MEASUREMENTS OF THE B PRODUCTION CROSS SECTION IN $P\overline{P}$ COLLISIONS AT $\sqrt{S} = 1.96$ TEV USING SEMILEPTIONIC DECAYS OF B HADRONS.

BY

JAMES ALEXANDER KRAUS

B.S., University of Toledo, 1999
M.S., University of Illinois, 2002

DISSERTATION

Submitted in partial fulfillment of the requirements
for the degree of Doctor of Philosophy in Physics
in the Graduate College of the
University of Illinois at Urbana-Champaign, 2006

Urbana, Illinois

Abstract

We present a measurement of the cross section of b hadron (H_b) production in $p\overline{p}$ collisions at $\sqrt{s} = 1.96$ TeV using the CDF II detector at the Fermilab Tevatron. We use 83 pb^{-1} of data taken between October 2002 and May 2003 that was collected with a trigger sensitive to high momentum muons and displaced tracks. We use partially reconstructed decays in the following modes: $H_b \to \mu^- \overline{\nu}_\mu D^0 X$, $D^0 \to K^-\pi^+$, and $H_b \to \mu^- \overline{\nu}_\mu D^{*+} X$, $D^{*+} \to D^0\pi^+$, $D^0 \to K^-\pi^+$, and their charge conjugates. We correct for the backgrounds from $c\overline{c}$ and $b\overline{b}$ decays, for trigger and reconstruction efficiencies, and for detector acceptance. We report the total cross section above a minimum transverse momentum (p_T) of 9 GeV/c for the rapidity range $|y| \leq 0.6$. We find

$$\sigma(p\overline{p} \to H_b) \times BR(H_b \to \mu^- \overline{\nu}_\mu D^0 X) \times BR(D^0 \to K^-\pi^+) = 3.53 \text{ nb } \pm 0.20 \text{ nb (stat.) } {}^{+0.34}_{-0.36} \text{ nb(syst.)}$$

and

$$\sigma(p\overline{p} \to H_b) \times BR(H_b \to \mu^- \overline{\nu}_\mu D^{*+} X) \times BR(D^{*+} \to D^0\pi^+) \times BR(D^0 \to K^-\pi^+) =$$

$$1.04 \text{ nb } \pm 0.13 \text{ nb (stat.) } \pm^{+0.12}_{-0.14} \text{ nb(syst.)}$$

Correcting for branching ratios, we find that the total H_b cross section is

$$\sigma(p\overline{p} \to H_b) = 1.34 \ \mu\text{b } \pm 0.08 \ \mu\text{b (stat.) } {}^{+0.13}_{-0.14}\mu\text{b (syst.) } \pm 0.07 \ \mu\text{b (BF)}$$

for events from $H_b \to \mu^- \overline{\nu}_\mu D^0 X$, $D^0 \to K^-\pi^+$ decays, and

$$\sigma(p\overline{p} \to H_b) = 1.47 \ \mu\text{b } \pm 0.18 \ \mu\text{b (stat.) } {}^{+0.17}_{-0.19} \ \mu\text{b (syst.) } \pm 0.11 \ \mu\text{b (BF)}$$

for events from $H_b \to \mu^- \overline{\nu}_\mu D^{*+} X$, $D^{*+} \to D^0\pi^+$, $D^0 \to K^-\pi^+$ decays.

dedicated to the memory of my mother, Susan Kraus

Acknowledgements

I would like to begin by acknowledging the contribution to this thesis by my advisor Kevin Pitts. I have been Kevin's student since 2000, and I have learned a great deal from him in that time about CDF and physics in general. He has always made time to give me advice when I haven't known how to deal with a problem, and when he did not personally have the information needed his knowledge of the collaboration was vital to finding someone who did. I doubt that this analysis would ever have come together without the effort he made, and I am extremely grateful.

I would also like to thank my fellow collaborators at CDF, both for their comments on this analysis and for helping me learn how to work at CDF. My collaborators Ting Miao, Yuri Gotra, and Mary Bishai involved me the the J/ψ cross-section analysis, and without this experience I don't know if this analysis would have gone so well. For this analysis, Matt Herndon, Ivan Furic, Guillelmo Ceballos, Cheng-Ju Lin, Stefan Giagu, Jonathan Lewis, Steve Nahn, and Aart Heijboier have all given excellent comments and made good suggestions at various points in this research, which have led to a better result. I would also like to than Steve and Dee Hahn, Morris Binkely, and others who helped me get my feet under me when I first joined CDF.

I would like to express my appreciation to my fellow UIUC-CDF group members, past and present, including professors Tony Liss, Tom Junk, postdocs Nathan Eddy, Lucio Cerrito, Anyes Taffard, Greg Veramendi, Catalin Ciobanu, Xiaojian Zhang, Heather Gerberich, and Hyunsoo Kim, and grad students Christopher Marino, Ulysses Grunder, Alice Abulencia, Ed Rogers, Kevin Lannon, Trevor Vickey, Raeghan Byrne, and James Holloway. I would also like to thank the engineers Mike Kasten and Allison Sibert for their work on the XTRP and for patiently explaining how various electrical doodads work, the HEPG group business office staff including Donna Guzy, Tom Shaw, Rene Dunham, and others, for working out the occasional funding snafus that have arisen over the course of my graduate school career. Also, I would like to thank the undergrad Charles Wilson who worked with me on part of this project.

Thank you to my friends at UIUC, without whom I probably would not have survived my seven years of graduate school. I particularly wish to thank the other physics grads I started with in 1999, for the

mutual support on the sixth floor of ESB and Friday lunches in the Union. Special thanks to John Veysey, Ken Esler, Mike Lawler, and Eun-Ah Kim, for letting me stay on their couch, which was more comfortable than it looked. Thank you also to Dom Ricci, Aaron Andrus, Dutyman Das, Ziggy Mahundar, Hector Garcia, Tommy Angelini, Jack Sadleir, Mary Upton, Matt Gordon, Jeff Reifenberger, and others I am forgetting for helping me move, listening to me complain, and other random acts of friendship. I would also like to acknowledge my friends in Red Bison, including Mark Uchanski, Lori Kae Schwab, Frank Hassler, Paul Heiberger, Val Sivicek, and Chris Letourneau, for times spent away from flourescent lighting and the occasional (controlled) prarie fire. I will miss you all.

I would like to thank my family for their love and support, particularly my father Gerard Kraus, my sister Jennifer Kraus, my Grandmother Ruth Shoedel, and my late Grandmother Regina Kraus. I would also like to acknowledge my stepmother Lani Kraus; Troy, Lindsey, Kyle, and Mason Maki; Greg, Robin, Elliot, Adam, and Claire Hornkohl; Laura Saterfield, and Landon Saterfield.

I would also like to express my love and gratitude to my girlfriend Sarah Budd, whose love and encouragement and pestering actually got me to the point that I had my thesis written.

This thesis was supported in part by the United States Department of Energy under grant DE-FG02-91ER40677.

Table of Contents

List of Tables . . . . . **ix**

List of Figures . . . . . **xii**

Chapter 1 Introduction **1**

Chapter 2 Theory **4**
2.1 QCD 4
2.2 The Parton Model 7
2.3 Fragmentation 8
2.4 D^0 Mixing (or the lack thereof) 9
2.5 History of B cross-section results 10

Chapter 3 CDF Detector **13**
3.1 Overview 13
3.2 Tracking System 14
3.2.1 Helix Parameters at CDF 14
3.2.2 The Central Outer Tracker 14
3.2.3 Silicon Vertex Detector 16
3.3 Muon System 18
3.4 CDF Cherenkov Luminosity Monitor 20
3.5 CDF Trigger System 23
3.5.1 The Track Trigger 29
3.5.2 Interface With Trigger System 29

Chapter 4 Datasets, Triggers, and Monte Carlo Generation **33**
4.1 Overview 33
4.2 Triggers 33
4.2.1 B Semileptonic Trigger 33
4.2.2 CMUP8 trigger 34
4.2.3 The Two Track Trigger 35
4.2.4 The B Semileptonic Backup trigger 35
4.2.5 The J/ψ CMU-CMU trigger 36
4.2.6 The J/ψ CMU-CMX trigger 36
4.3 Data Quality 37
4.4 Monte Carlo Generation 37
4.4.1 Bgenerator 37
4.4.2 Pythia 38
4.4.3 FakeEvent 39
4.4.4 EvtGen 39
4.4.5 Full Detector Simulation 39

Chapter 5 Trigger Efficiencies . . . 40
5.1 Introduction . . . 40
5.2 L1 Efficiency . . . 41
5.3 L2 efficiency . . . 45
5.3.1 XFT Efficiency . . . 46
5.3.2 SVT Efficiency . . . 49
5.4 L3 Efficiency . . . 53
5.5 Summary . . . 53

Chapter 6 Offline Efficiencies and Partial Acceptances . . . 101
6.1 Introduction . . . 101
6.2 SVX Efficiency . . . 101
6.3 Second Leg SVX Efficiency . . . 104
6.4 CMU Efficiency x Acceptance . . . 104
6.5 CMP Efficiency x Acceptance . . . 106
6.6 COT Efficiency . . . 108
6.7 Summary . . . 110

Chapter 7 Cross Section Results . . . 148
7.1 Introduction . . . 148
7.2 Generator Level Monte Carlo . . . 148
7.3 Monte Carlo with Full Detector Simulation . . . 149
7.4 $\mu + D^0$ from the Semileptonic B Trigger . . . 151
7.5 Vertex and Fit Model Efficiency . . . 153
7.6 Data to MC Comparison . . . 155
7.7 Charm Backgrounds . . . 156
7.7.1 $c\bar{c}$ Background Estimate . . . 156
7.7.2 $b\bar{b}$ Background Estimate . . . 157
7.7.3 $B \to DD$ and $B \to D\tau$ Background Events . . . 158
7.8 Branching Fraction Uncertainties . . . 159
7.9 $H_b \to \mu D^0 X$, $D^0 \to \pi K$ Cross-Section . . . 159
7.10 $H_b \to \mu D^{*+} X$, $D^{*+} \to D^0 \pi$, $D^0 \to \pi K$ Cross-Section . . . 161
7.11 Comparison With Theory and Previous Measurements . . . 162
7.12 Summary and Possible Future Directions . . . 162

Appendix A Glossary . . . 207

Appendix B SVT Efficiency Plots . . . 209

Appendix C CDF Default Author List from July 2006 to January 2007 . . . 276

References . . . 282

Author's Biography . . . 285

List of Tables

3.1 Some features of the COT 17
3.2 Some features of the SVX II 21
3.3 Some features of the CDF Muon System. 21
3.4 Quantities extracted from the lookup RAMs. 28
3.5 Typical values used in XTRP extrapolation. 30

5.1 The error matrix returned by the binned fit to the L1 efficiency vs $1/p_T$ of equation 5.4 after the L1 efficiency vs $1/p_T$ was reweighted by the L1 efficiency vs. η. 55
5.2 The values returned by binned fits to the L2 XFT efficiency in the various $|\eta|$ bins for the first run range for π. 56
5.3 The error matrix returned by binned fit to the L2 XFT efficiency for $0 < |\eta| < 0.2$ bin for the first run range for π. 56
5.4 The error matrix returned by binned fit to the L2 XFT efficiency for $0.2 < |\eta| < 0.4$ bin for the first run range for π. 56
5.5 The error matrix returned by binned fit to the L2 XFT efficiency for $0.4 < |\eta| < 0.6$ bin for the first run range for π. 56
5.6 The error matrix returned by binned fit to the L2 XFT efficiency for $0.6 < |\eta| < 0.8$ bin for the first run range for π. 56
5.7 The error matrix returned by binned fit to the L2 XFT efficiency for $0.8 < |\eta| < 1.0$ bin for the first run range for π. 57
5.8 The values returned by binned fits to the L2 XFT efficiency in the various $|\eta|$ bins for the first run range for K. 57
5.9 The error matrix returned by binned fit to the L2 XFT efficiency for $0 < |\eta| < 0.2$ bin for the first run range for K. 57
5.10 The error matrix returned by binned fit to the L2 XFT efficiency for $0.2 < |\eta| < 0.4$ bin for the first run range for K. 57
5.11 The error matrix returned by binned fit to the L2 XFT efficiency for $0.4 < |\eta| < 0.6$ bin for the first run range for K. 57
5.12 The error matrix returned by binned fit to the L2 XFT efficiency for $0.6 < |\eta| < 0.8$ bin for the first run range for K. 58
5.13 The error matrix returned by binned fit to the L2 XFT efficiency for $0.8 < |\eta| < 1.0$ bin for the first run range for K. 58
5.14 The values returned by binned fits to the L2 XFT efficiency in the various $|\eta|$ bins for π with $\phi_{SL6} < 225°$ or $345° < \phi_{SL6}$ (the top of the detector) in the second run range. 58
5.15 The error matrix returned by binned fit to the L2 XFT efficiency for $0 < |\eta| < 0.2$ bin for π with $\phi_{SL6} < 225°$ or $345° < \phi_{SL6}$ (the top of the detector) in the second run range. 58
5.16 The error matrix returned by binned fit to the L2 XFT efficiency for $0.2 < |\eta| < 0.4$ bin for π with $\phi_{SL6} < 225°$ or $345° < \phi_{SL6}$ (the top of the detector) in the second run range. 58
5.17 The error matrix returned by binned fit to the L2 XFT efficiency for $0.4 < |\eta| < 0.6$ bin for π with $\phi_{SL6} < 225°$ or $345° < \phi_{SL6}$ (the top of the detector) in the second run range. 59

5.18 The error matrix returned by binned fit to the L2 XFT efficiency for $0.6 < |\eta| < 0.8$ bin for π with $\phi_{SL6} < 225°$ or $345° < \phi_{SL6}$ (the top of the detector) in the second run range. 59
5.19 The error matrix returned by binned fit to the L2 XFT efficiency for $0.8 < |\eta| < 1.0$ bin for π with $\phi_{SL6} < 225°$ or $345° < \phi_{SL6}$ (the top of the detector) in the second run range. 59
5.20 The values returned by binned fits to the L2 XFT efficiency in the various $|\eta|$ bins for K with $\phi_{SL6} < 225°$ or $345° < \phi_{SL6}$ (the top of the detector) in the second run range. 59
5.21 The error matrix returned by binned fit to the L2 XFT efficiency for $0 < |\eta| < 0.2$ bin for K with $\phi_{SL6} < 225°$ or $345° < \phi_{SL6}$ (the top of the detector) in the second run range. 59
5.22 The error matrix returned by binned fit to the L2 XFT efficiency for $0.2 < |\eta| < 0.4$ bin for K with $\phi_{SL6} < 225°$ or $345° < \phi_{SL6}$ (the top of the detector) in the second run range. . . . 60
5.23 The error matrix returned by binned fit to the L2 XFT efficiency for $0.4 < |\eta| < 0.6$ bin for K with $\phi_{SL6} < 225°$ or $345° < \phi_{SL6}$ (the top of the detector) in the second run range. . . . 60
5.24 The error matrix returned by binned fit to the L2 XFT efficiency for $0.6 < |\eta| < 0.8$ bin for K with $\phi_{SL6} < 225°$ or $345° < \phi_{SL6}$ (the top of the detector) in the second run range. . . . 60
5.25 The error matrix returned by binned fit to the L2 XFT efficiency for $0.8 < |\eta| < 1.0$ bin for K with $\phi_{SL6} < 225°$ or $345° < \phi_{SL6}$ (the top of the detector) in the second run range. . . . 60
5.26 The values returned by binned fits to the L2 XFT efficiency in the various $|\eta|$ bins for π with $225° < \phi_{SL6} < 345°$ (the bottom of the detector) in the second run range. 60
5.27 The error matrix returned by binned fit to the L2 XFT efficiency for $0 < |\eta| < 0.2$ bin for π with $225° < \phi_{SL6} < 345°$ (the bottom of the detector) in the second run range. 61
5.28 The error matrix returned by binned fit to the L2 XFT efficiency for $0.2 < |\eta| < 0.4$ bin for π with $225° < \phi_{SL6} < 345°$ (the bottom of the detector) in the second run range. 61
5.29 The error matrix returned by binned fit to the L2 XFT efficiency for $0.4 < |\eta| < 0.6$ bin for π with $225° < \phi_{SL6} < 345°$ (the bottom of the detector) in the second run range. 61
5.30 The error matrix returned by binned fit to the L2 XFT efficiency for $0.6 < |\eta| < 0.8$ bin for π with $225° < \phi_{SL6} < 345°$ (the bottom of the detector) in the second run range. 61
5.31 The error matrix returned by binned fit to the L2 XFT efficiency for $0.8 < |\eta| < 1.0$ bin for π with $225° < \phi_{SL6} < 345°$ (the bottom of the detector) in the second run range. 61
5.32 The values returned by binned fits to the L2 XFT efficiency in the various $|\eta|$ bins for K with $225° < \phi_{SL6} < 345°$ (the bottom of the detector) in the second run range. 62
5.33 The error matrix returned by binned fit to the L2 XFT efficiency for $0 < |\eta| < 0.2$ bin for K with $225° < \phi_{SL6} < 345°$ (the bottom of the detector) in the second run range. 62
5.34 The error matrix returned by binned fit to the L2 XFT efficiency for $0.2 < |\eta| < 0.4$ bin for K with $225° < \phi_{SL6} < 345°$ (the bottom of the detector) in the second run range. 62
5.35 The error matrix returned by binned fit to the L2 XFT efficiency for $0.4 < |\eta| < 0.6$ bin for K with $225° < \phi_{SL6} < 345°$ (the bottom of the detector) in the second run range. 62
5.36 The error matrix returned by binned fit to the L2 XFT efficiency for $0.6 < |\eta| < 0.8$ bin for K with $225° < \phi_{SL6} < 345°$ (the bottom of the detector) in the second run range. 62
5.37 The error matrix returned by binned fit to the L2 XFT efficiency for $0.8 < |\eta| < 1.0$ bin for K with $225° < \phi_{SL6} < 345°$ (the bottom of the detector) in the second run range. 63
5.38 Layers of the SVX excluded due to low efficiency 64
5.39 The values returned by the binned fit to the L2 SVT efficiency relative to XFT and offline of equation 5.11. 65
5.40 The error matrix returned by the binned fit to the L2 SVT efficiency relative to XFT and offline of equation 5.11. 65
5.41 The error matrix returned by the binned fit to the L3 μ+SVT efficiency relative to L1, L2, and offline of equation 5.13. 66

6.1 The results of the fit of equation 6.5 to the CMP stub acceptance 111
6.2 The error matrix of the fit of equation 6.5 to the CMP stub acceptance 111

7.1 The results of of the fit to the generator level acceptance with loose cuts vs. b hadron p_T for $H_b \to \mu D^0 X$ events. 163

7.2 The error matrix of the fit to the generator level acceptance with loose cuts for $H_b \to \mu D^0 X$ events. . . . 163
7.3 The yields for the number of D^0 and D^{*+} events per μD^0 p_T bin, without SVT efficiency correction. . . . 164
7.4 The systematic errors of the $d\sigma(p\overline{p} \to B)/dp_T$ measurement. . . . 165
7.5 Differential cross section $d\sigma(p\overline{p} \to B)/dp_T$ times branching fraction of $H_b \to \mu D^0 X$, $D^0 \to K\pi$. . . . 166
7.6 Branching fractions used in this analysis, taken from [3]. . . . 166
7.7 The results of of the fit to the generator level acceptance with loose cuts vs. b hadron p_T for $H_b \to \mu D^{*+} X$ events. . . . 167
7.8 The error matrix of the fit to the generator level acceptance with loose cuts for $H_b \to \mu D^{*+} X$ events. . . . 167
7.9 Differential cross section $d\sigma(p\overline{p} \to B)/dp_T$ times branching fraction $H_b \to \mu D^{*+} X$, $D^{*+} \to D^0\pi$, $D^0 \to K\pi$. . . . 168

List of Figures

1.1 An example of an $H_b \to \mu^+ \overline{D}^0$, $\overline{D}^0 \to K^+\pi^-$ decay. . . . 2
1.2 An example of an $H_b \to \mu^+ D^{*-}$, $D^{*-} \to \overline{D}^0 \pi^- \ \overline{D}^0 \to K^+\pi^-$ decay. . . . 3

2.1 The leading order $O(\alpha_s^2)$ Feynman diagrams for heavy quark production. . . . 6
2.2 The next to leading order $O(\alpha_s^3)$ Feynman diagrams for heavy quark production. . . . 6
2.3 D^0 Mixing Diagram . . . 10
2.4 H_b cross section results from Run I of CDF and D0, plotted with the NLO QCD prediction. Data is roughly twice the size of the NLO prediction. . . . 12
2.5 The CDF Run II $\sigma(p\overline{p} \to H_b)$, $H_b \to J/\psi X$ cross section shown with the Run I $B \to J/\psi K$ cross section and FONLL theory. Theory and data agree well. . . . 12

3.1 An overview of the Collider Detector of Fermilab in its Run II configuration. . . . 15
3.2 A cut-away view of one quadrant of the CDF II detector showing the tracking region surrounded by the solenoid, calorimeters and CMU. . . . 15
3.3 A helix in the transverse plane with the impact parameter d_0 and ϕ_0 labeled. The radius of the helix is $1/2C$, where C is the curvature. . . . 16
3.4 1/6 section of the COT end plate. For each super layer is given the average radius. . . . 17
3.5 An end view of the SVX II detector. . . . 19
3.6 A side view of half of the CDF Run II silicon system on a scale in which the z coordinate is highly compressed. . . . 19
3.7 Location of the muon detector components in azimuth ϕ and pseudorapidity η for CDF Run II. 22
3.8 Number of absorption lengths as a function of pseudorapidity averaged over azimuthal acceptance of the CMU, CMP, and CMX systems. . . . 22
3.9 The average number of interactions ($\bar{N}$) for various conditions at CDF. 36 bunches is equivalent to 396 ns crossings. . . . 23
3.10 The functional block diagram of the CDF II data flow. . . . 25
3.11 The block diagram the CDF II trigger system . . . 25
3.12 An overview of the XTRP system. . . . 26
3.13 Event Count vs $\Delta\phi_{\text{SL6-CMU}} \times p_T(\mu)$ and $\Delta\phi_{\text{SL6-CMU}}$ vs. $p_T(\mu)$ . . . 32
3.14 Event Count vs $\Delta\phi_{\text{SL6-CMX}} \times p_T(\mu)$ and $\Delta\phi_{\text{SL6-CMX}}$ vs. $p_T(\mu)$ . . . 32

5.1 The J/ψ dimuon mass peak from the CMUP8 trigger. . . . 67
5.2 L1 CMUP4 efficiency vs. η for $p_T > 4.45$ GeV/c. . . . 68
5.3 L1 CMUP4 efficiency vs. $1/p_T$ after being reweighted by the η efficiency. . . . 69
5.4 L1 CMUP4 efficiency vs. $1/p_T$ both before and after being reweighted by the η efficiency. . . . 70
5.5 L1 CMUP4 efficiency vs. $1/p_T$ for $-0.6 < \eta < -0.2$, $-0.2 < \eta < 0.2$, and $0.2 < \eta < 0.6$, before and after being adjusted so that the plateau efficiency for each track is 1. . . . 71
5.6 Efficiency vs. $1/p_T$ for the TCMD and XFT. . . . 72
5.7 L1 CMUP4 efficiency vs. ϕ_{SL6}. . . . 73
5.8 L1 CMUP4 efficiency vs. track isolation within 30° of ϕ_0. . . . 74

5.9 The $D^+ \to K^-\pi^+\pi^+$ mass peak from the B_CHARM_LOWPT_L1_DPS trigger. The fitted curve was used to define signal and sideband regions, and there are about 200,000 events beneath the Gaussian. 75
5.10 The $\phi^0 \to K^+K^-$ mass peak from the B_CHARM_LOWPT_L1_DPS trigger used in the reconstruction of $D^+_{(s)} \to \phi^0\pi^+$. We use only events that have a K^+K^- mass between 1.0144 and 1.0256 GeV/c^2. 76
5.11 The $D^+_{(s)} \to \phi^0\pi^+$, $\phi^0 \to K^+K^-$ mass peaks from the B_CHARM_LOWPT_L1_DPS trigger. The fitted curve was used to define signal and sideband regions, and there are about 9,558 events beneath the D^+ Gaussian and 18,456 beneath the D^+_s Gaussian. 77
5.12 XFT efficiency (for the L2 measurement) vs. ϕ_{SL6} for runs between 152636 and 158000 (left) and runs between 158000 and 163117 (right) for π (red) and K (blue). 78
5.13 XFT efficiency vs.$1/|p_T|$ for $0 < |\eta| < 0.6$ for runs between 152636 and 158000 for π (red) and K (blue). 79
5.14 XFT efficiency vs.$1/|p_T|$ for $0.6 < |\eta| < 1.0$ for runs between 152636 and 158000 for π (red) and K (blue). 80
5.15 XFT efficiency vs.$1/|p_T|$ for $0 < |\eta| < 0.6$ for runs between 158000 and 163117 for π (red) and K (blue) within $\phi_{SL6} < 225°$ or $\phi_{SL6} > 345°$ (the top of the detector). 81
5.16 XFT efficiency vs.$1/|p_T|$ for $0.6 < |\eta| < 1.0$ for runs between 158000 and 163117 for π (red) and K (blue) within $\phi_{SL6} < 225°$ or $\phi_{SL6} > 345°$ (the top of the detector). 82
5.17 XFT efficiency vs.$1/|p_T|$ for $0 < |\eta| < 0.6$ for runs between 158000 and 163117 for π (red) and K (blue) within $225° < \phi_{SL6} < 345°$ (the bottom of the detector). 83
5.18 XFT efficiency vs.$1/|p_T|$ for $0.6 < |\eta| < 1.0$ for runs between 158000 and 163117 for π (red) and K (blue) within $225° < \phi_{SL6} < 345°$ (the bottom of the detector). 84
5.19 XFT efficiency vs. $|\eta|$ for runs between 152636 and 158000 (top left), 158000 and 163117 within $\phi_{SL6} < 225°$ or $\phi_{SL6} > 345°$, and 158000 and 163117 within $225° < \phi_{SL6} < 345°$ (bottom left) for π (red) and K (blue). 85
5.20 XFT efficiency vs. $1/|p_T|$ for π from $D^+ \to K^-\pi^+\pi^+$ that came in on the B_CHARM_HIGHPT trigger. The black points use pions from events that came in on the B_CHARM_HIGHPT when the B_CHARM_LOWPT_L1_DPS prescale was set to 1, and the red points use pions from events that came in on the B_CHARM_HIGHPT when the B_CHARM_LOWPT_L1_DPS prescale was set to greater than 1. 86
5.21 XFT efficiency vs. the number of tracks with $p_T > 1.5$ GeV/c within $\Delta\phi_0 < 10°$ for pions (red) and kaons (blue). 87
5.22 XFT efficiency vs. $|\eta|$ for π (left) and K (right) for the preshutdown (top) and postshutdown (bottom) run ranges. The blue point are for tracks that had positive η and the red point are for that had negative η. 88
5.23 The figure on the left shows the $K\pi\pi$ mass spectrum for track combinations that were also found within the $\phi\pi$ mass window. There is a $D^+ \to K^-\pi^+\pi^-$ peak with 1500 events. The figure on the right shows the track combinations that were under the $D^+ \to K^-\pi^+\pi^-$ peak on the left with the $\phi\pi$ mass assignments. 89
5.24 SVT efficiency vs. $z_{r=8cm}$ (upper left), SVT efficiency vs. $\phi_{r=8cm}$ (upper right), and SVT efficiency vs. $|\eta|$ (lower left). 90
5.25 SVT efficiency vs.$|d_0|$ (left) and SVT efficiency vs. $|d_0 - 8\mu m|$ (right). The points with positive SVX d0 are in red, and those with negative d0 are in blue. These points are averaged over all p_T and ISO. 91
5.26 SVT efficiency vs. $|d_0 - 8\mu$m| for $p_T > 2.255$ GeV/c. 92
5.27 SVT efficiency vs. $|d_0 - 8\mu$m| for tracks with a $p_T > 2.255$ GeV/c. Points in red represent the efficiency found using the muon tracks from $J/\psi \to \mu^+\mu^-$ decays, and points in blue come from tracks in the CMUP8 sample. There is no cut on ISO. 93
5.28 SVT efficiency vs. ISO for tracks with $p_T > 2.255$ GeV/c and 350μm $< |d_0 - 8\mu m| < 850\mu$m. Points in red represent the efficiency found using the muon tracks from $J/\psi \to \mu^+\mu^-$ decays, and points in blue come from tracks in the CMUP8 sample. 94

5.29 Distribution of tracks passing all numerator and denominator cuts vs. ISO normalized so that the sum over all bins for each histogram is one. Points in red represent the efficiency found using the muon tracks from $J/\psi \to \mu^+\mu^-$ decays, points in blue come from tracks in the CMUP8 sample, and points in black come from $D^0 \to \pi K$ decays in the signal sample, with sideband subtraction. 95
5.30 L3 μ+SVT efficiency vs. the inverse of the absolute value of the muons' transverse momentum (curvature) for various slices of the SVT tracks' momenta. The curves are the one dimensional projections of the two dimensional binned fit to the data. 96
5.31 L3 μ+SVT efficiency vs. the inverse of the absolute value of the muons' transverse momentum (curvature) for various slices of the SVT tracks' momenta. The curves are the one dimensional projections of the two dimensional binned fit to the data. 97
5.32 L3 μ+SVT efficiency vs. the inverse of the absolute value of the SVT tracks' transverse momentum (curvature) for various slices of the SVT tracks' momenta. The curves are the one dimensional projections of the two dimensional binned fit to the data. 98
5.33 L3 μ+SVT efficiency vs. the inverse of the absolute value of the SVT tracks' transverse momentum (curvature) for various slices of the SVT tracks' momenta. The curves are the one dimensional projections of the two dimensional binned fit to the data. 99
5.34 L3 μ+SVT efficiency vs. the inverse of the absolute value of the SVT tracks' transverse momentum (curvature) for various slices of the SVT tracks' momenta. The curves are the one dimensional projections of the two dimensional binned fit to the data. 100

6.1 The J/ψ dimuon mass peak for the SVX Efficiency measurement. 112
6.2 The SVX offline efficiency vs. $z_{r=8cm}$. The gaps in the efficiency are at points which were excluded due to low and rapidly changing efficiency in the SVT. 113
6.3 The SVX offline efficiency vs. $1/p_T$ 114
6.4 The SVX offline efficiency vs. run number 115
6.5 The SVX offline efficiency vs. $\phi_{r=8cm}$ 116
6.6 The SVX offline efficiency vs. η 117
6.7 The distributions of the μ track η (black histogram) and MC track η (red histogram), both normalized to one. 118
6.8 The SVX offline efficiency vs. $z_{r=8cm}$. The black points show the measurement with the J/ψ CMU μ track η, and the red points show the efficiency after reweighting the η distribution to match that from the MC. 119
6.9 The SVX offline efficiency vs. the number of tracks with a $p_T > 400$ MeV/c within$\Delta\phi_{r=8cm} < 5^\circ$. The slope of the fitted curve indicated that the efficiency drops 0.5% for every additional track added to the cone. 120
6.10 The distribution of the number of tracks with a $p_T > 400$ MeV/c within$\Delta\phi_{r=8cm} < 5^\circ$ that pass SVX offline cuts for the J/ψ (red points) and $\mu + D^0$ (black points) samples. The $\mu + D^0$ distribution has been corrected for the SVT efficiency, and sideband subtraction about the D^0 peak has been used. 121
6.11 The J/ψ dimuon mass peak for the CMU Efficiency measurement for events that fired the μSVT trigger. The fitted curve was used to define signal and sideband regions, and there are about 2223 events beneath the Gaussian. 122
6.12 The J/ψ dimuon mass peak for the CMU Efficiency measurement for events that fired the CMUP8 trigger. The fitted curve was used to define signal and sideband regions, and there are about 3258 events beneath the Gaussian. 123
6.13 The difference between the predicted and actual CMU stub positions in ϕ 124
6.14 The difference between the predicted and actual CMU stub positions in z. The black points indicate the difference for my algorithm, and the red points indicate the difference from the offline muon matching code. 125
6.15 The difference between the predicted and actual CMP stub positions in ϕ 126
6.16 The difference between the predicted and actual CMU stub positions in ϕ for μ^+ (red) and μ^- (blue). 127

6.17 The difference between the predicted and actual CMP stub positions in ϕ for μ^+ (red) and μ^- (blue). . . . 128
6.18 The CMU Efficiency measurement vs. muon $1/p_T$. . . . 129
6.19 The CMU Efficiency measurement vs. the predicted ϕ_{CMU}. . . . 130
6.20 The CMU Efficiency measurement vs. muon track η. . . . 131
6.21 CMP stub acceptance vs. η for various slices of muon transverse momentum. The curves are the one dimensional projections of the two dimensional binned fit to the data. . . . 132
6.22 CMP stub acceptance vs. η for various slices of muon transverse momentum. The curves are the one dimensional projections of the two dimensional binned fit to the data. . . . 133
6.23 CMP stub acceptance vs. $1/p_T$ for various slices of muon η. The curves are the one dimensional projections of the two dimensional binned fit to the data. . . . 134
6.24 CMP stub acceptance vs. $1/p_T$ for various slices of muon η. The curves are the one dimensional projections of the two dimensional binned fit to the data. . . . 135
6.25 CMP stub acceptance vs. $1/p_T$ for various slices of muon η. The curves are the one dimensional projections of the two dimensional binned fit to the data. . . . 136
6.26 The CMP stub acceptance measurement vs. the predicted ϕ_{CMP}. . . . 137
6.27 The CMP stub acceptance measurement vs. η for events with the unweighted ϕ_{CMP} distribution (in black) and the ϕ_{CMP} distribution reweighted to match the ϕ_{CMP} distribution of the $\mu + D^0$ sample. . . . 138
6.28 The CMP stub acceptance measurement vs. $1/p_T$ for events with the unweighted ϕ_{CMP} distribution (in black) and the ϕ_{CMP} distribution reweighted to match the ϕ_{CMP} distribution of the $\mu + D^0$ sample. . . . 139
6.29 The COT tracking efficiency vs. $1/p_T$ for K^-. The red points are from Bgenerator Monte Carlo with no matching cuts, the black points are from Bgenerator MC with matching cuts, and the blue points are from track embedding with matching cuts. . . . 140
6.30 The COT tracking efficiency vs. $1/p_T$ for K^+. The red points are from Bgenerator Monte Carlo with no matching cuts, the black points are from Bgenerator MC with matching cuts, and the blue points are from track embedding with matching cuts. . . . 141
6.31 The COT tracking efficiency vs. $1/p_T$ for μ^+. The red points are from Bgenerator Monte Carlo with no matching cuts, the black points are from Bgenerator MC with matching cuts, and the blue points are from track embedding with matching cuts. . . . 142
6.32 The COT tracking efficiency vs. $1/p_T$ for μ^-. The red points are from Bgenerator Monte Carlo with no matching cuts, the black points are from Bgenerator MC with matching cuts, and the blue points are from track embedding with matching cuts. . . . 143
6.33 The COT tracking efficiency vs. $1/p_T$ for π^-. The red points are from Bgenerator Monte Carlo with no matching cuts, the black points are from Bgenerator MC with matching cuts, and the blue points are from track embedding with matching cuts. The points between 1.0 and 2.5 $(\mathrm{GeV}/c)^-1$ are only needed for the soft π from the D^{*-} decays. . . . 144
6.34 The COT tracking efficiency vs. $1/p_T$ for π^+. The red points are from Bgenerator Monte Carlo with no matching cuts, the black points are from Bgenerator MC with matching cuts, and the blue points are from track embedding with matching cuts. The points between 1.0 and 2.5 $(\mathrm{GeV}/c)^-1$ are only needed for the soft π from the D^{*+} decays. . . . 145
6.35 A comparison of soft π p_T between data and CDF sample+track embedding MC (right) and the $m(K^-\pi^+\pi^+) - m(K^-\pi^+)$ mass difference plot (left) used to get the soft π p_T shape from data. Sideband subtraction was used on the peak, with the signal region defined as $0.142933\ \mathrm{GeV}/c < \Delta m < 0.147987\ \mathrm{GeV}/c$ and the sideband region defined as $0.149672\ \mathrm{GeV}/c < \Delta m < 0.153523\ \mathrm{GeV}/c$. . . . 146
6.36 A comparison of the $D^{*+} - D^0$ mass difference in pure Bgenerator Monte Carlo between events where the π_{soft} passed (black histogram) and failed (red histogram) the $\Delta curv$ and $\Delta\phi_0$ matching cuts. . . . 147

7.1 The generator level acceptance for the loose cuts on MC made with the CDF b spectrum versus b hadron p_T. . . . 169

7.2 The generator level acceptance for the loose cuts on MC made with the CDF b spectrum versus b hadron rapidity. . . . 170
7.3 The χ^2 of the vertex fits of the π K, with sideband subtraction. This indicates that the $\chi^2 < 1000$ cut is not throwing away a significant number of events. . . . 171
7.4 The π^+K^- mass, for events with 9 GeV/$c < p_T(\mu^-K^-\pi^+) <$ 11 GeV/c. . . . 172
7.5 The π^+K^- mass, for events with 11 GeV/$c < p_T(\mu^-K^-\pi^+) <$ 13 GeV/c. . . . 173
7.6 The π^+K^- mass, for events with 13 GeV/$c < p_T(\mu^-K^-\pi^+) <$ 17 GeV/c. . . . 174
7.7 The π^+K^- mass, for events with 17 GeV/$c < p_T(\mu^-K^-\pi^+) <$ 29 GeV/c. . . . 175
7.8 The π^+K^- mass, for events with 29 GeV/$c < p_T(\mu^-K^-\pi^+) <$ 40 GeV/c. . . . 176
7.9 The π^+K^- mass, for all events 177
7.10 The dimuon mass distribution without vertex fitting, fit to the sum of two Gaussians plus a linear background. There are 624723 ± 5577 J/ψ events beneath the two Gaussians. . . . 178
7.11 The dimuon mass distribution with vertex fitting, fit to the sum of two Gaussians plus a linear background. There are 623774 ± 5526 J/ψ events beneath the two Gaussians. . . . 179
7.12 The sideband subtracted vertex fit χ^2 for J/ψ events. . . . 180
7.13 The vertex fit χ^2 for the MC $D^0 \to K^-\pi^+$ events. . . . 181
7.14 The reconstructed D^0 mass from MC b events. There are 29207 ± 171 events beneath the mass peak. . . . 182
7.15 A comparison of the two MC samples to data, plotted vs. the p_T of the $\mu + D^0$. The data points are in black, the CDF MC is in red, and the MRSD0 MC is in blue. The spectrum from the CDF sample is slightly softer than the data. The MRSD0 MC is closer, but somewhat harder than the data. . . . 183
7.16 A comparison of the two MC samples to data, plotted vs. η. The data points are in black, the MC using the spectrum from the $b \to J/\psi$ cross section is in red, and the MRSD0 MC is in blue. . . . 184
7.17 A comparison of the two MC samples to data, plotted vs. the p_T of the μ. The data points are in black, the CDF MC is in red, and the MRSD0 MC is in blue. . . . 185
7.18 A comparison of the two MC samples to data, plotted vs. the p_T of the D^0. The data points are in black, the CDF MC is in red, and the MRSD0 MC is in blue. . . . 186
7.19 A comparison of invariant mass distributions of the μD^0 from data and the two MC samples. The data points are in black, the CDF MC is in red, and the MRSD0 MC is in blue. . . . 187
7.20 Ratio of the number of events per μD^0 mass bin of data to Monte Carlo. The plots on the left use the CDF phenomenological MC distribution, and the plots on the right use the MRSD0 distribution. Top plots use PHOTOS in the B decays, and bottom plots do not. The black lines show the fit of the points to a flat line, and red show the fit to a linear slope. Error bars show statistical errors only. . . . 188
7.21 The D^0 impact parameter distribution for the data, after sideband subtraction 189
7.22 The D^0 impact parameter distribution for the MC generated with the $b \to J/\psi$ spectrum (top left), the MRSD0 spectrum (top right), and direct charm MC (bottom) 190
7.23 The invariant mass of $D^0 \to K\pi$ from MC with the K and π masses swapped. Top plots show the mass from the CDF sample, and the bottom plots are from the MRSD0 sample. The plots on the left use the COT track properties to get the invariant mass, and those on the right use the direct MC track properties. . . . 191
7.24 The fit of a Gaussian to the wrong sign D^0 mass, with a linear background plus the auto-reflection of the right sign D^0 peak constrained to be a Gaussian with the mean and σ set by MC and the number taken from the reconstructed right sign peak. . . . 192
7.25 The generator level acceptance for the loose cuts on MC made with the CDF and MRSD0 b spectra versus b hadron p_T for events with a D^0(left) and a D^{*+} (right). The blue points have 50% more $B \to \mu D^{**}$ events, that red point have 50% fewer $B \to \mu D^{**}$ events, and the black points are the default acceptances. . . . 193
7.26 The differential cross section times branching ratio for $H_b \to \mu^- D^0 X$, $D^0 \to K^-\pi^+$. . . . 194
7.27 The differential cross section from $H_b \to \mu^- D^0 X$, $D^0 \to K^-\pi^+$. Branching ratios corrected for using PDG branching fractions. . . . 195

7.28 The $m(K^-\pi^+\pi^+) - m(K^-\pi^+)$ mass difference, with 9 GeV/c < $p_T(\mu^- K^-\pi^+)$ < 11 GeV/c . 196
7.29 The $m(K^-\pi^+\pi^+) - m(K^-\pi^+)$ mass difference, with 11 GeV/c < $p_T(\mu^- K^-\pi^+)$ < 13 GeV/c 197
7.30 The $m(K^-\pi^+\pi^+) - m(K^-\pi^+)$ mass difference, with 13 GeV/c < $p_T(\mu^- K^-\pi^+)$ < 17 GeV/c 198
7.31 The $m(K^-\pi^+\pi^+) - m(K^-\pi^+)$ mass difference, with 17 GeV/c < $p_T(\mu^- K^-\pi^+)$ < 29 GeV/c 199
7.32 The $m(K^-\pi^+\pi^+) - m(K^-\pi^+)$ mass difference, with 29 GeV/c < $p_T(\mu^- K^-\pi^+)$ < 40 GeV/c 200
7.33 The $m(K^-\pi^+\pi^+) - m(K^-\pi^+)$ mass difference, for all events 201
7.34 The generator level acceptance for the loose cuts on MC made with the CDF b spectrum versus b hadron p_T for events with a D^{*+}. 202
7.35 The differential cross section times branching ratio for $H_b \to \mu^- D^{*+} X$, $D^{*+} \to D^0\pi^+$, $D^0 \to K^-\pi^+$. 203
7.36 The differential cross section from $H_b \to \mu^- D^{*+} X$, $D^{*+} \to D^0\pi^+$, $D^0 \to K^-\pi^+$. Branching ratios corrected for using PDG branching fractions. 204
7.37 The differential cross section from $H_b \to J/\psi X$, $J/\psi \to \mu^+\mu^-$ (black points), $H_b \to \mu^- D^0 X$, $D^0 \to K^-\pi^+$ (blue points), and $H_b \to \mu^- D^{*+} X$, $D^{*+} \to D^0\pi^+$, $D^0 \to K^-\pi^+$ (red points). All three measurements have been corrected for the appropriate branching fractions, and all three have $|y(H_b)| < 0.6$. 205
7.38 The differential cross section from $H_b \to \mu^- D^0 X$, $D^0 \to K^-\pi^+$ (blue points) and $H_b \to \mu^- D^{*+} X$, $D^{*+} \to D^0\pi^+$, $D^0 \to K^-\pi^+$ (red points), compared to prediction made using FONLL theory with CTEQ6M PDF's (solid black line). Errors on theory are shown as dashed black lines. All measurements have been corrected for the appropriate branching fractions, and plots three have $|y(H_b)| < 0.6$. 206

B.1 SVT efficiency vs. $|d_0 - 8\mu\text{m}|$, ISO = 0, 2.00 GeV/c < p_T <2.42 GeV/c 210
B.2 SVT efficiency vs. $|d_0 - 8\mu\text{m}|$, ISO = 0, 2.42 GeV/c < p_T <3.53 GeV/c 211
B.3 SVT efficiency vs. $|d_0 - 8\mu\text{m}|$, ISO = 0, 3.53 GeV/c < p_T <10 GeV/c 212
B.4 SVT efficiency vs. $|d_0 - 8\mu\text{m}|$, ISO = 1, 2.00 GeV/c < p_T <2.42 GeV/c 213
B.5 SVT efficiency vs. $|d_0 - 8\mu\text{m}|$, ISO = 1, 2.42 GeV/c < p_T <3.53 GeV/c 214
B.6 SVT efficiency vs. $|d_0 - 8\mu\text{m}|$, ISO = 1, 3.53 GeV/c < p_T <10 GeV/c 215
B.7 SVT efficiency vs. $|d_0 - 8\mu\text{m}|$, ISO = 2, 2.00 GeV/c < p_T <2.42 GeV/c 216
B.8 SVT efficiency vs. $|d_0 - 8\mu\text{m}|$, ISO = 2, 2.42 GeV/c < p_T <3.53 GeV/c 217
B.9 SVT efficiency vs. $|d_0 - 8\mu\text{m}|$, ISO = 2, 3.53 GeV/c < p_T <10 GeV/c 218
B.10 SVT efficiency vs. $|d_0 - 8\mu\text{m}|$, ISO = 3 or 4, 2.00 GeV/c < p_T <2.42 GeV/c 219
B.11 SVT efficiency vs. $|d_0 - 8\mu\text{m}|$, ISO = 3 or 4, 2.42 GeV/c < p_T <3.53 GeV/c 220
B.12 SVT efficiency vs. $|d_0 - 8\mu\text{m}|$, ISO = 3 or 4, 3.53 GeV/c < p_T <10 GeV/c 221
B.13 SVT efficiency vs. $|d_0 - 8\mu\text{m}|$, ISO = 5, 6 or 7, 2.00 GeV/c < p_T <2.42 GeV/c 222
B.14 SVT efficiency vs. $|d_0 - 8\mu\text{m}|$, ISO = 5, 6 or 7, 2.42 GeV/c < p_T <3.53 GeV/c 223
B.15 SVT efficiency vs. $|d_0 - 8\mu\text{m}|$, ISO = 5, 6 or 7, 3.53 GeV/c < p_T <10 GeV/c 224
B.16 SVT efficiency vs. $|d_0 - 8\mu\text{m}|$, 8≤ ISO ≤16, 2.00 GeV/c < p_T <2.42 GeV/c 225
B.17 SVT efficiency vs. $|d_0 - 8\mu\text{m}|$, 8≤ ISO ≤16, 2.42 GeV/c < p_T <3.53 GeV/c 226
B.18 SVT efficiency vs. $|d_0 - 8\mu\text{m}|$, 8≤ ISO ≤16, 3.53 GeV/c < p_T <10.00 GeV/c 227
B.19 SVT efficiency vs. $1/p_T$, ISO = 0, 120 μm< $|d_0 - 8\mu\text{m}|$ <220 μm 228
B.20 SVT efficiency vs. $1/p_T$, ISO = 0, 220 μm< $|d_0 - 8\mu\text{m}|$ <570 μm 229
B.21 SVT efficiency vs. $1/p_T$, ISO = 0, 570 μm< $|d_0 - 8\mu\text{m}|$ <850 μm 230
B.22 SVT efficiency vs. $1/p_T$, ISO = 1, 120 μm< $|d_0 - 8\mu\text{m}|$ <220 μm 231
B.23 SVT efficiency vs. $1/p_T$, ISO = 1, 220 μm< $|d_0 - 8\mu\text{m}|$ <570 μm 232
B.24 SVT efficiency vs. $1/p_T$, ISO = 1, 570 μm< $|d_0 - 8\mu\text{m}|$ <850 μm 233
B.25 SVT efficiency vs. $1/p_T$, ISO = 2, 120 μm< $|d_0 - 8\mu\text{m}|$ <220 μm 234
B.26 SVT efficiency vs. $1/p_T$, ISO = 2, 220 μm< $|d_0 - 8\mu\text{m}|$ <570 μm 235
B.27 SVT efficiency vs. $1/p_T$, ISO = 2, 570 μm< $|d_0 - 8\mu\text{m}|$ <850 μm 236
B.28 SVT efficiency vs. $1/p_T$, ISO = 3 or 4, 120 μm< $|d_0 - 8\mu\text{m}|$ <220 μm 237
B.29 SVT efficiency vs. $1/p_T$, ISO = 3 or 4, 220 μm< $|d_0 - 8\mu\text{m}|$ <570 μm 238
B.30 SVT efficiency vs. $1/p_T$, ISO = 3 or 4, 570 μm< $|d_0 - 8\mu\text{m}|$ <850 μm 239
B.31 SVT efficiency vs. $1/p_T$, ISO = 5, 6 or 7, 120 μm< $|d_0 - 8\mu\text{m}|$ <220 μm 240

B.32 SVT efficiency vs. $1/p_T$, ISO = 5, 6, or 7, 220 μm< $|d_0 - 8\mu\text{m}|$ <570 μm 241
B.33 SVT efficiency vs. $1/p_T$, ISO = 5, 6, or 7, 570 μm< $|d_0 - 8\mu\text{m}|$ <850 μm 242
B.34 SVT efficiency vs. $1/p_T$, 8≤ ISO ≤16, 120 μm< $|d_0 - 8\mu\text{m}|$ <220 μm 243
B.35 SVT efficiency vs. $1/p_T$, 8≤ ISO ≤16, 220 μm< $|d_0 - 8\mu\text{m}|$ <570 μm 244
B.36 SVT efficiency vs. $1/p_T$, 8≤ ISO ≤16, 570 μm< $|d_0 - 8\mu\text{m}|$ <850 μm 245
B.37 SVT efficiency vs. ISO, 120 μm< $|d_0 - 8\mu\text{m}|$ <140 μm, 2.00 GeV/c < p_T <2.42 GeV/c 246
B.38 SVT efficiency vs. ISO, 120 μm< $|d_0 - 8\mu\text{m}|$ <140 μm, 2.42 GeV/c < p_T <3.53 GeV/c 247
B.39 SVT efficiency vs. ISO, 120 μm< $|d_0 - 8\mu\text{m}|$ <140 μm, 3.53 GeV/c < p_T <10.00 GeV/c . . . 248
B.40 SVT efficiency vs. ISO, 140 μm< $|d_0 - 8\mu\text{m}|$ <160 μm, 2.00 GeV/c < p_T <2.42 GeV/c 249
B.41 SVT efficiency vs. ISO, 140 μm< $|d_0 - 8\mu\text{m}|$ <160 μm, 2.42 GeV/c < p_T <3.53 GeV/c 250
B.42 SVT efficiency vs. ISO, 140 μm< $|d_0 - 8\mu\text{m}|$ <160 μm, 3.53 GeV/c < p_T <10.0 GeV/c 251
B.43 SVT efficiency vs. ISO, 160 μm< $|d_0 - 8\mu\text{m}|$ <190 μm, 2.00 GeV/c < p_T <2.42 GeV/c 252
B.44 SVT efficiency vs. ISO, 160 μm< $|d_0 - 8\mu\text{m}|$ <190 μm, 2.42 GeV/c < p_T <3.53 GeV/c 253
B.45 SVT efficiency vs. ISO, 160 μm< $|d_0 - 8\mu\text{m}|$ <190 μm, 3.53 GeV/c < p_T <10.00 GeV/c . . . 254
B.46 SVT efficiency vs. ISO, 190 μm< $|d_0 - 8\mu\text{m}|$ <220 μm, 2.00 GeV/c < p_T <2.42 GeV/c 255
B.47 SVT efficiency vs. ISO, 190 μm< $|d_0 - 8\mu\text{m}|$ <220 μm, 2.42 GeV/c < p_T <3.53 GeV/c 256
B.48 SVT efficiency vs. ISO, 190 μm< $|d_0 - 8\mu\text{m}|$ <220 μm, 3.53 GeV/c < p_T <10.00 GeV/c . . . 257
B.49 SVT efficiency vs. ISO, 220 μm< $|d_0 - 8\mu\text{m}|$ <280 μm, 2.00 GeV/c < p_T <2.42 GeV/c 258
B.50 SVT efficiency vs. ISO, 220 μm< $|d_0 - 8\mu\text{m}|$ <280 μm, 2.42 GeV/c < p_T <3.53 GeV/c 259
B.51 SVT efficiency vs. ISO, 220 μm< $|d_0 - 8\mu\text{m}|$ <280 μm, 3.53 GeV/c < p_T <10.00 GeV/c . . . 260
B.52 SVT efficiency vs. ISO, 280 μm< $|d_0 - 8\mu\text{m}|$ <350 μm, 2.00 GeV/c < p_T <2.42 GeV/c 261
B.53 SVT efficiency vs. ISO, 280 μm< $|d_0 - 8\mu\text{m}|$ <350 μm, 2.42 GeV/c < p_T <3.53 GeV/c 262
B.54 SVT efficiency vs. ISO, 280 μm< $|d_0 - 8\mu\text{m}|$ <350 μm, 3.53 GeV/c < p_T <10.00 GeV/c . . . 263
B.55 SVT efficiency vs. ISO, 350 μm< $|d_0 - 8\mu\text{m}|$ <450 μm, 2.00 GeV/c < p_T <2.42 GeV/c 264
B.56 SVT efficiency vs. ISO, 350 μm< $|d_0 - 8\mu\text{m}|$ <450 μm, 2.42 GeV/c < p_T <3.53 GeV/c 265
B.57 SVT efficiency vs. ISO, 350 μm< $|d_0 - 8\mu\text{m}|$ <450 μm, 3.53 GeV/c < p_T <10.00 GeV/c . . . 266
B.58 SVT efficiency vs. ISO, 450 μm< $|d_0 - 8\mu\text{m}|$ <570 μm, 2.00 GeV/c < p_T <2.42 GeV/c 267
B.59 SVT efficiency vs. ISO, 450 μm< $|d_0 - 8\mu\text{m}|$ <570 μm, 2.42 GeV/c < p_T <3.53 GeV/c 268
B.60 SVT efficiency vs. ISO, 450 μm< $|d_0 - 8\mu\text{m}|$ <570 μm, 3.53 GeV/c < p_T <10.00 GeV/c . . . 269
B.61 SVT efficiency vs. ISO, 570 μm< $|d_0 - 8\mu\text{m}|$ <700 μm, 2.00 GeV/c < p_T <2.42 GeV/c 270
B.62 SVT efficiency vs. ISO, 570 μm< $|d_0 - 8\mu\text{m}|$ <700 μm, 2.42 GeV/c < p_T <3.53 GeV/c 271
B.63 SVT efficiency vs. ISO, 570 μm< $|d_0 - 8\mu\text{m}|$ <700 μm, 3.53 GeV/c < p_T <10.00 GeV/c . . . 272
B.64 SVT efficiency vs. ISO, 700 μm< $|d_0 - 8\mu\text{m}|$ <850 μm, 2.00 GeV/c < p_T <2.42 GeV/c 273
B.65 SVT efficiency vs. ISO, 700 μm< $|d_0 - 8\mu\text{m}|$ <850 μm, 2.42 GeV/c < p_T <3.53 GeV/c 274
B.66 SVT efficiency vs. ISO, 700 μm< $|d_0 - 8\mu\text{m}|$ <850 μm, 3.53 GeV/c < p_T <10.00 GeV/c . . . 275

Chapter 1

Introduction

At CDF, the Collider Detector at Fermilab, we create new particles by colliding protons and anti-protons at high energy. The particles relevant to this work are b hadrons, H_b, which are either b mesons formed by $b\overline{q}$ or a b baryons formed by bqq, where the b is refers to the bottom quark and q refers to either a up (u), down (d), or strange (s) quark. This analysis is designed to measure the rate at which b quarks are produced, the b cross-section, by finding events where a b undergoes the following decay chain:

$$\begin{aligned} b \to H_b \to \mu^- \, \overline{\nu}_\mu \quad & D^0 \quad X \\ & D^0 \quad \to K^- \pi^+ \end{aligned}$$

Where X represents any other decay products of the H_b that are not found. An example of such a decay is shown if figure 1.1. In addition, we also look for events where the b undergoes the decay chain:

$$\begin{aligned} b \to H_b \to \mu^- \, \overline{\nu}_\mu \quad & D^{*+} \quad X \\ & D^{*+} \quad \to D^0 \pi^+ \\ & \qquad\quad D^0 \to K^- \pi^+ \end{aligned}$$

An example of such a decay is shown in figure 1.2. In both cases, we also use the charge conjugate decays; whenever one decay is listed the charge conjugate decay is implied. Our measurement is thus a measurement of the cross-section times the branching ratio for these decay chains. The production cross section can then be obtained by correcting for branching ratios using branching ratios obtained by other experiments.

The measurement of the $H_b \to \mu^- D^0 X$, $D^0 \to \pi^+ K^-$ cross-section times branching ratio and $H_b \to \mu^- D^{*+} X$, $D^{*+} \to D^0 \pi^+$, $D^0 \to \pi^+ K^-$ cross-section times branching ratio are complicated analyses with many different parts, so next we give a brief overview of our technique. The equation that is used to determine the cross-section times branching ratio is

$$\sigma(p\overline{p} \to H_b) \times BR = \frac{N(1-f_b)}{2 \times \alpha \times \epsilon \times \mathcal{L}} \tag{1.1}$$

where N is the measured number of $\mu^- D^0$ ($\mu^- D^{*+}$) events, f_b is the fraction of those events not from the decay of a b hadron, α is the acceptance of the detector for these events, *i.e.*, a measure of the fraction of the decays that occur which will have all of their decay products pass through active regions of the CDF detector, ϵ is the efficiency of the active regions of the CDF detector for finding those decay products, and $\mathcal{L}$ is the integrated luminosity of the beam delivered to the detector. The factor of two arises due to the fact that we include both $\mu^+ \overline{D}^0$ and $\mu^- D^0$, which means without the factor of 2 we would be measuring the b plus $\overline{b}$ cross section. By dividing by two, we get the b cross section alone.

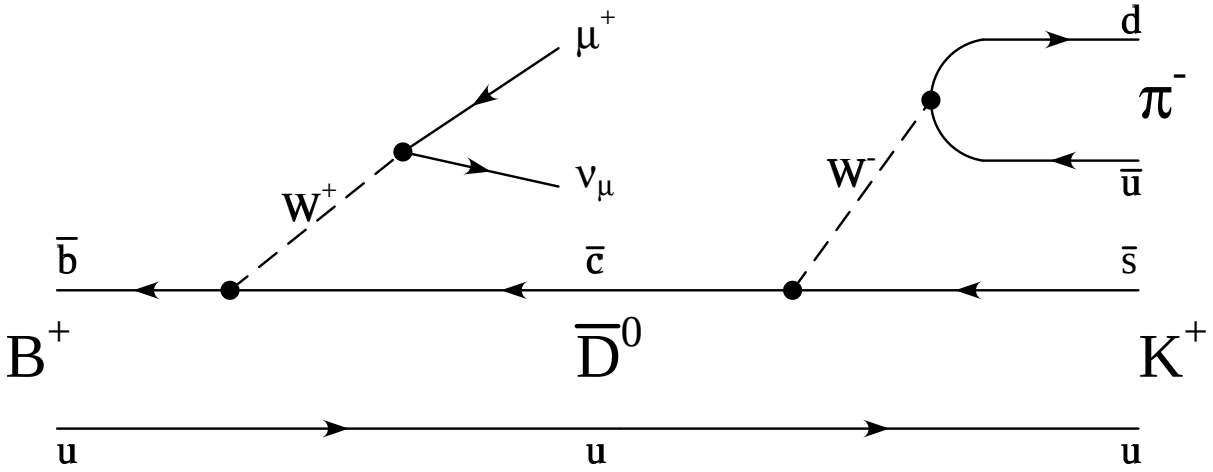

Figure 1.1: An example of an $H_b \to \mu^+ \overline{D}^0$, $\overline{D}^0 \to K^+ \pi^-$ decay.

This analysis uses data that was collected between October 2002 and May 2003, CDF run numbers 152636 to 163117. This run range includes 83 pb^{-1} of integrated luminosity.

In order to get N, we reconstruct $H_b \to \mu^- D^0$, $D^0 \to K^- \pi^+$ ($H_b \to \mu^- D^{*+}$, $D^{*+} \to D^0 \pi^+$, $D^0 \to K^- \pi^+$) events using data that satisfied the B semi-muonic trigger, which requires a high transverse momentum ($p_T = \sqrt{p_x + p_y}$) muon and a displaced track. A Gaussian function with a linear background is used to determine the number of μD^0 events and eliminate non-charm background. This does not, however, eliminate the the background due to $c\overline{c}$ and $b\overline{b}$ events, which are estimated by carefully comparing the data sample to theory/MC predictions to get f_b.

The acceptance, α, is determined by using Monte Carlo. We generate b quarks based on input transverse momentum - rapidity distributions taken from theoretical calculations and taken directly from previous cross section results. (The rapidity, y, is defined as $y = \frac{1}{2}\log(\frac{E+p_z}{E-p_z})$.) These b quarks are then paired with lighter

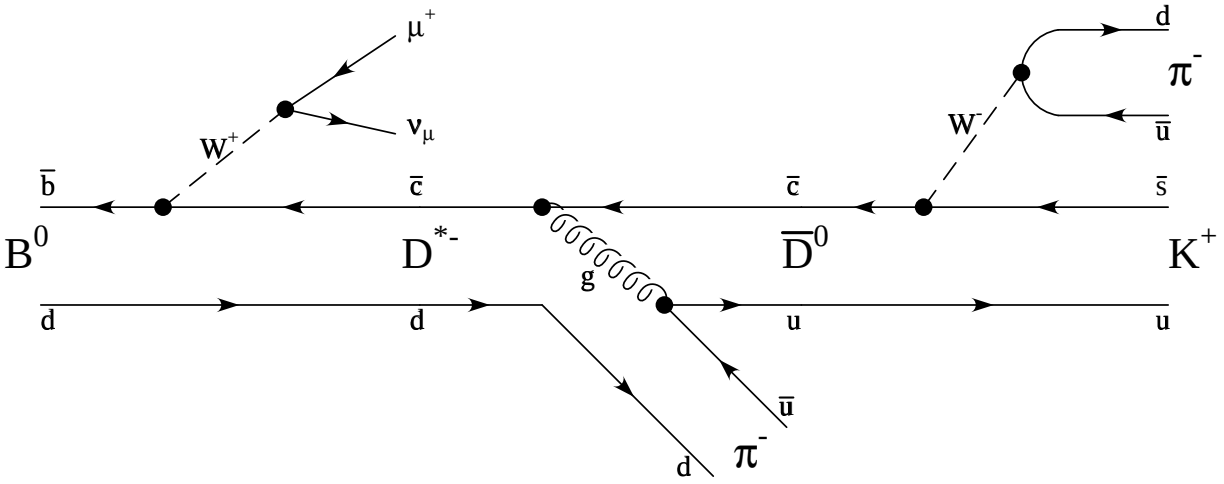

Figure 1.2: An example of an $H_b \to \mu^+ D^{*-}$, $D^{*-} \to \overline{D}^0 \pi^-$ $\overline{D}^0 \to K^+ \pi^-$ decay.

quarks to form hadrons and are decayed. The decay products are put through a simulation of our detector to see what fraction pass through our active detector components.

We have broken the measurement of the detector efficiency, ϵ, into nine separate measurements. Each efficiency is measured relative to the efficiency of another detector component except for the Central Outer Tracker (COT) efficiency, which is found in absolute terms. For example, the efficiency of the Central MUon (CMU) detector for finding a muon stub is determined relative to the efficiency of the COT for finding a muon track. The detector efficiency is determined primarily using data collected by backup triggers. Again, the exception is the COT efficiency, which is found using Monte Carlo.

These results are presented in the following order: chapter 5 shows how the efficiency of the trigger was found with respect to the offline efficiencies, and chapter 6 shows how those offline efficiencies were measured. Lastly, chapter 7 goes over the Monte Carlo acceptances and the determination of f_b, culminating in placing all of the pieces together with the μD^0 events from the signal sample to get the final result.

In the collisions which form the b quarks, the strong force is by far the dominant means of interaction. To understand the b cross section we must first understand the theory of the strong interaction, quantum chromodynamics (QCD).

Chapter 2

Theory

Beginning in the 1940's, cosmic ray experiments began discovering long lived particles, kaons, that decayed into multiple pions. When accelerators began to be able to produce these particles, it was found that their production cross section was larger than expected given the kaon lifetime. This lead to the introduction of the "strangeness" quantum number, which is conserved under strong interactions but violated in weak ones [1]. In 1963, Gell-Mann and Zweig proposed the quark model of nuclear structure, which could explain the hadron spectrum observed at the time. This model was confirmed in the SLAC-MIT deep inelastic scattering experiments. In 1973, Gross, Wilczek, and Politzer determined that only a non-Abelian gauge theory could result in asymptotic freedom. We refer to this theory as Quantum Chromodynamics, or QCD [2].

2.1 QCD

The QCD Lagrangian can be written as

$$\mathcal{L}_{QCD} = \frac{1}{2g_s^2} Tr(F^{\mu\nu}F_{\mu\nu}) + i\overline{\psi}\gamma^{\mu}(\partial_{\mu} + ig_s T^A G_{\mu}^A)\psi - m\overline{\psi}\psi \tag{2.1}$$

Where g_s is the coupling constant of the strong interaction, ψ is the quark field, γ^{μ} are the Dirac Matrices, $\overline{\psi} = \psi^{\dagger}\gamma^0$, $T^A = \frac{1}{2}\lambda^A$, where λ^A are the 8 Gell-Mann Matrices, G_{μ}^A is the gluon field, m is for the quark masses, and F is the QCD equivalent of the electromagnetic field strength tensor and is defined as $T^A F_{\mu\nu}^A = T^A(\partial_{\mu}G_{\nu}^A - \partial_{\nu}G_{\mu}^A)$. Summations over the repeated matrices μ, ν, and A are implied. The QCD Lagrangian has SU(3) gauge invariance, which means that the value of $\mathcal{L}$ does not vary under phase rotations that are unitary in SU(3), $U = e^{i\theta^A T^A}$,

$$\psi \rightarrow U\psi \tag{2.2}$$

$$\overline{\psi} \rightarrow U^{\dagger}\psi \tag{2.3}$$

$$T^A G^A_\mu \rightarrow U T^A G^A_\mu U^\dagger + \frac{i}{g_s}(\partial_\mu U)U^\dagger \tag{2.4}$$

Note that the 8 gluons are massless as the mass term $\mathcal{L} = m^2 G^A_\mu G^{\mu A}$ is not gauge invariant.

Let us define a term $\alpha_s = \frac{g_s^2}{4\pi}$, which is analogous to the fine structure constant in QED. Like the fine structure constant, the value of α_s depends on the scale of the virtual momentum transfer, Q. The formula for the running of α_s is

$$\alpha_s(Q) = \frac{\alpha_s(M)}{1 + \frac{\alpha_s(M)}{2\pi}(11 - \frac{2}{3}n_f)\log(Q/M)} \tag{2.5}$$

Where M is an arbitrary renormalization scale and n_f is the number of quark flavors. As there are 6 flavors of quark, we find that α_s decreases as Q increases, which leads to the asymptotic freedom of QCD. However, we see that this formula is dependent on an arbitrary renormalization scale, M. We prefer to write α_s in terms of a mass scale, Λ_{QCD}, defined as

$$1 = \frac{\alpha_s(M)}{2\pi}(11 - \frac{2}{3}n_f)\log(M/\Lambda_{QCD}) \tag{2.6}$$

so, by combining eq. 2.5 and 2.6, we can write

$$\alpha_s(Q) = \frac{2\pi}{(11 - \frac{2}{3}n_f)\log(Q/\Lambda_{QCD})} \tag{2.7}$$

Experimental measurements have yielded a value of Λ_{QCD} of approximately 200 MeV. This is important because for values of Q much larger than Λ_{QCD}, perturbation theory can be applied to quark production [2]. Characteristic Q values for this measurement are given by $Q \approx \sqrt{m_b^2 + p_T^2} > 7.5$ GeV, where $m_b \approx 4.5$ GeV/c^2 is the b quark mass [3]. Since this is well above Λ_{QCD}, we may apply perturbation theory to b production.

Figures 2.1 and 2.2 show the leading order and next-to-leading order processes for heavy quark production from light quarks and gluons. Two of the leading order processes are s channel processes, one representing $q\overline{q}$ annihilation, and the other gluon fusion. The third LO process is gluon fusion occurring via the t channel. The minimum value of s in theses processes is $4m_b^2$, while the minimum value of t is m_b^2. The standard NLO calculations used in $p\overline{p}$ collisions comes from Nason, Dawson and Ellis [4, 5], and is generally referred to as NDE. The NDE calculations contain terms which are logarithmic in p_T/m_b. These contributions become important at $p_T \gg m_b$. These contributions have been calculated to next-to-leading logarithmic accuracy (NLL), *i.e.* to order $\alpha_s^2(\alpha_s \log p_T/m_b)^k$ with $k \geq 1$, matching the fixed order, exact NLO calculation. This calculation is referred to as FONLL (Fixed Order Next Leading Log). [6].

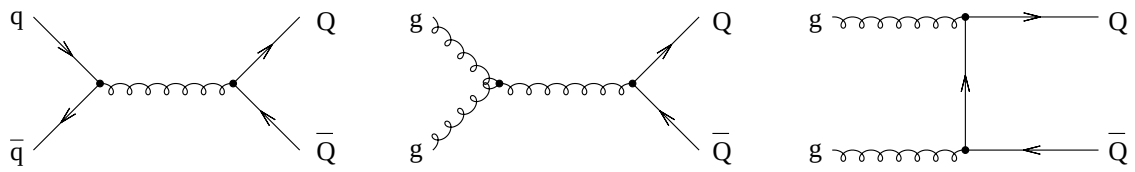

Figure 2.1: The leading order $O(\alpha_s^2)$ Feynman diagrams for heavy quark production. The left one is $q\overline{q}$ annihilation. The other two are gluon fusion.

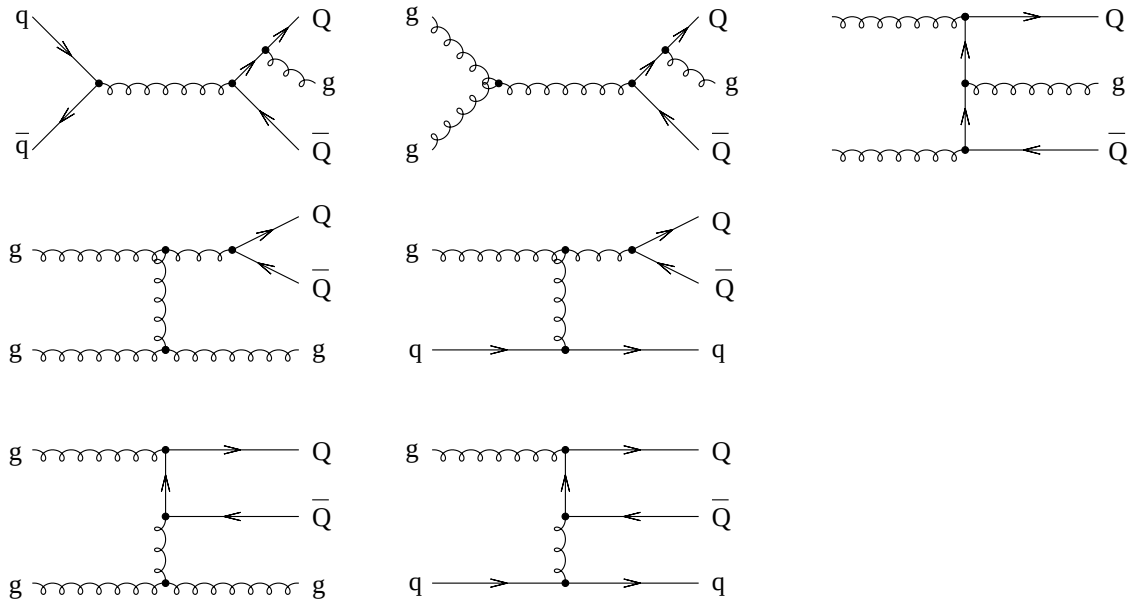

Figure 2.2: The next to leading order $O(\alpha_s^3)$ Feynman diagrams for heavy quark production. The top row is hard gluon radiation, the next is gluon splitting, and the bottom row is flavor excitation.

2.2 The Parton Model

Once one has the cross-section for $q\overline{q} \to b\overline{b}$, it is transformed into a cross-section for $p\overline{p} \to b\overline{b}$ by using the parton model of the proton. The partons are q, $\overline{q}$, and g. At high energies, such as those found at the Tevatron, the proton may be viewed as a bag of non-interacting quarks, anti-quarks, and gluons. Each parton carries a fraction x of the proton's momentum. The probability that parton f carries fraction x to $x + dx$ is $f(x)dx$, the parton distribution function (PDF) [2]. The quarks in the parton model are divided into sea quarks and valence quarks. The valence quarks are the two up quarks, and the down quark, which are the fundamental constituents of the proton. The sea quarks are the virtual quarks that are popped out of the vacuum by the proton's binding energy. Thus, it is required that

$$\int_0^1 [u(x) - \overline{u}(x)]dx = 2, \tag{2.8}$$

$$\int_0^1 [d(x) - \overline{d}(x)]dx = 1, \tag{2.9}$$

and that

$$\int_0^1 [s(x) - \overline{s}(x)]dx = \int_0^1 [c(x) - \overline{c}(x)]dx = \int_0^1 [b(x) - \overline{b}(x)]dx = \int_0^1 [t(x) - \overline{t}(x)]dx = 0. \tag{2.10}$$

Also, the momentum sum rule requires that

$$\int_0^1 x(\sum_{all q,\overline{q},g} f(x))dx = 1. \tag{2.11}$$

Thus, $\sigma(p\overline{p} \to b\overline{b})$ is given by

$$\sigma(p\overline{p} \to b\overline{b}) = \int\int\int dx_1 dx_2 q_i(x_1) q_i(x_2) d\sigma(q\overline{q} \to b\overline{b}). \tag{2.12}$$

Where we have taken advantage of the fact that q_i in the proton is the same as $\overline{q}_i$ in the anti-proton, due to charge conjugation symmetry. PDFs are determined experimentally via deep inelastic scattering (DIS) and other measurements. Examples of PDFs include the MRSD0 [7], which was derived using data from NMC, BCDMS, EMC, CDFR, CDHSW, WA70, and E605 experiments. The later PDFs MRST [8] and CTEQ5M [9] add in information from Hera and other experiments.

2.3 Fragmentation

When a b is produced by a hard collision between partons, it pulls one or more light $q\overline{q}$ pairs from the vacuum in order to form a hadron. This process, called fragmentation, is non-perturbative and so cannot be determined from first principles. Since the energy scale of fragmentation is much lower than that of heavy quark production, it is appropriate to treat these processes separately. Thus, the b hadron cross-section can be written

$$\frac{d\sigma}{dp} = \int dp_b dz \frac{d\sigma_b}{dp_b} D(z)\delta(p - zp_b) \tag{2.13}$$

where p is the H_b momentum, p_b is the b quark momentum before hadronization, z is the ratio p/p_b, and $D(z)$ is the probability density to find the b meson with momentum $p = zp_b$.

In practice, the non-perturbative effects are determined using a phenomenological fragmentation model in the non-perturbative regime, which is then convoluted with the perturbative cross-section prediction to get the prediction for the b meson cross section. Of several parameterizations, one of the most popular is the Peterson parameterization [10]. In the Peterson parameterization, it is assumed that when a light quark $\overline{q}$ is attached to a b to form the heavy meson $H(b\overline{q})$, the b is only slowed slightly and its momentum is almost the same as H. The corresponding transition amplitude is approximately inversely proportional to the energy transfer: $\Delta E = E_H + E_q - E_b$. Assuming m_H is roughly the same as m_b, we have

$$\Delta E = \sqrt{m_b^2 + z^2 p_b^2} + \sqrt{m_q^2 + (1-z)^2 p_b^2} - \sqrt{m_b^2 + p_b^2} \propto 1 - 1/z - \epsilon/(1-z) \tag{2.14}$$

where ϵ is the Peterson parameter, and is approximately m_q^2/m_b^2. Thus, the Peterson fragmentation function can be written

$$D(z) = \frac{N}{z[1 - 1/z - \epsilon/(1-z)]^2}, \tag{2.15}$$

where is is the normalization factor that is fixed by summing over all hadrons containing b,

$$\sum_H \int dz D(z) = 1 \tag{2.16}$$

The Peterson ϵ is determined experimentally to be roughly 0.006 for b quarks, depending on the model of hard radiation [11]. Recent studies have indicated that the value of ϵ may be smaller. However, as part of the $H_b \to J/\psi X$ cross section analysis, is was shown that moving the Peterson ϵ from 0 to 0.006 has a small effect on the shape of the H_b p_T spectrum above 9 GeV/c [12]. As our analysis only considers b mesons above this threshold, this is not a concern in this analysis.

2.4 D^0 Mixing (or the lack thereof)

The D^0 is a neutral meson formed by a $c\overline{u}$ pair, similar to a K^0 ($s\overline{d}$), B^0 ($b\overline{d}$), and B_s^0 ($b\overline{s}$). These states are not CP eigenstates, that is to say that under charge conjugation, C, and parity inversion, P, the particles change. Under CP transformations,

$$CP|K^0>=|\overline{K^0}>\,,\; CP|D^0>=|\overline{D^0}>\,,\; CP|B^0>=|\overline{B^0}>\,,\; CP|B_s^0>=|\overline{B_s^0}> \tag{2.17}$$

A CP eigenstate can be formed from these states by making the linear combinations $|K_S^0>=(|K^0>+|\overline{K^0}>)/\sqrt{2}$, $|K_L^0>=(|K^0>-|\overline{K^0}>)/\sqrt{2}$, and similarly for the other three neutral mesons. Because CP is (almost) conserved, these states have different decay modes and different masses. So while these particles must be created in an eigenstate of the weak force, they may oscillate into their anti-particles. In K^0, B^0, and B_s^0 systems this oscillation is observed, so that over the lifetime of the particle, the B^0 may transform into a $\overline{B^0}$. One might naively expect, therefore, to find that the D^0 also oscillates. However, this is not the case. This is due to the fact that D^0 mixing is Cabibbo suppressed because the charm and down quarks are different generations, while the decay of the D^0 is not Cabibbo suppressed (in the other three cases, both mixing and decays are Cabibbo suppressed, so the effects cancel). Also, the box diagram for D^0 mixing contains d, s, and b quarks (see figure 2.3), lacking the contribution the massive t quark makes to the box diagrams of the other neutral mesons listed [13]. The current upper limit on the mixing frequency of the D^0 CP eigenstates is 0.07 ps^{-1} at the 95% confidence level [3]. This means that the D^0 does not mix, or else mixes very slowly. This is important here because it means that, after the decay $H_b \to \mu^- D^0 X$, the D^0 will not mix into a $\overline{D^0}$. Thus, if we look for the two body decay $D^0 \to \pi^+ K^-$, we will find that the pion and the muon of the event have opposite charges. Since we do not distinguish between π and K tracks in our analysis based on their track properties alone, without muon information we would have two $K\pi$ masses for each oppositely charged track pair, one for each mass assignment. The incorrect mass assignment for $K\pi$ tracks from a D^0 decay leads to a mass distribution in the shape of a broad Gaussian that peaks near the D^0 mass, a phenomenon called auto-reflection. The lack of D^0 mixing combined with the muon charge information thus allows us to eliminate the auto-reflection of the $D^0 \to \pi^+ K^-$ peak, and substantially reduce the non-charm background.

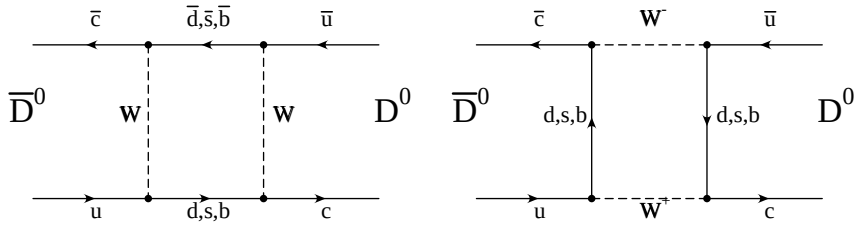

Figure 2.3: The lowest order Feynmann Diagrams for D^0 mixing. Note that the heaviest quark in the diagrams is the b quark; there is no contribution from top.

2.5 History of B cross-section results

In order to put our results into context, we give a brief overview of previous b cross section results. From the first measurements of $\sigma(p\overline{p} \to b)$ made at the Tevatron, there has been a factor of two difference between the observed cross section and the QCD predictions [15]. While the level of discrepancy has been reduced, some uncertainties remain. Also, a summary of existing measurements shows that previous experimental measurements are not entirely consistent with one another [14]. It is this historic difference that makes these cross section measurements interesting.

Cross section results fall into two general catagories, inclusive and exclusive measurements. In an inclusive measurement, the b hadron is not fully reconstructed. Instead, one looks for some of the H_b decay products, and based upon the found products and Monte Carlo simulations extrapolates the H_b cross section. Our measurement is an inclusive result, as we are unable to detect the neutrino produced in the H_b decay. Inclusive measurements have the benefit of usually having large statistics, but as the H_b p_T cannot be determined for a given event they are sensitive to errors in modelling. In exclusive measurements, the H_b is fully reconstructed. The CDF Run I measurement of $\sigma(p\overline{p} \to B^+)$ using the $B^+ \to J/\psi K^+$ decay mode was an exclusive measurement [16]. Exclusive measurements have the benefit of being able to determine the p_T of the H_b precisely, and therefore rely less on the Monte Carlo p_T spectrum to get the differential cross section. However, they generally have small sample sizes.

The $\sigma(p\overline{p} \to H_b)$ was first measured at the UA1 experiment at CERN, and published in 1987 [17]. This experiment was performed at a center of mass energy of 630 GeV, and was an inclusive measurement of $b\overline{b}$ to dimuons. The results agreed with the NLO theory calculation. The next measurement of the $\sigma(p\overline{p} \to H_b)$ cross section was made at CDF Run 0. This measurement was also conducted at 630 GeV, in the same decay mode. The CDF Run 0 result was 1.5σ higher than theory, but much was made of the fact that the ratio of experiment to theory was 5 to 1. At CDF Run I, this measurement was repeated at $\sqrt{s}$ of 1.8 TeV, and a factor of 2 discrepancy was still present [18]. It was at this point that the difference between experimental results and QCD predictions became significant [15].

CDF Run I also found the inclusive cross section in the $H_b \to J/\psi X$, $H_b \to \psi(2s)X$, $H_b \to \chi_c X$, and semileptonic electron decay modes [19, 20, 21]. Exclusive measurements in the decay modes $B^{\pm} \to J/\psi K^{\pm}$ and $B^0 \to J/\psi K^{*0}(892)$ were also made [16, 22]. The CDF Run I analyses were the first to include silicon vertex detector information (neither UA1 nor CDF Run 0 had silicon). These measurements were the first where the difference between theory and data became statistically significant.

The D0 experiment at the Tevatron also found a $\sigma(p\overline{p} \to H_b)$ at 1.8 TeV using semileptonic muon decays and $H_b \to J/\psi X$ decays. [23, 24, 25]. These results also showed a factor of two discrepancy (Figure 2.4). D0 also measured the cross section to a rapidity of 3 (previous results had all been at a $|y| < 1$), and found a factor of 4 discrepancy between its measurement and QCD [26].

Between Run I and Run II of the Tevatron, there were also several improvements to theory. There were changes made to the structure function of the proton due to results from the Hera experiment. The next leading log terms had been added to the QCD production calculation in FONLL. Also, the fragmentation function used changed [15]. Thus, when the first CDF Run II cross section which used $H_b \to J/\psi X$ decays was published, theory and experiment were shown to be in good agreement, as shown in figure 2.5 [12]. Most of the change took place on the part of the theory.

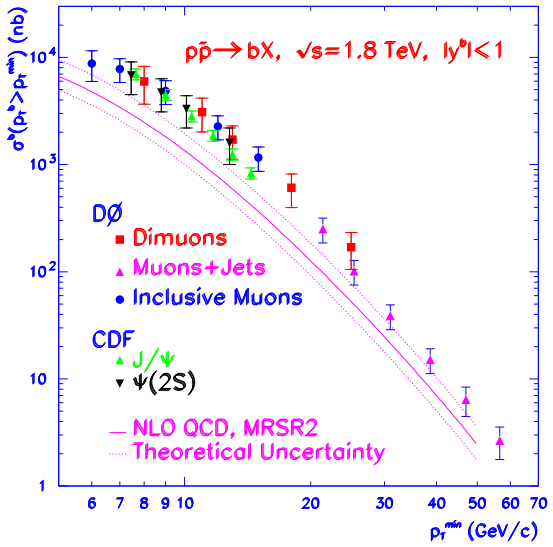

Figure 2.4: H_b cross section results from Run I of CDF and D0, plotted with the NLO QCD prediction. Data is roughly twice the size of the NLO prediction.

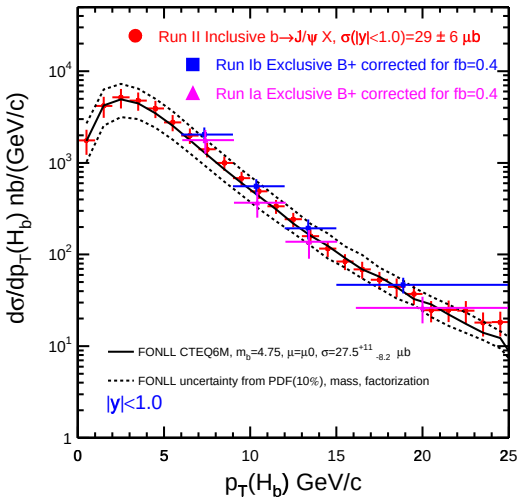

Figure 2.5: The CDF Run II $\sigma(p\overline{p} \to H_b)$, $H_b \to J/\psi X$ cross section shown with the Run I $B \to J/\psi K$ cross section and FONLL theory. Theory and data agree well.

Chapter 3

CDF Detector

3.1 Overview

The Collider Detector at Fermilab (CDF) is a general purpose experiment to study the $p\bar{p}$ collisions at the Fermilab Tevatron Collider. Since the first collision in October of 1985, at the center-of-mass energy of $\sqrt{s} = 1.8\,\text{TeV}$, the Tevatron and CDF performance has steadily improved and yielded large sample of data. The analysis of the experimental data has resulted in more than 100 published papers ranging over the entire state of the hadron collider physics [27].

After the shutdown of 1996, the Tevatron and CDF detector underwent major upgrades [28]. The modest increase in the Tevatron energy from $\sqrt{s} = 1.8\,\text{TeV}$ to $\sqrt{s} = 1.96\,\text{TeV}$ has a major impact on physics. (For example it increased the $t\bar{t}$ yield by 40 %.) The dramatic luminosity increase provided by the Main Injector gives us the capability to more precisely study hadron collider physics. Assuming that the proton and antiproton beams collide head-on without a crossing angle and with optimal alignment, the Tevatron's luminosity can be written as

$$\mathcal{L} = \frac{f_{\text{BC}} N_p N_{\bar{p}}}{2\pi T(\sigma_p^2 + \sigma_{\bar{p}}^2)} F(\frac{\sigma_l}{\beta^*}) \tag{3.1}$$

where $T \approx 21\,\mu\text{s}$ is the revolution period, f_{BC} is the number of bunches in each beam, N_p and $N_{\bar{p}}$ are the number of protons and antiprotons per bunch, σ_p and $\sigma_{\bar{p}}$ are the transverse beam sizes (RMS) at the interaction point, and F is a form factor that depends on the ratio between the bunch longitudinal RMS size σ_l, and the beta function β^* at the interaction point. At Run II, the Tevatron luminosity has increased most significantly by increasing the number of bunches per beam from 6 to 36, while keeping similar or even higher N_p and $N_{\bar{p}}$ than Run I. As of February of 2006, the total integrated luminosity at Tevatron Run II was $1\,\text{fb}^{-1}$, using instantaneous luminosities as high as $1.8 \times 10^{32}\,\text{cm}^{-2}\text{s}^{-1}$.

In order to accommodate the higher collision rate, and to best utilize the CDF physics program capabilities, most of the existing CDF detector has been rebuilt or upgraded. This chapter gives a general description of the CDF II detector with an emphasis on the elements relevant to this analysis. Figure 3.1 is

an overview of the detector, and Figure 3.2 shows a 1/4 slice of the detector with more detailed labeling of the components.

3.2 Tracking System

3.2.1 Helix Parameters at CDF

In the standard CDF coordinate system, the proton direction is defined as the $\hat{z}$ or longitudinal axis, which is opposite to the magnetic field direction. In the transverse plane looking in the proton direction, the 9 o'clock position defines the $\hat{x}$ axis and the 12 o'clock position is the $\hat{y}$ axis. The polar angle θ is measured starting from the positive $\hat{z}$ direction, and the pseudorapidity is defined as

$$\eta = -\log(\tan\frac{\theta}{2}) \tag{3.2}$$

In a homogeneous magnetic field the trajectory of a charged particle is a helix which axis is parallel to the magnetic field, as shown in Figure 3.3. At CDF the 5 tracking parameters [29] used to describe the helix of the charged particle are:

$$\vec{\alpha} = (\lambda, C, z_0, d_0, \phi_0) \tag{3.3}$$

where λ=cot θ, θ is the polar angle at the minimum approach. C is the half curvature and has the same sign as the particle charge. The z_0 and ϕ_0 terms are the z position and direction at the point of minimum approach to origin of helix respectively. d_0 is the signed impact parameter, its magnitude is equal to the distance between helix and origin at minimum approach. The impact parameter of a track has a sign that is defined by the following formula:

$$d_0 = \frac{\hat{z} \cdot (\vec{r} \times \vec{P}_T)}{|\vec{P}_T|}, \tag{3.4}$$

where $\vec{p}_T$ is the transverse momentum vector of the particle, $\vec{r}$ is the vector pointing from the primary vertex to the reconstructed particle trajectory at the point of closest approach to the primary in the $r - \phi$ plane and $\hat{z}$ is the unit vector along the z axis.

3.2.2 The Central Outer Tracker

The Central Outer Tracker (COT) is an open-cell drift chamber [28, 30]. The COT begins at a radius of 40 cm from the beam axis and ends at 137 cm. It has eight superlayers, each one is divided in ϕ into "super cells". There are 12 sense wires in each super cell with approximated same maximum drift distance, therefore

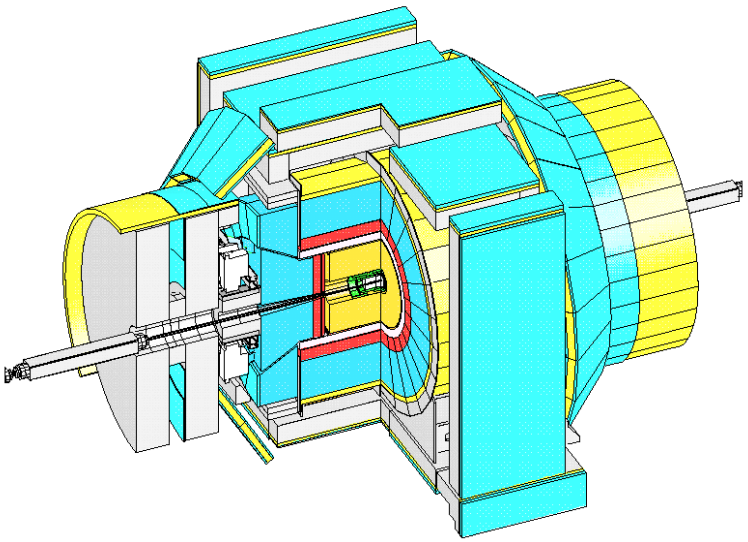

Figure 3.1: An overview of the Collider Detector of Fermilab in its Run II configuration.

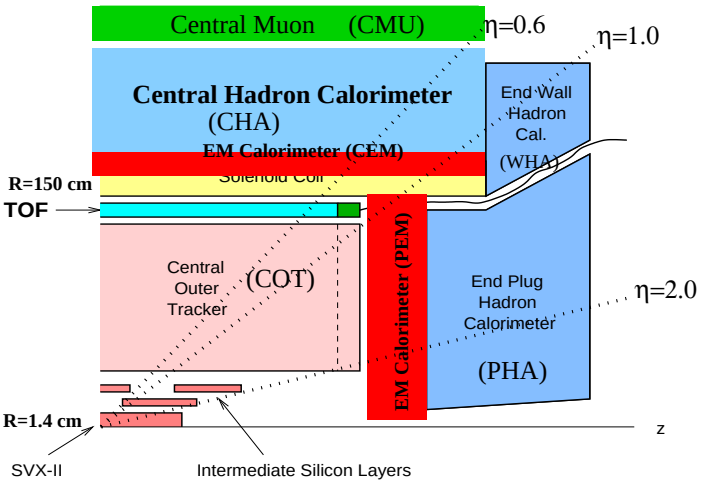

Figure 3.2: A cut-away view of one quadrant of the CDF II detector showing the tracking region surrounded by the solenoid, calorimeters and CMU.

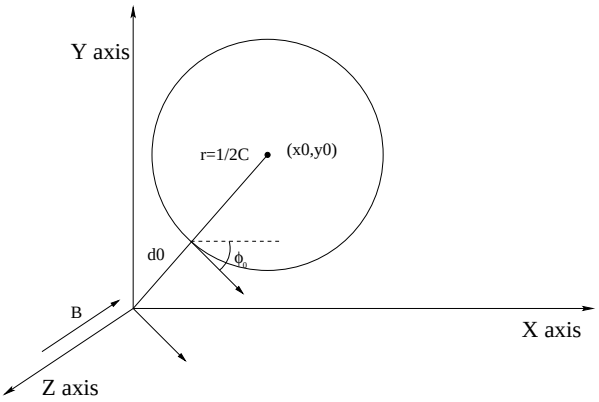

Figure 3.3: A helix in the transverse plane with the impact parameter d_0 and ϕ_0 labeled. The radius of the helix is $1/2C$, where C is the curvature.

the number of super cells in a given super layers is roughly proportional to the radius of the super layer. The super cell is tilted by 35° with respect to the radial direction, as illustrated in Figure 3.4. The super layer alternates between axial (parallel to the beam direction) alignment and small ±2° stereo alignment, where the tilt angle is a rotation about an axis in the radial direction. Table 3.1 gives some features of the COT. In the center of the COT (about $z = 0$ cm), the wires are supported by a polyester/fiber glass "protrusion" rod, called the spacer, that is epoxied to each wire in a wire plane to prevent the wires from moving due to electrostatic forces.

For a charged particle traveling trough the entire COT radially, the 4 axial and stereo superlayers provide 96 measurements. The drift time of ionization electrons in the gas is used to measure the spatial charged particle position. The total collected charge is encoded in the output discriminator pulse height, which is corresponding to the measurement of the energy loss through ionization of the gas per unit length (dE/dx). The dE/dx of a charged particle is a function of particle velocity that can be used to infer the particle mass by combining with the information of the particle's momentum.

While the data that is being used in this analysis was being collected, the COT was beginning to undergo rapid aging [31]. What this means is that the gain of the COT was decreasing, resulting in the efficiency of the detector dropping. While this has since been corrected, it effects several of our efficiency measurements.

3.2.3 Silicon Vertex Detector

CDF II has three silicon detectors [32]: Layer 00 (L00), the Silicon Vertex Detector (SVX II), and the Intermediate Silicon Layer (ISL). Figures 3.5 and 3.6 show the end view of the SVX II and the side view of the CDF Run II silicon system.

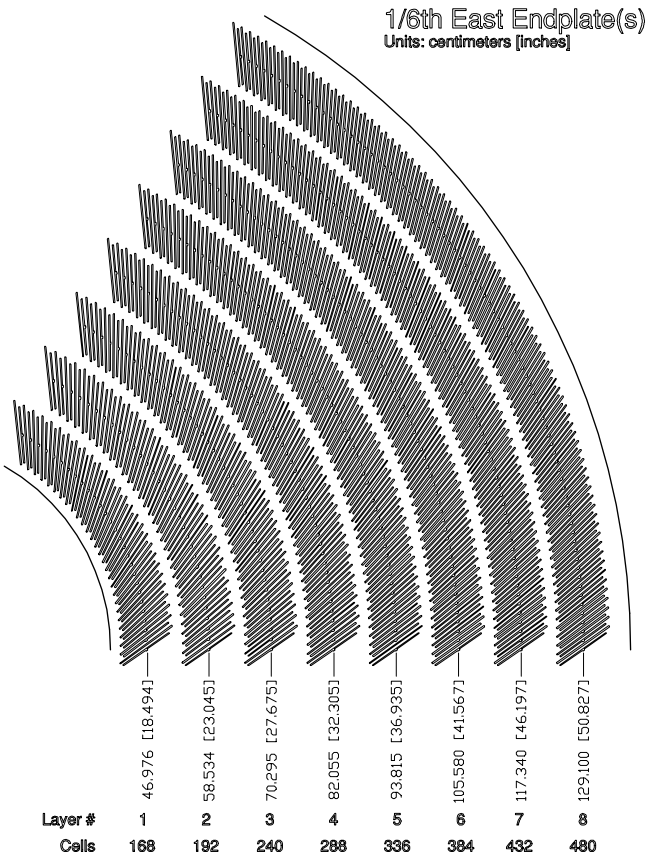

Figure 3.4: 1/6 section of the COT end plate. For each super layer is given the average radius.

COT	
Number of superlayers	8
Measurements per superlayer	12
Stereo Angle	+2 0 -2 0 +2 0 -2 0°
Cell/Layer	168 192 240 288 336 384 432 480
Radius at Center of SL	46 58 70 82 94 106 119 131 cm
Tilt Angle	35°
Length of Active Region	310 cm
Number of channels	30,240
Material thickness	1.3% X_0

Table 3.1: Some features of the COT

SVX II is the CDF Run II baseline detector, it is built in three cylindrical assemblies called "barrels". Each barrel is 29 cm long, they are positioned end-to-end along the beam axis and centered longitudinally with the detector. There are 12 wedges in ϕ per barrel, each has five layers of silicon staggered in radius numbered from 0 to 4. One layer consists of wire-bonded pair of double-sided silicon microstrip detectors. On the side facing the beamline, the strips are spaced in $r\phi$ by approximately 60 μm, and have implant widths of 14-15 μm. On the other side, both 90° and small angle stereo sensors are used, in the pattern (90 90 -1.2 90 +1.2) degrees from the innermost to the outmost SVX II layers. They are spaced by (141, 125.5, 60, 141, 65) μm, and have implant widths of 2- μm for the 90° strips and 15 μm for the small-angle stereo layers. The readout electronics chips are mounted on an electrical hybrid on the surface of the silicon detectors. Table 3.2 shows some of the SVX II features.

The ISL consists of a double-sided silicon layer, similar to the SVX II, placed at a radius of 22 cm in the central region. In the plug region, $1.0 \leq |\eta| \leq 2.0$, two layers of silicon are placed at the radii of 20 cm and 28 cm. Together with the SVX II, the ISL provides a stand-alone silicon tracking and b-tagging over the full region $|\eta| \leq 2.0$.

The Layer 00 detector is a single sided, radiation hard silicon layer placed immediately outside the beam pipe ($r \approx 1.5\,cm$), which greatly improves the track impact parameter resolution.

3.3 Muon System

Surrounding the calorimetry is a set of proportional chambers and scintillators used to identify muons [28]. There are 4 sets of proportional chambers, the Central Muon Detector (CMU), the Central Muon Upgrade (CMP), the Central Muon Extension (CMX), and Intermediate Muon Detector (IMU). The outside of the CMP (relative to the interaction point) is covered by a scintillator, the CSP, and the inner and outer sides of the CMX are also covered by scintillator, the CSX. The coverage of these detectors in $\eta - \phi$ is shown in figure 3.7. The CMU is a cylindrical detector on the outside of the Central Hadronic Calorimeter (CHA), which acts as an absorber for the CMU. The CMU is made up of 4 layers of single wire detectors, staggered slightly to give a course p_T resolution. The CMP is a box-like detector that surrounds the CMU. The north and south walls of the CMP are behind a 2 foot thick steel wall, while the top and bottom walls of the CMP are behind the magnetic field return yoke. Like the CMU, the CMP consists of 4 layers of staggered single cell drift chambers. The CMP was added for CDF Run I in order to increase the purity of high p_T muons. The CMX was added in the CDF Run I upgrade to extend the η range of the central muon detector. Unlike the CMP, there are gaps in the CMX near the top and bottom of the detector. The CMX is made

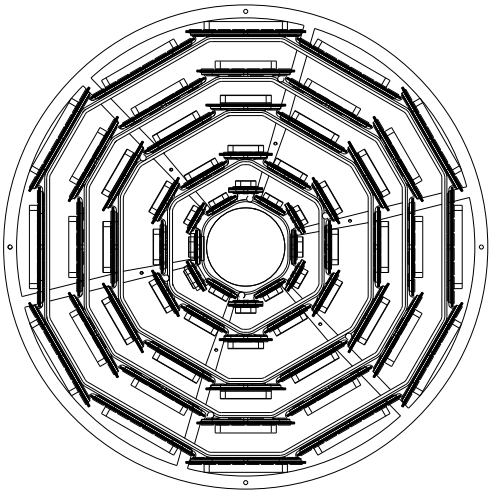

Figure 3.5: An end view of the SVX II detector.

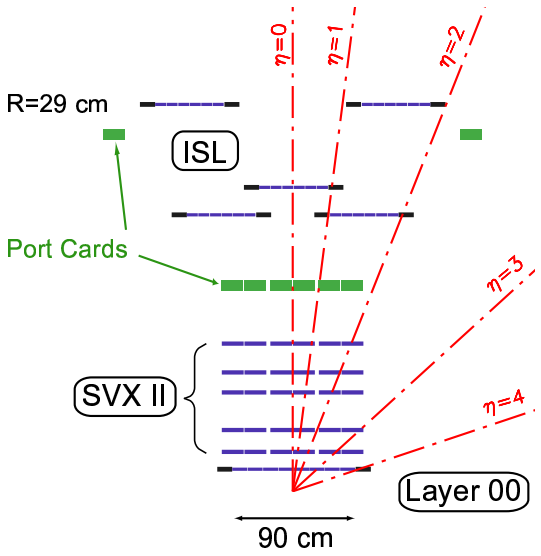

Figure 3.6: A side view of half of the CDF Run II silicon system on a scale in which the z coordinate is highly compressed.

up of 8 layers of staggered drift chambers. These chambers are identical to those in the CMP, except for length. Figure 3.8 shows the number of absorption lengths between interaction point and the CMU, CMP, and CMX. The IMU is placed to find muons in the forward region of the detector ($1 \leq |\eta| \leq 2$), and the IMU chambers are identical to the CMP chambers, except for size. Some properties of these detectors are shown in table 3.3.

3.4 CDF Cherenkov Luminosity Monitor

The luminosity $\mathcal{L}$ of hadron collider is often determined from the rate of inelastic $p\bar{p}$ interaction using the formula

$$\bar{N} f_{\mathrm{BC}} = \sigma_{\mathrm{in}} \mathcal{L} \tag{3.5}$$

where the $\bar{N}$ is the average number of interactions per beam crossing. The inelastic cross section $\sigma_{\mathrm{in}} \sim 60\,\mathrm{mb}$ at the center of mass energy 1.8 TeV at Tevatron was measured by CDF [33], E710 and E811 experiments with about 3 % uncertainty.

At CDF Run II, a Cherenkov Luminosity Counter (CLC) [34, 35, 36] has been implemented to measure $\bar{N}$ within a few percent uncertainty for Tevatron luminosity determination. There are two CLC detector modules in the CDF detector installed in "3-degree holes" inside the CDF end-plug calorimeter as illustrated in Figure 3.2, which covers the pseudorapidity range $3.7 \leq |\eta| \leq 4.7$. Each CLC module consists of 48 thin, long, conical, gas-filled, Cherenkov counters. These counters are arranged around beam pipe in three concentric layers with 16 counters each, and pointing to the interaction region. The counters in the outer two layers are 180 cm long, and the inner layers are 110 cm long due to geometrical constraints. The counter cross sections range between 2 and 6 cm in diameter. A photomultiplier tube is attached to the far end of each counter to collect the light of relativistic particles traveling through the CLC. A primary particle from $p\bar{p}$ interactions will transverse the full length of the counter and generate a large PMT signal, while the secondary particles produced in the beam pipe and materials surrounding the CLC cross the counter at different angles and yield much smaller signals. In addition, the Cherenkov counter is not sensitive to low momentum particles because of its momentum thresholds (2.6 GeV/c for pions), as well as the beam halo interaction.

The number of interactions in a bunch crossing follows Poisson statistics with mean $\bar{N}$. For traditional scintillator counter based luminosity measurement, by measuring the fraction of empty crossings we can calculate the $\bar{N}$. However, this approach fails at very high luminosity, where the average interaction numbers becomes too large to determine the no interaction crossing fraction with a small relative uncertainty. At

SVX II	
Readout coordinates	$r-\phi$; $r-z$
Number of barrels	3
Number of layers per barrel	5
Number of wedges per barrel	12
Ladder length	29.0 cm
Combined barrel length	87.0 cm
Radius at axial layers	2.545 4.120 6.520 8.220 10.095 cm
Radius at stereo layers	2.995 4.570 7.020 8.720 10.645 cm
number of ϕ strips	256 384 640 768 896
number of Z strips	256 576 640 512 896
ϕ strip pitch	60 62 60 60 65 μm
Z strip pitch	141 125.5 60 141 65 μm
Cell/Layer	168 192 240 288 336 384 432 480
Number of channels	405,504
Material thickness	3.5% X_0

Table 3.2: Some features of the SVX II

	CMU	CMP/CSP	CMX/CSX	IMU
Pseudorapidity coverage	$\lvert\eta\rvert \leq 0.6$	$\lvert\eta\rvert \leq 0.6$	$0.6 \leq \lvert\eta\rvert \leq 1.0$	$1.0 \leq \lvert\eta\rvert \leq 1.5$
Drift tube cross-section	2.68×6.35 cm	2.5×15 cm	2.5×15 cm	2.5×8.4 cm
Drift tube length	226 cm	640 cm	180 cm	363 cm
Pion interaction lengths	5.5	7.8	6.2	6.2 to 20
Minimum detectable muon p_T	1.4 GeV/c	2.2 GeV/c	1.4 GeV/c	1.4-2.0 GeV/c
Multiple scattering resolution	12 cm/p	15 cm/p	13 cm/p	13-25 cm/p

Table 3.3: Some features of the CDF Muon System. Pion interaction lengths and multiple scattering are computed at a reference angle of $\theta = 90°$ in the CMU and CMP/CSP, at an angle of $\theta = 55°$ in the CMX/CSX, and show a range of values for the IMU

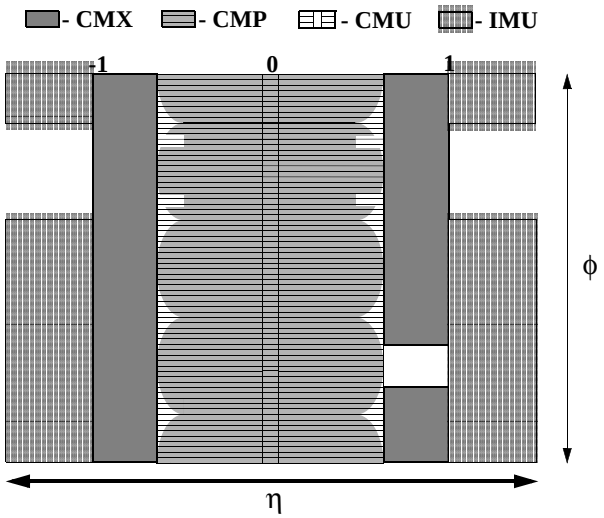

Figure 3.7: Location of the muon detector components in azimuth ϕ and pseudorapidity η for CDF Run II.

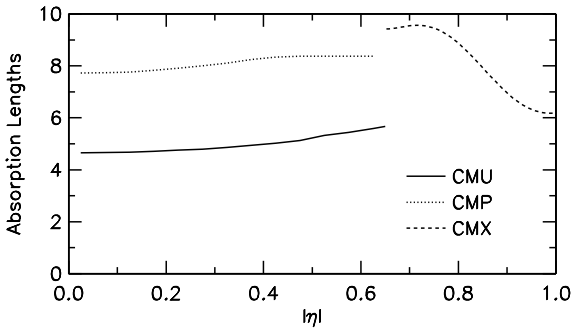

Figure 3.8: Number of absorption lengths as a function of pseudorapidity averaged over azimuthal acceptance of the CMU, CMP, and CMX systems.

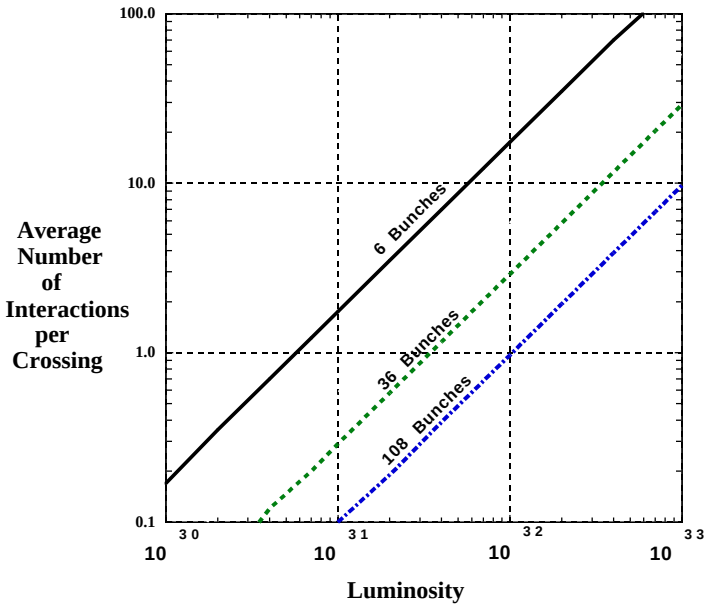

Figure 3.9: The average number of interactions ($\bar{N}$) for various conditions at CDF. 36 bunches is equivalent to 396 ns crossings.

CDF Run II, the expected $\bar{N}$ can reach as high as 4, as shown in Figure 3.9. As for the CLC, since the PMT signal amplitude collected by a Cherenkov counter is proportional to the primary particle number, it allows us to directly measure the $\bar{N}$ with high precision even at high luminosity. Moreover, collision data from zero biased and minimum biased triggers at CDF are continuously recorded through each run ($\sim$ 1 Hz), they are then analyzed in detail offline to produce the final luminosity measurement.

3.5 CDF Trigger System

At the Tevatron the $p\bar{p}$ collision rate is much higher than the rate at which the data can be recorded, and the cross section of the interesting physics events is only a small fraction of the total inelastic cross section. In CDF, a three level architecture trigger system has been implemented to select the most interesting events and reject large fraction of the inelastic background. Each trigger level provides a rate reduction sufficient to allow for processing in the next level with minimal deadtime.

The first level uses custom designed hardware to find physics objects such as clusters in the electromagnetic calorimeter or track-segments in the muon chambers. An eXtremely Fast Tracker (XFT) was built for Level-1 at CDF II, which allows tracks to be reconstructed on the transverse plane of the COT. An extrapolation unit (XTRP) matches a track to an electromagnetic calorimeter energy cluster for improved electron identification or to a stub in the muon system for better muon identification and momentum resolution. The

actual comparison of the extrapolated track to the muon chamber hits is done in Muon Matchbox (TCMD). The XTRP is also used alone for triggering. The Level-1 trigger makes a decision within 5.5 μs, while the event's data is still in the pipeline. The rejection factor is about 60, thus decreasing the event rate from 1.7 MHz to about 30 KHz.

The events accepted by the Level-1 system are processed by the Level-2 hardware, which has four asynchronous event buffers and a maximum input rate of 30 KHz. The Level-2 system has data from the central shower-max detector (CES) for improved identification of electrons and photons. Data from the silicon tracker (SVX II) is also available at Level-2; it can be associated with XFT tracks by the Silicon Vertex Trigger (SVT) [37, 38] to provide precise measurements of track impact parameter d_0, which is defined as the minimum distance between the origin and the track trajectory. The Level-2 accept rate is around 300 Hz, with a rejection of about 100.

The Level-3 trigger consists of a farm of PCs running Linux. It uses the full detector to reconstruct and filter events with a maximum 75 Hz written rate to permanent storage.

The purpose of the XTRP is to receive tracking information from the XFT and distribute the tracks and information derived from the tracks to the Level-1 and Level-2 trigger subsystems. After receiving the tracks from the XFT, signals are sent to the Level-1 Muon system (L1 MUON), the Level-1 Calorimeter trigger (L1 CAL), and the Level-1 Track Trigger (L1 TRACK) as shown in Fig. 3.11. The tracks are also put into a storage pipeline and upon receiving a Level-1 accept are sent to the SVT and the decision Level-2 processor.

The XTRP system consists of one Clock/Control board, 12 Data Boards, and the Track Trigger board. Information enters and leaves the XTRP crate via transition modules placed on the back of the crate. The Clock/Control board receives L1 Accepts and the CDF Clock from the rest of the trigger system, and sends the track information to the Global Level 2 trigger and the SVT. The Data Boards receive the track information from the XFT. Each contains 24 segments, with each segment capable of containing the information on a single track. The Data Boards perform the extrapolation to the L1 Muon and L1 Cal systems, and pass track information to the track trigger board. The track trigger board gets its tracks from the data boards, determines which triggers are set in a given event, and passes this information to the L1 Global Trigger system. Figure 3.12 diagrams the flow of data in the XTRP.

The entire XTRP system resides in a single, 9U VME crate with a custom J3 backplane that satisfies the VIPA specifications [39]. The crate also contains a commercial VME CPU [40] and TRACER module which are common to all CDF-II VME crates. The TRACER (TRigger And Clock + Event Readout) is the gateway between the XTRP crate and the CDF-II trigger system. It receives CDF-specific timing signals as

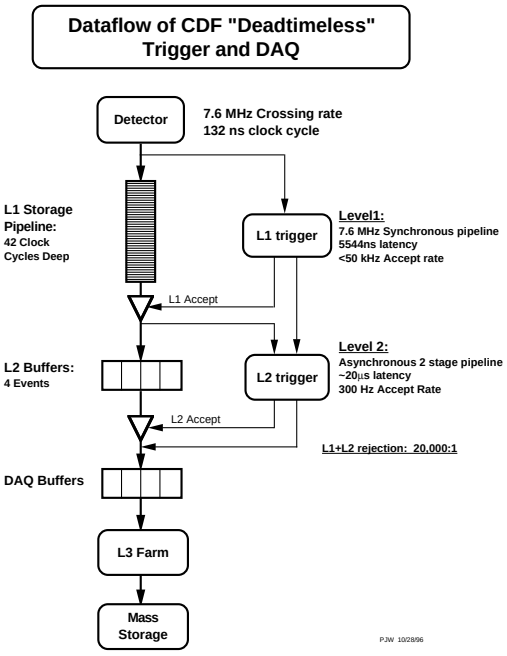

Figure 3.10: The functional block diagram of the CDF II data flow.

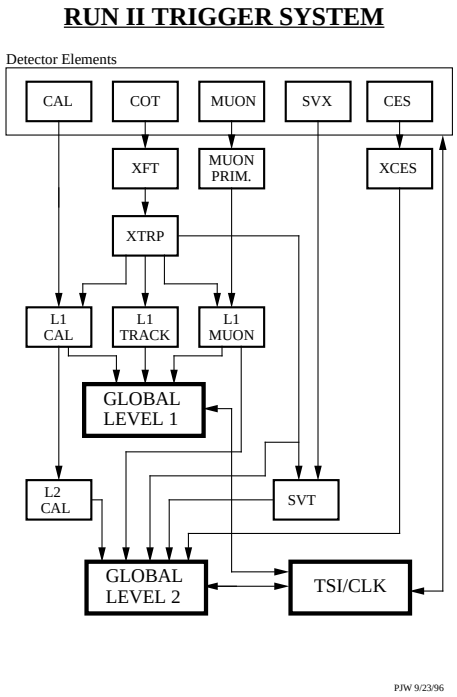

Figure 3.11: The block diagram the CDF II trigger system

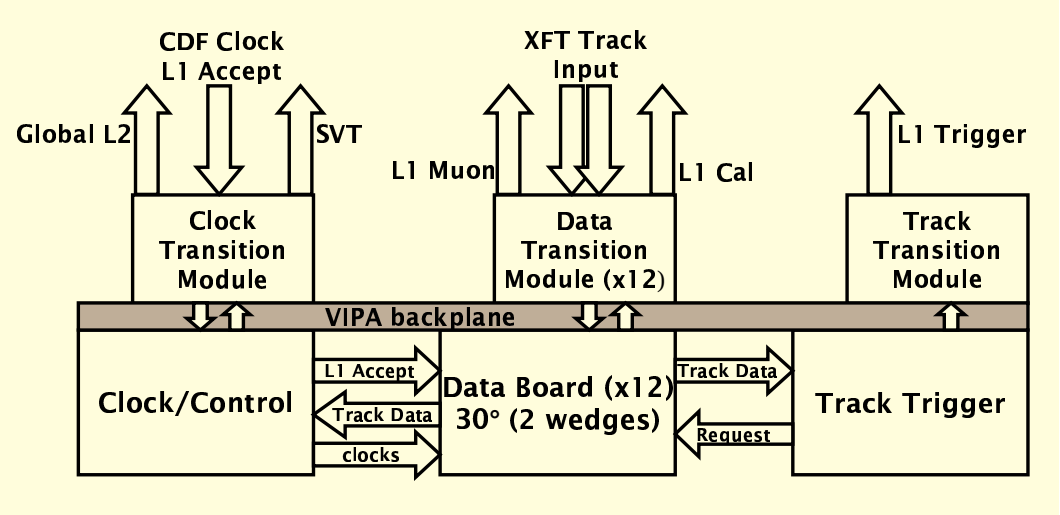

Figure 3.12: An overview of the XTRP system. Each 9U VME board (Clock/Control, 12 Data Boards, Track Trigger) has an associated transition module. Horizontal arrows between the boards indicate data transferred within the system via the VIPA backplane. Vertical arrows within the backplane indicate pass-through I/O between the board and its transition module. Vertical arrows at the top of the picture indicate cables connections which are data interfaces with other trigger systems. All cables connect to the system through transition modules as shown in the figure.

well as Level-1 and Level-2 Trigger Decisions [28]. The 9U VME crate, TRACER and CPU are common to all CDF front-end data acquisition and trigger systems.

For each Tevatron bunch crossing, the XFT reports information for all 288 segments to the XTRP. Reporting a fixed amount of information on each bunch crossing lends itself nicely to the synchronous data processing performed in the Level-1 trigger system. Track finding in the XFT is complete 2.7 μsec after each $p\bar{p}$ collision [41]. All of the XFT data is transferred to the XTRP in 132 ns.

The XTRP receives the track data from the XFT and, through the use of lookup tables, calculates the relevant information required by other systems to construct trigger objects. For example, muon primitives (track segments in the central muon chambers) are found at the same time the XFT is finding tracks in the COT. The XFT tracks are sent to the XTRP, which informs the Level-1 Muon trigger of all locations where a track extrapolates to the central muon systems. The definition of a muon object in the trigger is a track in the central muon system that is consistent with an extrapolated central track. Similarly, an electron is defined as a track plus an electromagnetic shower, with the XTRP extrapolating the tracks into the calorimeter.

The following information is sent to the Level-1 trigger subsystems from the XTRP:

- **Central Muon systems (L1 MUON).** XFT tracks are extrapolated to the radii of the CMU, CMX and IMU. One or more bits, corresponding to 2.5° azimuthal segmentation, are set according to p_T,

ϕ, and amount of multiple scattering. These bits are sent to the Level-1 Muon Trigger system. Two separate p_T thresholds are available for each of the three (CMU, CMX, IMU) subsystems.

- **Central Calorimetry (L1 CAL).** XFT tracks are extrapolated to Central Calorimeter towers. A set of four bits for each 15° wedge is sent to the Central Calorimetry Level-1 trigger. These bits correspond to four separate momentum thresholds.

- **Level-1 Track Trigger (L1 TRACK).** The Level-1 Track Trigger is an adjunct to the XTRP. It resides in the same VME crate and provides Level-1 triggers based on XFT track information only. The XTRP modules select tracks above a given p_T threshold and passes them on a bus to the Track Trigger. The total number of tracks is counted. If more than 6 tracks are found an automatic Level-1 accept is generated. If there are 6 tracks or fewer, the p_T and ϕ information is used to interrogate look-up tables to generate up to 15 distinct Level-1 track-only triggers.

The XTRP must provide output information to the L1 CAL, L1 MUON and L1 TRACK systems within 300 ns of having received input XFT data. The L1 TRACK decisions must be available 396 ns after having received all of the input track data.

Upon receiving input data from the XFT, all segments are put into a pipeline and stored pending the Level-1 trigger decision. If a Level-1 accept is received the tracks are latched into Level-2 buffers. All non-trivial tracks are then extracted and put into two separate FIFO's for delivery to the Level-2 processor and to the SVT respectively.

Extrapolating Tracks to Calorimeter and Muon Systems

The extrapolation of each track to the muon chambers and calorimeter is handled by lookup RAMs. Each Data Board has 24 lookup RAMS, one for each 1.25° segment within the 30° wedge covered by the Data Board. Each lookup RAM is $32K \times 36$ with 15 address bits and the 36 output bits divided into two 18 bit outputs. Data pertaining to the Central Muon chambers (CMU) and Central Muon Extension chambers (CMX) are grouped into the "CM side" of the RAM. Data pertaining to the Intermediate Muon chambers (IMU), calorimetry (CAL), Track Trigger, TOF and ϕ-gap bits are grouped into the "IM side" of the RAM.

The RAM contains the extrapolation data for every possible track. Once track data has been decoded for a segment, the 13 bits of track data along with 2 "phase" bits are presented as the address to a segment RAM. The phase bits are used to differentiate different lookup tables for different subsystems or different momentum thresholds. The data which are stored in the RAMs are generated and downloaded before each running period depending upon specified trigger parameters, and is discussed in Section 3.5.2. The 13 bits

of track data remain fixed for a single event (132 ns) but the phase bits change every 33 ns. This provides four phases of output for every track. Given the dual output and four phases, eight separate lookups of extrapolation information are performed for each track, which are summarized in Table 3.4.

For the muon lookups: CMU, CMX, and IMU, each phase corresponds to a single p_T threshold. Each of the 18-bits of output information correspond to a 2.5° window in the muon system, so it is possible for a segment in one wedge to extrapolate to the adjacent wedges in the muon system. The ϕ-gap and TOF lookups have two bits (low and high p_T thresholds) for each 15° wedge. The Track Trigger output is a one bit (p_T threshold) per wedge. The Calorimeter lookup provides 16-bits of information, which is 8 p_T thresholds mapped to a 30° window in the CDF-II Calorimeter. Since the Calorimeter trigger has 15° granularity, this extrapolation allows for tracks to extrapolate from one wedge into the nearest neighbor wedge.

Table 3.4: Quantities extracted from the lookup RAMs. The 13-bit track data word is presented to the RAM for 132 ns, while the two phase bits cycle (00, 01, 10, 11 binary) each 33 ns. Each phase represents a different lookup on each "side" of the RAM. The output of each side is 18 bits of data, as described in the text.

lookup phase	CM side	IM side
0	CMU high p_T	Calorimeter ($8p_T$) + Track ($1p_T$)
1	CMU low p_T	ϕ gap ($2p_T$) + Time-of-Flight ($2p_T$)
2	CMX high p_T	IMU high p_T
3	CMX low p_T	IMU low p_T

Compression of Extrapolation Output

The result of each lookup (one per segment) is 18-data bits, corresponding to different p_T thresholds or detector ϕ segmentation. Since nearby tracks can extrapolate to the same location in the detector, the extrapolation information must be compressed ("OR"ed) so that the ultimate output maps exactly onto the detector geometry. This compression is carried out through in series of stages. Data progresses through the stages in 33 ns cycles. Intra-wedge compression, among adjacent segments, is performed first, followed by inter-wedge compression, among adjacent wedges. The inter-wedge compression must handle adjacent wedges across adjacent Data Boards. The compression patterns are slightly different between calorimetry data and muon data. To save space on the Data Boards, the calorimetry and muon compression functions are performed by the same TTL/GTL translators with open-collector outputs for wire-AND logic.

All stages within the compression region are accessible to VME, and one can read the state of each compression stage for data verification. Furthermore, the VME access allows one to override the data presented to a subsequent stage with simulated data.

3.5.1 The Track Trigger

The Track Trigger board is the one board in the XTRP system that directly renders trigger decisions. These decisions are based upon tracking information only. Events selected by the track-only path at Level-1 provide heavy flavor candidate events for SVT trigger at Level-2.

Details of the interface between the Data Boards and the Track Trigger are described above. On the Track Trigger board, the track data are routed to a set of six "Sort" FPGAs. One half of these FPGAs is dedicated to extracting p_T data (p_T + isolation + short track bits), the other half extracts the ϕ data. From the wedge and segment origin of each track, a 9-bit "global ϕ" is generated (1.25° segmentation). The local-ϕ information from the XFT is dropped.

The Track Trigger board receives a maximum of 6 tracks and must evaluate every possible two-track pair for the six tracks. This yields "6-pick-2" or 15 possible combinations of track pairs. Each of the the Sort FPGAs output data (segment or ϕ information) for 5 pairs of tracks.

The data are fed to a bank of lookup RAMs. There are 15 unique p_T RAMS and 15 unique ϕ RAMs, with each RAM corresponding to a specific track-pair. Trigger selection criteria are programmed into the RAMs. The lookup RAMs on the Track Trigger are $512K \times 8$, with 19 address bits and 8 data bits. Each track provides 9 bits to the lookup RAM, with the 19^{th} bit used as a "phase" bit to generate two sets of 8 trigger bits. For every track-pair, the p_T and ϕ lookup outputs are ANDed together to generate a trigger decision for that pair. All pairs are then ORed together to generate the trigger decision for the event. The RAMs output 8 decision bits every 66ns. The two 8-bit words are concatenated into a single 16-bit trigger word. Since one trigger bit is reserved for the auto-accept trigger (> 6 tracks) the Track Trigger is capable of generating 15 different track triggers. These 15 different triggers can be any combination of single-track and two-track selection criteria.

The resultant trigger data is piped to a Level 2 Buffer and fed through the backplane to the Track Trigger Transition Module. The trigger signals are converted to differential LVDS and sent to the global Level-1 decision crate over shielded twisted pair cable. The trigger signals are synchronized to the 132 ns CDF clock.

3.5.2 Interface With Trigger System

Since the extrapolation parameters may change during different running periods, the infrastructure was developed so that the values loaded in the lookup RAMs (both on the XTRP Data Boards and the Track Trigger Board) could be generated dynamically based upon the number and types of triggers utilized. In this section, we describe how the extrapolation parameters are generated and loaded into the XTRP system.

The XFT provides 13-bits of information per track, with 7 of those bits recording track p_T. Track p_T values reported by the XFT are encoded into 96 bins, with bins 0-47 corresponding to negatively charged tracks and bins 48-95 corresponding to positively charged tracks. If no track is found in a given segment, its momentum bits are assigned a value of 124. The "short" tracks have a poorer p_T resolution, hence the p_T bin definitions are different for short tracks.

The Data Board lookup RAMs contain the information which takes an input track and extrapolates it to the calorimetry or muon systems. The extrapolation must account for the geometry of the detector, track curvature from the axial magnetic field and multiple scattering. The extrapolation formula used is the same for all detectors. The extrapolation determines a "window" bounded by a minimum and maximum value of $\phi_{detector}$ within which a particle may be found. The extrapolation window is given by:

$$\phi_{detector} = K/p_T \pm \sqrt{(3\sigma_K/p_T)^2 + \sigma_a^2} + \phi_{XFT},$$

where the $\pm$ values yield the maximum and minimum values of $\phi_{detector}$ for a track that has a signed transverse momentum p_T. The terms K, σ_K and σ_a are constants that depend detector subsystem. The term K/p_T accounts for the deflection of the track caused by the 1.4T solenoidal magnetic field, σ_K accounts for multiple scattering of the particle as it passes through the material of the detector, and σ_a is present to account for any misalignment between the COT and the detector to which the track is being extrapolated. The values of these constants are different for each one of the five detectors to which the XTRP extrapolates tracks. The extrapolation window, which is the middle term in the formula, allows for a 3-sigma multiple scattering term combined in quadrature with a misalignment term. See Table 3.5 for typical values utilized in extrapolation.

Table 3.5: Typical values used in XTRP extrapolation. The values of K, σ_K, and σ_a are constants that were determined from data. The p_T thresholds are set in the trigger table and may change depending upon physics needs. In the case of the calorimeter trigger, electrons with a 2GeV/c threshold are identified separately from positrons with a 2GeV/c threshold. In all other cases, the charge of the track is not used to select leptons.

detector	K (°/(GeV/c))	σ_K (°/(GeV/c))	σ_a(°)	p_T thresholds (GeV/c)
CMU	14.8	2.7	1.5	1.5, 4.0
CMX	13.36	5.39	1.5	2.0, 8.0
IMU	0	6.11	5	5, 11.
CAL	8.72	1.22	1.5	2.0+, 2.0−, 4.0, 8.0

At the beginning of CDF Run II, the extrapolation windows were set using MC, with the values of σ_K and σ_a for the CMU (CMX) larger than necessary to avoid losing muons. In order to refine the constants, we looked at events taken with the $J/\psi \to \mu^+\mu^-$ CMU-CMU (CMU-CMX) triggers. In these events, we

reconstructed the J/ψ mass peak, and used sideband subtraction to get a sample of pure muons. We fit the distribution of $\Delta\phi_{SL6-CMUp_T}$ ($\Delta\phi_{SL6-CMXp_T}$) to a Gaussian, and took K and σ_K from the mean and σ of the fit. To demonstrate this, we show data from the $J/\psi \to \mu^+\mu^-$ CMUP-CMU ($J/\psi \to \mu^+\mu^-$ CMUP-CMX) triggers, which have one leg of the J/ψ unbiased in the L1 trigger (Figures 3.13 and 3.14). The value of σ_a was set to 1.5° because each segment of the CMU (CMX) in the trigger represents a 1.5° section of the relevant detector, so this value of σ_a would ensure that even for very high p_T tracks, at least 2 segments of the CMU (CMX) would be examined for hits.

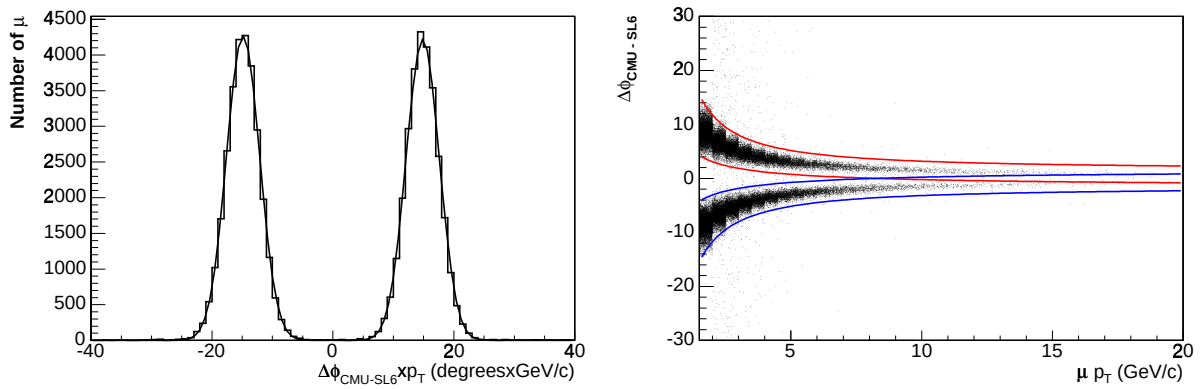

Figure 3.13: Plot of $\Delta\phi$ of μ between COT superlayer 6 and the CMU multiplied by the track's p_T on left. Plot of $\Delta\phi$ vs. p_T on the right. A sample of pure muons was obtained by reconstructing $J/\psi \to \mu^+\mu^-$ in the CMUP4-CMU trigger, which requires only a single high p_T muon at level 1. The tracks which filled this plot are the legs which did not trigger at level 1. The mean and σ of the two Gaussians are constrained to be equal.

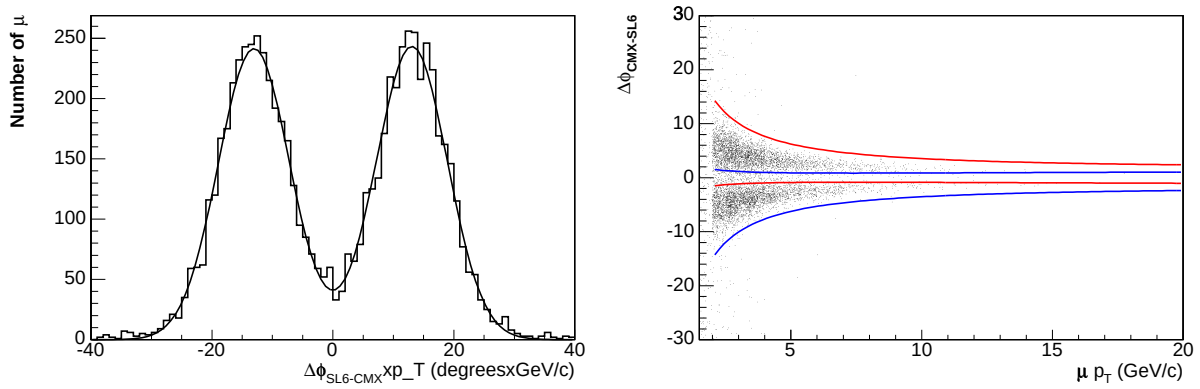

Figure 3.14: Plot of $\Delta\phi$ of μ between COT superlayer 6 and the CMX multiplied by the track's p_T on left. Plot of $\Delta\phi$ vs. p_T on the right. A sample of pure muons was obtained by reconstructing $J/\psi \to \mu^+\mu^-$ in the CMUP4-CMX trigger, which requires only a single high p_T muon at level 1. The tracks which filled this plot are the legs which did not trigger at level 1. The mean and σ of the two Gaussians are constrained to be equal.

Chapter 4

Datasets, Triggers, and Monte Carlo Generation

4.1 Overview

As mentioned in the previous chapter, not all events are written to tape due to the interaction rate being much higher than the maximum rate of data taking. Decisions on which events to keep and which to reject are made by a set of triggers [42], and events are grouped into different datasets depending on which trigger they came in on. (An event that fires multiple triggers may find itself in multiple datasets.) In this chapter, we give a brief description of the triggers that were used in this analysis. We also discuss briefly the offline validation of the data. Lastly, we go over the Monte Carlo simulations used in this analysis.

4.2 Triggers

4.2.1 B Semileptonic Trigger

The main trigger for this analysis is the B Semileptonic or μSVT Trigger, which was used to collect the μD^0 events. It was also used (along with CMUP8 events) in the determination of the offline CMU efficiency. At Level 1, this trigger requires that

- the XFT find a track with a p_T of at least 4 GeV/c
- the CMU must find a high p_T muon stub
- the XTRP extrapolates a high p_T track to the CMU stub which found the high p_T muon (there is no way to tell after the fact which XFT track set which XTRP muon bit, as two or more tracks could set the same bit.)
- the Muon Matchbox must extrapolate a CMP stub back to the high p_T CMU stub. This extrapolation is much looser than the extrapolation of the COT track to the CMU.

These requirements are collectively referred to as the L1_CMUP6_PT4 trigger. There was no muon information available for the L2 trigger in the runs used in this analysis. Instead, at Level 2 the trigger looks for a displaced track in the event. Passing the Level 2 trigger requires

- the XFT must find a track at Level 1.
- the SVT must find an SVX track that matches the XFT track. For this run period, the SVT required 4 ϕ layer hits in specific layers of the SVX. This is referred to as 4/4 SVT tracking.
- the found SVT track must have $120\mu\text{m} \leq |d_0| \leq 1\text{mm}$ and a $p_T > 2.0$ GeV/c.
- the χ^2 of the SVT track must be less than 25.

Note that, since there is no muon information available at Level 2, it is possible for a single track to fire both the L1 and L2 triggers. The L2 trigger requirements are collectively referred to as the L2_SVT_PT2_D120_CMUP6_PT4 trigger. At Level 3, full event reconstruction is done, except for the SVX. In order for the event to be accepted, Level 3 requires

- a muon with $p_T > 4$ GeV/c, a CMU stub with $\chi^2 < 9$, $dX < 15$ cm (here, dX means the difference in radius times ϕ between the predicted and found location of the muon stub), and a CMP $dX < 20$ cm.
- a COT track matched to an SVT track that passes the Level 2 cuts above.
- a difference ϕ_0 between the μ and SVT tracks of between 2° and 90°.
- the two tracks must have $\Delta z_0 < 5$ cm.
- the μ and SVT track combined have an invariant mass of less than 5 GeV/c^2, with the assumption that the SVT track is a pion.

The trigger requirements at L3 are collectively referred to as the B_SEMI_CMUP4_TRACK2_D120 trigger.

4.2.2 CMUP8 trigger

Events that came in on the CMUP8 trigger were used to find the efficiencies of the Level 1 trigger, the L2 SVT trigger, and (along with B Semileptonic events) the CMU offline efficiency. This trigger has the same requirements at Level 1 as the B Semileptonic trigger above. At Level 2, the only requirement is that the event contain an XFT track with $p_T > 8$ GeV/c. As there are no muons in Level 2, it is impossible to confirm at Level 2 that the 8 GeV/c track is actually a muon. At L3, it is required that a muon be found with $p_T > 8$ GeV/c, a CMU stub with $\chi^2 < 9$, $dX < 15$ cm, and a CMP $dX < 20$ cm.

4.2.3 The Two Track Trigger

Events that came in on the two track trigger, B_CHARM_LOWPT_L1_DPS, were used to determine the L2 XFT efficiency. The two track trigger has the following requirements at Level 1:

- two XFT tracks both with $p_T > 2$ GeV/c.
- $\Delta\phi_{SL6} < 90°$ between the tracks.

at Level 2, the event is required to have 2 SVT tracks with

- $p_T > 2$ GeV/c.
- $120\mu\text{m} \leq |d_0| \leq 1\text{mm}$
- $\chi^2 < 25$
- $2° < \Delta\phi_0 < 90°$
- $|L_{xy}| > 200\mu$m, where $|L_{xy}|$ is defined as the distance between the intersection point of two tracks and the primary vertex in the $r - \phi$ plane.

Then, at L3, it is required that

- both SVT tracks be matched to COT tracks with $p_T > 2$ GeV/c.
- the two tracks have $\Delta z_0 < 5$ cm.
- $2° < \Delta\phi_0 < 90°$

The two track trigger has a dynamic prescale at L1; this means that the rate at which the trigger at L1 is passed to L2 varies with luminosity. At the beginning of a run, only one event for every 250 triggers is passed to L2, but as the run progresses, this prescale may drop to the point that every triggered event is passed to L2.

4.2.4 The B Semileptonic Backup trigger

The B Semileptonic Backup trigger, B_SEMI_L3PS20_L2_TRK2_D120_L1_CMUP6_PT4, was used to determine the Level 3 efficiency. Its requirements are the same as the B Semileptonic trigger, except that it has no requirements at Level 3, and only 1 event of every 20 that fires the trigger is written to tape.

4.2.5 The J/ψ CMU-CMU trigger

The J/ψ CMU-CMU trigger was used, along with the J/ψ CMU-CMX trigger, to find the SVX offline efficiency. This trigger requires that at Level 1,

- at least 2 CMU muons be found
- both muons must have $p_T > 1.5$ GeV/c
- the CMU must find a low or high p_T muon stub
- the both CMU stubs must have the XTRP extrapolate an XFT track to it.
- in order to avoid the possibility that 2 adjacent CMU stubs are set due to crosstalk between them and then matched by a single XFT track, there is a $\Delta\phi$ cut of 5° (2 CMU stubs) in the CMU.

There are no cuts on this trigger at Level 2. At Level 3, it is required that

- there be 2 CMU muons found, both with $p_T > 1.5$ GeV/c, a CMU stub with $\chi^2 < 9$ and $dX < 30$ cm.
- the invariant mass of the di-muon pair must be between 2.7 GeV/c^2 and 4.0 GeV/c^2, so as to get both the J/ψ and ψ'
- the tracks must have opposite charges
- the two tracks must have $\Delta z_0 < 5$ cm.
- the $\Delta\phi_0$ between the two tracks must be less than 130°.

4.2.6 The J/ψ CMU-CMX trigger

The J/ψ CMU-CMX trigger was used, along with the J/ψ CMU-CMU trigger, to find the SVX offline efficiency. This trigger is the same as J/ψ CMU-CMU trigger, with the following exceptions. At Level 1, we require

- a CMU muon passing the L1 requirements for the J/ψ CMU-CMU trigger
- an XFT track with a $p_T > 2.0$ GeV/c
- a CMX low or high p_T stub
- the XTRP to have extrapolated an XFT track out to the CMX
- as the stubs are in different detectors, there is no $\Delta\phi_{CMU/X}$ cut

As before, there are no cuts at Level 2. At Level 3, the cuts are the same, except for the requirement that

- there be one CMU muon which meets the p_T and stub quality requirements of the J/ψ CMU-CMU trigger
- there be one CMX muon which has $p_T > 2.0$ GeV/c and $dX < 50$ cm.

4.3 Data Quality

In order for a run to be included in my sample, it must first pass certain data quality cuts. The first and most obvious is that all detector components that are used in my analysis must be included in the run. This means that we require the CLC, L1, L2, L3, COT, CMU, CMP, SVX, and SVT be active in every run used. In addition, we require that the COT, CMU, and CMP be declared good for use in the run offline. What this means is that the individuals responsible for maintaining the given detector have looked over the detector performance offline and declared it good. (Because the definition of a "good" run is somewhat more difficult for the other detector components used, this offline information is unavailable for the CLC, L1, L2, L3, SVX, and SVT. Instead, we check the data to make certain L1, L2, L3, SVX, and SVT make sense.)

4.4 Monte Carlo Generation

This analysis required a large amount of Monte Carlo to be generated in order to determine the kinematic and geometric acceptance of the detector, as well as the COT reconstruction efficiency. In all cases below, the Monte Carlo generated was run dependent, which means that the initial particles were created at the measured beamspot for a given run. All MC was generated using version 5.3.4 of the CDF software.

4.4.1 Bgenerator

A substantial amount of MC was required for this analysis, and the primary MC generator used was Bgenerator. The purpose of Bgenerator is to create and fragment b quarks with a given p_T and y spectrum [43, 44]. We generate b quarks using two different input spectra. The first spectrum is the default Bgenerator spectrum. It is set using the MRSD0 parton distribution function, and the b cross section is generated using theory provided in [4, 5]. The b quark mass for this sample was set to 4.75 GeV/c^2, and the normalization scale was set to $\mu = \mu_0 = \sqrt{m_b^2 + p_T^2}$. This first sample will be referred to later as simply the MRSD0 sample. The other MC sample generated used the results of the $H_b \to J/\psi X$, $J/\psi \to \mu\mu$ cross-section analysis

as its input spectrum, and will be referred to later as the CDF sample. In both cases, the b quarks were fragmented using the Peterson fragmentation function with $\epsilon = 0.006$ and the ratio of b hadrons created by the fragmentation was set to $B^0 : B^+ : B_s^0 : \Lambda_b : B_c^+ = 0.397 : 0.397 : 0.107 : 0.099 : 0.0$ in accordance with the production fractions found in [3]. There are no processes which result in $\Lambda_b \to \mu D^0 X$ in the standard CDF decay table or the PDG. There is a diagram for $\Lambda_b \to \mu \nu_\mu D^0 p$, but its branching fraction has not been measured and is not included in the standard CDF decay table. We have decided against adding it, as it is almost certainly a small contribution. The H_b are allowed to decay with their normal branching fractions, but we force the D^0 to decay to either $D^0 \to K^-\pi^+$, $D^0 \to K^+\pi^-$ (the doubly Cabibbo supressed decay), or to a μX.

There were two CDF samples produced. The first sample was only required to have a μ and a K and π that were produced in a D^0 decay. This first sample was generator level only and did not undergo the full detector simulation (see below). There were 370,000 events in that sample with a $|y(H_b)| < 0.6$. The second sample required that:

- The μ have $p_T > 3.6$ GeV/c and $|\eta| < 0.8$
- The event have a $D^0 \to K^\pm\pi^\mp$ decay. We kept the doubly Cabibbo suppressed decays.
- Both the π and K have $p_T > 0.5$ GeV/c and $|\eta| < 1.2$
- Either the π or K have $p_T > 1.4$

Events that passed these cuts went on to the full detector simulation. There were 782,000 of these events which passed these cuts and had an H_b with a $p_T > 9GeV/c$ and $|y| < 0.6$. Two equivalent samples were made using the MRSD0 distribution. There were 756,000 events in the MRSD0 sample with $p_T > 9GeV/c$ and $|y| < 0.6$ that underwent the full detector simulation, and additional 511,000 generator level only events.

4.4.2 Pythia

We used MC generated by Pythia to model in part the $c\overline{c}$ background of our measurement. Unlike Bgenerator, which creates single b quarks from a given input histogram, Pythia models entire physics events [45, 46]. In our case, we force Pythia to create a $c\overline{c}$ event in every interaction, and slightly boosted the RMS p_T of the events, so we could get a sample that would pass our basic trigger cuts (a μ with $p_T > 4.0$ GeV/c, a $D^0 \to \pi^+K^-$ with both π and K with $p_T > 1.0$ GeV/c, and at least one of the π or K with $p_T > 2.0$ GeV/c and an impact parameter greater than 120 μm. This sample was used primarily to confirm that the

D^0 impact parameter for $c\bar{c}$ is generally small, and has a distribution similar to that of D^0 mesons created directly by FakeEvent. We generated 20,000 of these Pythia events.

4.4.3 FakeEvent

FakeEvent is a simple particle gun which creates single particles based on a simple p_T, ϕ_0, and η spectrum. FakeEvent was used to estimate $c\bar{c}$ fraction in our data sample, and to generate the events used in the track embedding to find the COT efficiency. In the case of this analysis, all the p_T, ϕ_0, and η distributions were initially flat. For the $c\bar{c}$ estimate, the p_T spectrum was reweighted to match the spectrum from Pythia. We generated approximately 108,000 events for the COT efficiency study, and 876,000 events for the charm background estimate.

4.4.4 EvtGen

After the initial hadrons were created by Bgenerator, Pythia, or FakeEvent, they were decayed using EvtGen. EvtGen takes the particles created by the generators and decays them according to a set of input branching ratios [47]. This analysis for the most part used the default EvtGen branching ratios with one exception; the D^0 was forced to decay to $K\pi$. We kept both the favored and doubly Cabibbo suppressed decay modes, with their relative branching fractions kept to the values found in [3]. EvtGen does not decay μ, π, or K, which are left for GEANT in the full detector simulation.

4.4.5 Full Detector Simulation

The CDF detector is simulated in these studies using GEANT, which is designed to model the passage of elementary particles through matter [48]. A large amount of work has gone into modeling all of the CDF detector components, but relatively little of this is used in the current analysis. As most of the detector efficiencies were modelled using data, the only places the detector simulation is relied on is in the determination of the COT efficiency and in the estimation of the vertex reconstruction efficiency. In both cases, it is primarily the modelling of the COT and SVX that are used.

Chapter 5

Trigger Efficiencies

5.1 Introduction

This chapter reports the measurement the efficiency of the μSVT trigger path relative to the efficiencies of the associated offline detectors and selection cuts. We use techniques similar to those used in the J/ψ ([12]) and D^0 ([27],[49]) cross-section analysis. Specifically, we have used data taken using various backup triggers described in chapter 4 to estimate the efficiencies of the triggers in the μSVT trigger path.

All of the efficiency measurements come from data. We functionally parameterize the efficiencies using binned fits to the data. We have the events have been reconstructed using the 5.3.1 version of reconstruction.

This analysis uses data collected in the CDF run range 152636 to 163117. The beginning of the run range is set by the switch to the 1-miss XFT algorithm from the 2-miss XFT algorithm. What this means is that the XFT went from requiring 10 hits in each of the axial COT superlayers to requiring 11 hits in each axial superlayer. The end of the run range was set by the SVT switching from considering all XFT tracks to only XFT tracks with a transverse momentum greater than 2 GeV/c. In the entire run range, the SVT only examines SVX hits in 4 specific layers of the SVX, and a hit must be found in every one of those layers for an SVT track to be found. As stated in section 4.2.1, the semileptonic muon trigger path is:

- L1: L1_CMUP6_PT4
- L2: L2_SVT_PT2_D120_CMUP6_PT4
- L3: B_SEMI_CMUP4_TRACK2_D120

To get the overall efficiency of the trigger path, we find the efficiency of L1_CMUP6_PT4 with respect to offline reconstruction, the efficiency of L2_SVT_PT2_D120_CMUP6_PT4 with respect to L1_CMUP6_PT4 and offline reconstruction, and the efficiency of B_SEMI_CMUP4_TRACK2_D120 with respect to L1_CMUP6_PT4, L2_SVT_PT2_D120_CMUP6_PT4, and offline.

5.2 L1 Efficiency

The first trigger efficiency needed is the efficiency of the L1_CMUP6_PT4 trigger, henceforth referred to as the L1 efficiency, relative to offline:

$$\epsilon(\text{L1\_CMUP6\_PT4}) = \frac{\epsilon(\text{L1\_CMUP6\_PT4}) \times \epsilon(\text{offline})}{\epsilon(\text{offline})} \tag{5.1}$$

This trigger selects single 4 GeV/c muons. The L1 efficiency was measured using the unbiased legs of J/ψ events that came in on the CMUP8 trigger, and sideband subtraction was used to ensure a clean sample of muons (Figure 5.1). The CMUP8 trigger is described in section 4.2.2. We only examine runs that have good run bits set for run control, online, L1, L3, and the CLC, offline reconstruction, and COT, CMU, and CMP offline. One leg of the J/ψ is required to be an offline 8 GeV/c CMUP muon. To ensure that this muon actually fired the CMUP8 trigger at all levels, we require that the the offline track be matched to an XFT track with a momentum of at least 8 GeV/c, that the offline CMU and CMP stubs are matched with online CMU and CMP stubs, that the XTRP extrapolated a high p_T track to the CMU stub, and that the L1 CMP stub was extrapolated back to the CMU stub.

If the muon passes these criteria, it is consider the biased muon for the purposes of this measurement. The other J/ψ leg is a potential probe track, which must satisfy the following criteria (in addition to having a dimuon mass within the signal window defined below) to enter the denominator of our measurement:

- The offline muon must be a CMUP muon with a CMU $\chi^2 < 9$
- The offline CMU $dX < 15$ cm and offline CMP $dX < 20$ cm
- The $\Delta\phi_{CMU}$ between the probe and triggered muons must be at least 5°, to avoid overlapping hits in the muon chambers.
- The $\Delta\phi_{SL6}$ between the probe and triggered muons must be at least 2.5°, to avoid overlapping in the XFT.
- The offline muon $p_T > 4$ GeV/c.
- The track $|\eta| < 0.6$
- The track must not cross the spacer in the axial superlayers and must stay within the fiducial volume of the COT for all 8 Superlayers.
- The probe track must have at least 5 hits on each of two axial COT superlayers and each of two stereo COT superlayers.

- The probe track must have a $|z_0| < 47.25$ cm.
- The $|\Delta z_0|$ between the legs of the J/ψ must be less than 5 cm.
- The track of the offline muon is extrapolated out the the CMU and CMP by assuming the muon travels in a straight line after exiting the COT. We require that, when extrapolated out to the CMU, the track have a $|z_{CMU}| < 220$ cm and that for $z_{CMU} < 0$, the predicted stub not fall between 255° and 270° of ϕ_{CMU}, due to problems in that wedge of the CMU in our running period. We also require that the projected $|z_{CMP}| < 310$ cm.

To get into the numerator of the measurement, the probe muon must pass the following cuts:

- The offline probe muon track must be matched to an XFT track with a p_T of at least 4 GeV/c.
- The offline probe muon CMU stub must be associated with a high p_T L1 CMU stub
- The offline probe muon CMP stub must be associated with a L1 CMP stub.
- The XTRP must extrapolate a high p_T track to the L1 CMU stub associated with the offline muon.
- The muon matchbox must extrapolate a CMP stub back to the L1 CMU stub associated with the offline muon.

The workings of the XFT, XTRP, and Matchbox in the level 1 trigger have been described in section 3.5. The XFT and offline tracks are matched by requiring that the $|\delta(1/p_T)| < 0.1$ (GeV/c)$^{-1}$ and that the $|\delta(\phi_{SL6})| < 0.5°$. For the CMU stub matching, the offline CMU stub must have a hit in a tower that was also set online in the L1 Muon and which had an track with a $p_T > 4$ GeV/c extrapolated to it by the XTRP. For the CMP stub matching, we require at least one of the CMP towers associated with the muon be fired at L1, and that a CMP tower be extrapolated back to the appropriate CMU tower. If both J/ψ muons meet the criteria for a biased muon, then both are considered unbiased with respect to the other muon and are used as probe muons in this measurement.

We then check the mass of the J/ψ for sideband subtraction. The mass signal window for this measurement is between 3.0216 GeV/c^2 and 3.1655 GeV/c^2, and the sideband region is between 2.9016 GeV/c^2 and 2.9736 GeV/c^2 and between 3.2136 GeV/c^2 and 3.2856 GeV/c^2. There are 2008 probe tracks in the signal sample, of which 1833 passed, and there are 113 tracks in the sidebands, of which 104 passed. The efficiency is calculated bin by bin using the formula

$$\epsilon = \frac{N_{passingsignal} - N_{passingsideband}}{N_{totalsignal} - N_{totalsideband}} \tag{5.2}$$

and the errors, σ_ϵ, on the efficiency are given by

$$\sigma_\epsilon^2 = \frac{\epsilon(1-\epsilon)}{N_{totalsignal} - N_{totalsideband}} + \frac{2(N_{passingsideband}(1-2\epsilon) + N_{totalsideband}\epsilon^2)}{(N_{totalsignal} - N_{totalsideband})^2} \tag{5.3}$$

It was found that the efficiency depends on $1/p_T$ (curvature) and the absolute value of η of the muon ([12],[50],[51]). The shape of the efficiency curve vs. $1/p_T$ is given by

$$\epsilon = \epsilon_{plateau} \times \mathrm{erf}((1/p_{T50} - 1/p_T)/\sigma_{1/p_T}) \tag{5.4}$$

where $\epsilon_{plateau}$ is the plateau efficiency, p_{T50} is the value for transverse momentum where the efficiency falls to 50%, and σ_{1/p_T} is indicative of the trigger's momentum resolution. The erf term refers to the error function, defined as:

$$\mathrm{erf}(x) = \frac{1}{\sqrt{2\pi}} \int_{-\infty}^{x} e^{-u^2/2} du \tag{5.5}$$

The efficiency increases with increasing $|\eta|$, but is asymmetric due to the aging that took place in the COT during this period (Section 3.2.2). We believe that the shape of the efficiency curve with respect to $1/p_T$ is independent of η, and vice versa. To take advantage of this, we propose to parameterize the efficiency in the following manner. First, we find the efficiency of the L1 CMUP4 trigger vs. η for tracks with a $p_T > 4.45$ GeV/c, which is above the turn on curve for the trigger (Figure 5.2). Then, we find the efficiency for the muons binned in both η and p_T, weight the efficiency in each bin according by its efficiency vs *eta*, and sum over the eta bins to get the efficiency vs. $1/p_T$, using the formula:

$$\epsilon^j_{1/p_T} = \frac{\sum_{i=1}^{N_\eta} \epsilon^{i,j}_{1/p_T,\eta} / (\epsilon^i_\eta \sigma^{i,j2}_{1/p_T,\eta})}{\sum_{i=1}^{N_\eta} 1/\sigma^{i,j2}_{1/p_T,\eta}} \tag{5.6}$$

and

$$1/\sigma^{j2}_{1/p_T} = \sum_{i=1}^{N_\eta} \frac{1}{\sigma^{i,j2}_{1/p_T,\eta}} \tag{5.7}$$

The bin centers were weighted to reflect the distribution of track $1/p_T$ within each bin, and a χ^2 binned fit is performed to get the values of $\epsilon_{plateau}$, p_{T50}, and σ_{1/p_T} (Figure 5.3). We find that $\epsilon_{plateau} = 1.0150$, $1/p_{T50} = 0.25637$ (GeV/c)$^{-1}$, and $\sigma_{1/p_T} = 0.21089$ (GeV/c)$^{-1}$. The error matrix can be found in table 5.1. To get the efficiency of a track with a given p_T and η the efficiency is found by plugging the p_T into the formula above using the values of $\epsilon_{plateau}$, p_{T50}, and σ_{1/p_T} from the fit and multiplying by the efficiency of

the plateau in the η bin of the track.

Of course, we must show that it is reasonable that the effects of changing $1/p_T$ and η on the efficiency are separable in this manner. We show this in three ways. First, we plot the efficiency of the L1 CMUP4 trigger vs. $1/p_T$ both before and after the adjustment is made, showing that the fitted curves have values of p_{T50}, and σ_{1/p_T} that agree within error (Figure 5.4). Next, we plot ϵ vs. $1/p_T$ for $-0.6 < \eta < -0.2$, $-0.2 < \eta < 0.2$, and $0.2 < \eta < 0.6$, showing the tracks both with and without the plateau efficiencies adjusted to 1 (Figure 5.5). We see that after the adjustment, the turn-on curves for the three plots agree reasonably well within errors. Lastly, we plot ϵ vs. $1/p_T$ both for the TCMD bank finding the muon stub and for the XFT finding the track (Figure 5.6). Because the amount of material the μ must pass through to get to the CMU depends on η, we would expect that if there were an unfactorizable contribution to the efficiency, it would come from finding the CMU stub. However, we see that the efficiency for finding a CMU stub is flat with respect to $1/p_T$, with the turn on curve coming entirely from the XFT. These three results show that the L1 CMUP4 efficiency is factorizable into η and $1/p_T$ components.

During part the run period when this data was collected, there was a noticeable offset of the XFT beamspot with respect to the CDF beamspot, and the COT was suffering from the effects of aging, which also effected the XFT efficiency. To see if this effected the L1 efficiency, the efficiency was plotted against ϕ_{SL6} to look for a possible systematic error (Figure 5.7). There may be a small effect, however this is overwhelmed by the statistical errors on the data points so no systematic is assessed.

There is some concern that, since the tracking environment of $H_b \to \mu D^0 X$ events differs from that in J/ψ events, the L1_CMUP6_PT4 efficiency may not be the same. To address this concern, we examined the efficiency vs. the number of tracks with a p_T greater than 1.5 GeV/c in a cone of $\Delta\phi_0 < 30°$ (see Figure 5.8). It was found that the efficiency is at most only weakly dependent on the track isolation, so it should be possible to employ this measurement to muons in $H_b \to \mu D^0 X$ events.

The L1_CMUP6_PT4 efficiency has been found to be between 89% and 92% at the high p_T plateau, depending on value of $|\eta|$ of the track, with a higher efficiency at higher $|\eta|$. This has been accomplished using $J/\psi \to \mu^+\mu^-$ events collected on the CMUP8 trigger. The efficiency divided into bins based on the p_T and $|\eta|$ of the muon tracks with a reasonably small uncertainty in each bin. The efficiency was then parameterized in each $|\eta|$ bin by an error function dependent on $1/|p_T|$. The efficiency has been found to be independent of other variables.

5.3 L2 efficiency

For this measurement, we need the efficiency of the L2_SVT_PT2_D120_CMUP6_PT4 trigger. This trigger requires a CMUP4 trigger in L1 and an SVT track with a p_T greater than 2 GeV/c and a d_0 between 120 μm and 1 mm at L2. The muon in level 2 is the same muon that fired the trigger at level 1. All that happens at level 2 is that the event is examined for an SVT track with an impact parameter between 120 μm and 1 mm and a p_T greater than 2 GeV/c. The SVT uses tracks found by the XFT at level 1 as seeds to look for tracks in the SVX, so to get an SVT track an XFT track must first be found. The efficiency that we wish to measure is:

$$\frac{\epsilon_{\text{SVT\_PT2\_D120}} \times \epsilon_{\text{XFT}} \times \epsilon_{\text{L1\_CMUP6\_PT4}} \times \epsilon_{\text{offline\_MUON}} \times \epsilon_{\text{offline\_SVX}} \times \epsilon^2_{\text{offline\_COT}}}{\epsilon_{\text{L1\_CMUP6\_PT4}} \times \epsilon_{\text{offline\_MUON}} \times \epsilon_{\text{offline\_SVX}} \times \epsilon^2_{\text{offline\_COT}}} \tag{5.8}$$

Unfortunately, there is not sample of tracks that is unbiased with respect to both XFT and SVT that is large enough to measure this efficiency all at once. Therefore, we take advantage of the fact that one must have an XFT track to get an SVT track by first finding the XFT efficiency for tracks that feed into the SVT trigger, and then in a separate sample find the SVT efficiency of a track given that an XFT track has already been found. Note that the XFT efficiency that we are now measuring is not the same as that measured for the L1_CMUP6_PT4 trigger; in particular, for that measurement we required that the offline and XFT p_T be greater than 4 GeV/c while for this measurement the offline p_T must be greater than 2 GeV/c and the XFT only needs to find the track. In terms of efficiency formulas, we now wish to find:

$$\frac{\epsilon_{\text{XFT}} \times \epsilon_{\text{L1\_CMUP6\_PT4}} \times \epsilon_{\text{offline\_MUON}} \times \epsilon_{\text{offline\_SVX}} \times \epsilon^2_{\text{offline\_COT}}}{\epsilon_{\text{L1\_CMUP6\_PT4}} \times \epsilon_{\text{offline\_MUON}} \times \epsilon_{\text{offline\_SVX}} \times \epsilon^2_{\text{offline\_COT}}} \tag{5.9}$$

and

$$\frac{\epsilon_{\text{SVT\_PT2\_D120}} \times \epsilon_{\text{XFT}} \times \epsilon_{\text{L1\_CMUP6\_PT4}} \times \epsilon_{\text{offline\_MUON}} \times \epsilon_{\text{offline\_SVX}} \times \epsilon^2_{\text{offline\_COT}}}{\epsilon_{\text{XFT}} \times \epsilon_{\text{L1\_CMUP6\_PT4}} \times \epsilon_{\text{offline\_MUON}} \times \epsilon_{\text{offline\_SVX}} \times \epsilon^2_{\text{offline\_COT}}} \tag{5.10}$$

As equations 5.9 and 5.10 multiplied together give equation 5.8.

The measurements that are actually made are somewhat different. For part one, we use events that came in on the B_CHARM_LOWPT_L1_DPS trigger. We do this because, due to aging, the XFT efficiency is different for π and K, and three-body decays that came in on the B_CHARM_LOWPT_L1_DPS are the only sufficiently large source of pure π and K available. This should not make a large difference, since in both

cases we are for the most part examining tracks that originated in a B decay. For part two, we use events that came in on the CMUP8 trigger, using the non-muon tracks in the events as probe tracks. The trigger does not use silicon, so the tracks are unbiased with respect to the SVT. The environment is harder than in the average CMUP4 event, but the requirement in the μSVT trigger for a second track tends to make those event harder that the one that come in on the CMUP4 prescaled trigger.

5.3.1 XFT Efficiency

The XFT measurement is complicated by the fact that, due to aging, the XFT efficiency for pions and kaons are different. This means that pure samples of pions and kaons are needed to measure the relevant efficiencies. These samples are obtained by reconstructing the decays $D^+ \to K^-\pi^+\pi^+$ and $D^+_{(s)} \to \phi^0\pi^+$, $\phi^0 \to K^+K^-$ (and charge conjugate decays) using events that came in on either the B_CHARM_LOWPT_L1_DPS trigger. The requirements for this trigger are outlined in section 4.2.3. We require two of the tracks from the D^+ decay to fulfill the trigger requirements, and use the third track as the probe track in our measurement. Despite the dynamic prescale, which varies between 250 and 1, we use events from this trigger because it has no opposite charge requirement. We only examine runs that have good run bits set by run control and the shift crew, as well as for online L1, L2, L3, SVT, SVX and the CLC, offline reconstruction, and COT, CMU, and CMP offline. To make it into the denominator of our sample, the probe track must have the following properties:

- The mass of the $D^+ \to K^-\pi^+\pi^+$ must fall between 1.84374 and 1.89126 GeV/c^2. Sideband subtraction is used (Figure 5.9).
- The mass of the $D^+_{(s)}$ from the $D^+_{(s)} \to \phi^0\pi^+$, $\phi^0 \to K^+K^-$ decay must fall between either 1.84943 and 1.88678 GeV/c^2 (for the D^+) or between 1.94733 and 1.98636 GeV/c^2 (for the D^+_s). Sideband subtraction is used. We require that the ϕ^0 in the decay have a mass between 1.0144 and 1.0256 GeV/c^2. See Figures 5.10 and 5.11.
- In order to further reduce the possibility of a misassigned charge in the $D^+_{(s)} \to \phi^0\pi^+$, $\phi^0 \to K^+K^-$ decay, we require that the event have one and only one $D^+_{(s)}$ decay that passes both the trigger requirement and the mass cut on the ϕ^0.
- The p_T of the probe track must be greater than 2 GeV/c
- $|\eta| < 1$
- $|z_0| < 47.25$ cm

- The track must not cross the spacer in the axial superlayers and must stay within the fiducial volume of the COT for all 8 Superlayers.
- The probe track must have at least 5 hits on each of two axial superlayers and each of two stereo superlayers.
- The track must be the highest p_T track within 2.5° of ϕ at superlayer 6. We also do not use the track if either of the other tracks from the D decay was within 2.5° of ϕ at superlayer 6, regardless of their relative momenta.

In order to make it into the numerator of this measurement, the probe track must also be found by the XFT. The XFT and offline tracks are matched by requiring that the $|\delta(1/p_T)| < 0.1$ (GeV/c)$^{-1}$ and that the $|\delta(\phi_{SL6})| < 0.5°$, just as in section 5.2. The XFT finds tracks down to 1.5 GeV/c, but since the SVT examined all XFT tracks, we simply require that a track was found without demanding the XFT p_T be greater than 2 GeV/c.

This measurement is separated into two run ranges. The first run range, encompassing the runs between 152636 and 158000, contains all the runs between the beginning of 1-miss XFT until the shutdown. The second run range, running from 158000 and 163117, contains all the post-shutdown data in our sample. We parameterize the efficiency in terms of inverse p_T and $|\eta|$ in the first run range. We examined the efficiency with respect to ϕ_{SL6} for both π and K in the first run range (Figure 5.12), and found in the efficiency was roughly flat with respect to ϕ_{SL6} for π and only a very weak dependence for K. However, given that the effect is small and we expect the events to be uniformly distributed in ϕ_{SL6}, we do not parameterize the efficiency in ϕ_{SL6} for either π or K in the first run range. In the second run range, the effects of the COT aging and an offset in the XFT beamspot are great enough that we also take ϕ_{SL6} into account. In the first run range, a linear fit is performed in $1/p_T$ with bin centers weighted to reflect the distribution of $1/p_T$ in each bin for each of the $|\eta|$ bins (Figures 5.13 and 5.14). After getting the efficiencies with respect to $1/p_T$, we use a linear extrapolation in $|\eta|$ to get the true efficiency for a given track (Figure 5.19). For the second run range, we divided the sample into two ϕ_{SL6} ranges, one for $225° < \phi_{SL6} < 345°$, and the other for $\phi_{SL6} < 225°$ or $345° < \phi_{SL6}$. In each ϕ_{SL6} and $|\eta|$ range, a linear fit is performed in $1/p_T$ with bin centers weighted to reflect the distribution of $1/p_T$ (Figures 5.15 through 5.18). After getting the efficiencies with respect to inverse p_T, we use a linear extrapolation in $|\eta|$ to get the true efficiency for a given track, but we do not extrapolate between ϕ_{SL6} ranges. The values for each fit and the associated error matrices are in tables 5.2 through 5.37.

We do not attempt to adjust the results to account for the dynamic prescale, which means that we are not evenly sampling our dataset. This may mean that there is a difference between the efficiency measured using this sample and our signal sample, which is unprescaled and therefore will have a higher fraction of high luminosity events. In order to account for this, we look at events that came in on the unprescaled B_CHARM_HIGHPT trigger. This trigger has an opposite charge requirement, so we cannot use $D^+ \to K^-\pi^+\pi^+$ to measure the K efficiency. However, we can make a measurement of the π XFT efficiency using this sample, putting the same numerator and denominator requirements on the track as listed above, except requiring that two of the legs meet the B_CHARM_HIGHPT requirements. We can use this to check the luminosity dependence of the XFT trigger in our run range by measuring the pion efficiency in this sample for the periods in which the prescale of the B_CHARM_LOWPT_L1_DPS was greater than one, and for when the B_CHARM_LOWPT_L1_DPS had a prescale of 1 (Figure 5.20). This shows only a very small difference in efficiency. Additionally, we check the XFT efficiency versus track isolation, as a large drop in efficiency as the number of tracks increases might indicate that there would be luminosity dependence, but again we see little effect (Figure 5.21). Therefore, we assess a -0.5% systematic to account for any luminosity dependence in the efficiency.

In the second run range, there is a z-dependence in the COT aging which leads to a slight asymmetry between positive and negative η. In order to account for this, we assign a $\pm 0.5\%$ systematic uncertainty to the efficiencies in the second run range. We looked for a similar dependence in the earlier run ranges, but saw none (Figure 5.22).

Lastly, we note that in figure 5.11, there is a small bump in the $\phi^0\pi^+$ mass distribution just above the D_s^+ peak. By looking at events that were reconstructed both in the $\phi^0\pi^+$ and $K^-\pi^+\pi^+$ distributions, we see that there is a small $D^+ \to K^-\pi^+\pi^+$ reflection (with a π being misreconstructed as a K) of about 1500 events in the $\phi^0\pi^+$ distribution, peaking around 2.03 GeV/c^2. As our high sideband region runs from 1.9994 to 2.0189 GeV/c^2, there is some of the tail of this distribution in our sidebands. This is a concern because if there is an excess of pions in the kaon background, it could result in the measured kaon efficiency being lower than the true efficiency. However, we see that there are only 725 events in the sideband region that, when one track assigned the K mass is instead assigned the π mass, fall within 3σ of the D^+ peak. However, there is a large background beneath the D^+ peak, and only about 20% of the events in that 3σ window are actually D^+ events. So we believe that the excess is at most about 145 events over our entire sample. In comparison, there are about 130,000 K tracks after sideband subtraction, so at most this could be a 0.1% effect. We consider this negligible and do not assign a systematic (Figure 5.23).

5.3.2 SVT Efficiency

Like the L1 measurement, the SVT measurement is made using the CMUP8 sample (section 4.2.2). We are using the CMUP8 sample because it provides a large number of tracks that are not biased with respect to the SVT and have kinematics somewhat similar to those in the μ+SVT events. We only examine runs that have good run bits set by run control and the shift crew, as well as for online L1, L2, L3, SVT, SVX and the CLC, offline reconstruction, and COT, CMU, and CMP offline. To get into the denominator of our measurement, we require that each track in the sample pass the following requirements:

- The event must have a muon with an offline $p_T > 8$ GeV/c that also fired the L1 CMUP4 trigger and had an XFT $p_T > 8$ GeV/c.
- The probe track must have a 0.035 rad $< \Delta\phi_0 <$ 1.57 rad and the invariant mass of the track+muon must be less than 5 GeV/c^2, assuming the pion mass for the track.
- $p_T > 2$ GeV/c.
- The probe track must have at least 5 hits on each of two axial superlayers and each of two stereo superlayers.
- The probe track must be matched an XFT track (with the same criteria as detailed above), and the track must have the greatest transverse momentum of any track within $\Delta\phi_{SL6} < 2.5°$, in order to avoid fratricide in the XFT.
- $|\eta| < 1.0$ (Figure 5.24 shows the efficiency vs. $|\eta|$.)
- The probe track must not cross the spacer in the axial superlayers and must stay within the fiducial volume of the COT for all 8 Superlayers.
- All SVX electrical barrel crossers and wedge crossers were excluded. This was done by requiring all denominator tracks to have all of their hits in a single wedge and electrical barrel.
- The track must have been associated with SVX hits in all four SVX layers used by the SVT.
- $120\mu\text{m} < |d_0 - 8\mu\text{m}| < 850\mu\text{m}$
- $|z0| < 47.25$ cm
- The SiExpected method [52] from the TrackingSI method was used to predict which layers of the silicon would be crossed by the track. We require that SiExpected predict that the track not cross

any electrical barrel or wedge boundary. We also require that SiExpected predict that the track pass through all for SVX layers in the SVT, and that those layers must be integrated according to the database. We found that some layers used in the SVT which the database said were integrated had 0 or close to 0 efficiency, and tracks passing through these layers were also excluded. A list of these layers is provided in table 5.38.

- The efficiency was found to drop near the edges of the mechanical barrels and wedges. Therefore, regions near mechanical barrel and wedge boundaries were excluded to eliminate areas where the efficiency was changing rapidly (Figure 5.24 shows the efficiencies for the included sections). The excluded sections in $\phi_{r=8cm}$ were
  - $8.75° < \phi_{r=8cm} < 18.75°$
  - $42.5° < \phi_{r=8cm} < 50°$
  - $70° < \phi_{r=8cm} < 77.75°$
  - $103.75° < \phi_{r=8cm} < 107.5°$
  - $132.5° < \phi_{r=8cm} < 138.75°$
  - $161.25° < \phi_{r=8cm} < 171.25°$
  - $191.25° < \phi_{r=8cm} < 197.5°$
  - $216.25° < \phi_{r=8cm} < 230°$
  - $251.25° < \phi_{r=8cm} < 256.25°$
  - $282.5° < \phi_{r=8cm} < 287.5°$
  - $310° < \phi_{r=8cm} < 321.25°$
  - $340° < \phi_{r=8cm} < 348.75°$

  The excluded sections in $z_{r=8cm}$ were
  - $-45cm < z_{r=8cm}$
  - $-17cm < z_{r=8cm} < -15cm$
  - $15cm < z_{r=8cm} < 18cm$
  - $z_{r=8cm} < 45cm$.

Our sample contains a little over 71,000 tracks which meet all these requirements. To get into the numerator of the measurement, the track had to additionally satisfy the following criteria:

- The offline track had to be matched to a SVT track[53] with a matching $\chi^2 < 25$.
- The track p_T of the matched SVT track had to be greater than 2 GeV/c
- The SVT $|d_0|$ had to be between 120 μm and 1000 μm.
- The SVT $\chi^2 < 25$.

The reason for the asymmetric cut on SVX d_0 has to do with the way the SVT rounds the impact parameter when it sends the track information to the L2 processor. The SVT granularity is 10 microns, and it appears that the SVT rounds the impact parameter down. This means that the -120 μm bin has tracks with impact parameters between -111 and -120 microns, while the 120 μm bin has tracks with between 120 and 129 microns. This means that there are more tracks trigger with negative d_0 than with positive d_0. Due to the statistical limitations of our sample, we wish to parameterize the efficiency in terms of absolute d_0, so we have dealt with this asymmetry in the SVT d_0 by making our SVX d_0 range asymmetric (Figure 5.25).

For the purposes of the $H_b \to \mu D^0 X$ cross-section measurement, we wish to avoid regions in $|d_0 - 8\mu\text{m}|$ where there are poor statistics and the efficiency is rapidly changing. For this reason, we plan to exclude $|d_0 - 8\mu\text{m}|$ turn-off region. Examining figure 5.26, we choose to place our cut off at 850 microns.

Also, we found that the SVT efficiency has a dependence on the track environment. In particular, the efficiency was seen to decrease as more tracks were found within a $\Delta\phi_{r=8cm} < 5^\circ$ of the probe track. We do not, however, want to cut tracks in high occupancy environments from our sample, as this would kinematically bias our signal sample in ways that are difficult to take into account. Instead, we define the variable ISO as being the number of tracks with a $p_T > 400$ MeV/c that are within 5° of the probe track at a radius of 8 cm, and measure the SVT efficiency with respect to this variable.

The resulting efficiency was divided into 11 bins of p_T and 10 bins of $|d_0 - 8\mu\text{m}|$, and 16 bins of ISO. There were 1194 bins with tracks. We use a three dimensional fit of the form

$$\epsilon = (\epsilon_0 + \epsilon_{1p_T}\frac{1}{p_T} + \epsilon_{1d0}|d_0 - 8\mu\text{m}| + \epsilon_{2d0}|d_0 - 8\mu\text{m}|^2 + \epsilon_{ISO}ISO) \times \text{erf}(\frac{1/p_{T50} - 1/p_T}{\sigma_{pT}}) \times \text{erf}(\frac{|d_0 - 8\mu\text{m}| - d_{50+}}{\sigma_{d0+}}) \tag{5.11}$$

Where ϵ is the efficiency, ϵ_0 is the plateau efficiency, p_{T50} is the transverse momentum at which the efficiency is 1/2 the plateau efficiency with d_0 and ISO held constant, σ_{pT} indicates the width of the turn on region, d_{50+} indicates where on the turn on curve the efficiency is 1/2 the plateau efficiency with p_T and ISO held constant, σ_{d0+} indicates the width of the turn on region, and erf refers to the error function, defined in equation 5.5. The terms ϵ_{1p_T}, ϵ_{1d0}, and ϵ_{2d0} have been added to account for the fact that the plateau is not well fit by a flat line. The ϵ_{ISO} term accounts for the effect of the isolation on the SVT efficiency. The

bin centers were weighted to reflect the average value of inverse p_T and $|d_0 - 8\mu\text{m}|$ in each bin. The fitted values and associated error matrix can be found on tables 5.39 and 5.40. Figures B.1 through B.18 show the SVT efficiency versus impact parameter for the various slices in ISO and p_T, with sections of the three dimensional fit laid over the points. Similarly, figures B.19 through B.36 show the SVT efficiency versus $1/p_T$ for the slices in ISO and $|d_0 - 8\mu\text{m}|$, with sections of the three dimensional fit laid over the points. Next, figures B.37 through B.66 show the SVT efficiency versus ISO for the slices in $1/p_T$ and $|d_0 - 8\mu\text{m}|$, with sections of the three dimensional fit laid over the points.

It is worth noting that in previous attempts to measure this efficiency, we used muons from $J/\psi \to \mu^+\mu^-$ decays that were recorded on the CMU-CMU and CMU-CMX triggers. The numerator and denominator cuts were the same as listed above, except that we place a $\pm 3\sigma$ cut on the J/ψ invariant mass and used sideband subtraction to get a pure muon sample, and there was no $\Delta\phi_0$ cut between the muon tracks. However, when we compared the efficiency obtained from this sample to the efficiency obtained from the CMUP8 sample, we saw that the efficiency was much higher in the J/ψ sample (Figure 5.27). This was because we were not examining ISO; at the time, we were only looking at $1/p_T$ and d_0. We then plotted the efficiency on the $1/p_T$ and d_0 plateaus for both samples vs. ISO and as seen in figure 5.28 they agree to within statistical error. The muon tracks in the J/ψ sample tend to be more isolated than the tracks in the CMUP8 sample, and thus have a higher average efficiency. Examining the ISO distributions of tracks from the the J/ψ, CMUP8, and B semileptonic sample (which is our signal sample), we see that the distribution from signal sample falls between that of the CMUP8 and J/ψ samples (Figure 5.29). Also, the CMUP8 sample has better statistics than the J/ψ sample. Therefore, we chose to use the CMUP8 sample rather than the J/ψ for our measurement. (We chose not to use both to avoid situations where the event fired both the CMUP8 trigger and the J/ψ trigger.)

The measurement of the L2_SVT_PT2_D120_CMUP6_PT4 efficiency has been broken into two parts, one for the XFT efficiency of the tracks which feed into the SVT trigger, and the other for the SVT efficiency with respect to the XFT+offline. The XFT efficiency was measured using events that came in on the L3 B_CHARM_LOWPT_L1_DPS trigger. This efficiency was binned according to p_T, $|\eta|$, and run number, as well as ϕ_{SL6} in the second run range. The errors on the efficiency in each of the bins were reasonably small, and the efficiency was parameterized by either linear fit in $1/|p_T|$ in each $|\eta|$ bin. The SVT efficiency was measured using events that came in on the CMUP8 trigger. This efficiency was binned according to p_T, track isolation, and d_0. The errors on the efficiency in each of the bins were reasonably small, and the efficiency was parameterized by a three dimensional fit.

5.4 L3 Efficiency

The L3 trigger used in this analysis is the B_SEMI_CMUP4_TRACK2_D120 trigger, or L3 μSVT trigger. We only examine runs that have good run bits set by run control and the shift crew, as well as for online L1, L2, L3, SVT, SVX and the CLC, offline reconstruction, and COT, CMU, and CMP offline. We need to get the efficiency of this trigger relative to the L1 and L2 triggers plus offline:

$$\frac{\epsilon(\text{B\_SEMI\_CMUP4\_TRACK2\_D120}) \times \epsilon(\text{SVT\_PT2\_D120}) \times \epsilon(\text{XFT}) \times \epsilon(\text{L1\_CMUP6\_PT4}) \times \epsilon(\text{offline})}{\epsilon(\text{SVT\_PT2\_D120}) \times \epsilon(\text{XFT}) \times \epsilon(\text{L1\_CMUP6\_PT4}) \times \epsilon(\text{offline})} \tag{5.12}$$

To get the efficiency, we use events that came in on the B_SEMI_L3PS20_L2_TRK2_D120_L1_CMUP6_PT4 trigger, described in section 4.2.4. For an event to make it into the denominator of our measurement, there must be an offline CMUP muon and a second offline track matched to an SVT track, where the CMUP muon satisfies all the L1 numerator and denominator cuts and the second track satisfies all the L2 numerator and denominator cuts. To enter the numerator of the measurement, the B_SEMI_CMUP4_TRACK2_D120 trigger must have fired. Note that in the runs used in this analysis, there was no SVX reconstruction in L3; the impact parameter of the track was gotten by matching a L3 COT track with an SVT track. Examining the kinematic distributions of the CMUP muon and the second track, we find that there is a sharp but present turn-on curve at low transverse momentum for both tracks. We fit this efficiency distribution two a two dimensional fit in the inverse p_T of the muon and the inverse p_T of the second track, using the error function to characterize the turn on curves:

$$\epsilon = \epsilon_{plateau} \times \text{erf}(\frac{1/p_{T\mu 50} - 1/p_T}{\sigma_{1/p_{T\mu}}}) \times \text{erf}(\frac{1/p_{TSVT50} - 1/p_T}{\sigma_{1/p_{TSVT}}}) \tag{5.13}$$

The results of the binned fit to the data give $\epsilon_{plateau} = 0.97066$, $1/p_{T\mu 50} = 0.25092$ $(1/(\text{GeV}/c))$, $\sigma_{1/p_{T\mu}} = 0.0055054$ $(1/(\text{GeV}/c))$, $1/p_{TSVT50} = 0.50143$ $(1/(\text{GeV}/c))$ and $\sigma_{1/p_{TSVT}} = 0.0061269$ $(1/(\text{GeV}/c))$. The bin centers used in the fit were weighted to reflect the average values of the inverse muon and SVT track p_T. The error matrix associated with the fit can be found in table 5.41, and the efficiency is plotted against the μ and SVT $1/p_T$ in figures 5.30 through 5.34.

5.5 Summary

The efficiency of the B Semileptonic trigger path has been measured using data taken in the run range 152636 to 163117. The level 1 L1_CMUP6_PT4 was found using J/ψ events that came in on the CMUP8

trigger. The level 2 L2_SVT_PT2_D120_CMUP6_PT4 efficiency was measured in two parts using $D^+ \to K^-\pi^+\pi^+$ and $D^+_{(s)} \to \phi^0\pi^+$, $\phi^0 \to K^+K^-$ that came in on the B_CHARM_LOWPT_L1_DPS trigger for the XFT half of the efficiency, and events that came in on the CMUP8 trigger for the SVT section. The level 3 B_SEMI_CMUP4_TRACK2_D120 trigger efficiency was determined using the events from the B_SEMI_L3PS20_L2_TRK2_D120_L1_CMUP6_PT4 trigger. These efficiencies were binned according to p_T, η, ϕ, run number, isolation, or impact parameter as appropriate, an had reasonably small error bars in most bins. These efficiencies were then parameterized using polynomial fits or fits to the error function.

$\chi^2/ndf = 10.273/5$	$\epsilon_{plateau}$	$1/p_{T50}$ (1/(GeV/c))	σ_{1/p_T} (1/(GeV/c))
$\epsilon_{plateau}$	0.41331E-04	0.27925E-05	0.78373E-05
$1/p_{T50}$ (1/(GeV/c))	0.27925E-05	0.19652E-04	0.24122E-04
σ_{1/p_T} (1/(GeV/c))	0.78373E-05	0.24122E-04	0.34976E-04

Table 5.1: The error matrix returned by the binned fit to the L1 efficiency vs $1/p_T$ of equation 5.4 after the L1 efficiency vs $1/p_T$ was reweighted by the L1 efficiency vs. η.

Here are the fitted values for the L2 XFT efficiency measurement in the first run range for π:

$$\epsilon = b + m * (1/p_T) \tag{5.14}$$

$\|\eta\|$ range	b	m (GeV/c)
0 to 0.2	0.96570	-0.16684
0.2 to 0.4	0.97083	-0.10890
0.4 to 0.6	0.98004	-0.058907
0.6 to 0.8	0.99474	-0.038996
0.8 to 1.0	1.0140	-0.070710

Table 5.2: The values returned by binned fits to the L2 XFT efficiency in the various $|\eta|$ bins for the first run range for π.

$\chi^2/ndf = 5.3437/9$	b	m (GeV/c)
b	0.24689E-03	-0.77989E-03
m (GeV/c)	-0.77989E-03	0.27849E-02

Table 5.3: The error matrix returned by binned fit to the L2 XFT efficiency for $0 < |\eta| < 0.2$ bin for the first run range for π.

$\chi^2/ndf = 15.763/9$	b	m (GeV/c)
b	0.17053E-03	-0.54354E-03
m (GeV/c)	-0.54354E-03	0.19636E-02

Table 5.4: The error matrix returned by binned fit to the L2 XFT efficiency for $0.2 < |\eta| < 0.4$ bin for the first run range for π.

$\chi^2/ndf = 7.4666/9$	b	m (GeV/c)
b	0.12573E-03	-0.39069E-03
m (GeV/c)	-0.39069E-03	0.13594E-02

Table 5.5: The error matrix returned by binned fit to the L2 XFT efficiency for $0.4 < |\eta| < 0.6$ bin for the first run range for π.

$\chi^2/ndf = 11.194/9$	b	m (GeV/c)
b	0.83395E-04	-0.26584E-03
m (GeV/c)	-0.26584E-03	0.95155E-03

Table 5.6: The error matrix returned by binned fit to the L2 XFT efficiency for $0.6 < |\eta| < 0.8$ bin for the first run range for π.

$\chi^2/ndf = 13.031/9$	b	m (GeV/c)
b	0.11778E-03	-0.36882E-03
m (GeV/c)	-0.36882E-03	0.12943E-02

Table 5.7: The error matrix returned by binned fit to the L2 XFT efficiency for $0.8 < |\eta| < 1.0$ bin for the first run range for π.

Here are the fitted values for the L2 XFT efficiency measurement in the first run range for K:

$$\epsilon = b + m * (1/p_T) \tag{5.15}$$

$|\eta|$ range	b	m (GeV/c)
0 to 0.2	0.89077	-0.35974
0.2 to 0.4	0.94397	-0.37938
0.4 to 0.6	0.96628	-0.23526
0.6 to 0.8	0.98017	-0.11753
0.8 to 1.0	1.0195	-0.15335

Table 5.8: The values returned by binned fits to the L2 XFT efficiency in the various $|\eta|$ bins for the first run range for K.

$\chi^2/ndf = 11.492/9$	b	m (GeV/c)
b	0.36177E-03	-0.10459E-02
m (GeV/c)	-0.10459E-02	0.33373E-02

Table 5.9: The error matrix returned by binned fit to the L2 XFT efficiency for $0 < |\eta| < 0.2$ bin for the first run range for K.

$\chi^2/ndf = 6.0023/9$	b	m (GeV/c)
b	0.26390E-03	-0.76740E-03
m (GeV/c)	-0.76740E-03	0.24694E-02

Table 5.10: The error matrix returned by binned fit to the L2 XFT efficiency for $0.2 < |\eta| < 0.4$ bin for the first run range for K.

$\chi^2/ndf = 7.2276/9$	b	m (GeV/c)
b	0.17330E-03	-0.50174E-03
m (GeV/c)	-0.50174E-03	0.16073E-02

Table 5.11: The error matrix returned by binned fit to the L2 XFT efficiency for $0.4 < |\eta| < 0.6$ bin for the first run range for K.

$\chi^2/ndf = 6.2596/9$	b	m (GeV/c)
b	0.14826E-03	-0.42465E-03
m (GeV/c)	-0.42465E-03	0.13294E-02

Table 5.12: The error matrix returned by binned fit to the L2 XFT efficiency for $0.6 < |\eta| < 0.8$ bin for the first run range for K.

$\chi^2/ndf = 6.4377/9$	b	m (GeV/c)
b	0.19850E-03	-0.57173E-03
m (GeV/c)	-0.57173E-03	0.17853E-02

Table 5.13: The error matrix returned by binned fit to the L2 XFT efficiency for $0.8 < |\eta| < 1.0$ bin for the first run range for K.

Here are the fitted values for the L2 XFT efficiency measurement in the second run range for π with $\phi_{SL6} < 225°$ or $345° < \phi_{SL6}$ (the top of the detector):

$$\epsilon = b + m * (1/p_T) \tag{5.16}$$

$|\eta|$ range	b	m (GeV/c)
0 to 0.2	0.96487	-0.18079
0.2 to 0.4	0.98430	-0.13877
0.4 to 0.6	0.98919	-0.065533
0.6 to 0.8	0.97996	-0.0078088
0.8 to 1.0	0.98856	-0.0080328

Table 5.14: The values returned by binned fits to the L2 XFT efficiency in the various $|\eta|$ bins for π with $\phi_{SL6} < 225°$ or $345° < \phi_{SL6}$ (the top of the detector) in the second run range.

$\chi^2/ndf = 9.1179/9$	b	m (GeV/c)
b	0.20142E-03	-0.62395E-03
m (GeV/c)	-0.62395E-03	0.21811E-02

Table 5.15: The error matrix returned by binned fit to the L2 XFT efficiency for $0 < |\eta| < 0.2$ bin for π with $\phi_{SL6} < 225°$ or $345° < \phi_{SL6}$ (the top of the detector) in the second run range.

$\chi^2/ndf = 7.3388/9$	b	m (GeV/c)
b	0.15218E-03	-0.47115E-03
m (GeV/c)	-0.47115E-03	0.16354E-02

Table 5.16: The error matrix returned by binned fit to the L2 XFT efficiency for $0.2 < |\eta| < 0.4$ bin for π with $\phi_{SL6} < 225°$ or $345° < \phi_{SL6}$ (the top of the detector) in the second run range.

$\chi^2/ndf = 10.918/9$	b	m (GeV/c)
b	0.10089E-03	-0.31157E-03
m (GeV/c)	-0.31157E-03	0.10876E-02

Table 5.17: The error matrix returned by binned fit to the L2 XFT efficiency for $0.4 < |\eta| < 0.6$ bin for π with $\phi_{SL6} < 225°$ or $345° < \phi_{SL6}$ (the top of the detector) in the second run range.

$\chi^2/ndf = 13.345/9$	b	m (GeV/c)
b	0.91554E-04	-0.28507E-03
m (GeV/c)	-0.28507E-03	0.99516E-03

Table 5.18: The error matrix returned by binned fit to the L2 XFT efficiency for $0.6 < |\eta| < 0.8$ bin for π with $\phi_{SL6} < 225°$ or $345° < \phi_{SL6}$ (the top of the detector) in the second run range.

$\chi^2/ndf = 11.444/9$	b	m (GeV/c)
b	0.12363E-03	-0.37484E-03
m (GeV/c)	-0.37484E-03	0.12645E-02

Table 5.19: The error matrix returned by binned fit to the L2 XFT efficiency for $0.8 < |\eta| < 1.0$ bin for π with $\phi_{SL6} < 225°$ or $345° < \phi_{SL6}$ (the top of the detector) in the second run range.

Here are the fitted values for the L2 XFT efficiency measurement in the second run range for K with $\phi_{SL6} < 225°$ or $345° < \phi_{SL6}$ (the top of the detector):

$$\epsilon = b + m * (1/p_T) \tag{5.17}$$

$\lvert\eta\rvert$ range	b	m (GeV/c)
0 to 0.2	0.91265	-0.38628
0.2 to 0.4	0.92357	-0.30810
0.4 to 0.6	0.94896	-0.19148
0.6 to 0.8	0.97928	-0.15564
0.8 to 1.0	0.99607	-0.090003

Table 5.20: The values returned by binned fits to the L2 XFT efficiency in the various $|\eta|$ bins for K with $\phi_{SL6} < 225°$ or $345° < \phi_{SL6}$ (the top of the detector) in the second run range.

$\chi^2/ndf = 15.175/9$	b	m (GeV/c)
b	0.28800E-03	-0.82648E-03
m (GeV/c)	-0.82648E-03	0.26158E-02

Table 5.21: The error matrix returned by binned fit to the L2 XFT efficiency for $0 < |\eta| < 0.2$ bin for K with $\phi_{SL6} < 225°$ or $345° < \phi_{SL6}$ (the top of the detector) in the second run range.

$\chi^2/ndf = 9.1452/9$	b	m (GeV/c)
b	0.22882E-03	-0.65834E-03
m (GeV/c)	-0.65834E-03	0.20861E-02

Table 5.22: The error matrix returned by binned fit to the L2 XFT efficiency for $0.2 < |\eta| < 0.4$ bin for K with $\phi_{SL6} < 225°$ or $345° < \phi_{SL6}$ (the top of the detector) in the second run range.

$\chi^2/ndf = 9.0117/9$	b	m (GeV/c)
b	0.16097E-03	-0.45478E-03
m (GeV/c)	-0.45478E-03	0.14098E-02

Table 5.23: The error matrix returned by binned fit to the L2 XFT efficiency for $0.4 < |\eta| < 0.6$ bin for K with $\phi_{SL6} < 225°$ or $345° < \phi_{SL6}$ (the top of the detector) in the second run range.

$\chi^2/ndf = 2.6716/9$	b	m (GeV/c)
b	0.13141E-03	-0.37405E-03
m (GeV/c)	-0.37405E-03	0.11646E-02

Table 5.24: The error matrix returned by binned fit to the L2 XFT efficiency for $0.6 < |\eta| < 0.8$ bin for K with $\phi_{SL6} < 225°$ or $345° < \phi_{SL6}$ (the top of the detector) in the second run range.

$\chi^2/ndf = 9.3900/9$	b	m (GeV/c)
b	0.16213E-03	-0.46012E-03
m (GeV/c)	-0.46012E-03	0.14204E-02

Table 5.25: The error matrix returned by binned fit to the L2 XFT efficiency for $0.8 < |\eta| < 1.0$ bin for K with $\phi_{SL6} < 225°$ or $345° < \phi_{SL6}$ (the top of the detector) in the second run range.

Here are the fitted values for the L2 XFT efficiency measurement in the second run range for π with $225° < \phi_{SL6} < 345°$ (the bottom of the detector):

$$\epsilon = b + m * (1/p_T) \tag{5.18}$$

$\|\eta\|$ range	b	m (GeV/c)
0 to 0.2	0.95854	-0.30134
0.2 to 0.4	0.93918	-0.23496
0.4 to 0.6	0.96039	-0.058717
0.6 to 0.8	0.96392	-0.044611
0.8 to 1.0	1.0080	-0.099275

Table 5.26: The values returned by binned fits to the L2 XFT efficiency in the various $|\eta|$ bins for π with $225° < \phi_{SL6} < 345°$ (the bottom of the detector) in the second run range.

$\chi^2/ndf = 5.1653/9$	b	m (GeV/c)
b	0.71152E-03	-0.21611E-02
m (GeV/c)	-0.21611E-02	0.73895E-02

Table 5.27: The error matrix returned by binned fit to the L2 XFT efficiency for $0 < |\eta| < 0.2$ bin for π with $225° < \phi_{SL6} < 345°$ (the bottom of the detector) in the second run range.

$\chi^2/ndf = 9.4748/9$	b	m (GeV/c)
b	0.49341E-03	-0.15013E-02
m (GeV/c)	-0.15013E-02	0.51597E-02

Table 5.28: The error matrix returned by binned fit to the L2 XFT efficiency for $0.2 < |\eta| < 0.4$ bin for π with $225° < \phi_{SL6} < 345°$ (the bottom of the detector) in the second run range.

$\chi^2/ndf = 3.3985/9$	b	m (GeV/c)
b	0.29327E-03	-0.92685E-03
m (GeV/c)	-0.92685E-03	0.32694E-02

Table 5.29: The error matrix returned by binned fit to the L2 XFT efficiency for $0.4 < |\eta| < 0.6$ bin for π with $225° < \phi_{SL6} < 345°$ (the bottom of the detector) in the second run range.

$\chi^2/ndf = 4.0431/9$	b	m (GeV/c)
b	0.23580E-03	-0.73770E-03
m (GeV/c)	-0.73770E-03	0.25778E-02

Table 5.30: The error matrix returned by binned fit to the L2 XFT efficiency for $0.6 < |\eta| < 0.8$ bin for π with $225° < \phi_{SL6} < 345°$ (the bottom of the detector) in the second run range.

$\chi^2/ndf = 11.444/9$	b	m (GeV/c)
b	0.26828E-03	-0.80011E-03
m (GeV/c)	-0.80011E-03	0.27113E-02

Table 5.31: The error matrix returned by binned fit to the L2 XFT efficiency for $0.8 < |\eta| < 1.0$ bin for π with $225° < \phi_{SL6} < 345°$ (the bottom of the detector) in the second run range.

Here are the fitted values for the L2 XFT efficiency measurement in the second run range for K with $225° < \phi_{SL6} < 345°$ (the bottom of the detector):

$$\epsilon = b + m * (1/p_T) \tag{5.19}$$

$\|\eta\|$ range	b	m (GeV/c)
0 to 0.2	0.77564	-0.30894
0.2 to 0.4	0.83860	-0.36190
0.4 to 0.6	0.93984	-0.35030
0.6 to 0.8	0.95825	-0.16630
0.8 to 1.0	1.0055	-0.13468

Table 5.32: The values returned by binned fits to the L2 XFT efficiency in the various $|\eta|$ bins for K with $225° < \phi_{SL6} < 345°$ (the bottom of the detector) in the second run range.

$\chi^2/ndf = 11.779/9$	b	m (GeV/c)
b	0.88545E-03	-0.25008E-02
m (GeV/c)	-0.25008E-02	0.76977E-02

Table 5.33: The error matrix returned by binned fit to the L2 XFT efficiency for $0 < |\eta| < 0.2$ bin for K with $225° < \phi_{SL6} < 345°$ (the bottom of the detector) in the second run range.

$\chi^2/ndf = 17.937/9$	b	m (GeV/c)
b	0.62609E-03	-0.17875E-02
m (GeV/c)	-0.17875E-02	0.56151E-02

Table 5.34: The error matrix returned by binned fit to the L2 XFT efficiency for $0.2 < |\eta| < 0.4$ bin for K with $225° < \phi_{SL6} < 345°$ (the bottom of the detector) in the second run range.

$\chi^2/ndf = 5.2913/9$	b	m (GeV/c)
b	0.43073E-03	-0.12335E-02
m (GeV/c)	-0.12335E-02	0.38992E-02

Table 5.35: The error matrix returned by binned fit to the L2 XFT efficiency for $0.4 < |\eta| < 0.6$ bin for K with $225° < \phi_{SL6} < 345°$ (the bottom of the detector) in the second run range.

$\chi^2/ndf = 10.589/9$	b	m (GeV/c)
b	0.31460E-03	-0.91491E-03
m (GeV/c)	-0.91491E-03	0.29306E-02

Table 5.36: The error matrix returned by binned fit to the L2 XFT efficiency for $0.6 < |\eta| < 0.8$ bin for K with $225° < \phi_{SL6} < 345°$ (the bottom of the detector) in the second run range.

$\chi^2/ndf = 9.6585/9$	b	m (GeV/c)
b	0.39116E-03	-0.11265E-02
m (GeV/c)	-0.11265E-02	0.35519E-02

Table 5.37: The error matrix returned by binned fit to the L2 XFT efficiency for $0.8 < |\eta| < 1.0$ bin for K with $225° < \phi_{SL6} < 345°$ (the bottom of the detector) in the second run range.

first run	last run	barrel	end	wedge	layer
152636	163117	0	1	0	0
162453	162478	1	0	0	0
153616	155392	1	1	2	0
153325	163117	1	0	5	0
155342	155391	1	0	6	0
152636	156489	1	0	8	0
152636	156489	0	0	11	0
152636	155298	1	1	8	1
162238	162252	0	0	6	1
163113	163117	1	0	9	1
160346	160532	1	0	1	2
155742	161440	0	1	5	2
163064	163117	2	0	5	2
154449	163117	1	0	9	2
154653	155392	0	1	10	2
152636	163117	2	0	6	3
163064	163117	1	0	1	3
162836	163117	1	1	1	3
162982	163117	1	0	3	3
162982	163117	1	1	11	3
155113	155394	0	0	8	3
152636	163117	1	1	0	4
152636	163117	1	1	1	4
152636	156489	1	0	4	4
155364	156368	0	1	5	4
154653	156489	0	0	6	4
154653	156368	2	1	6	4
152636	163117	1	0	7	4
152636	155298	1	1	8	4

Table 5.38: These are the layers of the SVX which the database indicated were integrated but were nevertheless excluded from my measurement due to low efficiency. Note that my measurement only includes runs between 152636 and 163117, so layers with this run range indicated may have problems over a longer period. Also, we concentrated on layers that were used in the SVT, so the layer being taken out of the 'bad' list may indicate that a different layer was selected for use in the SVT.

ϵ_0	ϵ_{1p_T}	ϵ_{1d0}	ϵ_{2d0}	$1/p_{T50}$ $(1/(\mathrm{GeV}/c))$	σ_{pT} $(1/(\mathrm{GeV}/c))$	$d0_{50+}$ (cm)	σ_{d0+} (cm)	ϵ_{ISO}
0.92791	-0.16321	2.1460	-18.553	0.50114	0.022584	0.011508	0.0052810	-0.025679

Table 5.39: The values returned by the binned fit to the L2 SVT efficiency relative to XFT and offline of equation 5.11.

$\chi^2/ndf = 769.89/646$	ϵ_0	ϵ_{1p_T}	ϵ_{1d0}	ϵ_{2d0}	$1/p_{T50}$ $((\mathrm{GeV}/c)^{-1})$
ϵ_0	0.17232E-03	-0.65269E-04	-0.66988E-02	0.65879E-01	-0.57623E-06
ϵ_{1p_T}	-0.65269E-04	0.22461E-03	-0.46758E-04	-0.25139E-03	0.29064E-05
ϵ_{1d0}	-0.66988E-02	-0.46758E-04	0.30995	-3.1223	-0.49452E-05
ϵ_{2d0}	0.65879E-01	-0.25139E-03	-3.1223	32.298	0.45573E-04
$1/p_{T50}$ $((\mathrm{GeV}/c)^{-1})$	-0.57623E-06	0.29064E-05	-0.49452E-05	0.45573E-04	0.12089E-05
σ_{pT} $((\mathrm{GeV}/c)^{-1})$	-0.23762E-05	0.11080E-04	-0.15405E-04	0.13322E-03	0.22026E-05
$d0_{50+}$ (cm)	-0.38881E-07	0.46813E-07	-0.24039E-06	0.91307E-05	0.70715E-09
σ_{d0+} (cm)	0.18122E-05	-0.20678E-07	-0.73834E-04	0.68628E-03	0.30498E-09
ϵ_{ISO}	-0.21047E-05	0.96273E-06	0.29154E-04	-0.25732E-03	-0.41908E-08

	σ_{pT} $((\mathrm{GeV}/c)^{-1})$	$d0_{50+}$ (cm)	σ_{d0+} (cm)	ϵ_{ISO}	
ϵ_0	-0.23762E-05	-0.38881E-07	0.18122E-05	-0.21047E-05	
ϵ_{1p_T}	0.11080E-04	0.46813E-07	-0.20678E-07	0.96273E-06	
ϵ_{1d0}	-0.15405E-04	-0.24039E-06	-0.73834E-04	0.29154E-04	
ϵ_{2d0}	0.13322E-03	0.91307E-05	0.68628E-03	-0.25732E-03	
$1/p_{T50}$ $((\mathrm{GeV}/c)^{-1})$	0.22026E-05	0.70715E-09	0.30498E-09	-0.41908E-08	
σ_{pT} $((\mathrm{GeV}/c)^{-1})$	0.49168E-05	0.86471E-09	-0.41669E-10	0.14194E-07	
$d0_{50+}$ (cm)	0.86471E-09	0.97979E-08	-0.16877E-07	0.19576E-08	
σ_{d0+} (cm)	-0.41669E-10	-0.16877E-07	0.60355E-07	-0.60440E-08	
ϵ_{ISO}	0.14194E-07	0.19576E-08	-0.60440E-08	0.71030E-06	

Table 5.40: The error matrix returned by the binned fit to the L2 SVT efficiency relative to XFT and offline of equation 5.11.

$\chi^2/ndf = 149.82/125$	$\epsilon_{plateau}$	$1/p_{T\mu 50}$	$\sigma_{1/p_{T\mu}}$	$1/p_{TSVT50}$	$\sigma_{1/p_{TSVT}}$
$\epsilon_{plateau}$	0.10380E-05	0.22833E-07	0.61040E-07	0.82349E-07	0.13901E-06
$1/p_{T\mu 50}$	0.22833E-07	0.20728E-06	0.24905E-06	0.29383E-08	0.43844E-08
$\sigma_{1/p_{T\mu}}$	0.61040E-07	0.24905E-06	0.35844E-06	0.44874E-08	0.57851E-08
$1/p_{TSVT50}$	0.82349E-07	0.29383E-08	0.44874E-08	0.12869E-05	0.15282E-05
$\sigma_{1/p_{TSVT}}$	0.13901E-06	0.43844E-08	0.57851E-08	0.15282E-05	0.19821E-05

Table 5.41: The error matrix returned by the binned fit to the L3 μ+SVT efficiency relative to L1, L2, and offline of equation 5.13.

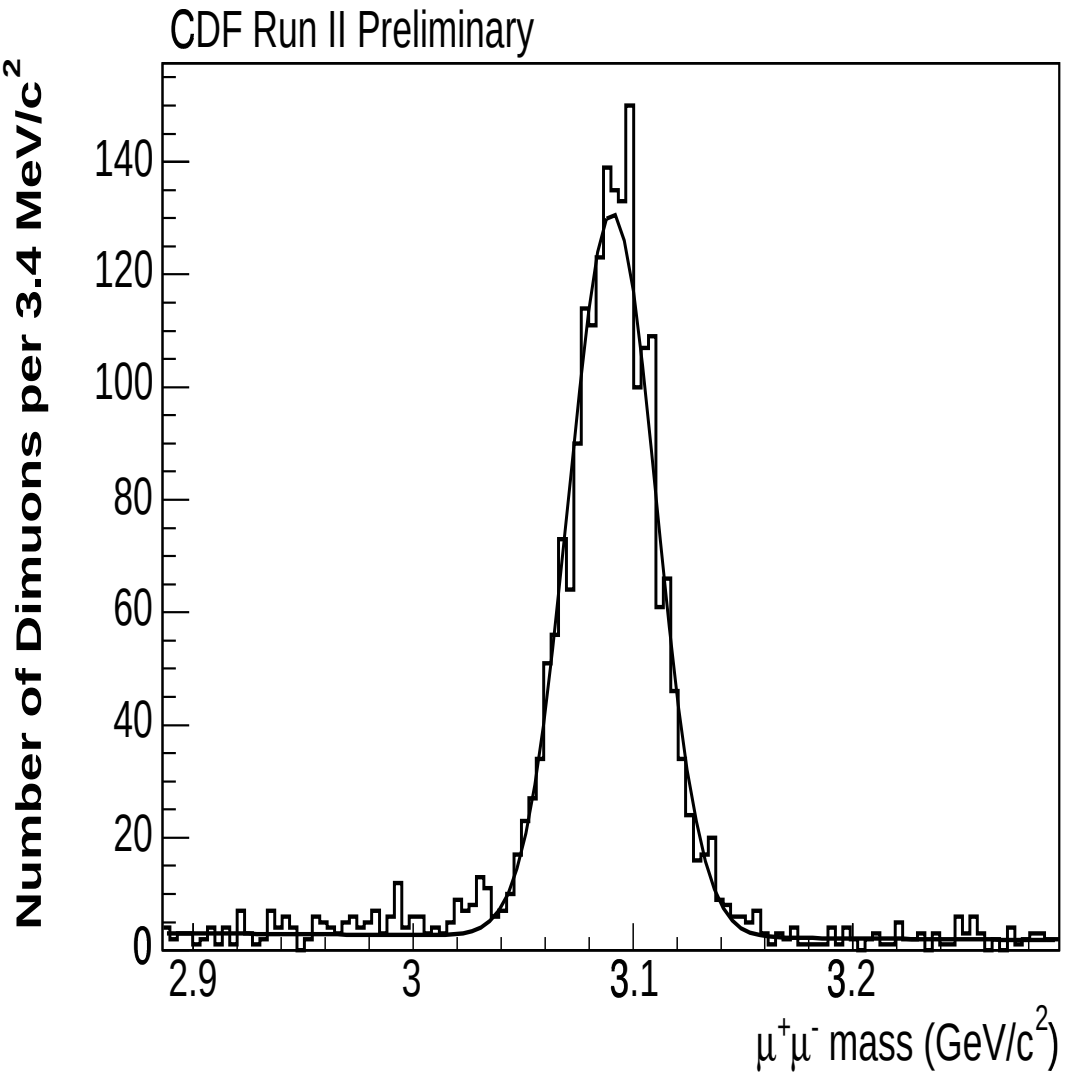

Figure 5.1: The J/ψ dimuon mass peak from the CMUP8 trigger. The fitted curve was used to define signal and sideband regions, and there are about 1887 events beneath the Gaussian.

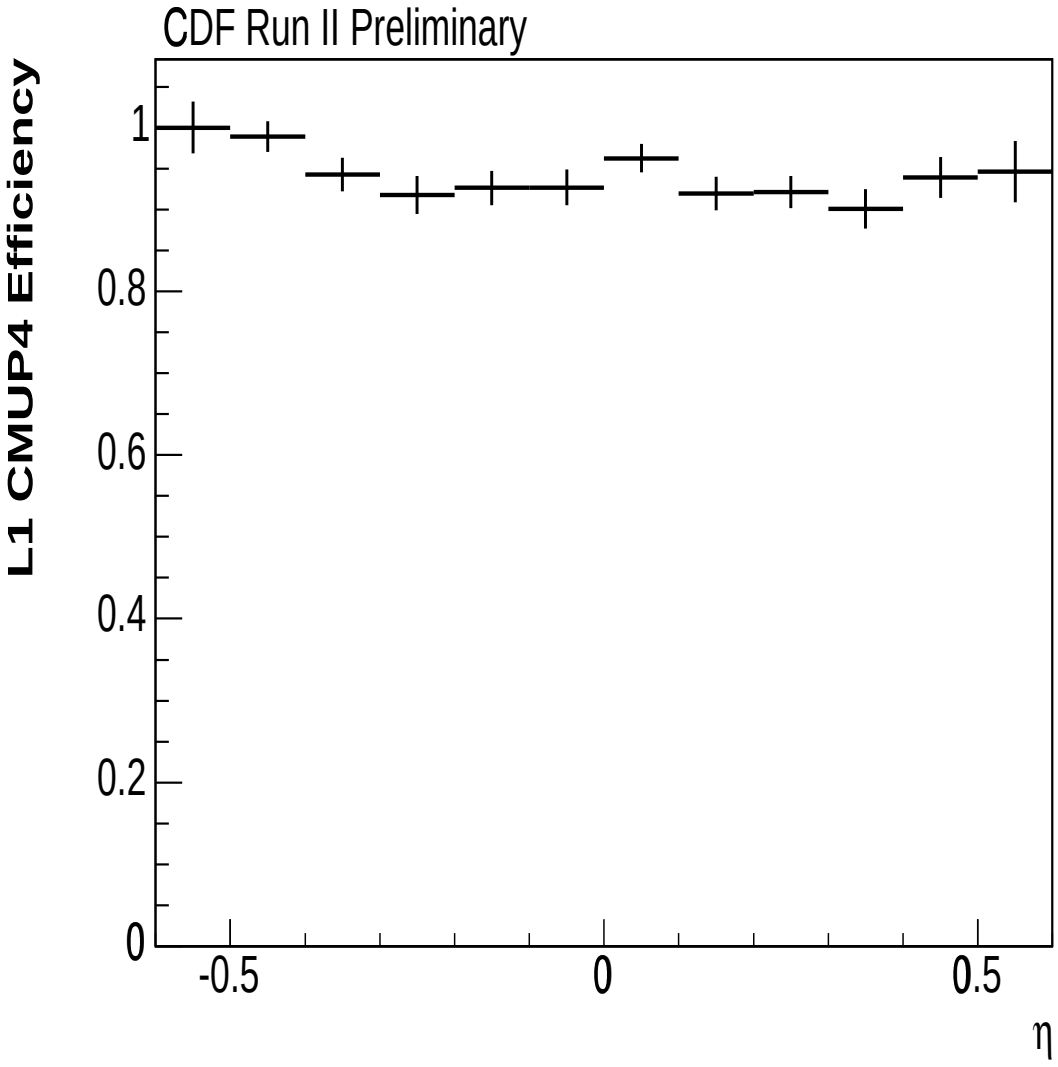

Figure 5.2: L1 CMUP4 efficiency vs. η for $p_T > 4.45$ GeV/c.

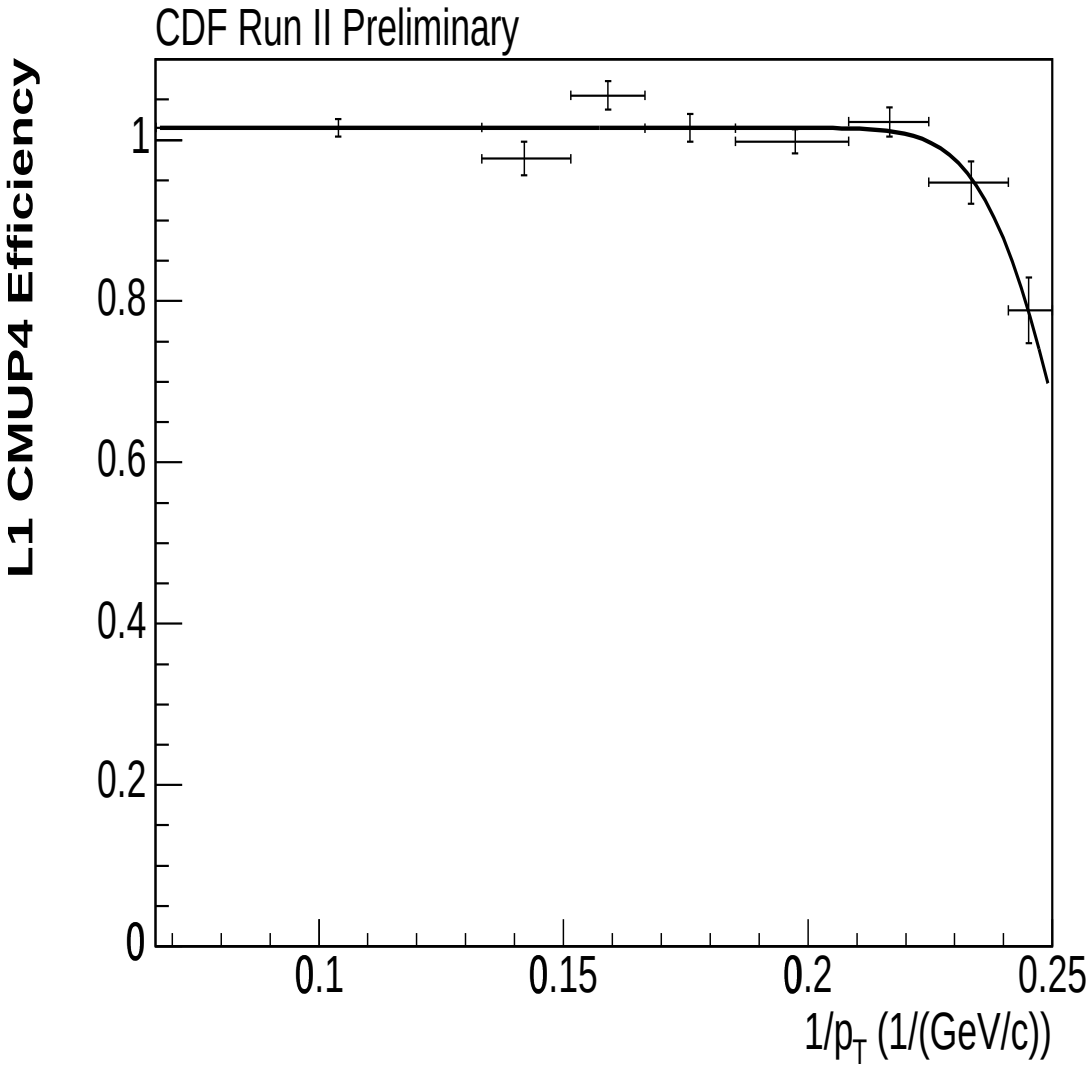

Figure 5.3: L1 CMUP4 efficiency vs. $1/p_T$ after being reweighted by the η efficiency.

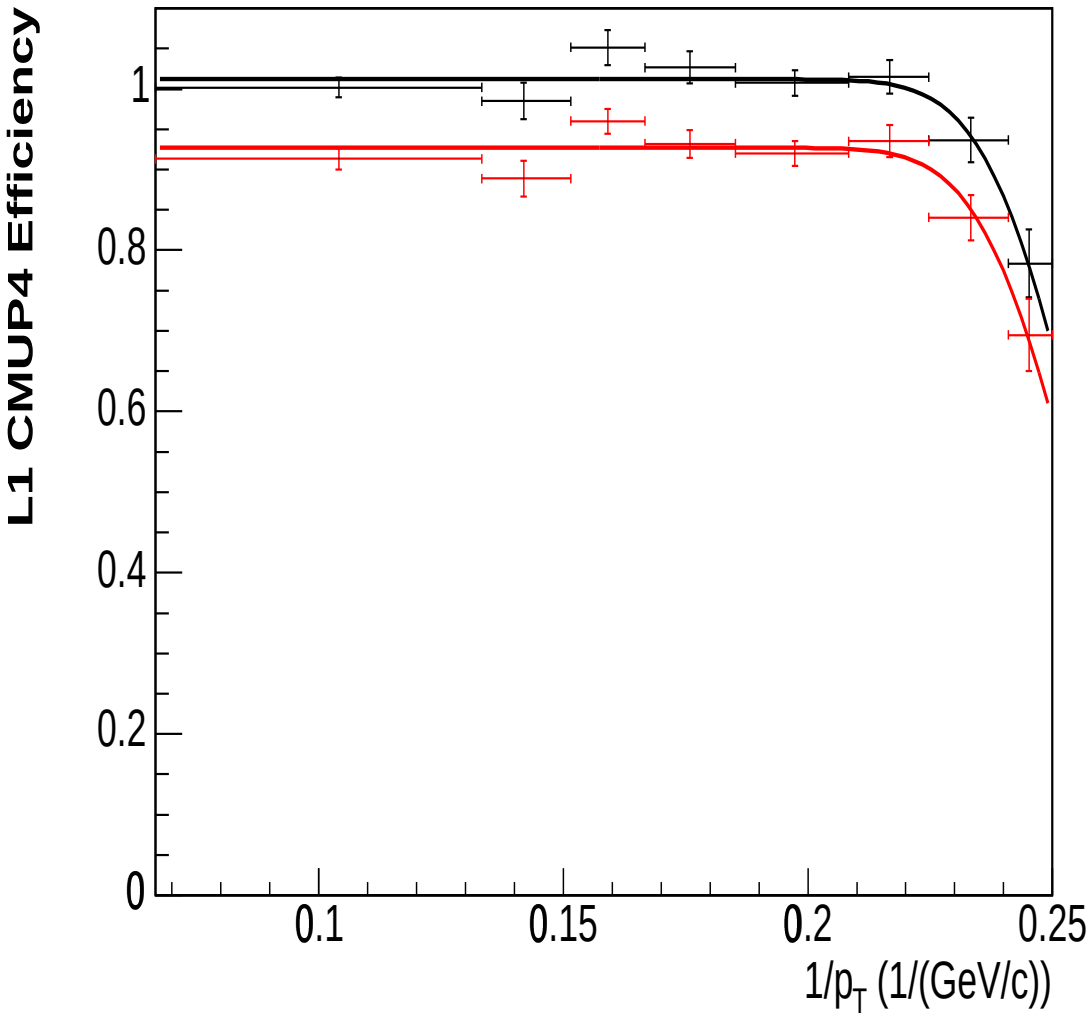

Figure 5.4: L1 CMUP4 efficiency vs. $1/p_T$ both before (red points) and after (black points) being reweighted by the η efficiency.

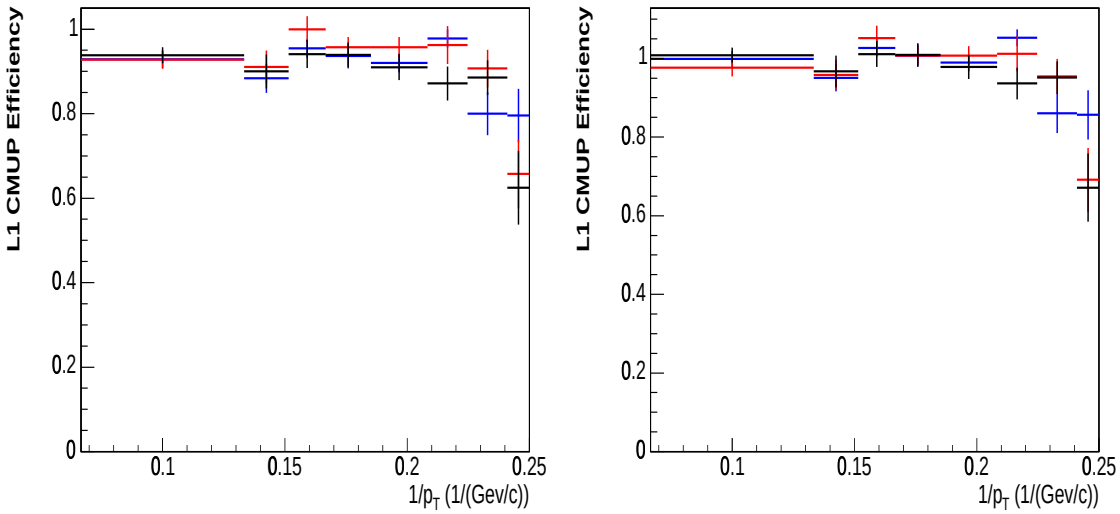

Figure 5.5: L1 CMUP4 efficiency vs. $1/p_T$ for $-0.6 < \eta < -0.2$ (red points), $-0.2 < \eta < 0.2$ (blue points), and $0.2 < \eta < 0.6$ (black points), before (left) and after (right) being adjusted so that the plateau efficiency for each track is 1.

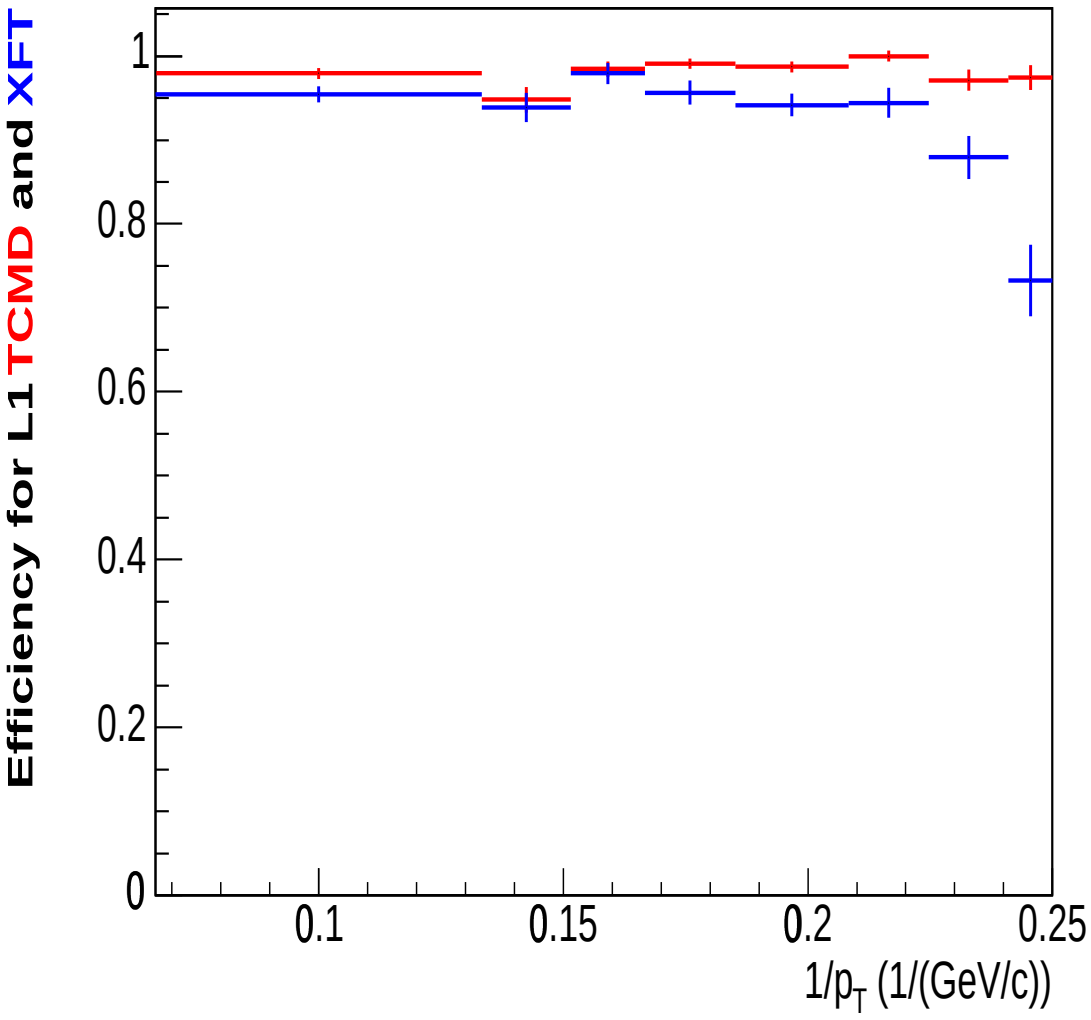

Figure 5.6: Efficiency vs. $1/p_T$ for the TCMD (red points) and XFT (blue points).

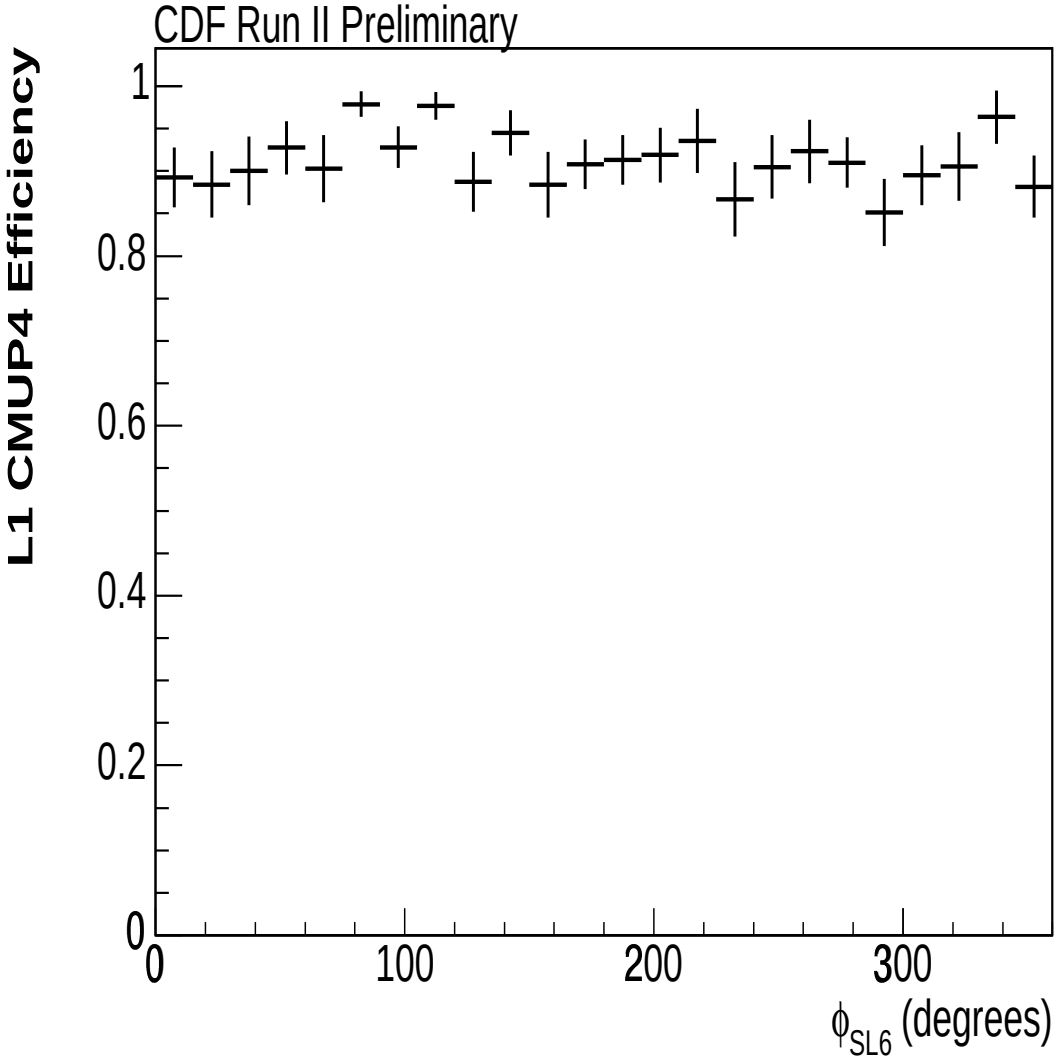

Figure 5.7: L1 CMUP4 efficiency vs. ϕ_{SL6}.

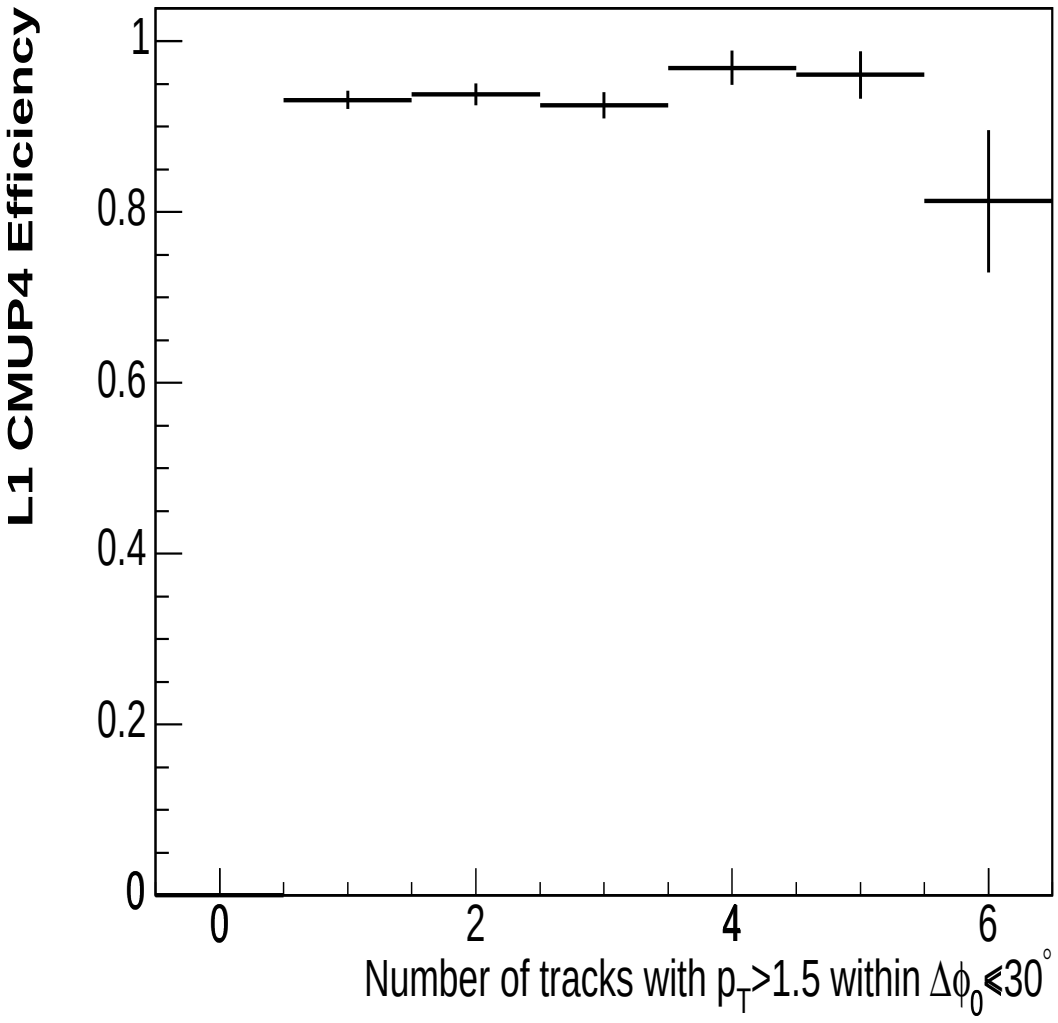

Figure 5.8: L1 CMUP4 efficiency vs. track isolation within 30° of ϕ_0.

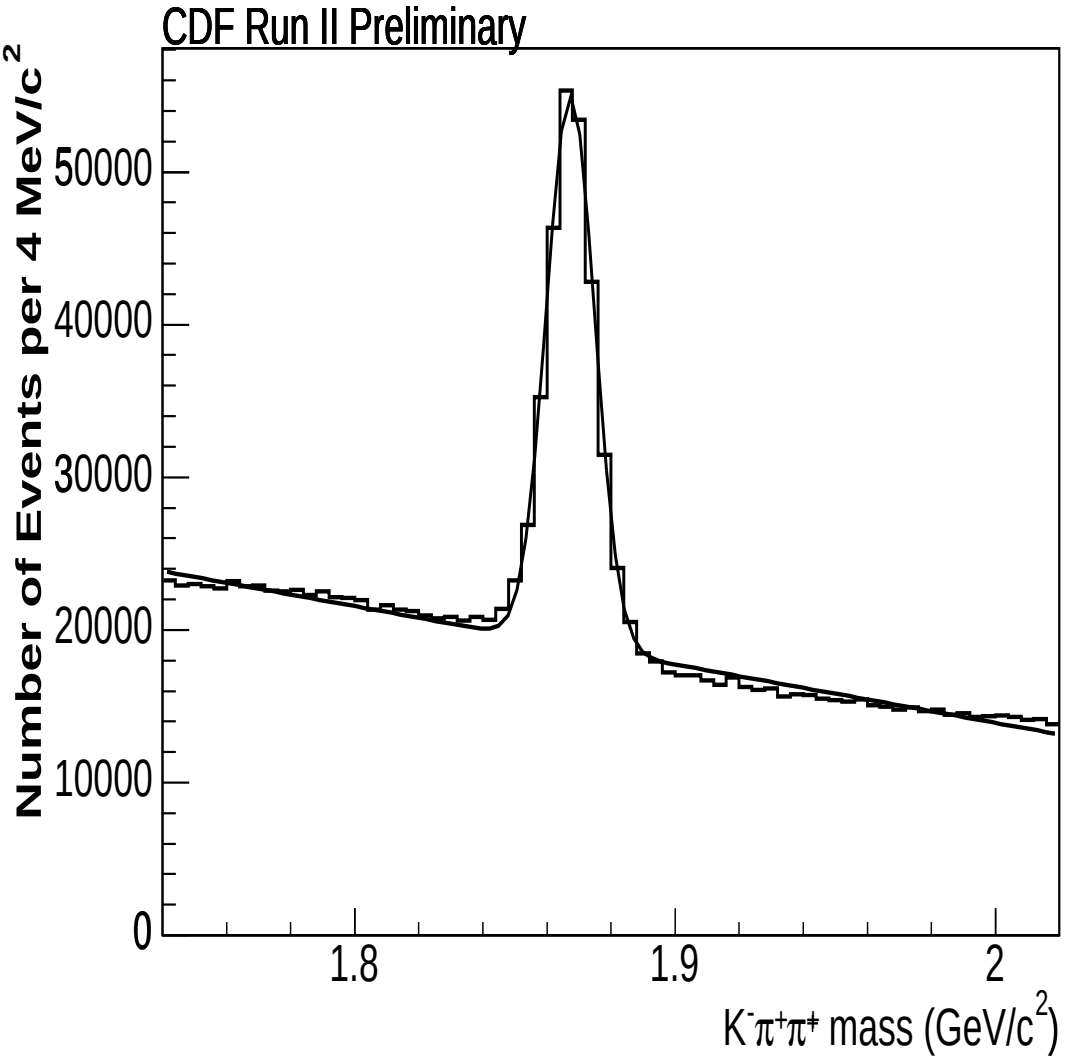

Figure 5.9: The $D^+ \to K^-\pi^+\pi^+$ mass peak from the B_CHARM_LOWPT_L1_DPS trigger. The fitted curve was used to define signal and sideband regions, and there are about 200,000 events beneath the Gaussian.

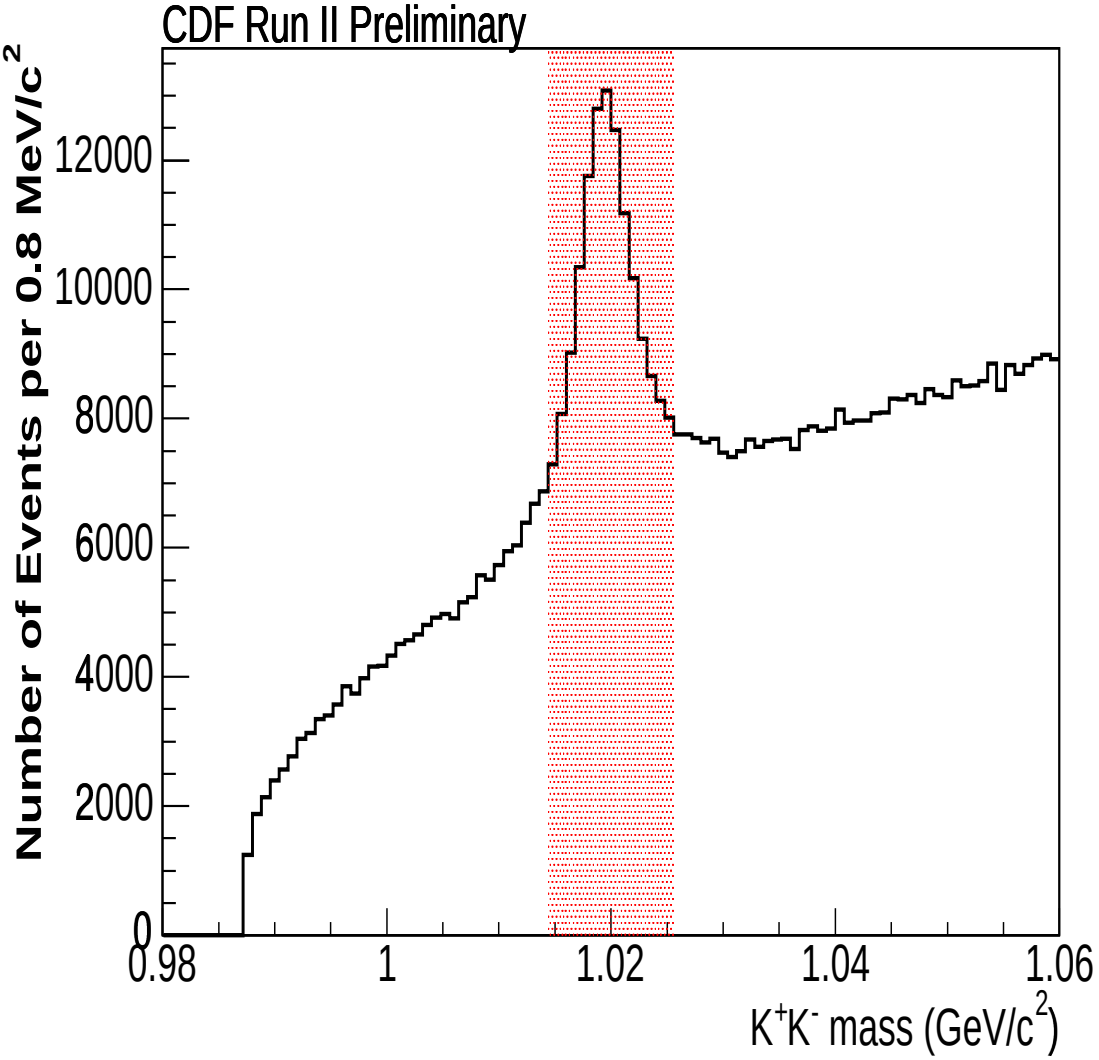

Figure 5.10: The $\phi^0 \to K^+K^-$ mass peak from the B_CHARM_LOWPT_L1_DPS trigger used in the reconstruction of $D^+_{(s)} \to \phi^0\pi^+$. We use only events that have a K^+K^- mass between 1.0144 and 1.0256 GeV/c^2.

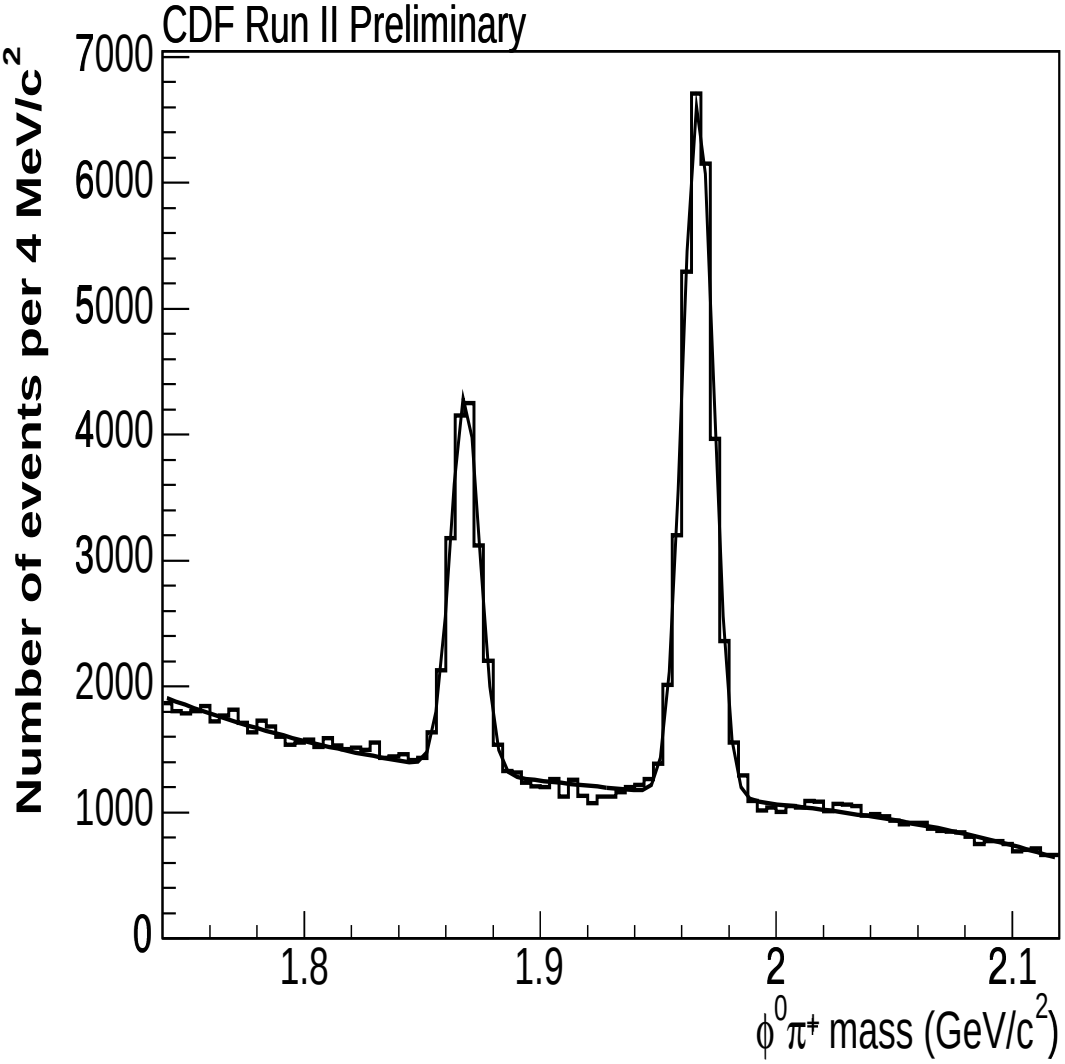

Figure 5.11: The $D^+_{(s)} \to \phi^0\pi^+$, $\phi^0 \to K^+K^-$ mass peaks from the B_CHARM_LOWPT_L1_DPS trigger. The fitted curve was used to define signal and sideband regions, and there are about 9,558 events beneath the D^+ Gaussian and 18,456 beneath the D^+_s Gaussian.

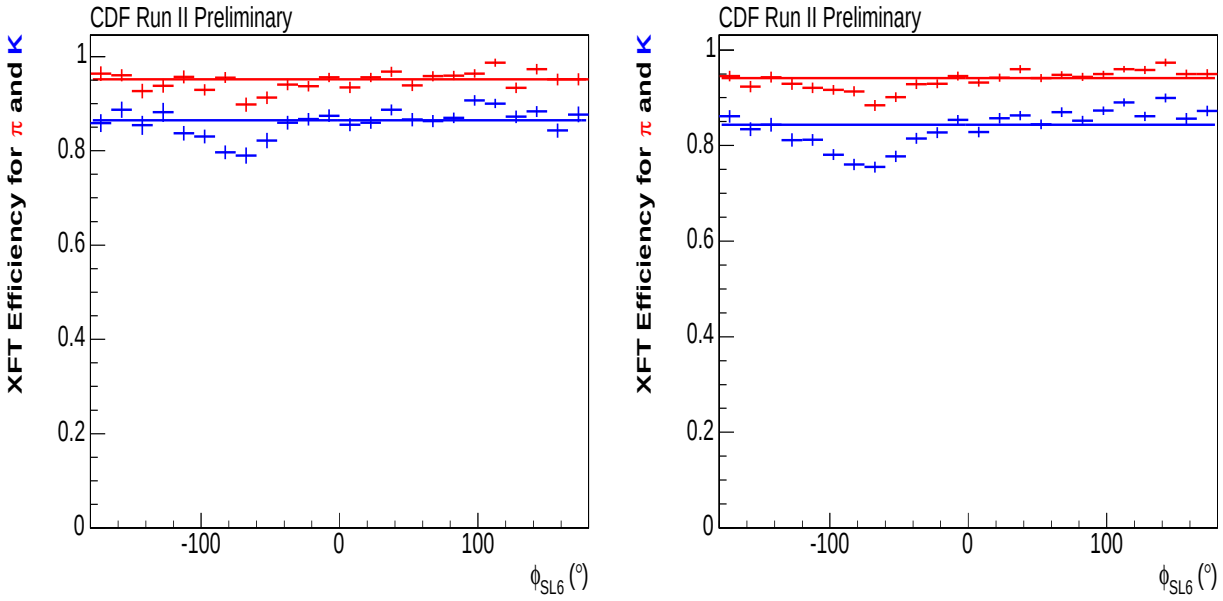

Figure 5.12: XFT efficiency (for the L2 measurement) vs. ϕ_{SL6} for runs between 152636 and 158000 (left) and runs between 158000 and 163117 (right) for π (red) and K (blue).

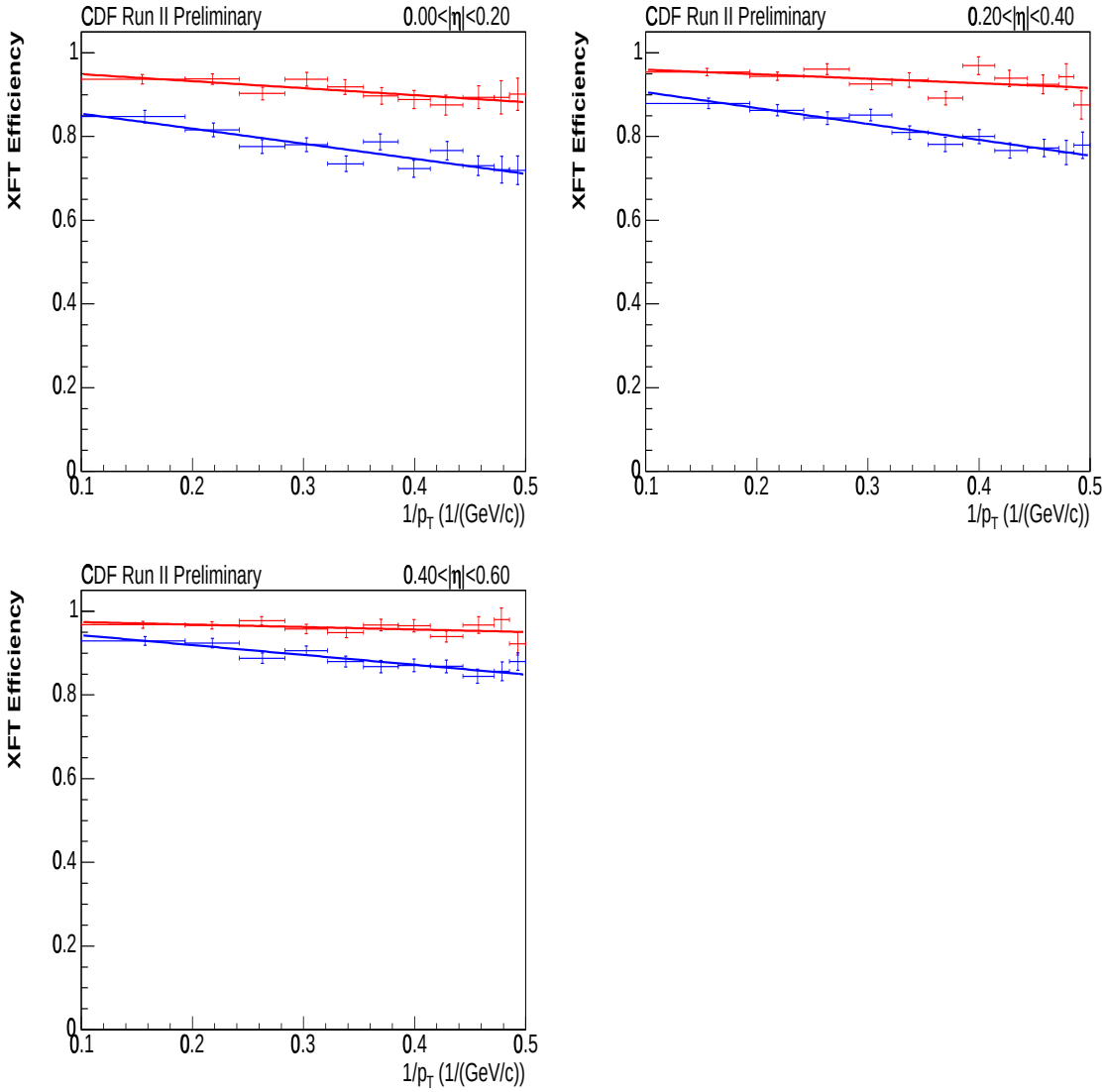

Figure 5.13: XFT efficiency vs.$1/|p_T|$ for $0 < |\eta| < 0.6$ for runs between 152636 and 158000 for π (red) and K (blue).

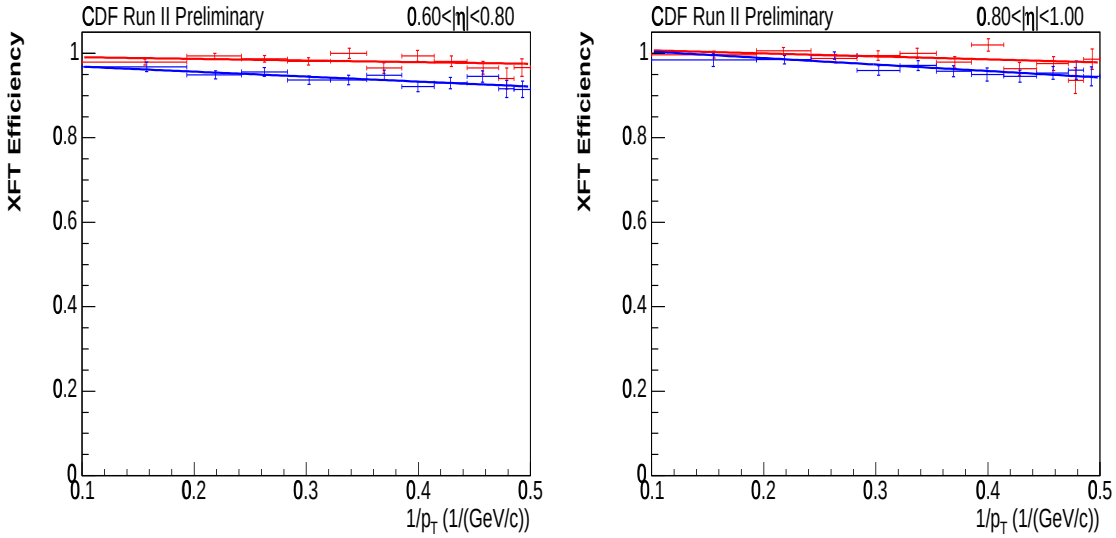

Figure 5.14: XFT efficiency vs.$1/|p_T|$ for $0.6 < |\eta| < 1.0$ for runs between 152636 and 158000 for π (red) and K (blue).

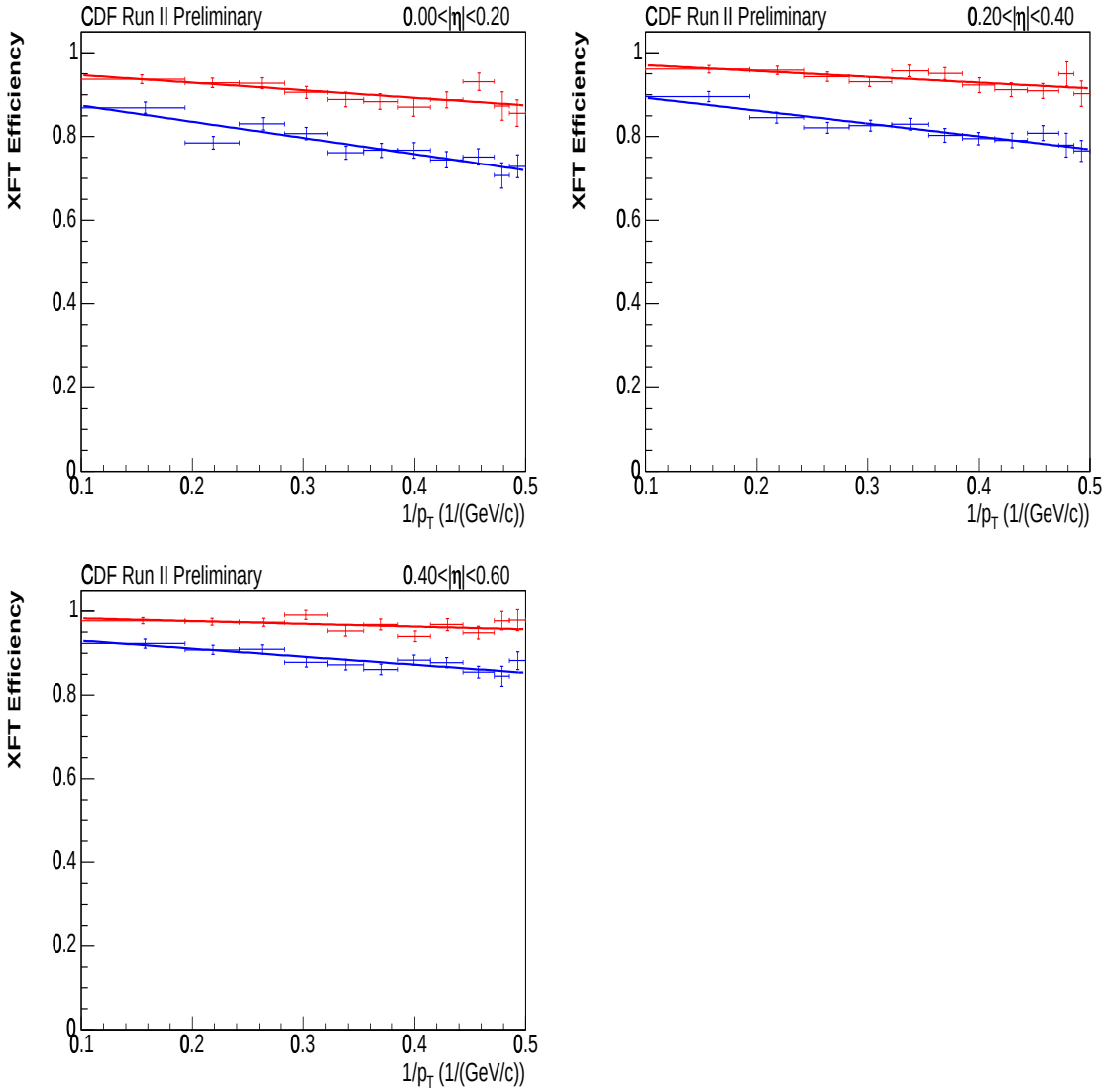

Figure 5.15: XFT efficiency vs.$1/|p_T|$ for $0 < |\eta| < 0.6$ for runs between 158000 and 163117 for π (red) and K (blue) within $\phi_{SL6} < 225°$ or $\phi_{SL6} > 345°$ (the top of the detector).

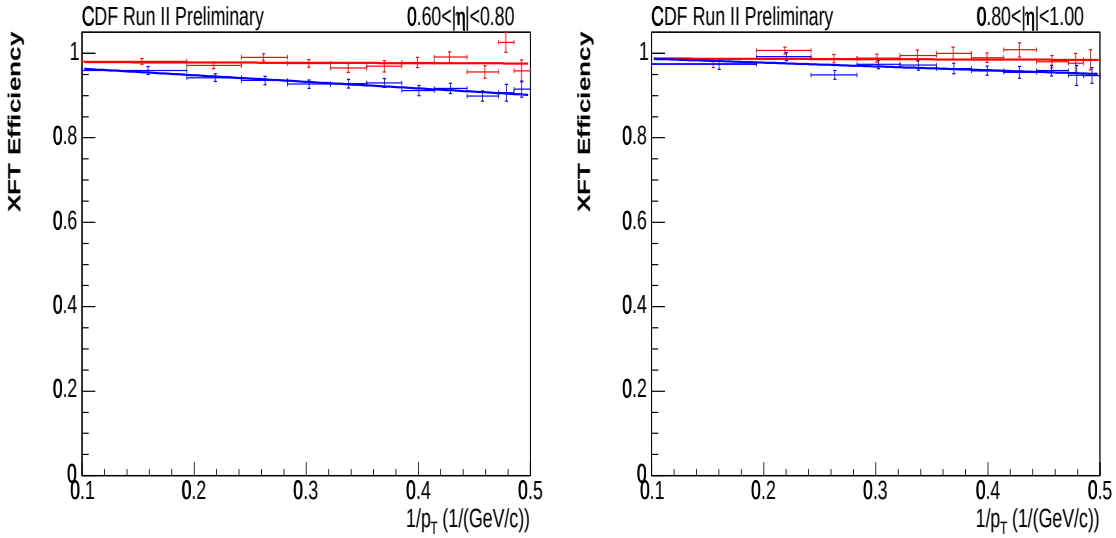

Figure 5.16: XFT efficiency vs.$1/|p_T|$ for $0.6 < |\eta| < 1.0$ for runs between 158000 and 163117 for π (red) and K (blue) within $\phi_{SL6} < 225°$ or $\phi_{SL6} > 345°$ (the top of the detector).

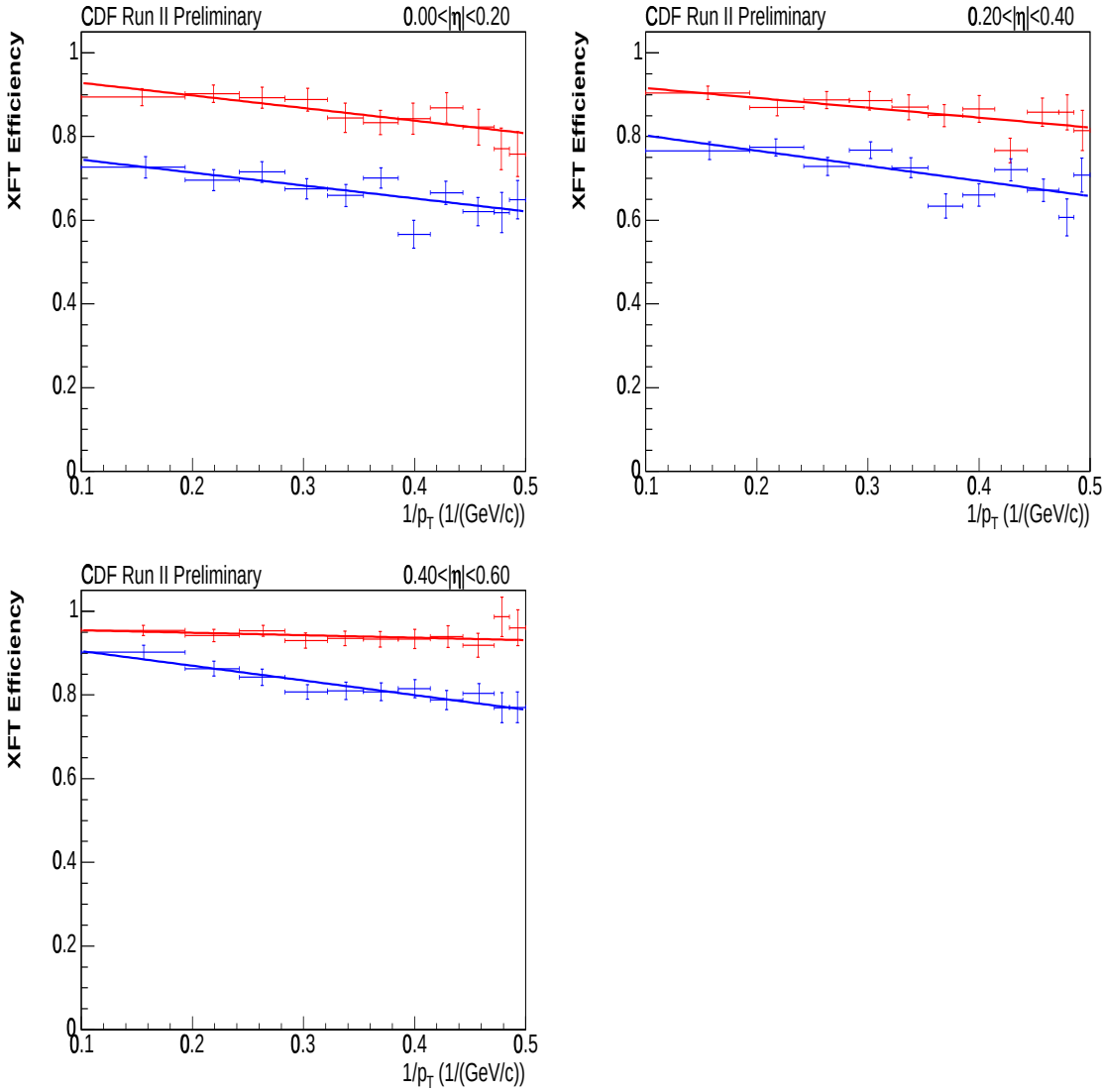

Figure 5.17: XFT efficiency vs.$1/|p_T|$ for $0 < |\eta| < 0.6$ for runs between 158000 and 163117 for π (red) and K (blue) within $225° < \phi_{SL6} < 345°$ (the bottom of the detector).

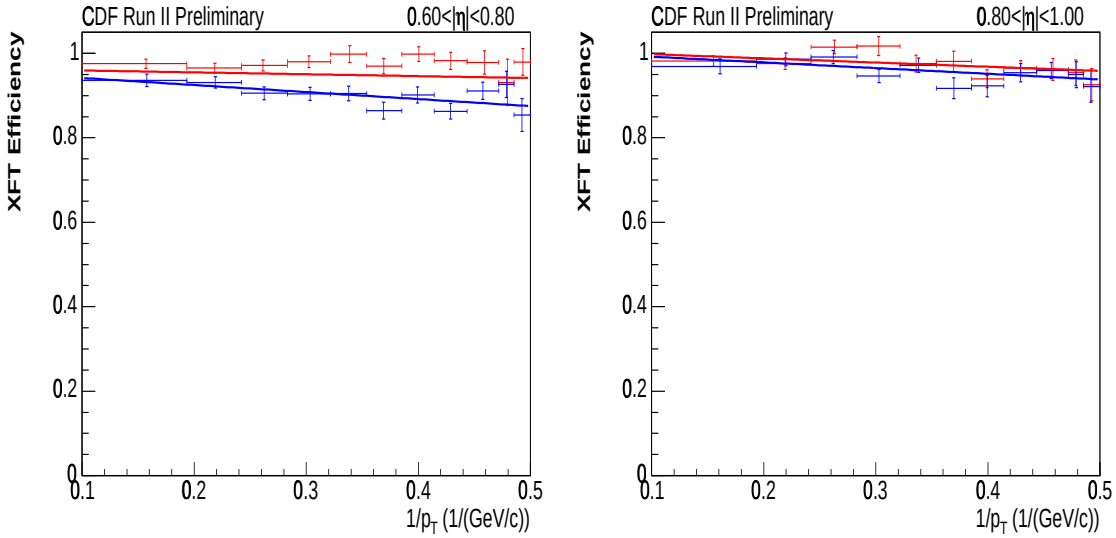

Figure 5.18: XFT efficiency vs.$1/|p_T|$ for $0.6 < |\eta| < 1.0$ for runs between 158000 and 163117 for π (red) and K (blue) within $225° < \phi_{SL6} < 345°$ (the bottom of the detector).

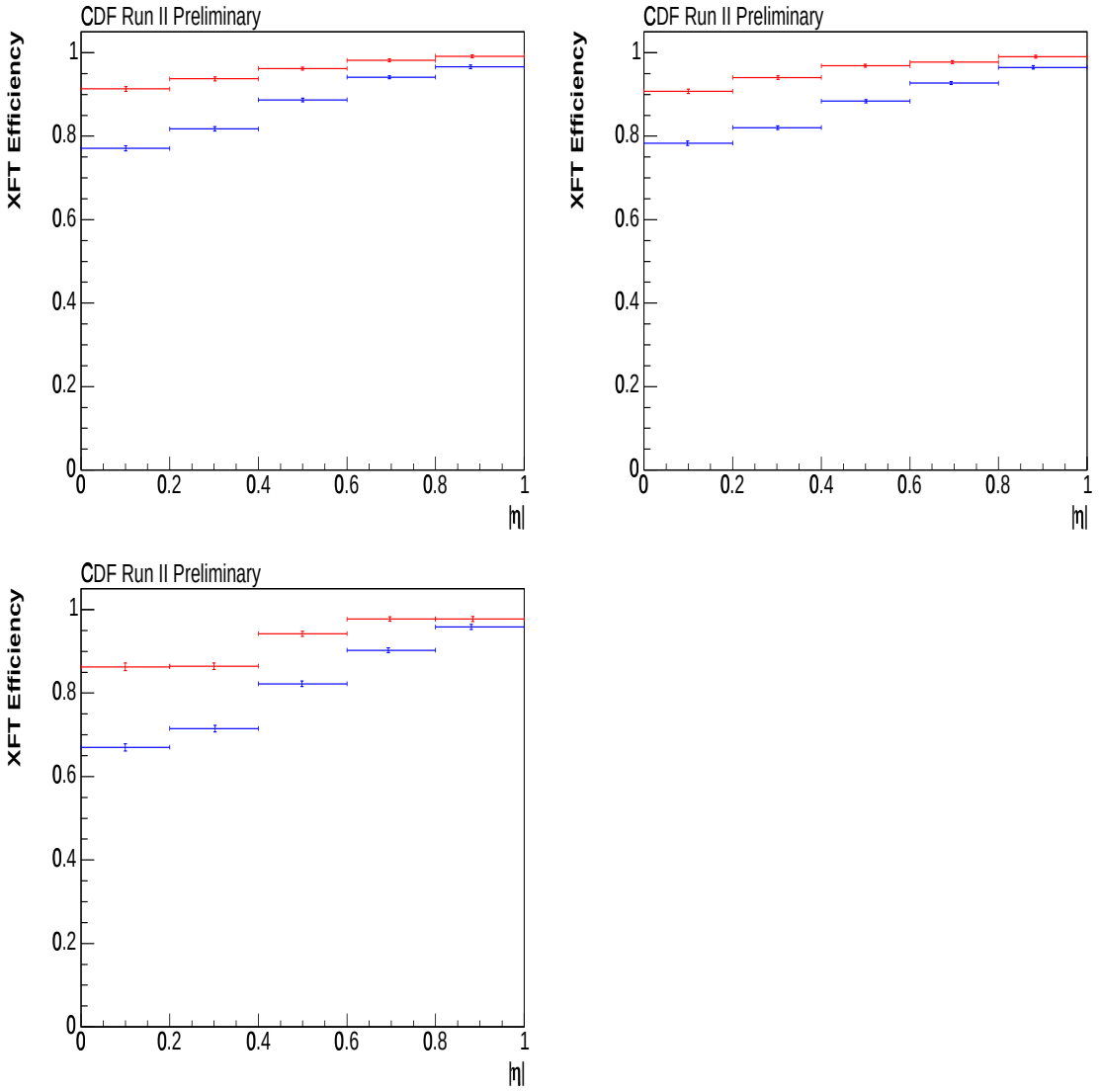

Figure 5.19: XFT efficiency vs. $|\eta|$ for runs between 152636 and 158000 (top left), 158000 and 163117 within $\phi_{SL6} < 225°$ or $\phi_{SL6} > 345°$, and 158000 and 163117 within $225° < \phi_{SL6} < 345°$ (bottom left) for π (red) and K (blue).

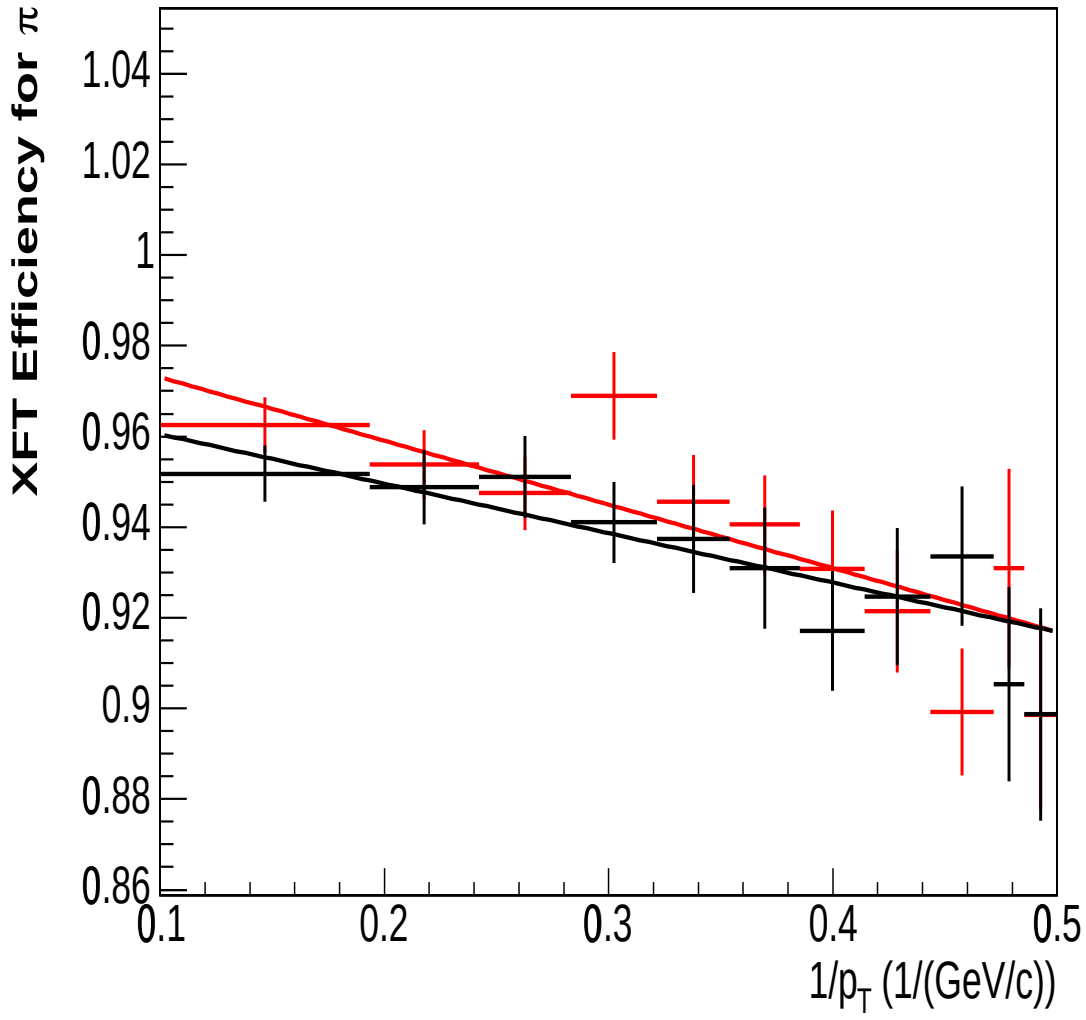

Figure 5.20: XFT efficiency vs. $1/|p_T|$ for π from $D^+ \to K^-\pi^+\pi^+$ that came in on the B_CHARM_HIGHPT trigger. The black points use pions from events that came in on the B_CHARM_HIGHPT when the B_CHARM_LOWPT_L1_DPS prescale was set to 1, and the red points use pions from events that came in on the B_CHARM_HIGHPT when the B_CHARM_LOWPT_L1_DPS prescale was set to greater than 1.

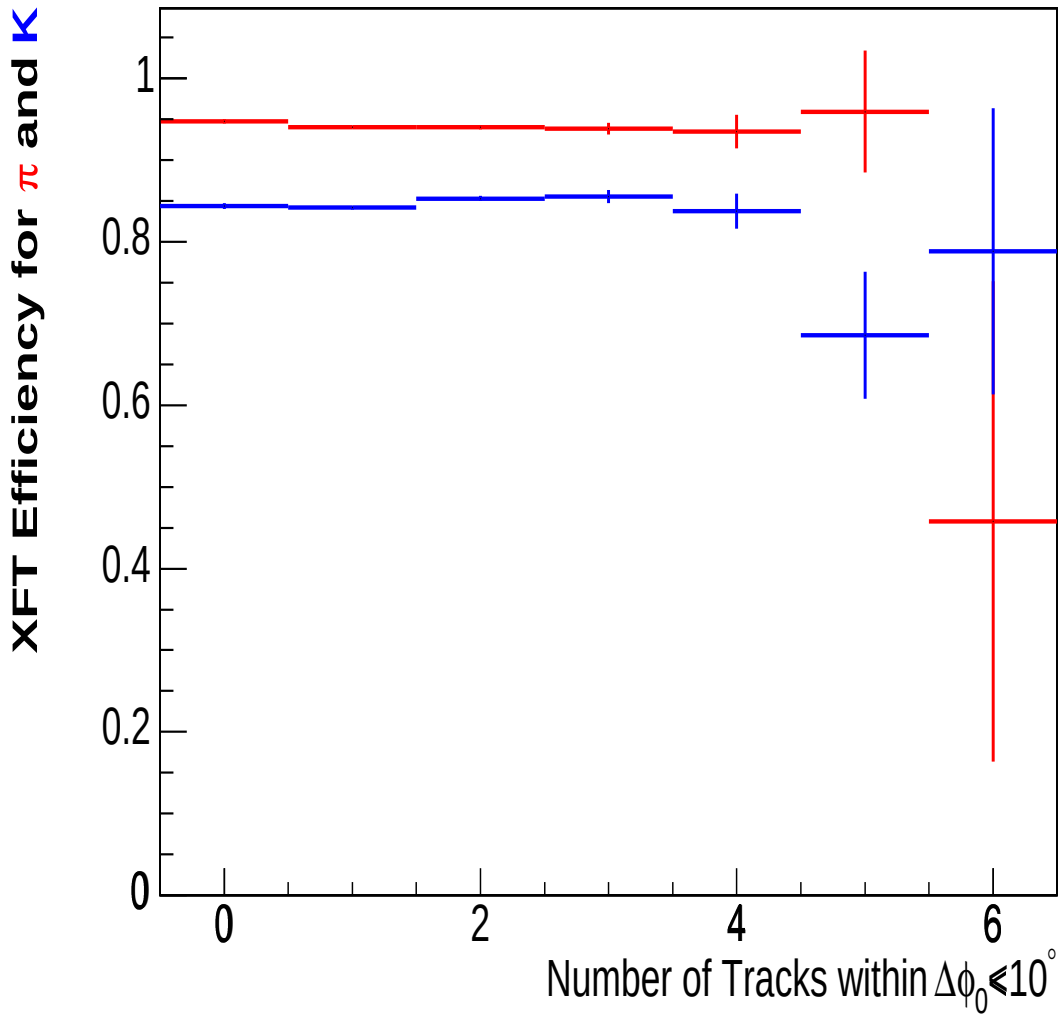

Figure 5.21: XFT efficiency vs. the number of tracks with $p_T > 1.5$ GeV/c within $\Delta\phi_0 < 10°$ for pions (red) and kaons (blue).

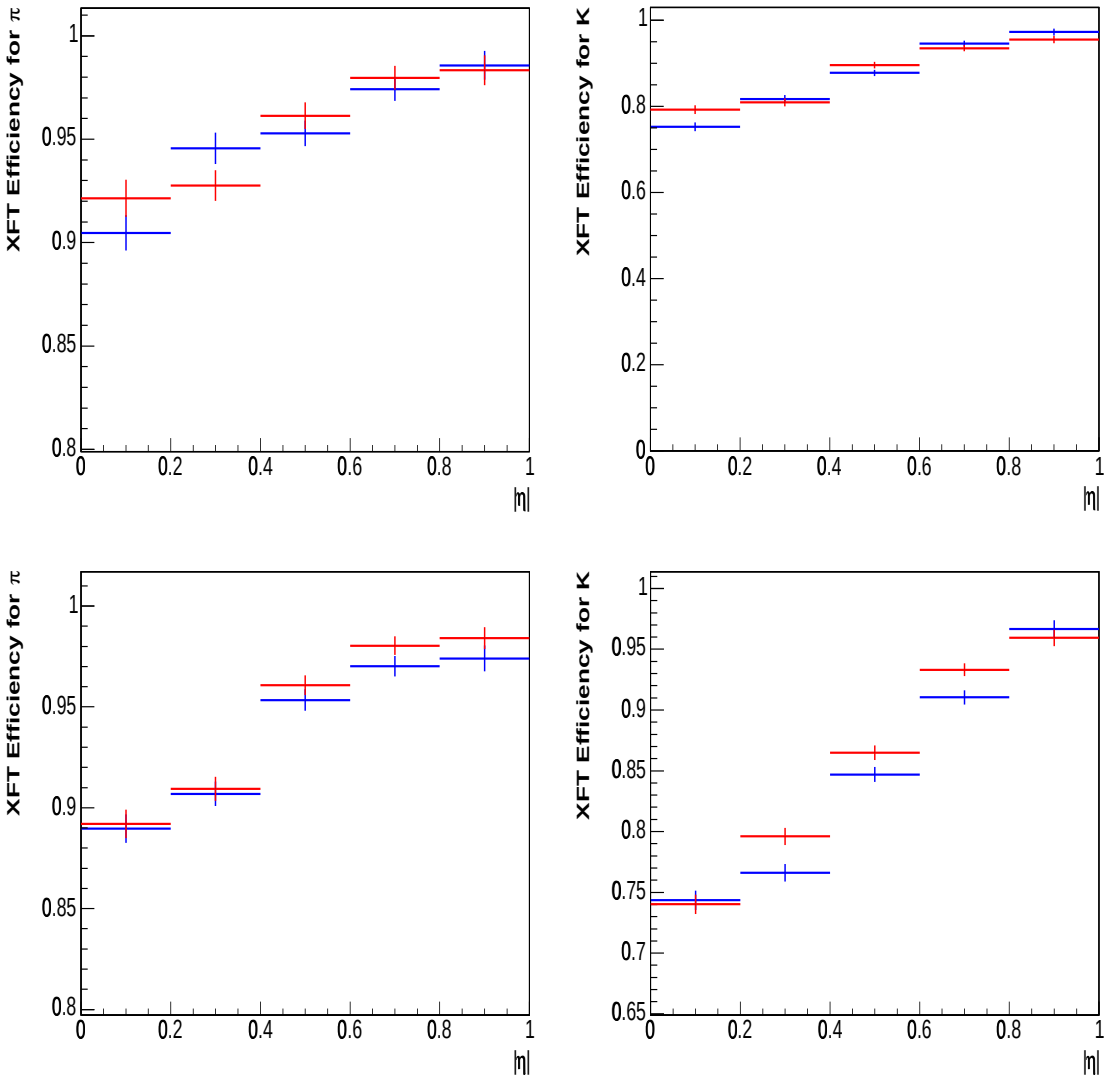

Figure 5.22: XFT efficiency vs. $|\eta|$ for π (left) and K (right) for the preshutdown (top) and postshutdown (bottom) run ranges. The blue point are for tracks that had positive η and the red point are for that had negative η.

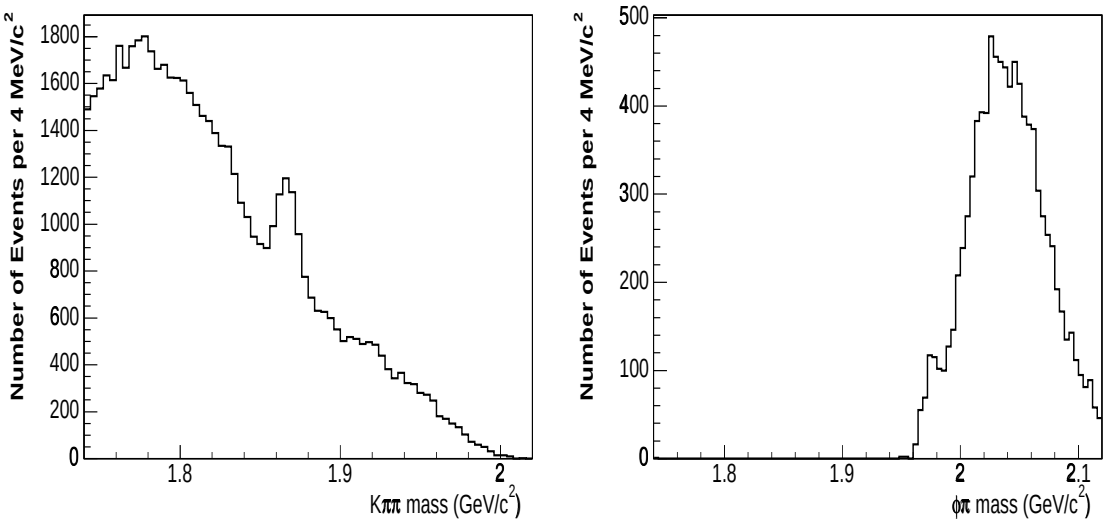

Figure 5.23: The figure on the left shows the $K\pi\pi$ mass spectrum for track combinations that were also found within the $\phi\pi$ mass window. There is a $D^+ \to K^-\pi^+\pi^-$ peak with 1500 events. The figure on the right shows the track combinations that were under the $D^+ \to K^-\pi^+\pi^-$ peak on the left with the $\phi\pi$ mass assignments.

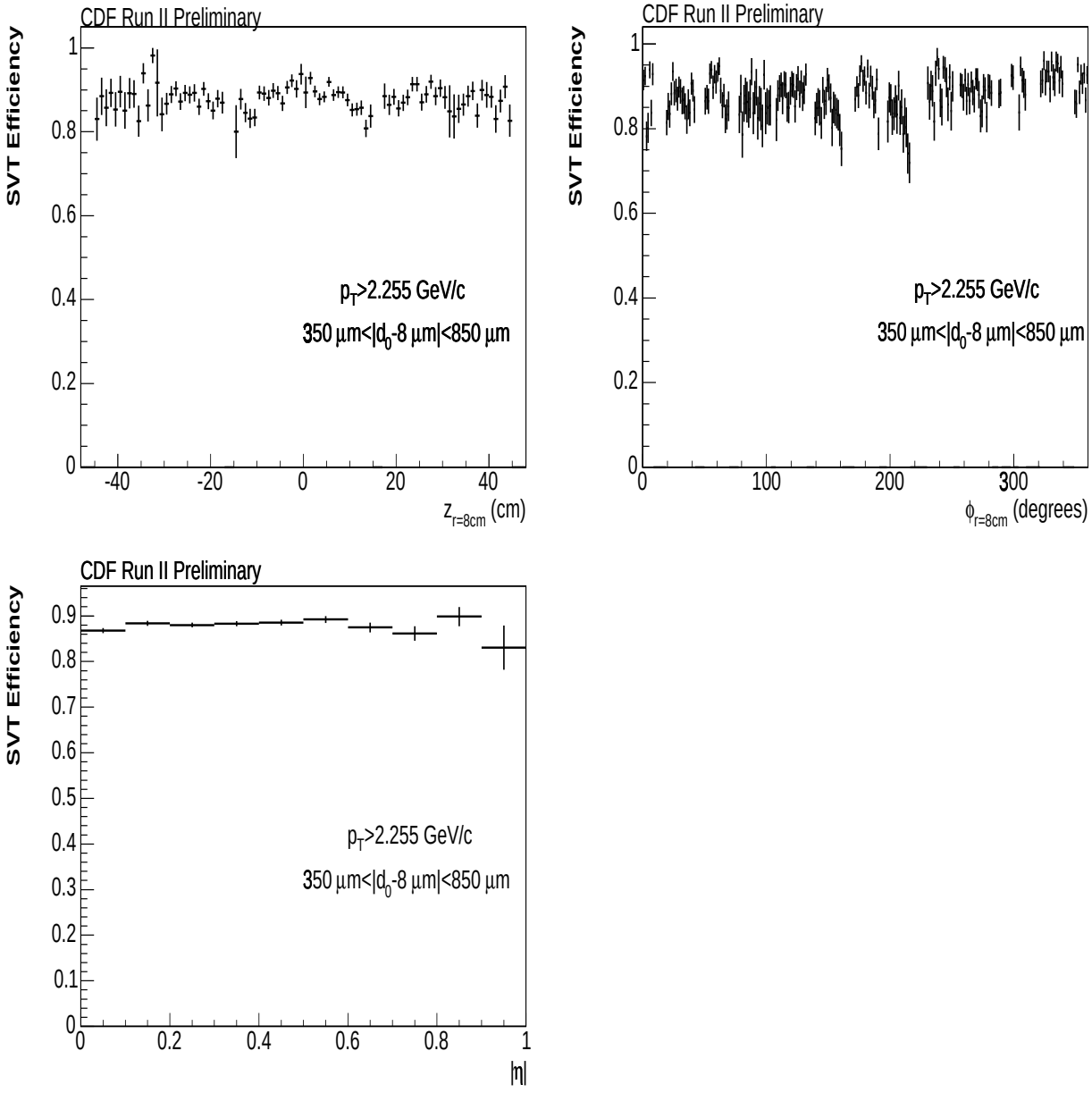

Figure 5.24: SVT efficiency vs. $z_{r=8cm}$ (upper left), SVT efficiency vs. $\phi_{r=8cm}$ (upper right), and SVT efficiency vs. $|\eta|$ (lower left).

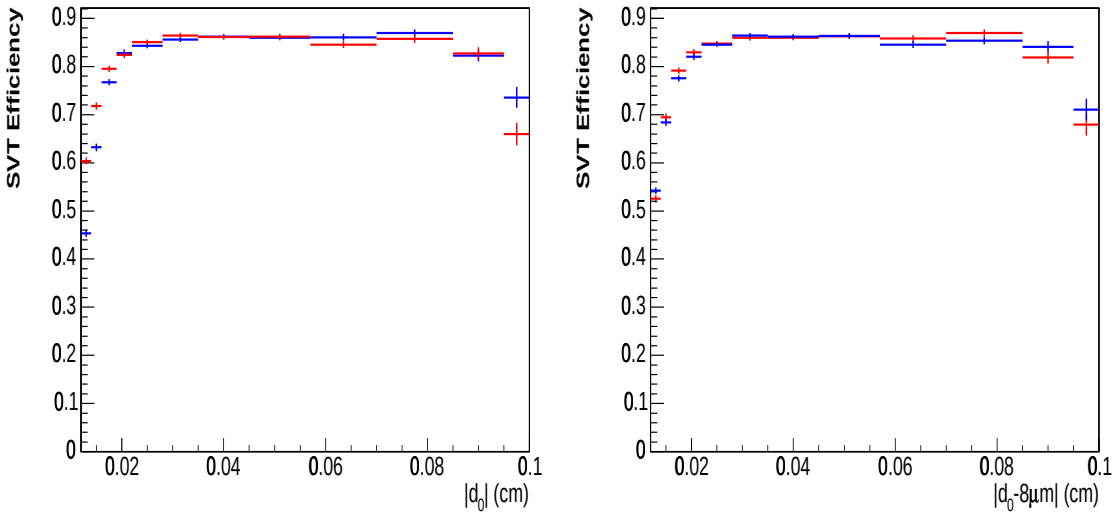

Figure 5.25: SVT efficiency vs.$|d_0|$ (left) and SVT efficiency vs. $|d_0 - 8\mu m|$ (right). The points with positive SVX d0 are in red, and those with negative d0 are in blue. These points are averaged over all p_T and ISO.

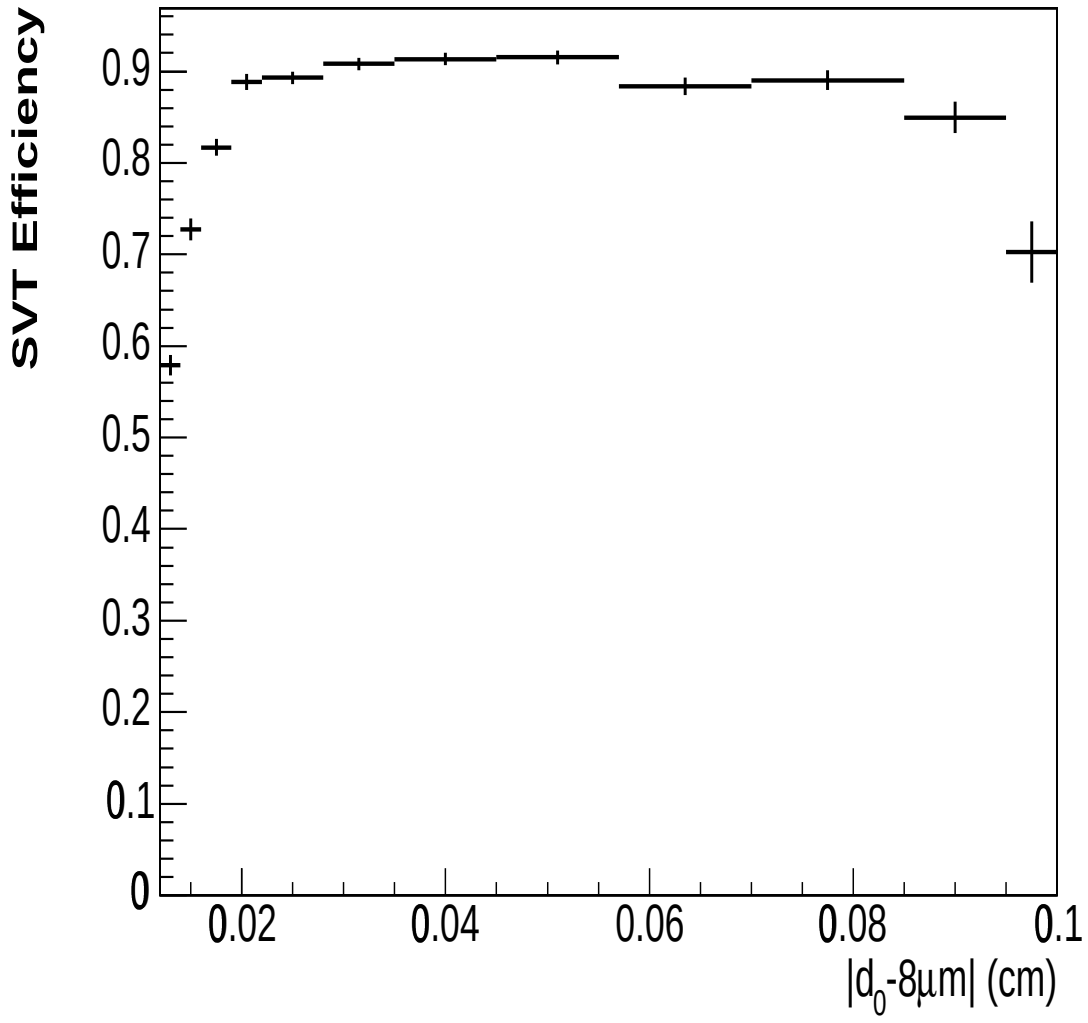

Figure 5.26: SVT efficiency vs. $|d_0 - 8\mu\text{m}|$ for $p_T > 2.255$ GeV/c.

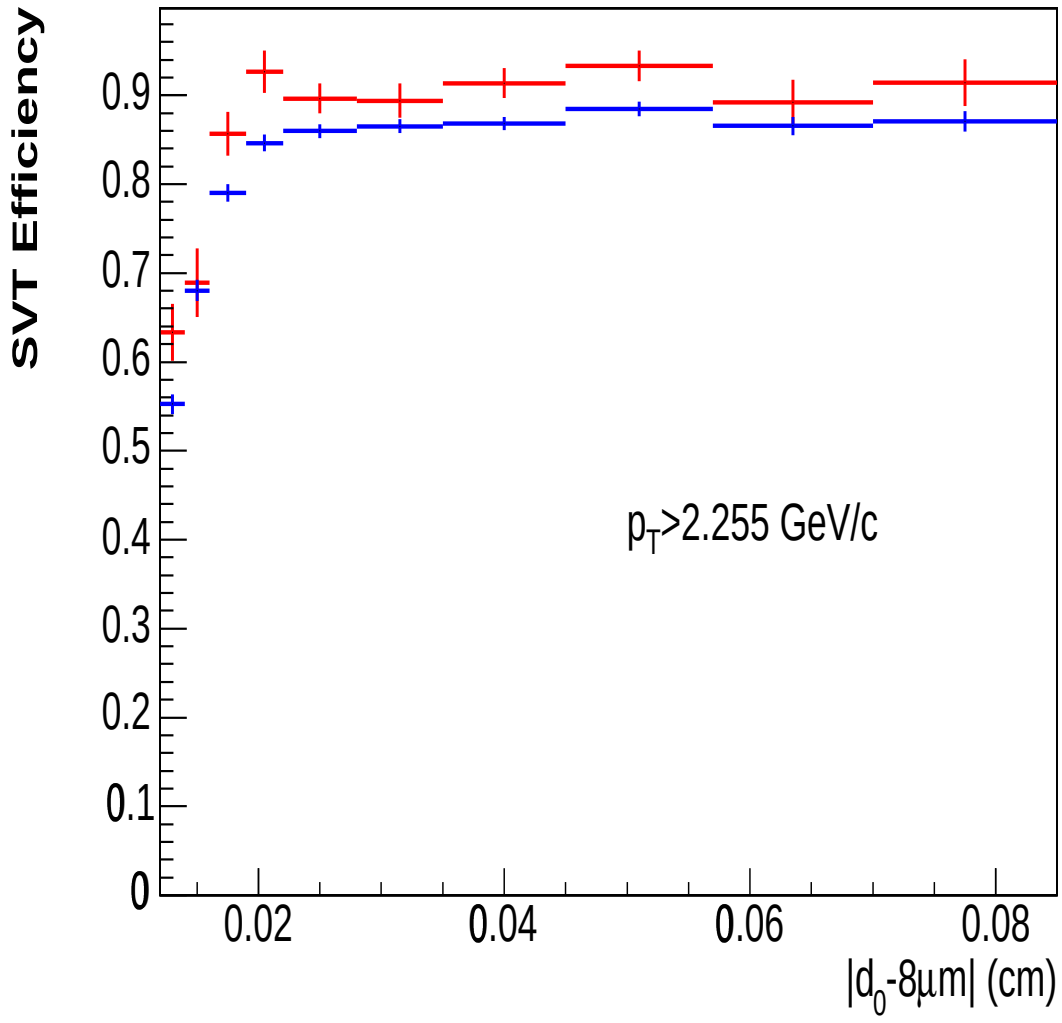

Figure 5.27: SVT efficiency vs. $|d_0 - 8\mu\text{m}|$ for tracks with a $p_T > 2.255$ GeV/c. Points in red represent the efficiency found using the muon tracks from $J/\psi \to \mu^+\mu^-$ decays, and points in blue come from tracks in the CMUP8 sample. There is no cut on ISO.

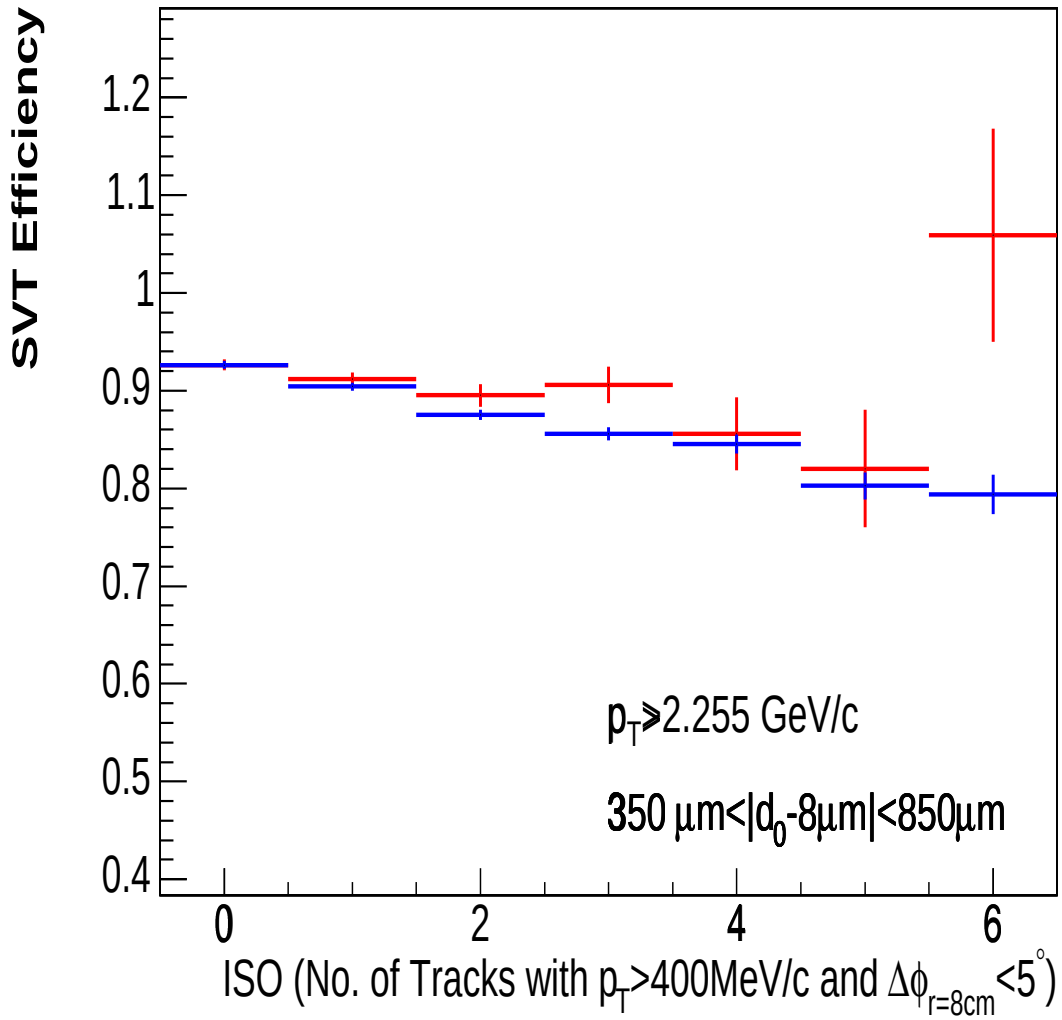

Figure 5.28: SVT efficiency vs. ISO for tracks with $p_T > 2.255$ GeV/c and $350\mu\text{m} < |d_0 - 8\mu m| < 850\mu\text{m}$. Points in red represent the efficiency found using the muon tracks from $J/\psi \to \mu^+\mu^-$ decays, and points in blue come from tracks in the CMUP8 sample.

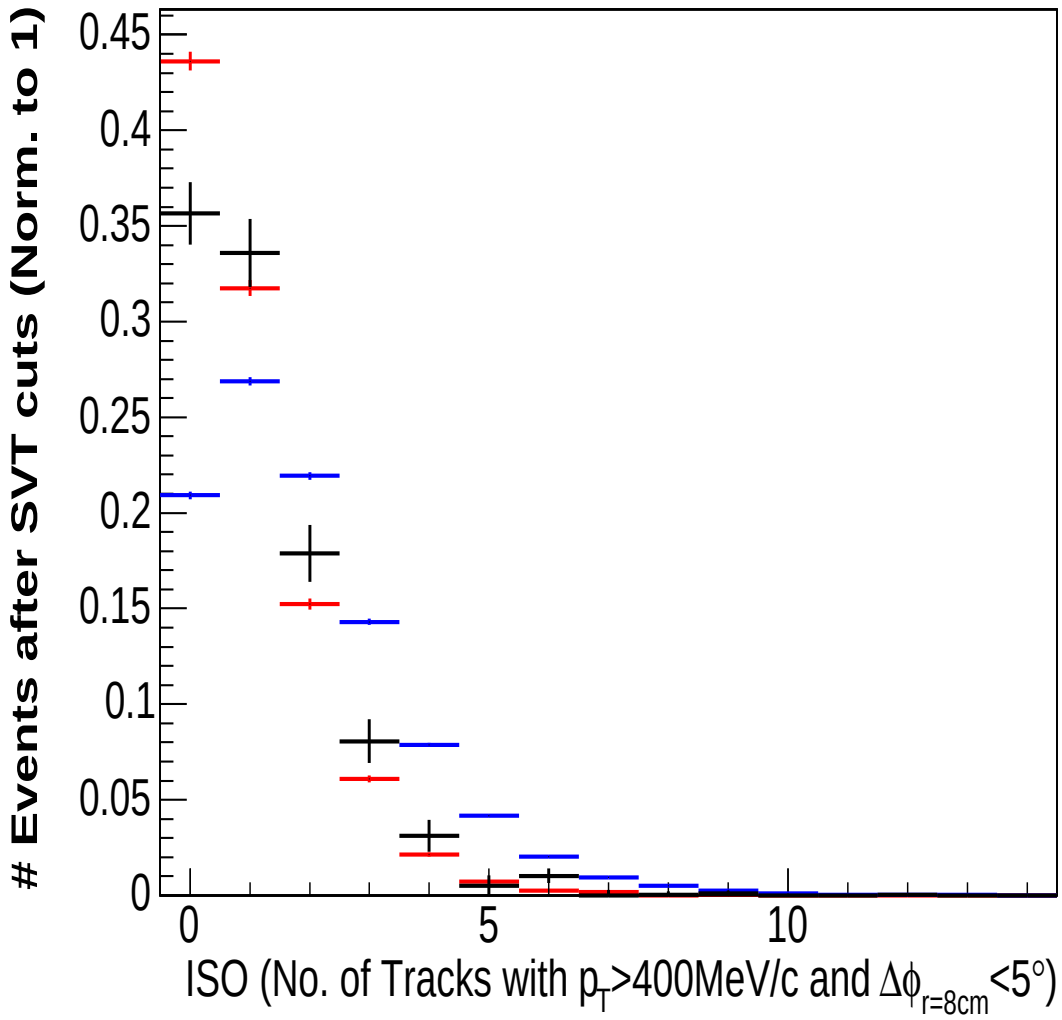

Figure 5.29: Distribution of tracks passing all numerator and denominator cuts vs. ISO normalized so that the sum over all bins for each histogram is one. Points in red represent the efficiency found using the muon tracks from $J/\psi \to \mu^+\mu^-$ decays, points in blue come from tracks in the CMUP8 sample, and points in black come from $D^0 \to \pi K$ decays in the signal sample, with sideband subtraction.

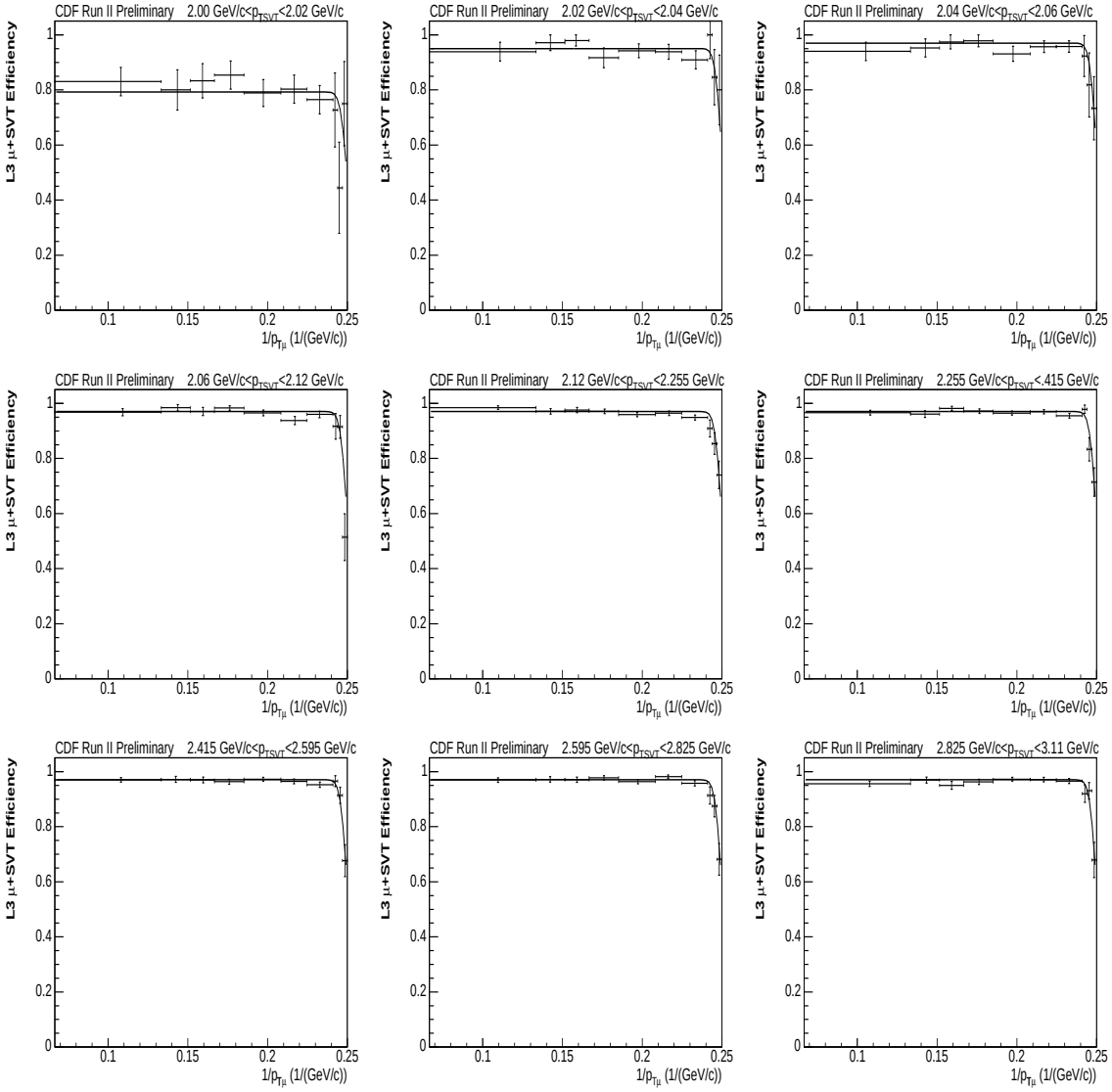

Figure 5.30: L3 μ+SVT efficiency vs. the inverse of the absolute value of the muons' transverse momentum (curvature) for various slices of the SVT tracks' momenta. The curves are the one dimensional projections of the two dimensional binned fit to the data.

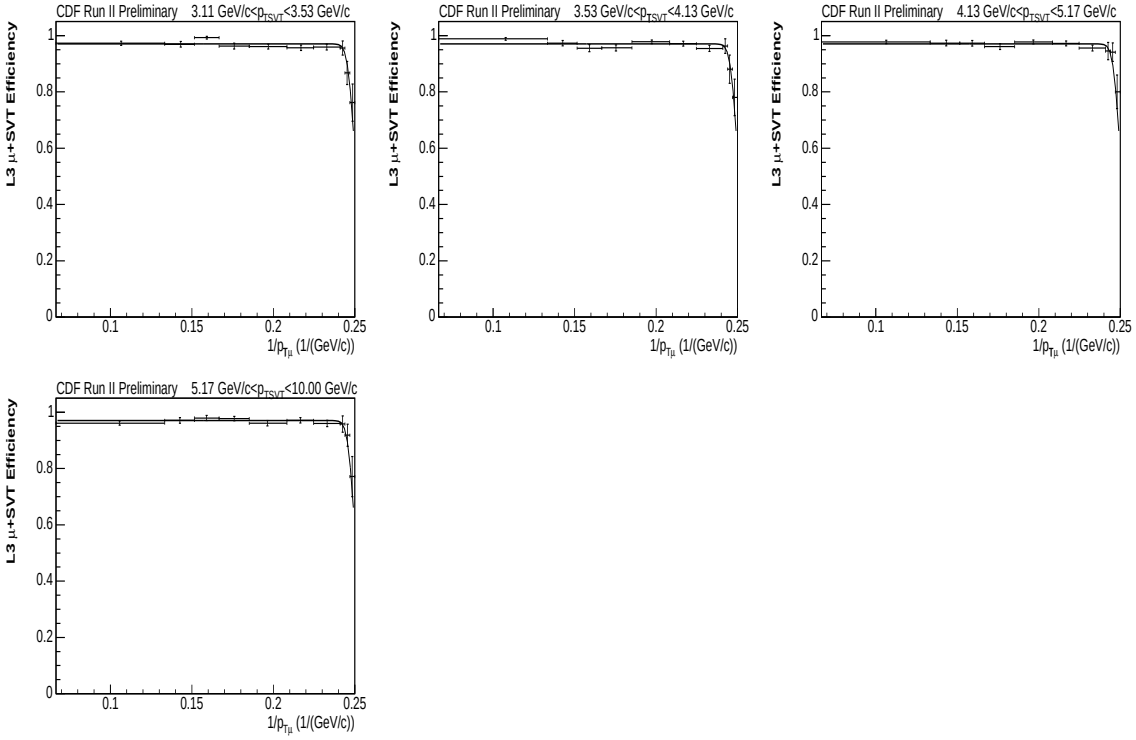

Figure 5.31: L3 μ+SVT efficiency vs. the inverse of the absolute value of the muons' transverse momentum (curvature) for various slices of the SVT tracks' momenta. The curves are the one dimensional projections of the two dimensional binned fit to the data.

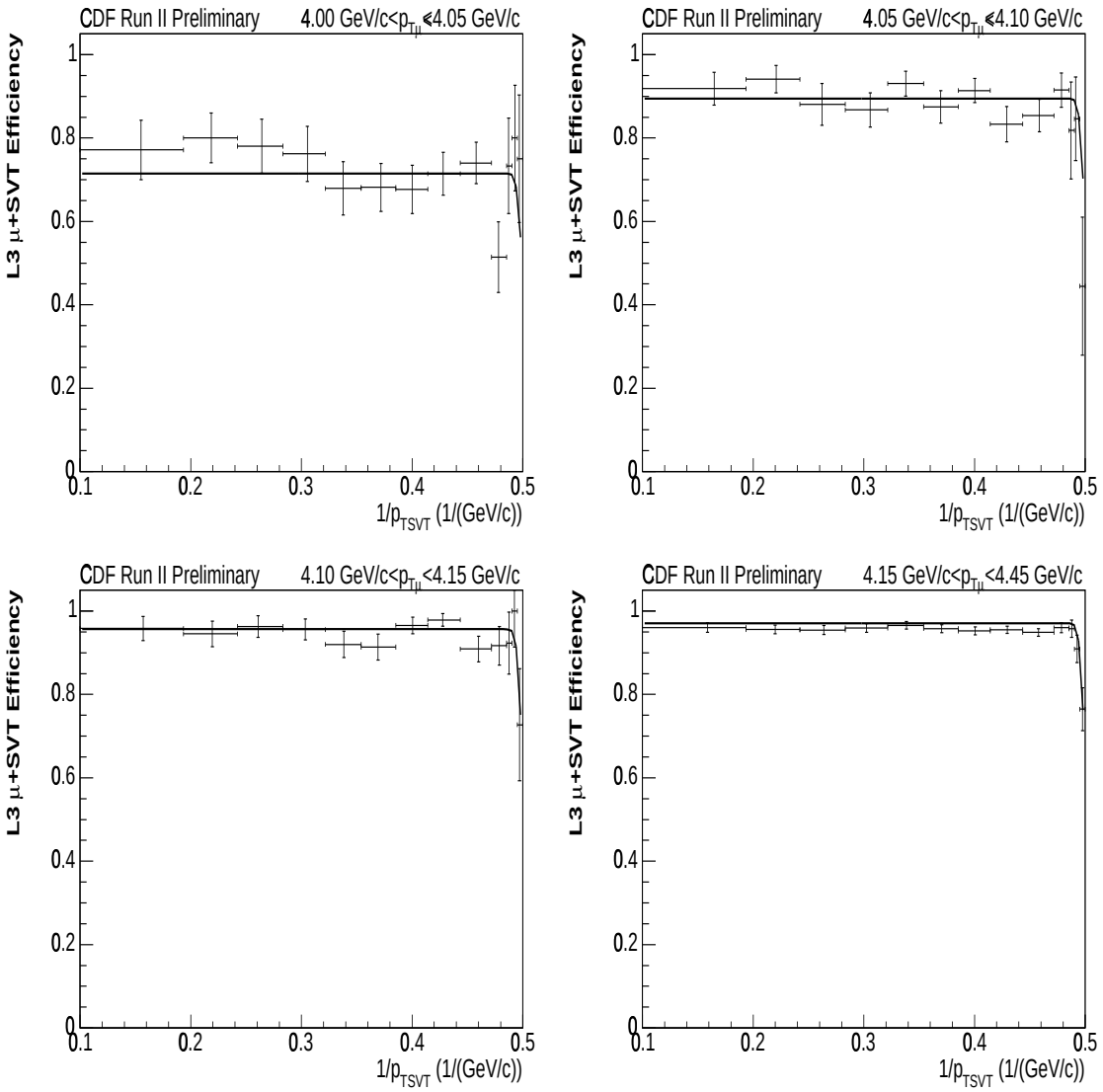

Figure 5.32: L3 μ+SVT efficiency vs. the inverse of the absolute value of the SVT tracks' transverse momentum (curvature) for various slices of the SVT tracks' momenta. The curves are the one dimensional projections of the two dimensional binned fit to the data.

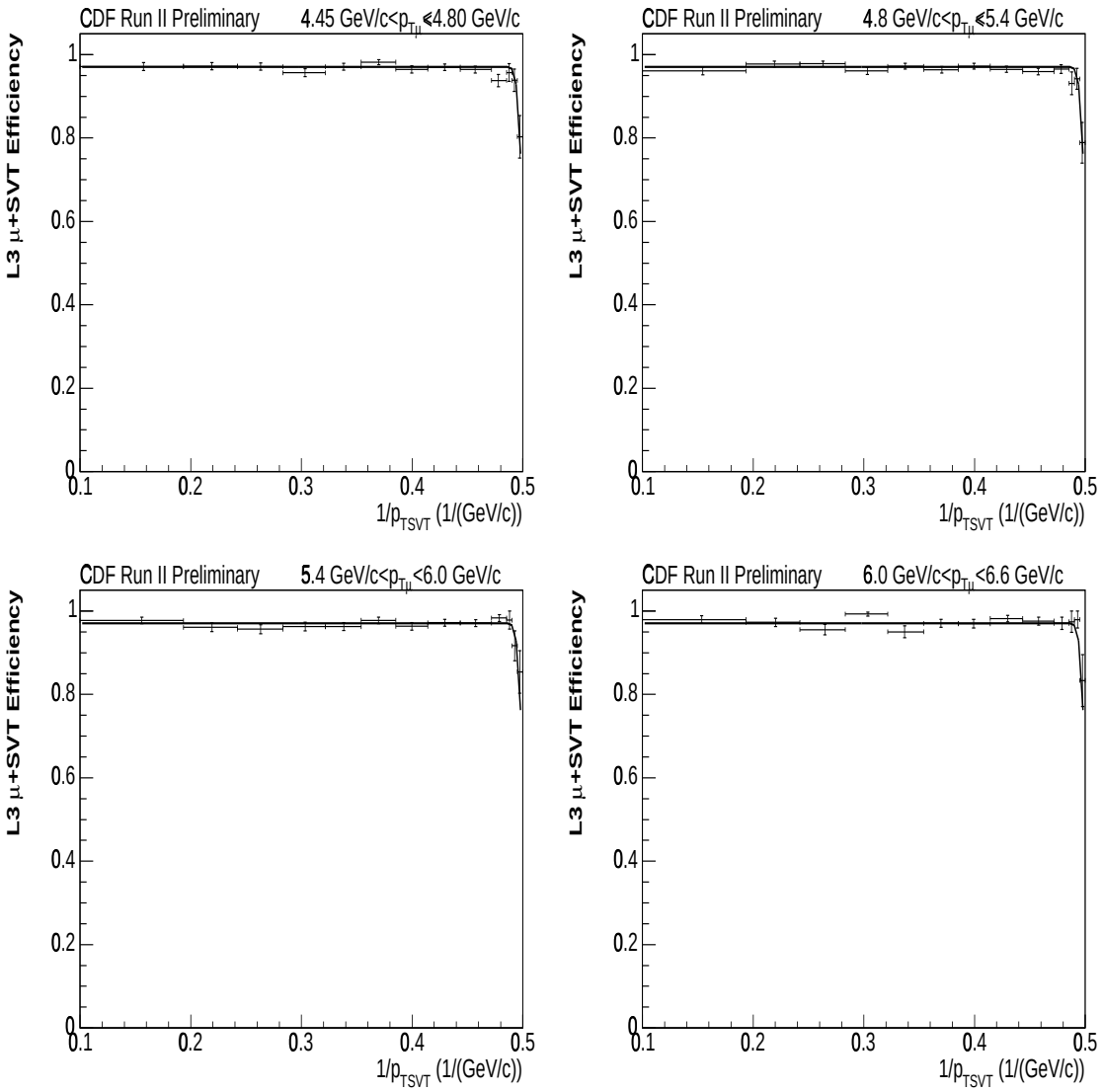

Figure 5.33: L3 μ+SVT efficiency vs. the inverse of the absolute value of the SVT tracks' transverse momentum (curvature) for various slices of the SVT tracks' momenta. The curves are the one dimensional projections of the two dimensional binned fit to the data.

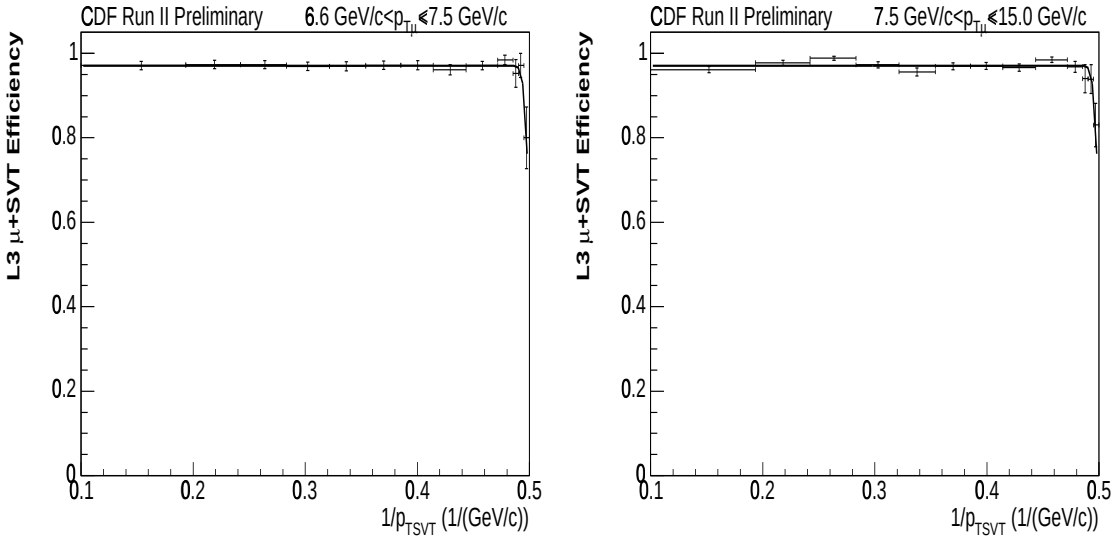

Figure 5.34: L3 μ+SVT efficiency vs. the inverse of the absolute value of the SVT tracks' transverse momentum (curvature) for various slices of the SVT tracks' momenta. The curves are the one dimensional projections of the two dimensional binned fit to the data.

Chapter 6

Offline Efficiencies and Partial Acceptances

6.1 Introduction

In the previous chapter, the measurements of the trigger efficiencies were made relative to the offline efficiencies. In this chapter, the offline efficiencies are found.

The SVX and muon stub efficiencies are measured using data. We find the efficiency of the SVX relative to the COT efficiency using J/ψ events that were taken on the dimuon triggers. We find the CMU efficiency times acceptance relative to the COT efficiency using reconstructed J/ψ events from the μSVT and CMUP8 triggers, and the efficiency times acceptance of the CMP relative to the efficiency of both the CMU and COT, using J/ψ events from the CMU-CMU trigger. The acceptances of the muon chambers that are measured include the geometric acceptances of the CMU and CMP detectors, and the kinematic acceptances associated with the muon tracks ranging out before arriving at the detectors. It does not, of course, include the acceptance due to part of the p_T and η spectrum of the muon tracks in the signal sample falling outside of our cuts. That component of the acceptance is calculated in the next chapter using Monte Carlo.

The COT efficiency is determined using MC and the track embedding method (See [12], [27]). In the track embedding method, MC track are fired into data events, near the z_0 of the highest momentum track in a given event. The hits from the MC track are then merged with the hits from the data event, and track reconstruction is then run to determine if the MC track is found in the COT.

6.2 SVX Efficiency

We have measured the SVX offline efficiency with respect to the COT tracking efficiency for tracks that SiExpected [52] predicts will pass through the 4 layers of the SVX which can fire the trigger:

$$\frac{\epsilon(\text{SVX offline}) \times \epsilon(\text{COT offline})}{\epsilon(\text{COT offline})} \tag{6.1}$$

We have made this measurement using muon tracks that came in on the $J/\psi \rightarrow \mu^+\mu^-$ CMU-CMU and CMU-CMX triggers (see sections 4.2.5 and 4.2.6). In order to get into our denominator, the tracks must pass the following cuts:

- The invariant di-muon mass must be within the range 3.04668 GeV/c^2 to 3.13222 GeV/c^2, which is a $\pm 3\sigma$ window about the J/ψ mass peak. Sideband subtraction is used (Figure 6.1).
- The track must have $p_T > 2.0$ GeV/c.
- The track must have $|\eta| < 1$
- The track must have $|z_0| < 47.25$ cm
- We use the SiExpected algorithm to predict which SVX layers the track would have crossed. We require that the track not be expected to cross any mechanical barrels or wedges. In addition, the track must be predicted to hit all 4 SVX layers which were used in the SVT for that wedge. We found that some layers used in the SVT which the database said were integrated had 0 or close to 0 efficiency, and tracks passing through these layers were also excluded. A list of these layers is provided in table 5.38.
- The track must pass COT fiducial cuts. Specifically, it must have a $|z_{SL8}| < 151$ cm and have more than 4 hits in two axial and two stereo superlayers.
- The track is not allowed to cross the spacer in the COT in a superlayer used by the XFT. Specifically, it must have a $|z| > 1.5$ cm in superlayers 2,4,6, and 8.
- We exclude sections of the SVX in ϕ measured at a radius of 8 cm from the beamline where the SVX efficiency is changing rapidly. We also exclude sections of the SVX in z measured at a radius of 8 cm from the beamline which were previously excluded in the measurement of the SVT efficiency in Section 5.3.2. The excluded sections in $\phi_{r=8cm}$ were
  - $8.75^\circ < \phi_{r=8cm} < 18.75^\circ$
  - $42.5^\circ < \phi_{r=8cm} < 50^\circ$
  - $70^\circ < \phi_{r=8cm} < 77.75^\circ$
  - $103.75^\circ < \phi_{r=8cm} < 107.5^\circ$
  - $132.5^\circ < \phi_{r=8cm} < 138.75^\circ$
  - $161.25^\circ < \phi_{r=8cm} < 171.25^\circ$

- $191.25° < \phi_{r=8cm} < 197.5°$
- $216.25° < \phi_{r=8cm} < 230°$
- $251.25° < \phi_{r=8cm} < 256.25°$
- $282.5° < \phi_{r=8cm} < 287.5°$
- $310° < \phi_{r=8cm} < 321.25°$
- $340° < \phi_{r=8cm} < 348.75°$

The excluded sections in $z_{r=8cm}$ were

- -45 cm $< z_{r=8cm}$
- -17cm $< z_{r=8cm} < -15$ cm
- 15cm $< z_{r=8cm} < 17$ cm
- $z_{r=8cm} < 45$ cm.

In order to get into the numerator of our measurement, the track must be reconstructed with SVX phi hits in the 4 SVX layers used in the SVT.

Looking at the efficiency vs. $z_{r=8cm}$, we see that the efficiency varies by more than 20% depending on z position. Therefore, we find the SVX efficiency with respect to $z_{r=8cm}$, using 1 cm wide z bins shown in figure 6.2. We examine the efficiency for dependence on p_T, but see none (Figure 6.3). The efficiency is also roughly flat with respect to run number (Figure 6.4). The efficiency also varies somewhat with respect to $\phi_{r=8cm}$ (Figure 6.5), but not to the point that a systematic seems necessary.

There is a very slight dependence on the η of the track (Figure 6.6). In order to assess a systematic on the η dependence, we compare the η distribution in the J/ψ CMU/CMX track sample with the η distribution of tracks from the CDF MC sample (described in Sec. 4.4.1) which pass all the numerator cuts above (Figure 6.7). We then reweight the tracks that go into the SVX efficiency measurement so that the η distribution matches that from the MC sample. We find the SVX efficiency with respect to $z_{r=8cm}$, using 1 cm wide z bins with the η reweighting, and use this to assess a systematic (Figure 6.8).

We define the variable ISO, as in the SVT measurement, as the number of tracks with a $p_T > 400$ MeV/c within $\Delta\phi_{r=8cm} < 5°$, and plot the SVX efficiency versus this variable in figure 6.9. We see that the efficiency does vary systematically with respect to ISO; it appears that for every track added, the efficiency drops by 0.5%. We know from our previous study that our signal sample is less isolated than the tracks in the J/ψ sample, so we assign a -0.5% systematic to our efficiency measurement to account for the difference (Figure 6.10 compares the J/ψ and $\mu + D^0$ SVX isolation distributions).

6.3 Second Leg SVX Efficiency

For the $H_b \to \mu + D^0 + X$ cross-section times branching ratio analysis, we require that the leg of the D^0 which did not fire the SVT trigger have at least 3 SVX phi hits, in order to more accurately estimate charm backgrounds. This means that we need the efficiency of the SVX for the second leg. We can obtain this efficiency by reconstructing the D^0 peak in our signal sample both with and without requiring that second D^0 leg have 3 SVX phi hits. As we are making this measurement in the signal sample, no parameterization of the efficiency is necessary. We find that the single leg SVX efficiency is $93.21\% \pm 0.97\%$. This measurement is equivalent to:

$$\frac{\epsilon(\text{SVX } 2^{\text{nd}} \text{ leg}) \times \epsilon(\text{SVX offline}) \times \epsilon(\text{COT offline})^2}{\epsilon(\text{SVX offline}) \times \epsilon(\text{COT offline})^2} \tag{6.2}$$

6.4 CMU Efficiency x Acceptance

Next, we find the CMU stub offline efficiency times acceptance with respect to the COT offline efficiency:

$$\frac{\epsilon(\text{CMU offline}) \times \epsilon(\text{COT offline})}{\epsilon(\text{COT offline})} \tag{6.3}$$

To get this measurement, we reconstruct the $J/\psi \to \mu^+\mu^-$ mass peak in events that came in on the μSVT trigger and in events that came in on the CMUP8 trigger (section 4.2.2). In order to get into the denominator of the sample, a track must satisfy the following requirements:

- The invariant di-muon mass must be within the range 3.04006 GeV/c^2 to 3.13974 GeV/c^2 (3.033407 GeV/c^2 to 3.147853 GeV/c^2), which is a $\pm 3\sigma$ window about the J/ψ mass peak for the events that came in on the μSVT (CMUP8) trigger. Sideband subtraction is used (Figures 6.11 and 6.12).

- The biased leg of the J/ψ must be a CMUP muon with a $p_T > 4$ GeV/c(8 GeV/c) for tracks from the μ SVT (CMUP8) sample. The μ must be confirmed as passing the Level 1 CMUP4 trigger. The requirements for passing the L1 CMUP4 trigger are listed in section 4.2.1.

- For tracks coming on on the μ SVT trigger, the biased leg must have a $p_T < 8$ GeV/c. This avoids the possibility of double counting events that came in on both triggers.

- For events taken using the CMUP8 trigger, the biased leg must be matched to an XFT track with a $p_T > 8$ GeV/c.

- For events taken using the μ SVT trigger, the probe leg of the J/ψ must pass the SVT trigger requirements. Specifically, the track must
  - The offline track must be matched to an SVT track with a matching $\chi^2 < 25$ [53].
  - The SVT $p_T > 2$ GeV/c
  - The SVT $|d_0|$ must be between 120 μm and 1 mm.
  - The SVT $\chi^2 < 25$
- The probe track must have $p_T > 4.0$ GeV/c.
- The probe track must have $|\eta| < 0.6$
- The probe track must have $|z_0| < 47.25$ cm
- The track must pass COT fiducial cuts. Specifically, it must have a $|z_{SL8}| < 151$ cm and have at least 5 hits in two axial and two stereo superlayers.
- The track is not allowed to cross the spacer in the COT in a superlayer used by the XFT. Specifically, it must have a $|z| > 1.5$ cm in superlayers 2, 4, 6, and 8.
- The track is extrapolated out to the radius of the CMU. We require that the predicted 10 cm $< |z_{CMU}| < 220$ cm. Also, for $z_{CMU} < 0$, we exclude tracks between $255° < \phi_{CMU} < 270°$ (wedge 17), as wedge 17 is known to be less efficient in our run range. Also, there must be a separation of at least 7° between the predicted location of the probe stub in the CMU and the biased CMU stub.
- The track is extrapolated out to the CMP, and we require that the predicted $|z_{CMP}| < 310$ cm.

To test the algorithm used to extrapolate the tracks out to the CMU and CMP, we ran the algorithm on the muon tracks from the SVX offline efficiency measurement (section 6.2) and looked at the difference between the predicted and observed ϕ positions in the CMU (while requiring $dX_{CMU} < 15$ cm). We also compared the ϕ positions in the CMP (requiring $dX_{CMP} < 20$ cm) for muons with CMP stubs. Lastly, we checked the algorithm's z prediction in the CMU for muons that came in on the the B semileptonic backup trigger (section 4.2.4). We found a good level of agreement in all cases (See figures 6.13, 6.14, and 6.15). We also have checked the separation of the peaks for μ^+ and μ^- in the $\Delta\phi_{predicted-stub}$ distribution for both CMU and CMP distributions. The CMU difference is 0.18°, and the CMP difference is 0.80° (Figures 6.16 and 6.17).

In order for the track to enter the numerator of our measurement, it must pass the following requirements.

- The probe track must be the best match to an offline CMU stub.
- The CMU stub must have a $dX < 15$ cm and a $\chi^2 < 9$.

If both legs of the J/ψ pass all bias and probe cuts, then both legs are treated as probe tracks. We look at the CMU stub efficiency times acceptance versus p_T, ϕ_{CMU}, and η (Figures 6.18, 6.19, and 6.20). The CMU efficiency times acceptance does not have a strong dependence on any of these variables. We thus find that the CMU offline stub efficiency times acceptance is $79.5\% \pm 1.3\%$

6.5 CMP Efficiency x Acceptance

We find the CMP offline stub efficiency times acceptance with respect to the COT and CMU offline efficiencies:

$$\frac{\epsilon(\text{CMP offline}) \times \epsilon(\text{CMU offline}) \times \epsilon(\text{COT offline})}{\epsilon(\text{CMU offline}) \times \epsilon(\text{COT offline})} \tag{6.4}$$

To do this, we use muons that came in on the $J/\psi \to \mu^+\mu^-$ CMU-CMU trigger (section 4.2.5). In order to get into the denominator of our measurement, the track must satisfy the following:

- The invariant di-muon mass must be within the range 3.03865 GeV/c^2 to 3.13972 GeV/c^2, which is a $\pm 3\sigma$ window about the J/ψ mass peak. Sideband subtraction is used.
- The event must have come in on the L3 J/ψ CMU-CMU trigger.
- The $|\Delta z_0|$ between the 2 muons must be less than 5 cm.
- The non-probe track must have $p_T < 2.5$ GeV/c. This is to ensure that the two muons won't have CMP stubs close to one another which could alter the measurement.
- The probe track must have $p_T > 4.0$ GeV/c.
- The probe track must have $|\eta| < 0.6$
- The probe track must have $|z_0| < 47.25$ cm
- The track must pass COT fiducial cuts. Specifically, it must have a $|z_{SL8}| < 151$ cm and have at least 5 hits in two axial and two stereo superlayers.
- The track is not allowed to cross the spacer in the COT in a superlayer used by the XFT. Specifically, it must have a $|z| > 1.5$ cm in superlayers 2, 4, 6, and 8.

- The muon must have a CMU stub with a $dX < 15$ cm and a $\chi^2 < 9$.
- The track is extrapolated out to the radius of the CMU. We require that the predicted 10 cm $< |z_{CMU}| <$ 220 cm. Also, for $z_{CMU} < 0$, we exclude tracks between $255° < \phi_{CMU} < 270°$ (wedge 17), as wedge 17 is known to be less efficient in our run range.
- The track is extrapolated out to the CMP, and we require that the predicted $|z_{CMP}| < 310$ cm.

In order to get into the numerator of our measurement, the muon must be matched to a CMP stub with a $dX < 20$ cm.

The efficiency times acceptance is parameterized using the function:

$$\epsilon_{CMP} = (\epsilon_{plat} + \epsilon_{pT1} * 1/p_T + \epsilon_{pT2} * (1/p_T)^2) * \mathrm{erf}(\frac{\eta - \eta_-}{\sigma_{\eta-}}) * \mathrm{erf}(\frac{\eta_+ - \eta}{\sigma_{\eta+}}) \tag{6.5}$$

Where erf is the error function, defined in equation 5.5. The results of the fit of this function to the data can be found in table 6.1 and the corresponding error matrix is found in table 6.2. Slices of the fitted curve are plotted against the data points vs. $1/p_T$ and η in figures 6.21 through 6.25. One problem we have is that, while the efficiency times acceptance is well behaved in both η and $1/p_T$, the efficiency times acceptance versus ϕ_{CMP} varies by as much as 25%, in a manner that is difficult to parameterize (Figure 6.26). This is largely due to the fact that, unlike the other CDF detector components used in this analysis, the CMP is not cylindrically symmetric. Rather than try to parameterize the efficiency times acceptance in ϕ_{CMP}, we instead look at the ϕ_{CMP} of our signal sample, which satisfied the B semileptonic trigger (section 4.2.1). (We have looked at the efficiency of this trigger with respect to the offline efficiency in the previous chapter, and did not observe any variation in the muon trigger efficiency with respect ϕ.) We reconstruct the $D^0 \to \pi^+K^-$ peak in this sample, and use sideband subtraction based on the $D^0 \to \pi^+K^-$ peak in order to obtain a sample of muons that are all associated with a D^0 meson. (We require the π and μ to have opposite charges.) We found multiple ϕ_{CMP} distributions by varying the cuts on μD^0 p_T and η, and checked the ϕ_{CMP} distribution of the signal plus sidebands together. We compare the ϕ_{CMP} distributions from the μD^0 sample to the ϕ_{CMP} distribution of the J/ψ muons which pass both the numerator and denominator cuts above. We note that the distributions are somewhat different. To take this difference into account, we reweight the events that go into the CMP efficiency times acceptance so that its ϕ_{CMP} distribution matches that from the signal sample. For most of the distributions, the difference is negligible. The largest difference between the reweighted and unreweighted efficiencies was found to be from the distribution of signal and sidebands together, which raises the CMP efficiency times acceptance in all η and $1/p_T$ bins by about 1% or less. (figures 6.27 and 6.28). To be conservative, we therefore assess a 1.0% systematic due to the differing

ϕ_{CMP} distributions.

6.6 COT Efficiency

The COT offline reconstruction efficiency was measured using two different methods. The first was the track embedding method. Single μ, π, and K particles and anti-particles were fired using FakeEvent (section 4.4.3) into events that were taken using the μSVT trigger. The p_T distribution of the tracks fired into the event was based on that generated by in the Bgenerator CDF sample 4.4.1, and for π and K the tracks are place in the event around the highest momentum CMUP4 muon using the $dR = \sqrt{\Delta\phi_0^2 + \Delta\eta^2}$ distribution from the CDF sample. The μ tracks were also embedded within $dR < 1.4$ the CMUP4 muon. We also attempted to embed the tracks near a second track, if possible. The embedded tracks are placed within 5 cm of the z_0 of the highest momentum track in a given event. The MC tracks are integrated into the data events and production was run to see of the COT reconstruction could find the tracks. We used a small subsample of events that covered the range of runs and luminosities used in this analysis. Efficiencies are found separately for particles and anti-particles. In order for the MC particle to enter the efficiency measurement, we require that the $|z_{SL8}| < 151$cm. In order to enter the numerator of the measurement, we require that

- The Monte Carlo track be matched to a COT track.
- $|\Delta curv| < 0.00025$ cm^{-1} between the MC and COT track.
- $|\Delta\phi_0| < 0.03$ radians between the MC and COT track

These limits were set to find tracks down to low momentum.

In the other method, we simply used TrackMatchUtils to match COT tracks to the generator level tracks in the pure Monte Carlo generated with Bgenerator. The same $|\Delta curv|$ and $|\Delta\phi_0|$ cuts listed above were used. Because most of the COT inefficiency is due to either decay in flight or nuclear interactions with the material, both of which are well modelled by the Monte Carlo, the resulting efficiency agrees with the efficiency from track embedding to within less than a percent for tracks with a p_T above 1 GeV/c. For pions between 0.4 and 1.0 GeV/c, which are needed for the D^{*+} measurement, the efficiency from track embedding falls with respect to the efficiency in pure Monte Carlo. Between 0.40 and 0.41 GeV/c, the pion efficiency from track embedding is only $\approx 90\%$ of the value of the efficiency from the pure MC for that p_T range. However, the D^0/D^* double ratio study [54], indicates that the efficiency should not fall off as fast as it does in the track embedding sample. Therefore, we use the efficiency from TrackMatchUtils in pure Bgenerator MC as the default, and use the efficiency from the track embedding sample as a systematic by

weighting the events which pass in the Bgenerator sample by the ratio of the efficiency from track embedding to the efficiency from the pure MC. Plots of the COT efficiency from both track embedding and the pure Bgenerator MC can be found in figures 6.29 through 6.34.

We use π with transverse momenta down to 0.4 GeV/c as soft pions in the D^* measurement. In order to convince ourselves that the track embedding method adequately describes the COT efficiency down to low momentum, we embed the soft pions into the data with the p_T spectrum of soft pions from the CDF sample, after all cuts and efficiencies have been applied. We then compare the p_T spectrum of the tracks found by the COT with the p_T spectrum of the soft pions from data, after adjusting for the SVT efficiency and sideband subtraction. Above 0.4 GeV/c, the two curves agree to within errors as shown in figure 6.35. Also, we wish to be very certain that the efficiencies used for the soft pion systematics bracket the range of possible efficiencies. To see about this, we look at the $D^{*+} - D^0$ mass difference in the Bgenerator Monte Carlo, using COT tracks that were matched to the generator level tracks with TrackMatchUtils. First, we require both the π and the K from the D^0 decay to pass the matching cuts. We then compare the Δm distribution for events where the soft pion passed our $|\Delta curv|$ and $|\Delta\phi_0|$ cuts to the one for events where the soft pion was found by TrackMatchUtils but failed the matching cuts (fig. 6.36). The Δm distribution for events that failed the cuts is much wider than the one for events passing the cuts, and it is clear that many of the events that failed would not have given a Δm in the signal region. However, a significant fraction that failed the matching cuts are still in the Δm signal region, so we cannot discount these events entirely. This gives us confidence that the efficiency without matching cuts brackets the uncertainty.

Unfortunately, there is uncertainty as to the amount of material in the detector, which leads to an uncertainty the number of nuclear interactions we should expect. To take this into account, we so we weight events with a nuclear interaction by $\pm 25\%$, effectively varying the amount of material by 25%. This leads to roughly 1.5% systematic uncertainty on the π and K efficiencies.

We also examine the efficiency versus luminosity and isolation for systematic uncertainty. However, the luminosity is low enough in our sample (the highest instantaneous luminosity is 46.489×10^{30} cm^{-2}s^{-1}) that there is no significant effect on the COT efficiency. We assess a systematic based isolation, which here we define as

$$ISO_{std} = \frac{\text{embedded track } p_T}{\sum p_T \text{ of all COT tracks within } dR < 0.5} \tag{6.6}$$

The sum in the denominator of equation 6.6 includes the p_T of the COT track resulting from the embedded track, if it is found. When determining this systematic, we remove nuclear interactions and decays in flight, so these effects are not double counted. We see by looking at the COT efficiency vs. ISO_{std} distributions that there is about a 2.5% drop in efficiency from $ISO_{std} = 1.0$ to $ISO_{std} < 0.1$ for most of the particles.

It is somewhat more for muons. We know our embedded tracks are somewhat more isolated that the tracks in our data sample, so we assign a -1% systematic on the COT efficiencies.

In this measurement, we do not take into account any effects due to the aging of the COT. This may seem odd, given the impact aging had on measurements of the trigger efficiencies in chapter 5. The reason is that the XFT track finder used in the trigger requires that at least 11 of 12 possible hits be found in all 4 of the COT axial superlayers. This leads to small drops in the hit finding efficiency of a single wire causing large changes in the XFT efficiency. The COT offline tracking, on the other hand, requires only 5 or more hits on 2 of the axial superlayers and 2 of the stereo superlayers. These cuts are sufficiently forgiving that the small drop in hit efficiency in this period should not cause a noticeable drop on the COT offline reconstruction efficiency.

6.7 Summary

We have measured the offline efficiency for the SVX and the CMU and CMP stub efficiencies times acceptances. The SVX efficiency was measured using events that came in on the J/ψ CMU-CMU and CMU-CMX triggers, and parameterized in terms of $z_{r=8cm}$. The CMU stub efficiency times acceptance was measured using events that were taken by the $\mu + SVT$ and CMUP8 triggers, and the result was found to be a flat $79.5\% \pm 1.3\%$. The CMP stub efficiency times acceptance was measured using events that came in on the J/ψ CMU-CMU trigger, and was parameterized in terms of $1/p_T$ and η. The COT efficiency has been found using the track embedding method for μ, π, and K.

$\chi^2/ndf = 85.53/89$						
ϵ_{plat}	ϵ_{pT1} (GeV/c)	ϵ_{pT2} ((GeV/c)^2)	η_-	$\sigma_{\eta-}$	η_+	$\sigma_{\eta+}$
0.89570	0.96601	-5.0486	-0.75344	0.28185	0.75578	0.25326

Table 6.1: The results of the fit of equation 6.5 to the CMP stub acceptance

	ϵ_{plat}	ϵ_{pT1}(GeV/c)	ϵ_{pT2}((GeV/c)^2)	η_-	$\sigma_{\eta-}$	η_+	$\sigma_{\eta+}$
ϵ_{plat}	0.260E-02	-0.288E-01	0.764E-01	-0.317E-04	0.363E-04	0.722E-05	0.128E-04
ϵ_{pT1}(GeV/c)	-0.288E-01	0.326	-0.878	-0.321E-03	0.528E-03	0.358E-03	0.499E-03
ϵ_{pT2}((GeV/c)^2)	0.764E-01	-0.878	2.40	0.918E-03	-0.150E-02	-0.121E-02	-0.156E-02
η_-	-0.317E-04	-0.321E-03	0.918E-03	0.231E-02	-0.233E-02	-0.141E-03	-0.233E-03
$\sigma_{\eta-}$	0.363E-04	0.528E-03	-0.150E-02	-0.233E-02	0.248E-02	0.195E-03	0.321E-03
η_+	0.722E-05	0.358E-03	-0.121E-02	-0.141E-03	0.195E-03	0.201E-02	0.181E-02
$\sigma_{\eta+}$	0.128E-04	0.499E-03	-0.156E-02	-0.233E-03	0.321E-03	0.181E-02	0.178E-02

Table 6.2: The error matrix of the fit of equation 6.5 to the CMP stub acceptance

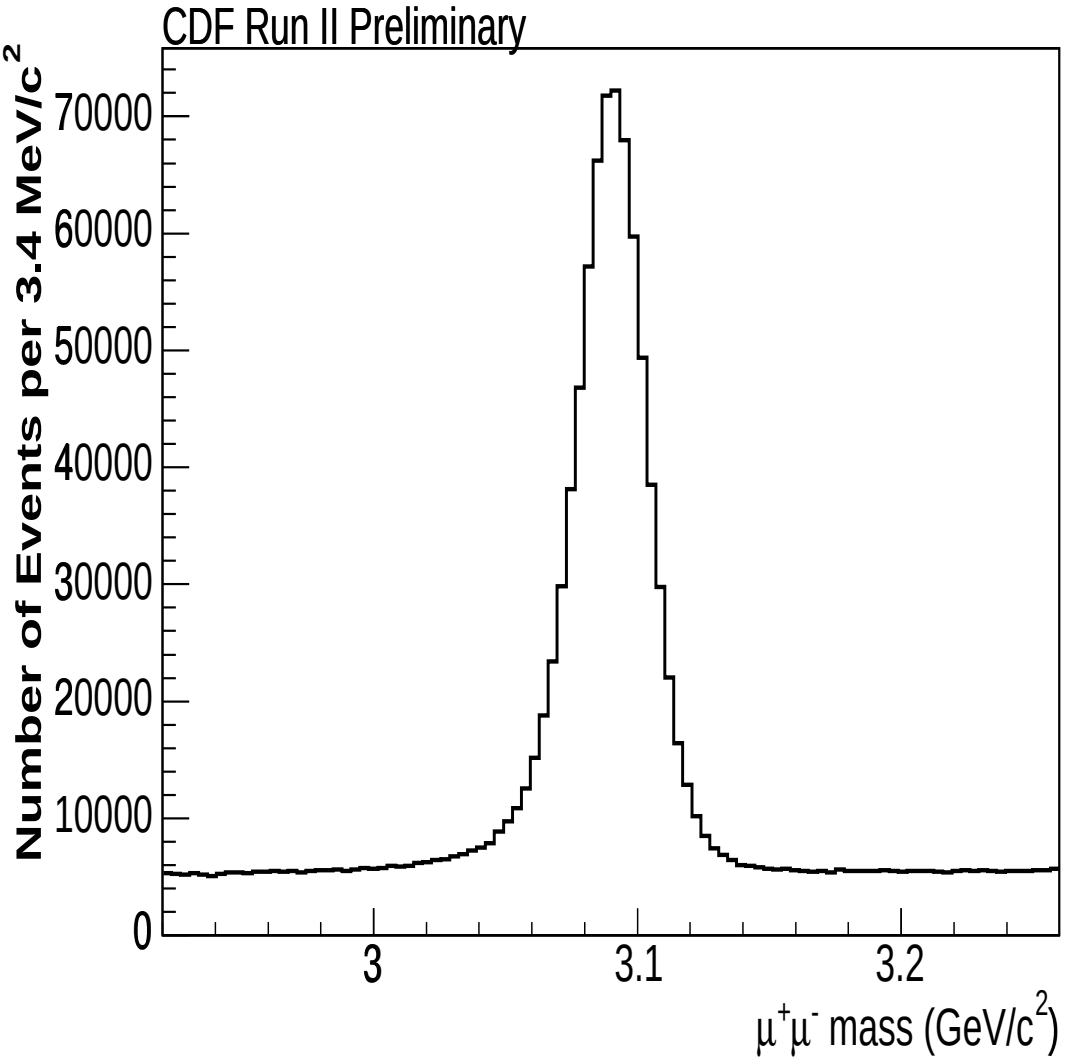

Figure 6.1: The J/ψ dimuon mass peak for the SVX Efficiency measurement.

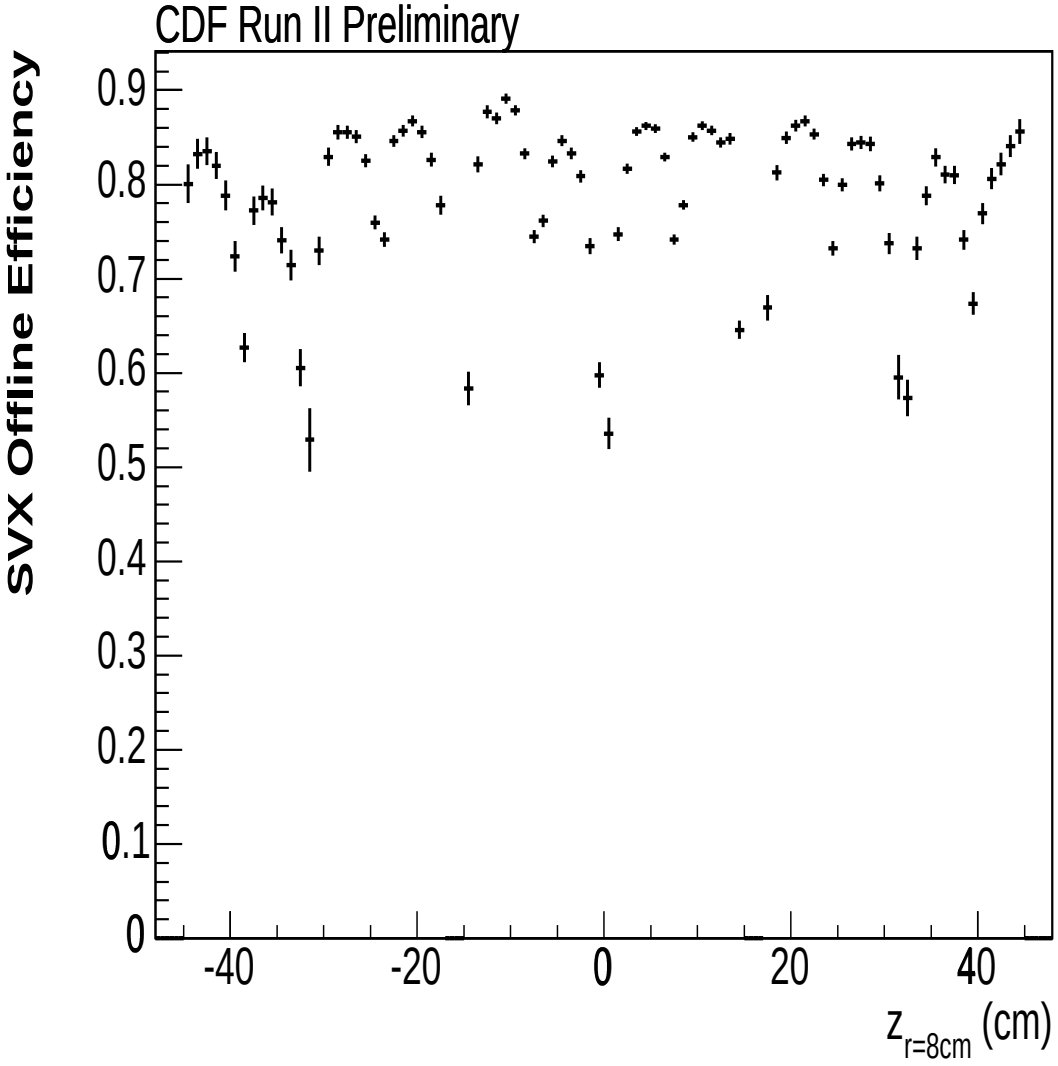

Figure 6.2: The SVX offline efficiency vs. $z_{r=8cm}$. The gaps in the efficiency are at points which were excluded due to low and rapidly changing efficiency in the SVT.

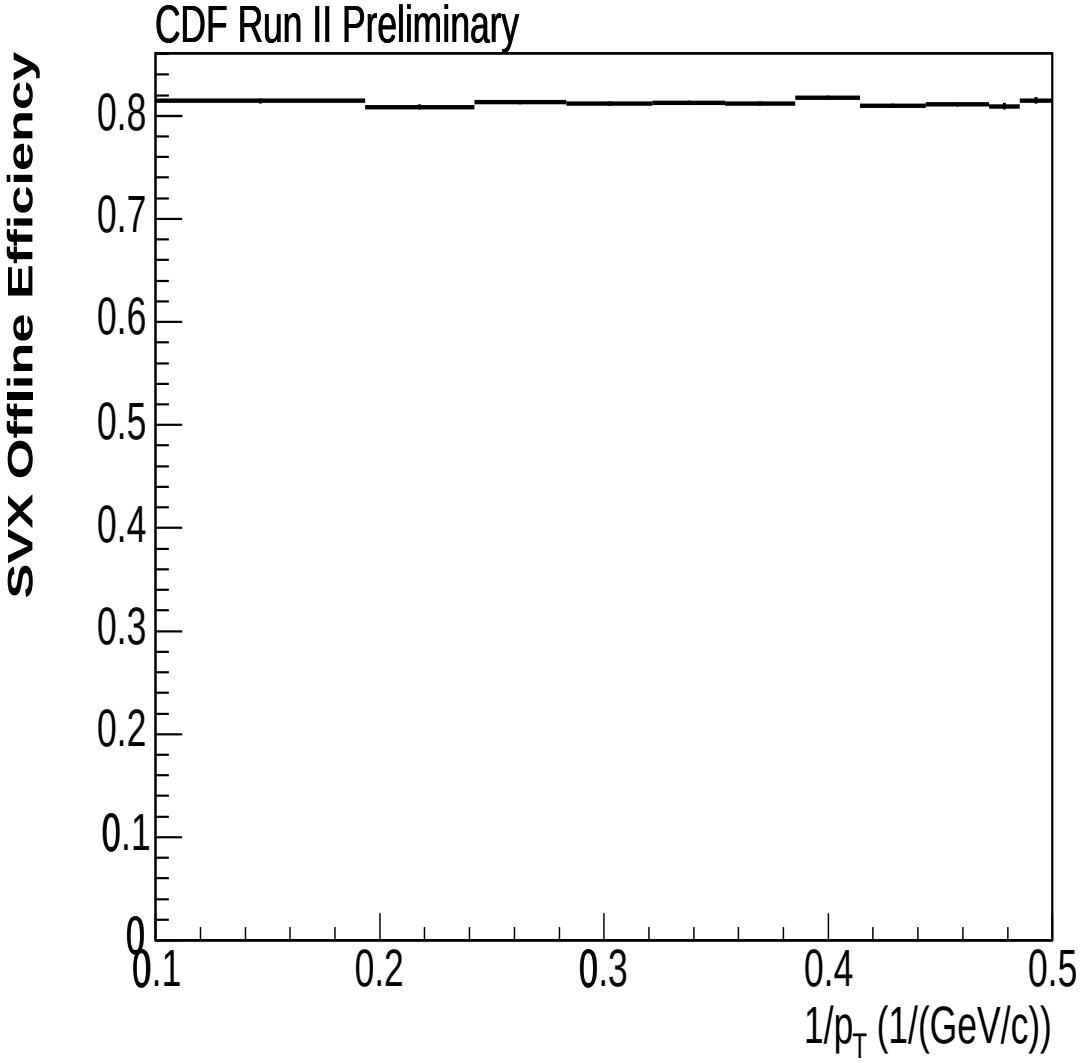

Figure 6.3: The SVX offline efficiency vs. $1/p_T$

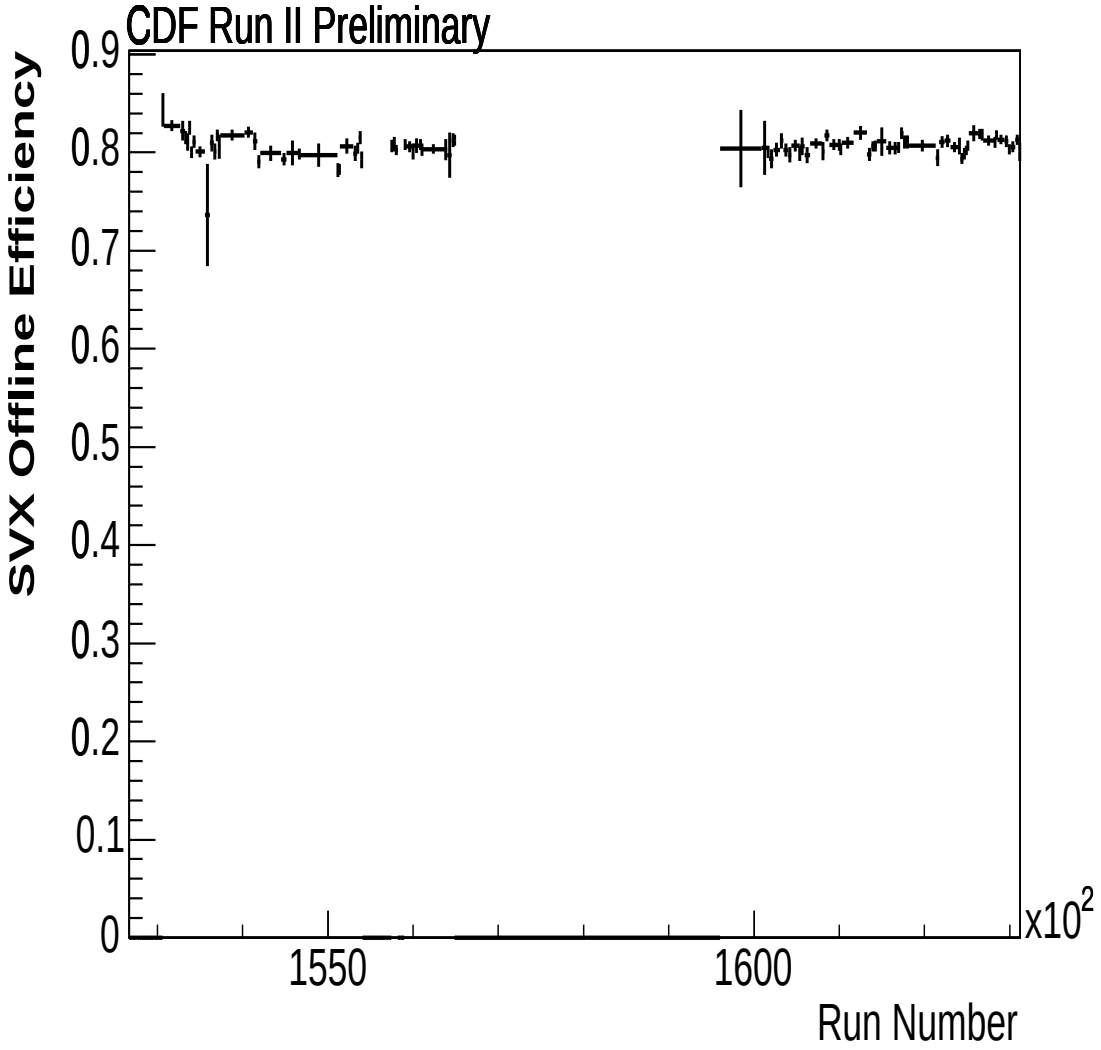

Figure 6.4: The SVX offline efficiency vs. run number

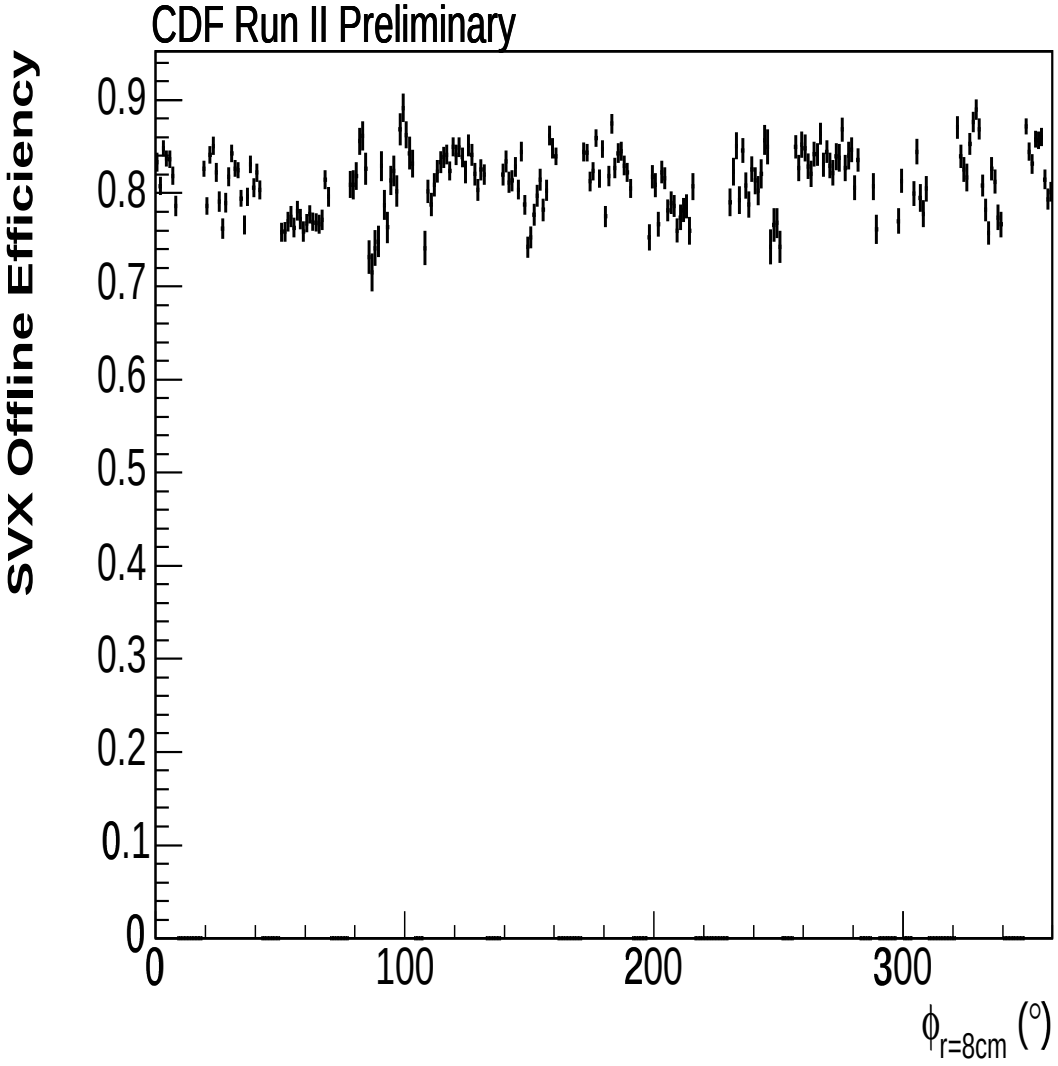

Figure 6.5: The SVX offline efficiency vs. $\phi_{r=8cm}$

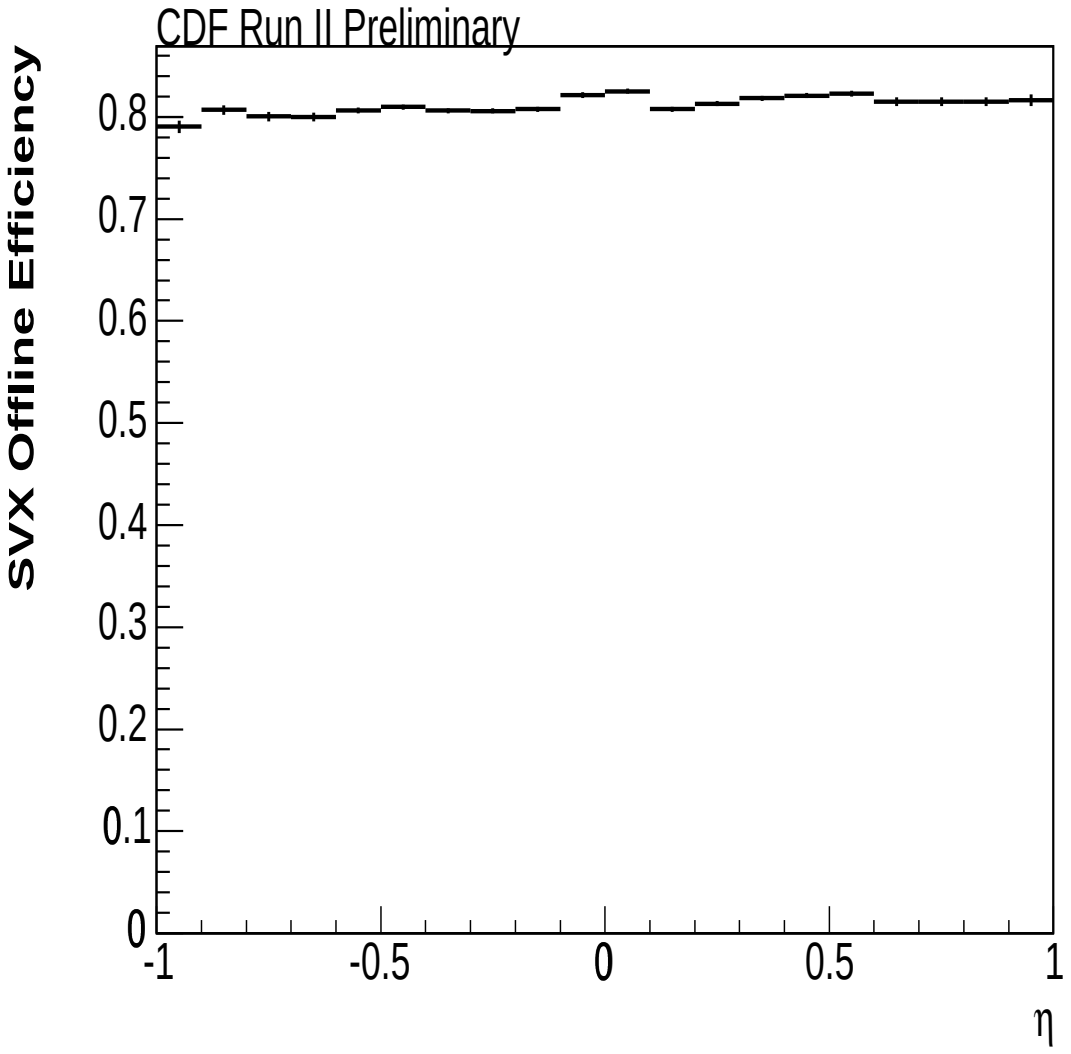

Figure 6.6: The SVX offline efficiency vs. η

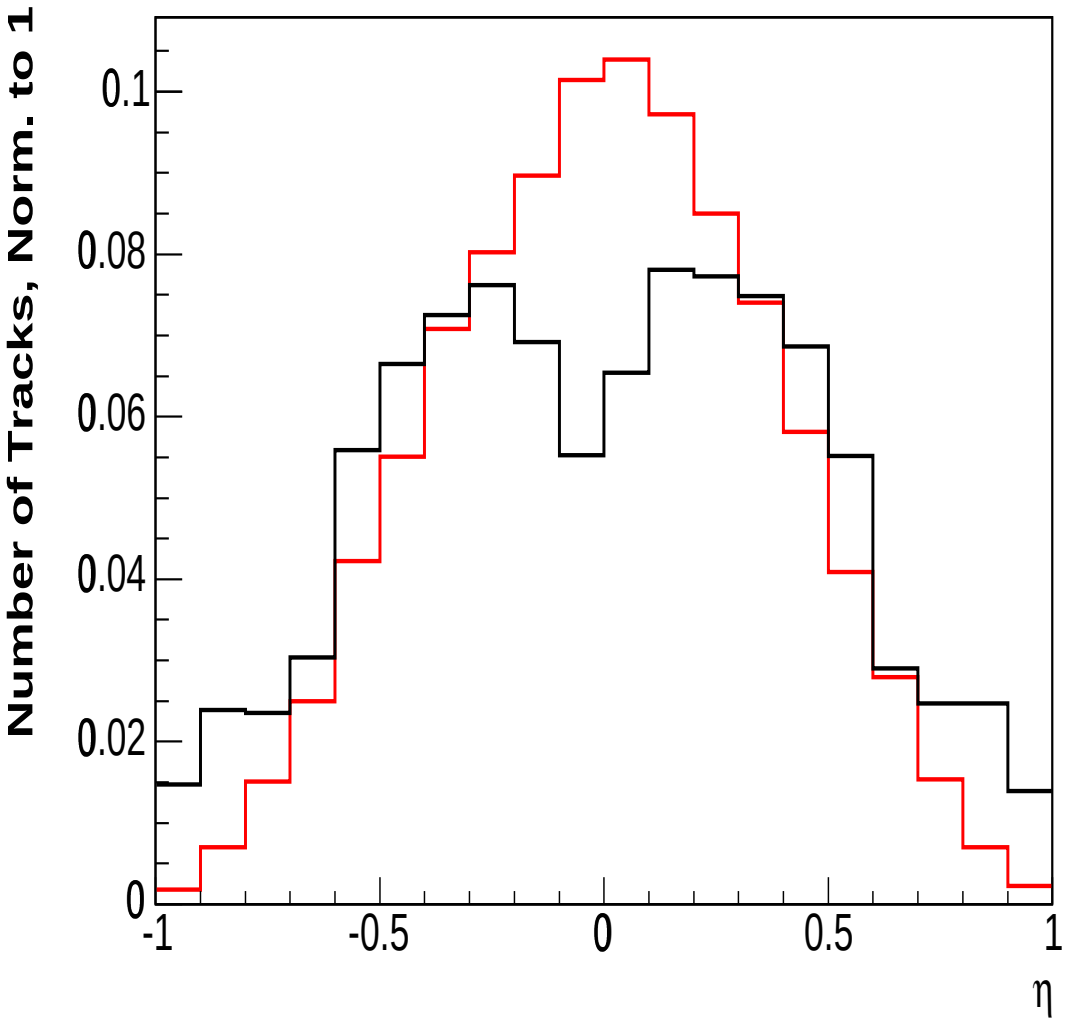

Figure 6.7: The distributions of the μ track η (black histogram) and MC track η (red histogram), both normalized to one.

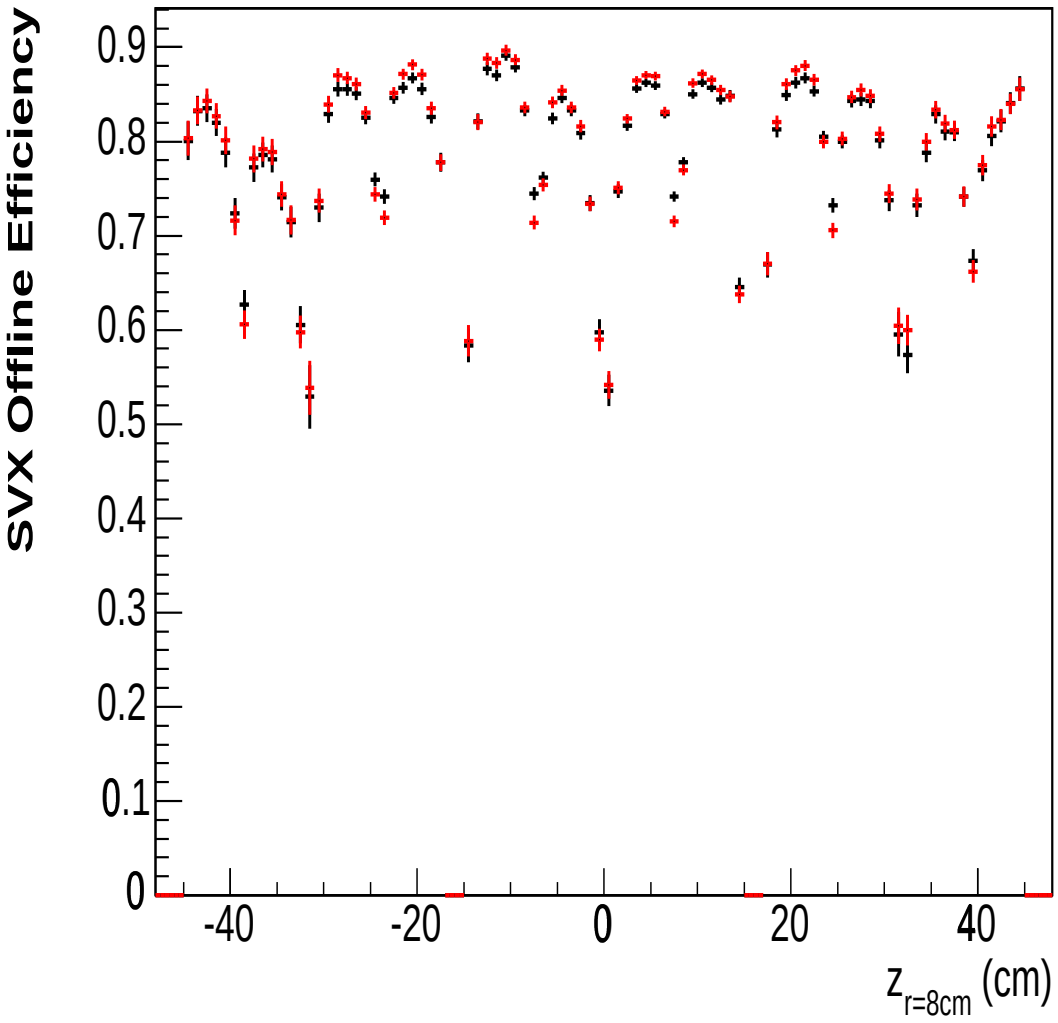

Figure 6.8: The SVX offline efficiency vs. $z_{r=8cm}$. The black points show the measurement with the J/ψ CMU μ track η, and the red points show the efficiency after reweighting the η distribution to match that from the MC.

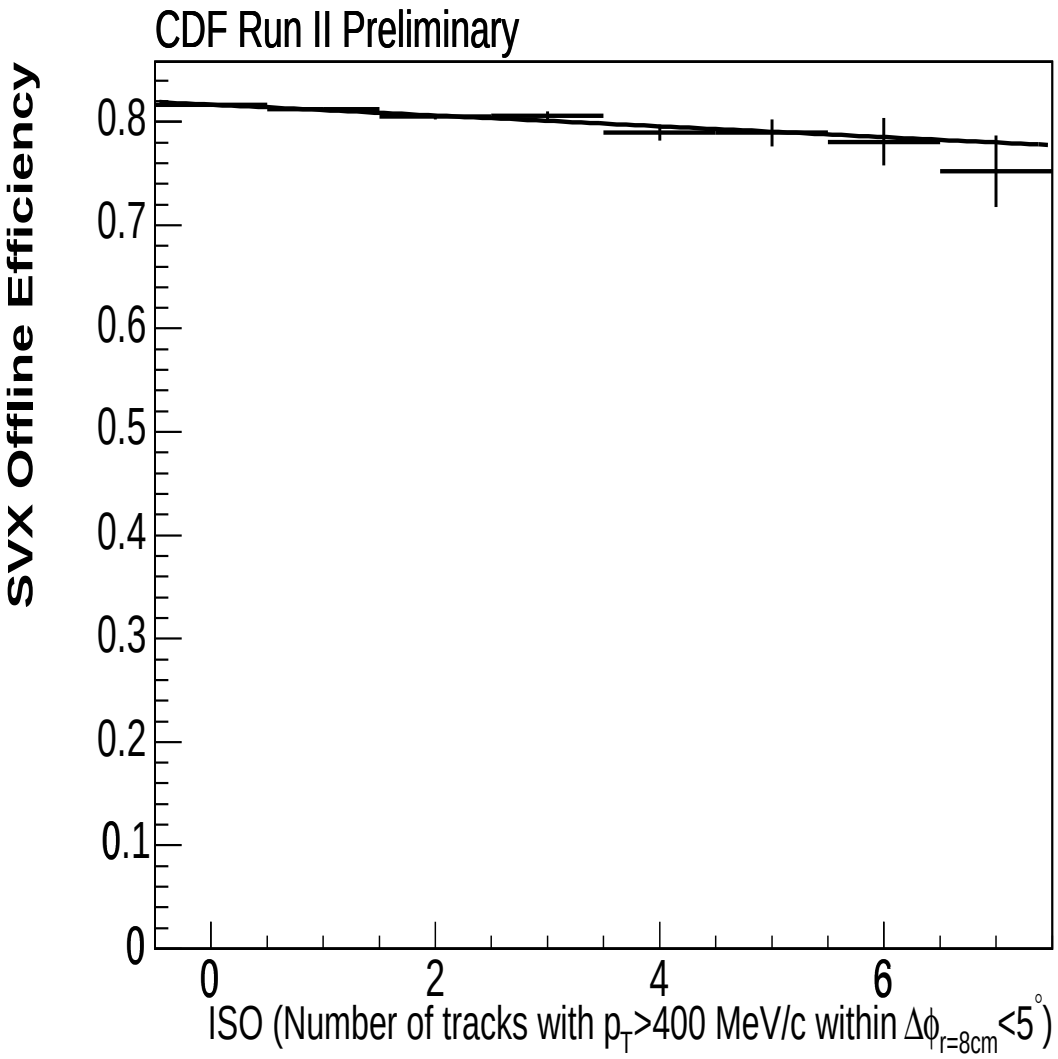

Figure 6.9: The SVX offline efficiency vs. the number of tracks with a $p_T > 400$ MeV/c within $\Delta\phi_{r=8cm} < 5°$. The slope of the fitted curve indicated that the efficiency drops 0.5% for every additional track added to the cone.

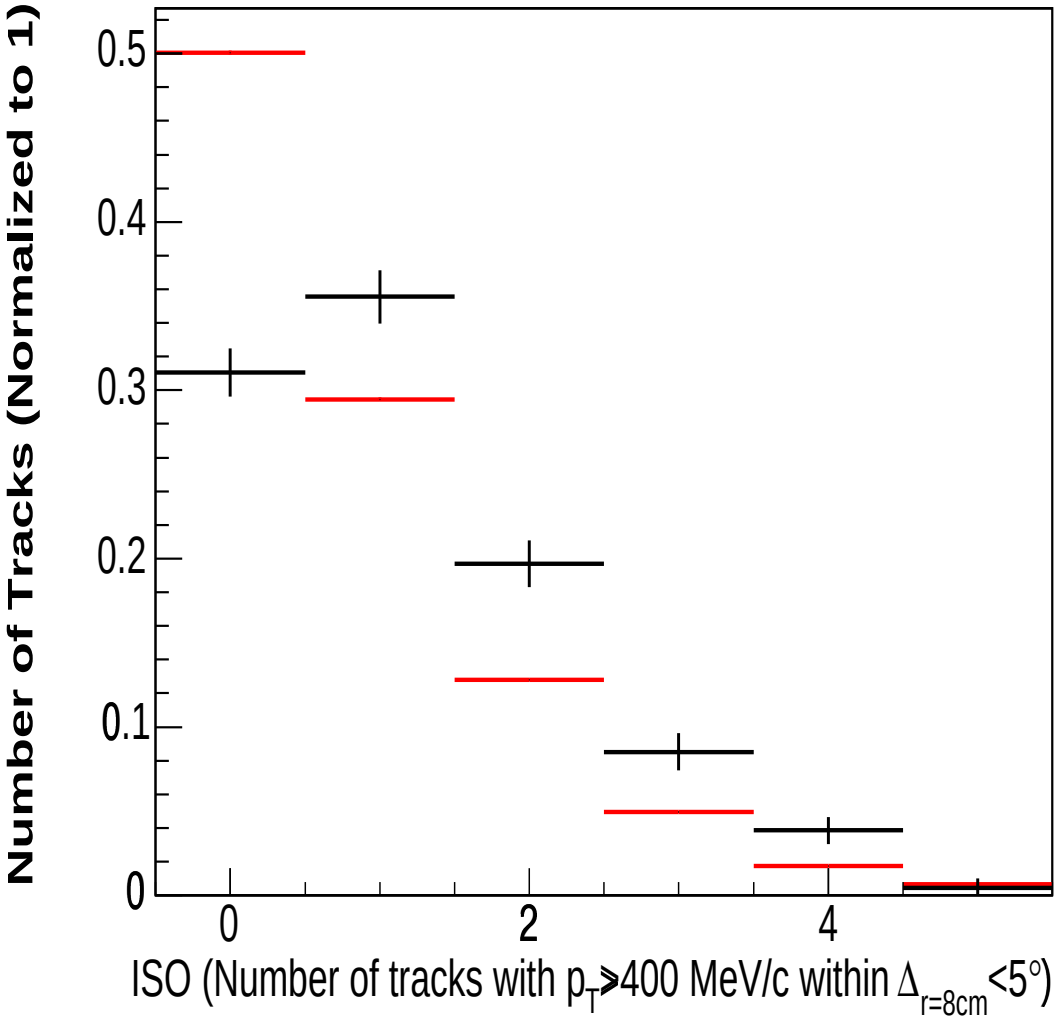

Figure 6.10: The distribution of the number of tracks with a $p_T > 400$ MeV/c within$\Delta\phi_{r=8cm} < 5°$ that pass SVX offline cuts for the J/ψ (red points) and $\mu + D^0$ (black points) samples. The $\mu + D^0$ distribution has been corrected for the SVT efficiency, and sideband subtraction about the D^0 peak has been used.

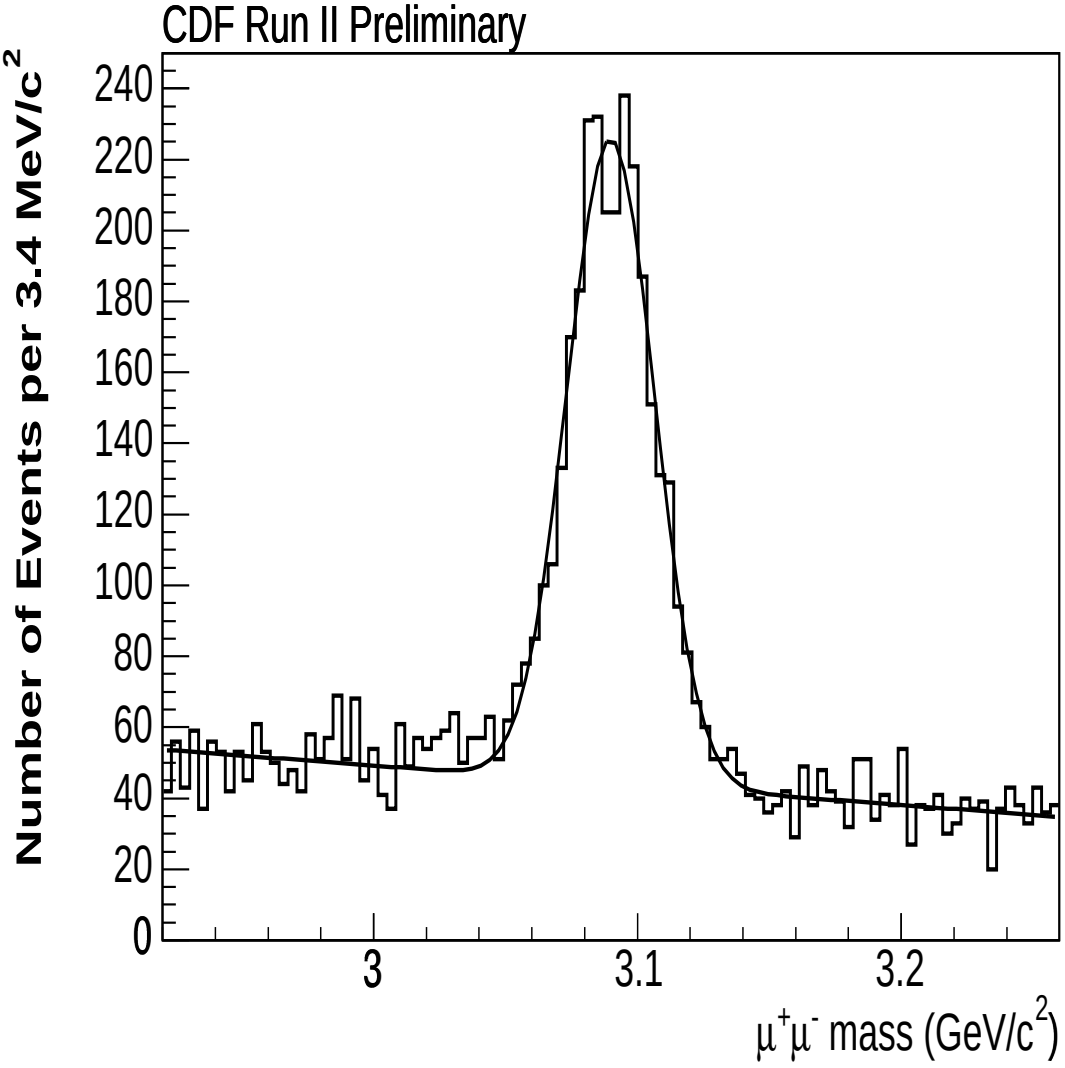

Figure 6.11: The J/ψ dimuon mass peak for the CMU Efficiency measurement for events that fired the μSVT trigger. The fitted curve was used to define signal and sideband regions, and there are about 2223 events beneath the Gaussian.

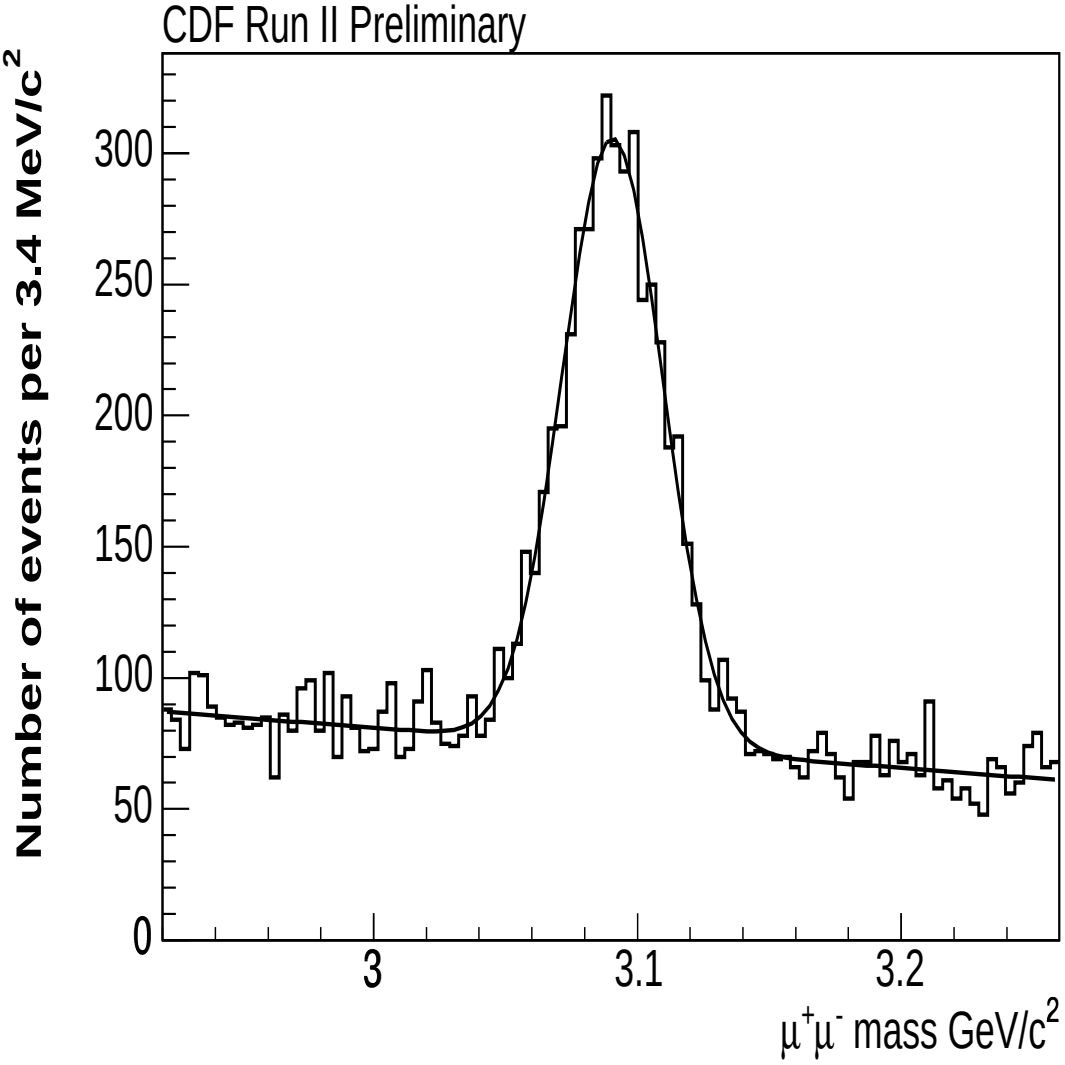

Figure 6.12: The J/ψ dimuon mass peak for the CMU Efficiency measurement for events that fired the CMUP8 trigger. The fitted curve was used to define signal and sideband regions, and there are about 3258 events beneath the Gaussian.

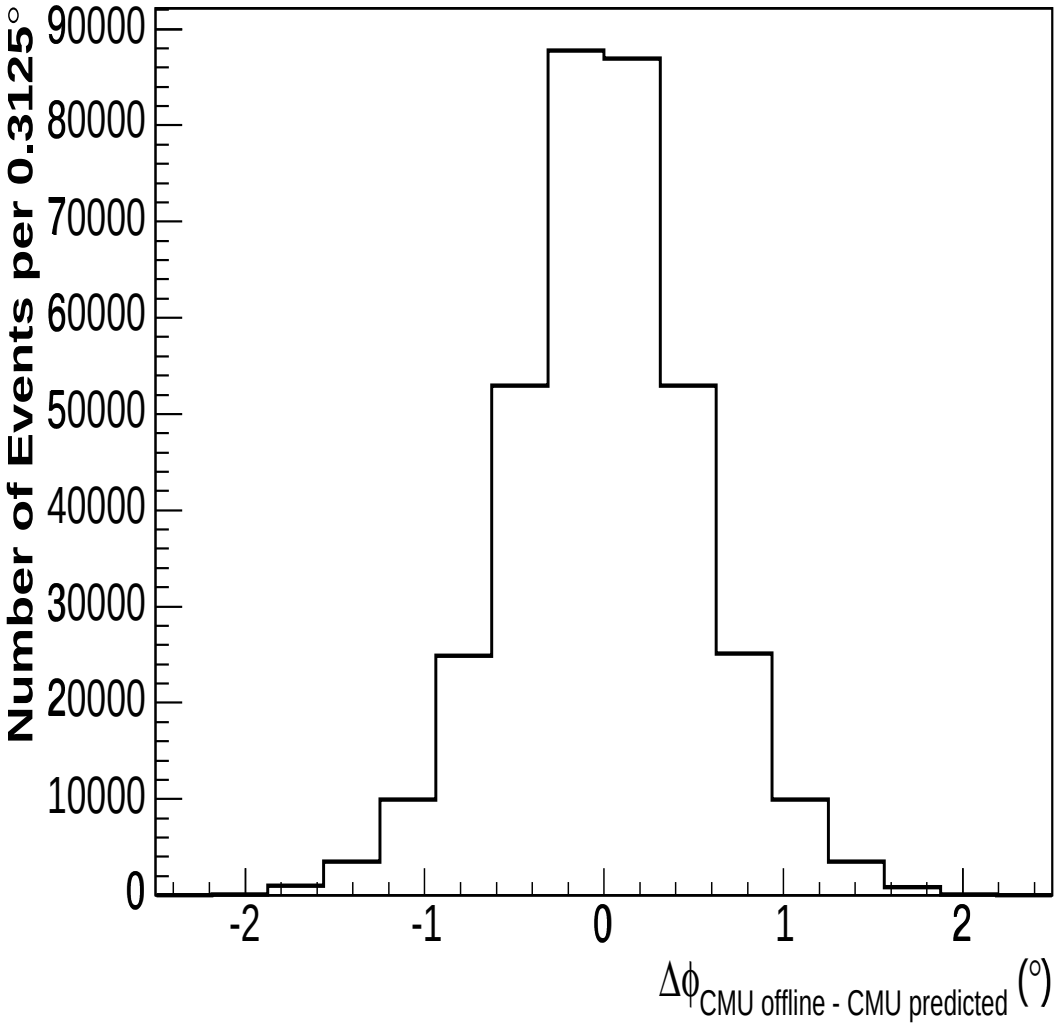

Figure 6.13: The difference between the predicted and actual CMU stub positions in ϕ

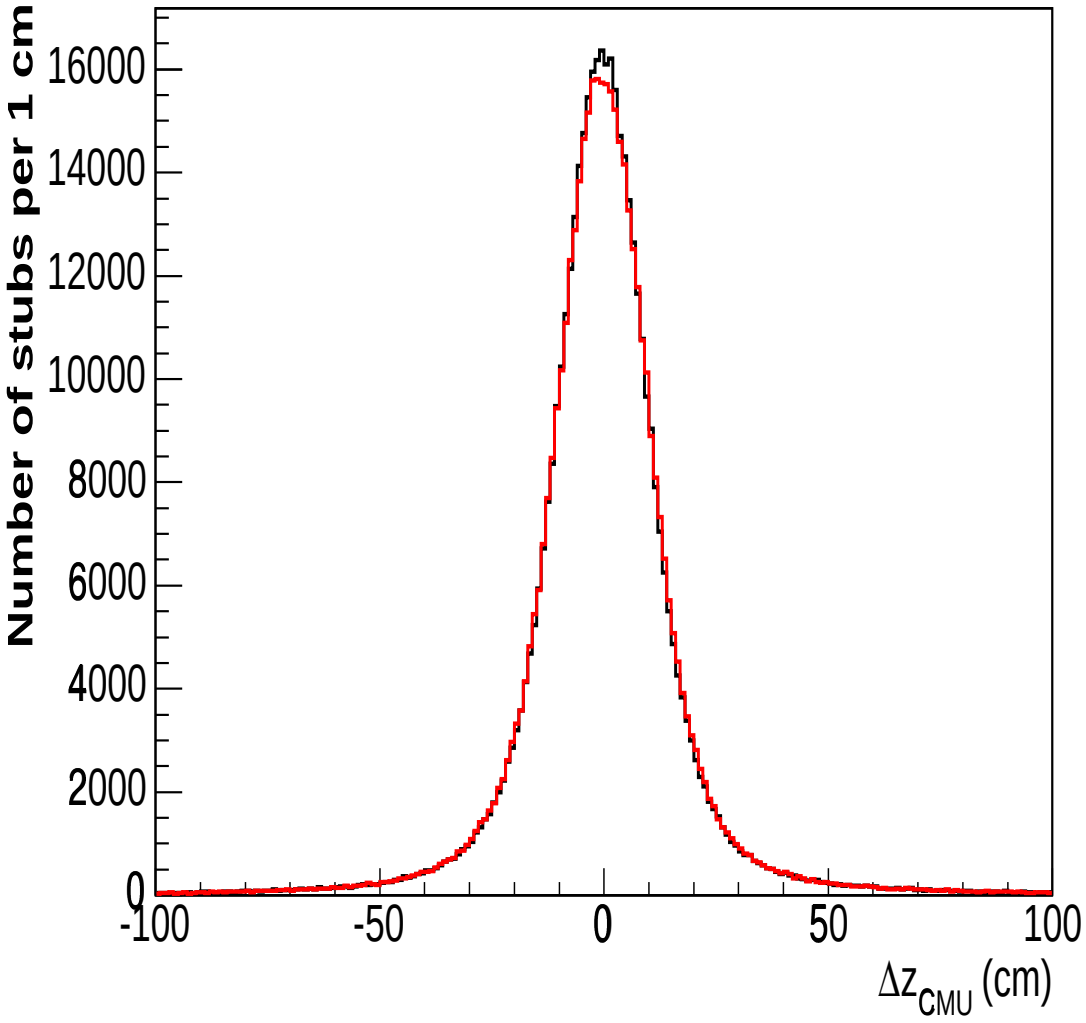

Figure 6.14: The difference between the predicted and actual CMU stub positions in z. The black points indicate the difference for my algorithm, and the red points indicate the difference from the offline muon matching code.

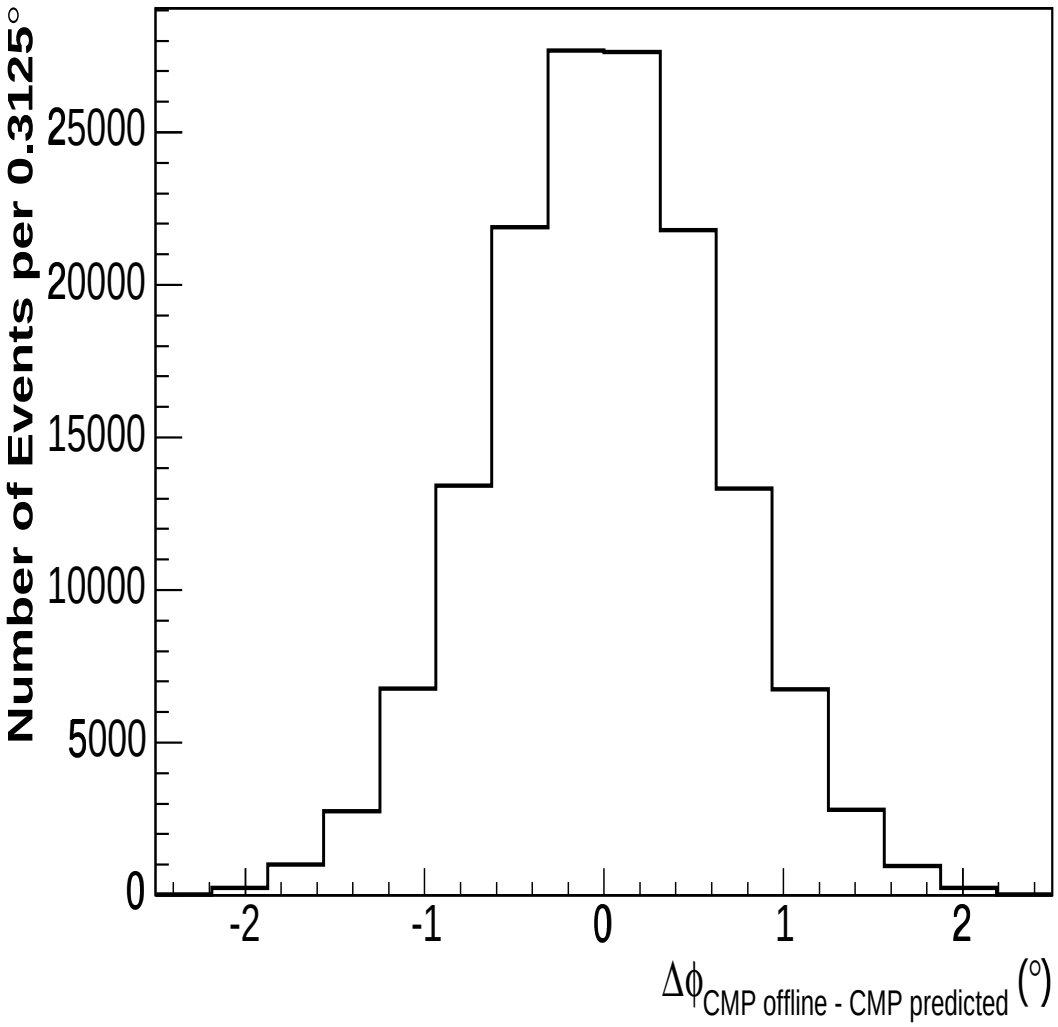

Figure 6.15: The difference between the predicted and actual CMP stub positions in ϕ

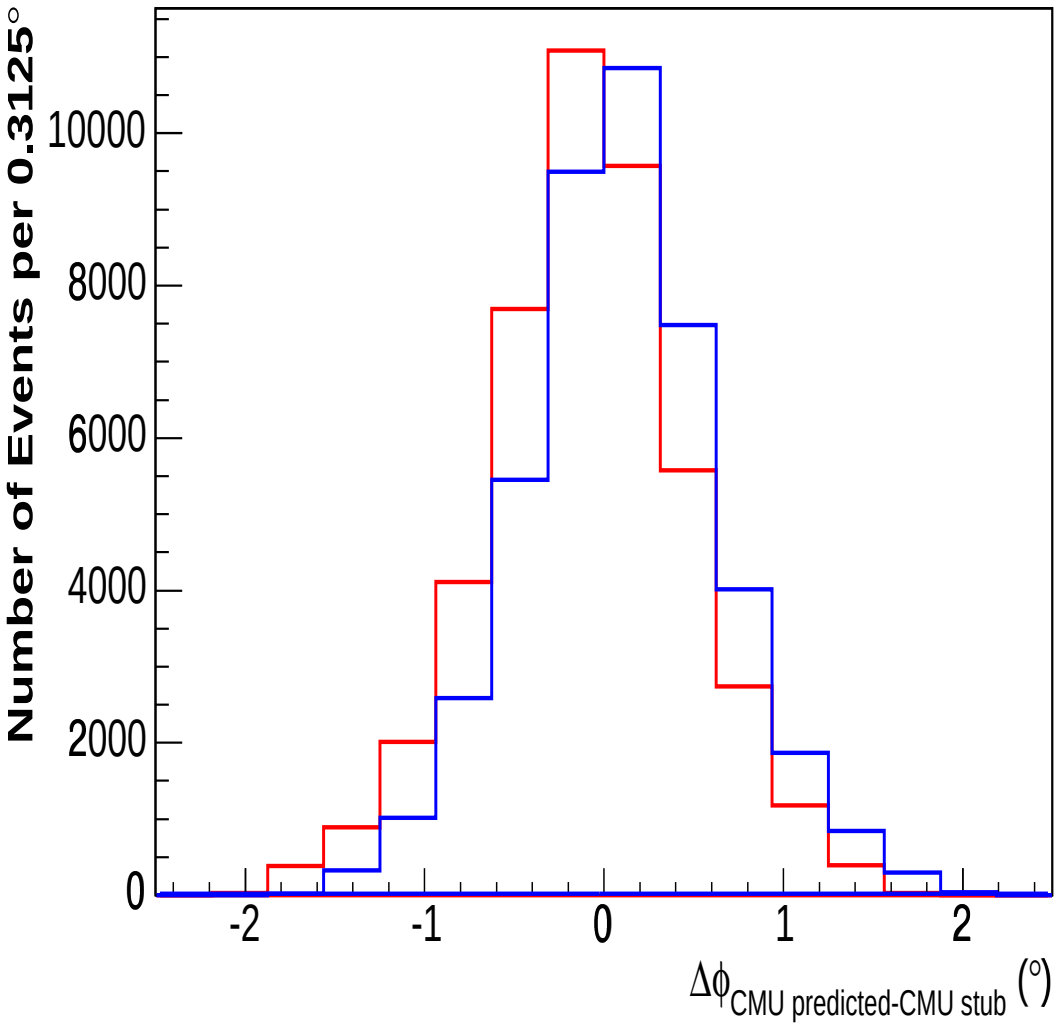

Figure 6.16: The difference between the predicted and actual CMU stub positions in ϕ for μ^+ (red) and μ^- (blue).

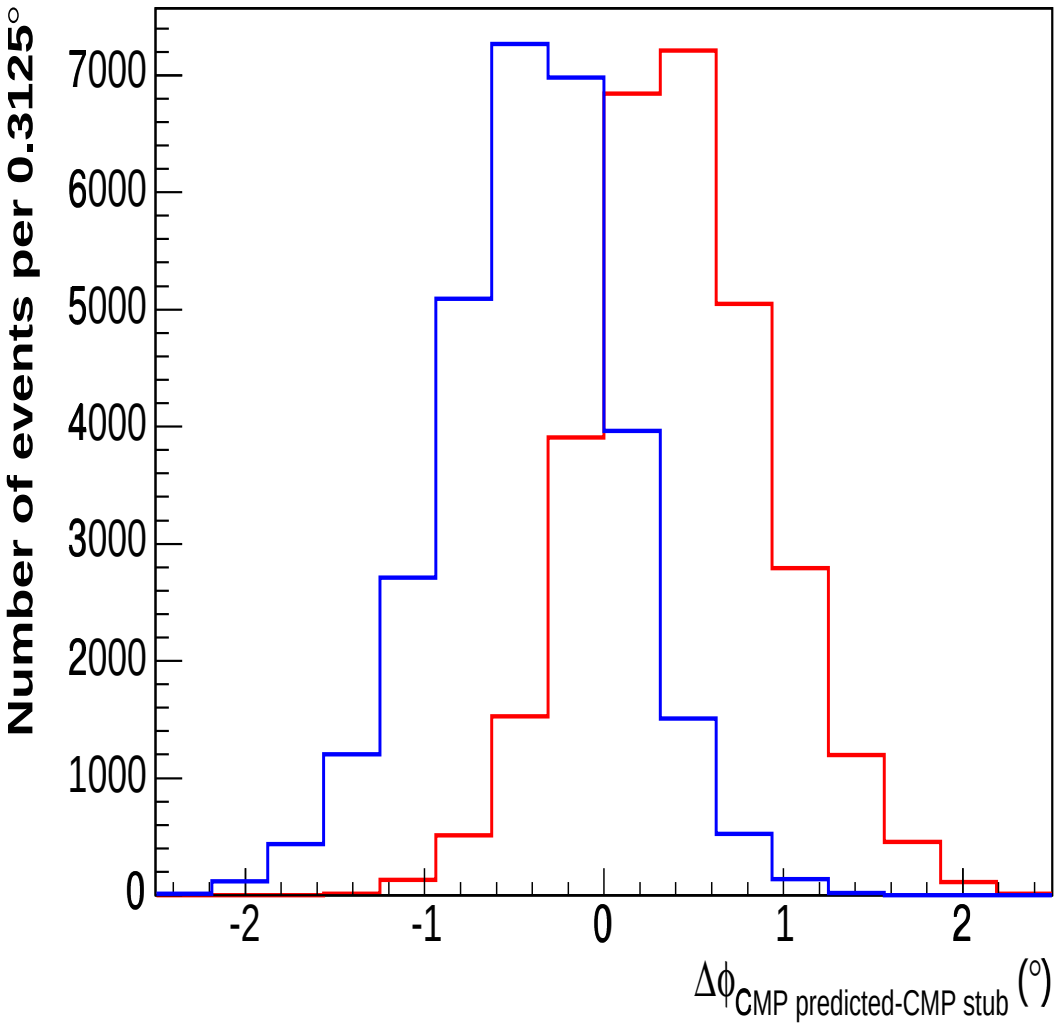

Figure 6.17: The difference between the predicted and actual CMP stub positions in ϕ for μ^+ (red) and μ^- (blue).

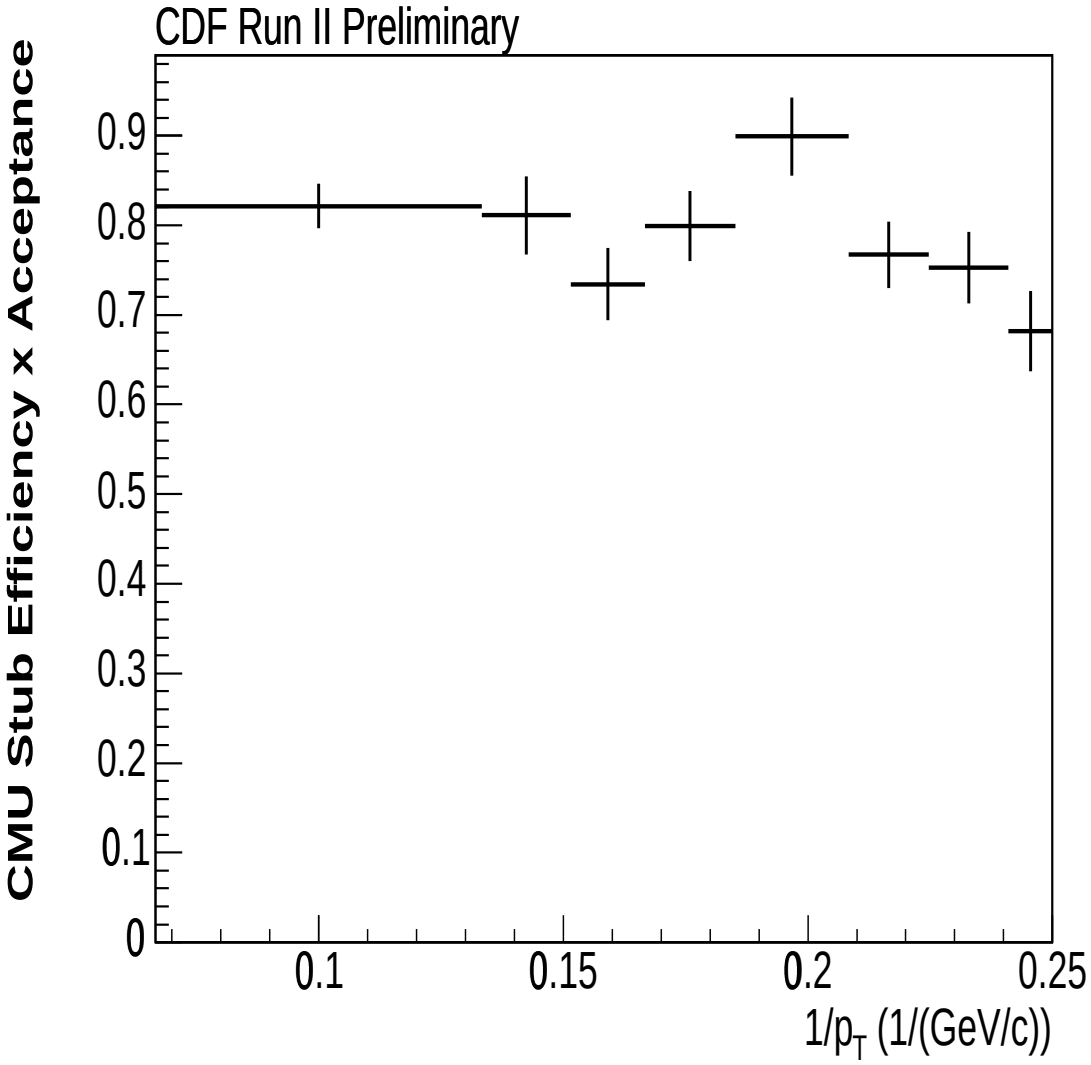

Figure 6.18: The CMU Efficiency measurement vs. muon $1/p_T$.

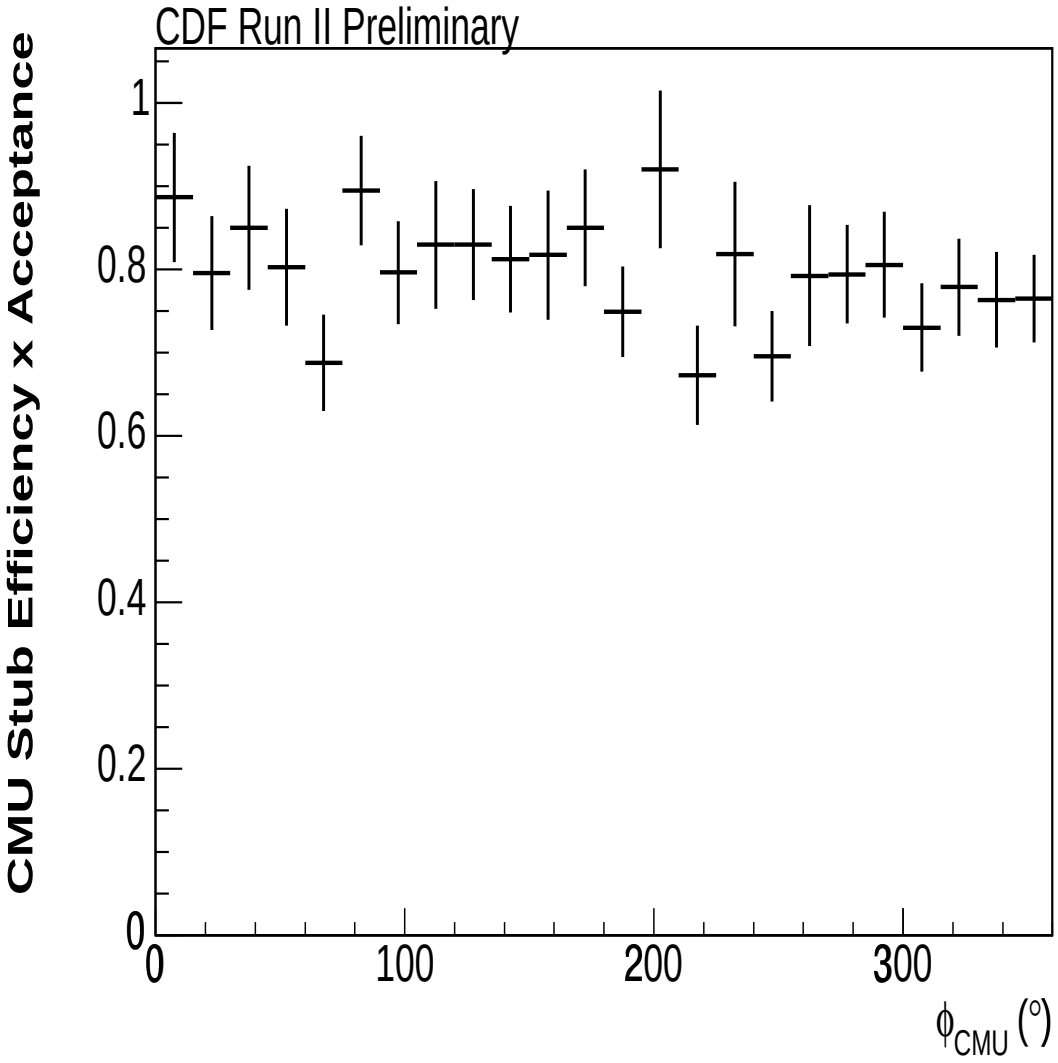

Figure 6.19: The CMU Efficiency measurement vs. the predicted ϕ_{CMU}.

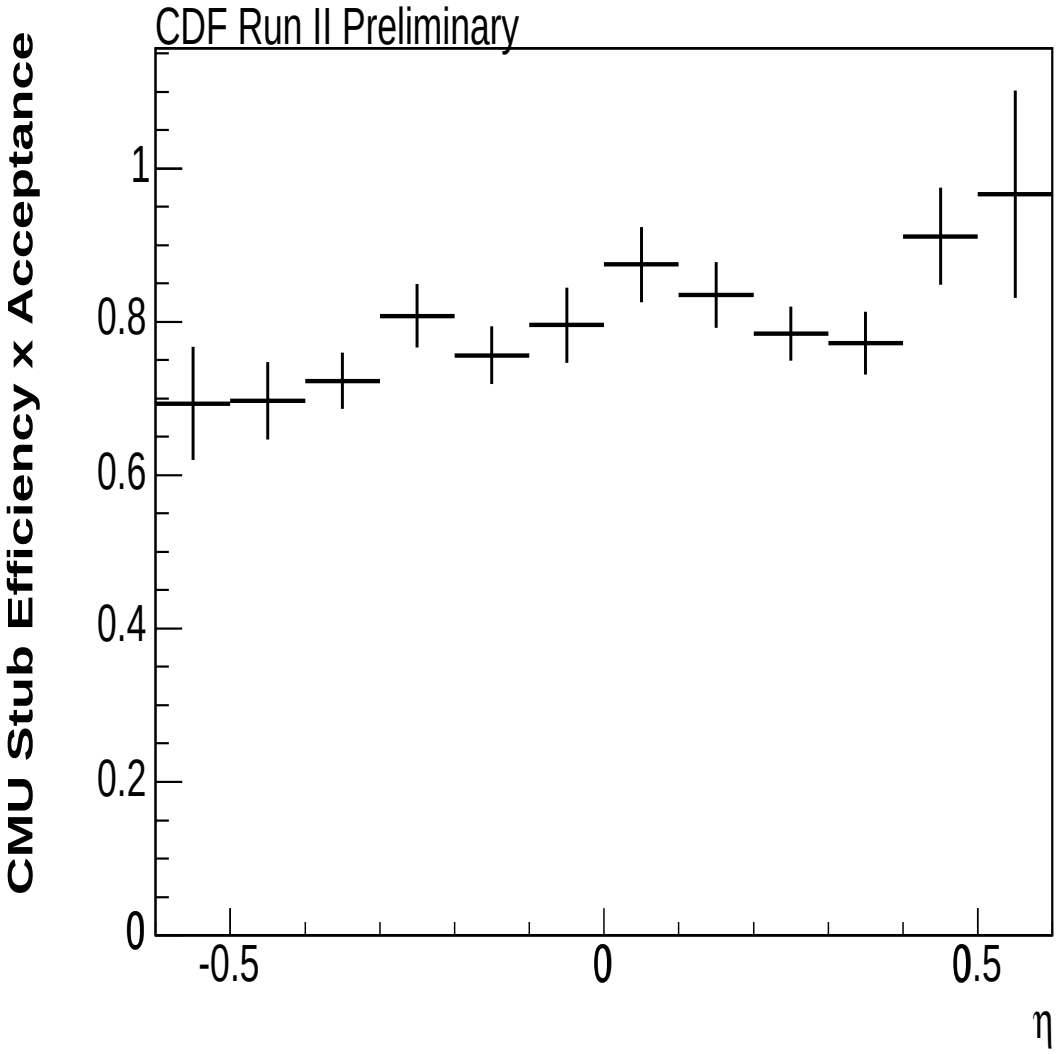

Figure 6.20: The CMU Efficiency measurement vs. muon track η.

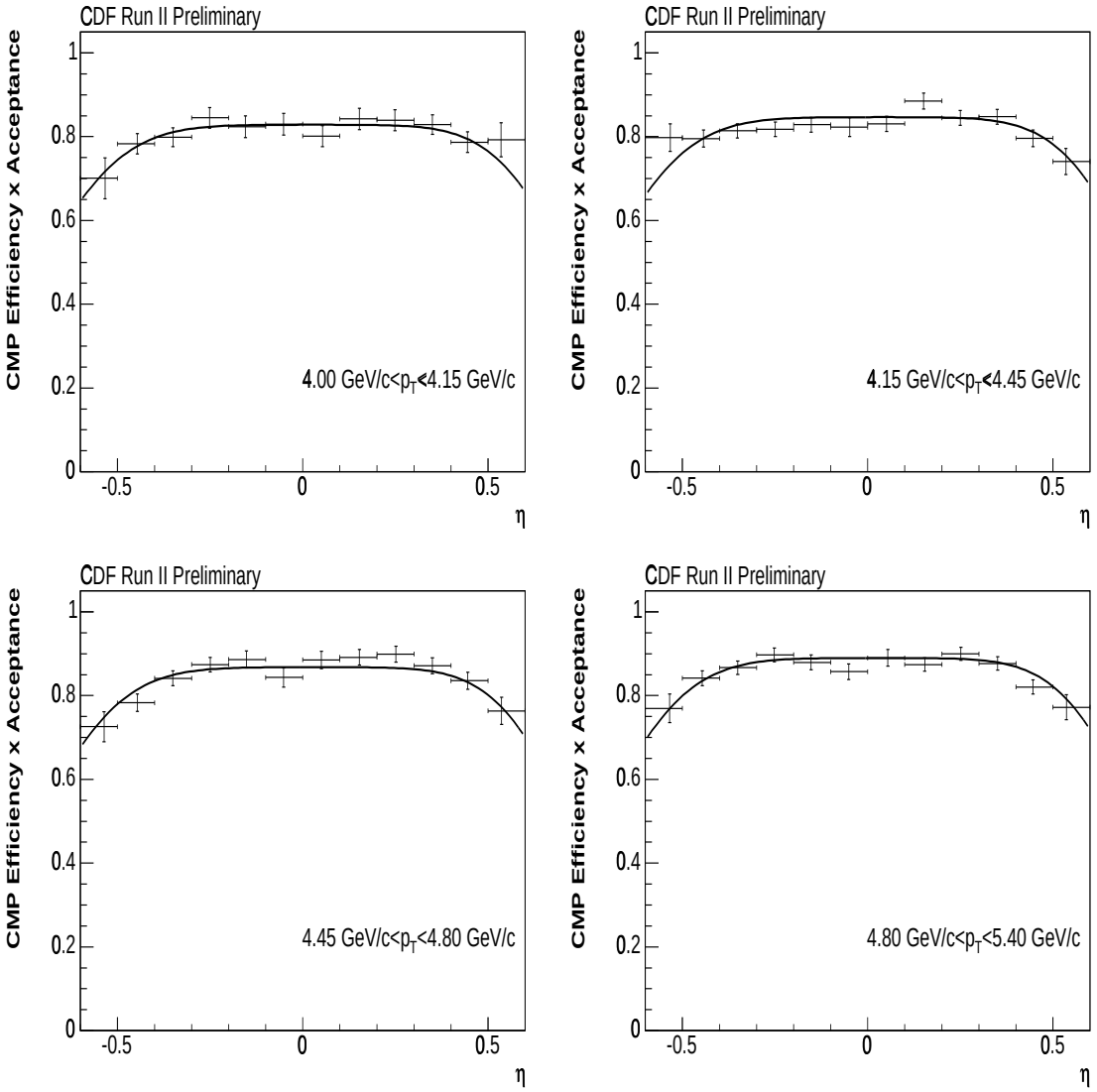

Figure 6.21: CMP stub acceptance vs. η for various slices of muon transverse momentum. The curves are the one dimensional projections of the two dimensional binned fit to the data.

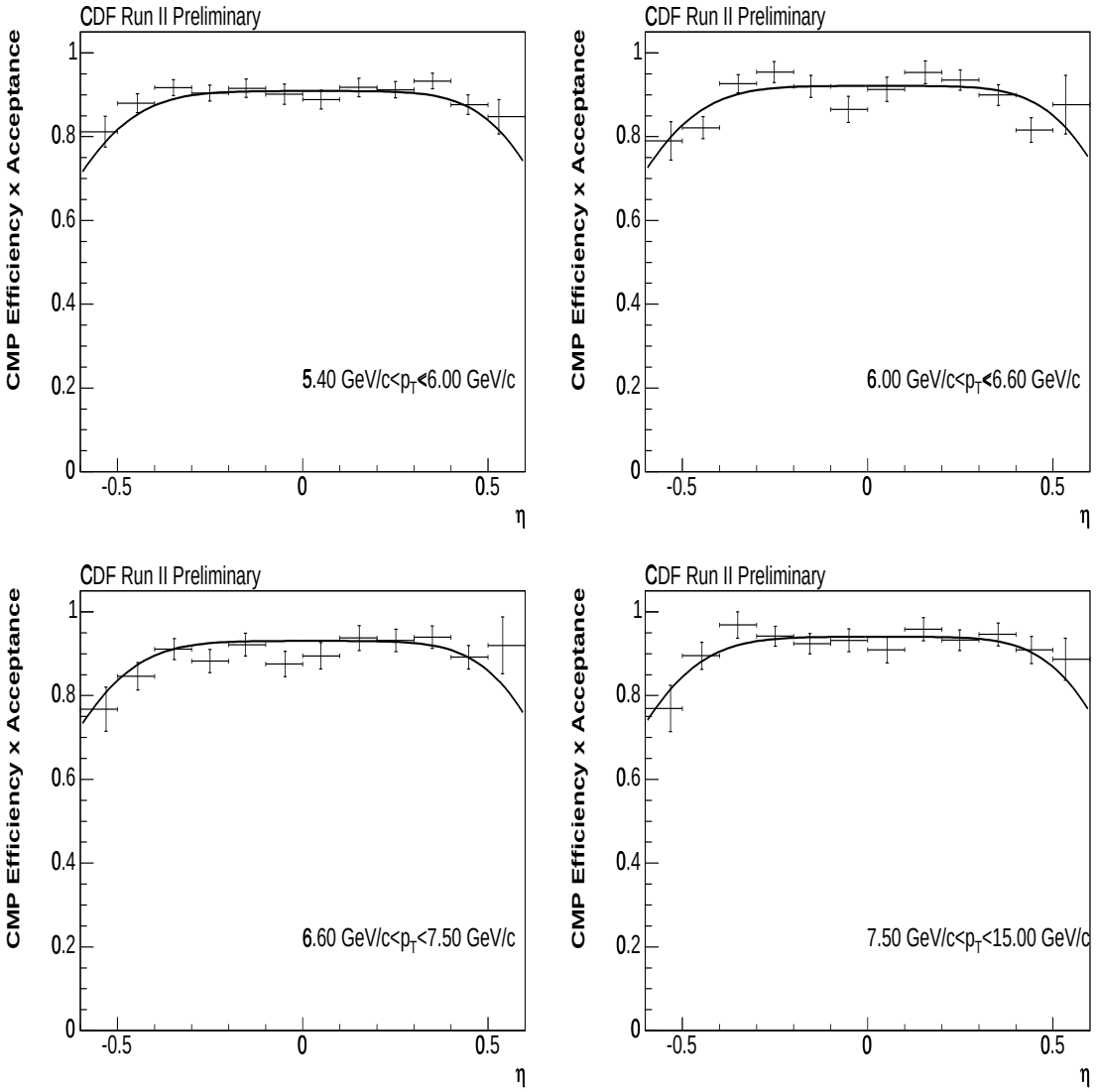

Figure 6.22: CMP stub acceptance vs. η for various slices of muon transverse momentum. The curves are the one dimensional projections of the two dimensional binned fit to the data.

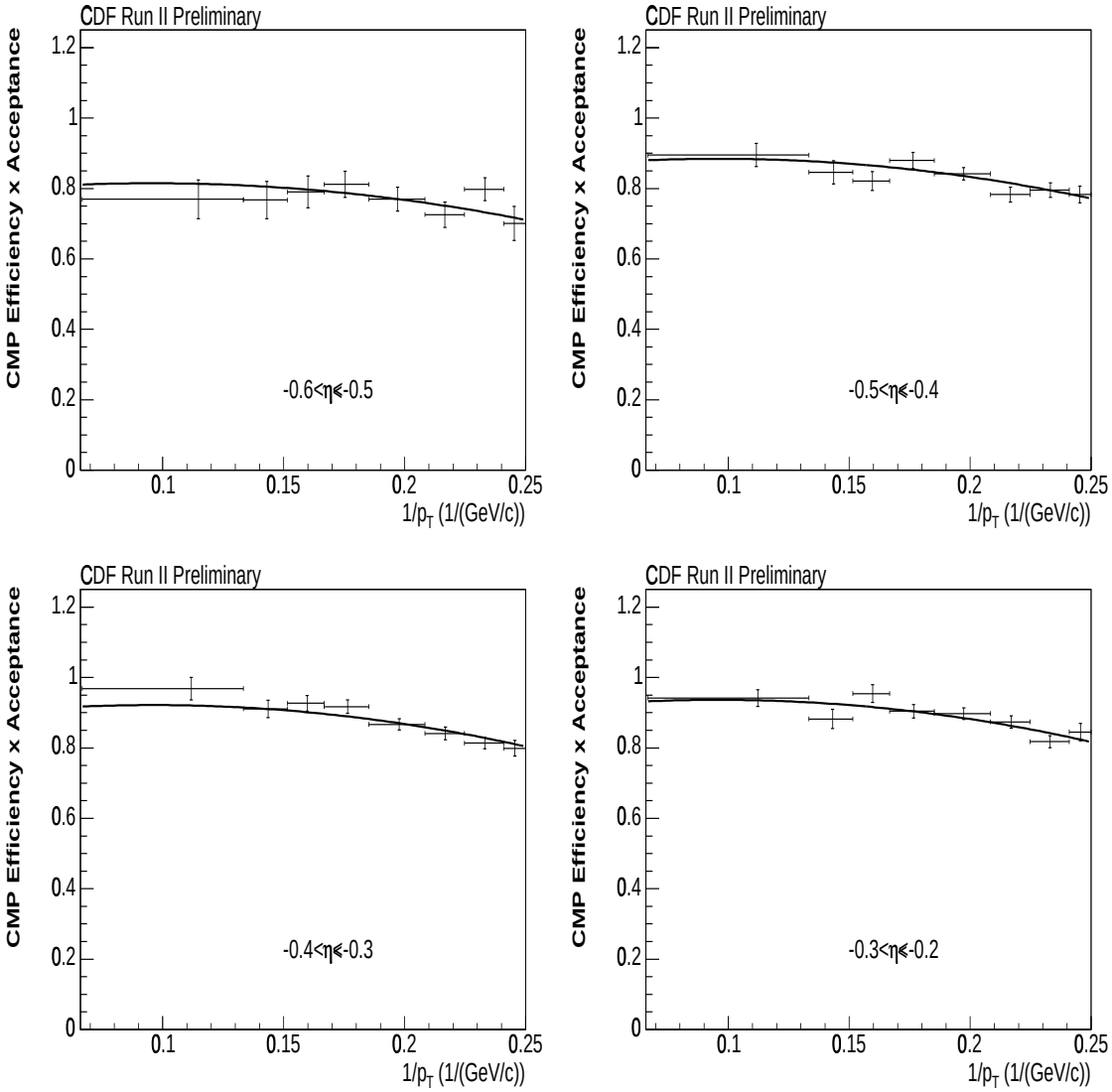

Figure 6.23: CMP stub acceptance vs. $1/p_T$ for various slices of muon η. The curves are the one dimensional projections of the two dimensional binned fit to the data.

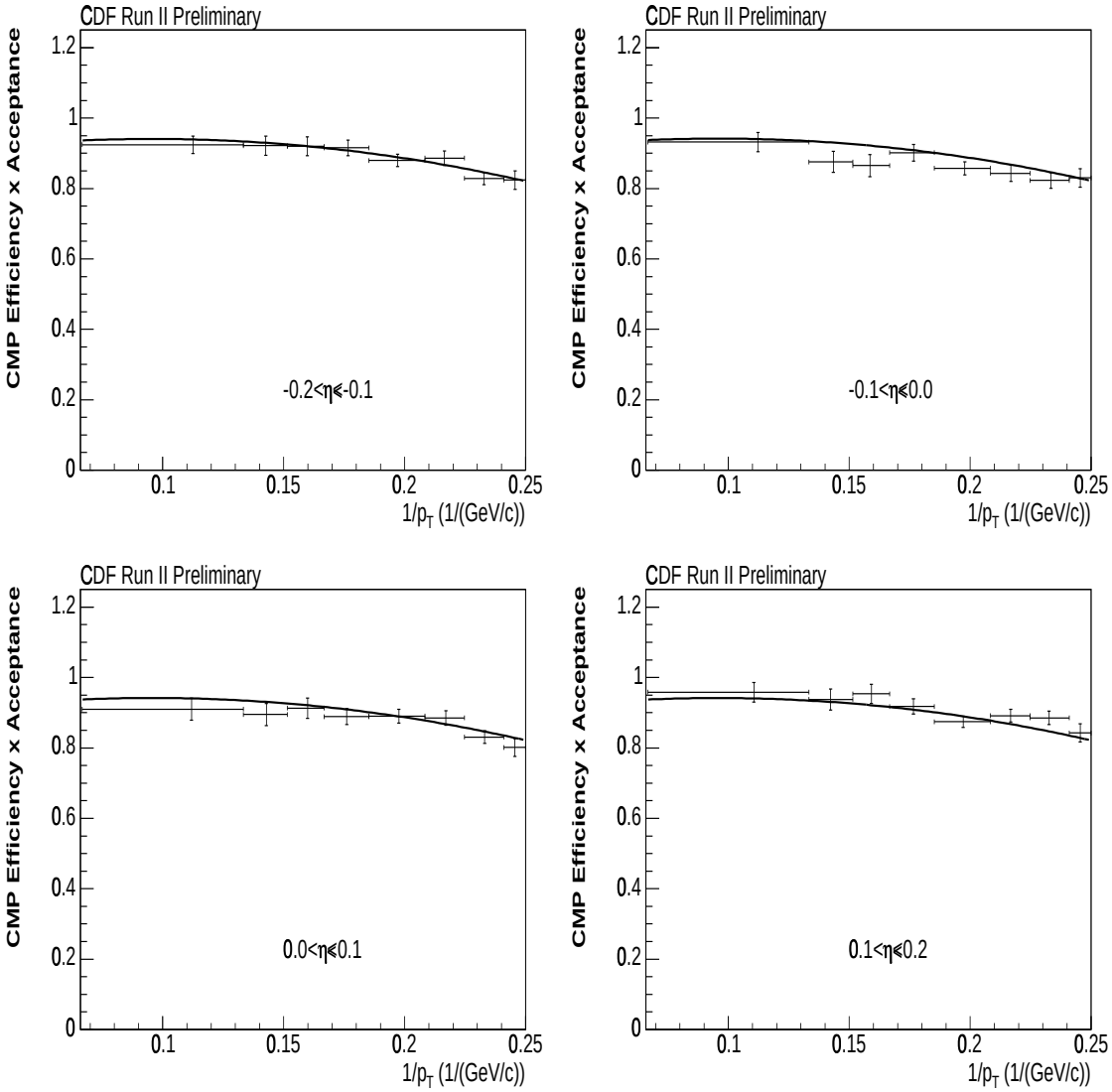

Figure 6.24: CMP stub acceptance vs. $1/p_T$ for various slices of muon η. The curves are the one dimensional projections of the two dimensional binned fit to the data.

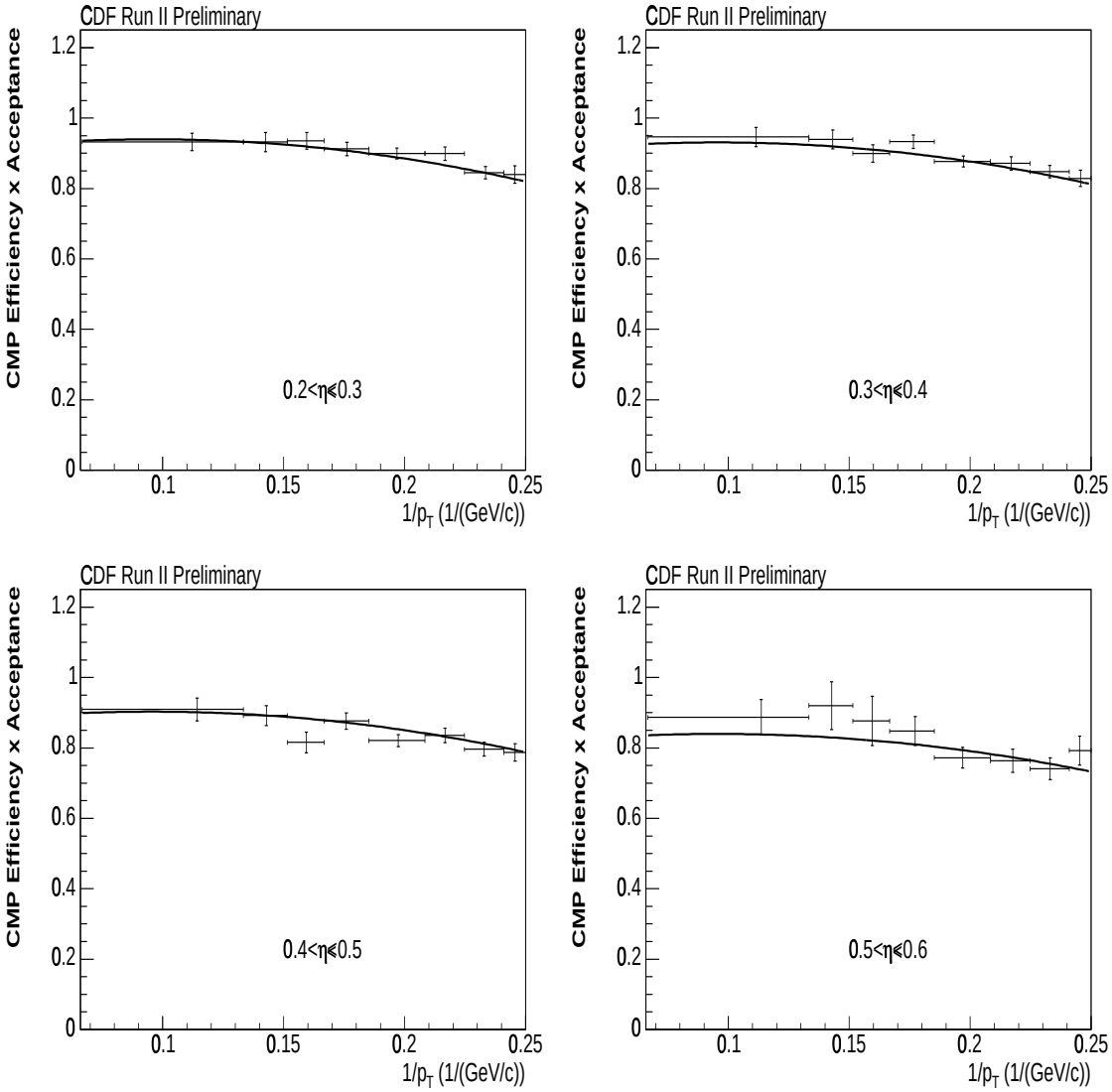

Figure 6.25: CMP stub acceptance vs. $1/p_T$ for various slices of muon η. The curves are the one dimensional projections of the two dimensional binned fit to the data.

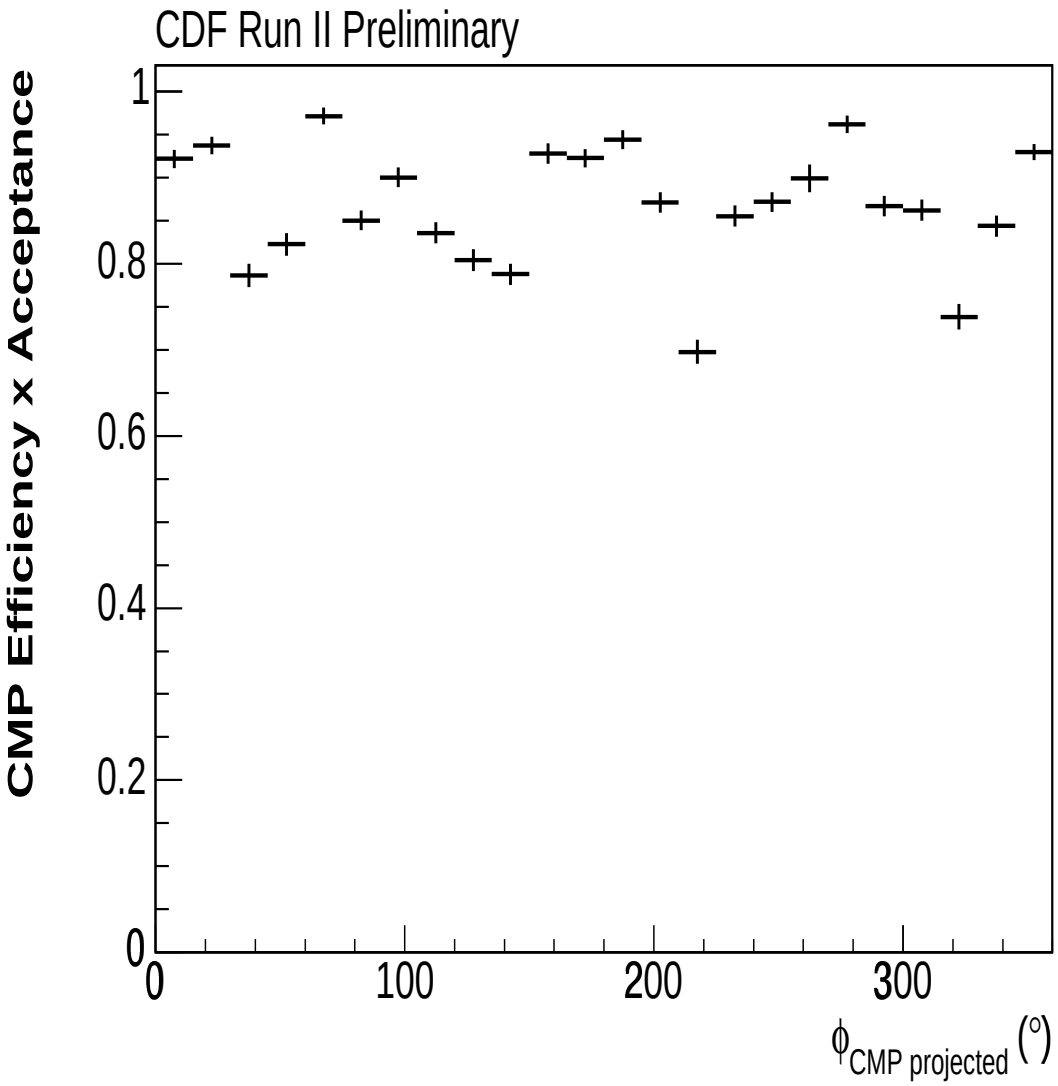

Figure 6.26: The CMP stub acceptance measurement vs. the predicted ϕ_{CMP}.

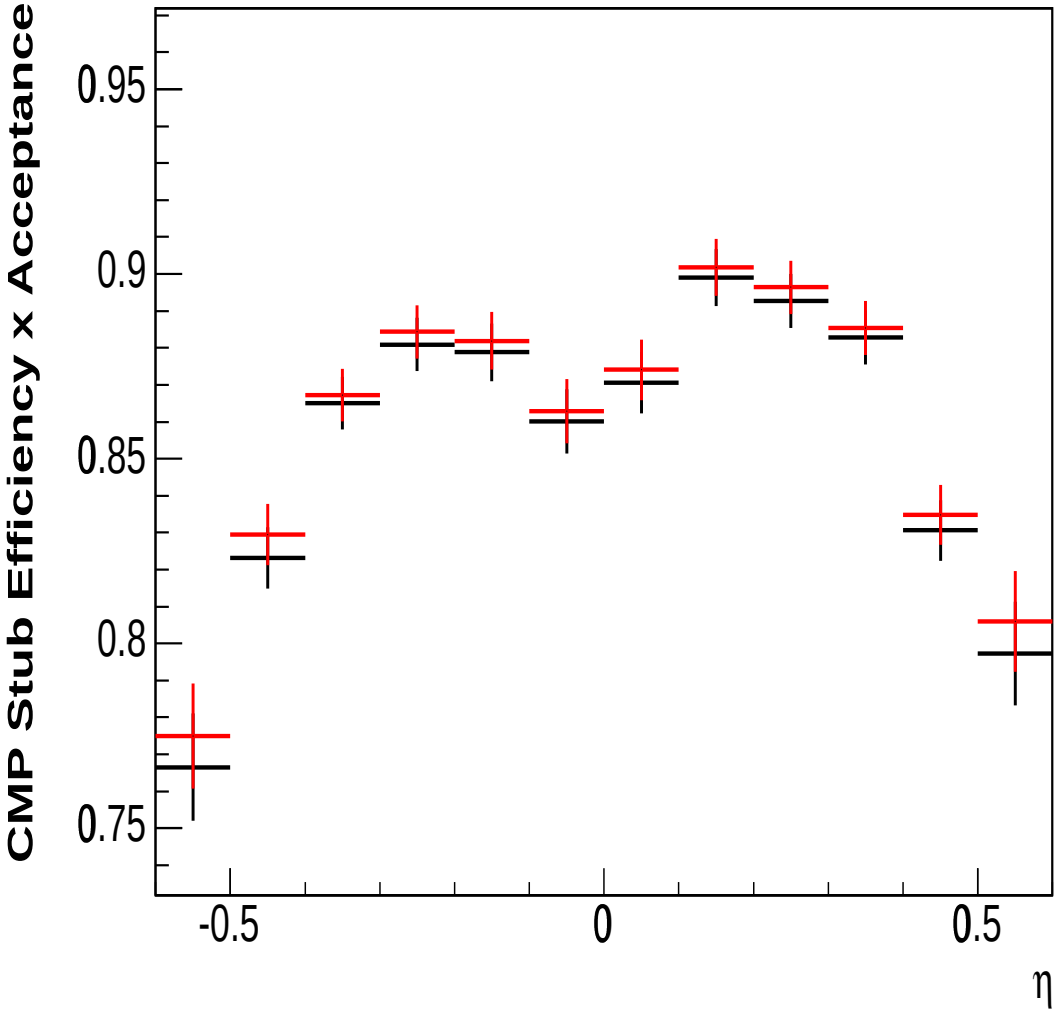

Figure 6.27: The CMP stub acceptance measurement vs. η for events with the unweighted ϕ_{CMP} distribution (in black) and the ϕ_{CMP} distribution reweighted to match the ϕ_{CMP} distribution of the $\mu + D^0$ sample.

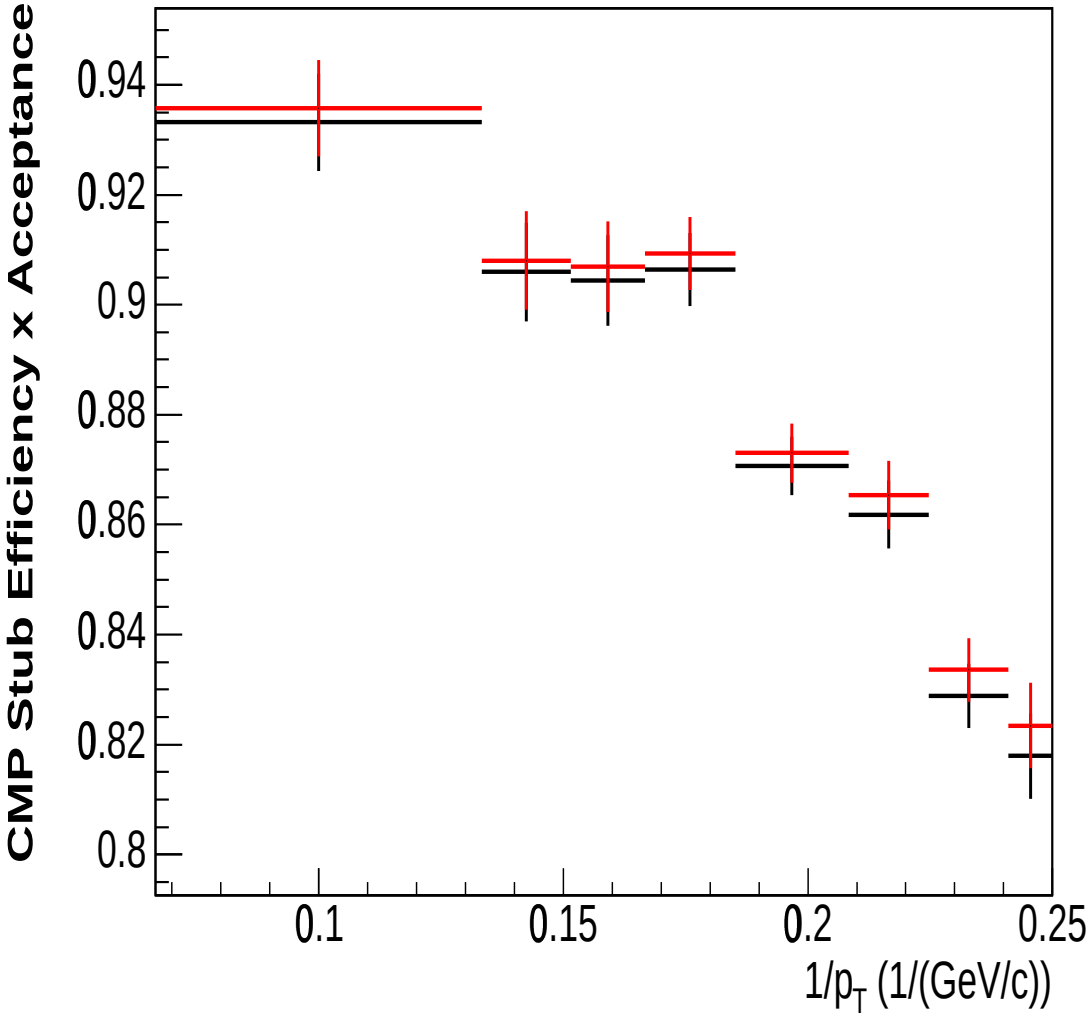

Figure 6.28: The CMP stub acceptance measurement vs. $1/p_T$ for events with the unweighted ϕ_{CMP} distribution (in black) and the ϕ_{CMP} distribution reweighted to match the ϕ_{CMP} distribution of the $\mu + D^0$ sample.

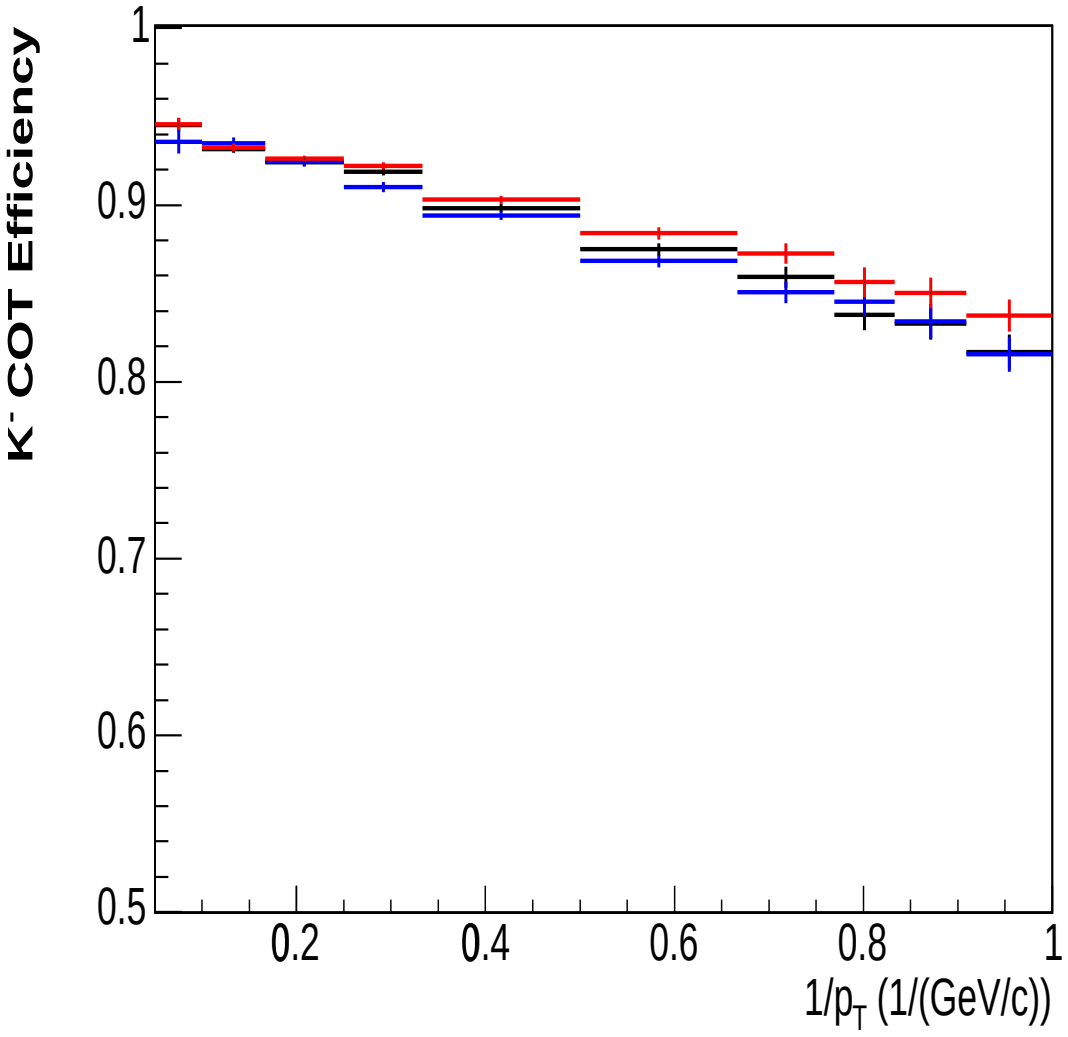

Figure 6.29: The COT tracking efficiency vs. $1/p_T$ for K^-. The red points are from Bgenerator Monte Carlo with no matching cuts, the black points are from Bgenerator MC with matching cuts, and the blue points are from track embedding with matching cuts.

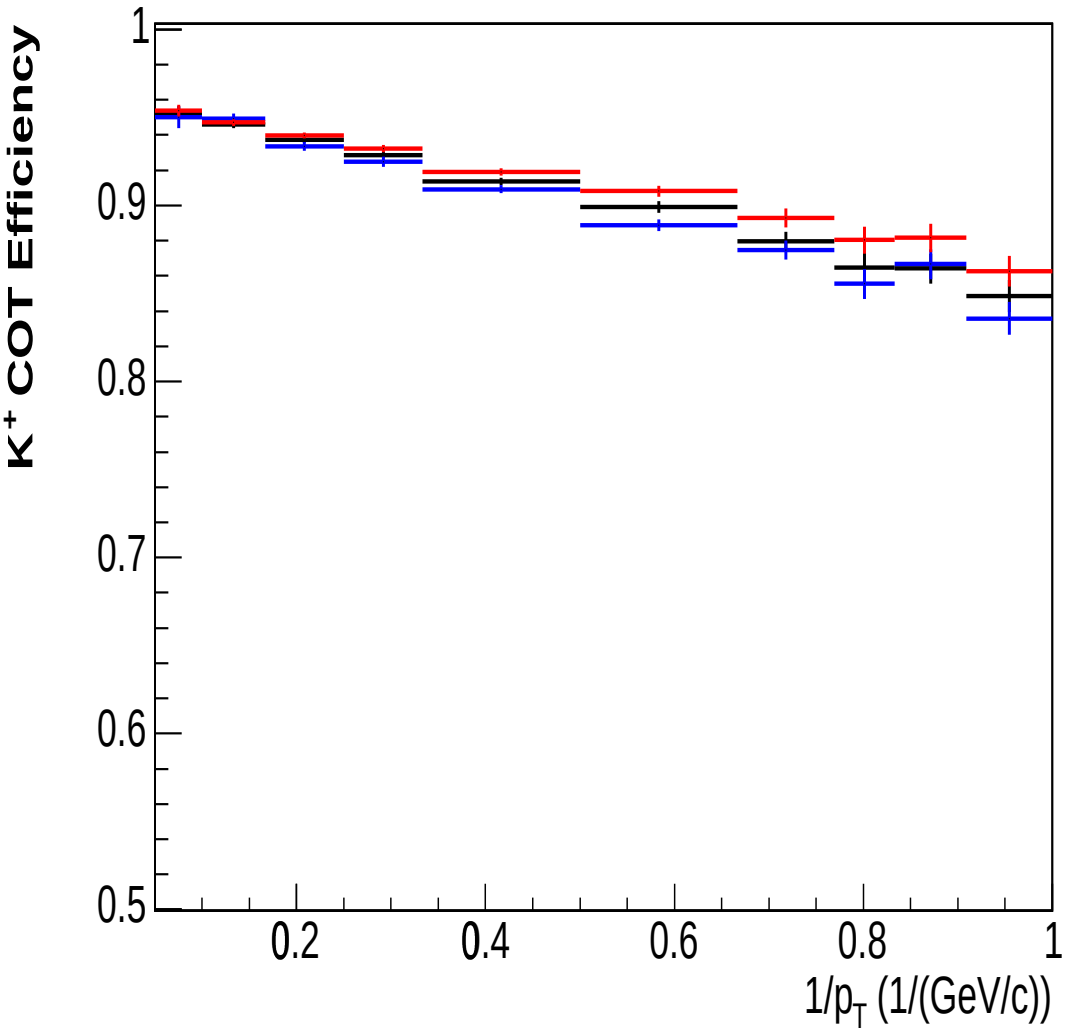

Figure 6.30: The COT tracking efficiency vs. $1/p_T$ for K^+. The red points are from Bgenerator Monte Carlo with no matching cuts, the black points are from Bgenerator MC with matching cuts, and the blue points are from track embedding with matching cuts.

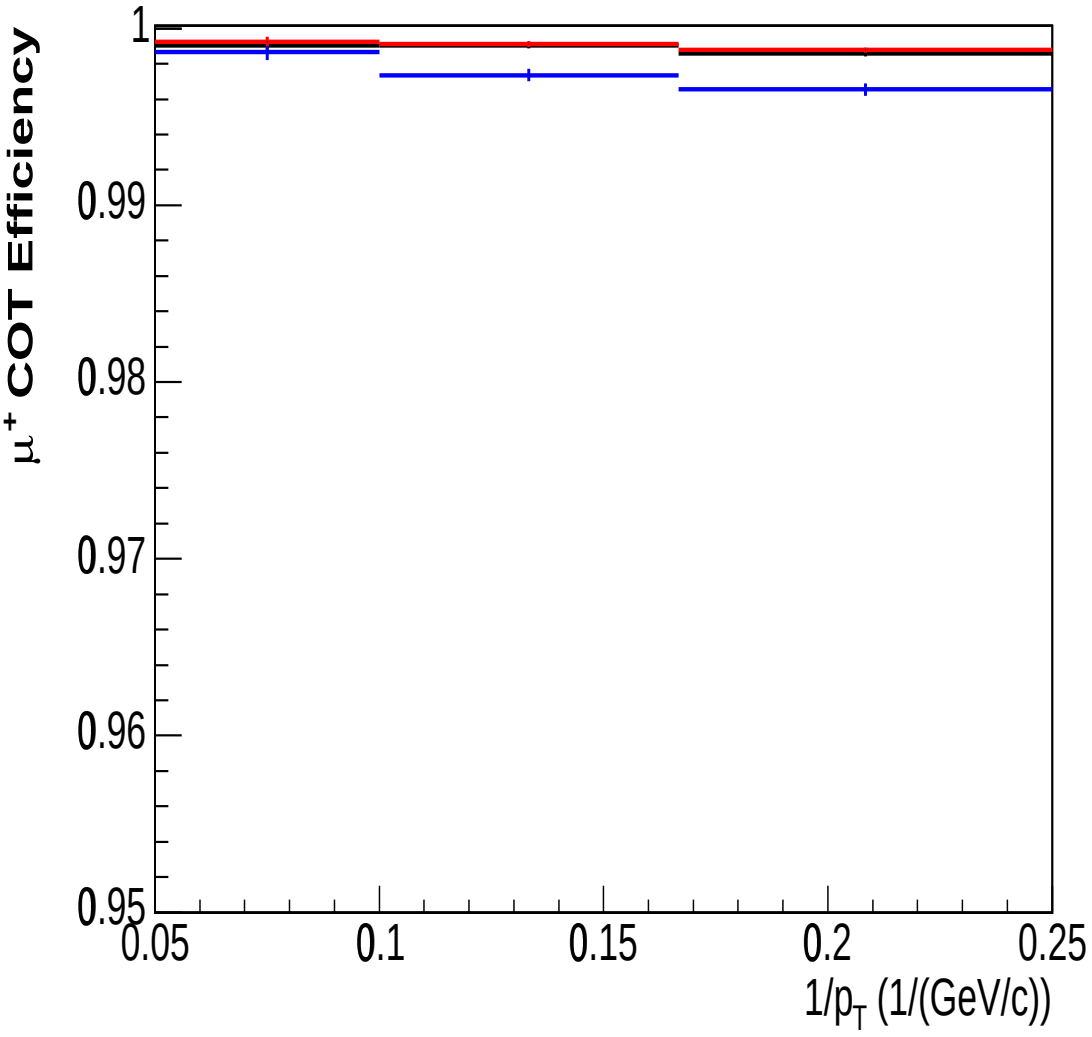

Figure 6.31: The COT tracking efficiency vs. $1/p_T$ for μ^+. The red points are from Bgenerator Monte Carlo with no matching cuts, the black points are from Bgenerator MC with matching cuts, and the blue points are from track embedding with matching cuts.

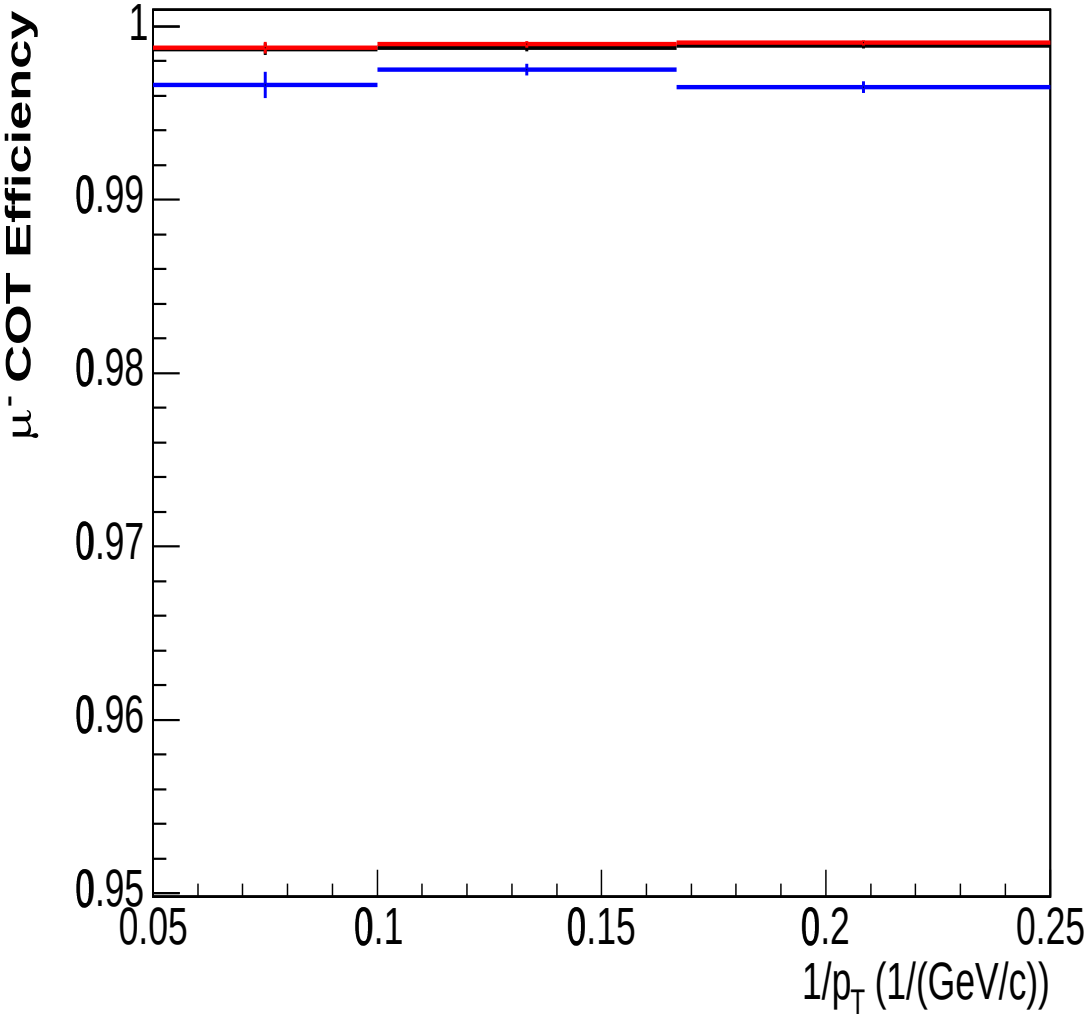

Figure 6.32: The COT tracking efficiency vs. $1/p_T$ for μ^-. The red points are from Bgenerator Monte Carlo with no matching cuts, the black points are from Bgenerator MC with matching cuts, and the blue points are from track embedding with matching cuts.

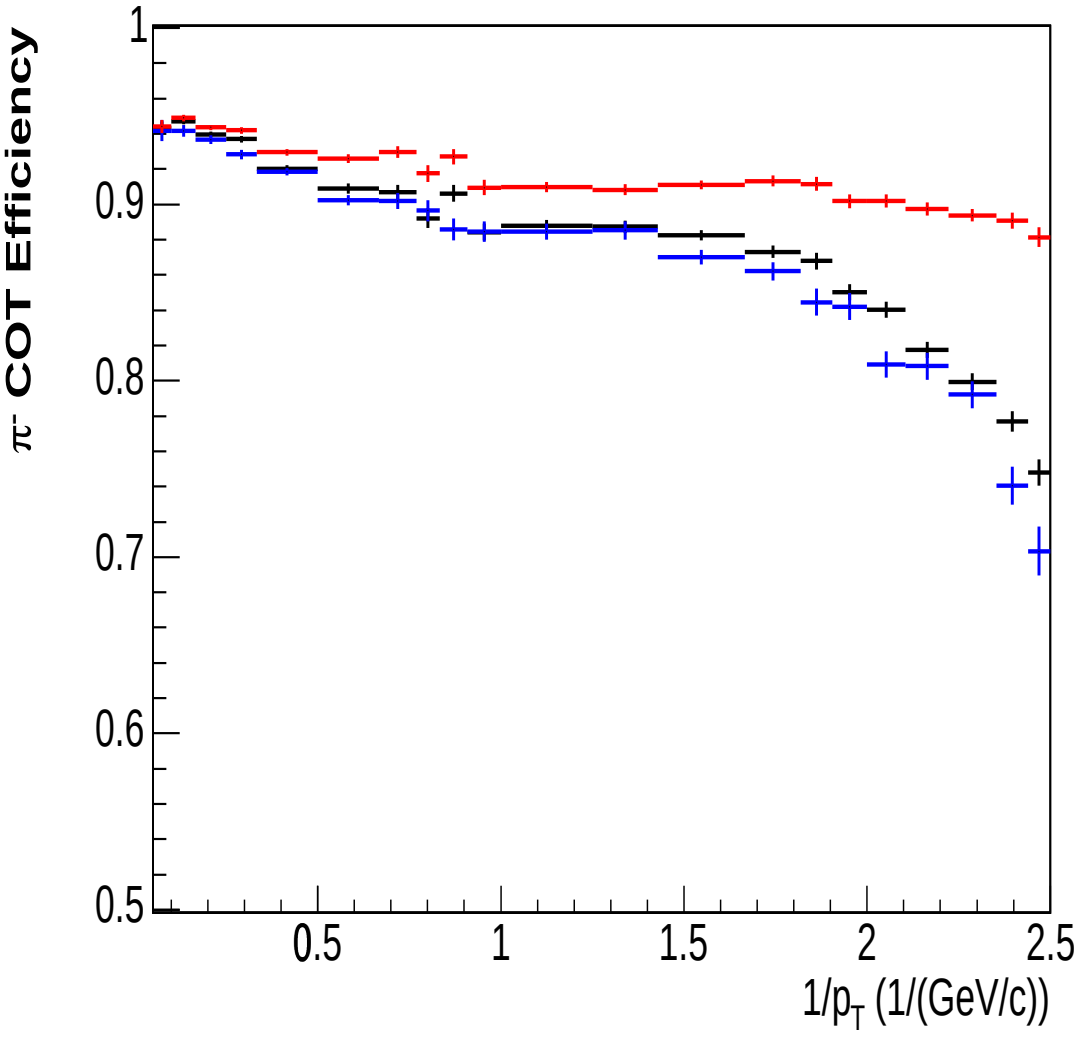

Figure 6.33: The COT tracking efficiency vs. $1/p_T$ for π^-. The red points are from Bgenerator Monte Carlo with no matching cuts, the black points are from Bgenerator MC with matching cuts, and the blue points are from track embedding with matching cuts. The points between 1.0 and 2.5 $(\mathrm{GeV}/c)^-1$ are only needed for the soft π from the D^{*-} decays.

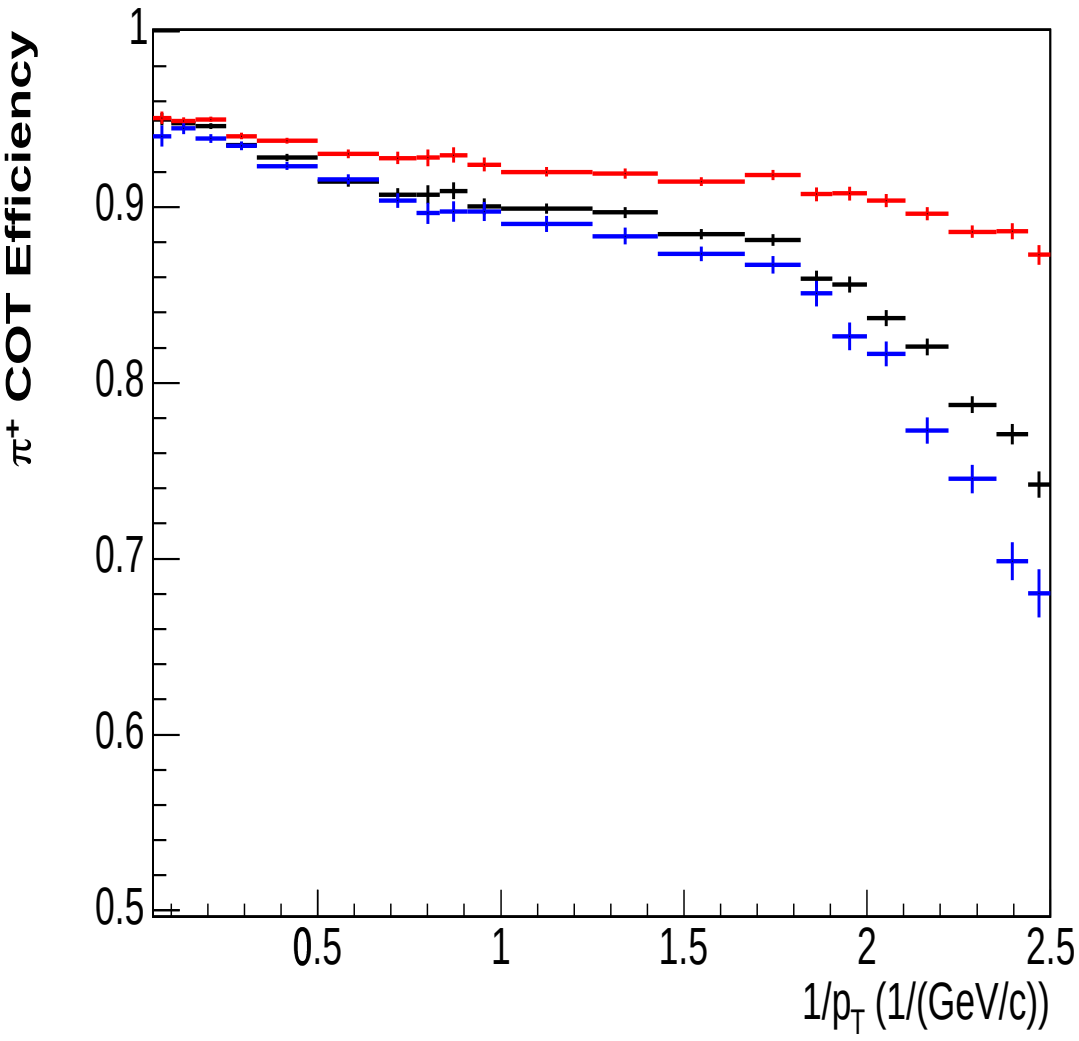

Figure 6.34: The COT tracking efficiency vs. $1/p_T$ for π^+. The red points are from Bgenerator Monte Carlo with no matching cuts, the black points are from Bgenerator MC with matching cuts, and the blue points are from track embedding with matching cuts. The points between 1.0 and 2.5 $(\mathrm{GeV}/c)^{-}1$ are only needed for the soft π from the D^{*+} decays.

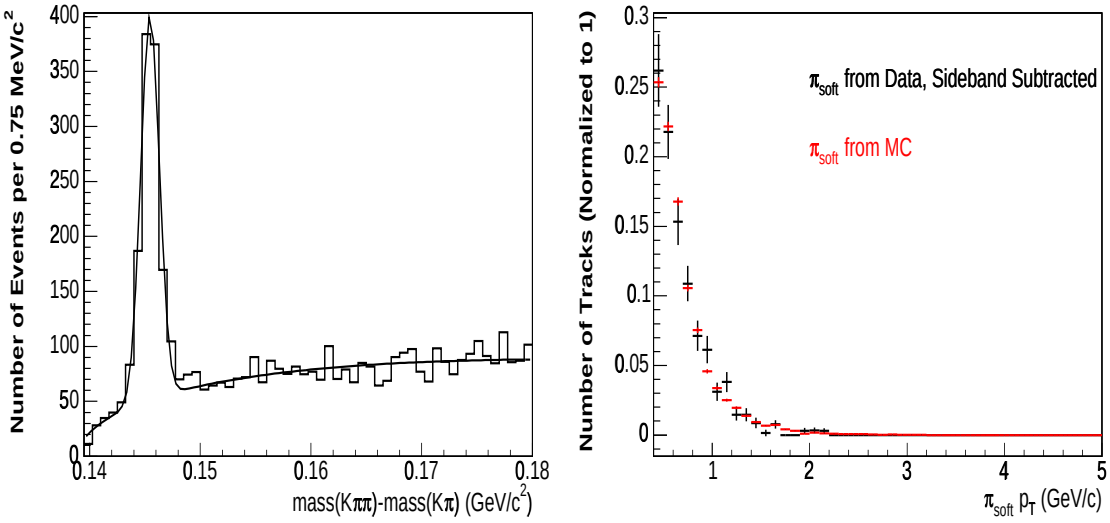

Figure 6.35: A comparison of soft π p_T between data and CDF sample+track embedding MC (right) and the $m(K^-\pi^+\pi^+) - m(K^-\pi^+)$ mass difference plot (left) used to get the soft π p_T shape from data. Sideband subtraction was used on the peak, with the signal region defined as 0.142933 GeV/c $< \Delta m <$ 0.147987 GeV/c and the sideband region defined as 0.149672 GeV/c $< \Delta m <$ 0.153523 GeV/c.

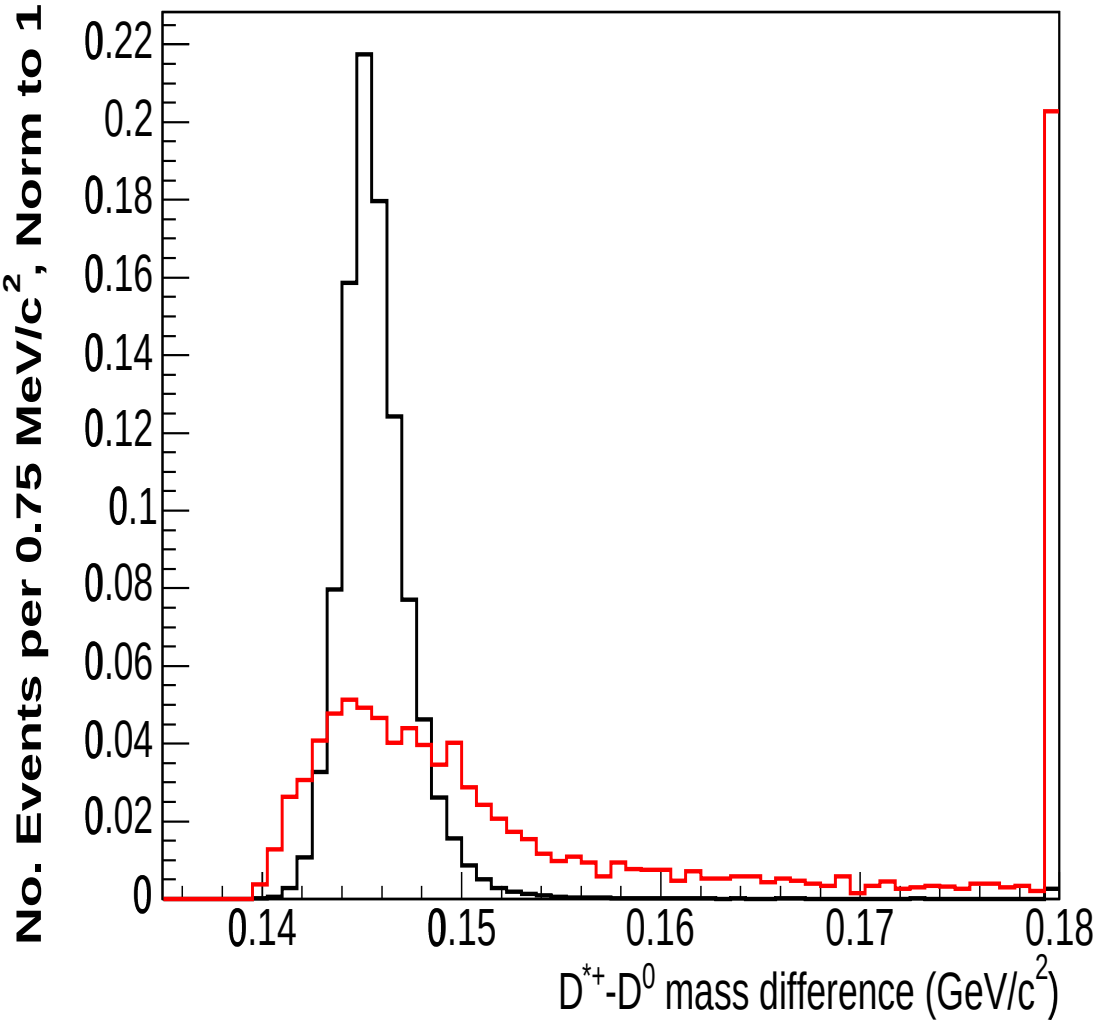

Figure 6.36: A comparison of the $D^{*+} - D^0$ mass difference in pure Bgenerator Monte Carlo between events where the π_{soft} passed (black histogram) and failed (red histogram) the $\Delta curv$ and $\Delta\phi_0$ matching cuts.

Chapter 7

Cross Section Results

7.1 Introduction

This chapter reports the measurement of the $H_b \to \mu^- D^0 X, D^0 \to K^- \pi^+$ cross-section times branching fraction. All events have been reconstructed using version 5.3.1 of the CDF software, and the MC was run using version 5.3.4. We reconstruct a sample of $\mu + D^0$ events that pass all relevant cuts place on the events used to find the efficiencies in the previous two chapters. This will give us the N term for use in equation 1.1. Thereafter, we describe how our Monte Carlo was generated and compared to our data. We use the efficiencies to correct the Monte Carlo acceptance event by event, which gives the ϵ term. We then discuss the estimation of charm backgrounds to arrive at the f_b term. As we have the luminosity measurement from the Cherenkov Luminosity Counter (Section 3.4), we can finally show the measurement itself, with both statistical and systematic errors.

7.2 Generator Level Monte Carlo

In order to reduce the amount of MC we needed to keep on disk, we generated 2.6×10^6 events using Bgenerator and decayed with EvtGen in version 5.3.4 of the CDF software without running the detector simulation, as described in section 4.4.1. These events formed the denominator of the first part of our acceptance measurement. We also require that the H_b have a rapidity of less than 0.6. In order to get into the numerator of the measurement, we require that:

- The μ must have $p_T > 3.6$ GeV/c and an $|\eta| < 0.8$.
- Both the π and the K must have a $p_T > 0.5$ GeV/c and an $|\eta| < 1.2$. Either the π or the K must have a $p_T > 1.4$ GeV/c.
- Neither the μ, the π, nor the K may have a $|z| > 151$ cm before traveling 50 cm radially.

The cuts were kept intentionally loose as we did not wish to cut any possibly good events from the full MC simulation. The resulting acceptance vs. p_T and acceptance vs. η curves can be seen in figures 7.1 and 7.2. A ninth-order polynomial was fit to the acceptance vs. $p_T(H_b)$ and used to correct the full detector simulation, below. The fit values and error matrix for the fit can be found in tables 7.1 and 7.2. The acceptance curves for the two input spectra agreed to with statistical uncertainties, so the full detector simulation was corrected with the acceptance curve from the $H_b \to J/\psi$ Monte Carlo in both cases. This is not a surprising result, as the binning in p_T is fine enough that the differences between the p_T spectra do not matter.

7.3 Monte Carlo with Full Detector Simulation

In addition to the generator level only Monte Carlo, we generated a larger sample of MC which was run with the full, run dependent detector simulation. This sample was also made using Bgenerator, and had all of the cuts listed for the generator only sample in both the numerator and denominator applied as filters before the event was passed to the full detector simulation. Events were generated with both p_T spectrums. The MC was decayed using EvtGen. All of the events that pass these cuts make it into our denominator and are weighted according to p_T by the polynomial curve fit to the generator level acceptance measurement. In order to then get into the numerator of our measurement, we required the events to fulfill the following:

- The μ, π, and K tracks must pass through all 8 superlayers of the COT, and none of the tracks may cross the spacer in one of the axial superlayers.
- The μ, π, and K tracks must have $|z_0| < 47.5$cm and no 2-track combination may have $|\Delta z_0| > 5$cm
- The μ must have a $p_T > 4.0$ GeV/c and have $|\eta| < 0.6$
- Both the π and K must have $p_T > 1.0$ GeV/c and $|\eta| < 1.0$
- The μD^0 must have $|\eta| < 0.6$.
- Either the π or the K must meet the following requirements:
  - The track must have $p_T > 2.0$ GeV/c
  - The track must be predicted to pass through at least 4 phi layers of the SVX by the SiExpected. Wedge and mechanical barrel crossers are excluded. Some layers that SiExpected reports should be good are excluded due to low efficiency. A complete list of these layers may be found in table 5.38.

- Some sections of the SVX are excluded by cutting on the ϕ and z of the track at a radius of 8 cm. The excluded sections in $\phi_{r=8cm}$ were
  - $8.75° < \phi_{r=8cm} < 18.75°$
  - $42.5° < \phi_{r=8cm} < 50°$
  - $70° < \phi_{r=8cm} < 77.75°$
  - $103.75° < \phi_{r=8cm} < 107.5°$
  - $132.5° < \phi_{r=8cm} < 138.75°$
  - $161.25° < \phi_{r=8cm} < 171.25°$
  - $191.25° < \phi_{r=8cm} < 197.5°$
  - $216.25° < \phi_{r=8cm} < 230°$
  - $251.25° < \phi_{r=8cm} < 256.25°$
  - $282.5° < \phi_{r=8cm} < 287.5°$
  - $310° < \phi_{r=8cm} < 321.25°$
  - $340° < \phi_{r=8cm} < 348.75°$

  The excluded sections in $z_{r=8cm}$ were
  - $-45cm < z_{r=8cm}$
  - $-17cm < z_{r=8cm} < -15cm$
  - $15cm < z_{r=8cm} < 18cm$
  - $z_{r=8cm} < 45cm$.
- The impact parameter of the track (according to track parameters taken directly from the input Monte Carlo, not what was determined from the detector simulation) must be $120\mu\text{m} < |d_0 - 8\mu\text{m}| < 850\mu\text{m}$. To adjust for the SVX resolution, the MC d_0 is smeared by a Gaussian resolution function with $\sigma = 30\mu$m . We vary the σ between 0 and 60 microns, and take the differences as a systematic.

- We extrapolate the muon out to the CMU and CMP using the method outlined in the previous chapter, and require that the predicted 10 cm $< |z_{CMU}| <$ 220 cm. Also, for $z_{CMU} < 0$, we exclude tracks between $255° < \phi_{CMU} < 270°$ (wedge 17), as wedge 17 is known to be less efficient in our run range. The muon track is also required to have a predicted $|z_{CMP}| <$ 310 cm.

If both the π and the K pass the tighter set of cuts, the event is counted twice in the numerator. Because all of the efficiencies determined above except for the CMU and second leg SVX efficiencies depend on

the kinematic properties of the events (μ and π or K p_T, for example), the numerator is weighted by the efficiencies event by event to get the overall efficiency times acceptance. The one exception is the SVT efficiency, which depends on the p_T, d_0, and isolation of the track. Since the Monte Carlo does not reproduce the underlying event, the SVT efficiency correction is applied by reweighting the data as described below.

7.4 $\mu + D^0$ from the Semileptonic B Trigger

We have reconstructed the decay $D^0 \to \pi^+ K^-$ in 83 pb^{-1} of data that came in on the B_SEMI_CMUP4_TRACK2_D120 trigger (described in section 4.2.1) between October 2002 and May 2003. All of the events in the sample must have the good run bits set for runcontrol, shiftcrew, the CLC online, L1, L2, and L3 triggers, SVT online, SVX online, offline, and COT, CMU, and CMP offline. We require that the events that enter our sample meet the following requirements:

- The μ and π from the $D^0 \to \pi K$ decay must have opposite charges. The Feynmann diagrams related to the decay of the $H_b \to \mu D^0$, $D^0 \to \pi K$ show that $Q_\mu \neq Q_\pi$ except for doubly Cabibbo suppressed decays. This cut avoids autoreflection of the D^0 peak.
- The μD^0 invariant mass must be less than 5.5 GeV/c^2.
- The μD^0 must have $|\eta| < 0.6$.
- The μ, π, and K tracks must pass through all 8 superlayers of the COT, and none of the tracks may cross the spacer in one of the axial superlayers.
- The μ, π, and K must have more than 4 hits on each of two axial superlayers and each of two stereo superlayers.
- The μ, π, and K tracks must have $|z_0| < 47.5$cm and no 2-track combination may have $|\Delta z_0| > 5$cm
- The μ must have a $p_T > 4.0$ GeV/c and have $|\eta| < 0.6$
- Both the π and K must have $p_T > 1.0$ GeV/c and $|\eta| < 1.0$
- Either the π or the K must meet the following requirements:
  - The track must have $p_T > 2.0$ GeV/c
  - The track must be predicted to pass through at least 4 phi layers of the SVX by the SiExpected [52]. Wedge and mechanical barrel crossers are excluded. Some layers that SiExpected reports

should be good are excluded due to low efficiency. A complete list of these layers may be found in 5.38.

- The track must have SVX phi hits in the layers that SiExpected predicts hits in.
- The track must be found by the SVX to have $120\mu m < |d_0 - 8\mu m| < 850\mu m$.
- The offline track had to be matched to a SVT track[53] with a matching $\chi^2 < 25$.
- The track p_T of the matched SVT track had to be greater than 2 GeV/c
- The SVT $|d_0|$ had to be between 120 μm and 1000 μm.
- The SVT $\chi^2 < 25$.
- Some sections of the SVX are excluded by cutting on the ϕ and z of the track at a radius of 8 cm. The excluded sections in $\phi_{r=8cm}$ were
  - $8.75^\circ < \phi_{r=8cm} < 18.75^\circ$
  - $42.5^\circ < \phi_{r=8cm} < 50^\circ$
  - $70^\circ < \phi_{r=8cm} < 77.75^\circ$
  - $103.75^\circ < \phi_{r=8cm} < 107.5^\circ$
  - $132.5^\circ < \phi_{r=8cm} < 138.75^\circ$
  - $161.25^\circ < \phi_{r=8cm} < 171.25^\circ$
  - $191.25^\circ < \phi_{r=8cm} < 197.5^\circ$
  - $216.25^\circ < \phi_{r=8cm} < 230^\circ$
  - $251.25^\circ < \phi_{r=8cm} < 256.25^\circ$
  - $282.5^\circ < \phi_{r=8cm} < 287.5^\circ$
  - $310^\circ < \phi_{r=8cm} < 321.25^\circ$
  - $340^\circ < \phi_{r=8cm} < 348.75^\circ$

  The excluded sections in $z_{r=8cm}$ were
  - $-45cm < z_{r=8cm}$
  - $-17cm < z_{r=8cm} < -15cm$
  - $15cm < z_{r=8cm} < 18cm$
  - $z_{r=8cm} < 45cm$.

- The offline muon must be a CMUP muon with a CMU $\chi^2 < 9$
- The offline CMU $dX < 15$ cm and offline CMP $dX < 20$ cm

- We extrapolate the muon out to the CMU and CMP using the method outlined above, and require that the predicted 10 cm $< |z_{CMU}| <$ 220 cm. Also, for $z_{CMU} < 0$, we exclude tracks between $255° < \phi_{CMU} < 270°$ (wedge 17), as wedge 17 is known to be less efficient in our run range. The muon track is also required to have a predicted $|z_{CMP}| <$ 310 cm.
- The muon track must be matched to an XFT track with a p_T of at least 4 GeV/c.
- The offline CMU stub must be associated with a high p_T L1 CMU stub
- The offline CMP stub must be associated with a L1 CMP stub.
- The XTRP must extrapolate a high p_T track to the L1 CMU stub associated with the offline muon.
- The muon matchbox must extrapolate a CMP stub back to the L1 CMU stub associated with the offline muon.
- We use the algorithm VertexFit, which calls the CTVMFT fitter [55], to fit the π and K of the D^0 to a common vertex. The fit must have $\chi^2 < 1000$. Figure 7.3 shows a plot of the χ^2 versus number of events.

If both the π and K legs of the D^0 pass all of the SVT leg cuts, the event is counted twice. As the SVT efficiency is sensitive to the track isolation, each event is weighted to correct for SVT efficiency of the track which fired the SVT trigger. The other efficiencies are taken into account in the Monte Carlo, as discussed above. Because the SVT efficiency is species independent, both the signal and background can be adjusted without knowing for certain the species content of the background. The number of $\mu + D^0$ events is determined by fitting the mass plots to a Gaussian function over a linear background. The error due to the uncertainty on the SVT efficiency measurement is determined by varying the fit to the SVT Efficiency measurement by $\pm 1\sigma$, calculated using the SVT fit error matrix (Table 5.40). The mass plots and fit results are shown in figures 7.4 through figures 7.8, and table 7.3 shows the yields from the fits without the SVT efficiency adjustment. Figure 7.9 shows the mass plot for all μD^0 with $p_T > 9$ GeV/c without the SVT efficiency adjustment.

7.5 Vertex and Fit Model Efficiency

In order to reconstruct the D^0, the π and K must be fit to a common vertex. The CTVMFT code used is very good, but not 100% efficient. We do not require a vertex to be fit when calculating the MC efficiency above, so the vertex fit efficiency must be calculated separately. Unfortunately, we cannot use the μD^0

sample for this purpose, since without vertexing the background completely overwhelms the D^0 peak, and no signal can be found.

We attempt to instead measure the vertexing efficiency using $J/\psi \to \mu^+\mu^-$ decays collected on the CMU-CMU and CMU-CMX triggers. In the events that enter the denominator of out measurement, we require that

- One of the μ must have at least 4 SVX phi hits.
- The other μ must have at least 3 SVX phi hits.
- Both muon tracks must have at least 5 hits in 2 axial and 2 stereo COT Superlayers.
- 2.7 GeV/c^2 $< m_{\mu\mu} <$ 3.4 GeV/c^2. The number of J/ψ events is estimated by fitting the J/ψ peak to the sum of two Gaussians with a linear background (Figure 7.10).

In order to get into the numerator of the measurement, we run VertexFit on the events and estimate the number of J/ψ events with two Gaussians plus linear background fit, as described above for the denominator (Figure 7.11). This gives a vertexing efficiency of $99.8\% \pm 0.005\%$. We look for a variation in efficiency with the sum of the p_T of the two muons, but see none. The sideband subtracted fit χ^2 distribution is shown in figure 7.12.

We consider the possibility that the fit efficiency for $D^0 \to K^-\pi^+$ is different than that for $J/\psi \to \mu^+\mu^-$. To do this, we use a subsample of the Monte Carlo above; the results are the same for both b p_T distributions. We require that the π and K are both found by the COT and have at least 3 SVX hits each. Both tracks must have a COT p_T greater than 1.0 GeV/c and one must have $p_T >$ 2.0GeV/c. At least one of the tracks must have a impact parameter within the SVT trigger track cut above. The μ p_T must be greater than 4.0 GeV/c with an $|\eta| < 0.6$. These requirements give a leave a sample of 69409 events, and vertex reconstruction efficiency of 99.69% $\pm$ 0.02%(stat). The fit χ^2 distribution is shown in figure 7.13. However, some of the found D^0 were reconstructed with masses far from the central value of 1.86 GeV/c^2. In order to account for this, the mass peak is fit to a Gaussian, as is done in the data (Figure 7.14). This also takes into account the fit model inefficiency due to the fact that the D^0 peak is not exactly Gaussian. From this, we get an efficiency of 97.41% $\pm$ 0.06%(stat). There is a small variation of the efficiency with b p_T, so we add on a 0.35% systematic error, leading to a combined vertex reconstruction and fit model efficiency of $97.41\% \pm 0.06\%(\text{stat}) \pm 0.35\%(\text{syst})$.

7.6 Data to MC Comparison

In order to see how well the two versions of the Monte Carlo reproduce the p_T and η distributions in from the data, we have made plots of the $\mu + D^0$ p_T and η distributions for the MC after all cuts and efficiencies have been applied, and of the data after all cuts and corrections for the SVT efficiency. These plots are shown in figures 7.15 and 7.16. We see that the MC p_T based that the $b \to J/\psi X$ cross section result is softer than the data, while the spectrum from the MRSD0 MC is somewhat harder than the data. We therefore measure the cross-section by taking the average of the cross section from the two measurements, and use one-half the difference as a systematic. Also, consider the events with μD^0 p_T between 6 and 9 GeV/c. We are concerned that, as these events are on the softer side of the spectrum with the lowest efficiency and acceptance, that they may be subject to poorly understood systematic effects. Because of this possibility, we exclude events with a $\mu + D^0$ p_T of less than 9 GeV/c. We also compare the muon (figure 7.17) and D^0 (figure 7.18) p_T spectra separately and find that the distributions from data, the CDF sample, and the MRSD0 sample agree reasonably well.

We also compare the invariant mass distribution of μD^0 in the data to the distributions of the two MC samples (fig 7.19). The mass distributions are all consistent with one another. The fitting the ratio of the MC to data for the two distributions to lines gives a slope that is 0.80σ from 0 for the CDF distribution, and 1.27σ from 0 for the MRSD0 distribution (fig 7.20). We can use this ratio to assess a radiative decay systematic for our cross section. We do this by creating MC samples from both distributions that have the PHOTOS package left out of the decay of the H_b, and measure the cross-section in these samples. Without PHOTOS, the slope of the invariant mass ratio is decreased, and by finding the mixture of samples with and without PHOTOS that gives a slope consistent with 0 gives the ratio of the PHOTOS/no PHOTOS samples to use in the systematic assessment. I get somewhat different results for the two samples. Unfortunately, while the slope of the mass ratio is smaller without PHOTOS than with PHOTOS, the slope for the CDF phenomenological sample is still positive. This means that it is impossible to combine the two slopes to get a slope consistent with 0. The MRSD0 sample without PHOTOS, on the other hand, is slightly negative, so that can be combined with the sample including PHOTOS to get a 0 slope. We have some concerns about this method, however, due to the presence of direct charm in our sample. Because the $c\overline{c}$ pair does not have to have an invariant mass consistent with a b hadron mass, the μD^0 mass distribution from these decays peaks at higher mass than those from the decays of H_b. We attempted to model this using Pythia Monte Carlo that was initially generated for a different study, but there were insufficient statistics to correct the mass distributions from our Bgenerator studies, and generating a large enough sample would require a prohibitive amount of time and computing power. Instead, to be conservative we take average of the

difference in the cross-sections with and without PHOTOS to be our systematic.

7.7 Charm Backgrounds

While fitting the D^0 peak to a Gaussian allows us to determine how many μD^0 events are in our sample and eliminate non-charm background, it is possible that there are real μD^0 events that are not part of our $H_b \to \mu D^0$ signal. One source of this charm background is direct $c\bar{c}$ production. It is possible for direct charm to mimic our signal by having one charm quark decay to a μ, and the other charm quark decay to a D^0. A second source of charm background is $b\bar{b}$ production, where one b quark decays to $D^0 X$, and the other b quark follows the decay chain $b \to c \to \mu$. Also, it is possible for a single H_b to decay to a $D\overline{D}X$ or a $D\tau X$, where subsequent decays of the one of the D mesons or the τ produces a muon. For our cross section measurement, we are only interested in events where the muon was produced directly by the H_b decay, so these processes are also considered backgrounds. Since it is not possible to remove these events from our sample, their contributions to the total number of μD^0 must be estimated to get the f_b term from equation 1.1.

7.7.1 $c\bar{c}$ Background Estimate

In order to estimate the fraction of events in our sample from direct charm, we use the impact parameter of the D^0. As the D^0 mesons from direct charm are created at the primary vertex, they ought to point back to the primary, to within the detector resolution. The D^0 from b decays, on the other hand, are created at the secondary b vertex, and are less likely to point back at the primary vertex. To get the impact parameter distribution for D^0 mesons from b decays, we use the same MC sample that was used to find the acceptance above. In order to get the d_0 distribution of the D^0 from direct charm, we generated 20,065 charm-anticharm events using Pythia and decay them using EvtGen. We force the D^0 to decay either semi-muonically or to πK, but other particles are allowed to decay normally. We require the direct charm events to satisfy the same cuts as were placed on our MC sample. In order to increase our statistics, we also generate 876152 D^0 mesons using FakeEvent. We then reweight the p_T spectrum of the events from FakeEvent so that it matches the p_T spectrum of the D^0 from Pythia events with a μ with $p_T > 4.0\text{GeV}/c$ and $|\eta| < 0.6$.

In both the direct charm and b to D^0 samples, calculate the impact parameter using generator level MC quantities. In order to estimate the error on the D^0 impact parameter due to detector resolution, we look at the sideband subtracted D^0 impact parameter error distribution from data, shown in figure 7.21. We see that the average error is approximately 34 microns, so we smear the MC impact parameters using a Gaussian

resolution function with a σ of 34 μm. We see that this gives the impact parameter distributions for D^0 mesons from direct charm and bottom decays shown in figure 7.22. We do a bin by bin χ^2 fit to determine the ratio of events from direct charm to those from bottom decays. We find that using the d_0 distribution from the b events generated with the $J\psi$ input spectrum, we get a charm fraction of $6.29\% \pm 2.11\%$, while using the d_0 distribution from the b events in the MRSD0 sample gives a charm fraction of $5.43\% \pm 2.13\%$. So as a final result, we use the charm fraction $5.86\% \pm 2.12\%(stat) \pm 0.43\%(syst)$.

7.7.2 $b\overline{b}$ Background Estimate

We also have background due to the presence of $b\overline{b}$ events where one bottom quark decays to a D^0 meson and the other follows the decay $\overline{b} \to \overline{c} \to \mu^- + X$. In this case, there will also be a $\mu + D^0$ with the μ and π having opposite charges, but since this is not a $H_b \to \mu^- D^0$ decay, we do not wish to include these events in our signal. Unfortunately, the impact parameter distribution for the D^0 meson in these events is expected to be the same as signal, since the D^0 mesons are coming from b hadrons. Therefore, we cannot use the same technique as we used for the $c\overline{c}$ background. Instead, we take advantage of the fact that when the second b decays directly to a μ, instead of first decaying to a charm quark, the muon that is produced has the same charge as the π from the D^0, rather than the opposite charge as in a $H_b \to \mu^- D^0$, $D^0 \to \pi^+ K^-$ decay. We expect that there will be more of these events than $b \to \overline{c} \to \mu + X$ events. Therefore, we look for a $D^0 \to \pi^+ K^-$ peak in events with $Q_\mu = Q_\pi$. This is complicated by two factors. The first is that there is a large peaking background in this sample from reflections of our signal sample of $H_b \to \mu^- D^0$, $D^0 \to \pi^+ K^-$ events. We account for this by finding the shape of this distribution using Monte Carlo, and fixing the number of events in the reflection peak to the number of D^0 events in our signal sample. The Monte Carlo wrong sign mass distribution was found to be insensitive to both the input b p_T spectrum used and whether direct MC track momentum was used or if the reconstructed COT momentum was used for the π and K tracks. These distributions are shown in figure 7.23. The second complication is that the double Cabibbo suppressed decay of the $D^0 \to \pi^- K^+$ is also expected to give a small peak, with a number of events equal to 0.0036 ± 0.0003 times the number of events in our signal peak. This number is arrived at from branching ratios listed in [3]. As there are 4069 ± 114 events in our signal peak (after correcting for SVT efficiency), we expect to have 15 ± 1 events from doubly Cabibbo suppressed decays. We now do a fit to the wrong sign distribution with a linear background, the reflection of right sign D^0 peak set to the number of events set to 4069.35 and the mean and σ set by MC, and a D^0 signal peak with its mean and σ set to the same values as in the right sign peak, but with the number of events allowed to float (see figure 7.24). This gives a peak of 188 ± 69 events. Taking into account the doubly Cabibbo suppressed peak, we get 173 ± 69 events.

To convert this number into a estimate of the number of right sign $b\bar{b}$ events, we look at a generator level sample of $b\bar{b}$ Monte Carlo generated using Pythia and decayed with the standard EvtGen decay table. In this sample, we look for events where one b decayed to a μ, and the other produced a D^0. This sample was initially generated without mixing for a different study, so to determine the number of mixed B^0 and B_s^0 events, we take the time integrated mixing probabilities of 0.186 and 0.50 respectively from [3], and use a random number generator to decide if the B mixed. We require that the μ have $p_T > 4.0$ GeV/c and $|\eta| < 0.6$, and that the D^0 decay to $K^-\pi^+$ where both the K and π have $p_T > 1.0$ GeV/c, $|\eta| < 1.0$, and at least one of the two has a $p_T > 2.0$ GeV/c. No other attempt is made to account for the detector efficiency or acceptance, with the assumption that these will cancel in the ratio of the right sign to wrong sign events. We find 107 right sign and 471 wrong sign event in this sample (after adjusting for mixing), giving a right to wrong sign ratio of 0.227 $\pm$ 0.024 (stat). To take into account the fact that the efficiencies are not exactly the same, we apply a 50% systematic, giving a final ratio of 0.227 $\pm$ 0.024 (stat) $\pm$ 0.113 (syst). As we found 173 ± 69 wrong sign events above, this gives 39.3 $\pm$ 16.2 (stat) $\pm$ 19.6 (syst). Dividing by the number of events in the signal peak, this gives a $b\bar{b}$ background fraction of 0.97% $\pm$ 0.40%$\pm$ 0.48%

7.7.3 $B \to DD$ and $B \to D\tau$ Background Events

In addition to backgrounds from $c\bar{c}$ and $b\bar{b}$ events, a background also comes from the decays of a single b meson. These events can occur when the decay $b \to c\bar{c}s$ or $b \to c\bar{c}d$ is followed by one of the charm quarks decaying to a μ, and the other decaying through $D^0 \to K\pi$. These events also can come from a decay of $b \to c\tau^-\overline{\nu}_\tau$, where the τ decays to a μ, and the c decays through $D^0 \to K\pi$. Because these events come from real b decays, the impact parameter of the D^0 will not necessarily point back to the primary vertex, and the nature of the decay means that the μ and the π from the decays will have opposite charges, as is the case in $b \to c\mu^-\nu_\mu$ events. Instead, we take these events into account using Monte Carlo only. When we generated the Monte Carlo for the acceptance measurement, we kept events with $B \to DD$ and $B \to D\tau$ decays, so long as they had both a μ^- and a $D^0 \to K^-\pi^+$ decay. We then include these events in the denominator of the weights to determine bin migration (described in section 7.9), but not in the numerator. Thus, these events are subtracted out. Unfortunately, the branching fractions for some of these decays are not extremely well known compared to decays for $b \to c\mu^-\nu_\mu$ events. Therefore, to assess an uncertainty on this background, we allow the number of events from $B \to DD$ and $B \to D\tau$ decays to vary by 50%.

7.8 Branching Fraction Uncertainties

Because we do not fully reconstruct the H_b, we have to consider effects on the cross section due to the uncertainties on the branching fractions of decays that lead to $H_b \to \mu D^0$. These uncertainties only matter to the extent that the different decay modes have different acceptances within our detector. In particular, we are concerned with the decays of $H_b \to \mu D^{**} X$, where the D^{**} decays to a D^0. Since the D^0 from these decays tend to be softer and have a larger spread in η than decays directly to D^0s or D^*, the acceptance is lower for these events than for the more direct decays. To get the uncertainty in the cross section due to $H_b \to \mu D^{**} X$ decays, we allow the number of $H_b \to \mu D^{**} X$ decays to vary by 50%. We find that this gives an uncertainty of 1.9% for the both the cross section from $H_b \to \mu D^0 X$ events, and the cross section from $H_b \to \mu D^{*+} X$ events. The acceptance vs. p_T of the H_b for D^0 and D^{*+} events for my loose cuts are shown in figure 7.25 with the $H_b \to \mu D^{**}$ branching fraction varied by 50%.

7.9 $H_b \to \mu D^0 X$, $D^0 \to \pi K$ Cross-Section

In order to turn the $\mu + D^0$ p_T distribution from the data into a b hadron differential cross-section times branching fraction measurement, we perform a convolution between that and the p_T distribution of the H_b from MC. We determine a weight, w_{ij}, that is defined as

$$w_{ij} = \frac{\text{No. } H_b \text{ in } p_T \text{ bin } i \ \& \ |y| < 0.6 \text{ decaying to a } \mu D^0 \text{ in } p_T \text{ bin } j \ \& \text{ passing all cuts in Sec. 7.3}}{\text{No. } \mu D^0 \text{ in } p_T \text{ bin } j \text{ and passing all cuts in section 7.3}} \tag{7.1}$$

We generate H_b with $|y| > 0.6$ in order to ensure these events are properly taken into account in the number of events in the μD^0 p_T bins, but these account for less than 1% of the μD^0 with $|\eta| < 0.6$. Note that for the determination of the weights w_{ij}, it is the slope of the H_b p_T curve, and not its absolute normalization that matters. Then, to get the differential cross section, we use the formula

$$N_i^{H_b} = \sum_{j=1}^{N} w_{ij} N_j^{\mu D^0} \tag{7.2}$$

Where $N_i^{H_b}$ is the number of H_b in p_T bin i, and $N_j^{\mu D^0}$ is the number of events in $\mu + D^0$ p_T bin j from data found in section 7.4. We now have all of the terms from equation 1.1 required to get the cross section.

The statistical error in each H_b p_T bin is given by

$$\delta_{stat}(N_i^{H_b}) = \sqrt{\sum_{j=1}^{N} w_{ij}\delta_{stat}^2(N_j^{\mu D^0})} \tag{7.3}$$

The systematic uncertainties were determined in general by varying the efficiency or acceptance in question by $\pm 1\sigma$, usually using the error matrix determined from a fit. The systematic due to the SVT efficiency found in this manner was only about 0.5%, which was felt to be too low as several of the data point used in the fit lie more than $1\sigma + 0.5\%$ from the fitted curve. To assess a fit model systematic, the cross section was determined using the data points from the SVT efficiency measurement, and the difference added in quadrature with the 1 σ systematic to get the total systematic uncertainty. The systematic uncertainty on the MC p_T spectrum is estimated by taking the fractional difference between the cross-section found using the CDF sample and the reweighted MRSD0 sample. A list of the systematic uncertainties is shown in table 7.4. It may be worth noting that the total systematic error for the MC p_T shape is less than the systematic error due to the MC p_T shape in most of the p_T bins. This is because uncertainty on the p_T shape primarily effects what fraction of the total cross section is in a specific p_T bin. When integrating over all bins, this effect is ameliorated. Also, when finding the acceptance for specific p_T bin, one can only use the MC events within that bin, while the overall measurement uses all of the MC events. This leads to a lower uncertainty due to MC statistics.

After applying all corrections to the data, we get the total cross-section times branching ratio of

$$3.53 \text{ nb} \pm 0.20 \text{ nb (stat.)} \; ^{+0.34}_{-0.36} \text{ nb(syst.)}$$

for b hadrons with $p_T > 9\text{GeV}/c^2$ and $y < 0.6$. Correcting for branching ratios of the the $H_b \to \mu D^0$ and $D^0 \to \pi K$ from [3], we get a total cross-section of

$$1.34 \; \mu\text{b} \pm 0.08 \; \mu\text{b (stat.)} \; ^{+0.13}_{-0.14} \; \mu\text{b (syst.)} \pm 0.07 \; \mu\text{b (BF)}$$

for b hadrons with $p_T > 9\text{GeV}/c^2$ and $y < 0.6$. The differential cross-section times branching ratio is shown in table 7.5, and displayed in figure 7.26, and the differential cross-section corrected for the branching ratios using the current best values is shown in figure 7.27. For convenience, we list the branching ratios used in table 7.6.

7.10 $H_b \to \mu D^{*+} X$, $D^{*+} \to D^0 \pi$, $D^0 \to \pi K$ Cross-Section

In addition to the measuring the H_b cross-section in the $H_b \to \mu D^0$, $D^0 \to \pi K$ channel, we extend this analysis to look at the cross section in the $H_b \to \mu D^{*+}$, $D^{*+} \to D^0 \pi^+_{soft}$, $D^0 \to \pi K$ channel. This extension is fairly straightforward. We place the same cuts on the $\mu + D^0$ in data as are listed in section 7.4. In addition, we require a soft pion be found in the event, which satisfies the following requirements:

- The π_{soft} must have a $p_T > 0.4$ GeV/c.
- The π_{soft} must have a $|\eta| < 1.0$;
- The Δz_0 between the π_{soft} and the μ, the π must all be less than 5 cm.
- The π_{soft} track must have at least 5 hits on two COT axial layers and 5 hits on two COT stereo layers.
- The D^0 associated with the soft pion must have a mass between 1.82 GeV/c^2 and 1.90 GeV/c^2. Since this includes an interval of 4.5σ about the D^0 peak, we do not correct for any D^{*+} that might be excluded.

The mass difference between the D^0 and the D^{*+} is only 0.145 GeV/c^2 [3], which is only slightly greater than the π^+ mass of 0.139 GeV/c^2 [3]. Therefore, in order to get a clear peak, we plot the mass difference between the $K\pi\pi$ and the $K\pi$ pair which are used to from the D^0. These mass plots are shown in figures 7.28 to 7.32. In order to make comparisons between the two measurements simple, we bin the data in the same bins of μD^0 p_T. The yields without the SVT efficiency adjustments are included on table 7.3. Figure 7.33 shows the mass difference plotted without the SVT efficiency adjustment.

All of the efficiencies for this measurement are the same as those for the $H_b \to \mu D^0$, $D^0 \to \pi K$, except that we need to add in the efficiency for the π_{soft}. This efficiency was discussed above in 6.6.

The generator level acceptance for D^{*+} events, described for general D^0 events in section 7.2, is somewhat higher for events that include a D^{*+}. We parameterize the generator level acceptance for D^{*+} events, with a seventh order polynomial. The fit constants and error matrix can be found on tables 7.7 and 7.8, and is plotted in figure 7.34.

Most of the systematics for the D^{*+} measurement are the same as those for the D^0 measurement on table 7.4, where they differ the table refers to D^0 or D^{*+} specifically.

After applying all corrections to the data, we get the total cross-section times branching ratio using $H_b \to \mu D^{*+}$, $D^{*+} \to D^0 \pi$, $D^0 \to \pi K$ decays of

$$1.04 \text{ nb} \pm 0.13 \text{ nb (stat.)} \, ^{+0.12}_{-0.14} \text{ nb(syst.)}$$

for b hadrons with $p_T > 9\text{GeV}/c^2$ and $y < 0.6$. Correcting for branching ratios of the the $H_b \to \mu D^{*+}$, $D^{*+} \to D^0\pi$, and $D^0 \to \pi K$ from [3], we get a total cross-section of

$$1.47\ \mu\text{b} \pm 0.18\ \mu\text{b (stat.)}\ ^{+0.17}_{-0.19}\ \mu\text{b (syst.)} \pm 0.11\ \mu\text{b (BF)}$$

for b hadrons with $p_T > 9\text{GeV}/c^2$ and $y < 0.6$. The differential cross-section times branching ratio is shown in table 7.9, and displayed in figure 7.35, and the differential cross-section corrected for the branching ratios using the current best values is shown in figure 7.36. For convenience, we list the branching ratios used in table 7.6.

7.11 Comparison With Theory and Previous Measurements

In order to get a sense of how our measurement compares with previous H_b cross section results, we compare our result with the measurement of the H_b cross section measured at CDF Run II using J/ψ decays [12]. The differential cross sections are compared in figure 7.37, where we see that the three cross section measurements agree to with experimental errors. We also look at a prediction made using FONLL theory for b production with CTEQ6M PDFs [56]. Comparing this to our result, we see good agreement within errors (Figure 7.38).

7.12 Summary and Possible Future Directions

We have measured the b cross section in $H_b \to \mu D^0 X$ and $H_b \to \mu D^{*+} X$ decays. This measurement is the first b cross section from CDF to use data collected with the SVT displaced track trigger. Other alternative production mechanisms of μD^0 events have been proposed [14], but the consistency of my results with the J/ψ cross section and theory makes a large contribution from new physics unlikely. There are several ways this analysis could be extended. By including data from later run periods, it would be possible to get a better measurement of the high momentum cross section. Also, one could look for additional high momentum muons in the events, in order to measure the $b\bar{b}$ cross section.

Acceptance, Background Estimate and Cross-Section Tables and Figures

Here is the fit result for the generator level acceptance with loose cuts vs. b hadron p_T using the formula:

$$\alpha = \alpha_0 + \alpha_1 * p_T + \alpha_2 * p_T^2 + \alpha_3 * p_T^3 + \alpha_4 * p_T^4 + \alpha_5 * p_T^5 + \alpha_6 * p_T^6 + \alpha_7 * p_T^7 + \alpha_8 * p_T^8 + \alpha_9 * p_T^9 \quad (7.4)$$

Note that the unit of p_T used in the fitter was 10 GeV/c, rather than GeV/c. Therefore, to get the correct acceptance for a 20 GeV/c b hadron, one must put in 2.0 into the formula above.

χ^2/ndf = 33.25476/30				
α_0	α_1	α_2	α_3	α_4
0.4315915	-1.954760	2.161378	1.525248	-4.281450
α_5	α_6	α_7	α_8	α_9
3.505121	-1.511293	0.3692517	-0.04835067	0.002639340

Table 7.1: The results of of the fit to the generator level acceptance with loose cuts vs. b hadron p_T for $H_b \to \mu D^0 X$ events.

	α_0	α_1	α_2	α_3	α_4
α_0	0.78081E-06	-0.14022E-05	0.35233E-06	0.16728E-06	-0.12383E-07
α_1	-0.14022E-05	0.32045E-05	-0.16976E-05	-0.26083E-07	0.72738E-07
α_2	0.35233E-06	-0.16976E-05	0.21764E-05	-0.71374E-06	-0.36745E-07
α_3	0.16728E-06	-0.26083E-07	-0.71374E-06	0.65404E-06	-0.11036E-06
α_4	-0.12383E-07	0.72738E-07	-0.36745E-07	-0.11036E-06	0.86504E-07
α_5	-0.98769E-08	0.14645E-07	0.13530E-07	-0.15197E-07	-0.10589E-07
α_6	-0.20088E-08	0.94033E-09	0.45290E-08	-0.85471E-09	-0.18318E-08
α_7	-0.15039E-09	-0.30987E-09	0.71112E-09	0.25834E-09	-0.19154E-09
α_8	0.58425E-10	-0.13736E-09	-0.14195E-10	0.11254E-09	0.19891E-10
α_9	0.35133E-10	-0.30871E-10	-0.59922E-10	0.25731E-10	0.20639E-10
	α_5	α_6	α_7	α_8	α_9
α_0	-0.98769E-08	-0.20088E-08	-0.15039E-09	0.58425E-10	0.35133E-10
α_1	0.14645E-07	0.94033E-09	-0.30987E-09	-0.13736E-09	-0.30871E-10
α_2	0.13530E-07	0.45290E-08	0.71112E-09	-0.14195E-10	-0.59922E-10
α_3	-0.15197E-07	-0.85471E-09	0.25834E-09	0.11254E-09	0.25731E-10
α_4	-0.10589E-07	-0.18318E-08	-0.19154E-09	0.19891E-10	0.20639E-10
α_5	0.85557E-08	-0.80684E-09	-0.14112E-09	-0.12806E-10	0.34420E-11
α_6	-0.80684E-09	0.75495E-09	-0.55592E-10	-0.10297E-10	-0.12054E-11
α_7	-0.14112E-09	-0.55592E-10	0.60375E-10	-0.46701E-11	-0.11583E-11
α_8	-0.12806E-10	-0.10297E-10	-0.46701E-11	0.41280E-11	-0.56430E-12
α_9	0.34420E-11	-0.12054E-11	-0.11583E-11	-0.56430E-12	0.20951E-12

Table 7.2: The error matrix of the fit to the generator level acceptance with loose cuts for $H_b \to \mu D^0 X$ events.

μD^0 p_T	D^0 yield	D^* yield
9 to 11 GeV/c	867.87 ± 53.47	82.3 ± 10.5
11 to 13 GeV/c	863.13 ± 45.82	142.6 ± 13.2
13 to 17 GeV/c	1016.77 ± 46.27	236.4 ± 16.9
17 to 29 GeV/c	669.59 ± 38.29	169.6 ± 14.1
29 to 40 GeV/c	67 ± 12.2	14.2 ± 4.27

Table 7.3: The yields for the number of D^0 and D^{*+} events per μD^0 p_T bin, without SVT efficiency correction.

		p_T bin width in GeV/c					
source	total p_T	9-11	11-13	13-17	17-23	23-29	29-40
Luminosity	6.0%	6.0%	6.0%	6.0%	6.0%	6.0%	6.0%
L1 Efficiency	2.6%	2.6%	2.6%	2.6 %	2.5 %	2.5 %	2.5%
L2 XFT Efficiency	1.0%	1.0%	1.0%	1.0%	1.0%	1.0%	1.0%
L2 SVT Efficiency	1.3%	1.6%	1.2%	0.8%	0.7%	0.7%	0.9%
L3 Efficiency	0.2%	0.2%	0.2%	0.2%	0.2%	0.1%	0.1%
CMU Efficiency	1.6%	1.6%	1.6%	1.6%	1.6%	1.6%	1.6%
CMP Efficiency	$^{+1.4\%}_{-1.3\%}$	$^{+1.4\%}_{-1.3\%}$	$^{+1.4\%}_{-1.3\%}$	$^{+1.4\%}_{-1.3\%}$	1.4%	1.5%	1.7%
SVX Efficiency	$^{+1.5\%}_{-1.0\%}$	$^{+1.5\%}_{-1.0\%}$	$^{+1.5\%}_{-1.0\%}$	$^{+1.5\%}_{-1.0\%}$	$^{+1.5\%}_{-1.1\%}$	$^{+1.5\%}_{-1.1\%}$	$^{+1.5\%}_{-1.0\%}$
SVX 2nd leg Eff.	1.0%	1.0%	1.0%	1.0%	1.0%	1.0%	1.0%
COT Eff. (D^0)	$^{+3.1\%}_{-4.1\%}$	$^{+3.2\%}_{-4.3\%}$	$^{+3.3\%}_{-4.2\%}$	$^{+3.0\%}_{-3.8\%}$	$^{+2.9\%}_{-3.5\%}$	$^{+2.8\%}_{-3.3\%}$	$^{+2.7\%}_{-3.1\%}$
COT Eff. (D^*)	$^{+7.0\%}_{-8.9\%}$	$^{+7.9\%}_{-9.7\%}$	$^{+7.1\%}_{-9.6\%}$	$^{+6.1\%}_{-8.2\%}$	$^{+5.3\%}_{-6.1\%}$	$^{+4.9\%}_{-5.0\%}$	$^{+4.5\%}_{-4.3\%}$
Vertex + Fit Eff	0.4%	0.4%	0.4%	0.4%	0.4%	0.4%	0.4%
$c\bar{c}$ Background	2.2%	2.2%	2.2%	2.2%	2.2%	2.2%	2.2%
$b\bar{b}$ Background	0.6%	0.6%	0.6%	0.6%	0.6%	0.6%	0.6%
d_0 Smearing	$^{+0.9\%}_{-2.6\%}$	$^{+1.1\%}_{-2.6\%}$	$^{+0.8\%}_{-2.8\%}$	$^{+0.7\%}_{-2.6\%}$	$^{+0.8\%}_{-2.3\%}$	$^{+1.0\%}_{-2.5\%}$	$^{+1.5\%}_{-1.4\%}$
FSR	1.2%	1.0%	1.8%	1.8%	0.7%	2.2%	4.0%
$B \to \mu D^{**} X$ BR (D^0)	1.9%	2.1%	1.7%	1.6%	2.0%	1.5%	1.7%
$B \to \mu D^{**} X$ BR (D^*)	1.9%	2.0%	1.9%	1.8%	2.3%	1.7%	2.0%
$B \to DD$, $B \to D\tau$ BR	2.4%	2.4%	2.4%	2.5%	2.6%	2.3%	2.4%
MC stat. (D^0)	0.5%	1.7%	1.1%	0.9%	1.0%	1.6%	2.1%
MC stat. (D^*)	1.2%	5.8%	3.4%	2.2%	2.2%	3.3%	4.4%
MC p_T shape (D^0)	3.4%	5.7%	3.0%	1.7%	2.2%	2.0%	2.5%
MC p_T shape (D^*)	4.4%	5.7%	4.4%	3.9%	4.0%	0.6%	2.8%
total (D^0)	$^{+9.6\%}_{-10.1\%}$	$^{+10.8\%}_{-11.4\%}$	$^{+9.6\%}_{-10.2\%}$	$^{+9.1\%}_{-9.6\%}$	$^{+9.1\%}_{-9.5\%}$	$^{+9.2\%}_{-9.6\%}$	$^{+10.1\%}_{-10.2\%}$
total (D^*)	$^{+11.8\%}_{-13.2\%}$	$^{+14.1\%}_{-15.3\%}$	$^{+12.3\%}_{-14.1\%}$	$^{+11.3\%}_{-12.7\%}$	$^{+10.9\%}_{-11.5\%}$	$^{+10.3\%}_{-10.5\%}$	$^{+11.5\%}_{-11.4\%}$

Table 7.4: The systematic errors of the $d\sigma(p\bar{p} \to B)/dp_T$ measurement.

p_T bin (GeV/c)	$d\sigma/dp_T \times Br$ (pb/(GeV/c))	stat. err (pb/(GeV/c))	syst. err (pb/(GeV/c))
9-11	789	90	$^{+85}_{-90}$
11-13	413	30	$^{+40}_{-42}$
13-17	180	9	$^{+16}_{-17}$
17-23	48.9	2.5	$^{+4.4}_{-4.6}$
23-29	12.7	1.0	1.2
29-40	3.31	0.36	0.34

Table 7.5: Differential cross section $d\sigma(p\overline{p} \to B)/dp_T$ times branching fraction of $H_b \to \mu D^0 X$, $D^0 \to K\pi$.

decay	branching fraction
$H_b \to \mu^- D^0 X$	6.89% ± 0.35%
$H_b \to \mu^- D^{*+} X$	2.75% ± 0.19%
$D^{*+} \to D^0 \pi^+$	67.7% ± 0.5%
$D^0 \to \pi^+ K^-$	3.81% ± 0.09%

Table 7.6: Branching fractions used in this analysis, taken from [3].

Here is the fit result for the generator level acceptance for μD^{*+} events with loose cuts vs. b hadron p_T using the formula:

$$\alpha = \alpha_0 + \alpha_1 * p_T + \alpha_2 * p_T^2 + \alpha_3 * p_T^3 + \alpha_4 * p_T^4 + \alpha_5 * p_T^5 + \alpha_6 * p_T^6 + \alpha_7 * p_T^7 \tag{7.5}$$

Note that the unit of p_T used in the fitter was 10 GeV/c, rather than GeV/c. Therefore, to get the correct acceptance for a 20 GeV/c b hadron, one must put in 2.0 into the formula above.

$\chi^2/ndf = 24.46741/33$							
α_0	α_1	α_2	α_3	α_4	α_5	α_6	α_7
0.6654247	-3.639978	7.082303	-6.183229	3.004793	-0.8346769	0.1236831	-0.007573609

Table 7.7: The results of of the fit to the generator level acceptance with loose cuts vs. b hadron p_T for $H_b \to \mu D^{*+} X$ events.

	α_0	α_1	α_2	α_3
α_0	0.31192E-05	-0.58317E-05	0.18103E-05	0.58614E-06
α_1	-0.58317E-05	0.13521E-04	-0.75138E-05	0.58394E-07
α_2	0.18103E-05	-0.75138E-05	0.88947E-05	-0.28693E-05
α_3	0.58614E-06	0.58394E-07	-0.28693E-05	0.25989E-05
α_4	-0.10839E-06	0.36482E-06	-0.88827E-07	-0.48832E-06
α_5	-0.44977E-07	0.61089E-07	0.63698E-07	-0.62038E-07
α_6	-0.35156E-08	-0.27900E-08	0.13431E-07	0.14214E-08
α_7	0.24741E-08	-0.49049E-08	-0.11821E-08	0.38724E-08

	α_4	α_5	α_6	α_7
α_0	-0.10839E-06	-0.44977E-07	-0.35156E-08	0.24741E-08
α_1	0.36482E-06	0.61089E-07	-0.27900E-08	-0.49049E-08
α_2	-0.88827E-07	0.63698E-07	0.13431E-07	-0.11821E-08
α_3	-0.48832E-06	-0.62038E-07	0.14214E-08	0.38724E-08
α_4	0.33280E-06	-0.45310E-07	-0.53459E-08	0.74324E-09
α_5	-0.45310E-07	0.34432E-07	-0.33244E-08	-0.50264E-09
α_6	-0.53459E-08	-0.33244E-08	0.27687E-08	-0.42109E-09
α_7	0.74324E-09	-0.50264E-09	-0.42109E-09	0.12047E-09

Table 7.8: The error matrix of the fit to the generator level acceptance with loose cuts for $H_b \to \mu D^{*+} X$ events.

p_T bin (GeV/c)	$d\sigma/dp_T \times Br$ (pb/(GeV/c))	stat. err (pb/(GeV/c))	syst. err (pb/(GeV/c))
9-11	228	63	$^{+32}_{-35}$
11-13	122	17	$^{+15}_{-17}$
13-17	56.0	4.5	$^{+6.3}_{-7.1}$
17-23	15.3	1.2	$^{+1.7}_{-1.8}$
23-29	3.83	0.45	$^{+0.39}_{-0.40}$
29-40	0.961	0.154	$^{+0.111}_{-0.110}$

Table 7.9: Differential cross section $d\sigma(p\overline{p} \to B)/dp_T$ times branching fraction $H_b \to \mu D^{*+} X$, $D^{*+} \to D^0 \pi$, $D^0 \to K\pi$.

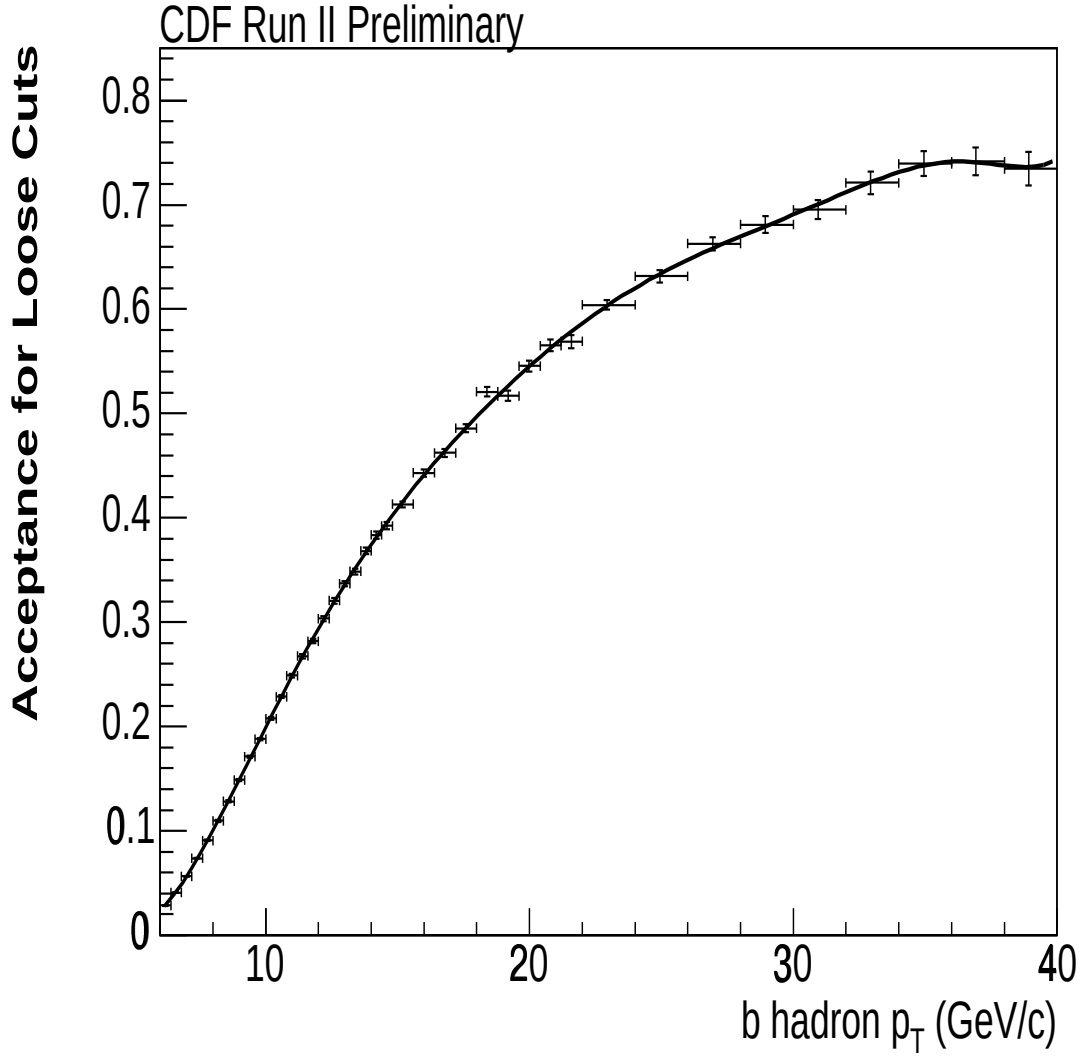

Figure 7.1: The generator level acceptance for the loose cuts on MC made with the CDF b spectrum versus b hadron p_T.

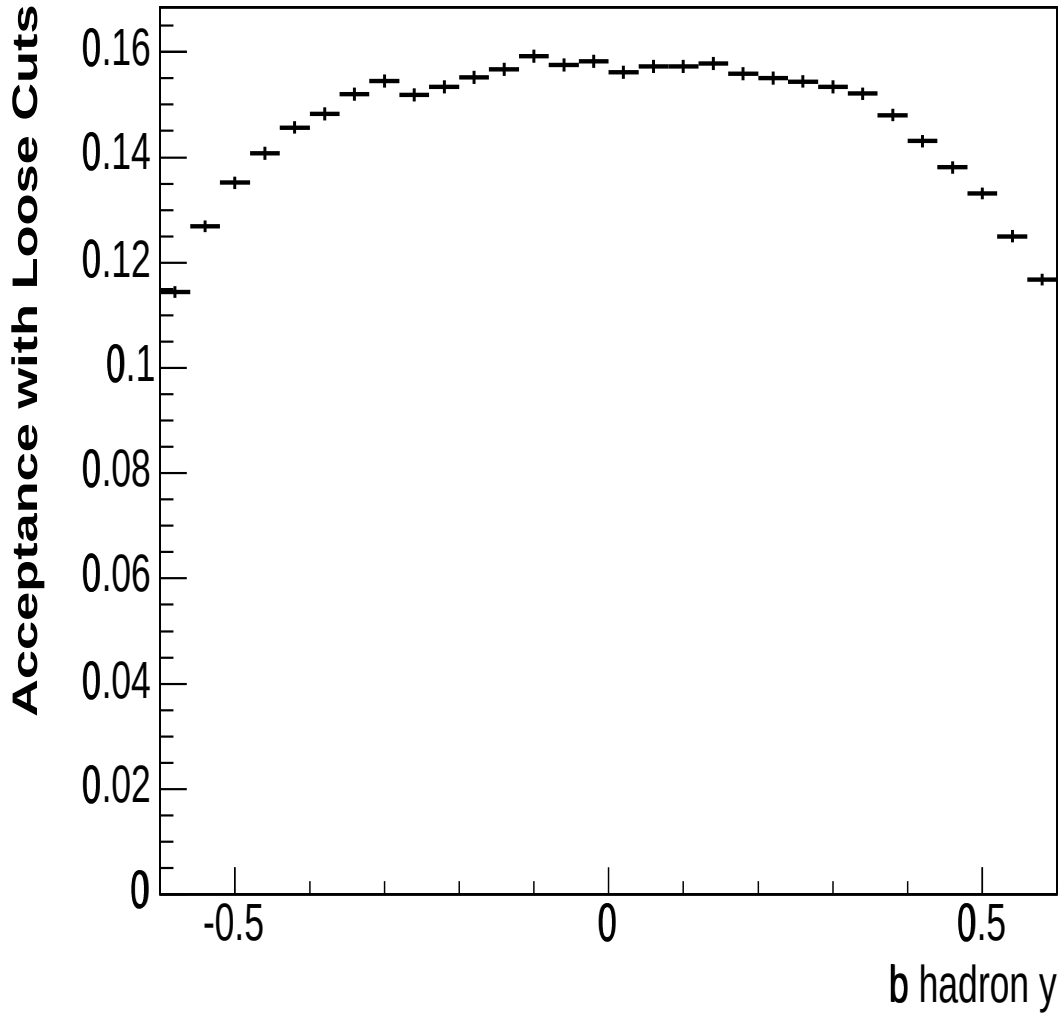

Figure 7.2: The generator level acceptance for the loose cuts on MC made with the CDF b spectrum versus b hadron rapidity.

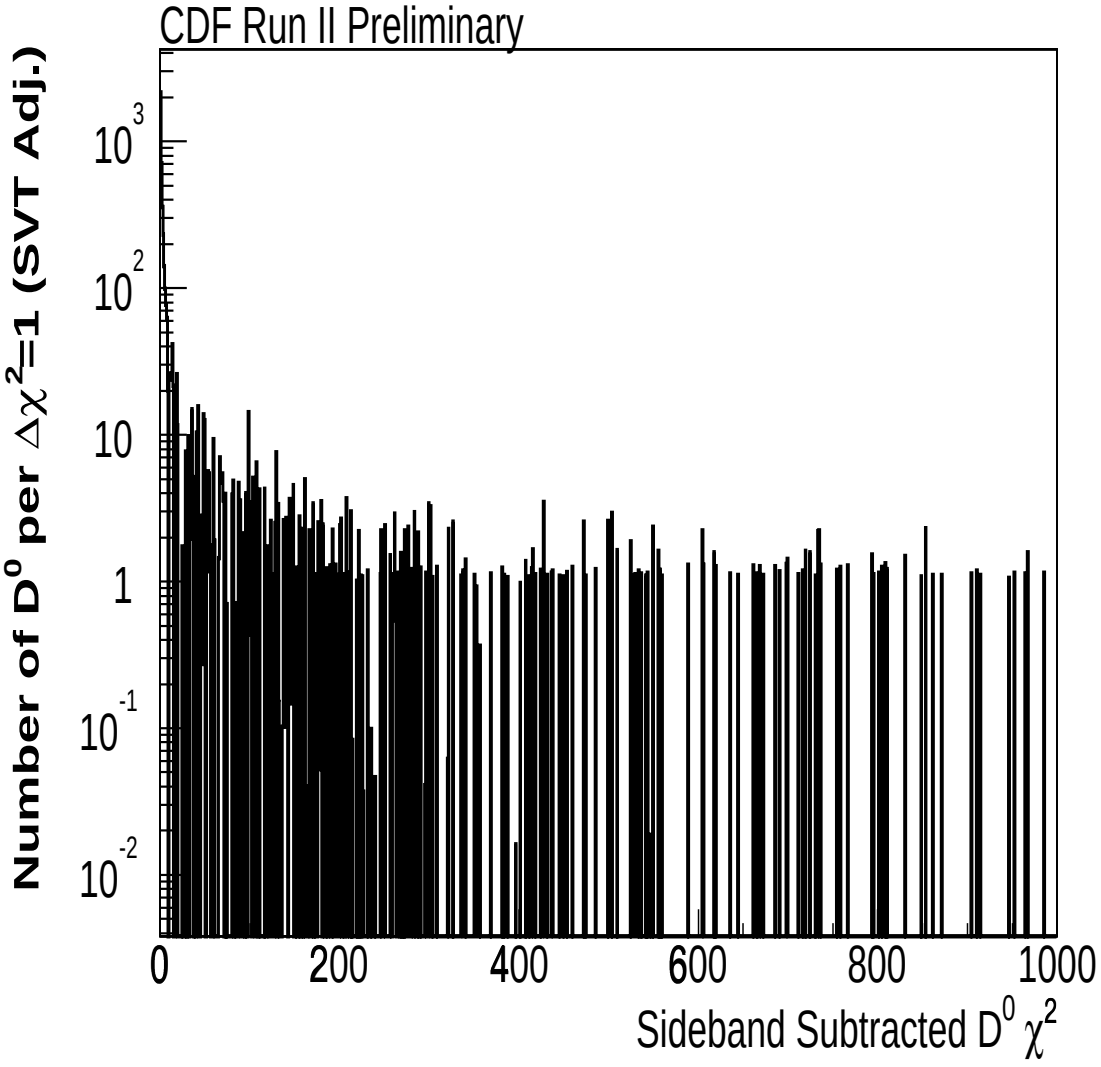

Figure 7.3: The χ^2 of the vertex fits of the π K, with sideband subtraction. This indicates that the $\chi^2 < 1000$ cut is not throwing away a significant number of events.

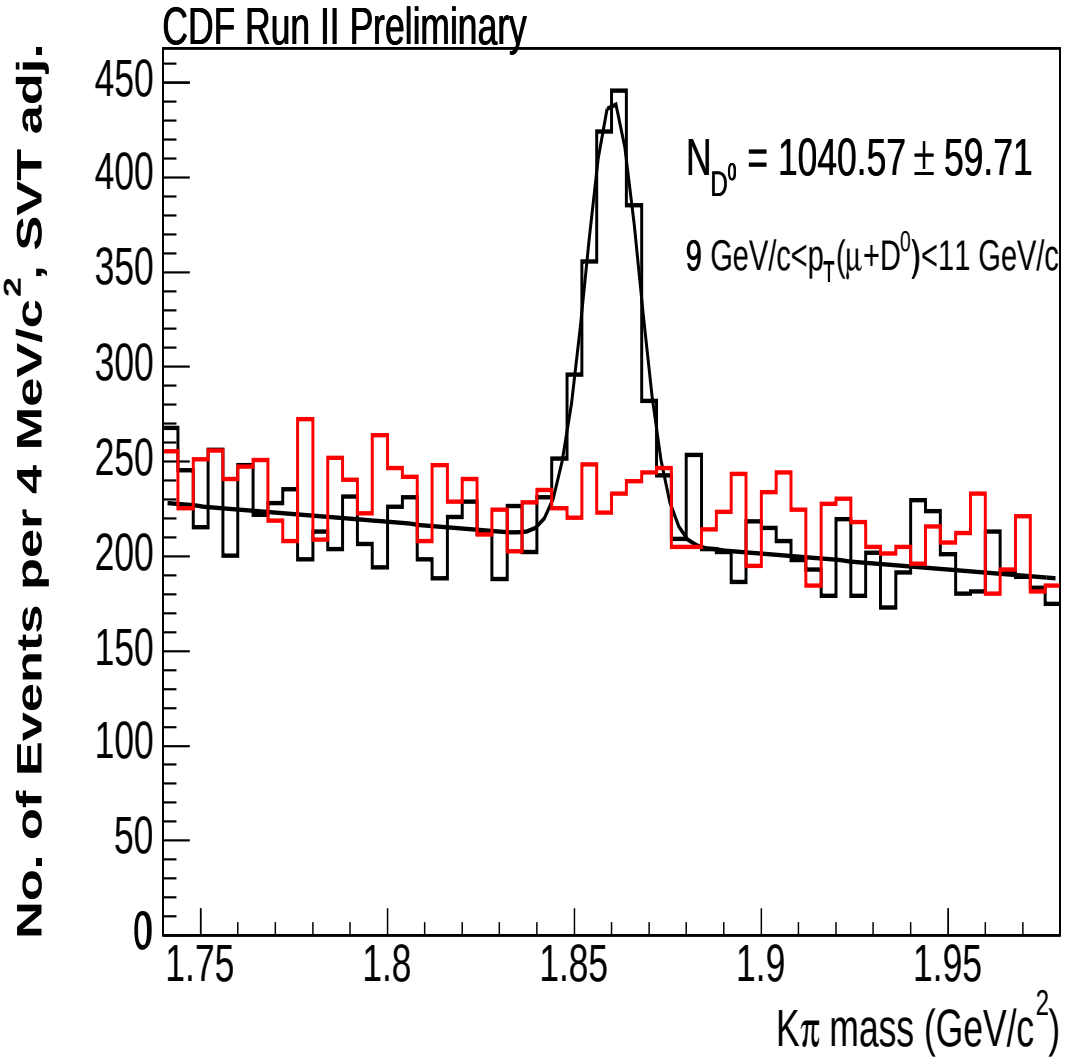

Figure 7.4: The π^+K^- mass, for events with 9 GeV/c < $p_T(\mu^-K^-\pi^+)$ < 11 GeV/c. The black and red plots are for $q_\pi \neq q_\mu$ and $q_\pi = q_\mu$, respectively. The mass was fit using a Gaussian plus linear background. The events have been weighted to take into account the SVT efficiency.

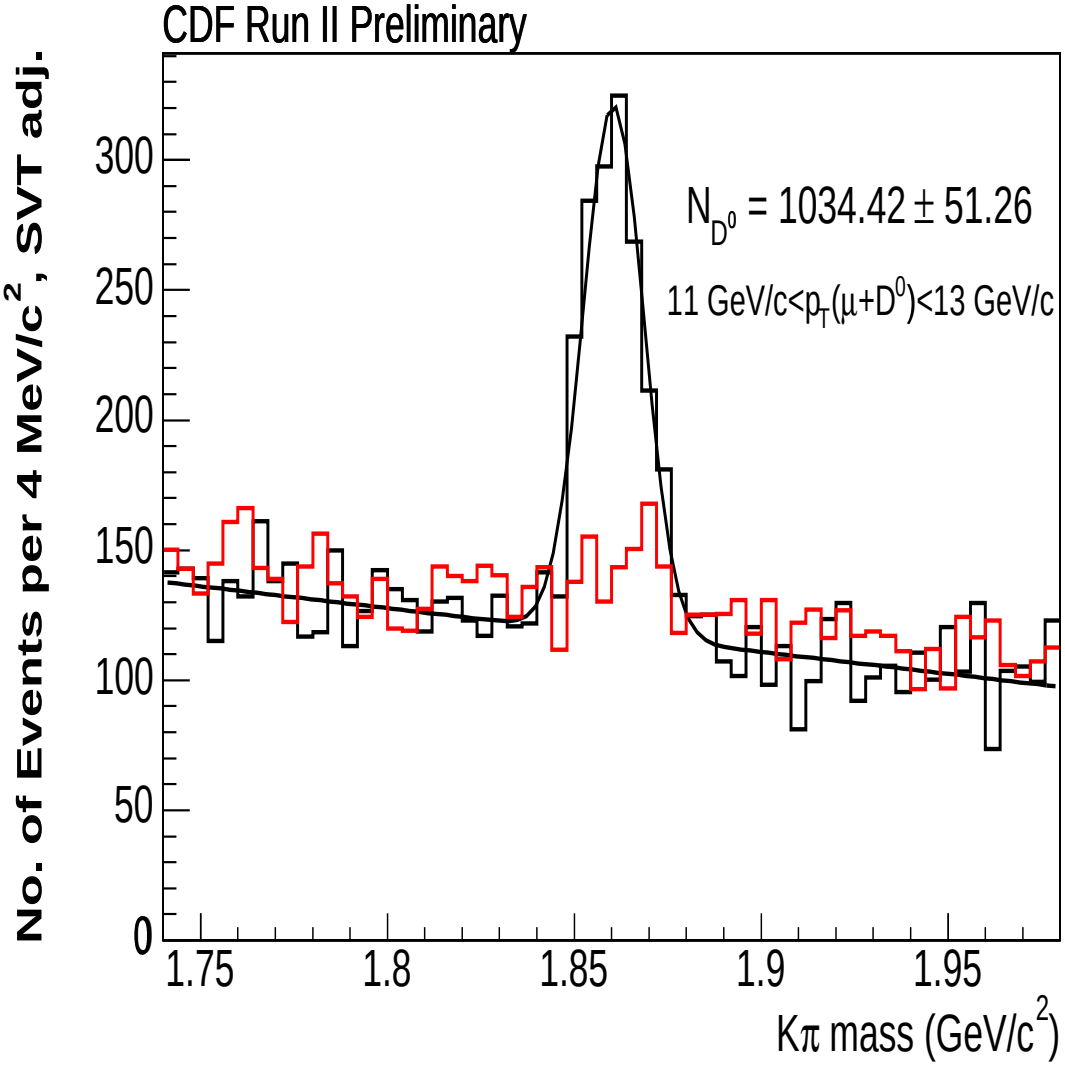

Figure 7.5: The π^+K^- mass, for events with 11 GeV/c < $p_T(\mu^-K^-\pi^+)$ < 13 GeV/c. The black and red plots are for $q_\pi \neq q_\mu$ and $q_\pi = q_\mu$, respectively. The mass was fit using a Gaussian plus linear background. The events have been weighted to take into account the SVT efficiency.

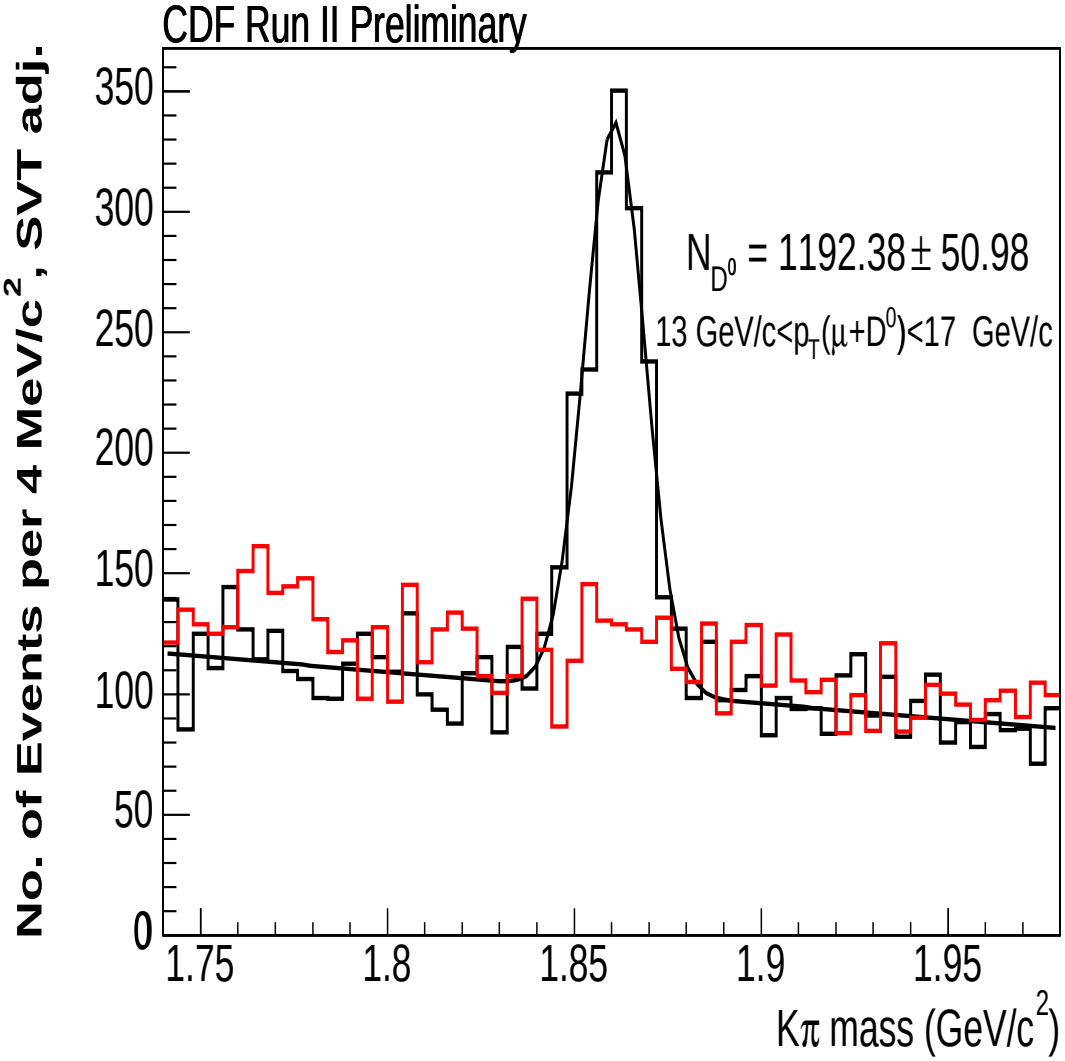

Figure 7.6: The π^+K^- mass, for events with 13 GeV/c < $p_T(\mu^-K^-\pi^+)$ < 17 GeV/c. The black and red plots are for $q_\pi \neq q_\mu$ and $q_\pi = q_\mu$, respectively. The mass was fit using a Gaussian plus linear background. The events have been weighted to take into account the SVT efficiency.

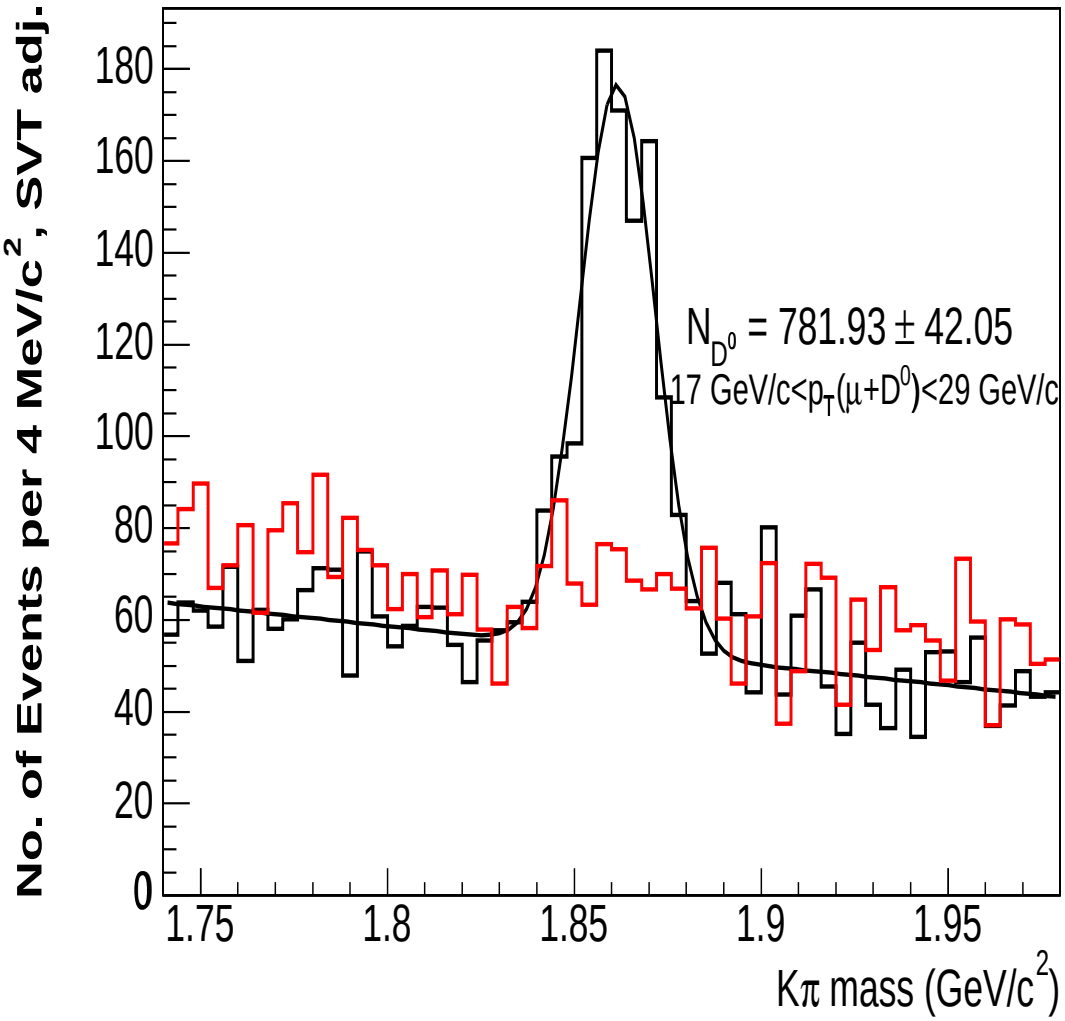

Figure 7.7: The π^+K^- mass, for events with 17 GeV/c < $p_T(\mu^-K^-\pi^+)$ < 29 GeV/c. The black and red plots are for $q_\pi \neq q_\mu$ and $q_\pi = q_\mu$, respectively. The mass was fit using a Gaussian plus linear background. The events have been weighted to take into account the SVT efficiency.

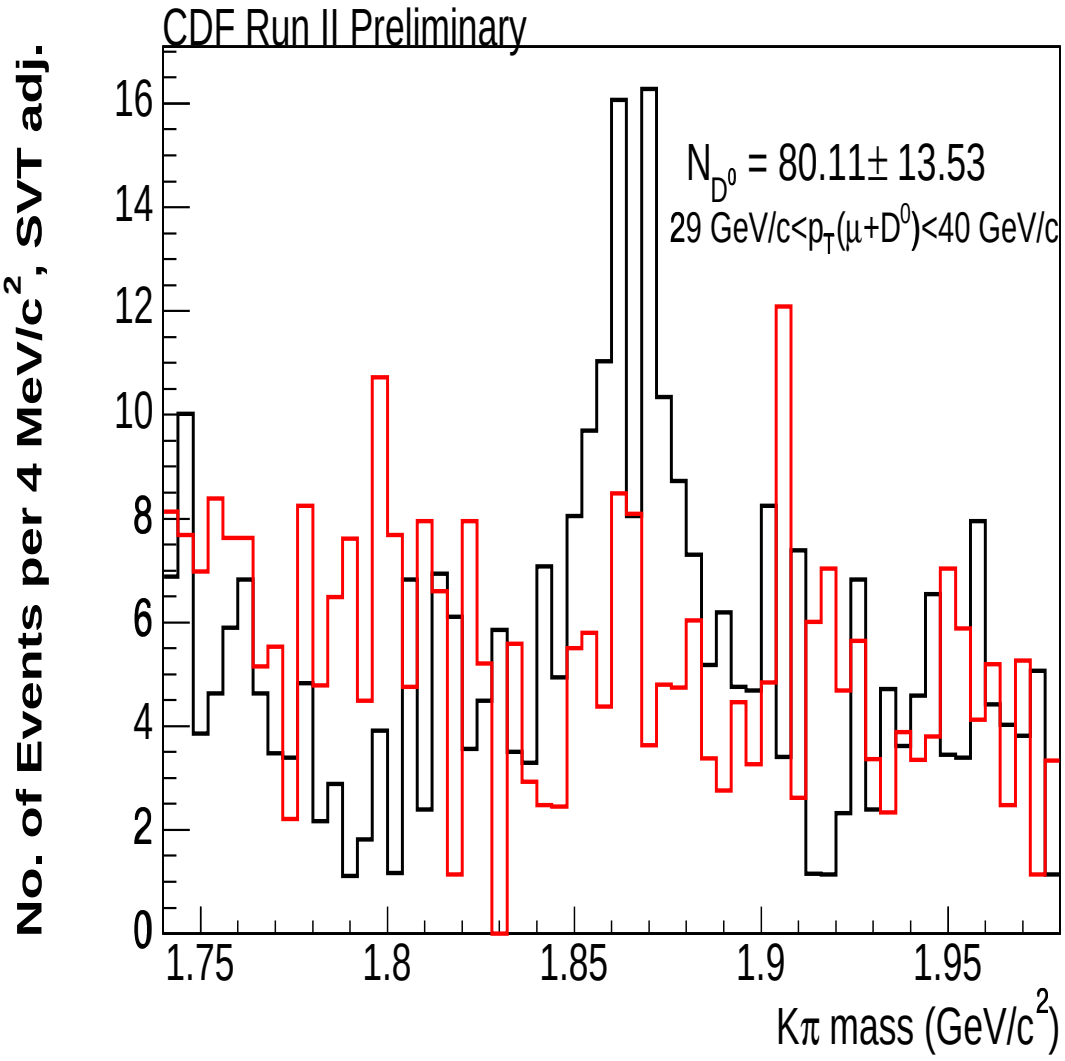

Figure 7.8: The π^+K^- mass, for events with 29 GeV/c < $p_T(\mu^-K^-\pi^+)$ < 40 GeV/c. The black and red plots are for $q_\pi \neq q_\mu$ and $q_\pi = q_\mu$, respectively. Because there were relatively few events, the number of events was found by sideband subtraction rather than a Gaussian fit. The signal range was 3σ about the mean of the Gaussian from the 17 GeV/c < p_T < 29 GeV/c bin fit, and the sideband range was 5 to 8 σ on either side of the peak. The events have been weighted to take into account the SVT efficiency.

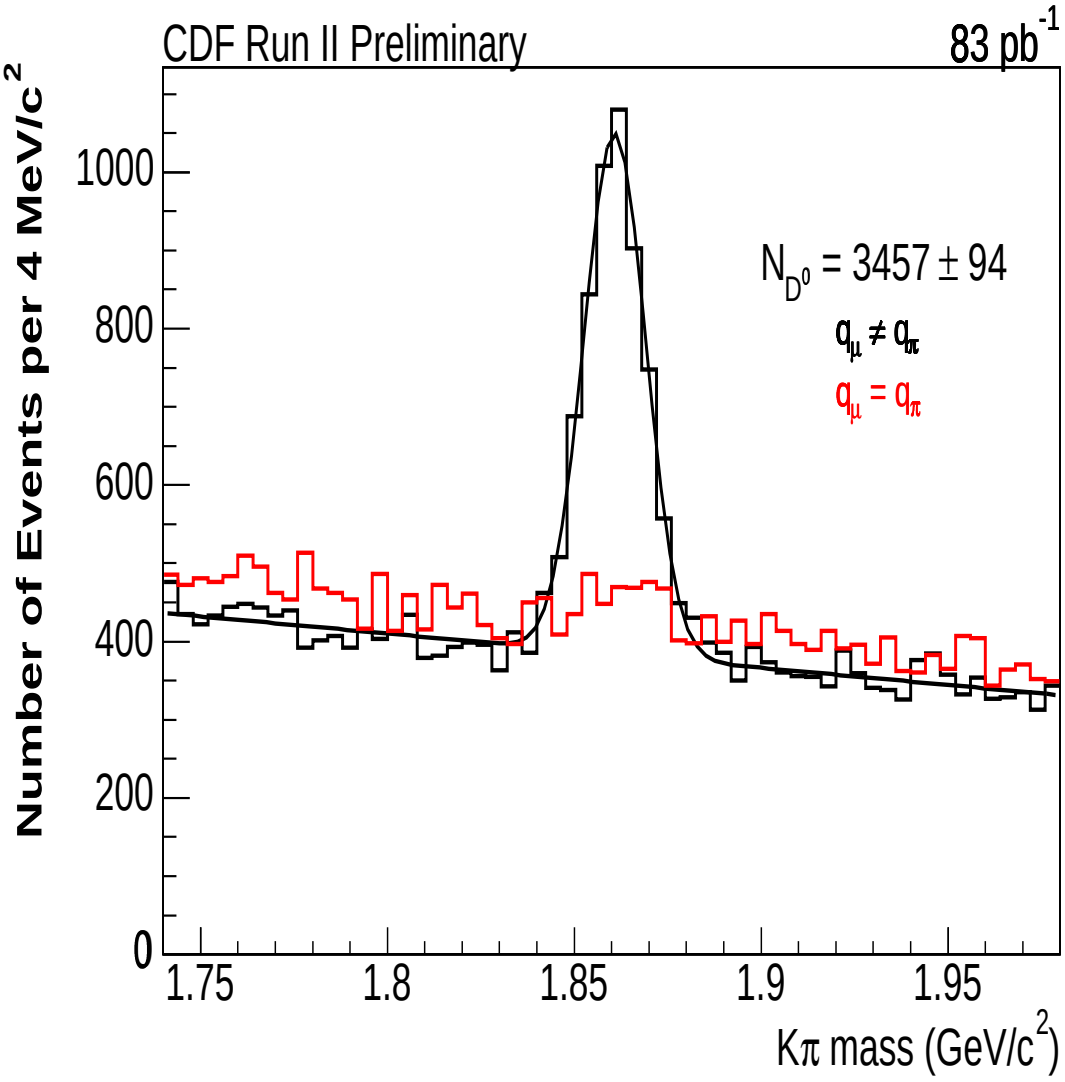

Figure 7.9: The π^+K^- mass, for events with $p_T(\mu^- K^- \pi^+) > 9.0$ GeV/c. The black and red plots are for $q_\pi \neq q_\mu$ and $q_\pi = q_\mu$, respectively. The mass was fit using a Gaussian plus linear background. There is no adjustment for the SVT efficiency.

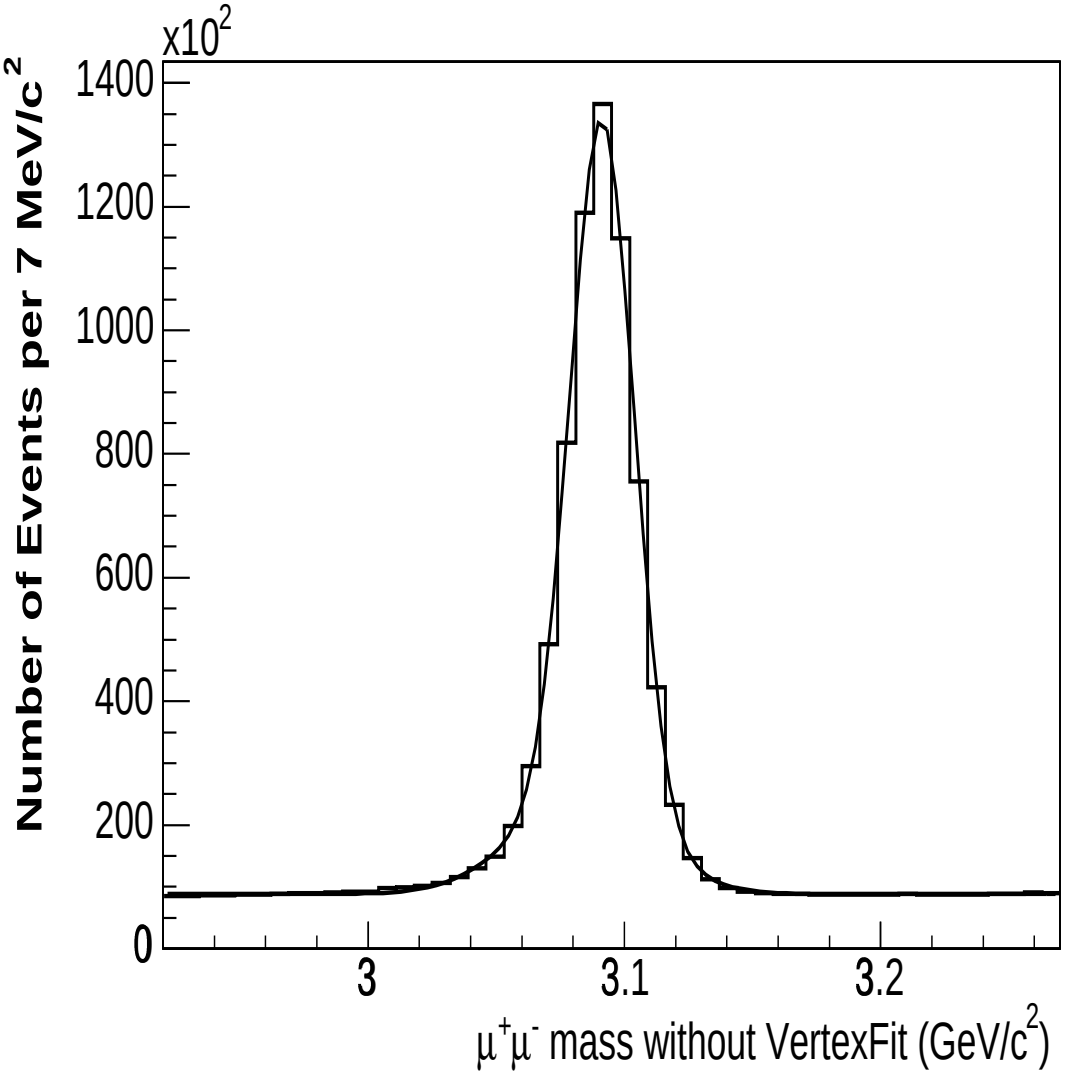

Figure 7.10: The dimuon mass distribution without vertex fitting, fit to the sum of two Gaussians plus a linear background. There are 624723 ± 5577 J/ψ events beneath the two Gaussians.

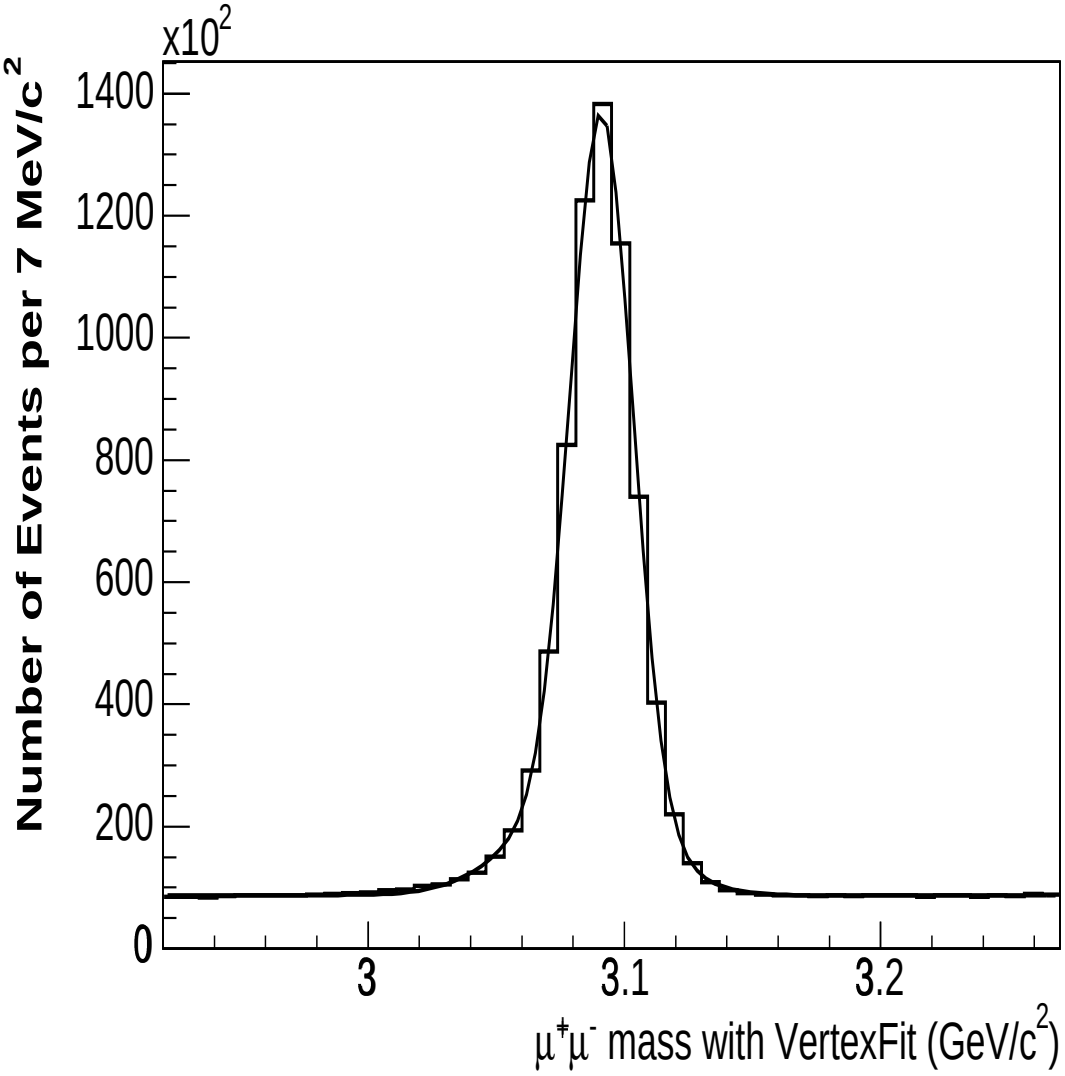

Figure 7.11: The dimuon mass distribution with vertex fitting, fit to the sum of two Gaussians plus a linear background. There are 623774 ± 5526 J/ψ events beneath the two Gaussians.

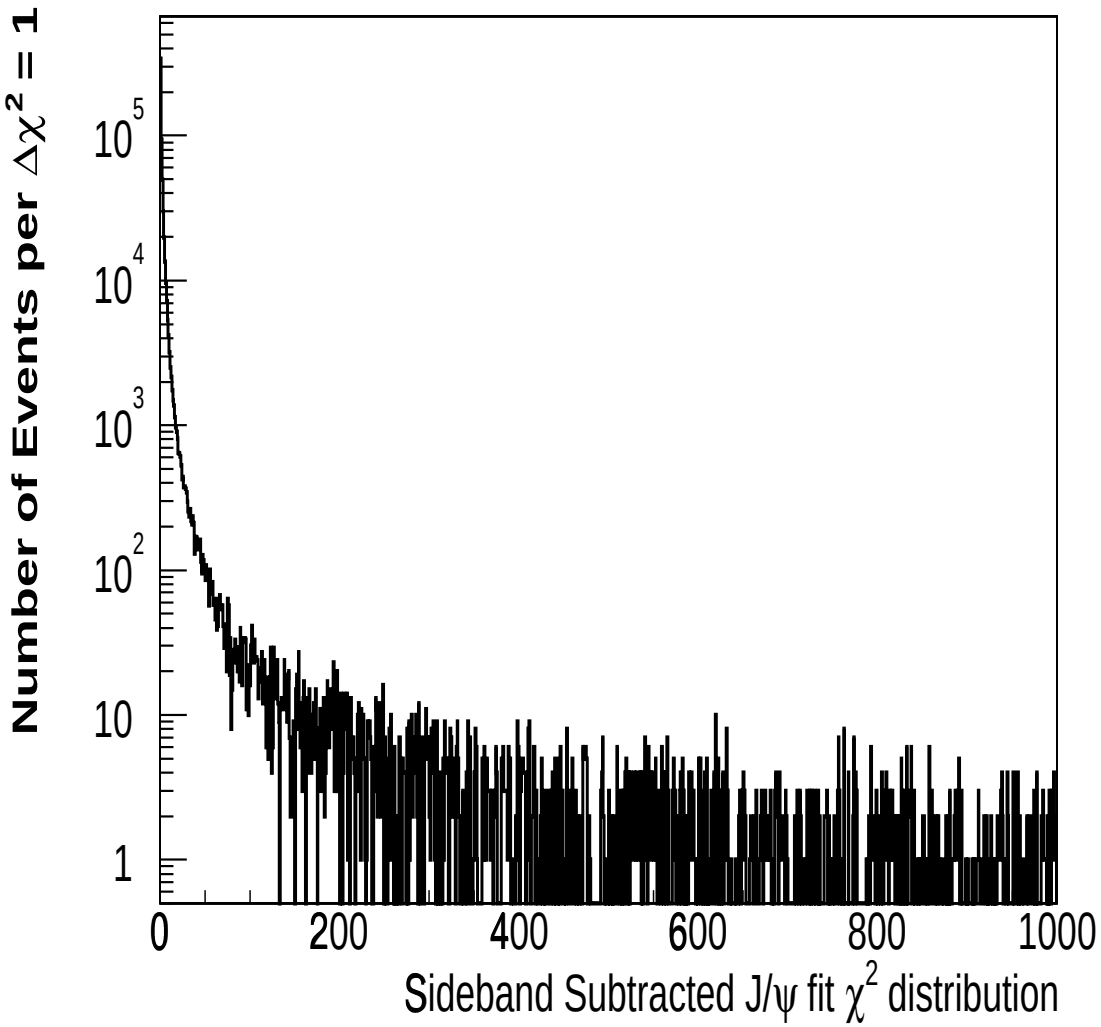

Figure 7.12: The sideband subtracted vertex fit χ^2 for J/ψ events.

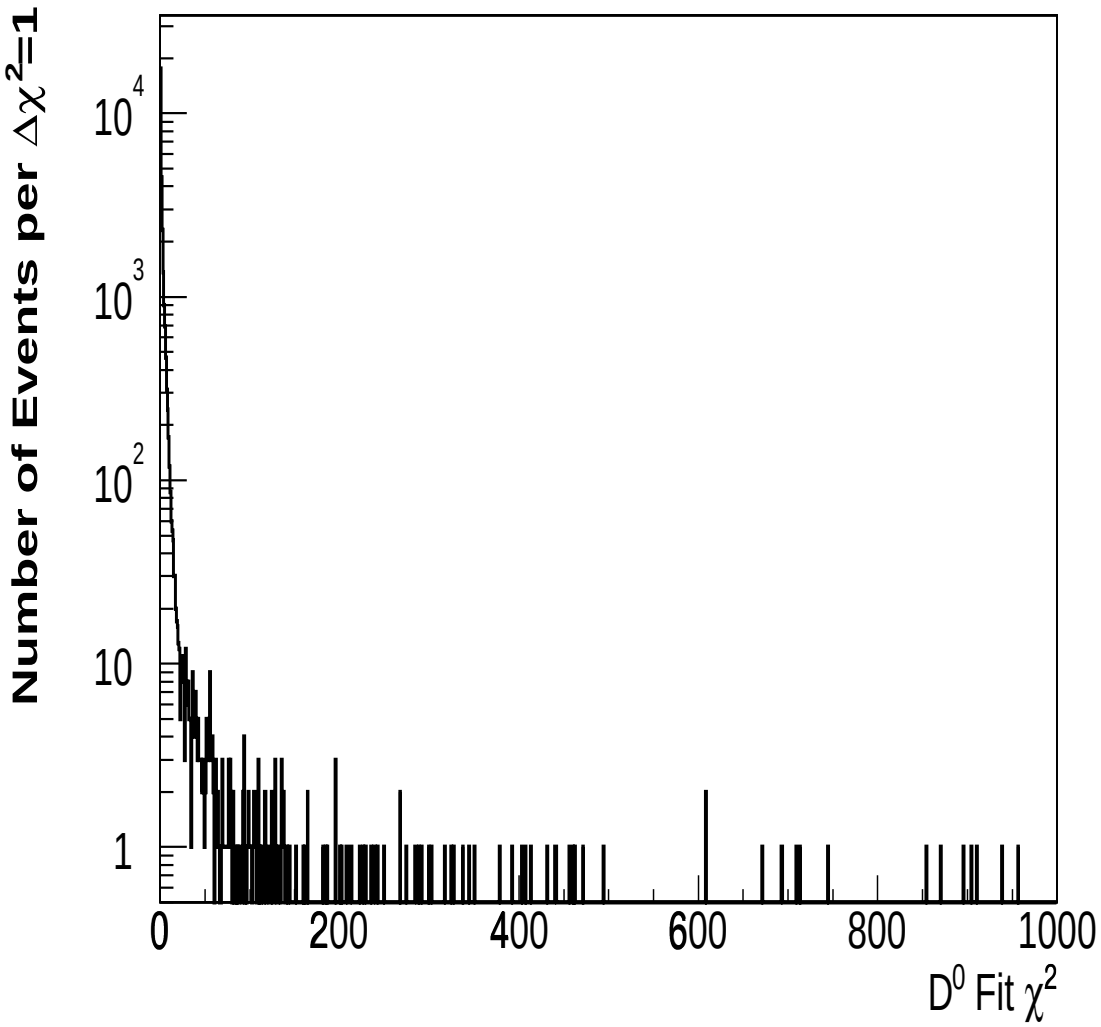

Figure 7.13: The vertex fit χ^2 for the MC $D^0 \to K^-\pi^+$ events.

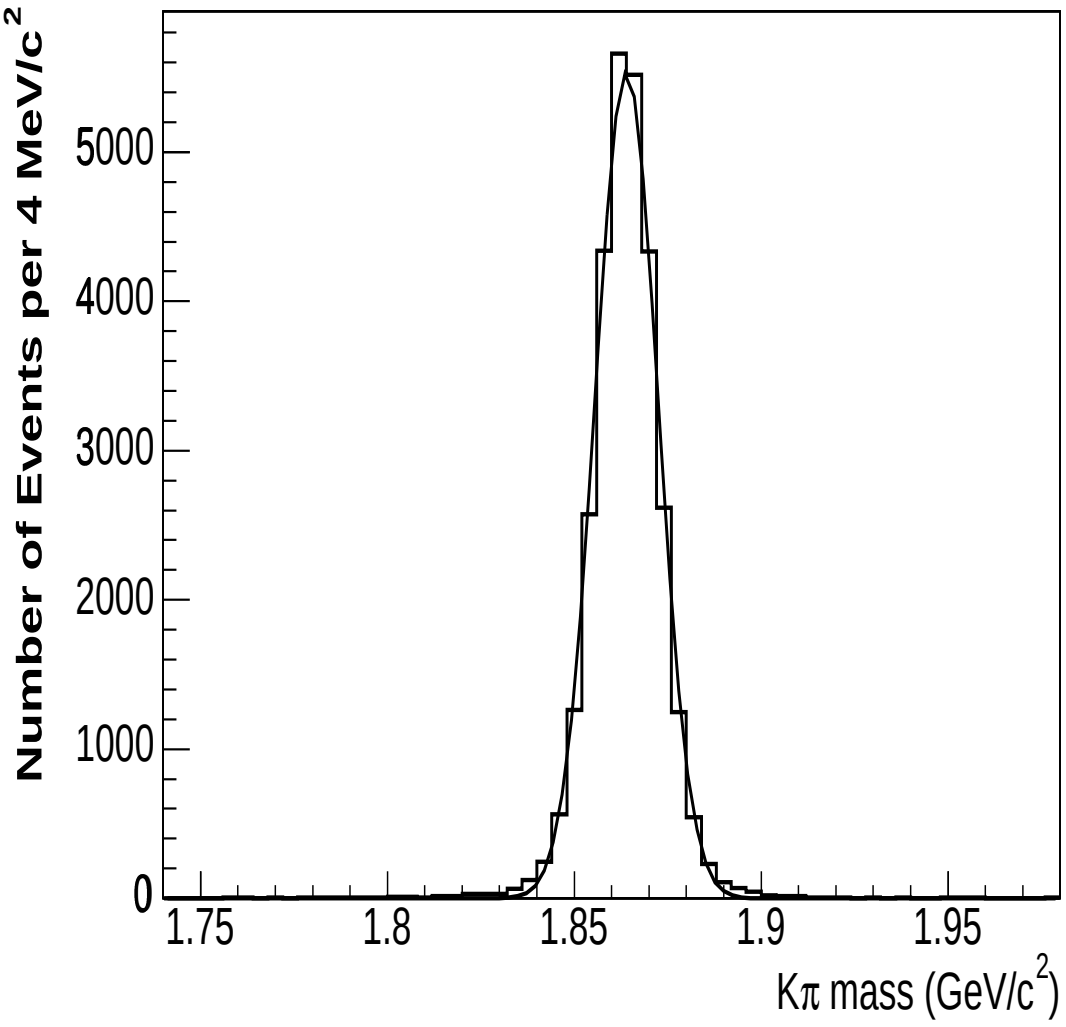

Figure 7.14: The reconstructed D^0 mass from MC b events. There are 29207 $\pm$ 171 events beneath the mass peak.

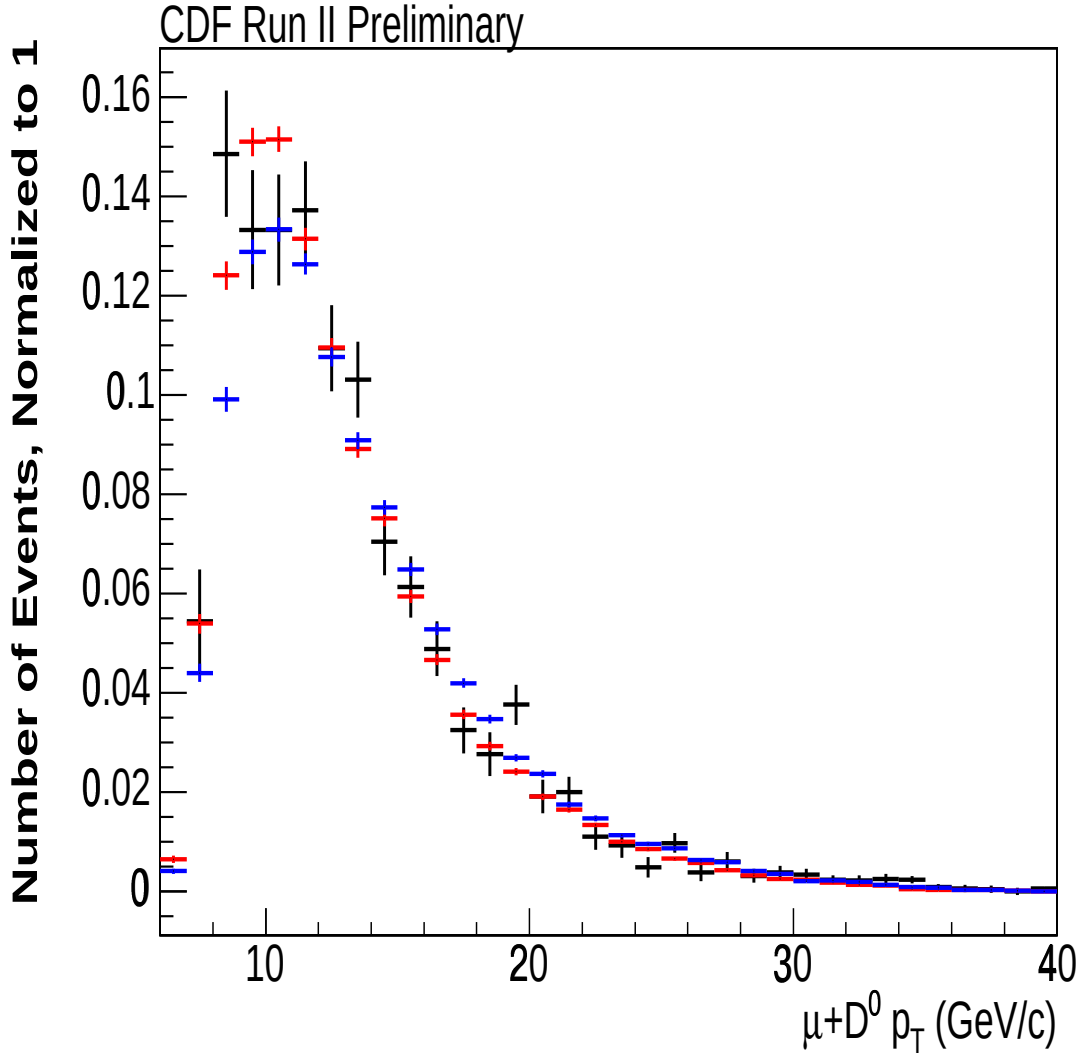

Figure 7.15: A comparison of the two MC samples to data, plotted vs. the p_T of the $\mu + D^0$. The data points are in black, the CDF MC is in red, and the MRSD0 MC is in blue. The spectrum from the CDF sample is slightly softer than the data. The MRSD0 MC is closer, but somewhat harder than the data.

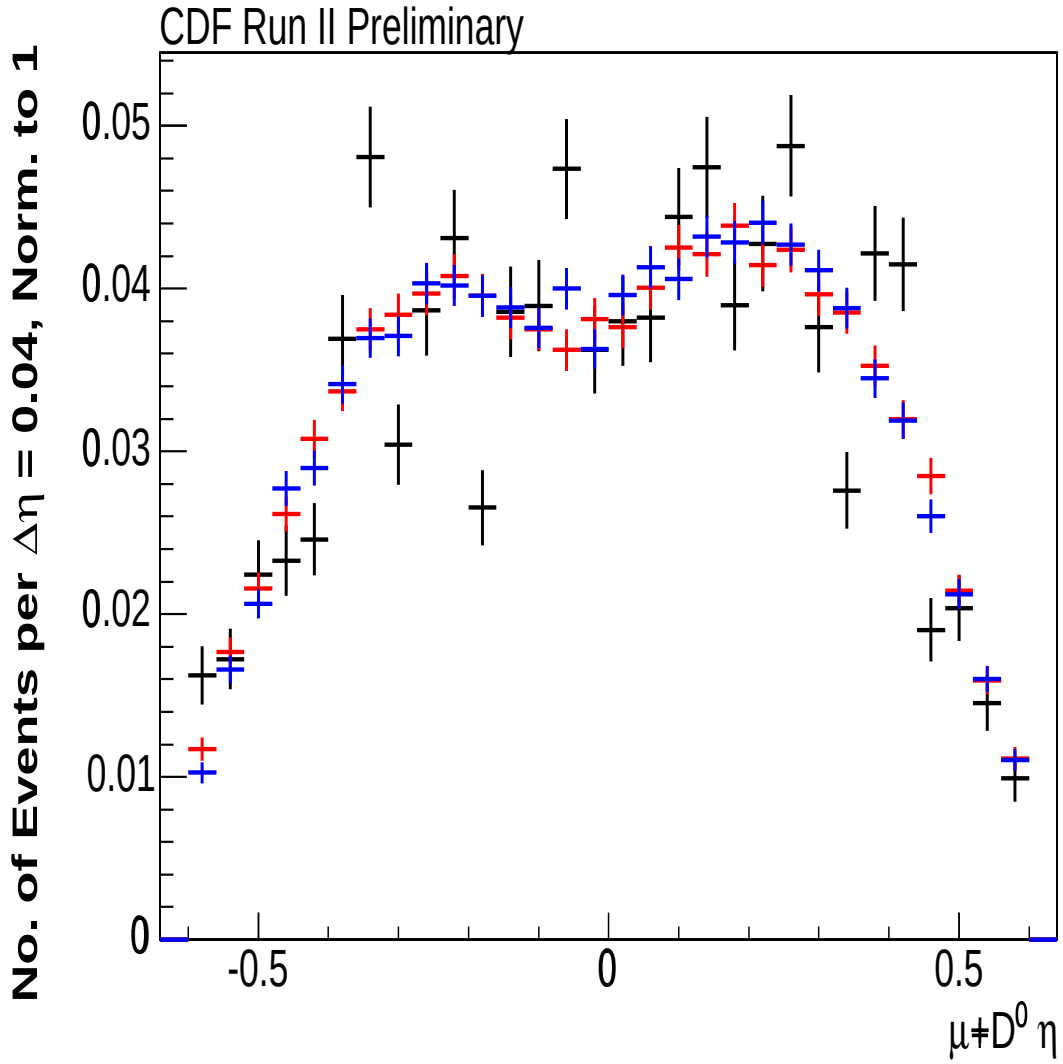

Figure 7.16: A comparison of the two MC samples to data, plotted vs. η. The data points are in black, the MC using the spectrum from the $b \to J/\psi$ cross section is in red, and the MRSD0 MC is in blue.

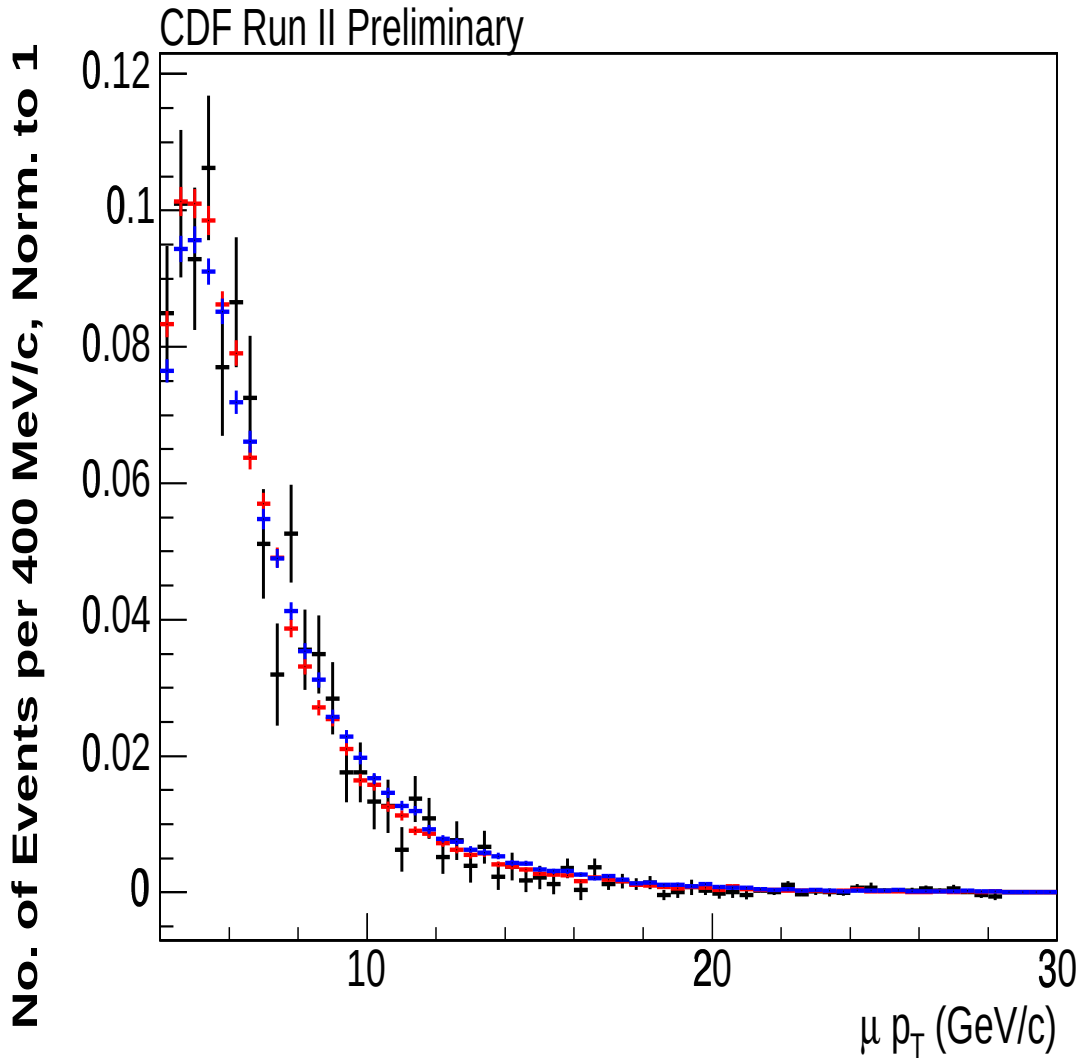

Figure 7.17: A comparison of the two MC samples to data, plotted vs. the p_T of the μ. The data points are in black, the CDF MC is in red, and the MRSD0 MC is in blue.

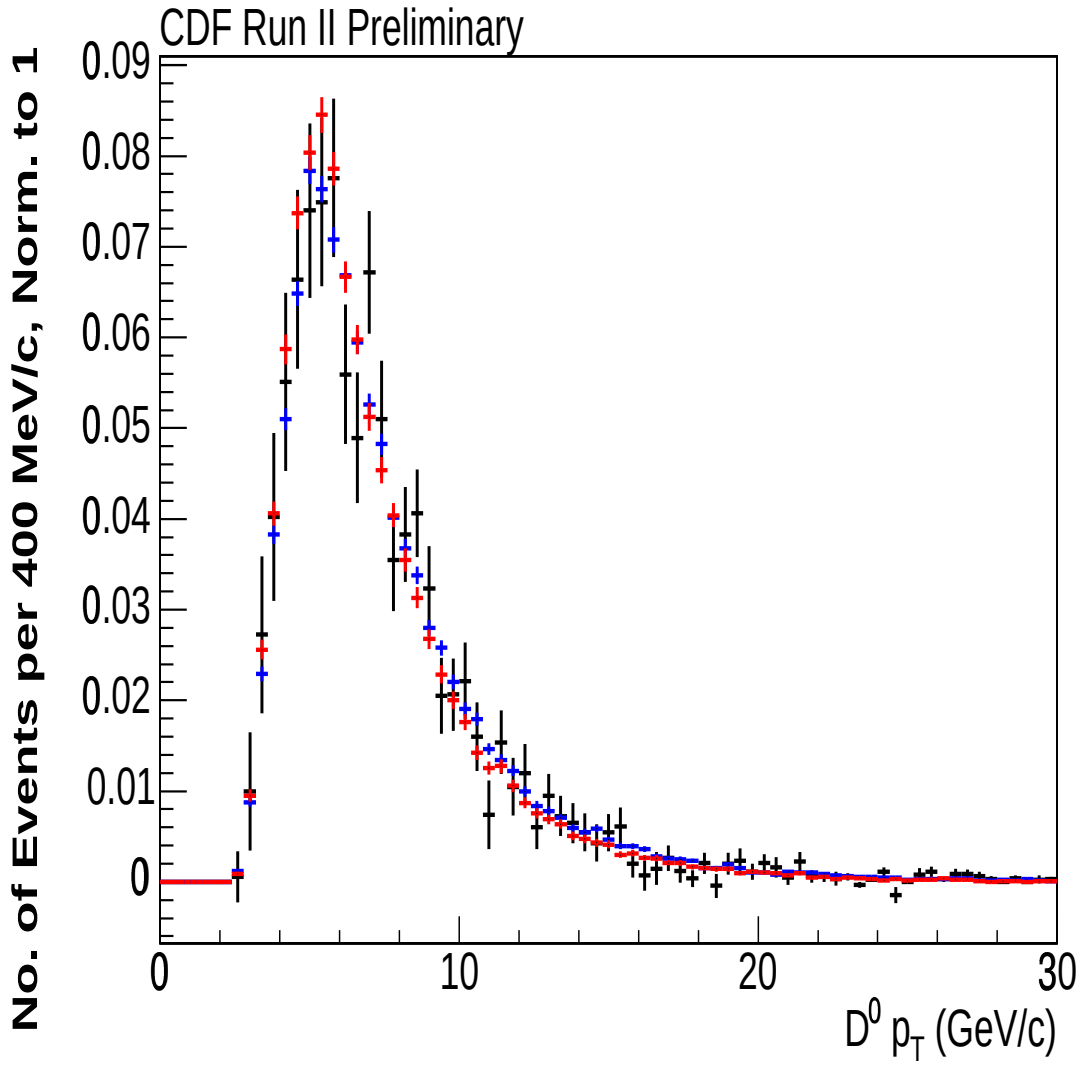

Figure 7.18: A comparison of the two MC samples to data, plotted vs. the p_T of the D^0. The data points are in black, the CDF MC is in red, and the MRSD0 MC is in blue.

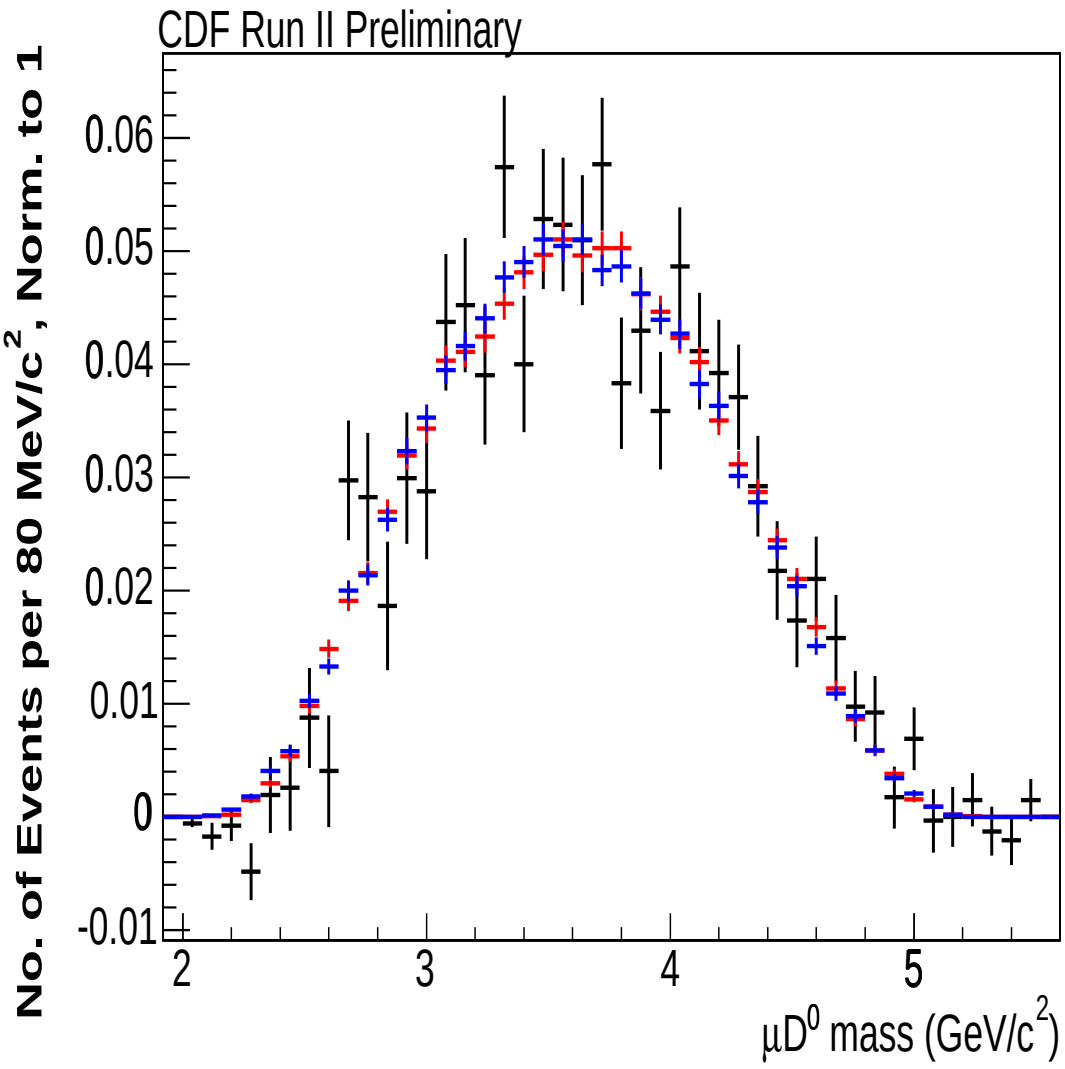

Figure 7.19: A comparison of invariant mass distributions of the μD^0 from data and the two MC samples. The data points are in black, the CDF MC is in red, and the MRSD0 MC is in blue.

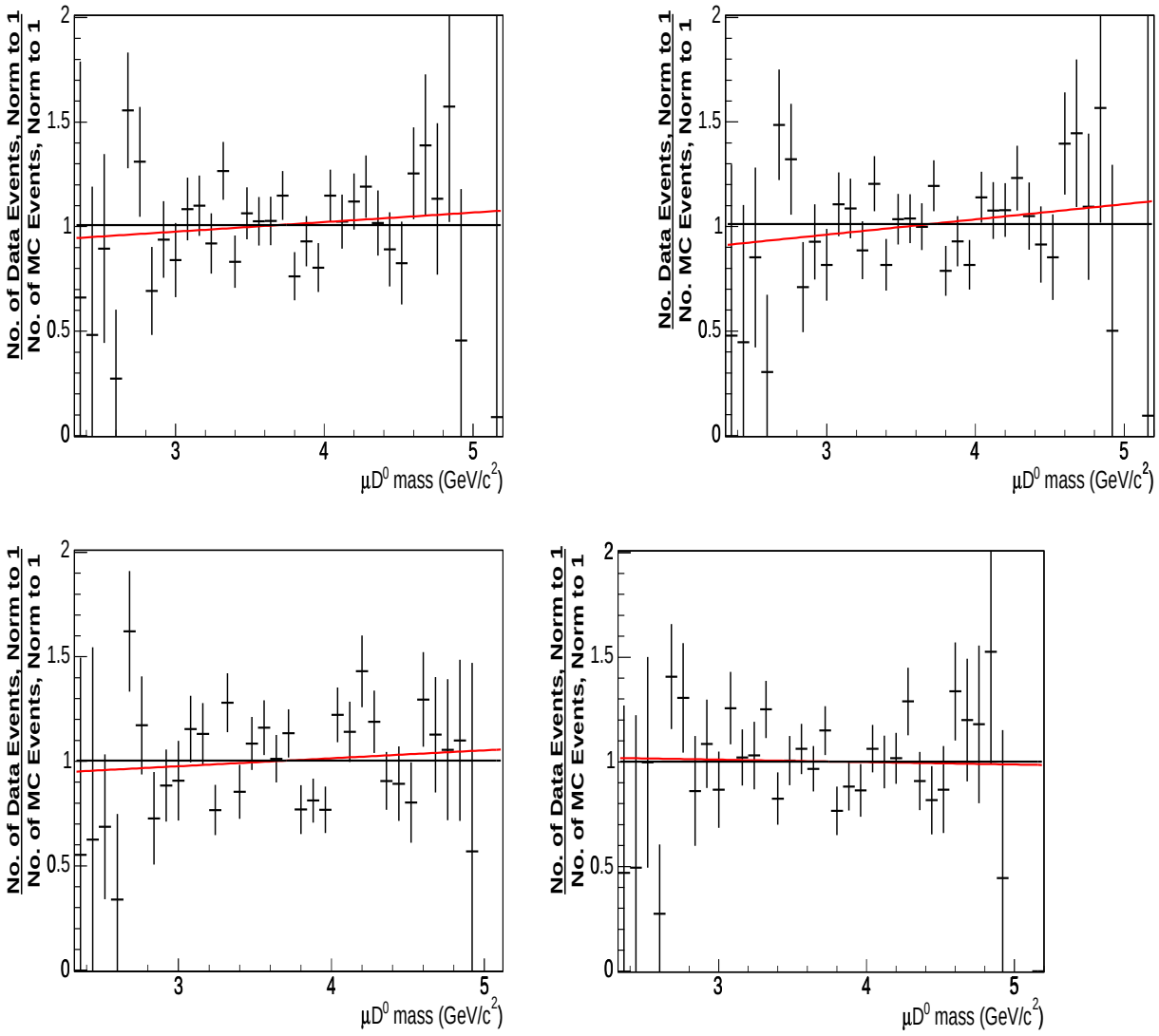

Figure 7.20: Ratio of the number of events per μD^0 mass bin of data to Monte Carlo. The plots on the left use the CDF phenomenological MC distribution, and the plots on the right use the MRSD0 distribution. Top plots use PHOTOS in the B decays, and bottom plots do not. The black lines show the fit of the points to a flat line, and red show the fit to a linear slope. Error bars show statistical errors only.

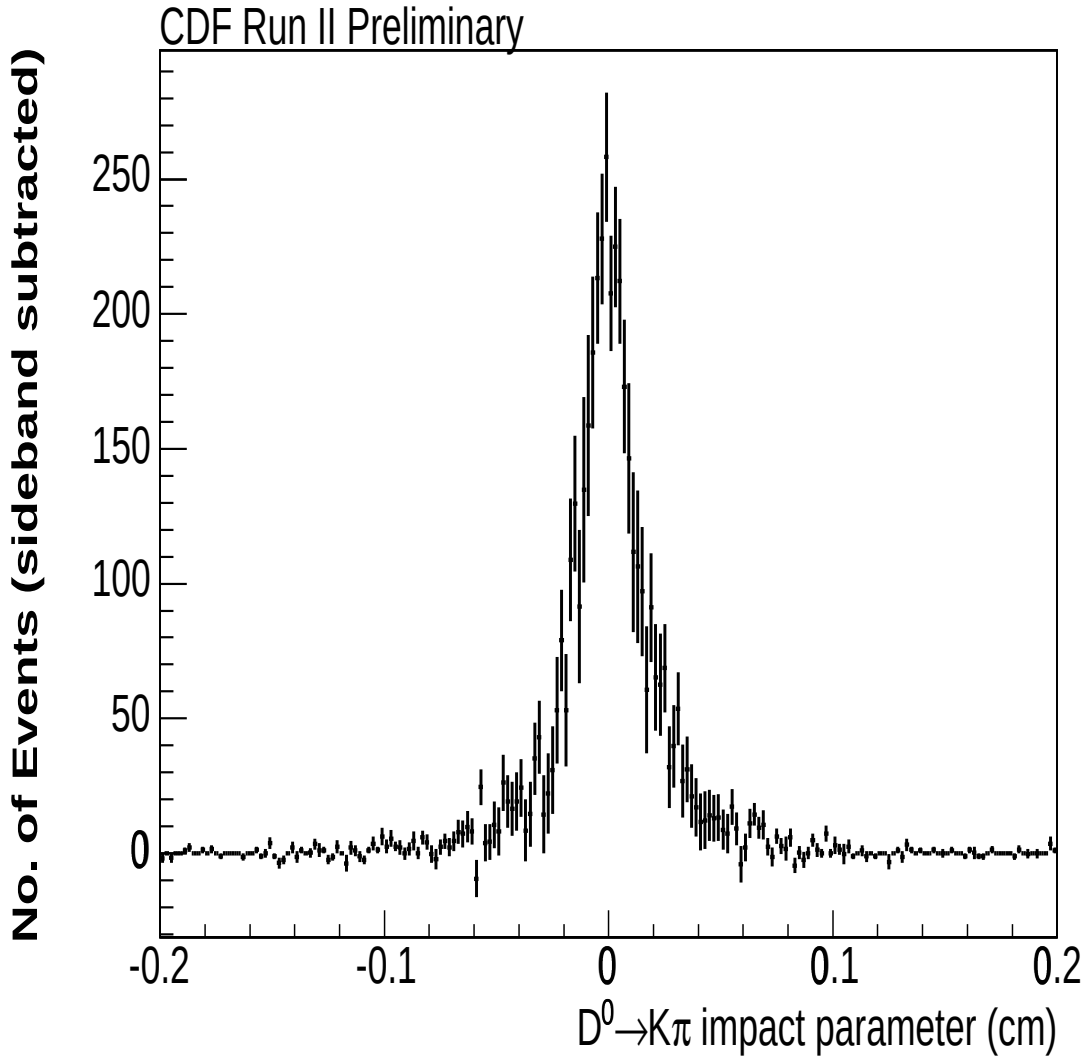

Figure 7.21: The D^0 impact parameter distribution for the data, after sideband subtraction

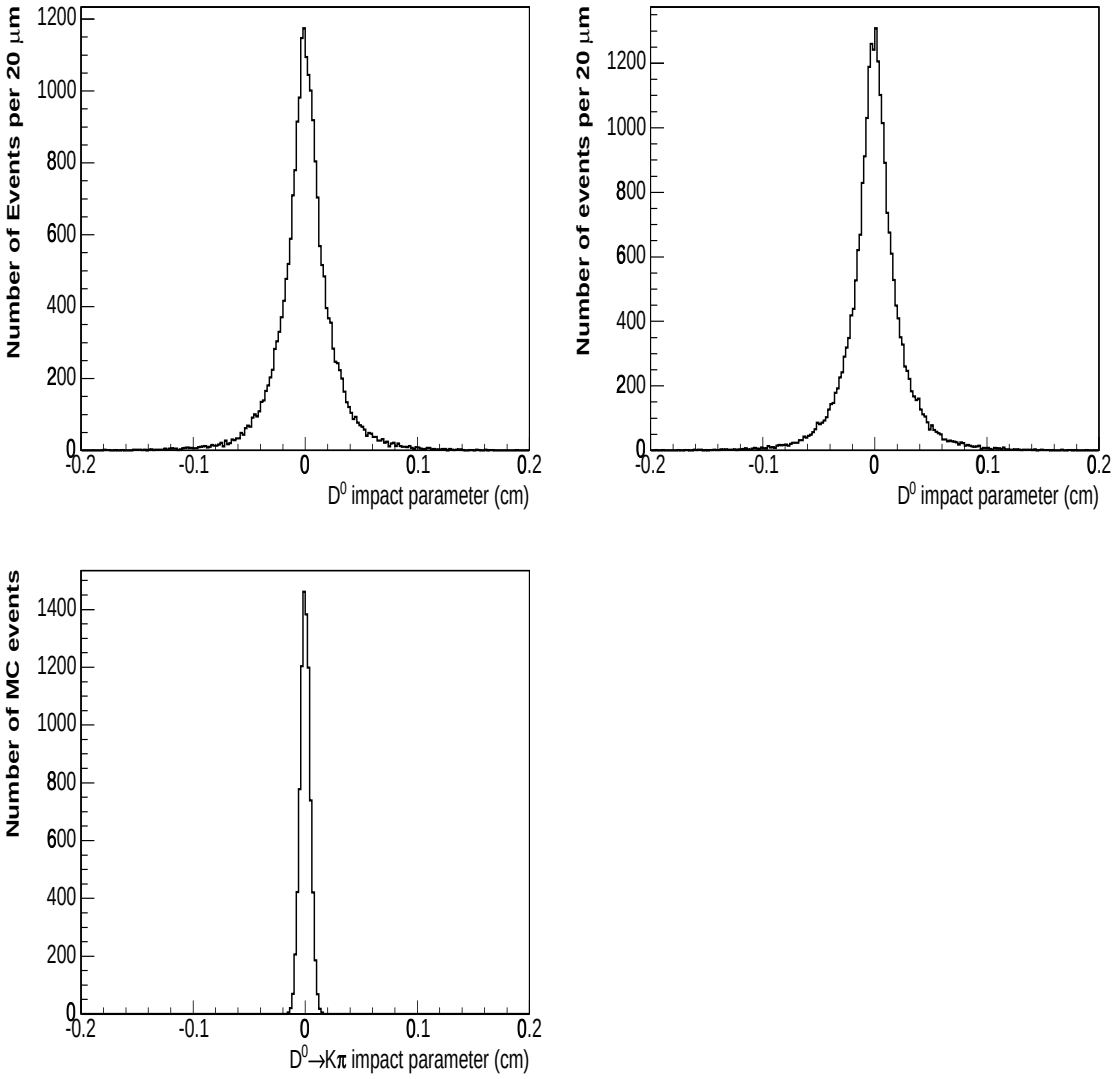

Figure 7.22: The D^0 impact parameter distribution for the MC generated with the $b \to J/\psi$ spectrum (top left), the MRSD0 spectrum (top right), and direct charm MC (bottom)

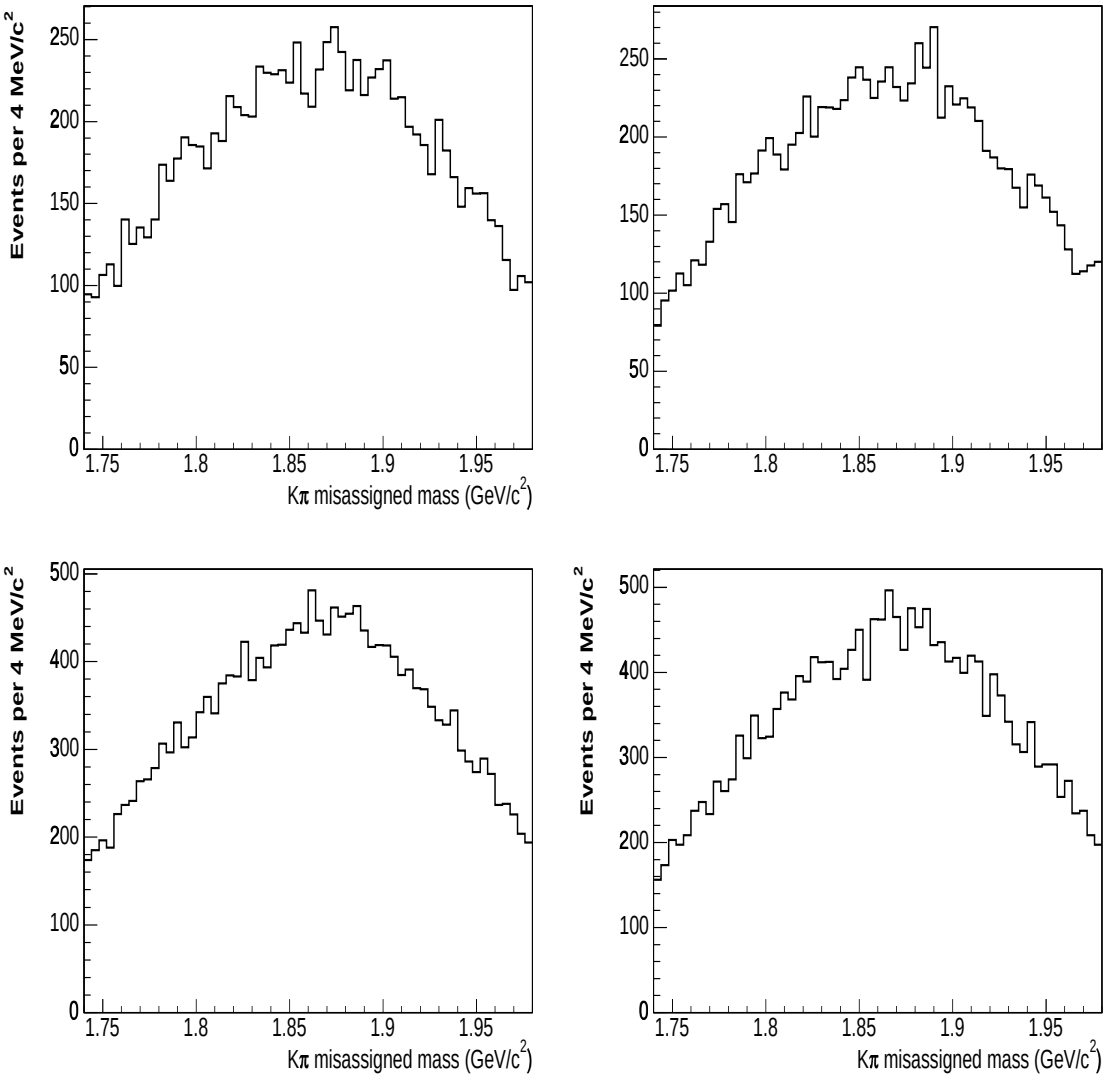

Figure 7.23: The invariant mass of $D^0 \to K\pi$ from MC with the K and π masses swapped. Top plots show the mass from the CDF sample, and the bottom plots are from the MRSD0 sample. The plots on the left use the COT track properties to get the invariant mass, and those on the right use the direct MC track properties.

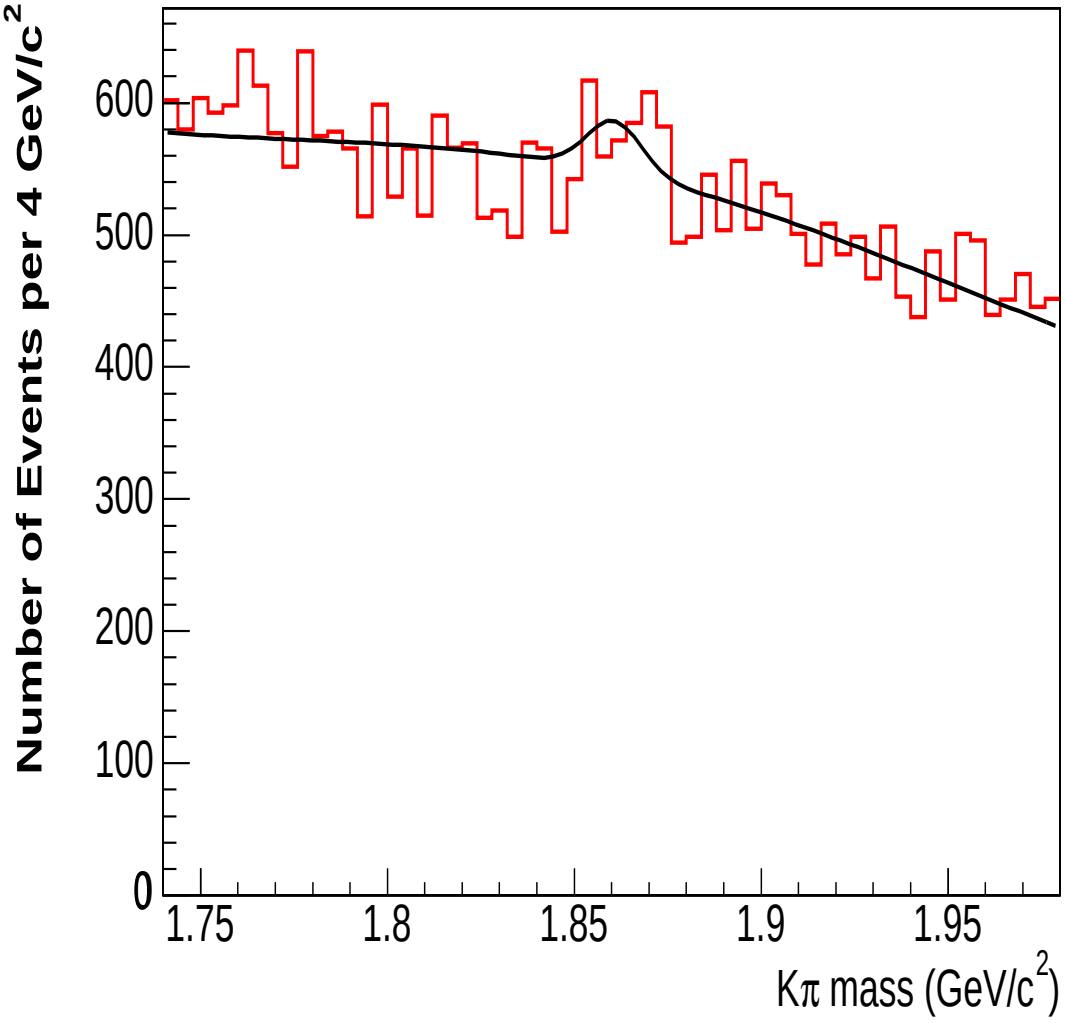

Figure 7.24: The fit of a Gaussian to the wrong sign D^0 mass, with a linear background plus the auto-reflection of the right sign D^0 peak constrained to be a Gaussian with the mean and σ set by MC and the number taken from the reconstructed right sign peak.

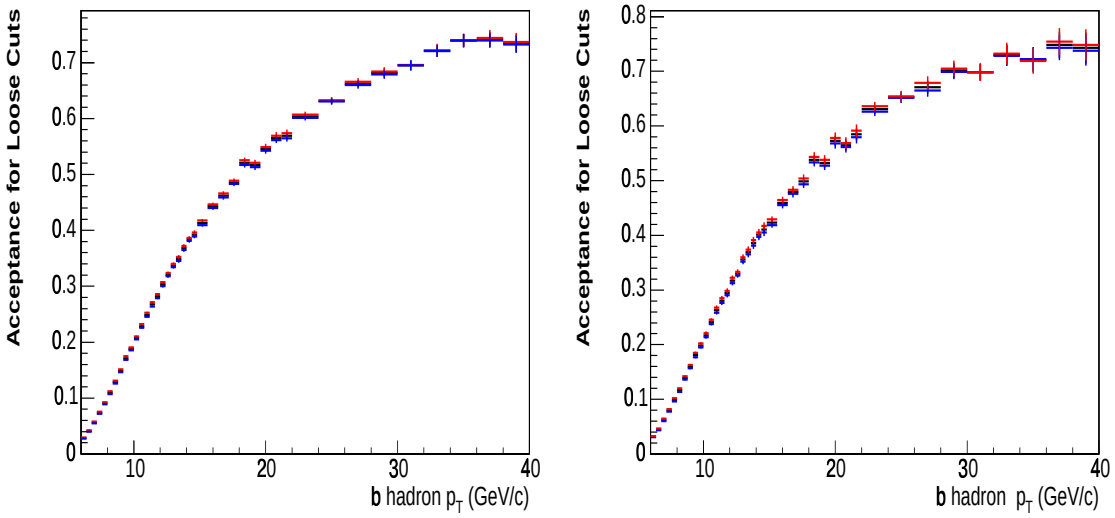

Figure 7.25: The generator level acceptance for the loose cuts on MC made with the CDF and MRSD0 b spectra versus b hadron p_T for events with a D^0(left) and a D^{*+} (right). The blue points have 50% more $B \to \mu D^{**}$ events, that red point have 50% fewer $B \to \mu D^{**}$ events, and the black points are the default acceptances.

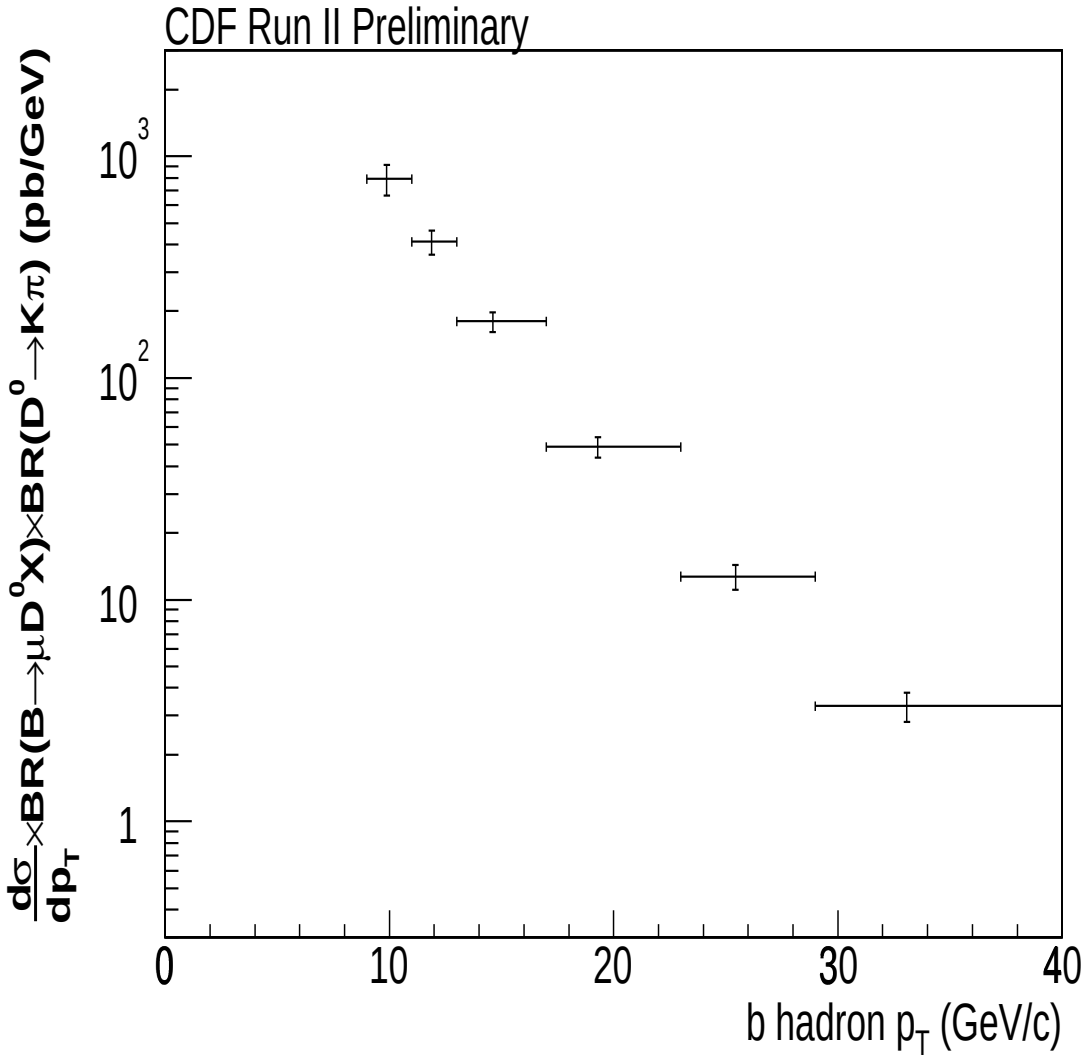

Figure 7.26: The differential cross section times branching ratio for $H_b \to \mu^- D^0 X$, $D^0 \to K^- \pi^+$.

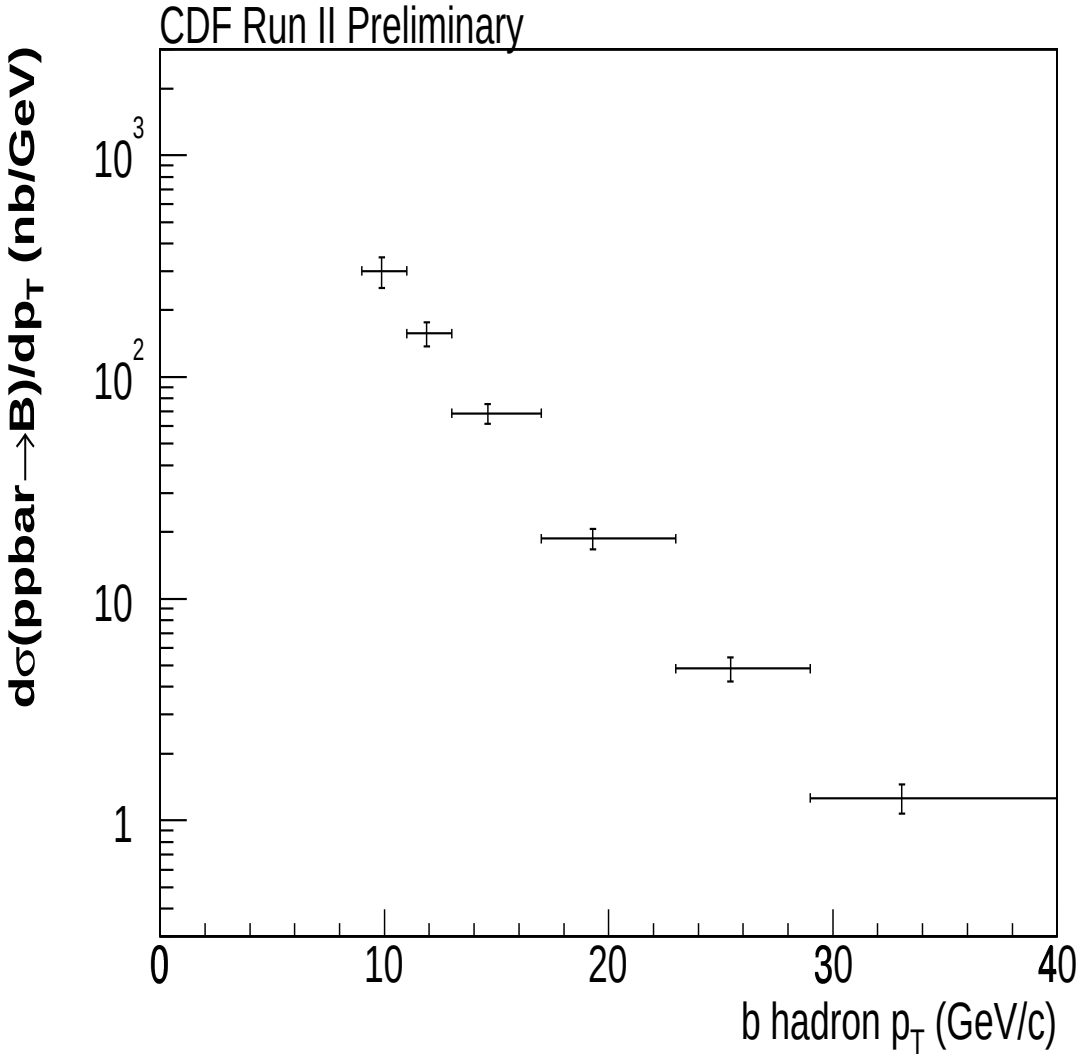

Figure 7.27: The differential cross section from $H_b \to \mu^- D^0 X$, $D^0 \to K^- \pi^+$. Branching ratios corrected for using PDG branching fractions.

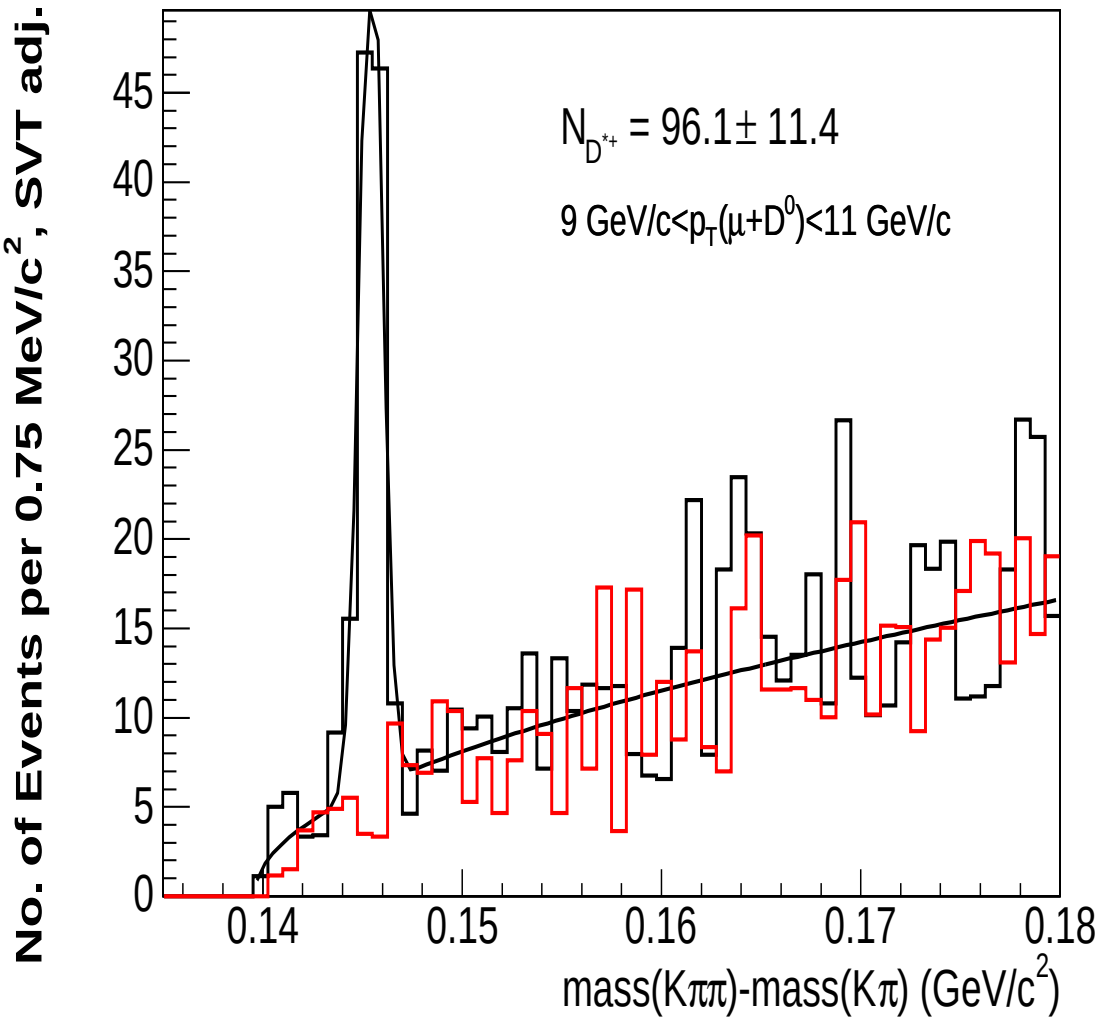

Figure 7.28: Plot of the $m(K^-\pi^+\pi^+) - m(K^-\pi^+)$ mass difference, where the $\mu^- K^-\pi^+$ has 9 GeV/c < p_T < 11 GeV/c and a mass between 3.82 GeV/c^2 and 3.90 GeV/c^2. The black and red plots are for $q_{\pi_{soft}} \neq q_\mu$ and $q_{\pi_{soft}} = q_\mu$, respectively. In both plots the μ and the π associated with the D^0 have opposite charges. The mass difference was fit using a Gaussian plus the background function $a\sqrt{\Delta m - m_\pi}exp(b\times(\Delta m - m_\pi))$, where a and b are allowed to float. The events have been weighted to take into account the SVT efficiency.

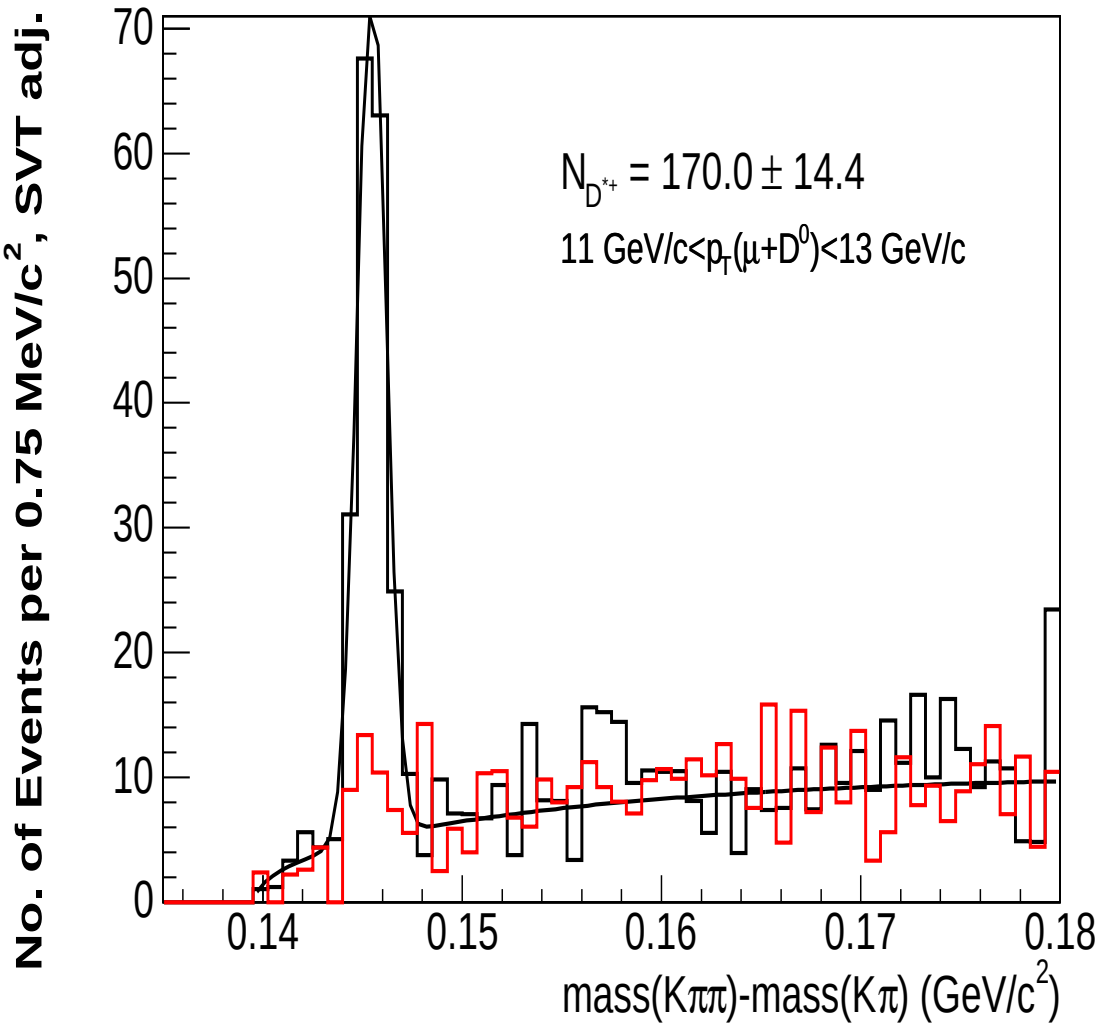

Figure 7.29: Plot of the $m(K^-\pi^+\pi^+) - m(K^-\pi^+)$ mass difference, where the $\mu^- K^-\pi^+$ has 11 GeV/$c < p_T <$ 13 GeV/c and a mass between 3.82 GeV/c^2 and 3.90 GeV/c^2. The black and red plots are for $q_{\pi_{soft}} \neq q_\mu$ and $q_{\pi_{soft}} = q_\mu$, respectively. In both plots the μ and the π associated with the D^0 have opposite charges. The mass difference was fit using a Gaussian plus the background function $a\sqrt{\Delta m - m_\pi}exp(b \times (\Delta m - m_\pi))$, where a and b are allowed to float. The events have been weighted to take into account the SVT efficiency.

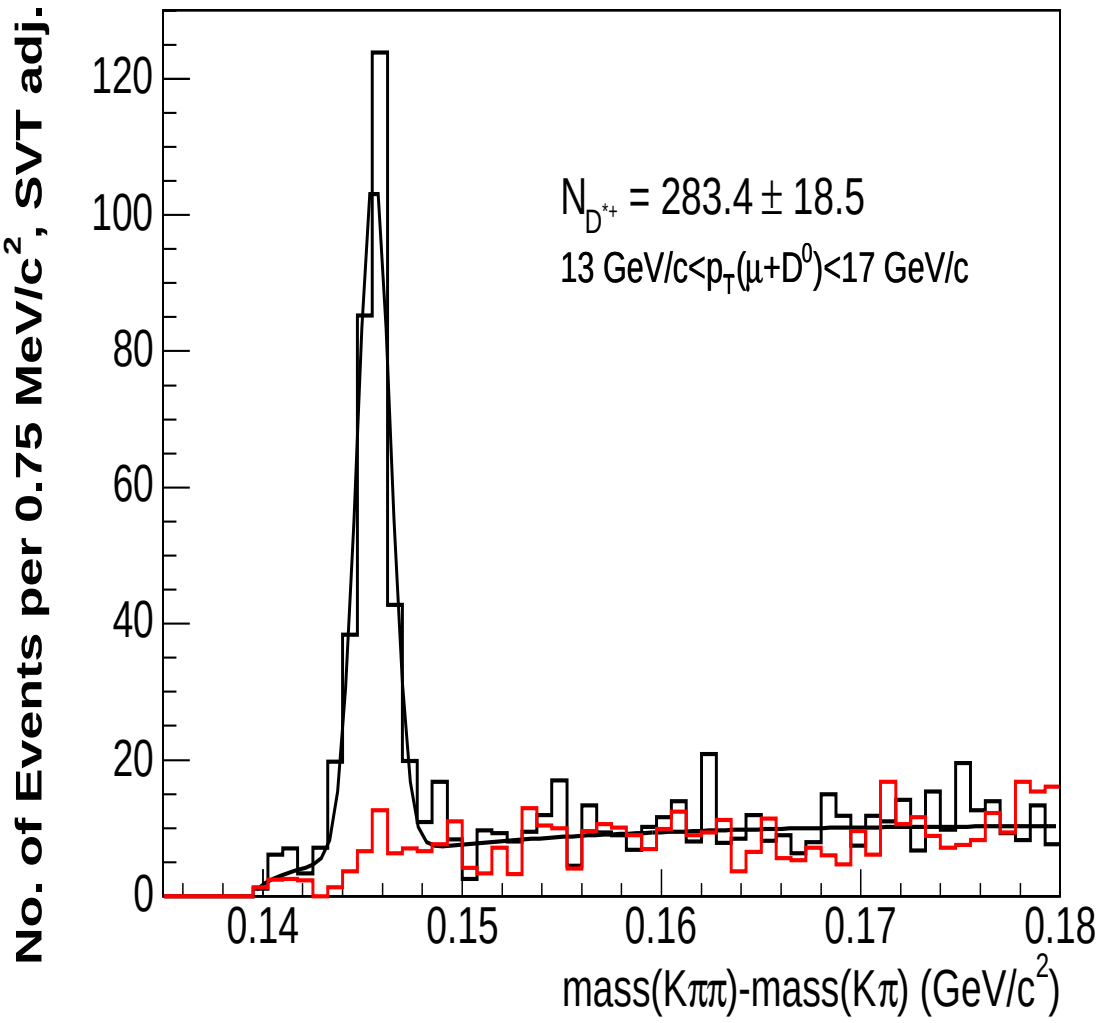

Figure 7.30: Plot of the $m(K^-\pi^+\pi^+) - m(K^-\pi^+)$ mass difference, where the $\mu^- K^-\pi^+$ has 13 GeV/$c < p_T <$ 17 GeV/c and a mass between 3.82 GeV/c^2 and 3.90 GeV/c^2. The black and red plots are for $q_{\pi_{soft}} \neq q_\mu$ and $q_{\pi_{soft}} = q_\mu$, respectively. In both plots the μ and the π associated with the D^0 have opposite charges. The mass difference was fit using a Gaussian plus the background function $a\sqrt{\Delta m - m_\pi}exp(b \times (\Delta m - m_\pi))$, where a and b are allowed to float. The events have been weighted to take into account the SVT efficiency.

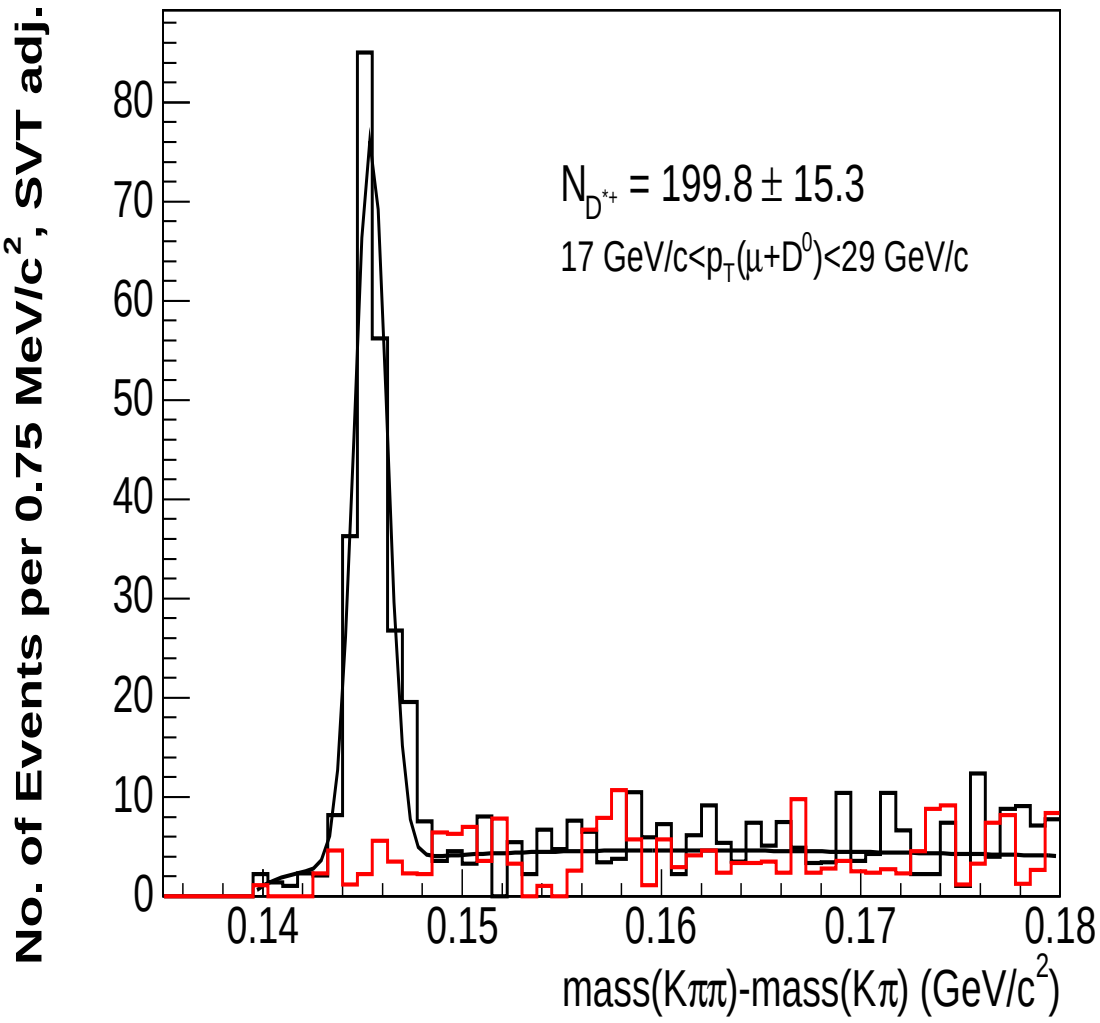

Figure 7.31: Plot of the $m(K^-\pi^+\pi^+) - m(K^-\pi^+)$ mass difference, where the $\mu^- K^-\pi^+$ has 17 GeV/$c < p_T <$ 29 GeV/c and a mass between 3.82 GeV/c^2 and 3.90 GeV/c^2. The black and red plots are for $q_{\pi_{soft}} \neq q_\mu$ and $q_{\pi_{soft}} = q_\mu$, respectively. In both plots the μ and the π associated with the D^0 have opposite charges. The mass difference was fit using a Gaussian plus the background function $a\sqrt{\Delta m - m_\pi}exp(b \times (\Delta m - m_\pi))$, where a and b are allowed to float. The events have been weighted to take into account the SVT efficiency.

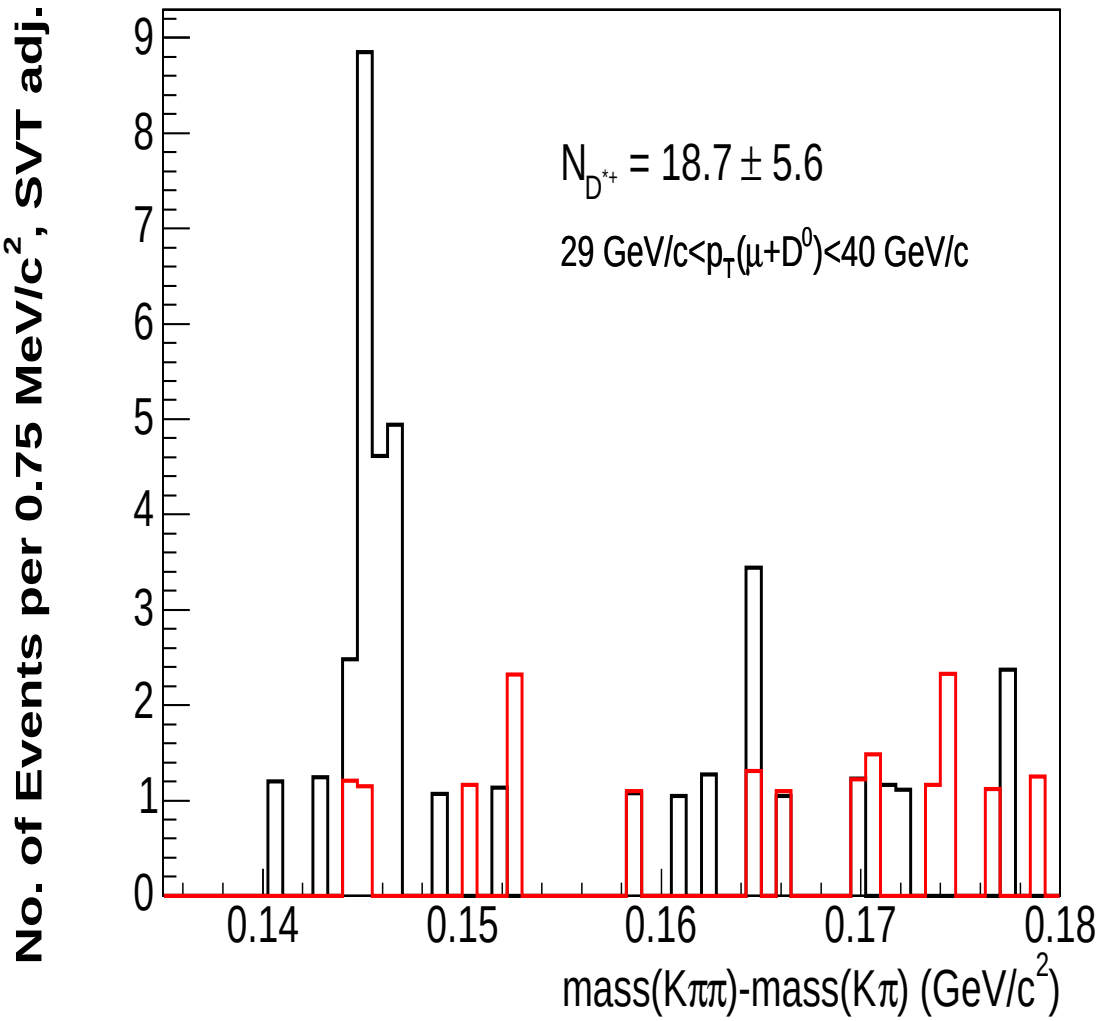

Figure 7.32: Plot of the $m(K^-\pi^+\pi^+) - m(K^-\pi^+)$ mass difference, where the $\mu^- K^-\pi^+$ has 29 GeV/c < p_T < 40 GeV/c and a mass between 3.82 GeV/c^2 and 3.90 GeV/c^2. The black and red plots are for $q_{\pi_{soft}} \neq q_\mu$ and $q_{\pi_{soft}} = q_\mu$, respectively. In both plots the μ and the π associated with the D^0 have opposite charges. Because there were relatively few events, the number of events was found by sideband subtraction rather than a Gaussian fit. The signal range was 3σ about the mean of the Gaussian from the 17 GeV/c < p_T < 29 GeV/c bin fit, and the sideband range was 5 to 8.4 σ above the peak. The sideband region was chosen so that, in the 17 GeV/c < p_T < 29 GeV/c bin fit, the area under the background fit in the sideband region is the same as in the signal region. The events have been weighted to take into account the SVT efficiency.

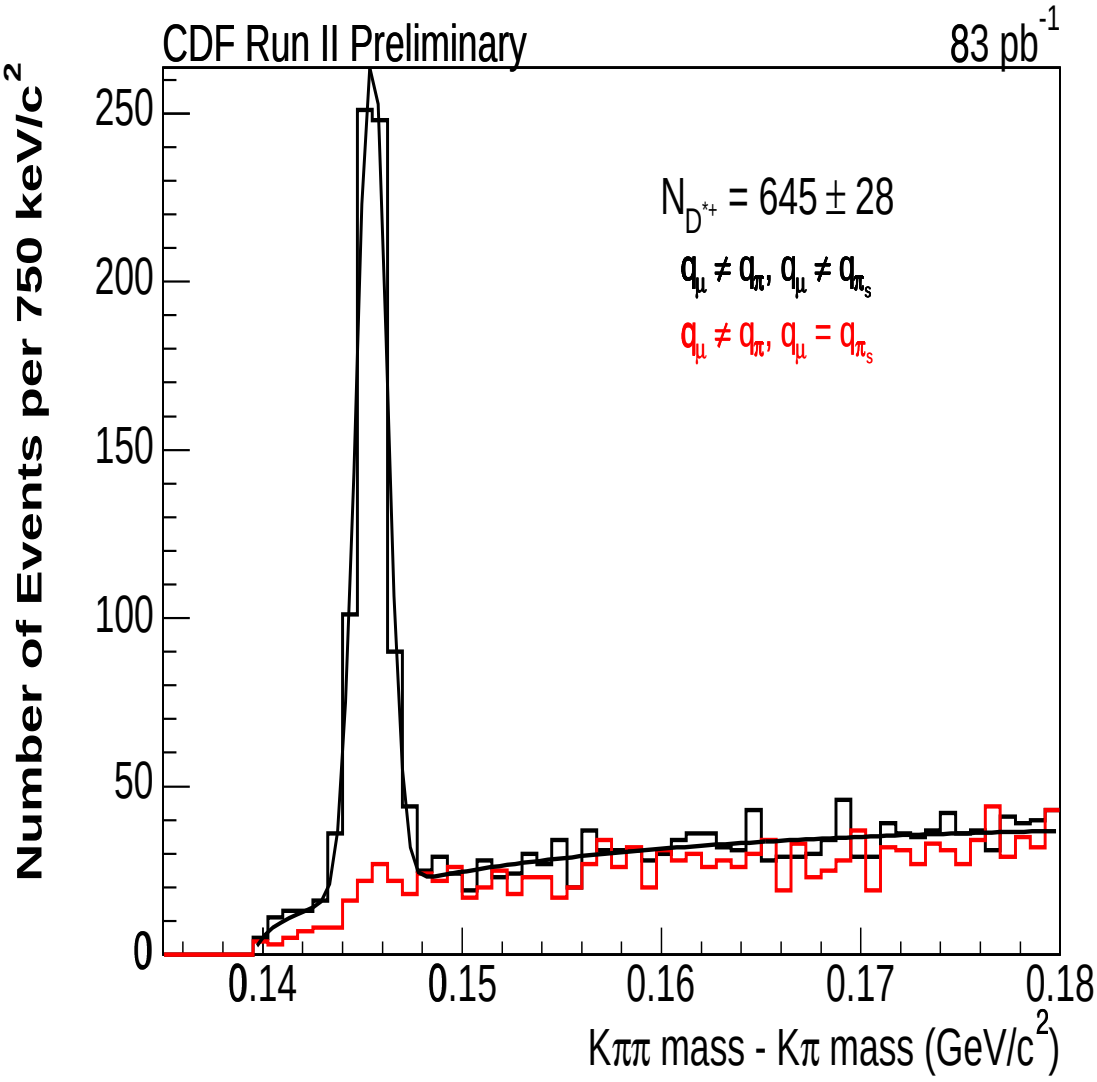

Figure 7.33: Plot of the $m(K^-\pi^+\pi^+) - m(K^-\pi^+)$ mass difference, for events with $p_T(\mu^- K^-\pi^+) > 9.0$ GeV/c. The black and red plots are for $q_{\pi_{soft}} \neq q_\mu$ and $q_{\pi_{soft}} = q_\mu$, respectively. In both plots the μ and the π associated with the D^0 have opposite charges. The mass difference was fit using a Gaussian plus the background function $a\sqrt{\Delta m - m_\pi}exp(b \times (\Delta m - m_\pi))$, where a and b are allowed to float. There is no adjustment for the SVT efficiency.

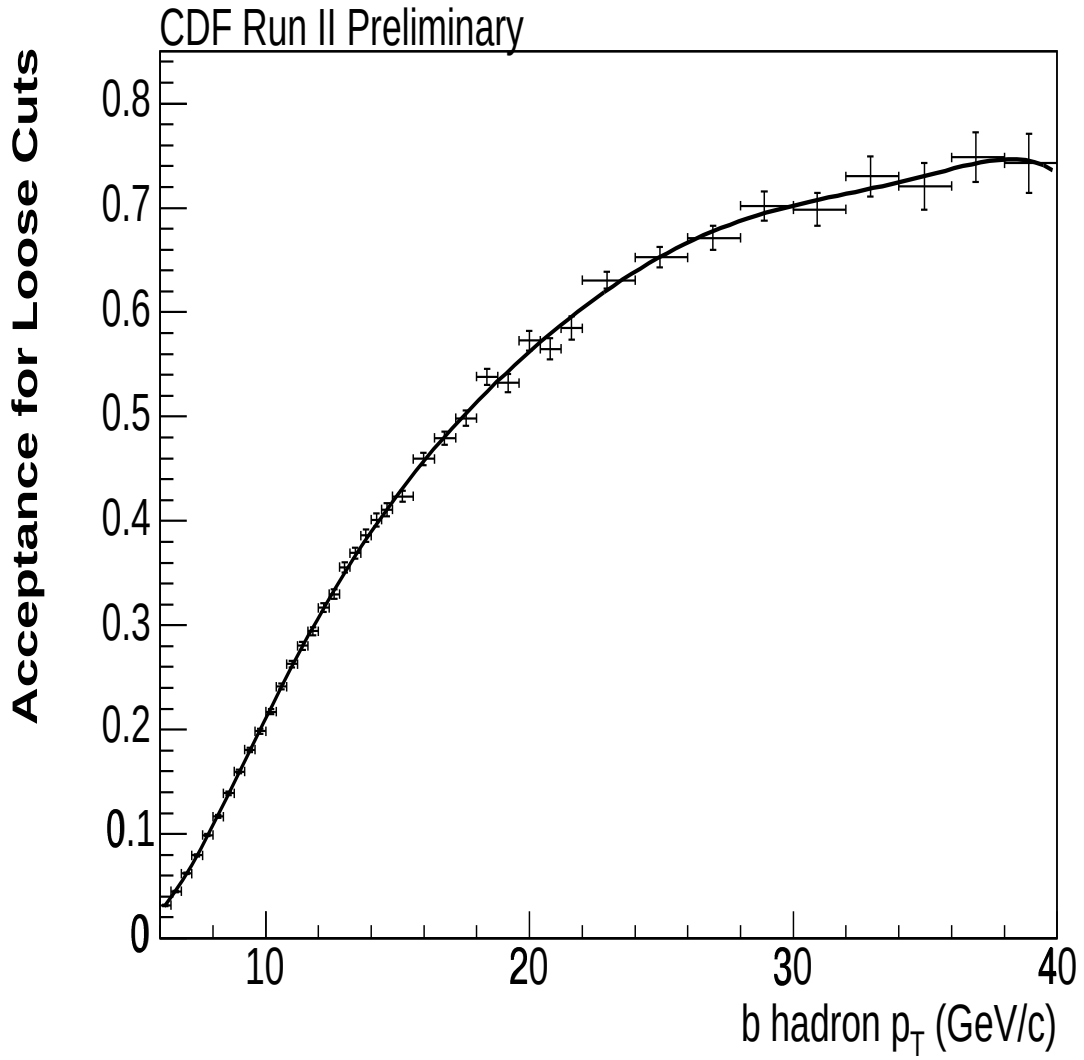

Figure 7.34: The generator level acceptance for the loose cuts on MC made with the CDF b spectrum versus b hadron p_T for events with a D^{*+}.

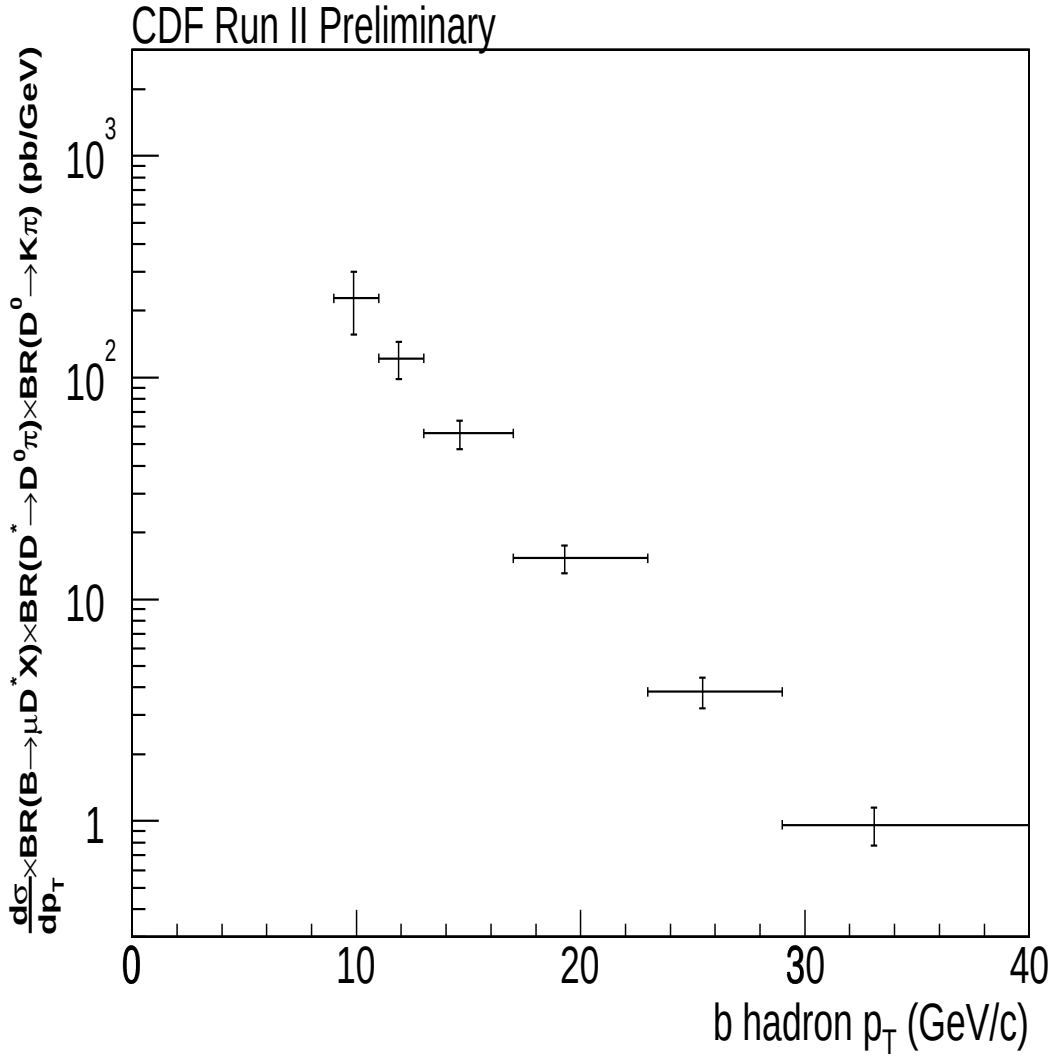

Figure 7.35: The differential cross section times branching ratio for $H_b \to \mu^- D^{*+} X$, $D^{*+} \to D^0 \pi^+$, $D^0 \to K^- \pi^+$.

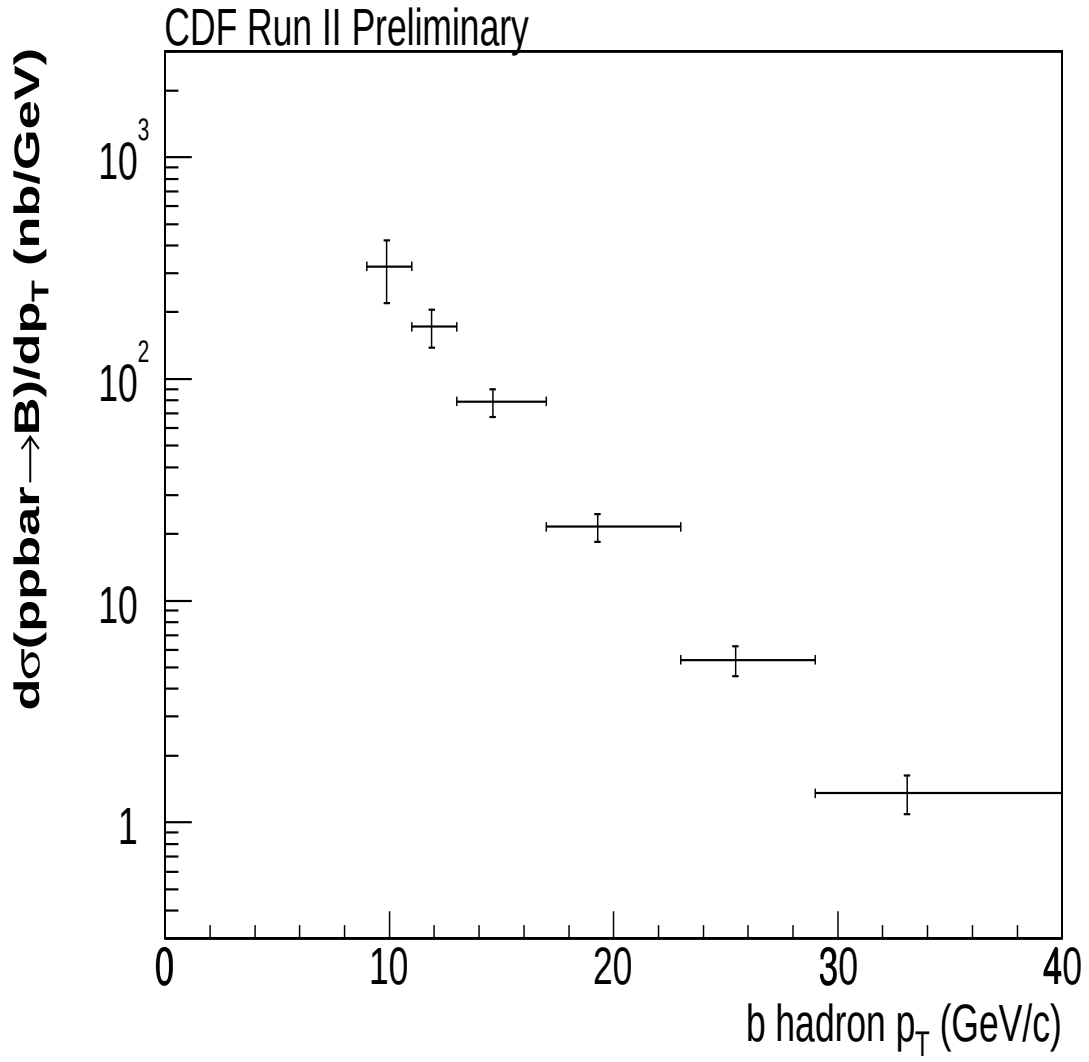

Figure 7.36: The differential cross section from $H_b \to \mu^- D^{*+} X$, $D^{*+} \to D^0 \pi^+$, $D^0 \to K^- \pi^+$. Branching ratios corrected for using PDG branching fractions.

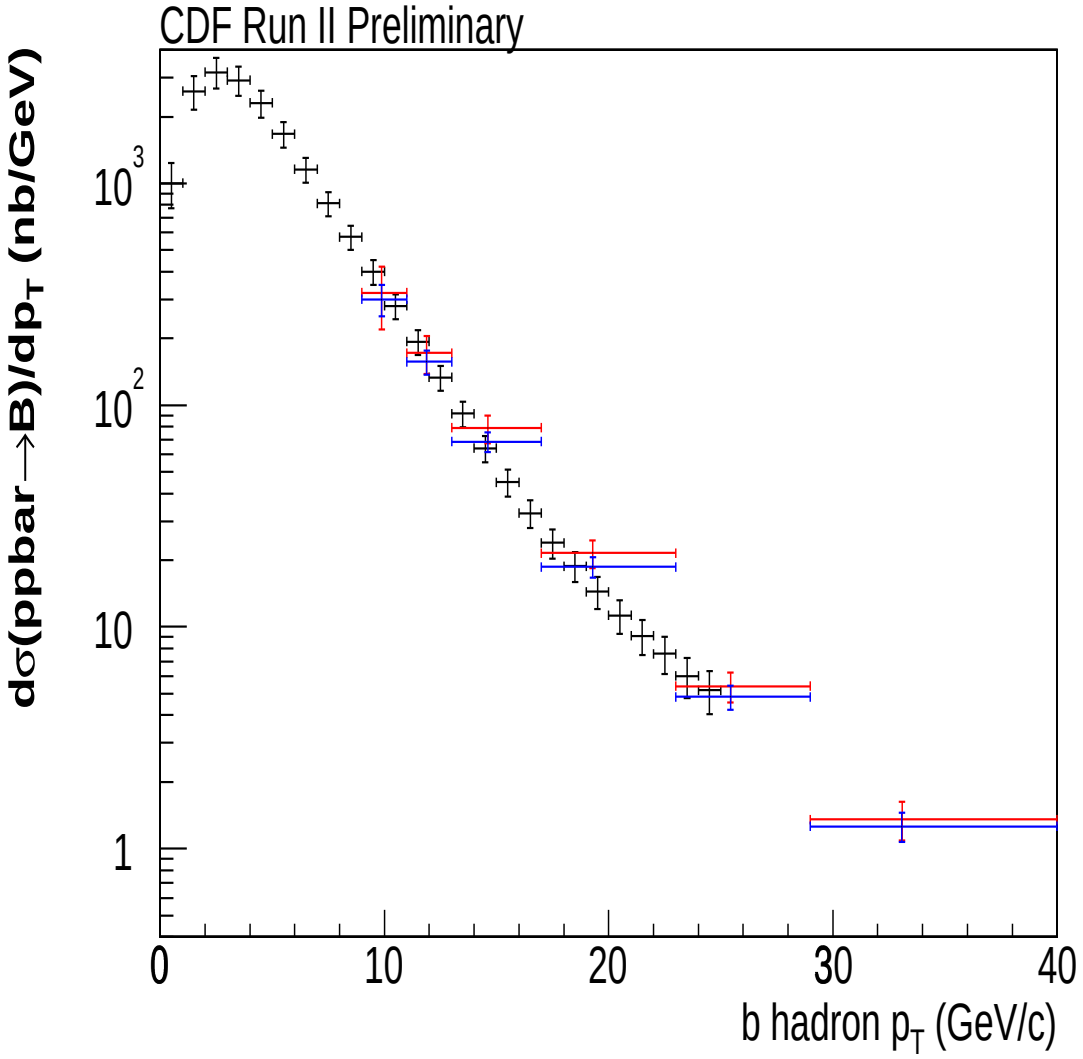

Figure 7.37: The differential cross section from $H_b \to J/\psi X$, $J/\psi \to \mu^+\mu^-$ (black points), $H_b \to \mu^- D^0 X$, $D^0 \to K^-\pi^+$ (blue points), and $H_b \to \mu^- D^{*+} X$, $D^{*+} \to D^0\pi^+$, $D^0 \to K^-\pi^+$ (red points). All three measurements have been corrected for the appropriate branching fractions, and all three have $|y(H_b)| < 0.6$.

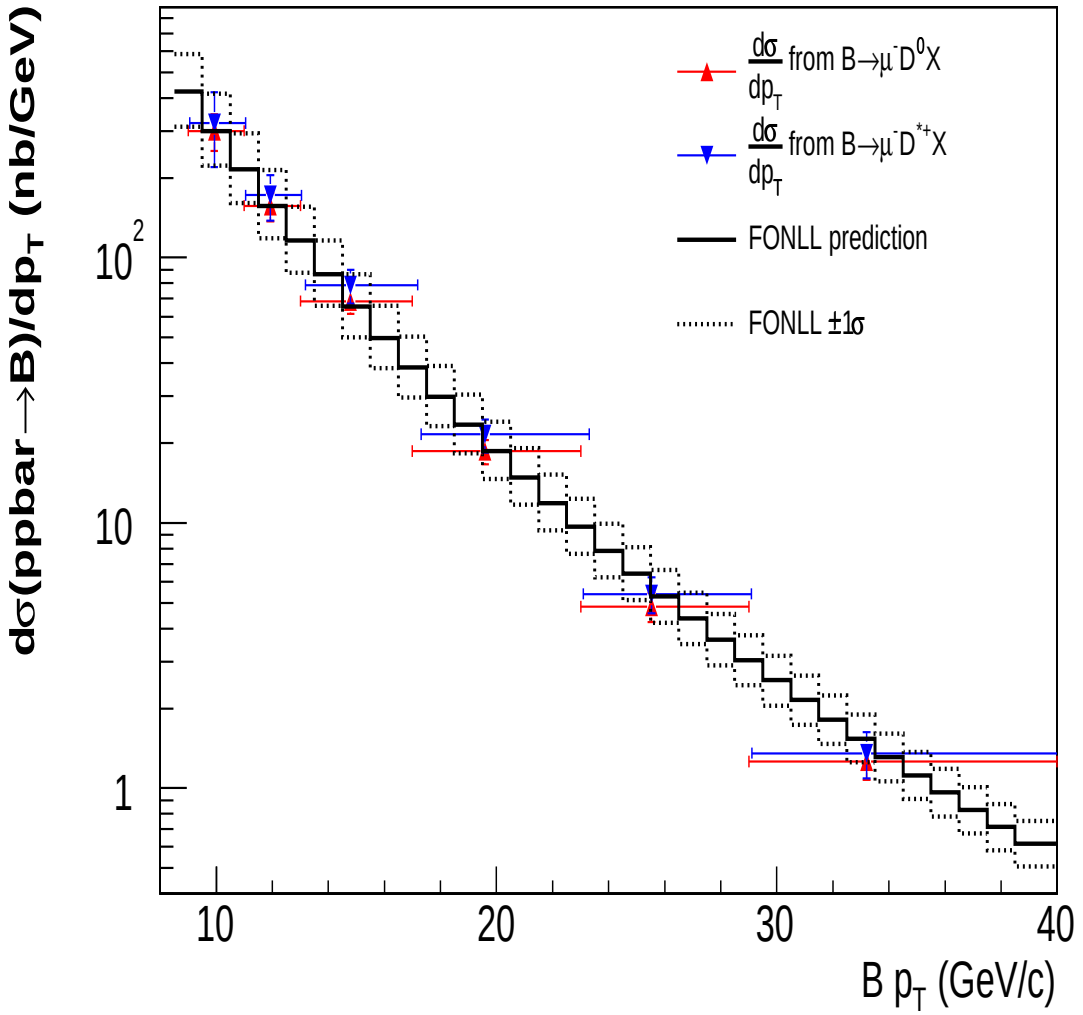

Figure 7.38: The differential cross section from $H_b \to \mu^- D^0 X$, $D^0 \to K^-\pi^+$ (blue points) and $H_b \to \mu^- D^{*+} X$, $D^{*+} \to D^0\pi^+$, $D^0 \to K^-\pi^+$ (red points), compared to prediction made using FONLL theory with CTEQ6M PDF's (solid black line). Errors on theory are shown as dashed black lines. All measurements have been corrected for the appropriate branching fractions, and plots three have $|y(H_b)| < 0.6$.

Appendix A

Glossary

B_CHARM_LOWPT_L1_DPS: Name of the trigger requiring 2 displaced tracks to fire. Used in the XFT efficiency measurement.

B_SEMI_CMUP4_TRACK2_D120: Name of the trigger used to collect the μD^0 events used in the cross section. Requires a high p_T muon with hits in the CMU and CMP chambers and a displaced track.

B_SEMI_L3PS20_L2_TRK2_D120_L1_CMUP6_PT4: Trigger similar to the B_SEMI_CMUP4_TRACK2_D120 trigger, but with no requirements at L3. Used to determine the L3 efficiency of the B_SEMI_CMUP4_TRACK2_D120 trigger.

CDF: Collider Detector at Fermilab. The name of the detector overall. The CLC, COT, SVX, CMU, and CMP are all subdetectors of the CDF detector.

CLC: Cherenkov Luminosity Counter. Used to measure the luminosity of beam delivered to CDF.

CMP: Central Muon uPgrade. Muon chambers placed behind the CMU and additional steel that cover the range $|\eta| < 0.6$

CMU: Central MUon Detector. Muon chambers placed directly outside the calorimeters that cover the range $|\eta| < 0.6$

CMUP8 Trigger: Trigger requiring a muon with a p_T of at least 8 GeV/c with hits in the CMU and CMP chambers. Used in the L1, SVT, and CMU efficiency measurements.

CMX: Central Muon eXtension. Muon chambers that cover the range $0.6 < |\eta| < 1.0$

COT: Central Outer Tracker. The CDF experiment's drift chamber, used for tracking and p_T measurement.

η: See Pseudorapidity.

FONLL: Fixed Order, Next Leading Log. Calculation of the b cross section using matrix elements out to NLO, and resumming over logarithmic terms of order $\alpha_s(\log\frac{p_T}{m_b})^k$ and $\alpha_s^2(\log\frac{p_T}{m_b})^k$, where $k \geq 1$.

H_b: A b hadron. Any particle contisting of a b quank and either an anti-quark or two other quarks.

J/ψ **CMU-CMU Trigger**: Trigger requiring two muons with hits in the CMU chambers that have an invariant mass consistent with a J/ψ. Used to determine the efficiency of the SVX offline reconstruction.

J/ψ **CMU-CMX Trigger**: Trigger requiring two muons, one with hits in a CMU chamber and the other

with hits in a CMX chamber, that have an invariant mass consistent with a J/ψ. Used to determine the efficiency of the SVX offline reconstruction. **L1**: Level 1 Trigger. First level of the CDF trigger. Accepts about one event in 60.

L2: Level 2 Trigger. Second level of the CDF trigger. Accepts about one event in 100.

L3: Level 3 Trigger. Third level of the CDF trigger. Accepts about one event in 4.

$\phi_{r=8cm}$: Azimuthal (ϕ) position of the track at a radius of 8 cm from the center of the beampipe.

Luminosity: The number of particles passing through a given area in a given time. At CDF, typical a typical luminosity is 10^{31} cm^{-2}s^{-1}. The formula used to find the luminosity at CDF is $\mathcal{L} = \frac{f_{\rm BC} N_p N_{\bar{p}}}{2\pi T(\sigma_p^2+\sigma_{\bar{p}}^2)} F(\frac{\sigma_l}{\beta^*})$,where $T \approx 21\,\mu$s is the revolution period, $f_{\rm BC}$ is the number of bunches in each beam, N_p and $N_{\bar{p}}$ are the number of protons and antiprotons per bunch, σ_p and $\sigma_{\bar{p}}$ are the transverse beam sizes (RMS) at the interaction point, and F is a form factor that depends on the ratio between the bunch longitudinal RMS size σ_l, and the beta function β^* at the interaction point.

Pseudorapidity: Typically represented by η, pseudorapidity is defined as $-\ln(\tan\frac{\theta}{2})$

p_T: see Transverse Momentum.

QCD: Quantum ChromoDynamics. The fundamental theory of the strong interaction.

Rapidity: $-\frac{1}{2}\log\frac{E+p_z}{E-p_z}$, where E is the particle energy and p_z is the component of the track's momentum parallel to the beam axis. Under a Lorentz boost in the z direction with velocity β, $y \to y + \tanh^{-1}\beta$, so $dy \to dy$.

SL: Superlayer. The COT in divided radially into 8 superlayers, each of which contains 12 layers of sense wires.

SVT: Silicon Vertex Trigger. Finds displaced tracks for use in the L2 trigger decision.

SVX: Silicon VerteX Tracker. Five layers of silicon strips used to precisely determine a track's impact parameter.

Transverse Momentum: Magnitude of the tracks momentum in the direction perpendicular to the beam axis.

XFT: eXtremely Fast Tracker. Reconstructs COT tracks for use the the L1 and L2 trigger decisions

XTRP: eXTRaPolation Unit. Extrapolates tracks reconstructed be the XFT to the calorimeters and muon chambers for use in the L1 trigger decision, and determines the L1 track only trigger decisions.

$z_{r=8cm}$: Position of the track along the beam axis direction (the z co-ordinate) at a radius of 8 cm from the center of the beampipe.

Appendix B

SVT Efficiency Plots

The following plots show the L2 SVT efficiency versus either $1/p_T$, $|d_0 - 8\ \mu\text{m}|$, or isolation, for a given range of the other two variables. The lines superimposed on the plots are the results of the 3-D fit to the data, with two of the variables fixed to their average value for that bin. For example, for the plot showing the efficiency versus $1/p_T$ for 120 μm$< |d_0 - 8\ \mu\text{m}| <$ 140 μm and ISO = 0, the plot shown is the result of the 3-D fit with ISO = 0 and the $|d_0 - 8\ \mu\text{m}|$ set to its average value within the bin. Because the lines shown include input from data points not on the plot, the lines do not show the most optimum fit to the lines within a single given plot.

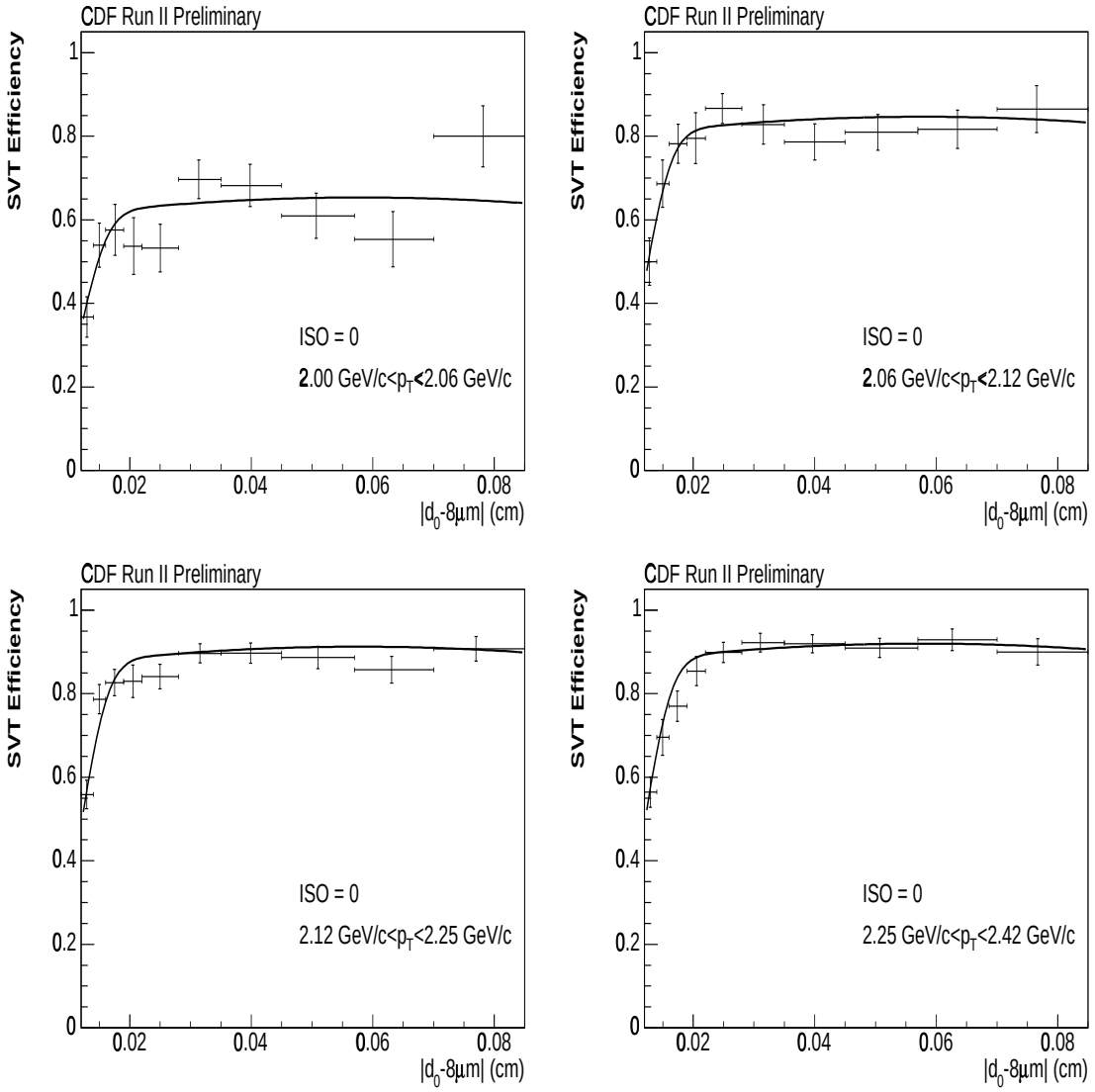

Figure B.1: SVT efficiency vs. $|d_0 - 8\mu\text{m}|$ for various slices of transverse momentum for tracks with no tracks having $p_T > 400$ MeV/c within $\Delta\phi_{r=8cm} < 5^\circ$ (ISO = 0). The curves are the one dimensional projections of the three dimensional binned fit to the data. Tracks with $|d_0 - 8\mu\text{m}| > 850$ microns have been excluded from the fit.

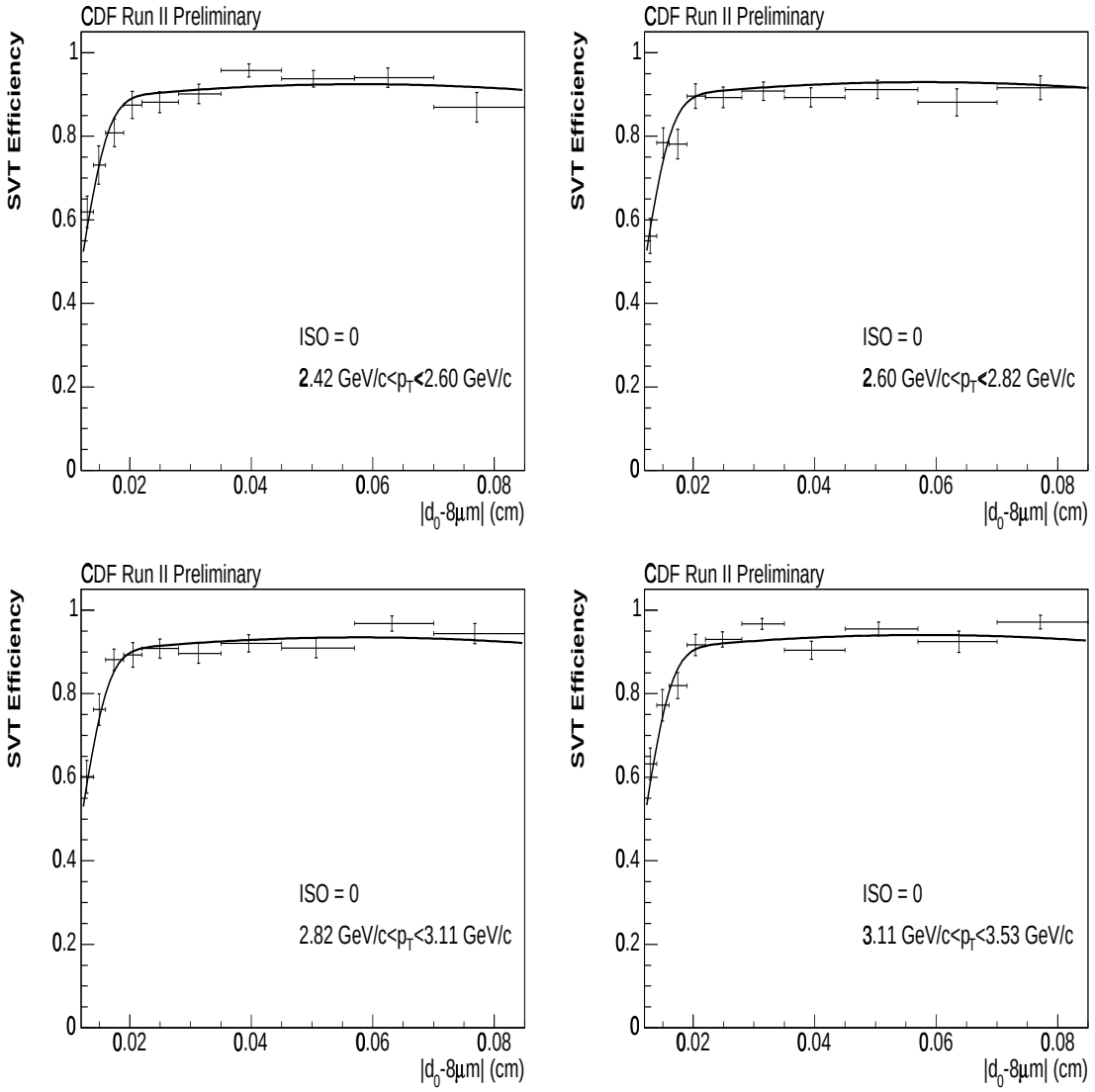

Figure B.2: SVT efficiency vs. $|d_0 - 8\mu\text{m}|$ for various slices of transverse momentum for tracks with no tracks having $p_T > 400$ MeV/c within $\Delta\phi_{r=8cm} < 5°$ (ISO = 0). The curves are the one dimensional projections of the three dimensional binned fit to the data. Tracks with $|d_0 - 8\mu\text{m}| > 850$ microns have been excluded from the fit.

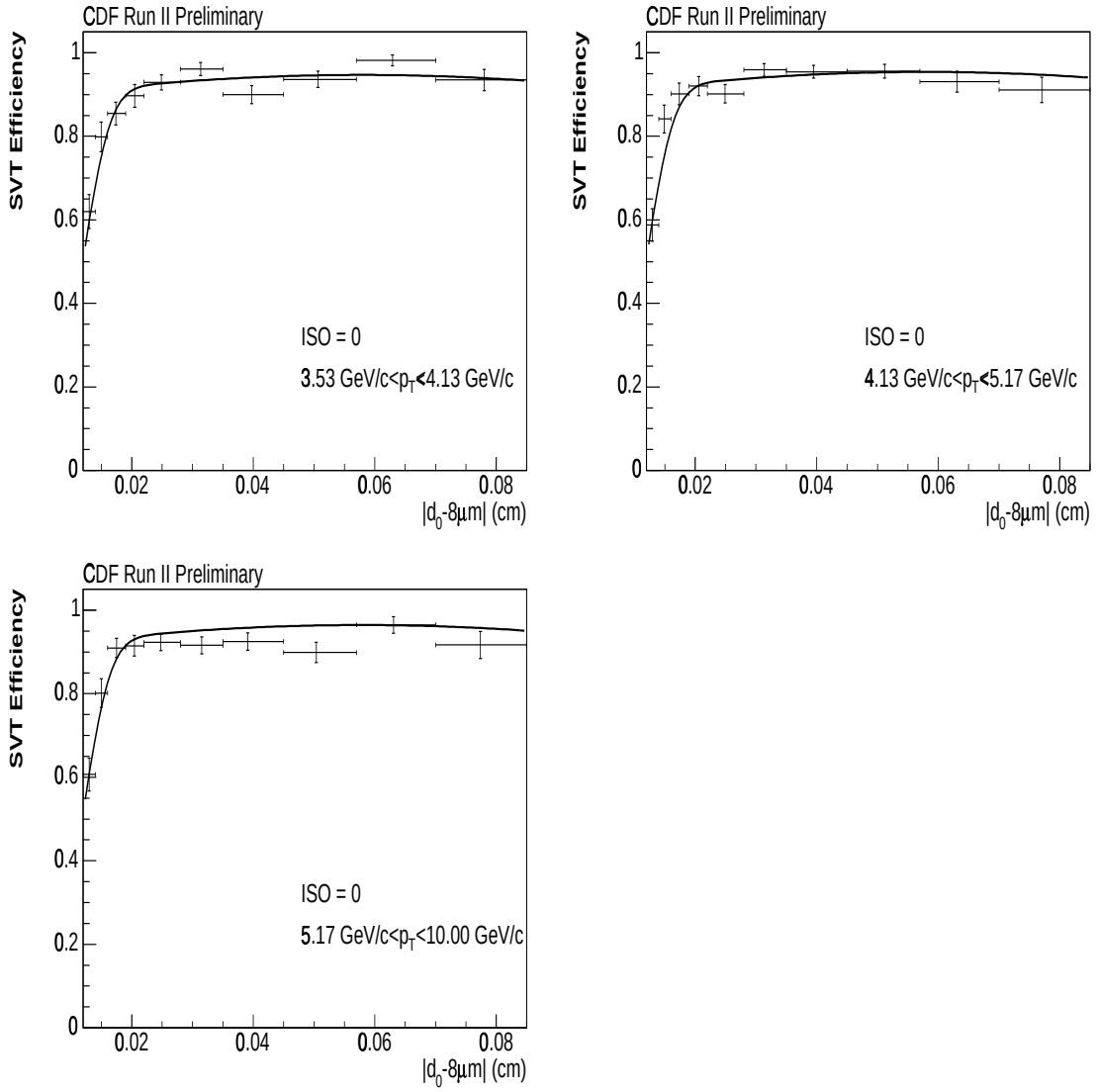

Figure B.3: SVT efficiency vs. $|d_0 - 8\mu\text{m}|$ for various slices of transverse momentum for tracks with no tracks having $p_T > 400$ MeV/c within $\Delta\phi_{r=8cm} < 5°$ (ISO = 0). The curves are the one dimensional projections of the three dimensional binned fit to the data. Tracks with $|d_0 - 8\mu\text{m}| > 850$ microns have been excluded from the fit.

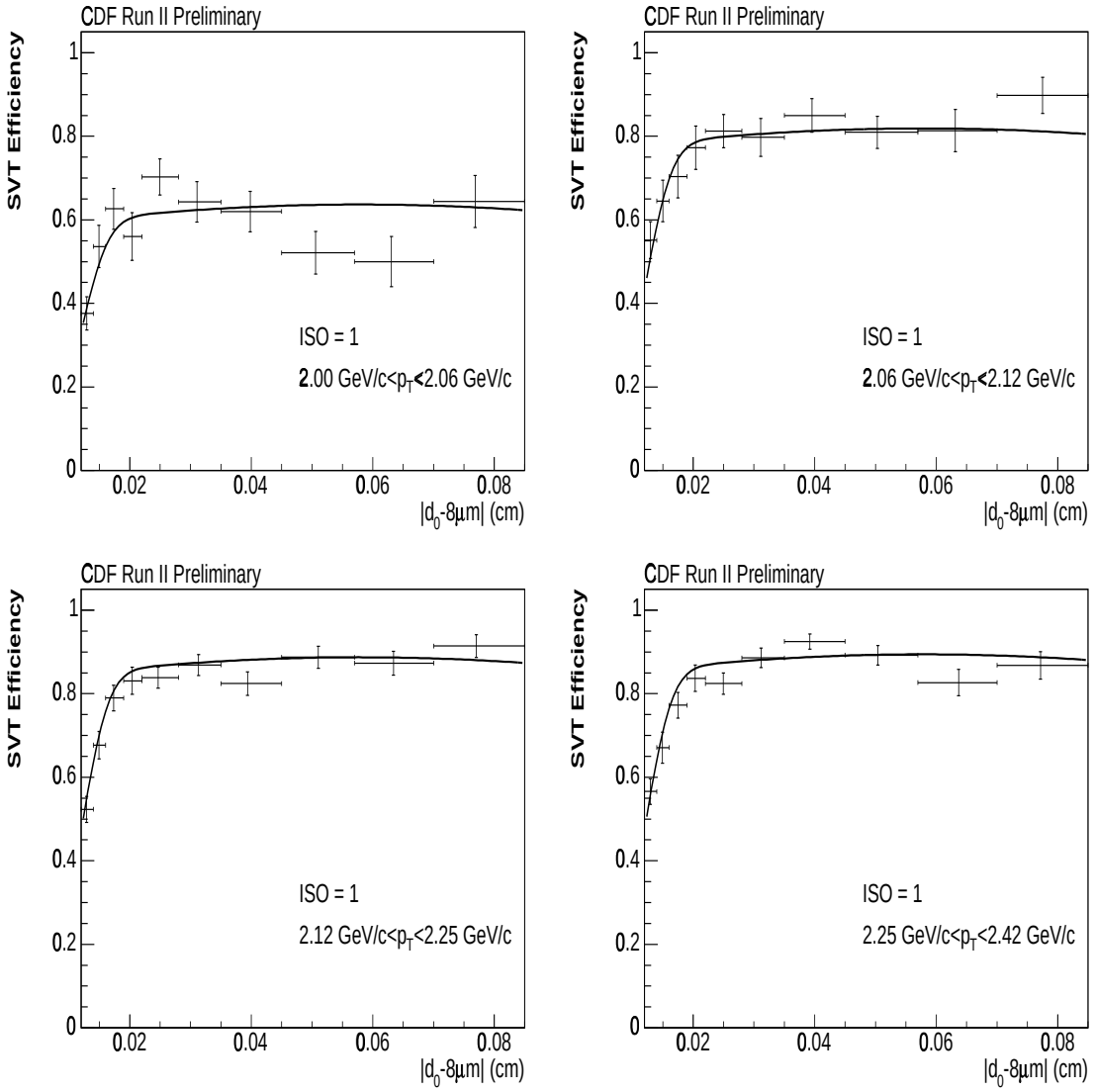

Figure B.4: SVT efficiency vs. $|d_0 - 8\mu\text{m}|$ for various slices of transverse momentum for tracks with 1 track having $p_T > 400$ MeV/c within $\Delta\phi_{r=8cm} < 5°$ (ISO = 1). The curves are the one dimensional projections of the three dimensional binned fit to the data. Tracks with $|d_0 - 8\mu\text{m}| > 850$ microns have been excluded from the fit.

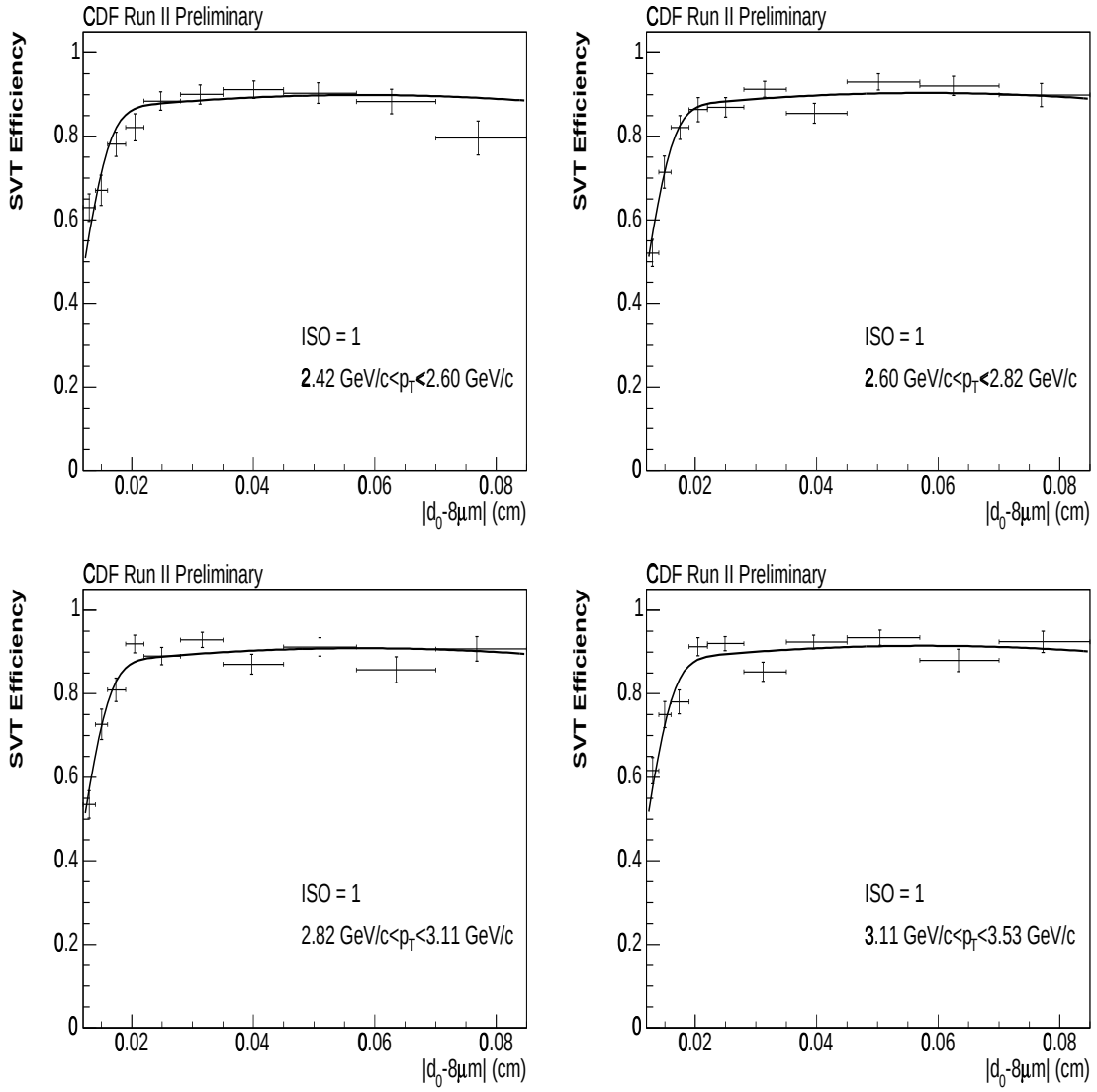

Figure B.5: SVT efficiency vs. $|d_0 - 8\mu\text{m}|$ for various slices of transverse momentum for tracks with 1 track having $p_T > 400$ MeV/c within $\Delta\phi_{r=8cm} < 5°$ (ISO = 1). The curves are the one dimensional projections of the three dimensional binned fit to the data. Tracks with $|d_0 - 8\mu\text{m}| > 850$ microns have been excluded from the fit.

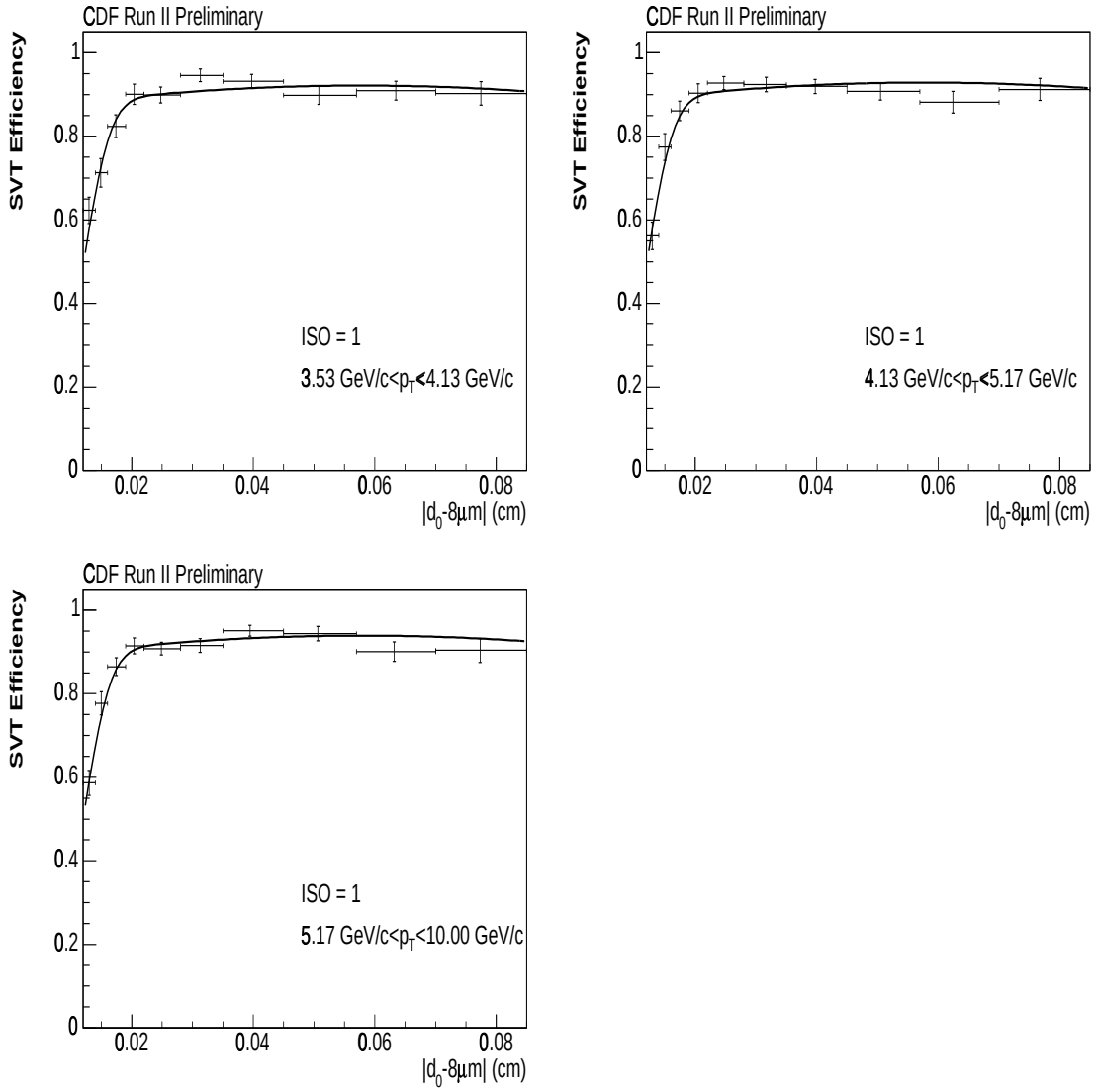

Figure B.6: SVT efficiency vs. $|d_0 - 8\mu\text{m}|$ for various slices of transverse momentum for tracks with 1 track having $p_T > 400$ MeV/c within $\Delta\phi_{r=8cm} < 5°$ (ISO = 1). The curves are the one dimensional projections of the three dimensional binned fit to the data. Tracks with $|d_0 - 8\mu\text{m}| > 850$ microns have been excluded from the fit.

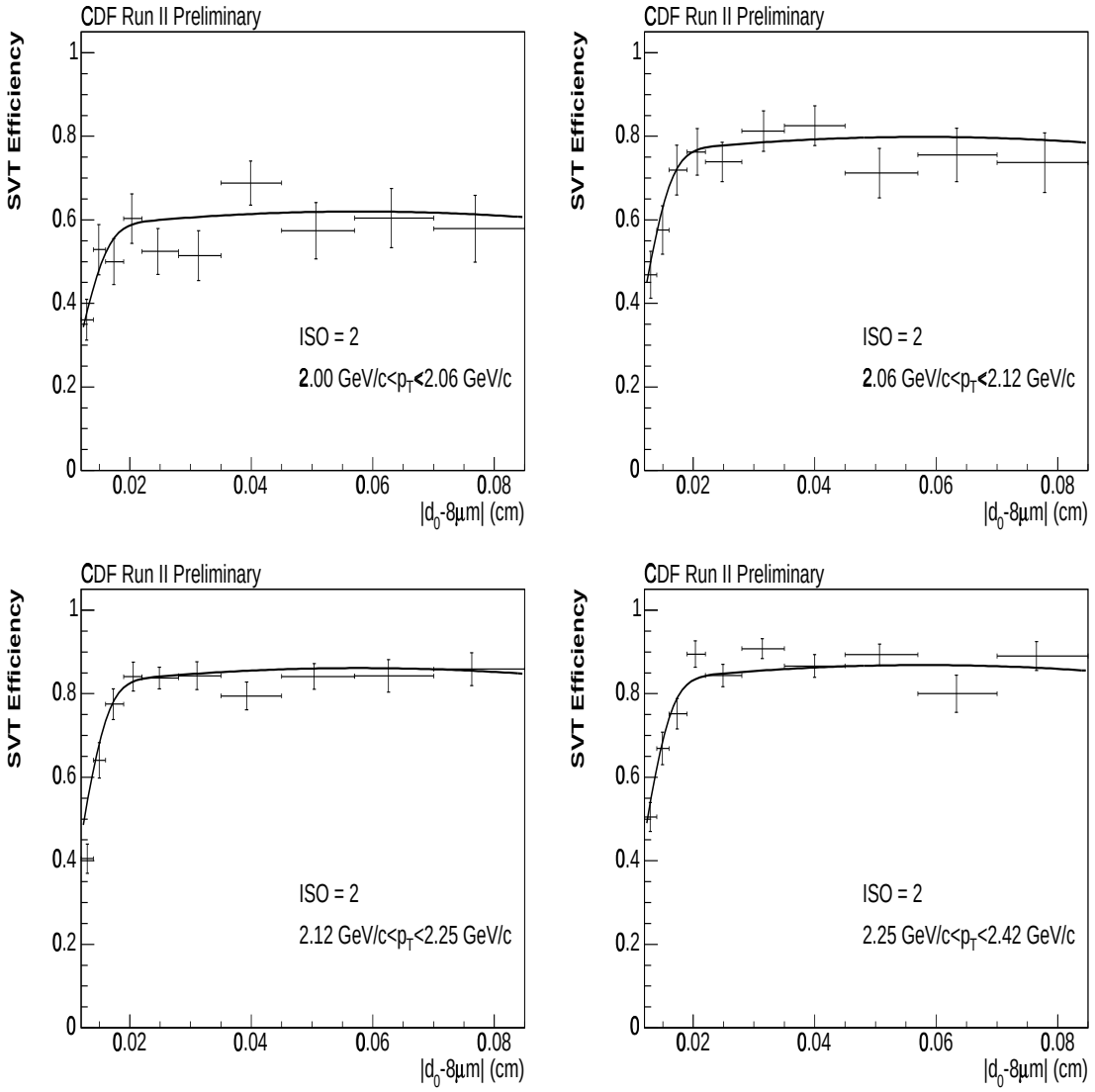

Figure B.7: SVT efficiency vs. $|d_0 - 8\mu\text{m}|$ for various slices of transverse momentum for tracks with 2 tracks having $p_T > 400$ MeV/c within $\Delta\phi_{r=8cm} < 5^\circ$ (ISO = 2). The curves are the one dimensional projections of the three dimensional binned fit to the data. Tracks with $|d_0 - 8\mu\text{m}| > 850$ microns have been excluded from the fit.

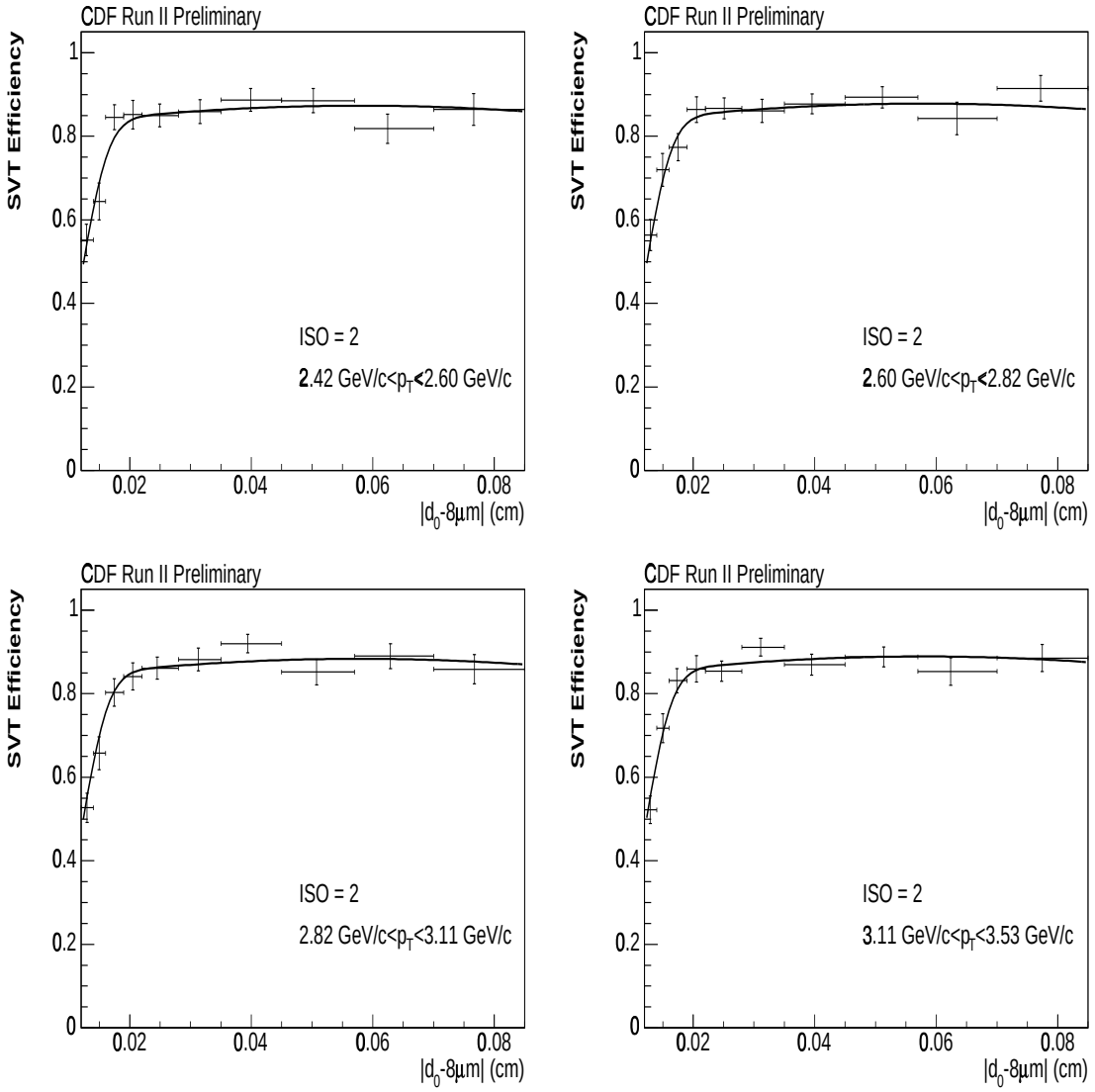

Figure B.8: SVT efficiency vs. $|d_0 - 8\mu\text{m}|$ for various slices of transverse momentum for tracks with 2 tracks having $p_T > 400$ MeV/c within $\Delta\phi_{r=8cm} < 5°$ (ISO = 2). The curves are the one dimensional projections of the three dimensional binned fit to the data. Tracks with $|d_0 - 8\mu\text{m}| > 850$ microns have been excluded from the fit.

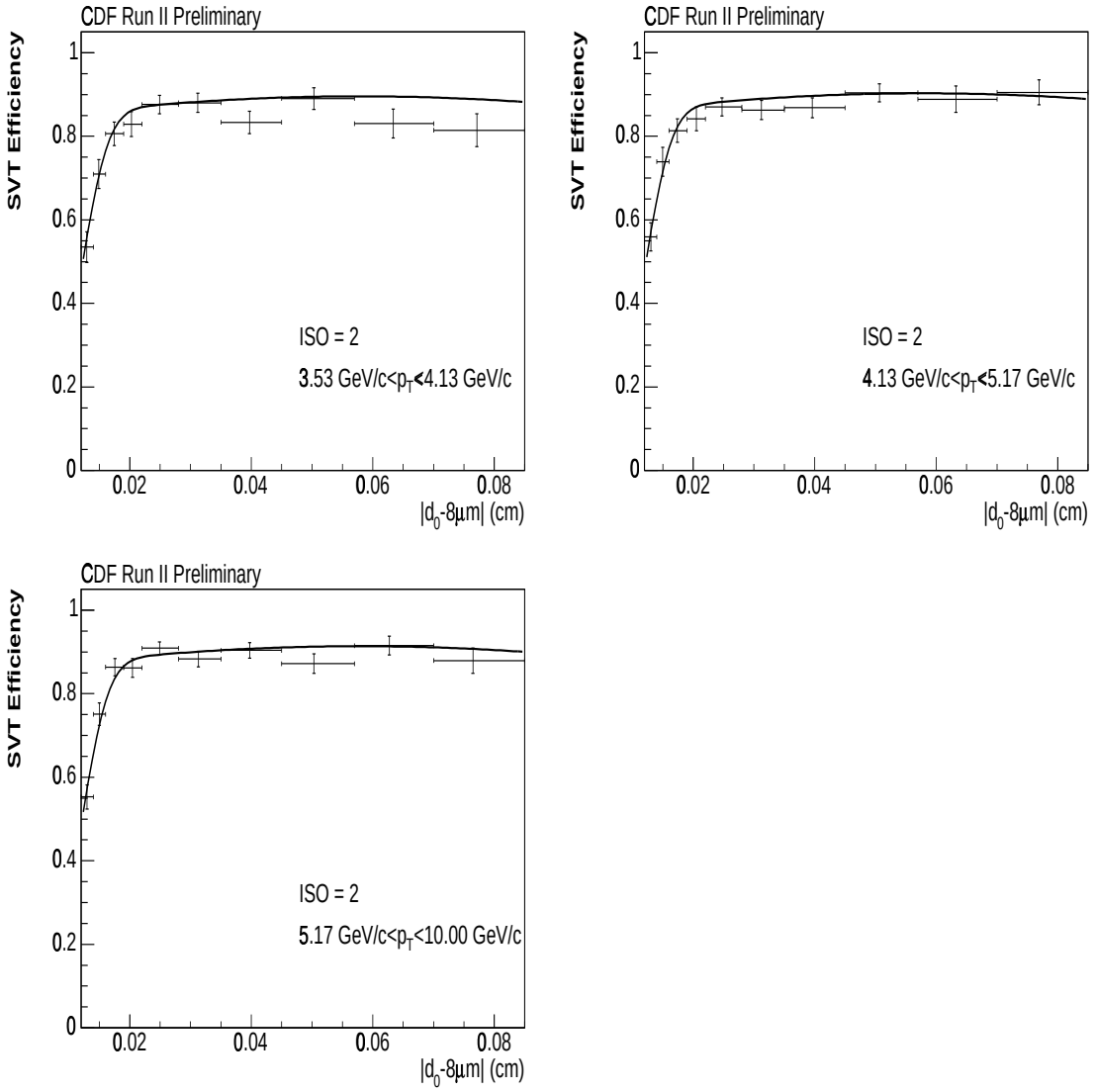

Figure B.9: SVT efficiency vs. $|d_0 - 8\mu\text{m}|$ for various slices of transverse momentum for tracks with 2 tracks having $p_T > 400$ MeV/c within $\Delta\phi_{r=8cm} < 5^\circ$ (ISO = 2). The curves are the one dimensional projections of the three dimensional binned fit to the data. Tracks with $|d_0 - 8\mu\text{m}| > 850$ microns have been excluded from the fit.

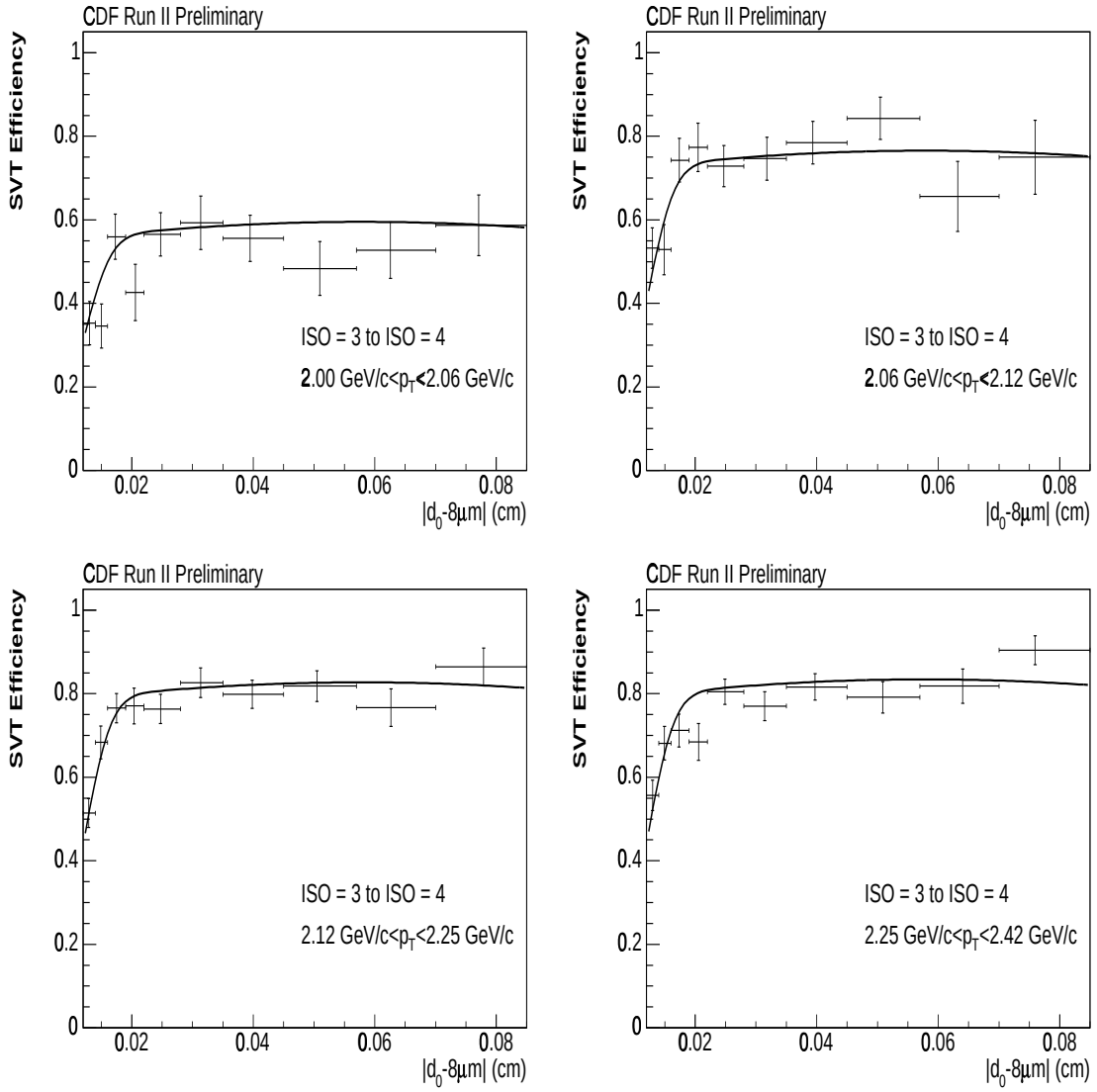

Figure B.10: SVT efficiency vs. $|d_0 - 8\mu\text{m}|$ for various slices of transverse momentum for tracks with 3 or 4 tracks having $p_T > 400$ MeV/c within $\Delta\phi_{r=8cm} < 5^\circ$ (ISO = 3 or 4). The curves are the one dimensional projections of the three dimensional binned fit to the data. Tracks with $|d_0 - 8\mu\text{m}| > 850$ microns have been excluded from the fit.

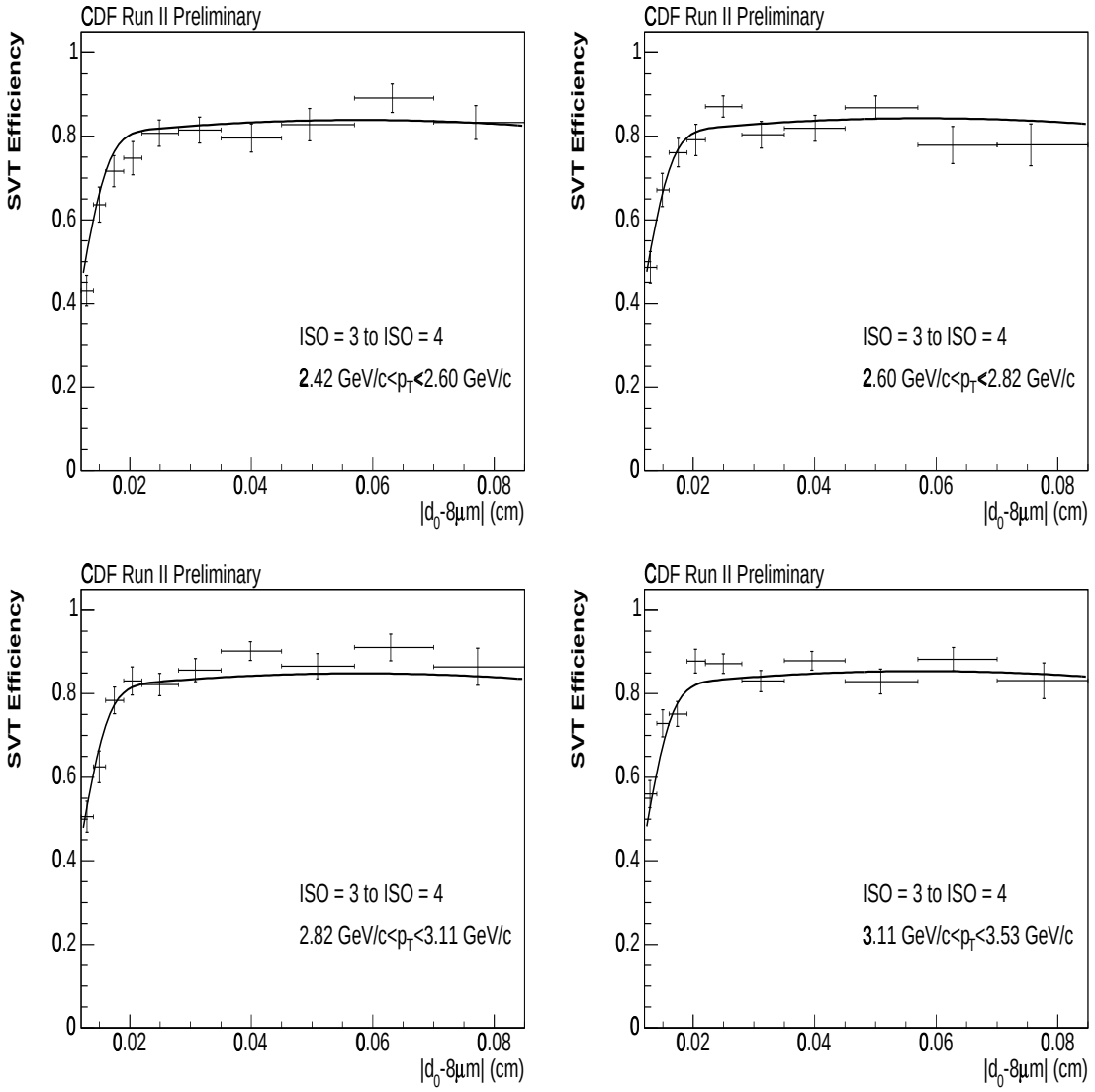

Figure B.11: SVT efficiency vs. $|d_0 - 8\mu\text{m}|$ for various slices of transverse momentum for tracks with 3 or 4 tracks having $p_T > 400$ MeV/c within $\Delta\phi_{r=8cm} < 5^\circ$ (ISO = 3 or 4). The curves are the one dimensional projections of the three dimensional binned fit to the data. Tracks with $|d_0 - 8\mu\text{m}| > 850$ microns have been excluded from the fit.

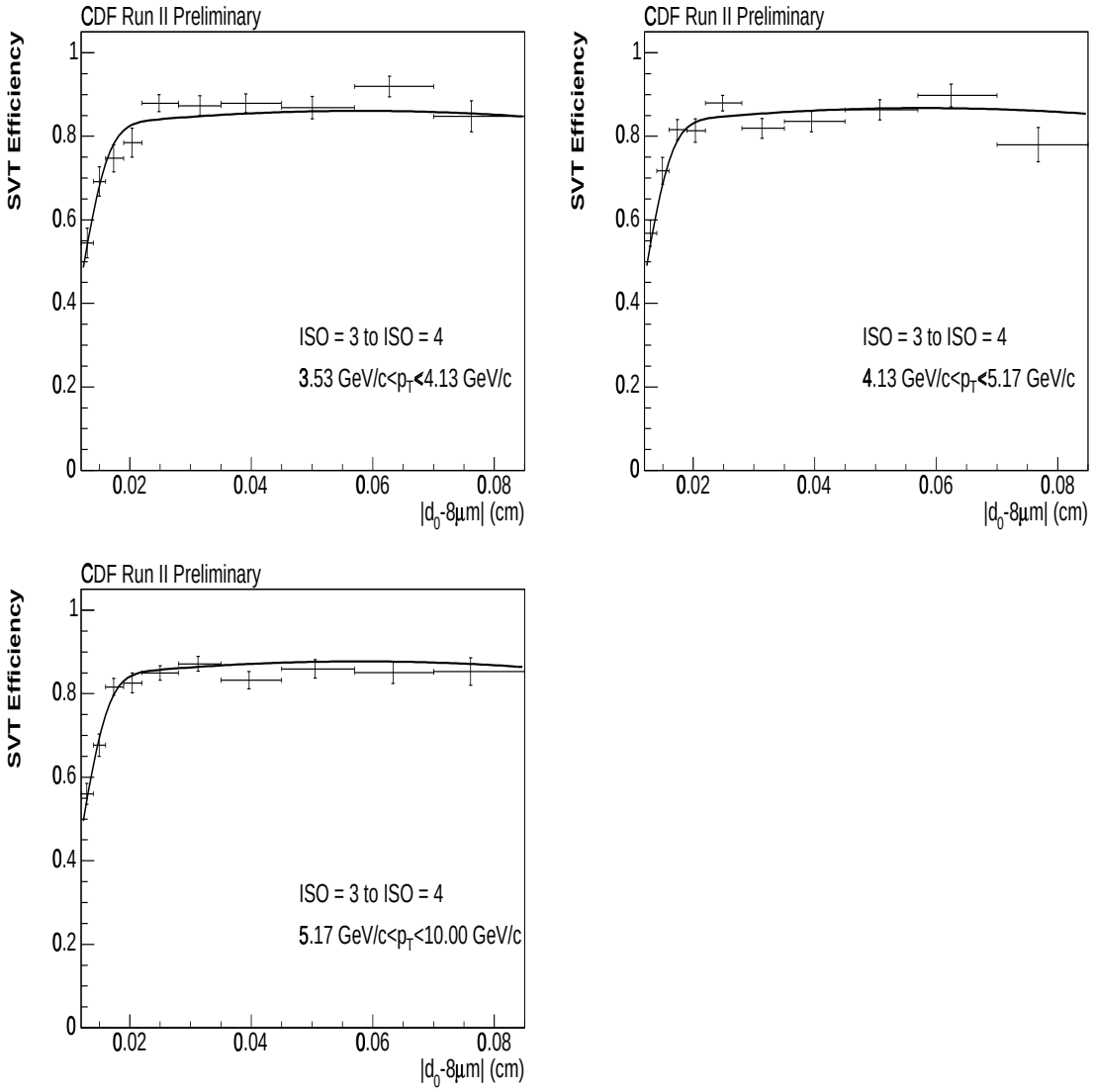

Figure B.12: SVT efficiency vs. $|d_0 - 8\mu\text{m}|$ for various slices of transverse momentum for tracks with 3 or 4 tracks having $p_T > 400$ MeV/c within $\Delta\phi_{r=8cm} < 5°$ (ISO = 3 or 4). The curves are the one dimensional projections of the three dimensional binned fit to the data. Tracks with $|d_0 - 8\mu\text{m}| > 850$ microns have been excluded from the fit.

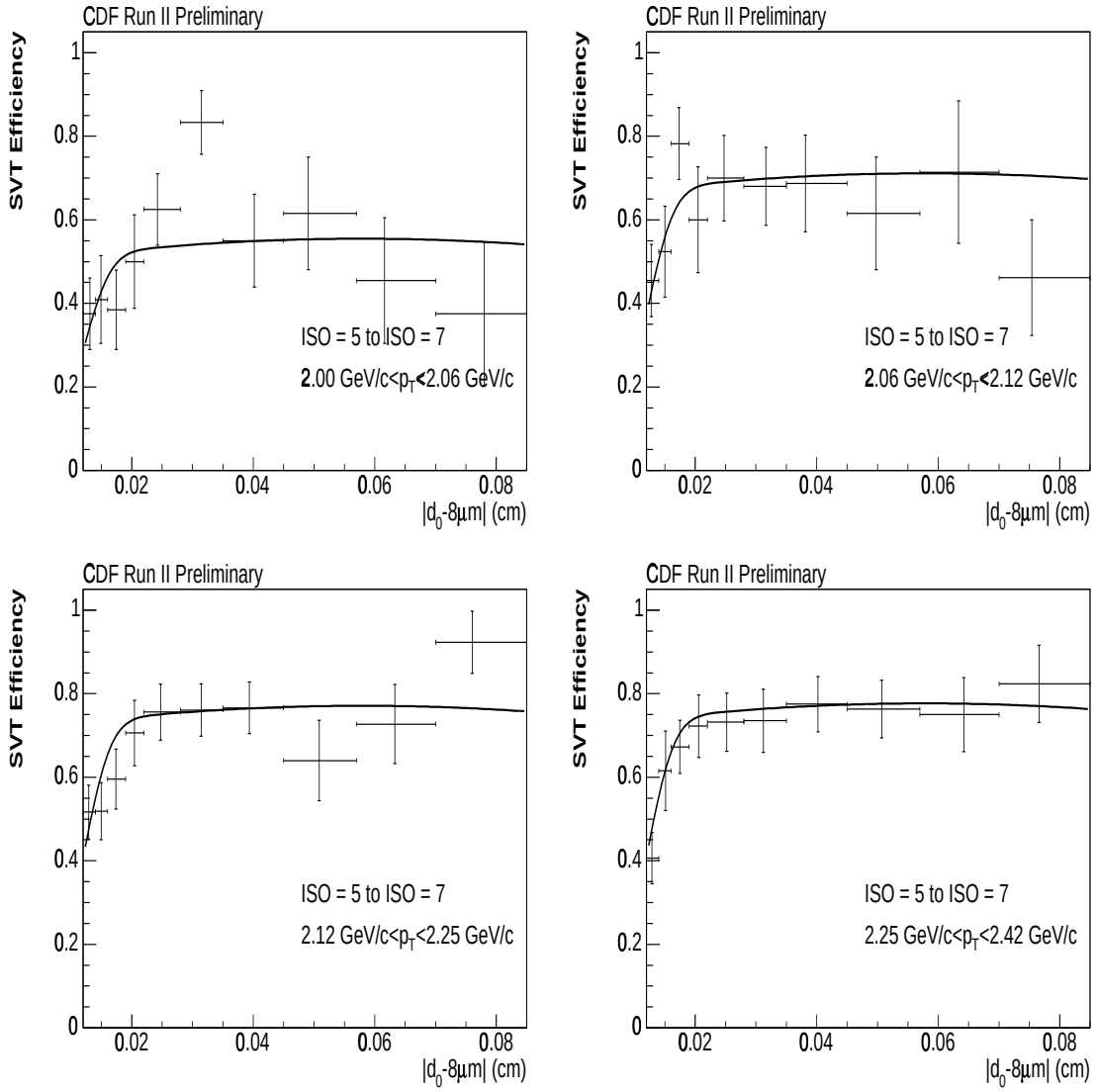

Figure B.13: SVT efficiency vs. $|d_0 - 8\mu\text{m}|$ for various slices of transverse momentum for tracks with 5, 6, or 7 tracks having $p_T > 400$ MeV/c within $\Delta\phi_{r=8cm} < 5°$ (ISO = 5, 6, or 7). The curves are the one dimensional projections of the three dimensional binned fit to the data. Tracks with $|d_0 - 8\mu\text{m}| > 850$ microns have been excluded from the fit.

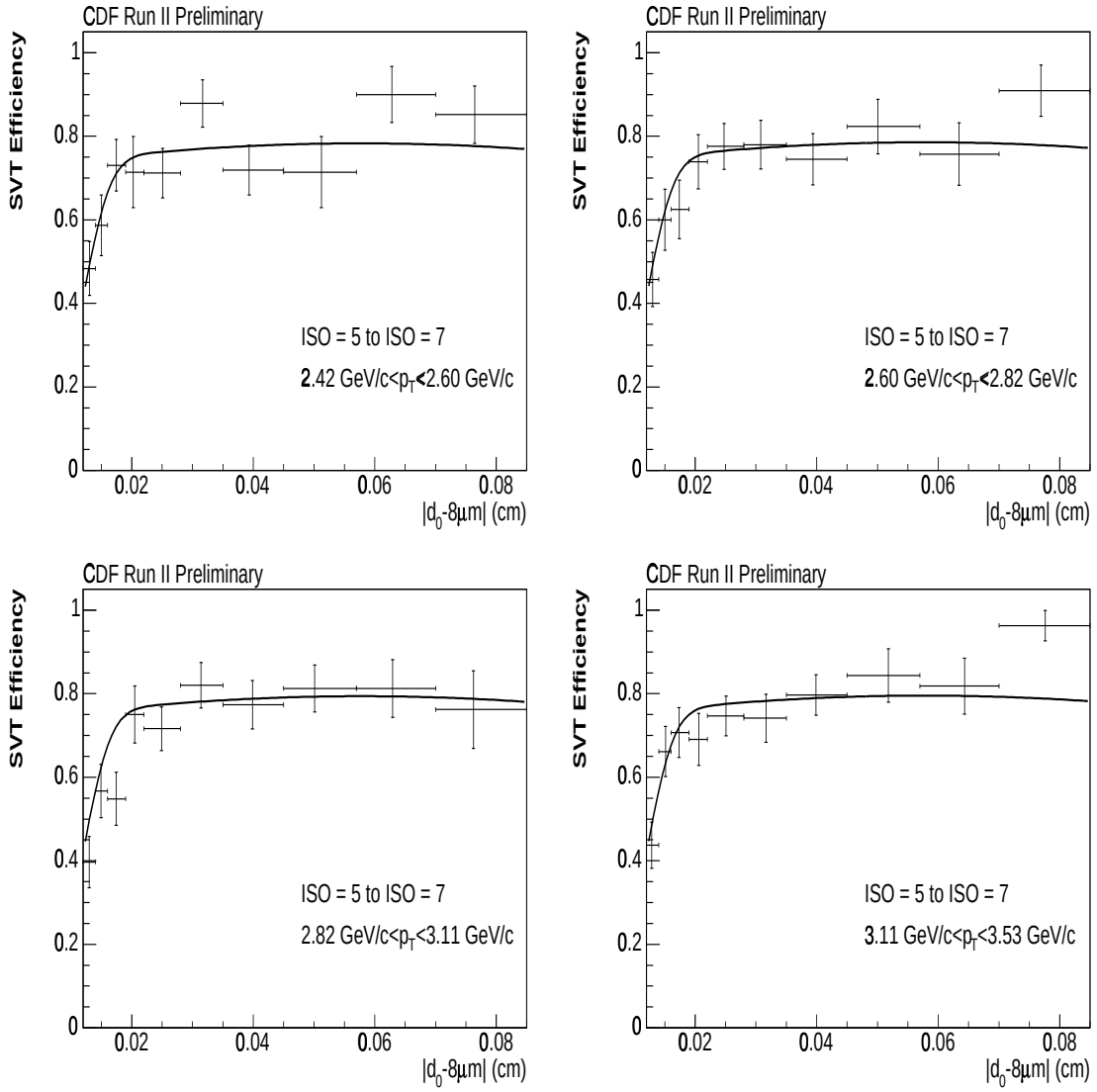

Figure B.14: SVT efficiency vs. $|d_0 - 8\mu\text{m}|$ for various slices of transverse momentum for tracks with 5, 6, or 7 tracks having $p_T > 400$ MeV/c within $\Delta\phi_{r=8cm} < 5°$ (ISO = 5, 6, or 7). The curves are the one dimensional projections of the three dimensional binned fit to the data. Tracks with $|d_0 - 8\mu\text{m}| > 850$ microns have been excluded from the fit.

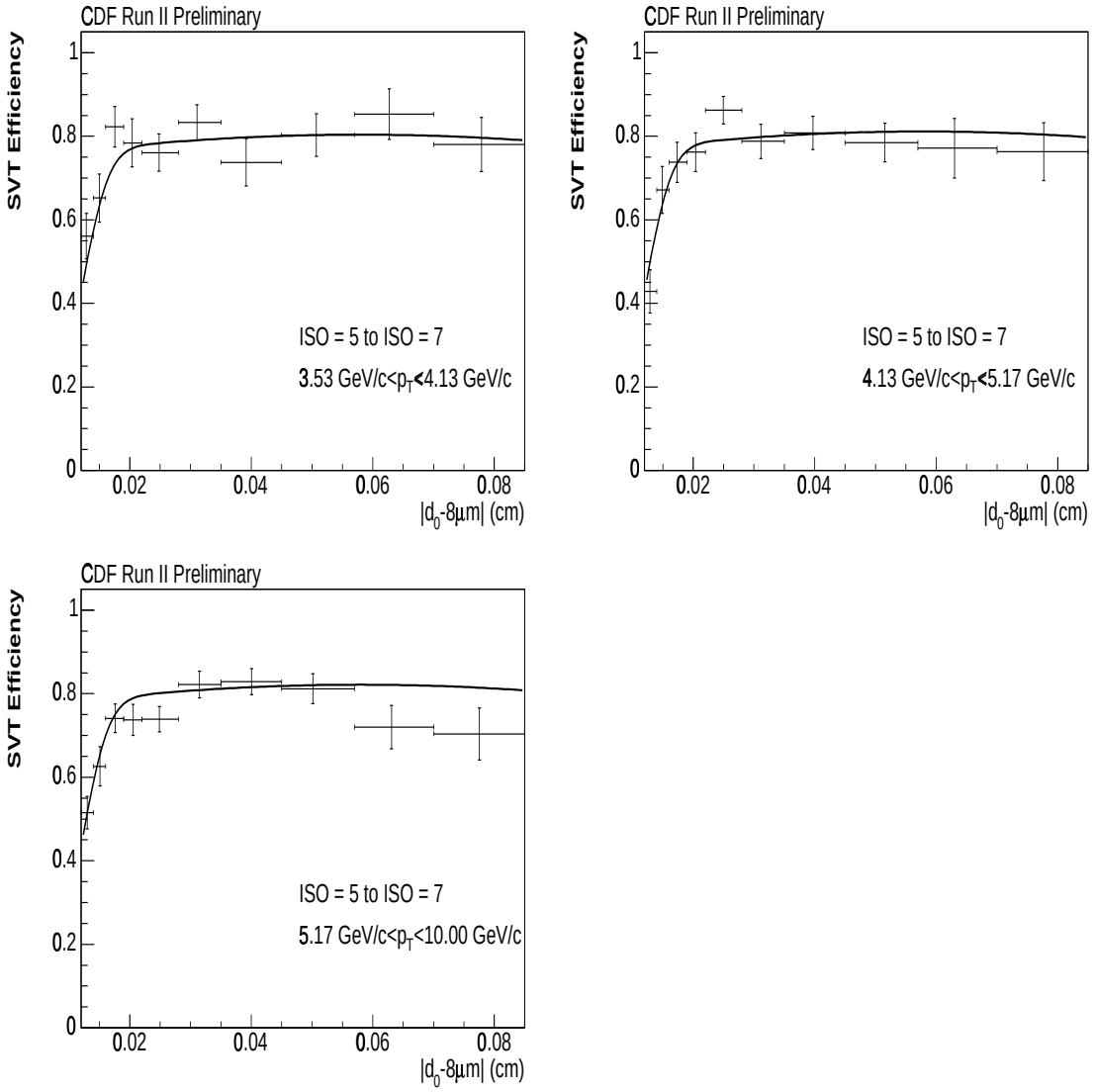

Figure B.15: SVT efficiency vs. $|d_0 - 8\mu\text{m}|$ for various slices of transverse momentum for tracks with 5, 6, or 7 tracks having $p_T > 400$ MeV/c within $\Delta\phi_{r=8cm} < 5°$ (ISO = 5, 6, or 7). The curves are the one dimensional projections of the three dimensional binned fit to the data. Tracks with $|d_0 - 8\mu\text{m}| > 850$ microns have been excluded from the fit.

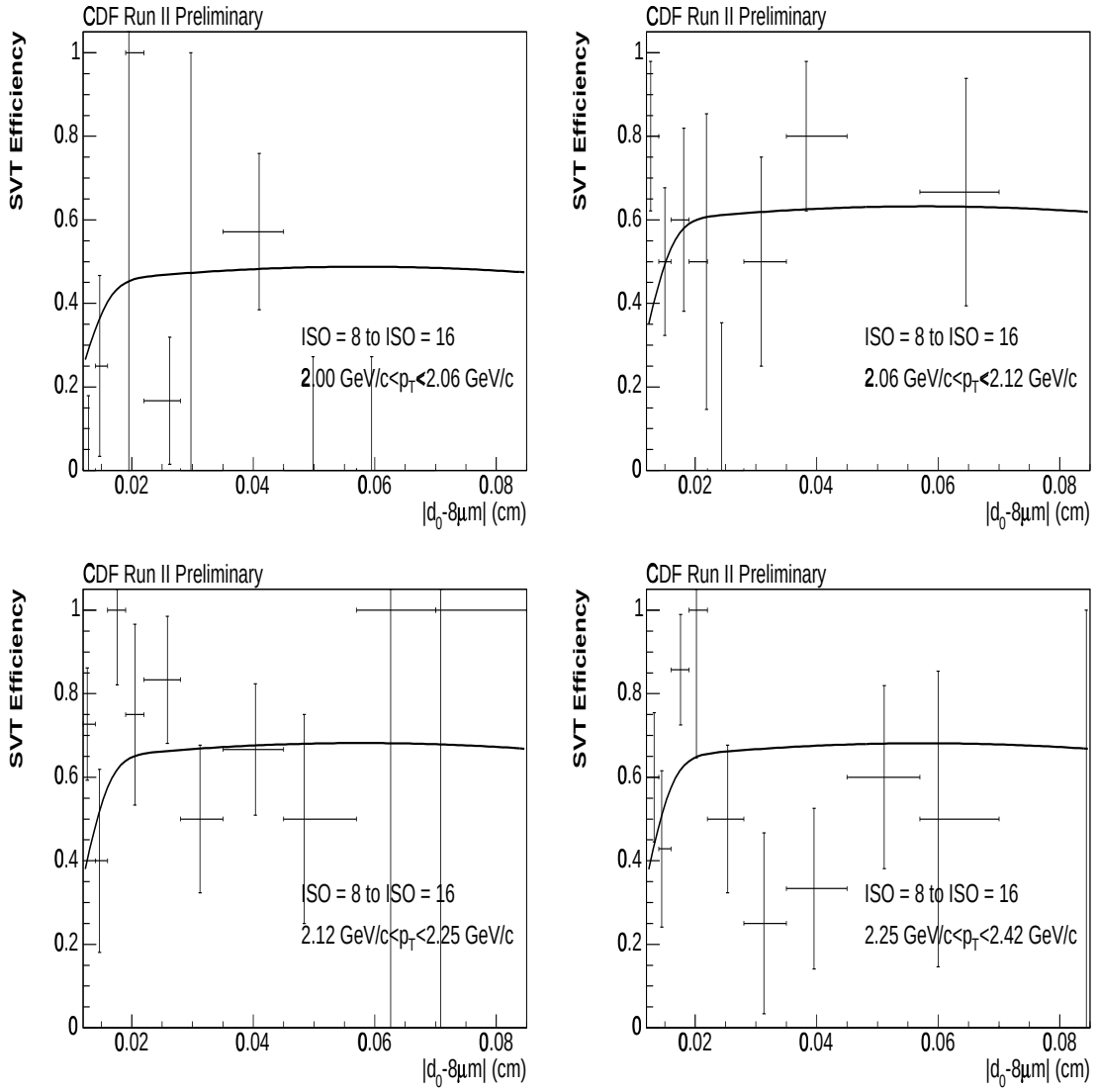

Figure B.16: SVT efficiency vs. $|d_0 - 8\mu\text{m}|$ for various slices of transverse momentum for tracks with 8 to 16 tracks having $p_T > 400$ MeV/c within $\Delta\phi_{r=8cm} < 5°$ (ISO = 8 to 16). The curves are the one dimensional projections of the three dimensional binned fit to the data. Tracks with $|d_0 - 8\mu\text{m}| > 850$ microns have been excluded from the fit.

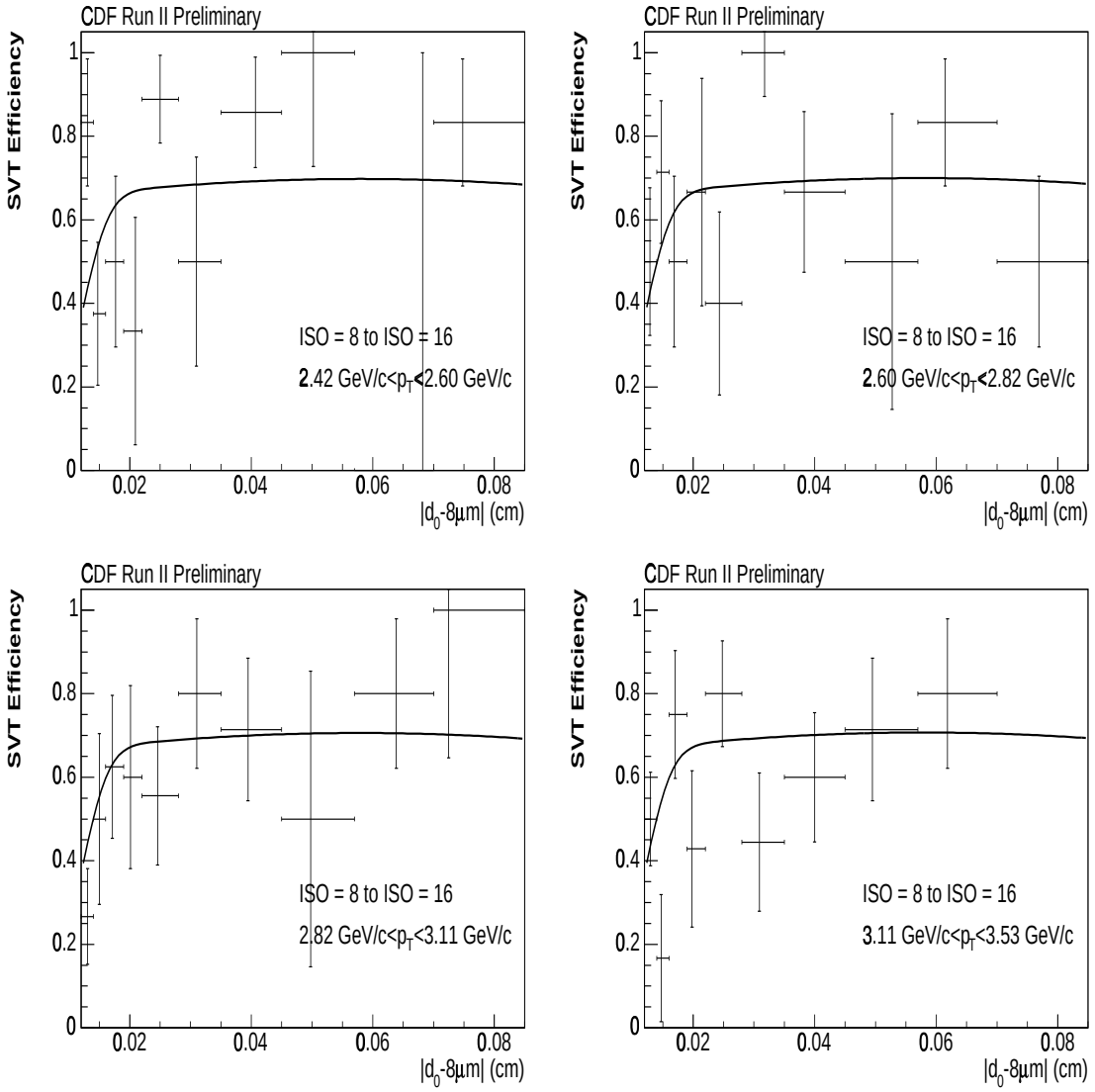

Figure B.17: SVT efficiency vs. $|d_0 - 8\mu\text{m}|$ for various slices of transverse momentum for tracks with 8 to 16 tracks having $p_T > 400$ MeV/c within $\Delta\phi_{r=8cm} < 5°$ (ISO = 8 to 16). The curves are the one dimensional projections of the three dimensional binned fit to the data. Tracks with $|d_0 - 8\mu\text{m}| > 850$ microns have been excluded from the fit.

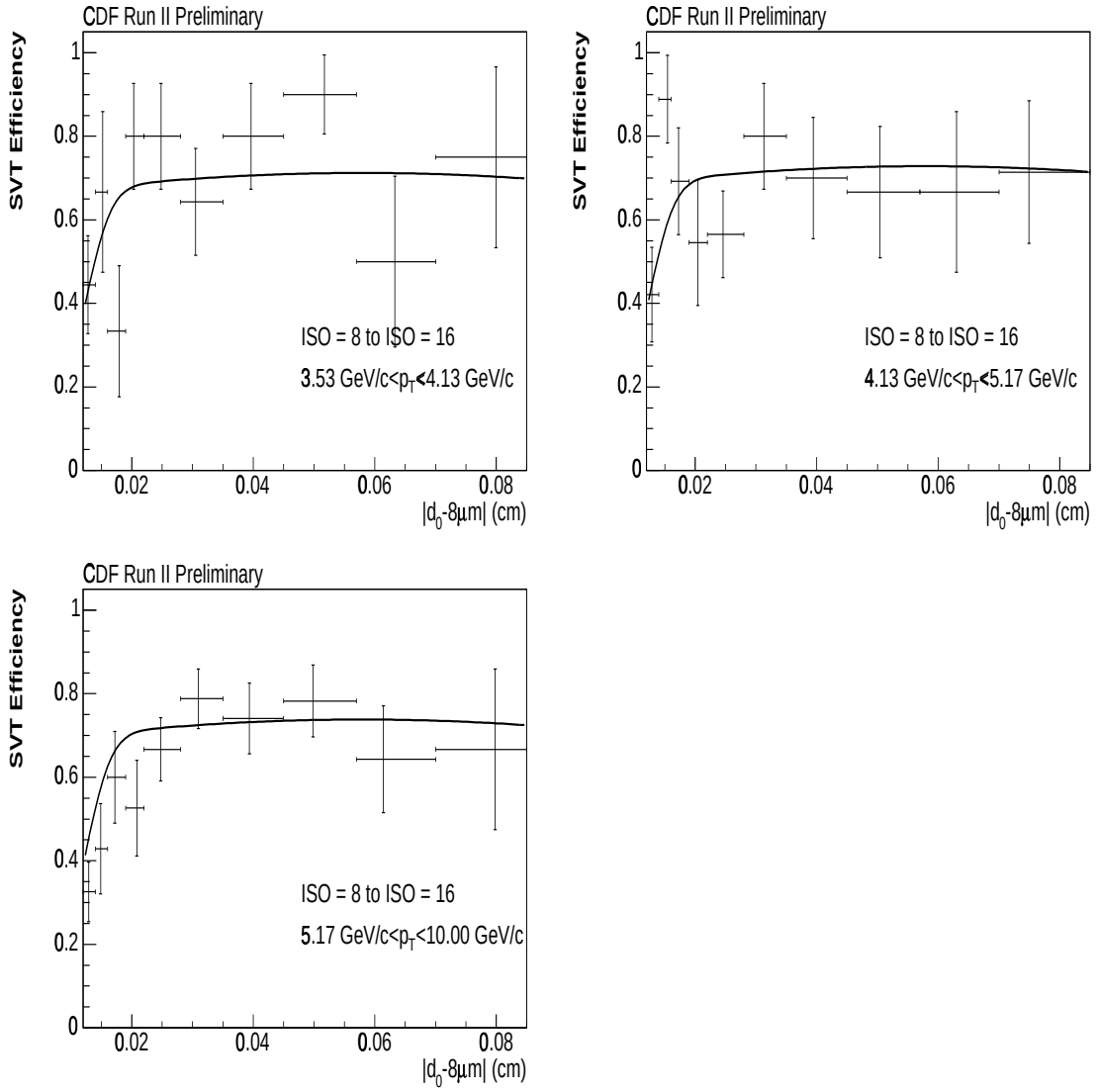

Figure B.18: SVT efficiency vs. $|d_0 - 8\mu\text{m}|$ for various slices of transverse momentum for tracks with 8 to 16 tracks having $p_T > 400$ MeV/c within $\Delta\phi_{r=8cm} < 5°$ (ISO = 8 to 16). The curves are the one dimensional projections of the three dimensional binned fit to the data. Tracks with $|d_0 - 8\mu\text{m}| > 850$ microns have been excluded from the fit.

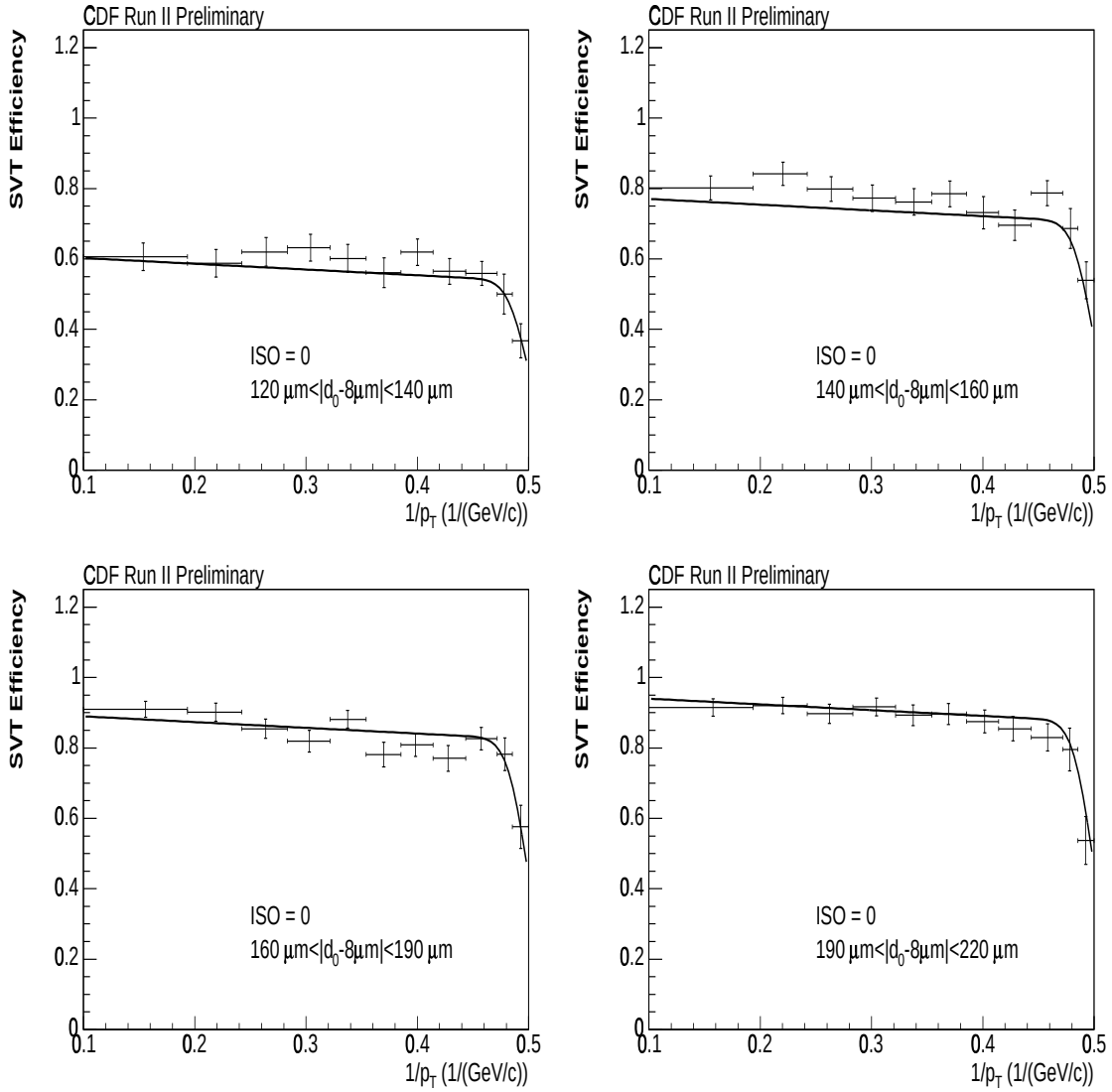

Figure B.19: SVT efficiency vs. $1/|p_T|$ for various slices of impact parameter for tracks with no tracks having $p_T > 400$ MeV/c within $\Delta\phi_{r=8cm} < 5°$ (ISO = 0). The curves are the one dimensional projections of the three dimensional binned fit to the data. Tracks with $|d_0 - 8\mu\text{m}| > 850$ microns have been excluded from the fit.

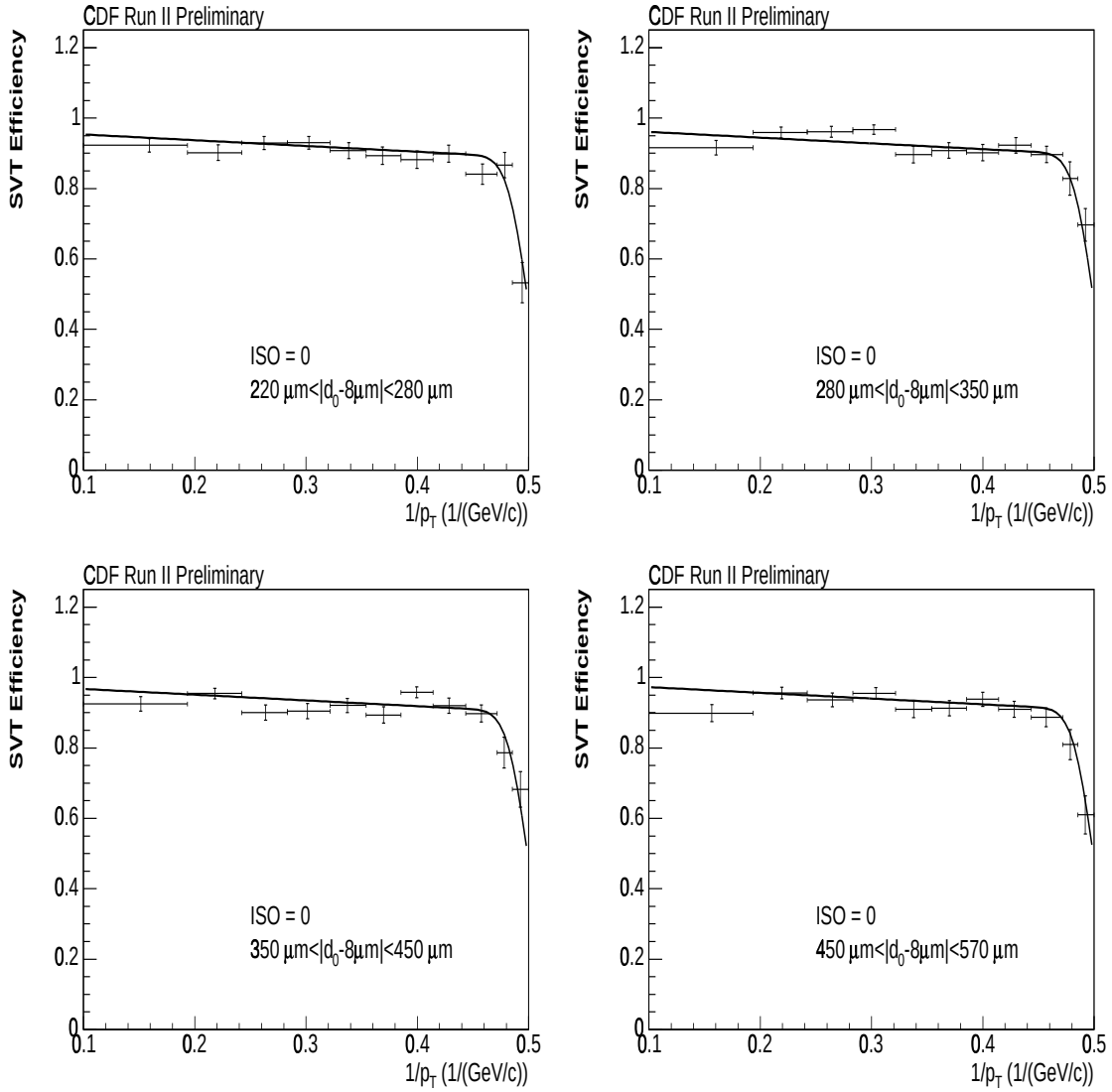

Figure B.20: SVT efficiency vs. $1/|p_T|$ for various slices of impact parameter for tracks with no tracks having $p_T > 400$ MeV/c within $\Delta\phi_{r=8cm} < 5^\circ$ (ISO = 0). The curves are the one dimensional projections of the three dimensional binned fit to the data. Tracks with $|d_0 - 8\mu\text{m}| > 850$ microns have been excluded from the fit.

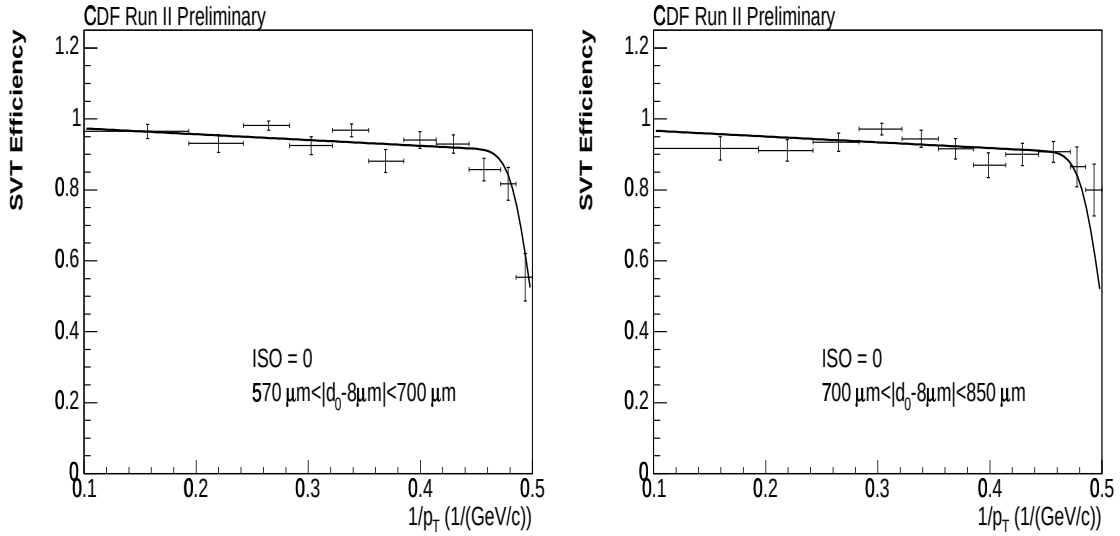

Figure B.21: SVT efficiency vs. $1/|p_T|$ for various slices of impact parameter for tracks with no tracks having $p_T > 400$ MeV/c within $\Delta\phi_{r=8cm} < 5°$ (ISO = 0). The curves are the one dimensional projections of the three dimensional binned fit to the data. Tracks with $|d_0 - 8\mu\text{m}| > 850$ microns have been excluded from the fit.

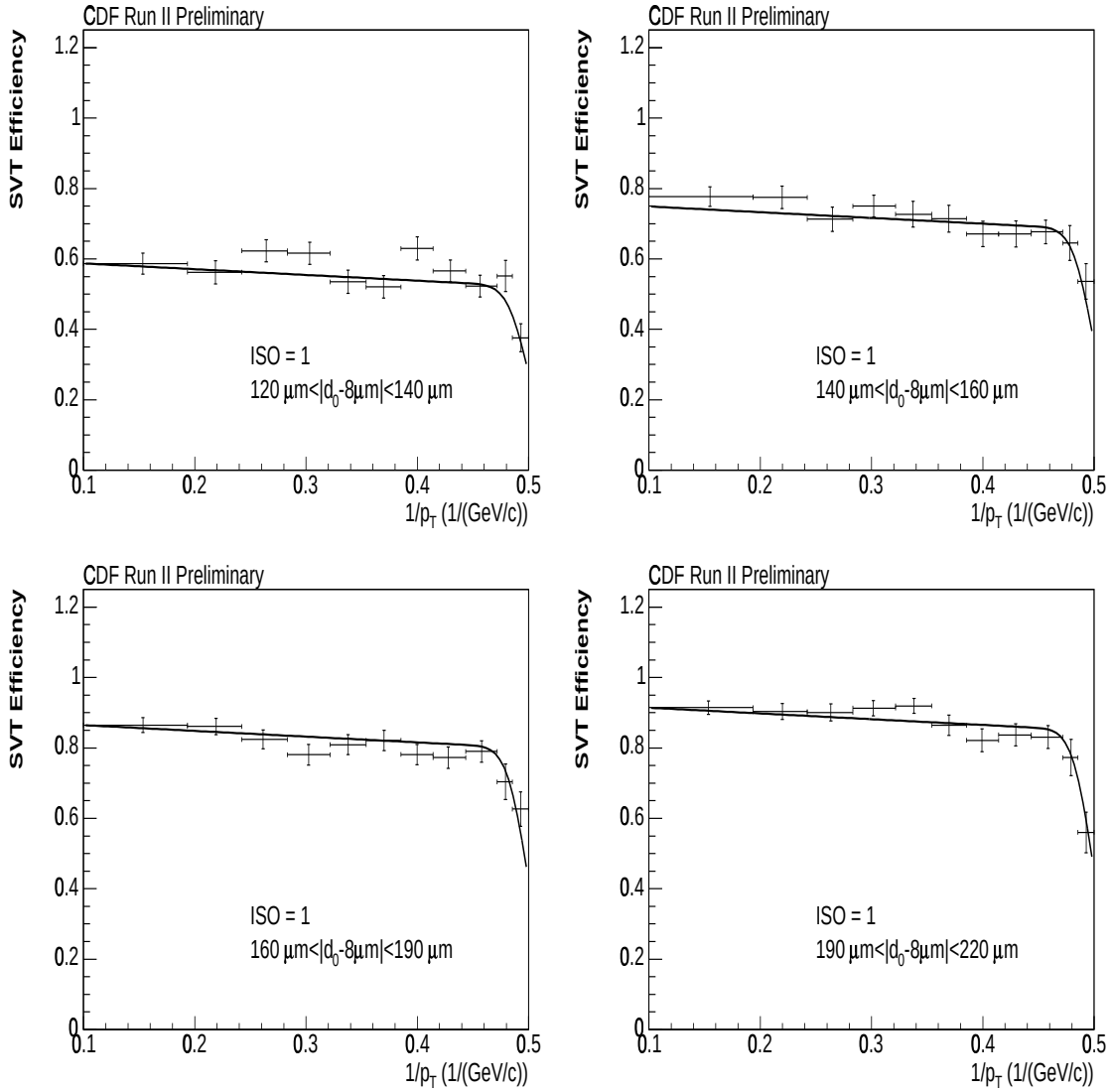

Figure B.22: SVT efficiency vs. $1/|p_T|$ for various slices of impact parameter for tracks with 1 track having $p_T > 400$ MeV/c within $\Delta\phi_{r=8cm} < 5°$ (ISO = 1). The curves are the one dimensional projections of the three dimensional binned fit to the data. Tracks with $|d_0 - 8\mu\text{m}| > 850$ microns have been excluded from the fit.

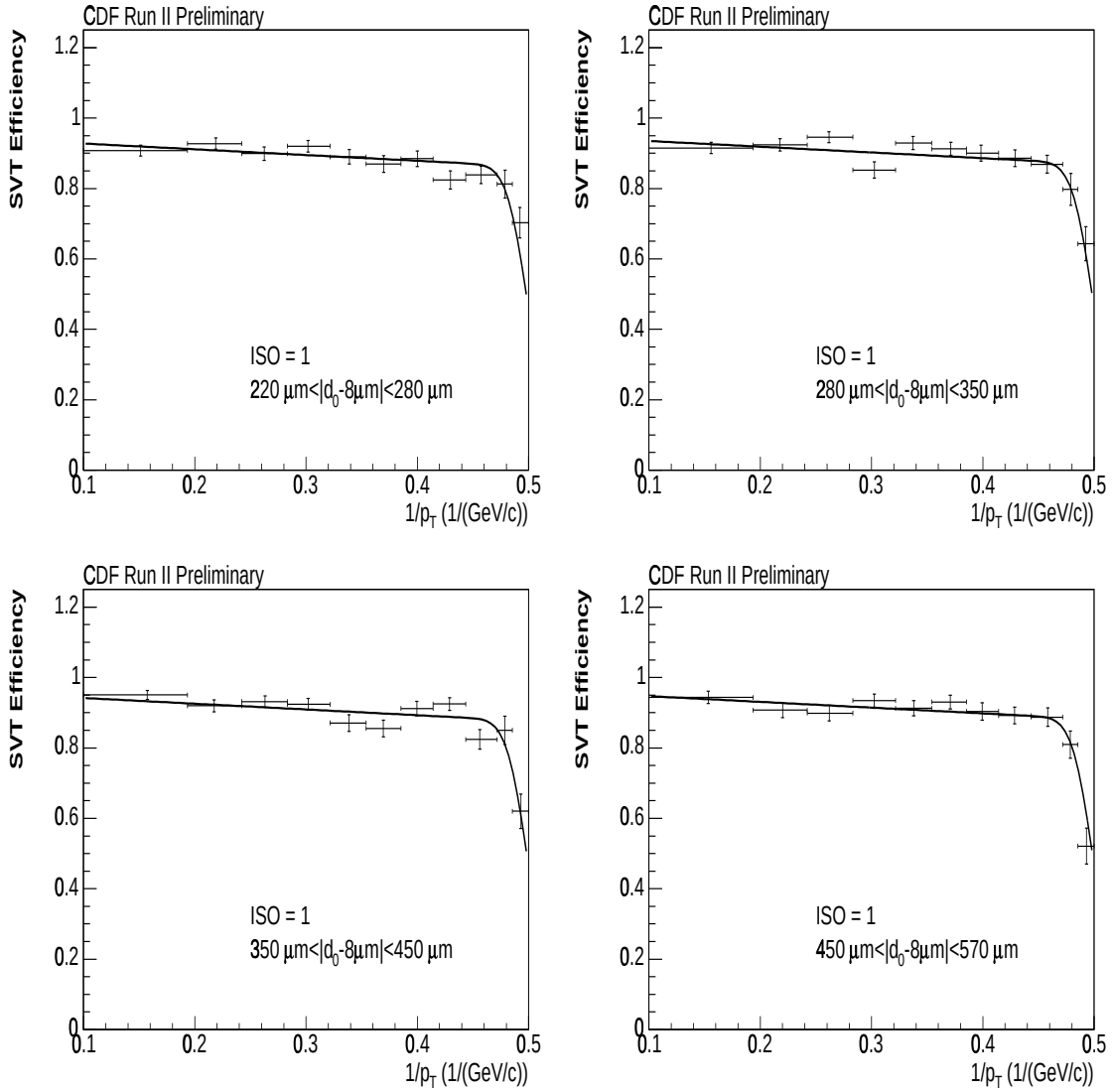

Figure B.23: SVT efficiency vs. $1/|p_T|$ for various slices of impact parameter for tracks with 1 track having $p_T > 400$ MeV/c within $\Delta\phi_{r=8cm} < 5°$ (ISO = 1). The curves are the one dimensional projections of the three dimensional binned fit to the data. Tracks with $|d_0 - 8\mu\text{m}| > 850$ microns have been excluded from the fit.

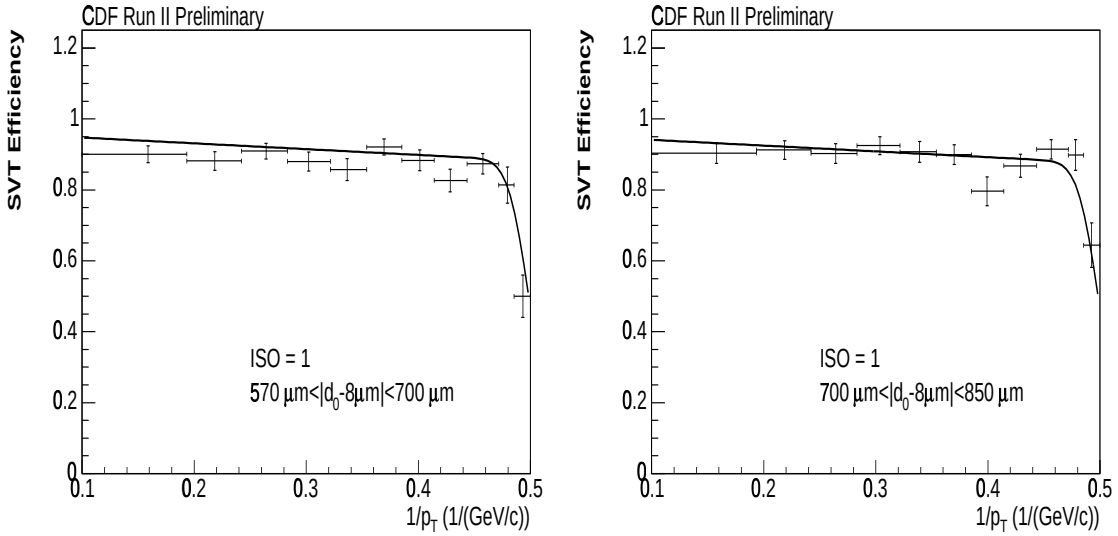

Figure B.24: SVT efficiency vs. $1/|p_T|$ for various slices of impact parameter for tracks with 1 track having $p_T > 400$ MeV/c within $\Delta\phi_{r=8cm} < 5°$ (ISO = 1). The curves are the one dimensional projections of the three dimensional binned fit to the data. Tracks with $|d_0 - 8\mu\text{m}| > 850$ microns have been excluded from the fit.

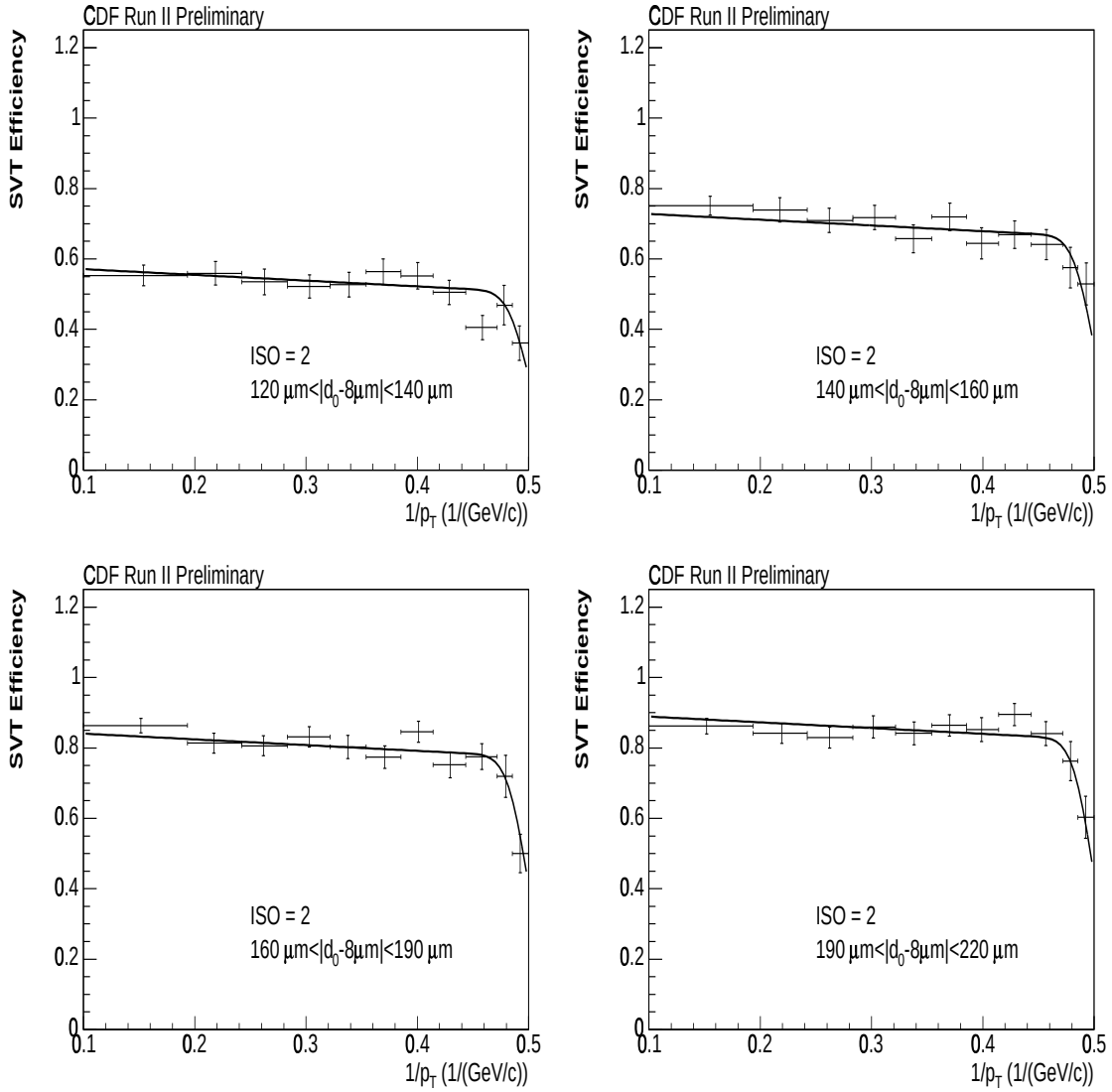

Figure B.25: SVT efficiency vs. $1/|p_T|$ for various slices of impact parameter for tracks with 2 tracks having $p_T > 400$ MeV/c within $\Delta\phi_{r=8cm} < 5°$ (ISO = 2). The curves are the one dimensional projections of the three dimensional binned fit to the data. Tracks with $|d_0 - 8\mu\text{m}| > 850$ microns have been excluded from the fit.

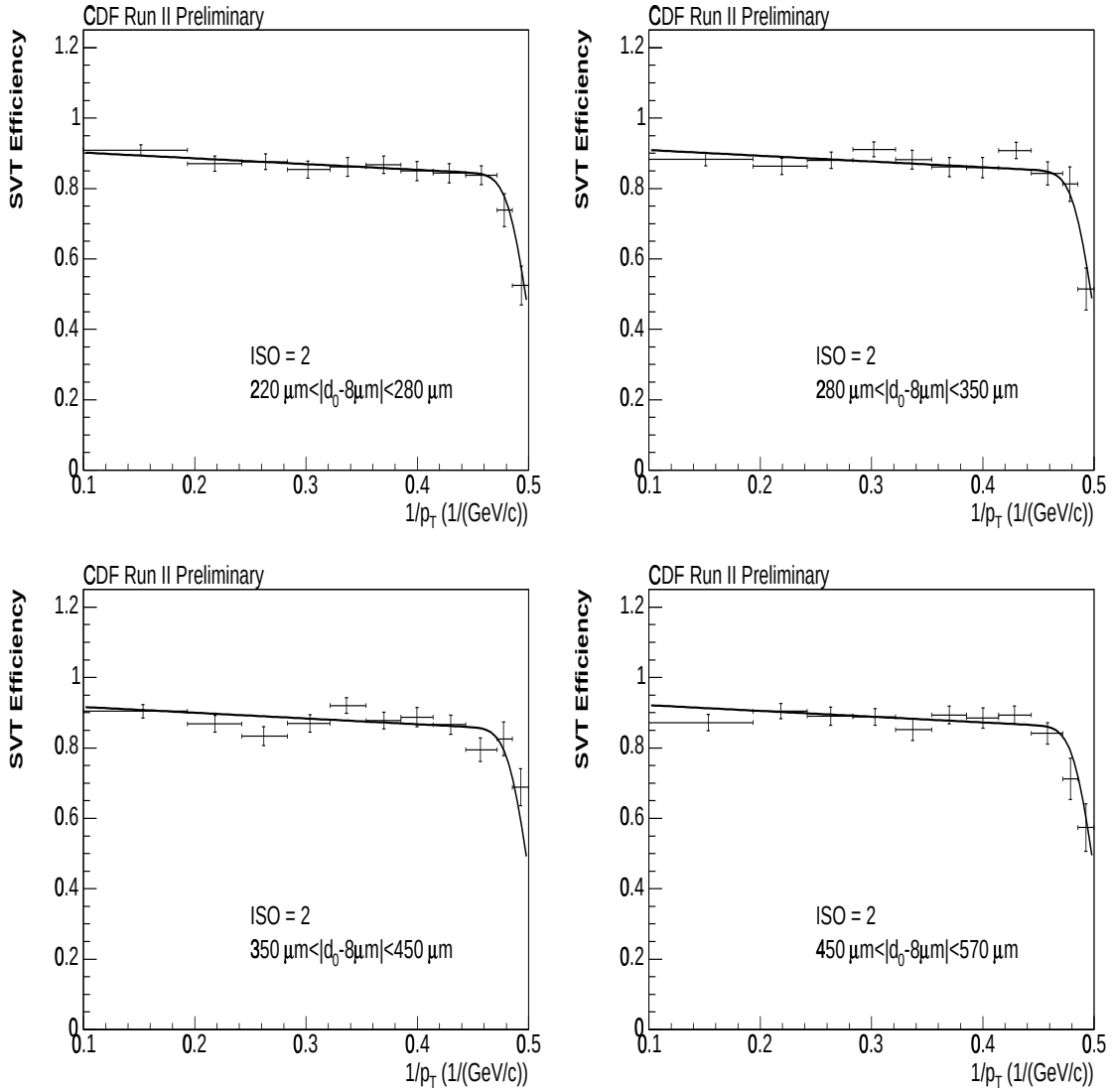

Figure B.26: SVT efficiency vs. $1/|p_T|$ for various slices of impact parameter for tracks with 2 tracks having $p_T > 400$ MeV/c within $\Delta\phi_{r=8cm} < 5°$ (ISO = 2). The curves are the one dimensional projections of the three dimensional binned fit to the data. Tracks with $|d_0 - 8\mu\text{m}| > 850$ microns have been excluded from the fit.

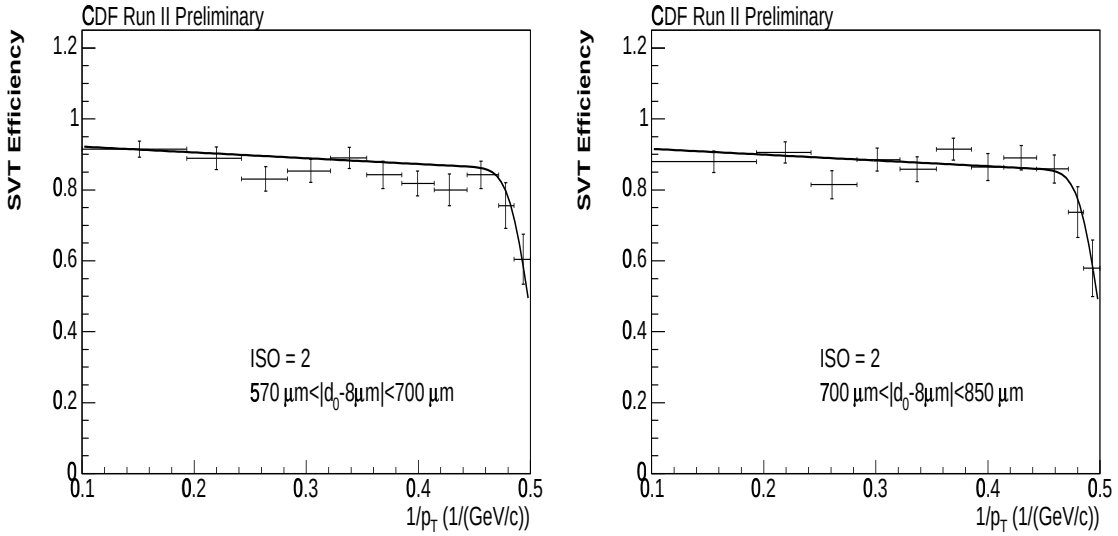

Figure B.27: SVT efficiency vs. $1/|p_T|$ for various slices of impact parameter for tracks with 2 tracks having $p_T > 400$ MeV/c within $\Delta\phi_{r=8cm} < 5°$ (ISO = 2). The curves are the one dimensional projections of the three dimensional binned fit to the data. Tracks with $|d_0 - 8\mu\text{m}| > 850$ microns have been excluded from the fit.

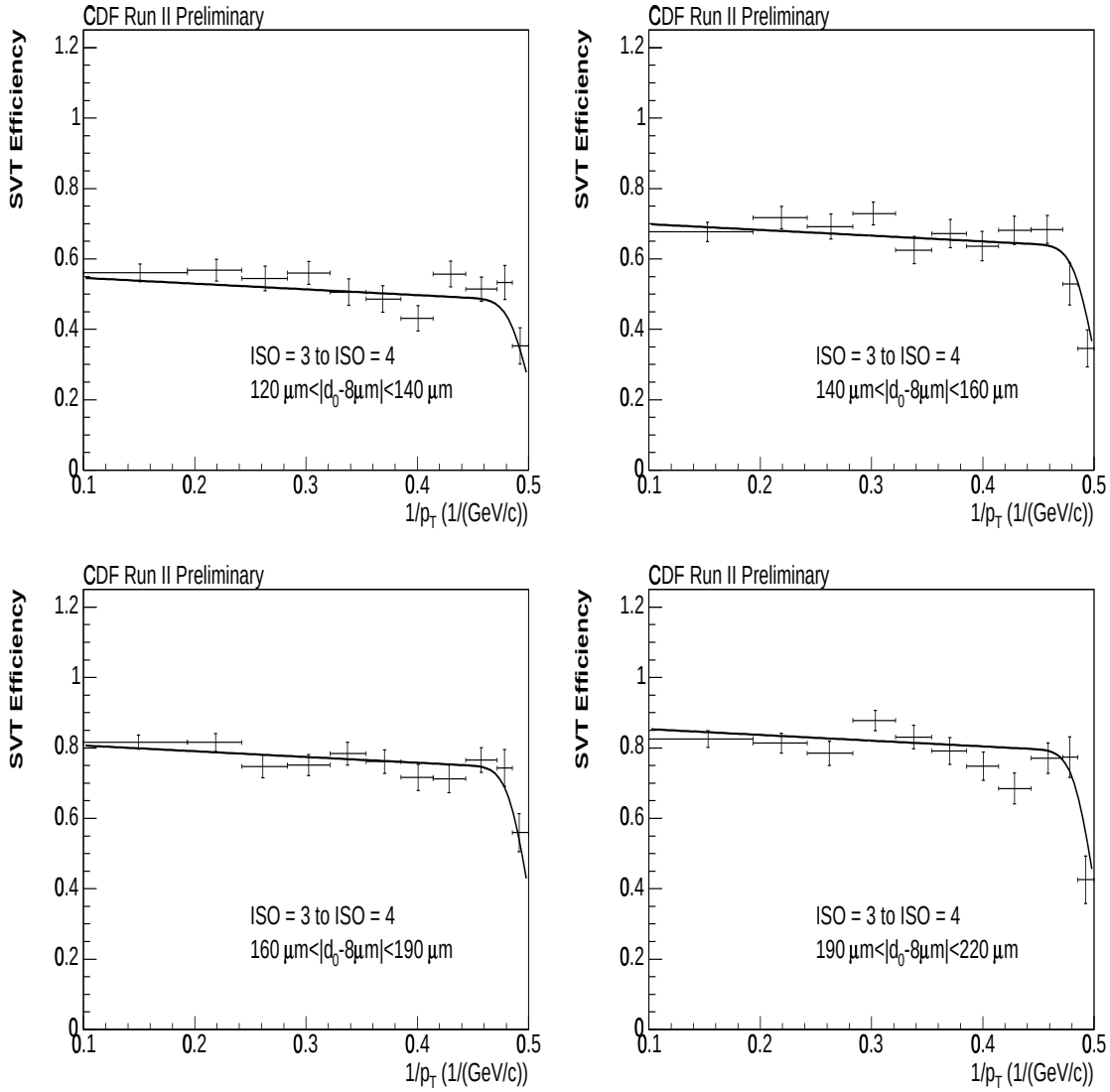

Figure B.28: SVT efficiency vs. $1/|p_T|$ for various slices of impact parameter for tracks with 3 or 4 tracks having $p_T > 400$ MeV/c within $\Delta\phi_{r=8cm} < 5°$ (ISO = 3 or 4). The curves are the one dimensional projections of the three dimensional binned fit to the data. Tracks with $|d_0 - 8\mu\text{m}| > 850$ microns have been excluded from the fit.

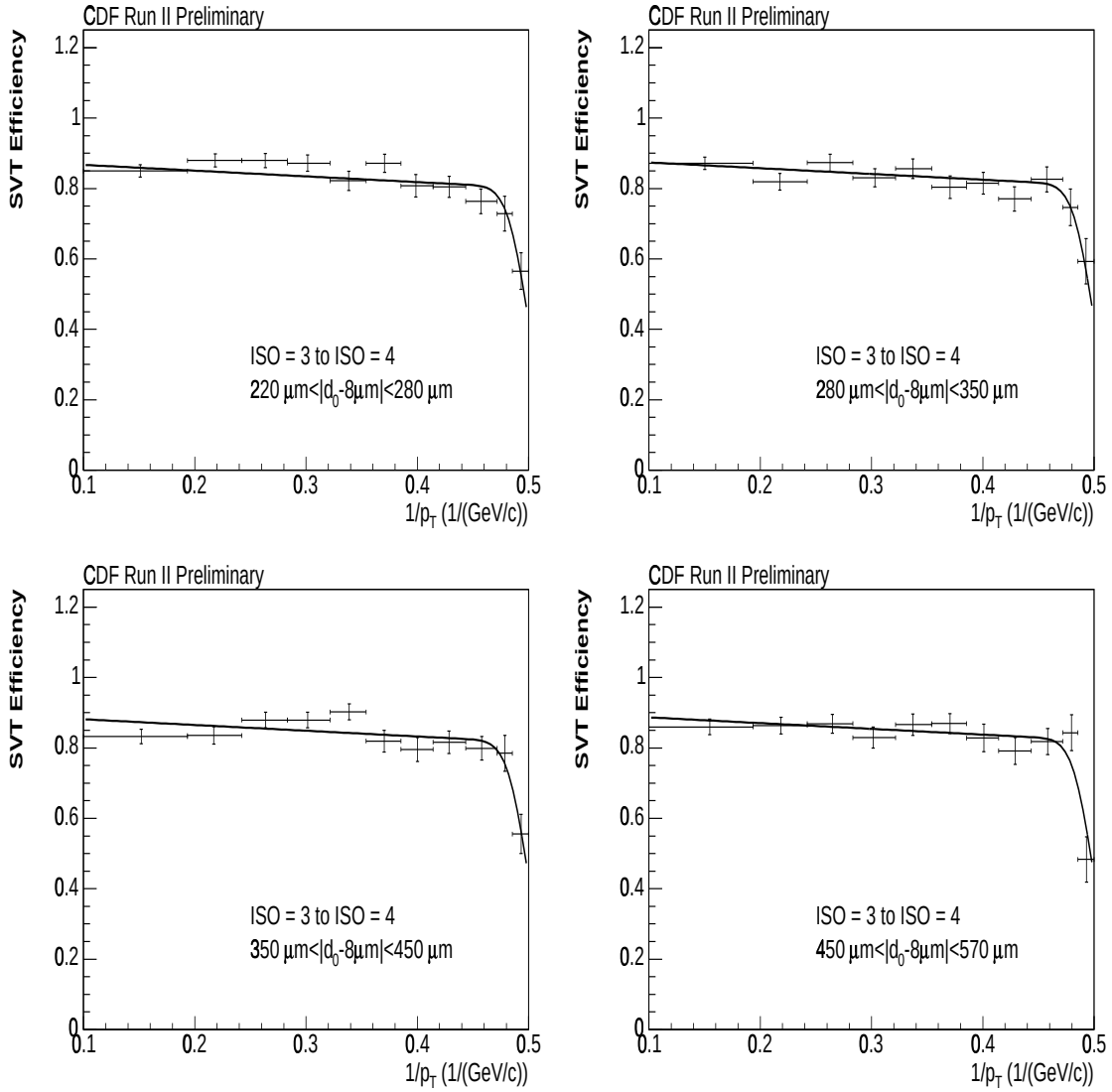

Figure B.29: SVT efficiency vs. $1/|p_T|$ for various slices of impact parameter for tracks with 3 or 4 tracks having $p_T > 400$ MeV/c within $\Delta\phi_{r=8cm} < 5°$ (ISO = 3 or 4). The curves are the one dimensional projections of the three dimensional binned fit to the data. Tracks with $|d_0 - 8\mu\text{m}| > 850$ microns have been excluded from the fit.

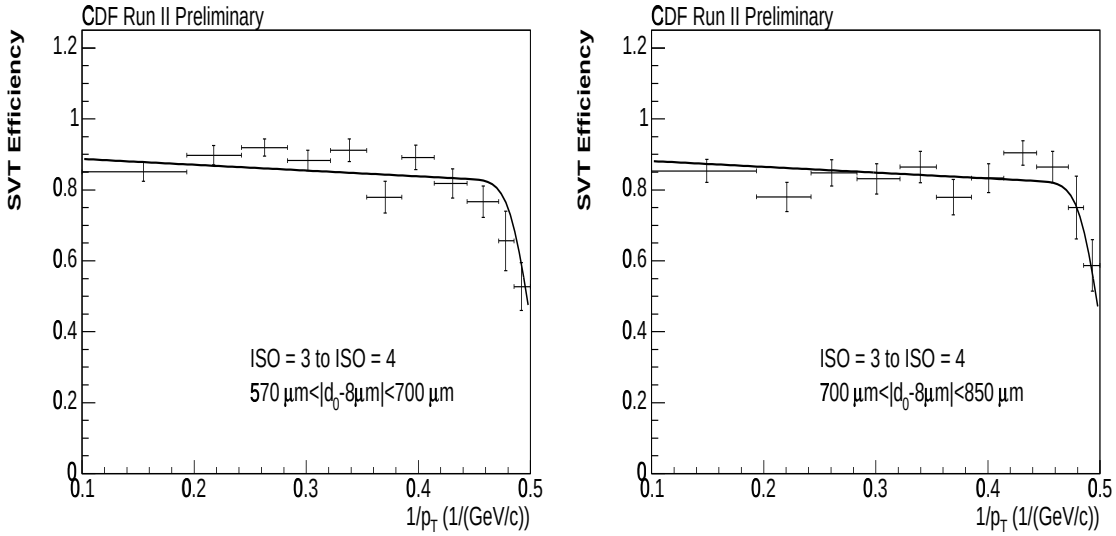

Figure B.30: SVT efficiency vs. $1/|p_T|$ for various slices of impact parameter for tracks with 3 or 4 tracks having $p_T > 400$ MeV/c within $\Delta\phi_{r=8cm} < 5°$ (ISO = 3 or 4). The curves are the one dimensional projections of the three dimensional binned fit to the data. Tracks with $|d_0 - 8\mu\text{m}| > 850$ microns have been excluded from the fit.

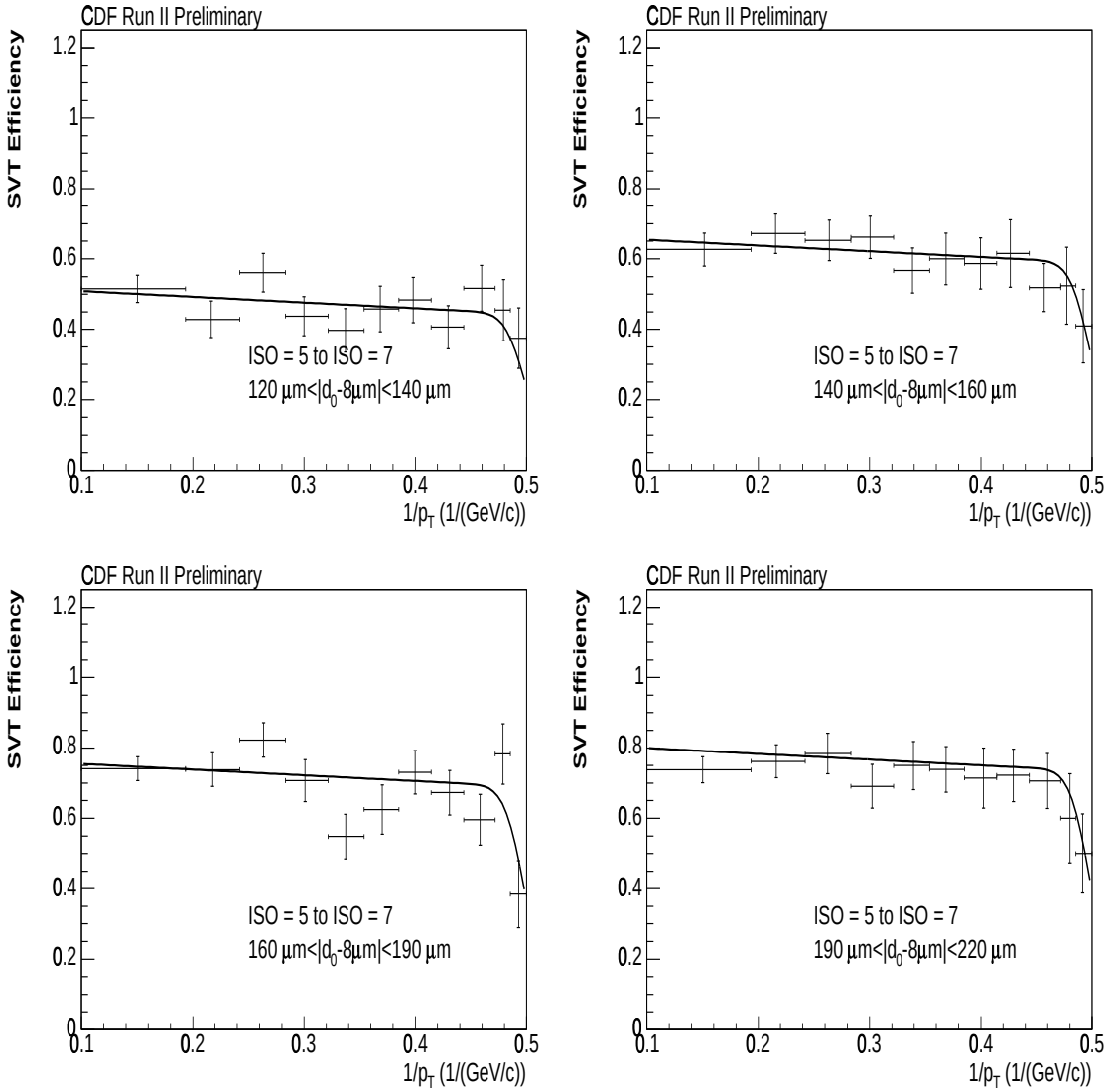

Figure B.31: SVT efficiency vs. $1/|p_T|$ for various slices of impact parameter for tracks with 5, 6, or 7 tracks having $p_T > 400$ MeV/c within $\Delta\phi_{r=8cm} < 5°$ (ISO = 5, 6, or 7). The curves are the one dimensional projections of the three dimensional binned fit to the data. Tracks with $|d_0 - 8\mu\text{m}| > 850$ microns have been excluded from the fit.

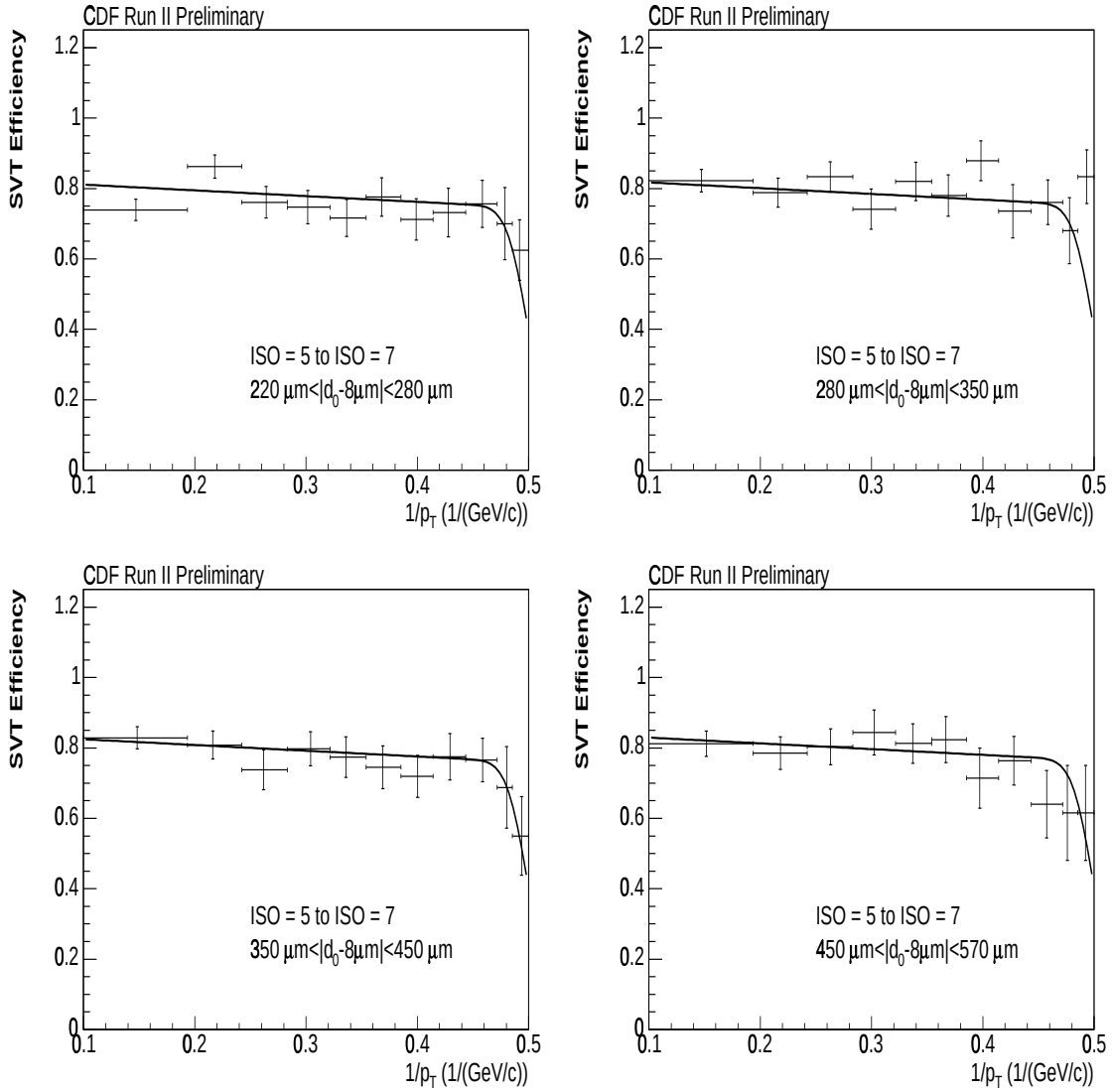

Figure B.32: SVT efficiency vs. $1/|p_T|$ for various slices of impact parameter for tracks with 5, 6, or 7 tracks having $p_T > 400$ MeV/c within $\Delta\phi_{r=8cm} < 5°$ (ISO = 5, 6, or 7). The curves are the one dimensional projections of the three dimensional binned fit to the data. Tracks with $|d_0 - 8\mu\text{m}| > 850$ microns have been excluded from the fit.

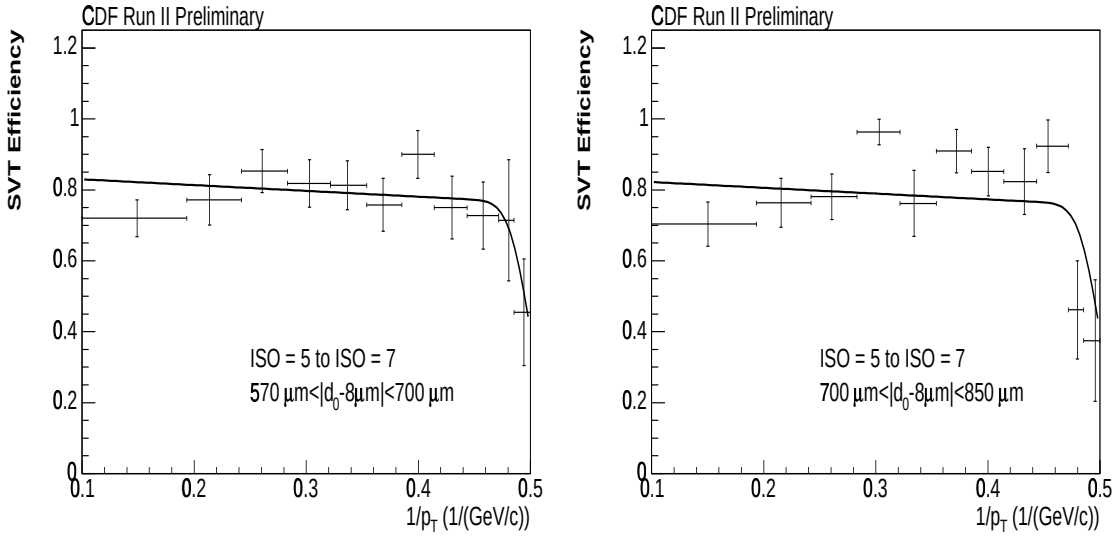

Figure B.33: SVT efficiency vs. $1/|p_T|$ for various slices of impact parameter for tracks with 5, 6, or 7 tracks having $p_T > 400$ MeV/c within $\Delta\phi_{r=8cm} < 5°$ (ISO = 5, 6, or 7). The curves are the one dimensional projections of the three dimensional binned fit to the data. Tracks with $|d_0 - 8\mu\text{m}| > 850$ microns have been excluded from the fit.

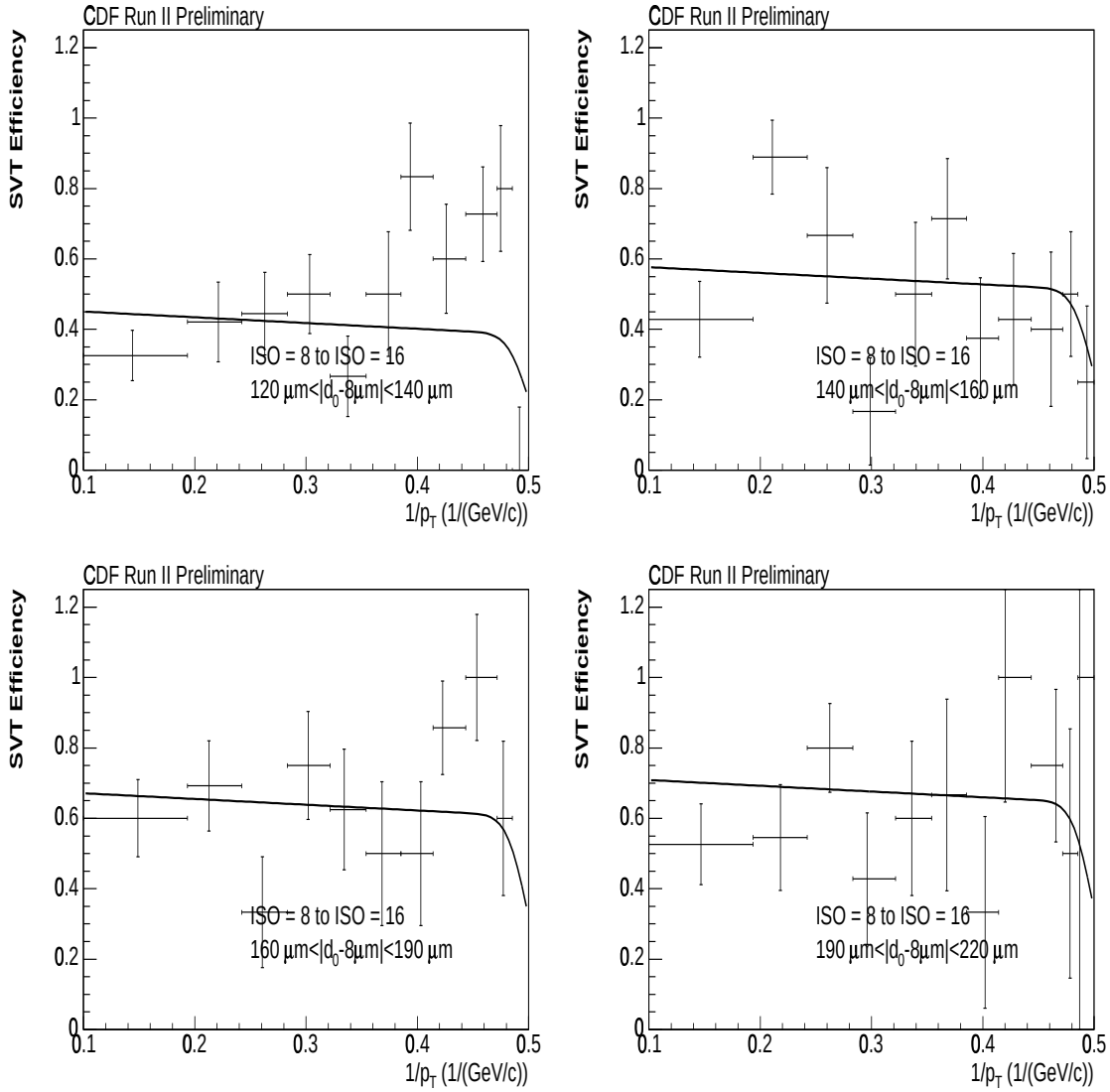

Figure B.34: SVT efficiency vs. $1/|p_T|$ for various slices of impact parameter for tracks with 8 to 16 tracks having $p_T > 400$ MeV/c within $\Delta\phi_{r=8cm} < 5°$ (ISO = 8 to 16). The curves are the one dimensional projections of the three dimensional binned fit to the data. Tracks with $|d_0 - 8\mu\text{m}| > 850$ microns have been excluded from the fit.

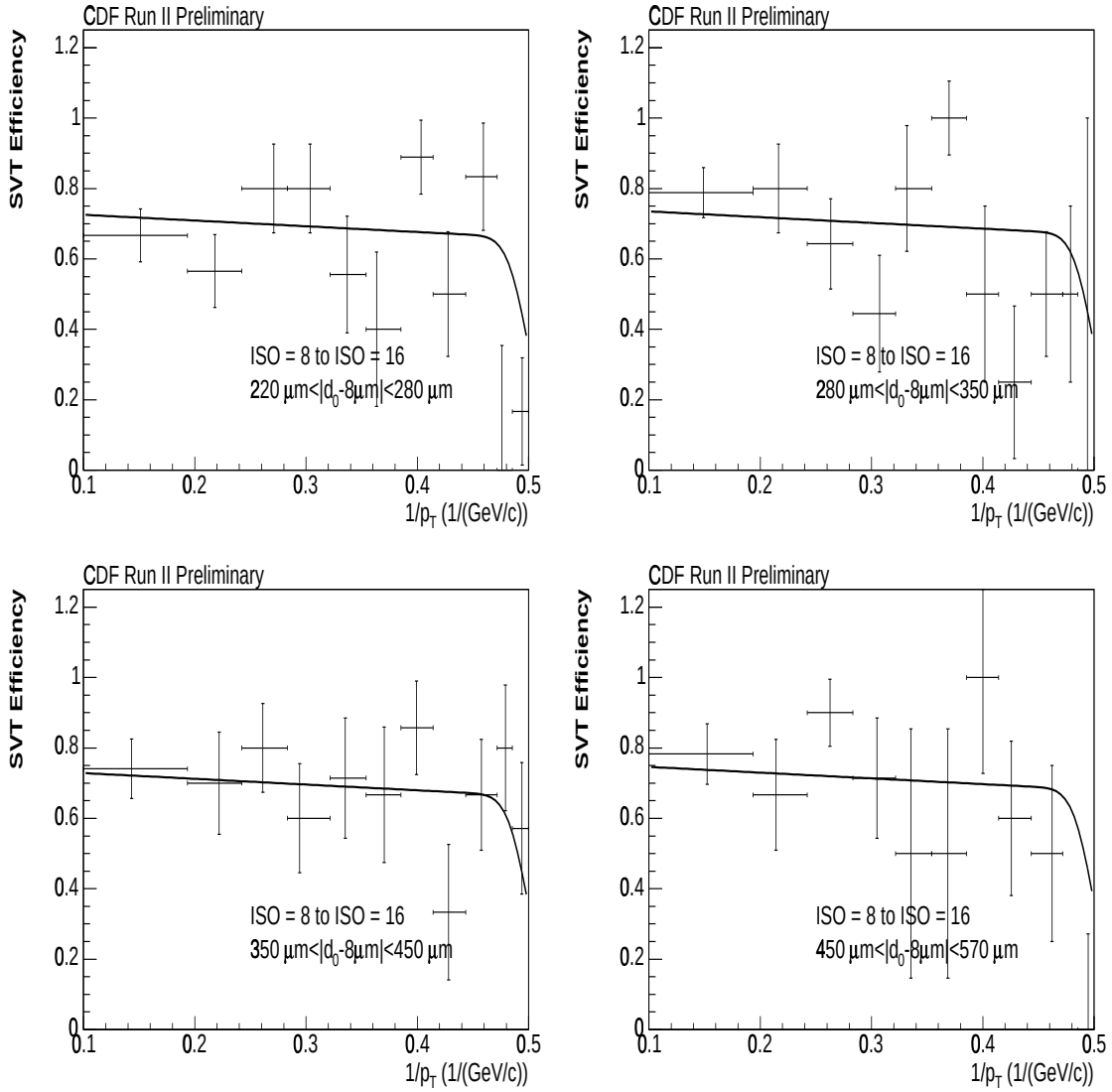

Figure B.35: SVT efficiency vs. $1/|p_T|$ for various slices of impact parameter for tracks with 8 to 16 tracks having $p_T > 400$ MeV/c within $\Delta\phi_{r=8cm} < 5°$ (ISO = 8 to 16). The curves are the one dimensional projections of the three dimensional binned fit to the data. Tracks with $|d_0 - 8\mu\text{m}| > 850$ microns have been excluded from the fit.

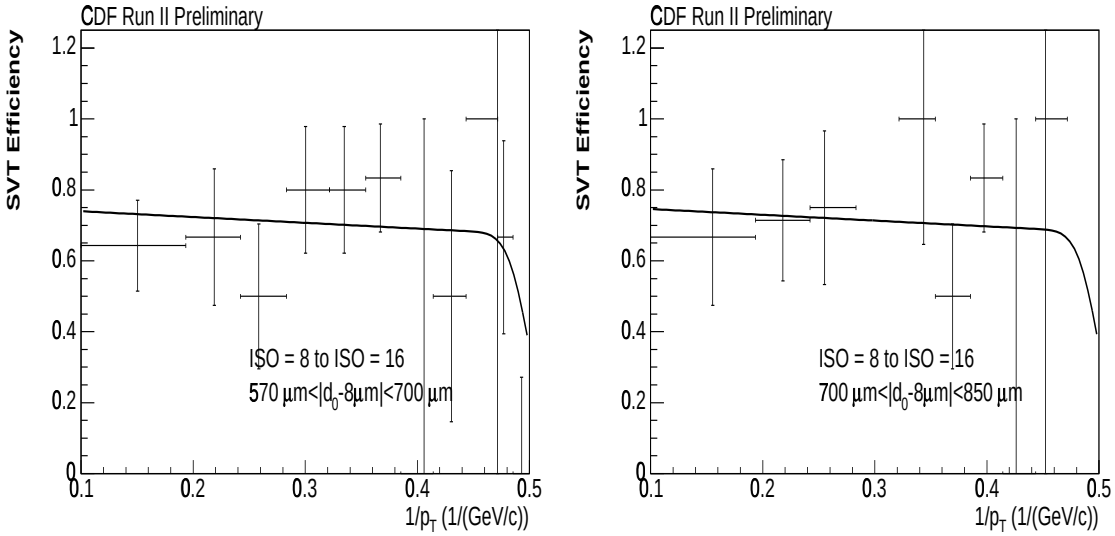

Figure B.36: SVT efficiency vs. $1/|p_T|$ for various slices of impact parameter for tracks with 8 to 16 tracks having $p_T > 400$ MeV/c within $\Delta\phi_{r=8cm} < 5°$ (ISO = 8 to 16). The curves are the one dimensional projections of the three dimensional binned fit to the data. Tracks with $|d_0 - 8\mu\text{m}| > 850$ microns have been excluded from the fit.

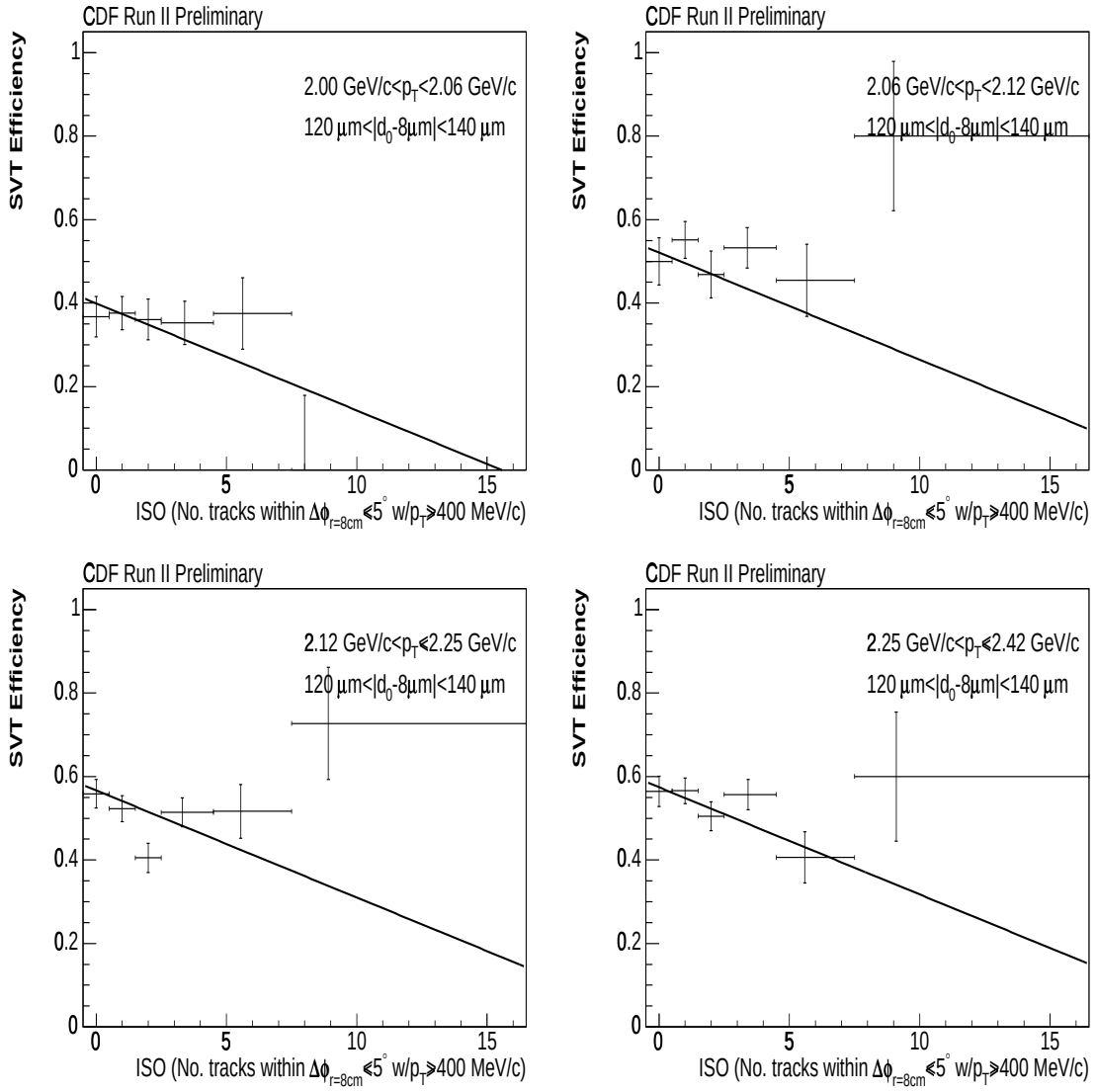

Figure B.37: SVT efficiency vs. ISO for various slices of transverse momentum and impact parameter. The curves are the one dimensional projections of the three dimensional binned fit to the data. Tracks with $|d_0 - 8\mu\text{m}| > 850$ microns have been excluded from the fit.

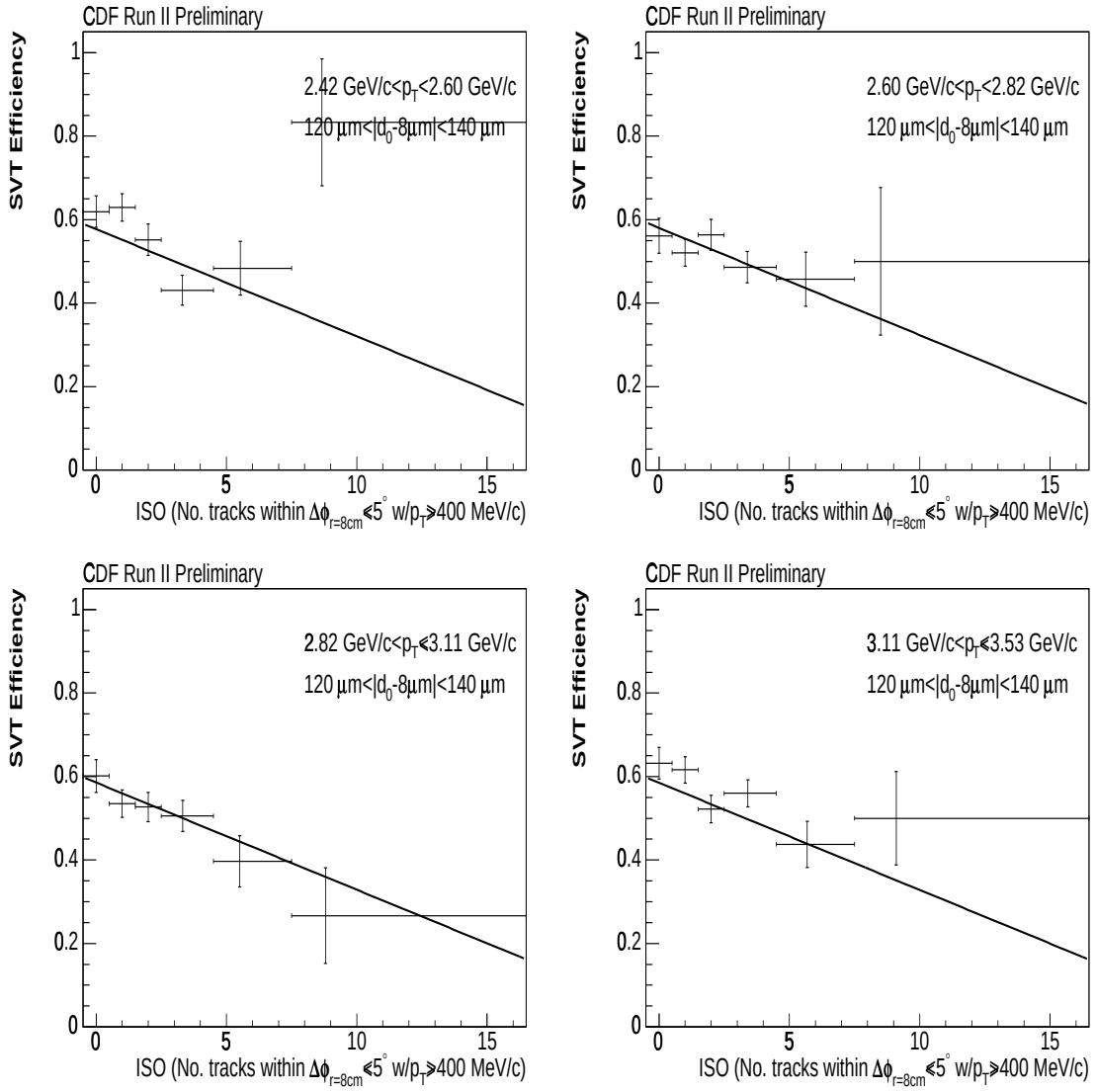

Figure B.38: SVT efficiency vs. ISO for various slices of transverse momentum and impact parameter. The curves are the one dimensional projections of the three dimensional binned fit to the data. Tracks with $|d_0 - 8\mu\text{m}| > 850$ microns have been excluded from the fit.

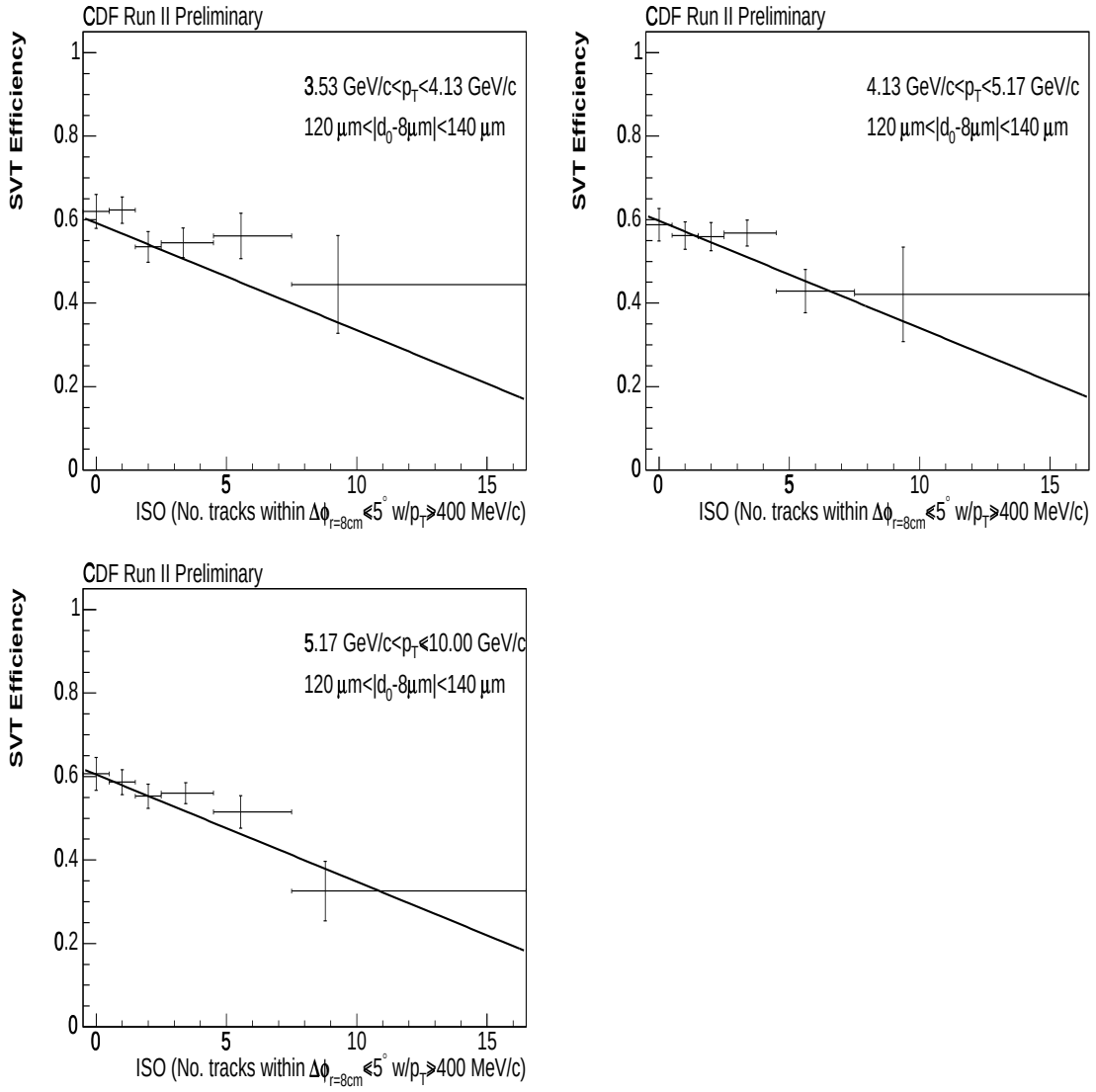

Figure B.39: SVT efficiency vs. ISO for various slices of transverse momentum and impact parameter. The curves are the one dimensional projections of the three dimensional binned fit to the data. Tracks with $|d_0 - 8\mu\text{m}| > 850$ microns have been excluded from the fit.

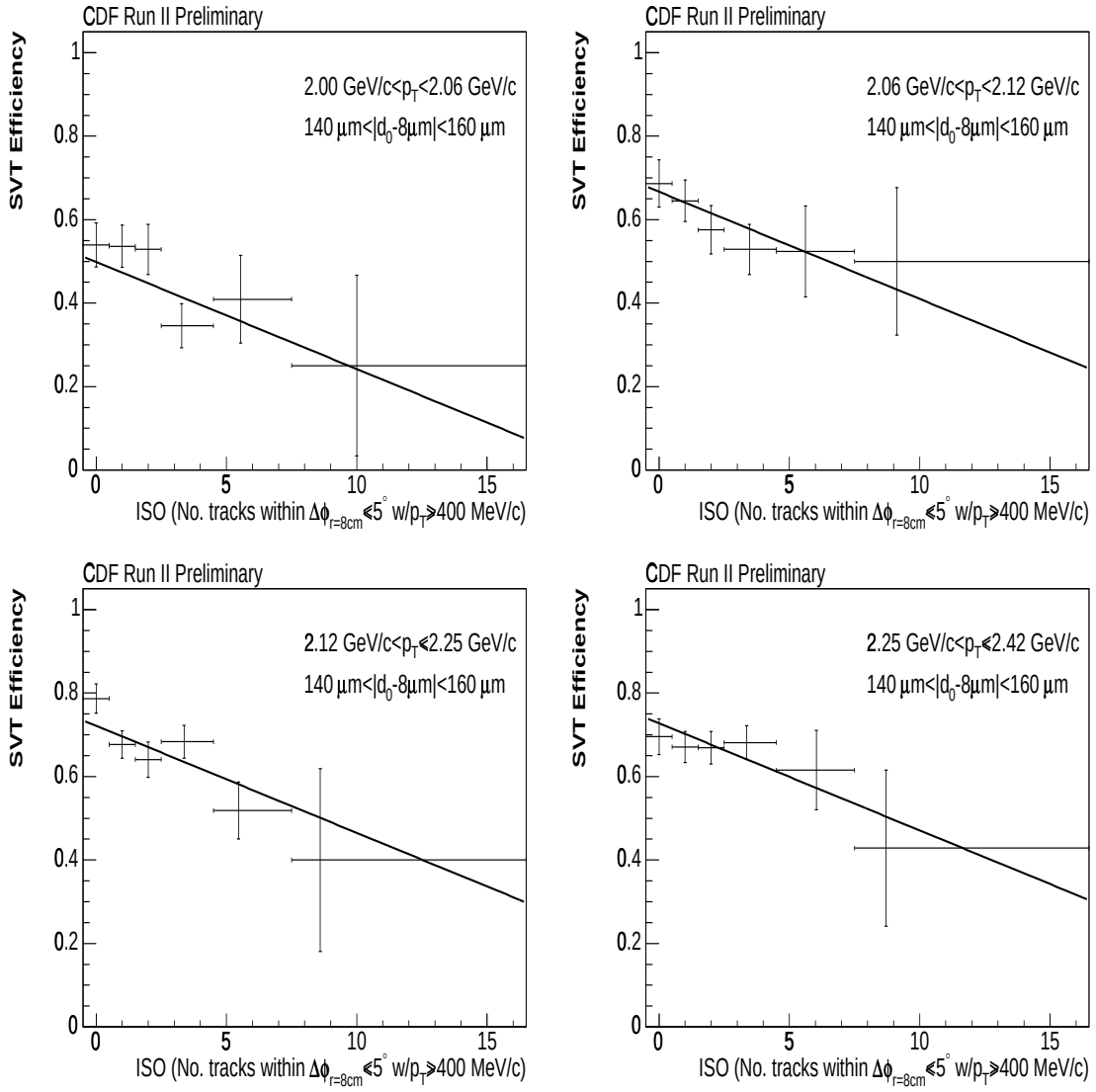

Figure B.40: SVT efficiency vs. ISO for various slices of transverse momentum and impact parameter. The curves are the one dimensional projections of the three dimensional binned fit to the data. Tracks with $|d_0 - 8\mu\text{m}| > 850$ microns have been excluded from the fit.

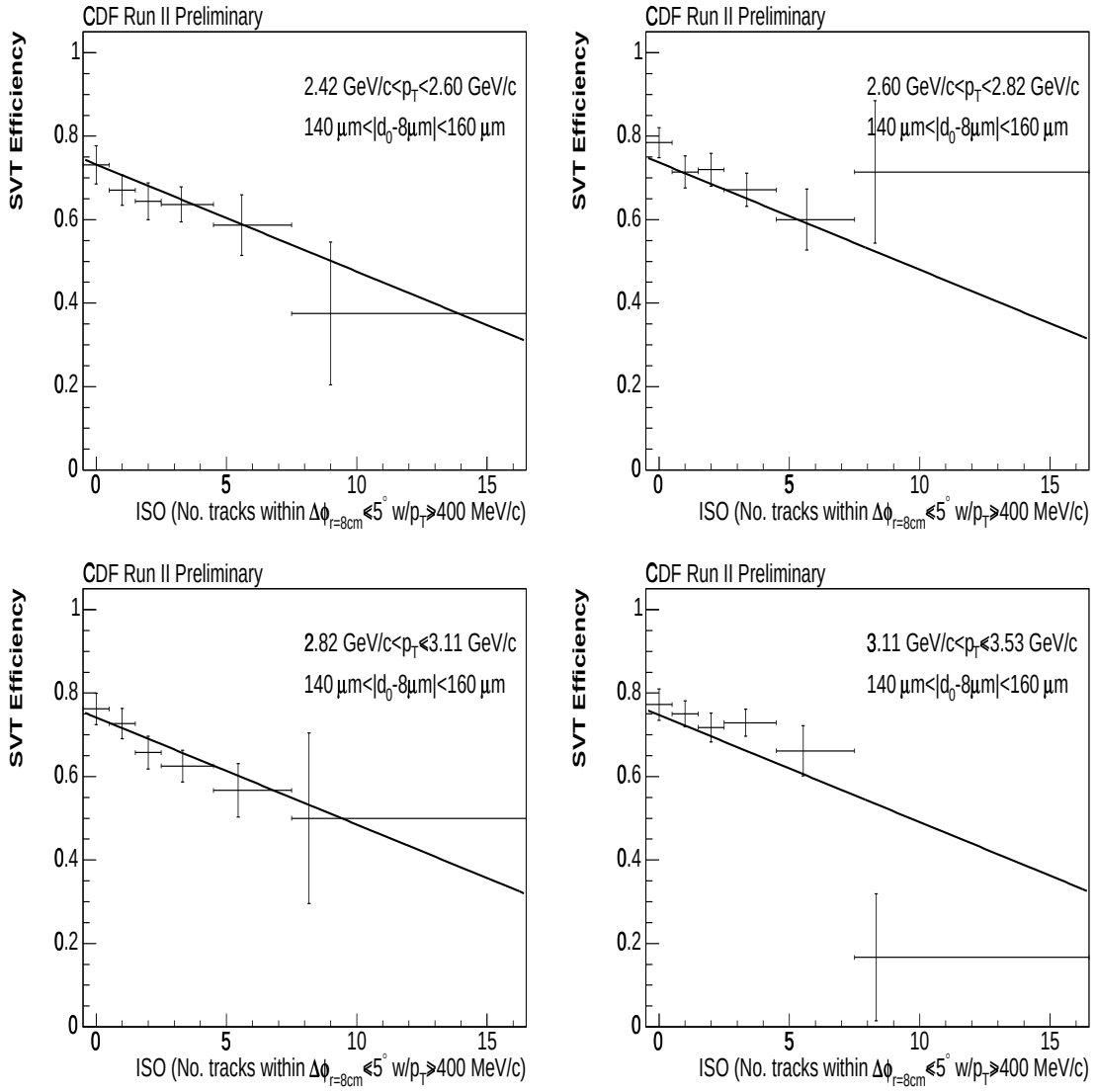

Figure B.41: SVT efficiency vs. ISO for various slices of transverse momentum and impact parameter. The curves are the one dimensional projections of the three dimensional binned fit to the data. Tracks with $|d_0 - 8\mu\text{m}| > 850$ microns have been excluded from the fit.

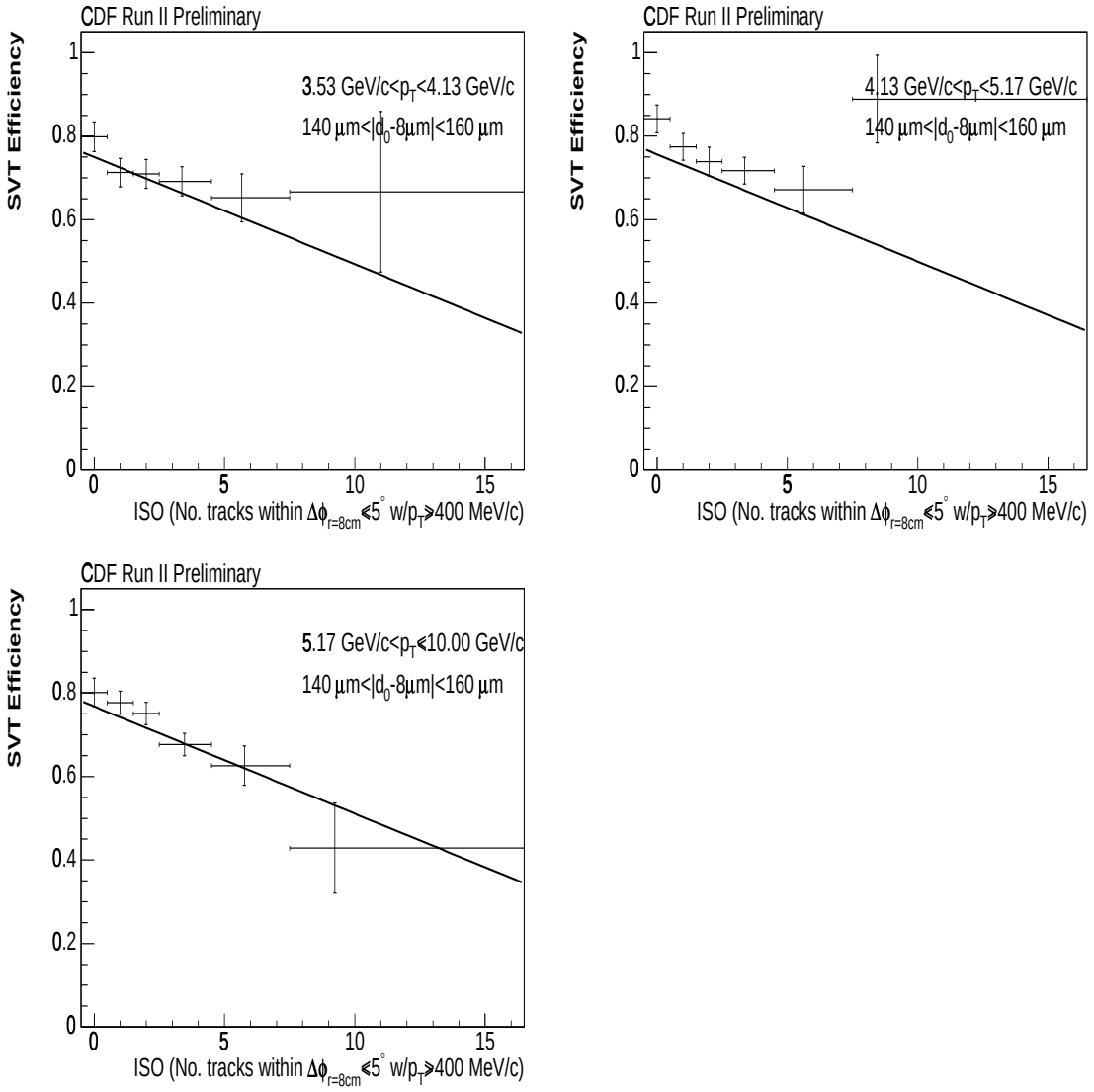

Figure B.42: SVT efficiency vs. ISO for various slices of transverse momentum and impact parameter. The curves are the one dimensional projections of the three dimensional binned fit to the data. Tracks with $|d_0 - 8\mu\text{m}| > 850$ microns have been excluded from the fit.

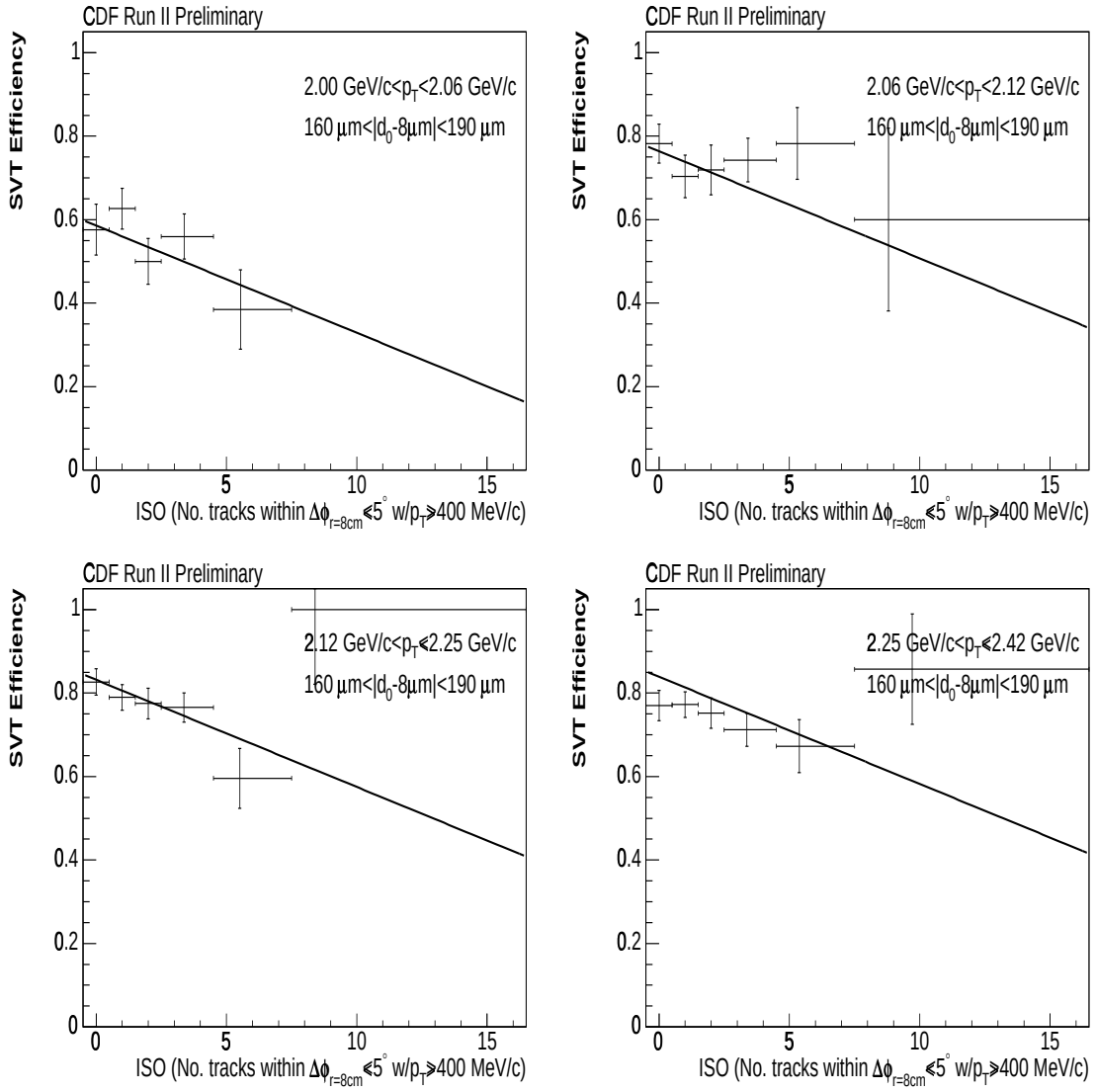

Figure B.43: SVT efficiency vs. ISO for various slices of transverse momentum for tracks with 2 tracks having $p_T > 400$ MeV/c within $\Delta\phi_{r=8cm} < 5°$ (D0 = 2). The curves are the one dimensional projections of the three dimensional binned fit to the data. Tracks with $|d_0 - 8\mu\text{m}| > 850$ microns have been excluded from the fit.

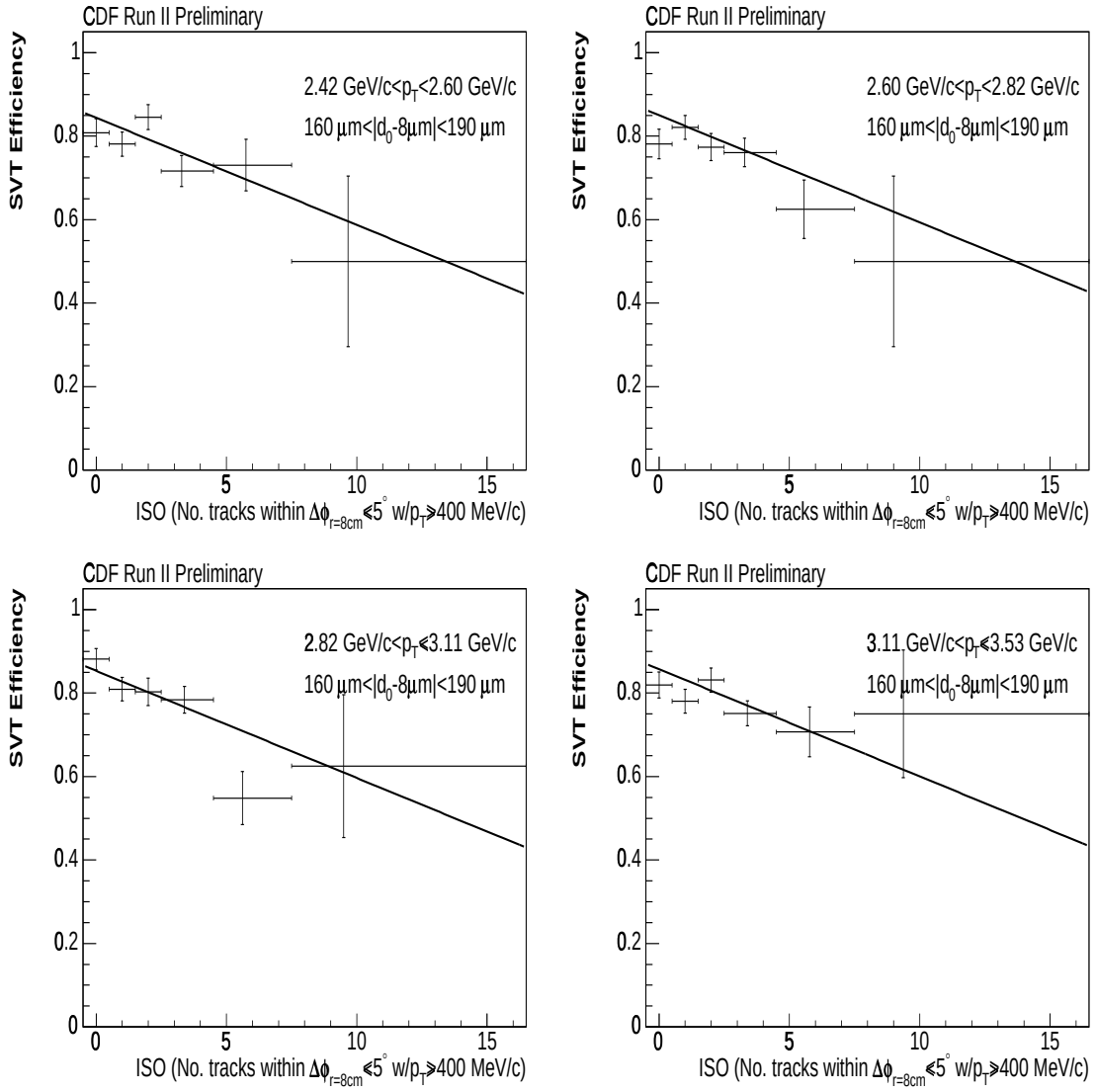

Figure B.44: SVT efficiency vs. ISO for various slices of transverse momentum and impact parameter. The curves are the one dimensional projections of the three dimensional binned fit to the data. Tracks with $|d_0 - 8\mu\text{m}| > 850$ microns have been excluded from the fit.

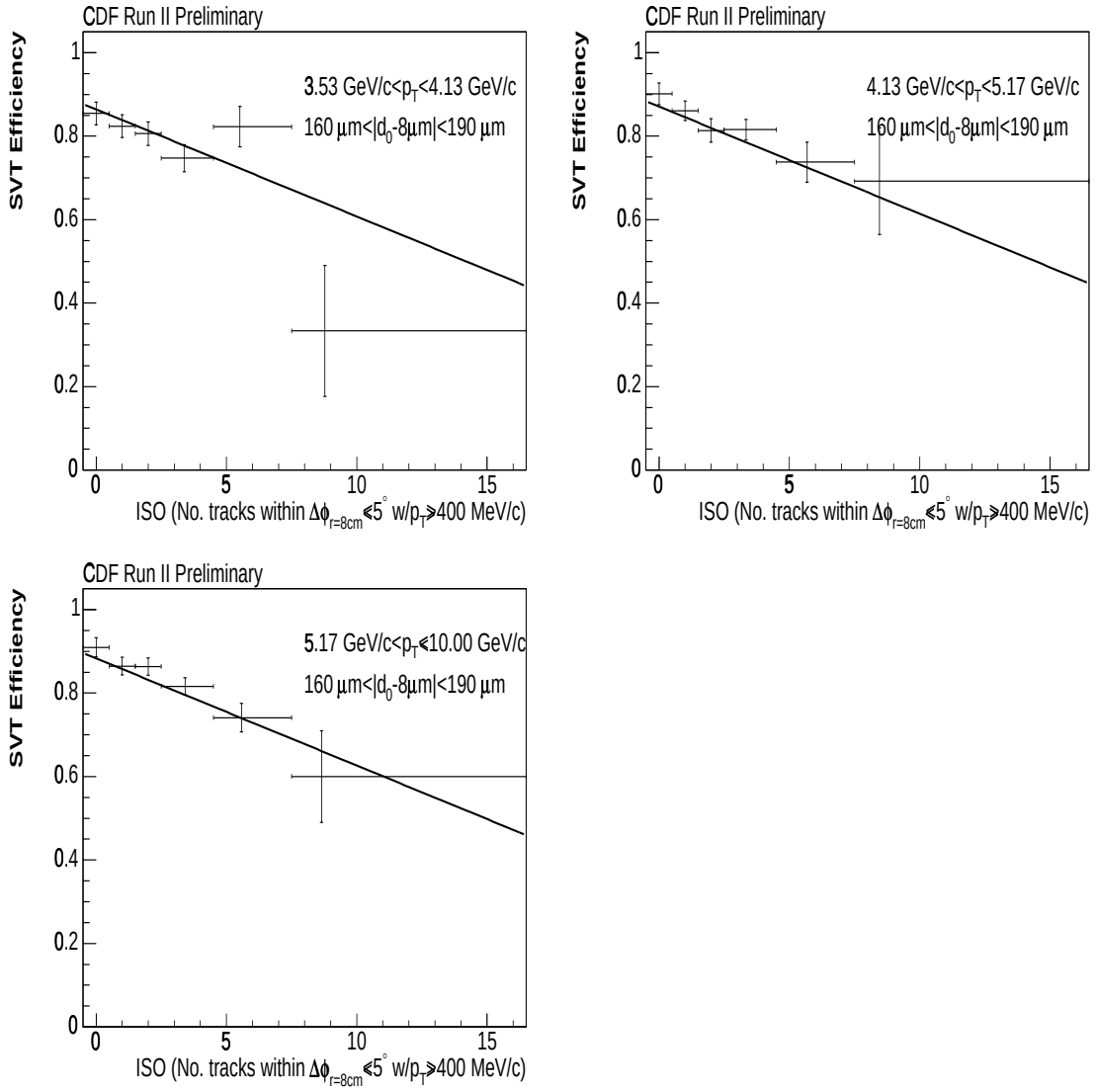

Figure B.45: SVT efficiency vs. ISO for various slices of transverse momentum and impact parameter. The curves are the one dimensional projections of the three dimensional binned fit to the data. Tracks with $|d_0 - 8\mu\text{m}| > 850$ microns have been excluded from the fit.

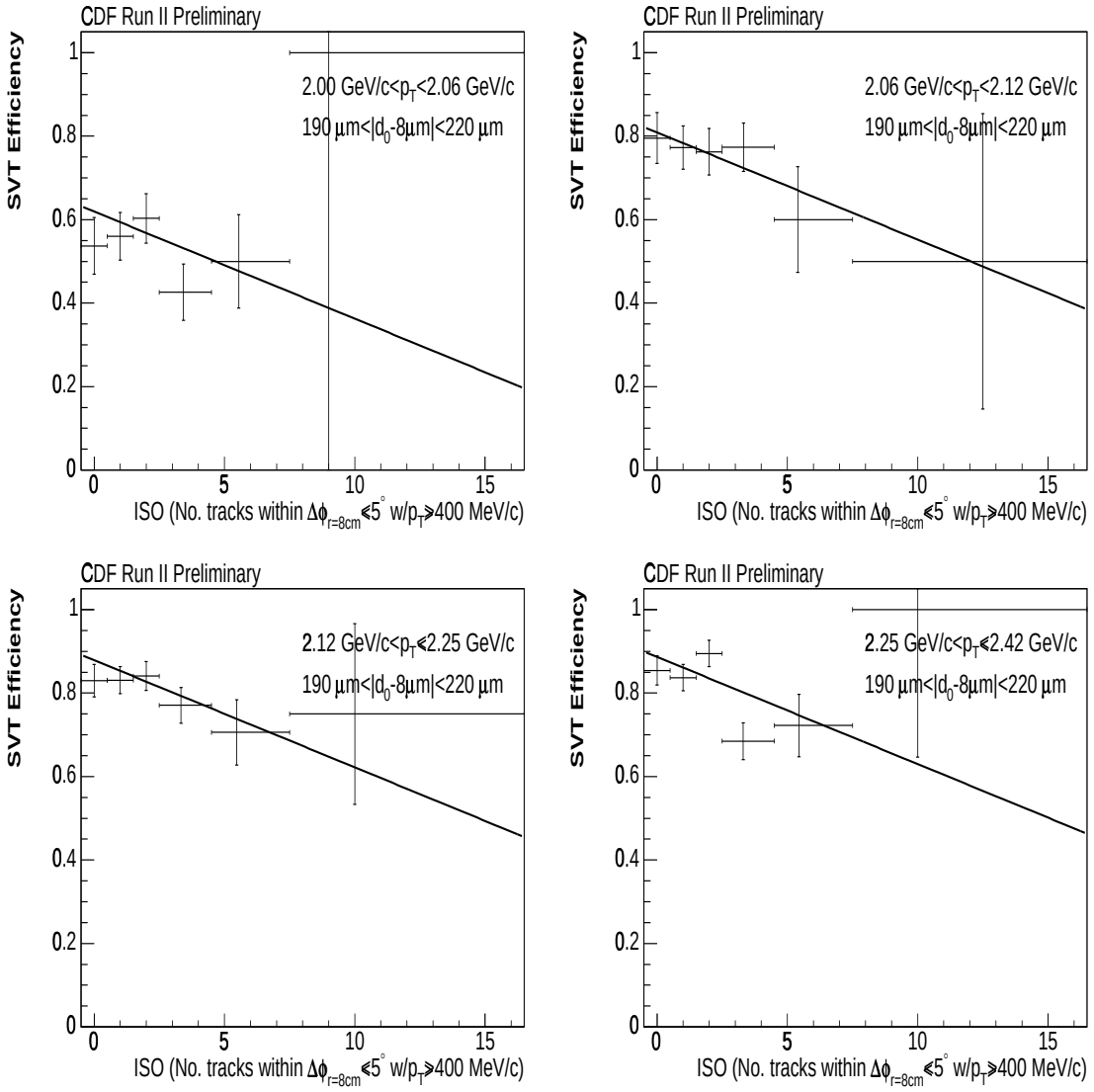

Figure B.46: SVT efficiency vs. ISO for various slices of transverse momentum and impact parameter. The curves are the one dimensional projections of the three dimensional binned fit to the data. Tracks with $|d_0 - 8\mu\text{m}| > 850$ microns have been excluded from the fit.

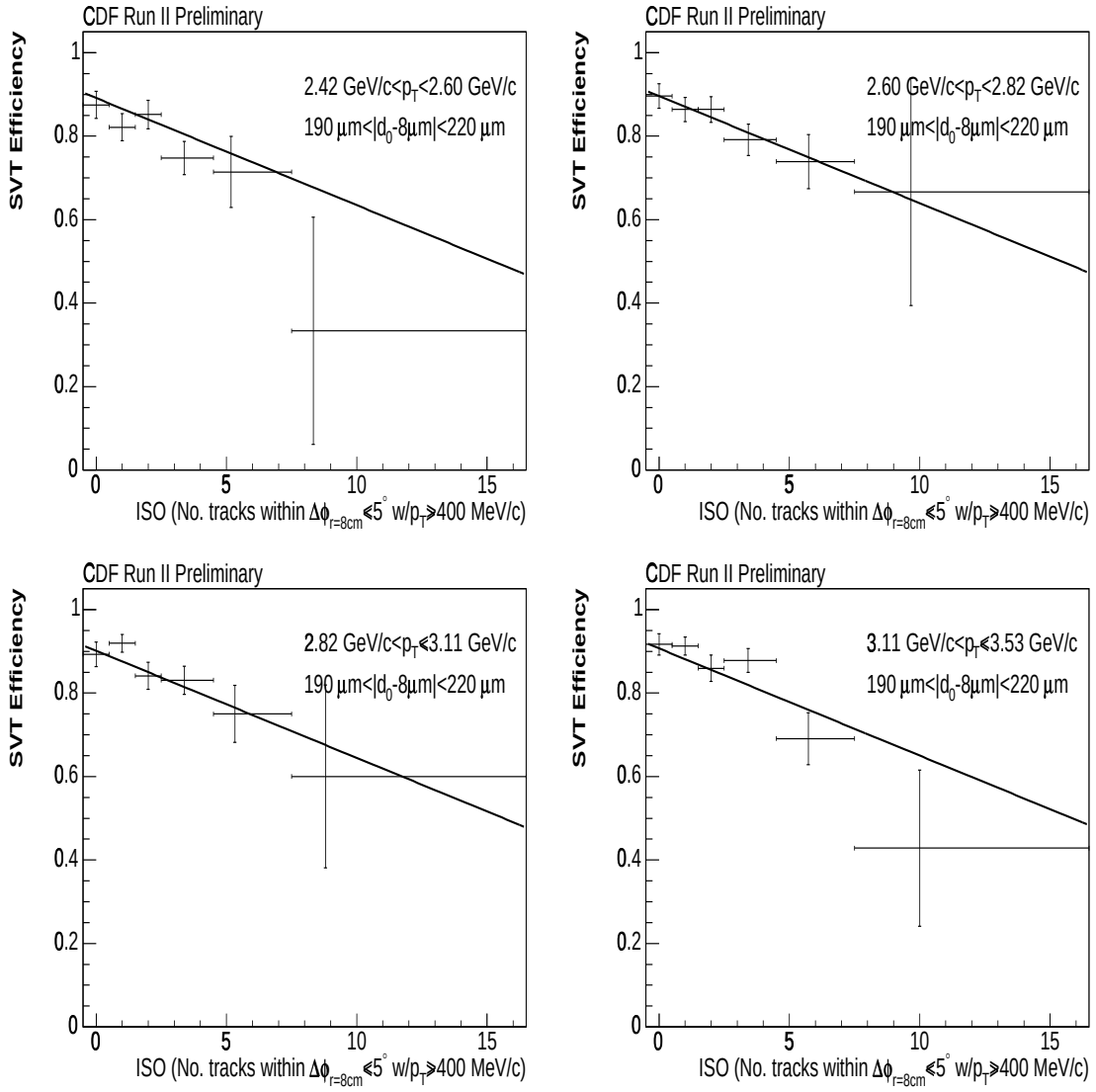

Figure B.47: SVT efficiency vs. ISO for various slices of transverse momentum and impact parameter. The curves are the one dimensional projections of the three dimensional binned fit to the data. Tracks with $|d_0 - 8\mu\text{m}| > 850$ microns have been excluded from the fit.

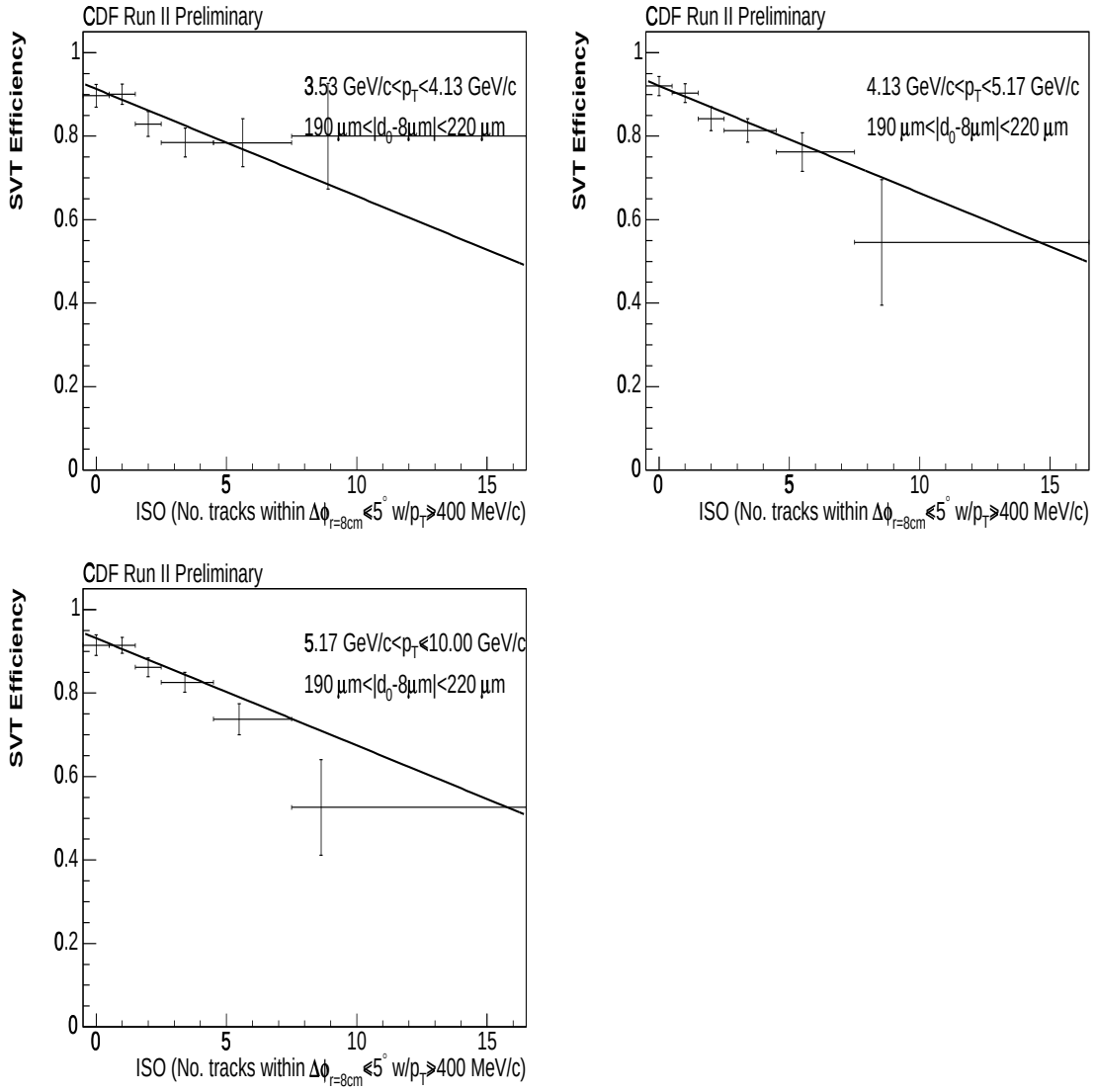

Figure B.48: SVT efficiency vs. ISO for various slices of transverse momentum and impact parameter. The curves are the one dimensional projections of the three dimensional binned fit to the data. Tracks with $|d_0 - 8\mu\text{m}| > 850$ microns have been excluded from the fit.

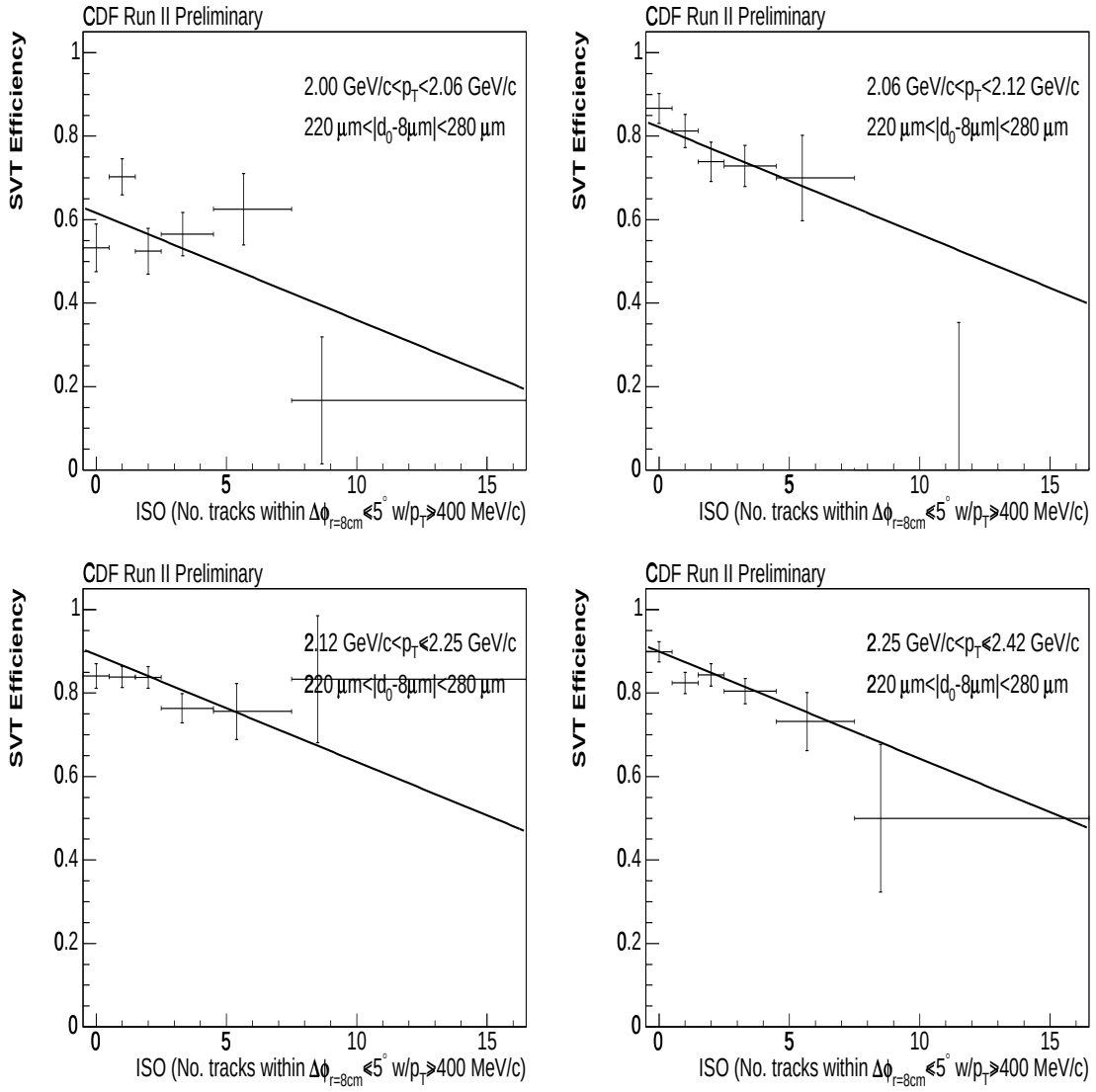

Figure B.49: SVT efficiency vs. ISO for various slices of transverse momentum for tracks with 5, 6, or 7 tracks having $p_T > 400$ MeV/c within $\Delta\phi_{r=8cm} < 5°$ (D0 = 5, 6, or 7). The curves are the one dimensional projections of the three dimensional binned fit to the data. Tracks with $|d_0 - 8\mu\text{m}| > 850$ microns have been excluded from the fit.

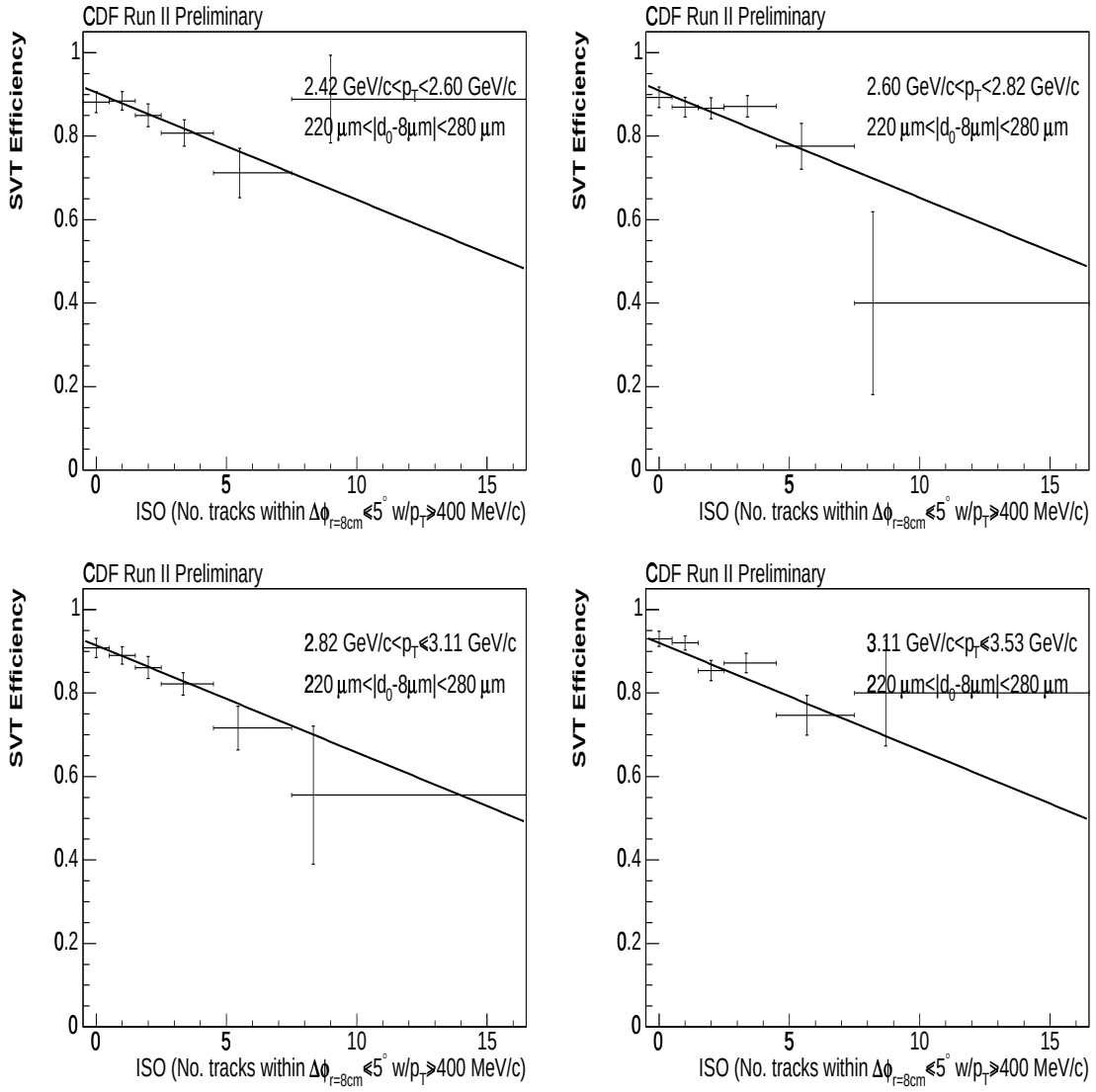

Figure B.50: SVT efficiency vs. ISO for various slices of transverse momentum and impact parameter. The curves are the one dimensional projections of the three dimensional binned fit to the data. Tracks with $|d_0 - 8\mu\text{m}| > 850$ microns have been excluded from the fit.

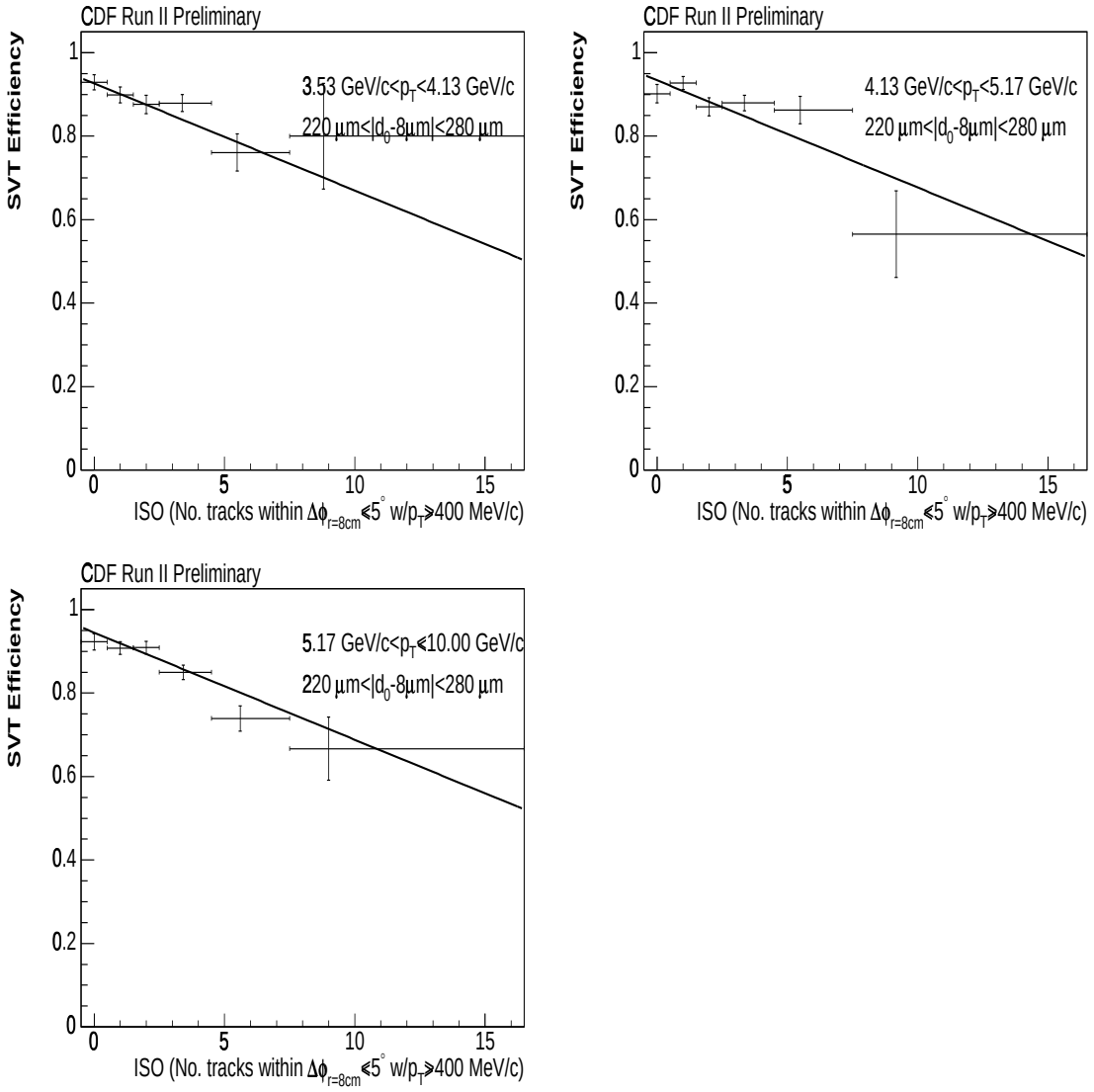

Figure B.51: SVT efficiency vs. ISO for various slices of transverse momentum and impact parameter. The curves are the one dimensional projections of the three dimensional binned fit to the data. Tracks with $|d_0 - 8\mu\text{m}| > 850$ microns have been excluded from the fit.

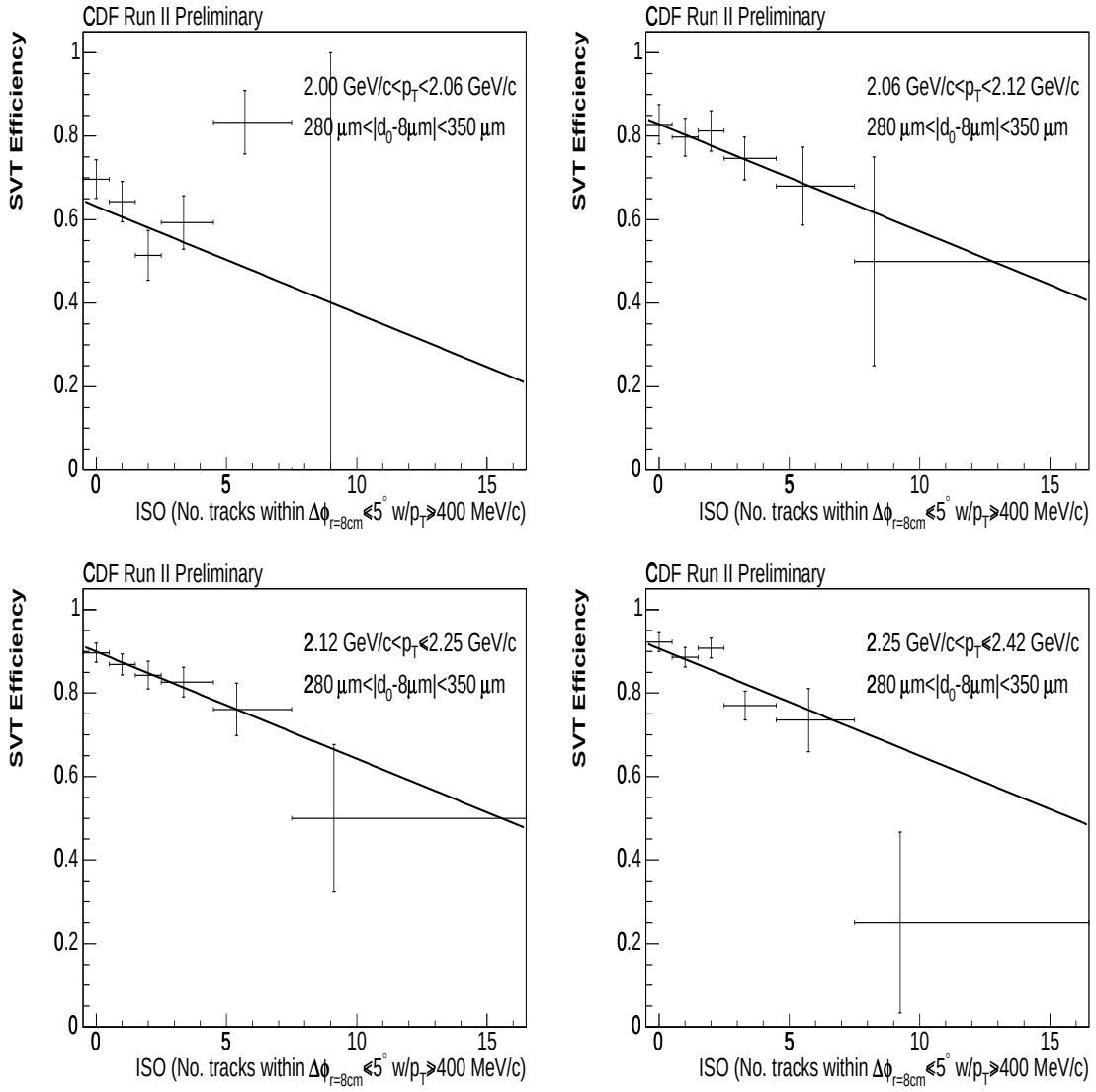

Figure B.52: SVT efficiency vs. ISO for various slices of transverse momentum and impact parameter. The curves are the one dimensional projections of the three dimensional binned fit to the data. Tracks with $|d_0 - 8\mu\text{m}| > 850$ microns have been excluded from the fit.

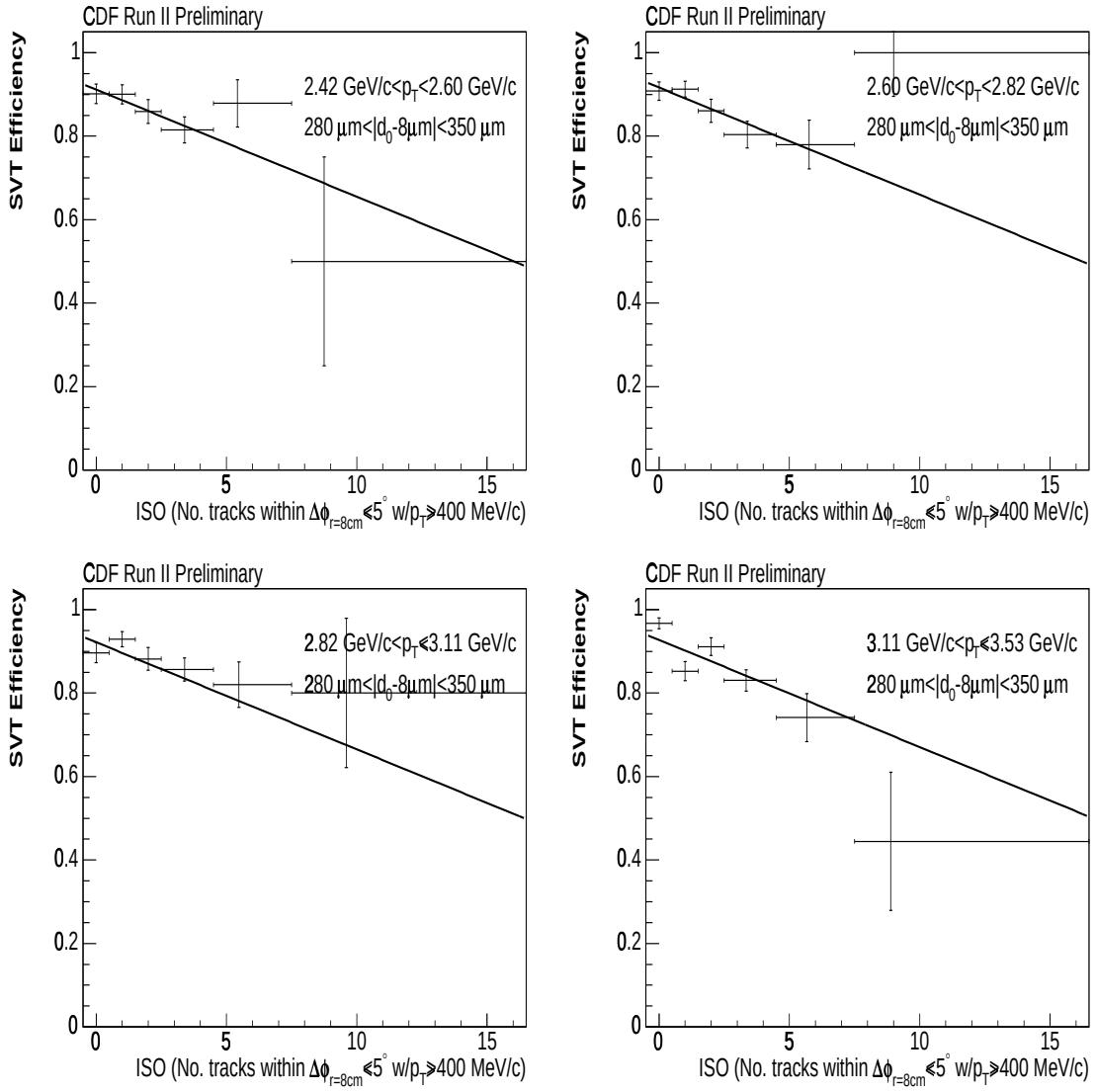

Figure B.53: SVT efficiency vs. ISO for various slices of transverse momentum and impact parameter. The curves are the one dimensional projections of the three dimensional binned fit to the data. Tracks with $|d_0 - 8\mu\text{m}| > 850$ microns have been excluded from the fit.

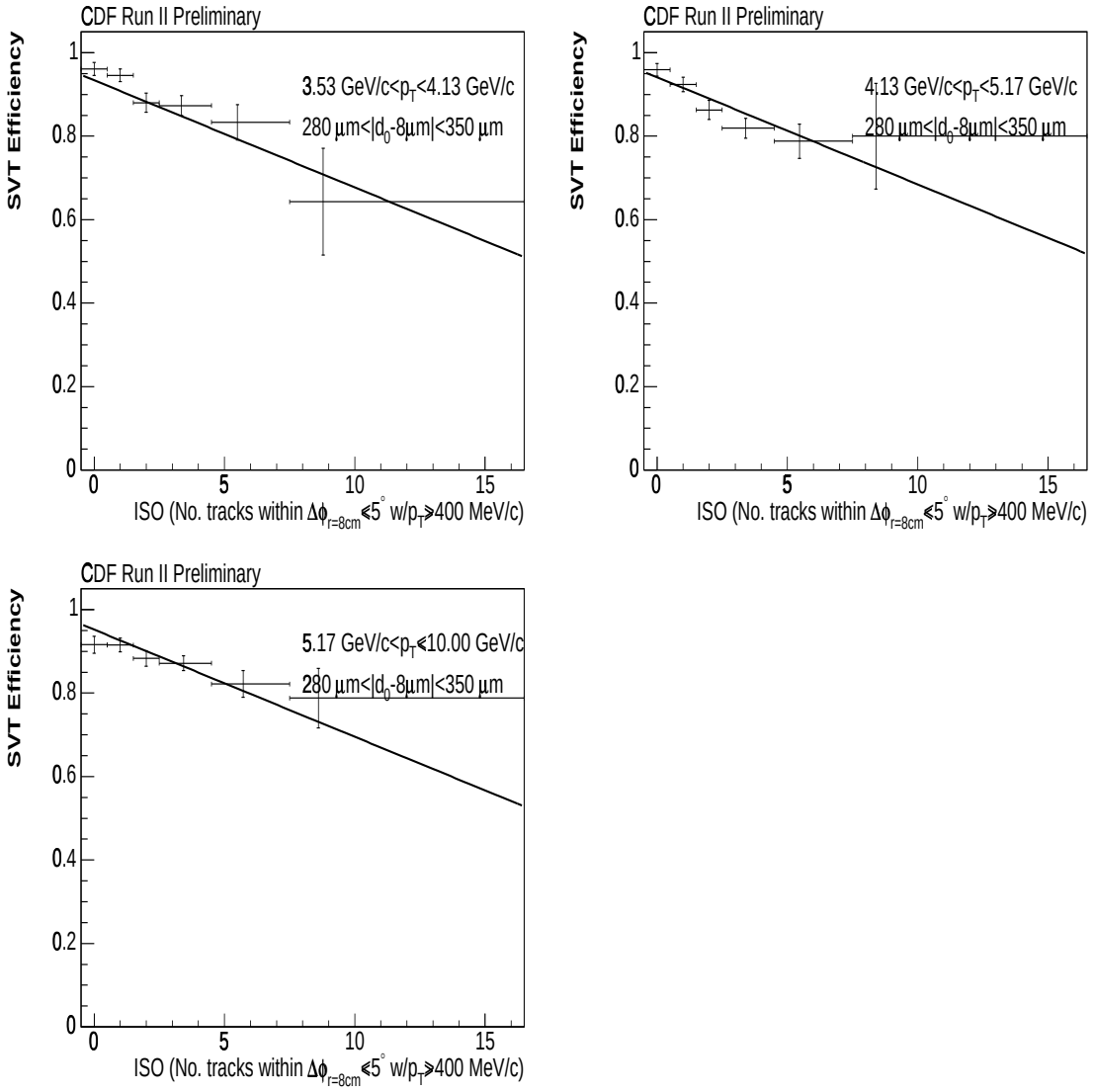

Figure B.54: SVT efficiency vs. ISO for various slices of transverse momentum and impact parameter. The curves are the one dimensional projections of the three dimensional binned fit to the data. Tracks with $|d_0 - 8\mu\text{m}| > 850$ microns have been excluded from the fit.

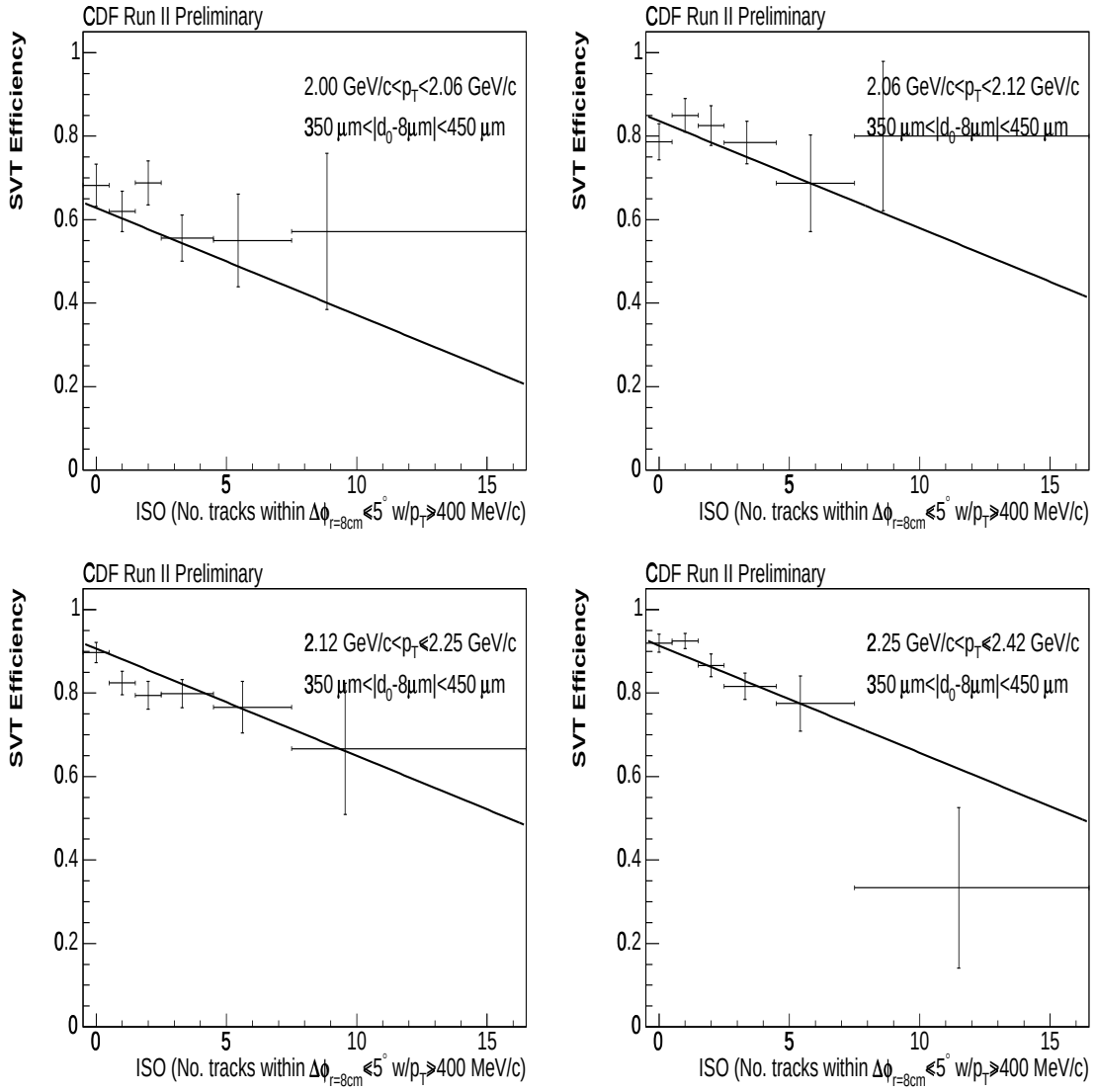

Figure B.55: SVT efficiency vs. ISO for various slices of transverse momentum and impact parameter. The curves are the one dimensional projections of the three dimensional binned fit to the data. Tracks with $|d_0 - 8\mu\text{m}| > 850$ microns have been excluded from the fit.

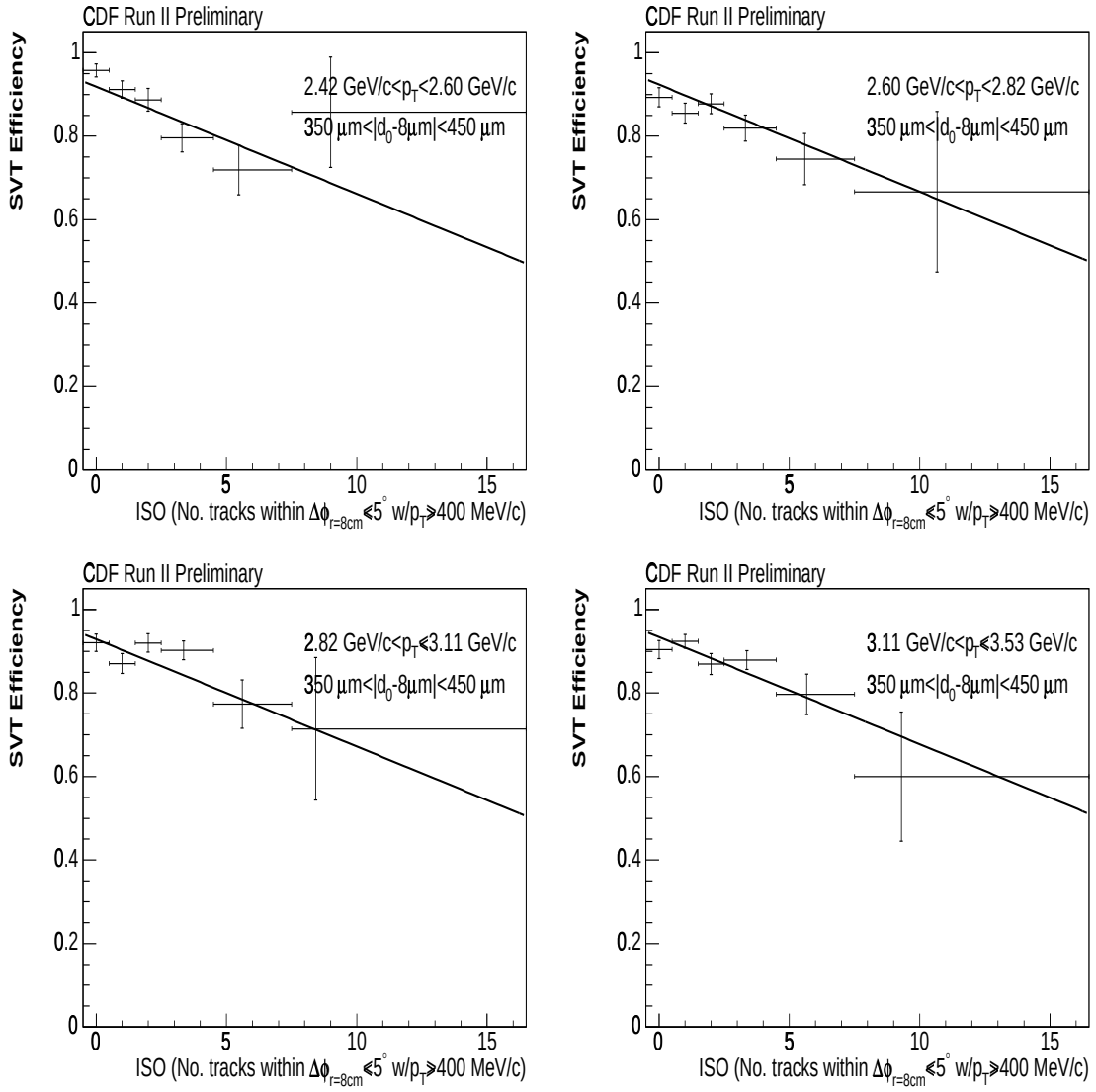

Figure B.56: SVT efficiency vs. ISO for various slices of transverse momentum and impact parameter. The curves are the one dimensional projections of the three dimensional binned fit to the data. Tracks with $|d_0 - 8\mu\text{m}| > 850$ microns have been excluded from the fit.

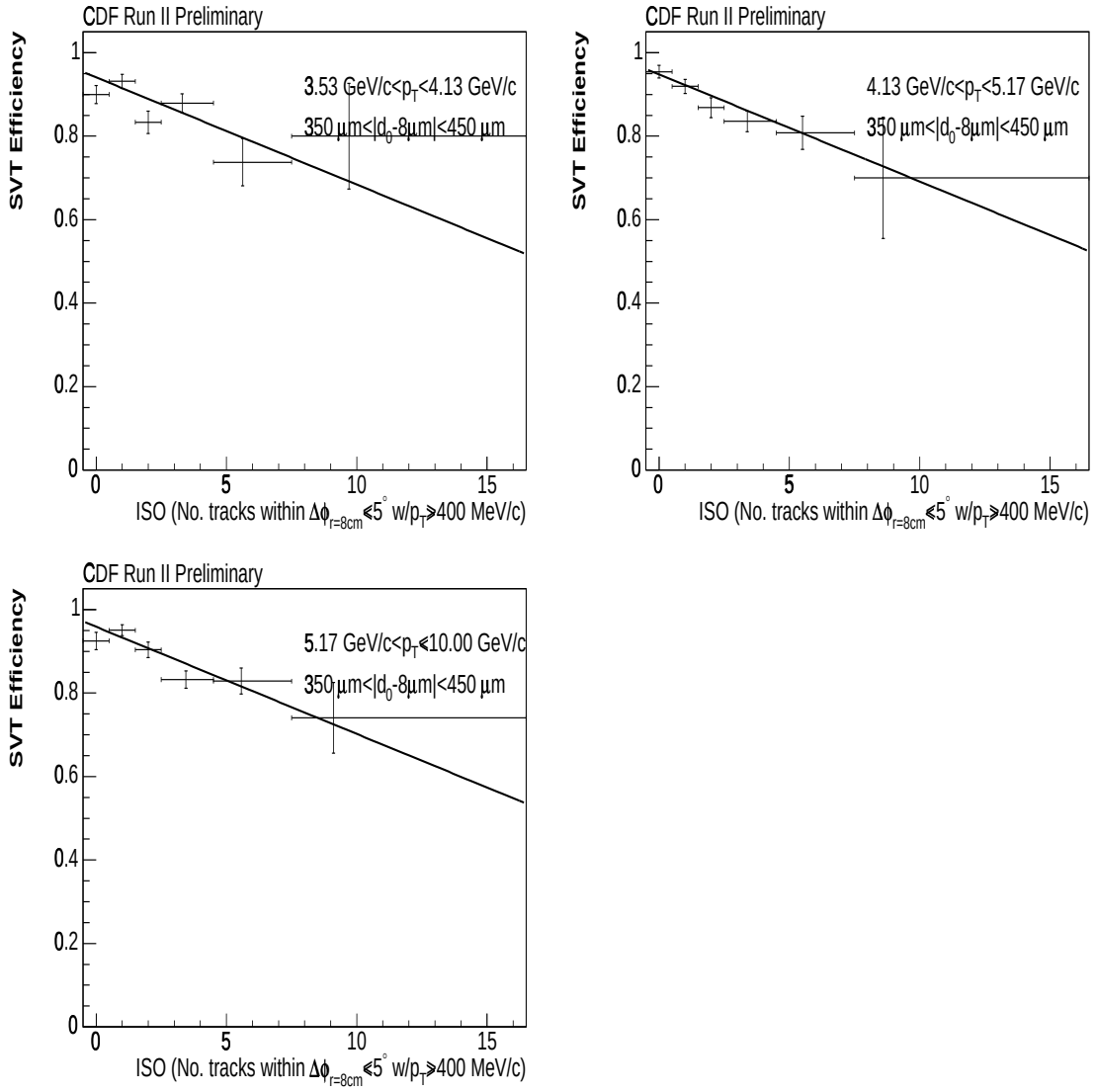

Figure B.57: SVT efficiency vs. ISO for various slices of transverse momentum and impact parameter. The curves are the one dimensional projections of the three dimensional binned fit to the data. Tracks with $|d_0 - 8\mu\text{m}| > 850$ microns have been excluded from the fit.

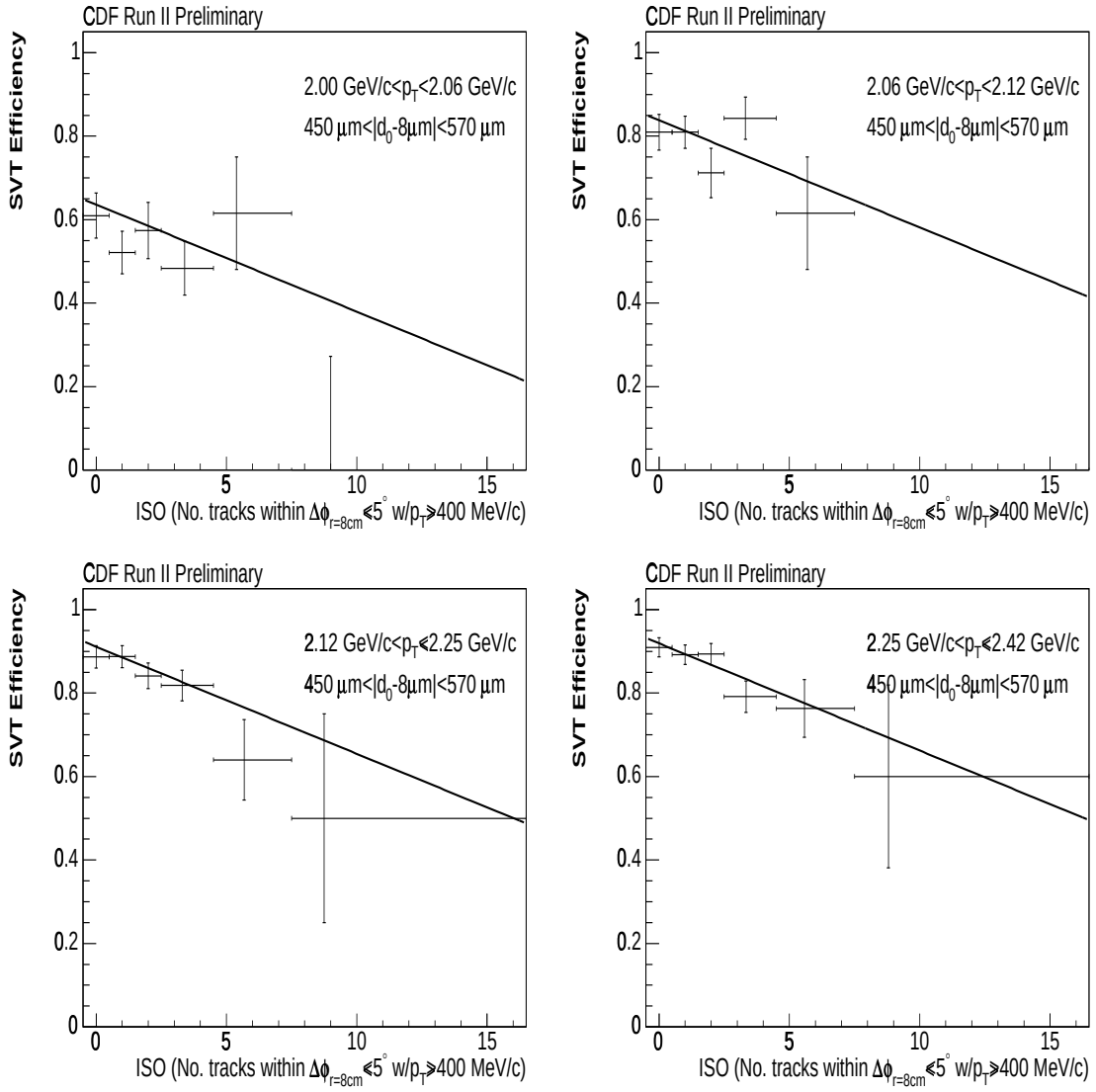

Figure B.58: SVT efficiency vs. ISO for various slices of transverse momentum and impact parameter. The curves are the one dimensional projections of the three dimensional binned fit to the data. Tracks with $|d_0 - 8\mu\text{m}| > 850$ microns have been excluded from the fit.

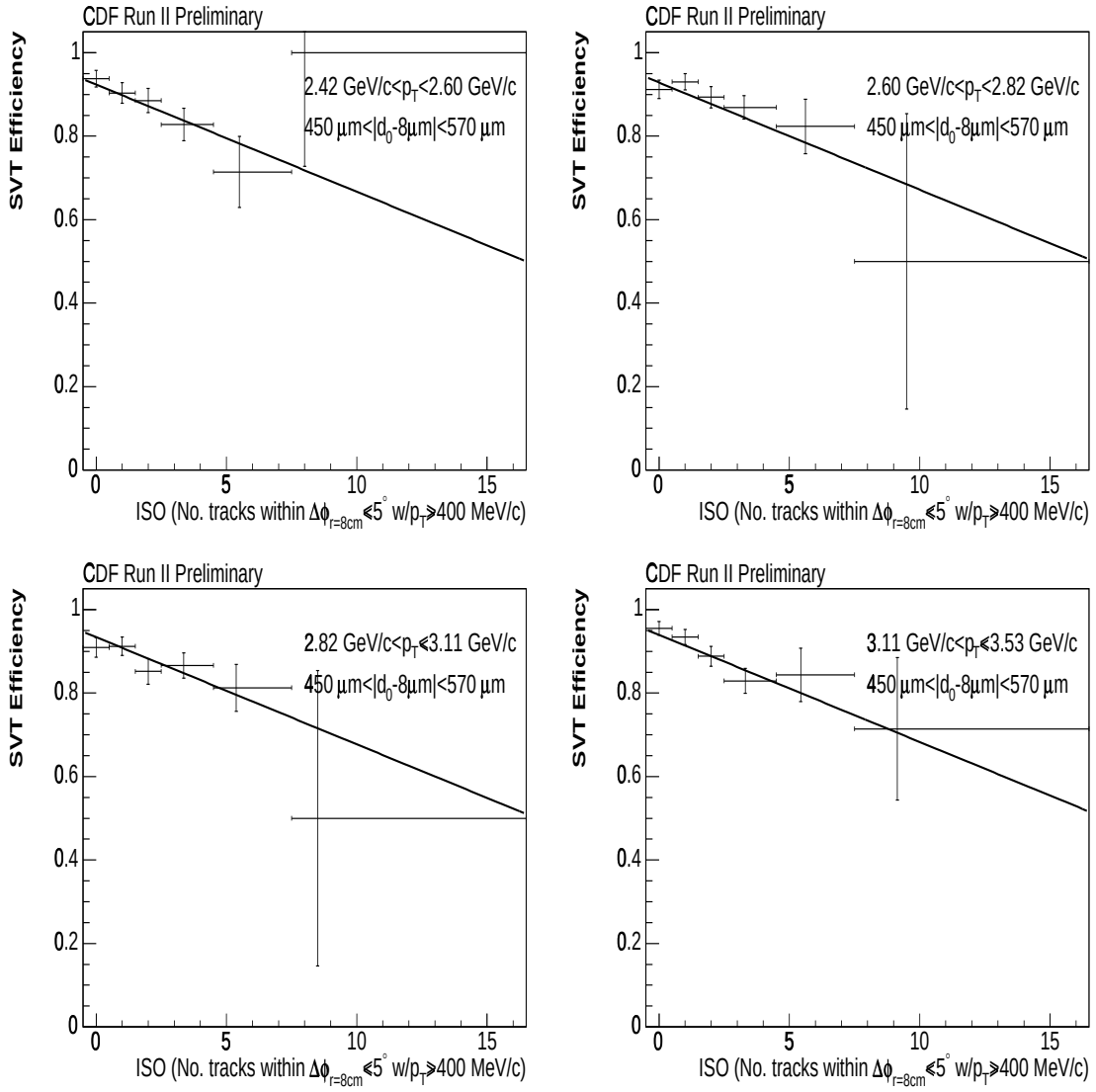

Figure B.59: SVT efficiency vs. ISO for various slices of transverse momentum and impact parameter. The curves are the one dimensional projections of the three dimensional binned fit to the data. Tracks with $|d_0 - 8\mu\text{m}| > 850$ microns have been excluded from the fit.

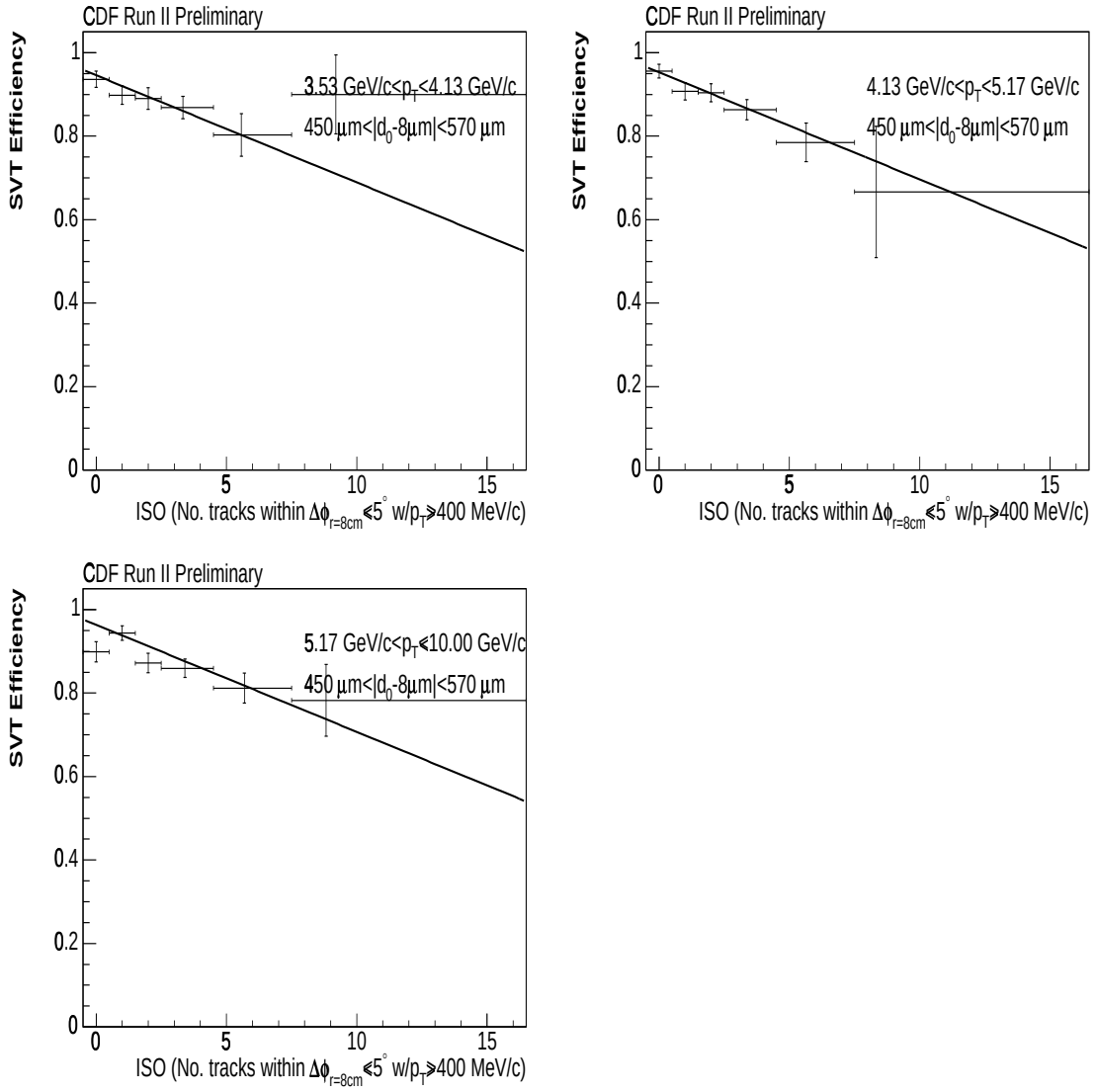

Figure B.60: SVT efficiency vs. ISO for various slices of transverse momentum and impact parameter. The curves are the one dimensional projections of the three dimensional binned fit to the data. Tracks with $|d_0 - 8\mu\text{m}| > 850$ microns have been excluded from the fit.

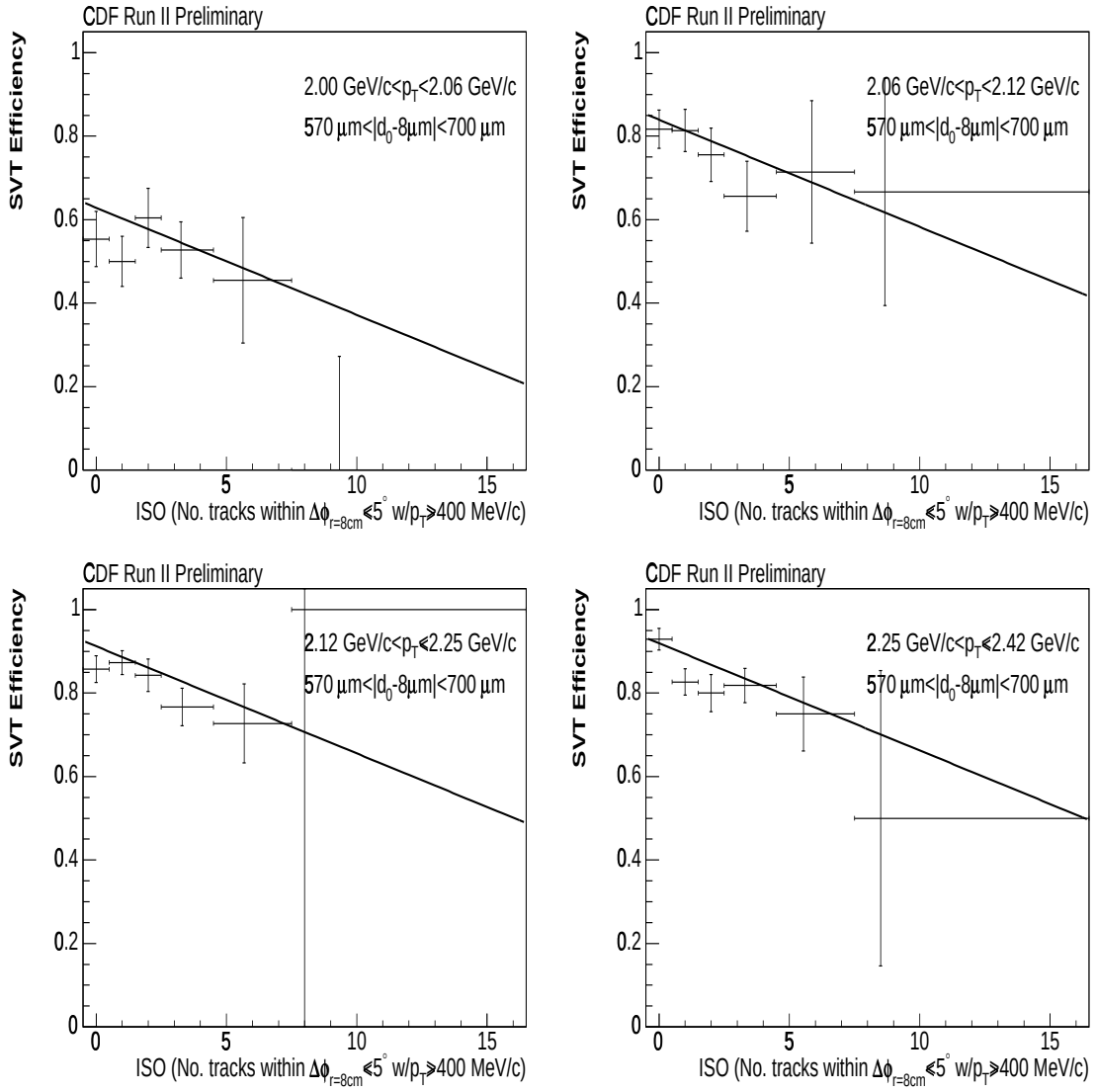

Figure B.61: SVT efficiency vs. ISO for various slices of transverse momentum for tracks with 2 tracks having $p_T > 400$ MeV/c within $\Delta\phi_{r=8cm} < 5°$ (D0 = 2). The curves are the one dimensional projections of the three dimensional binned fit to the data. Tracks with $|d_0 - 8\mu\text{m}| > 850$ microns have been excluded from the fit.

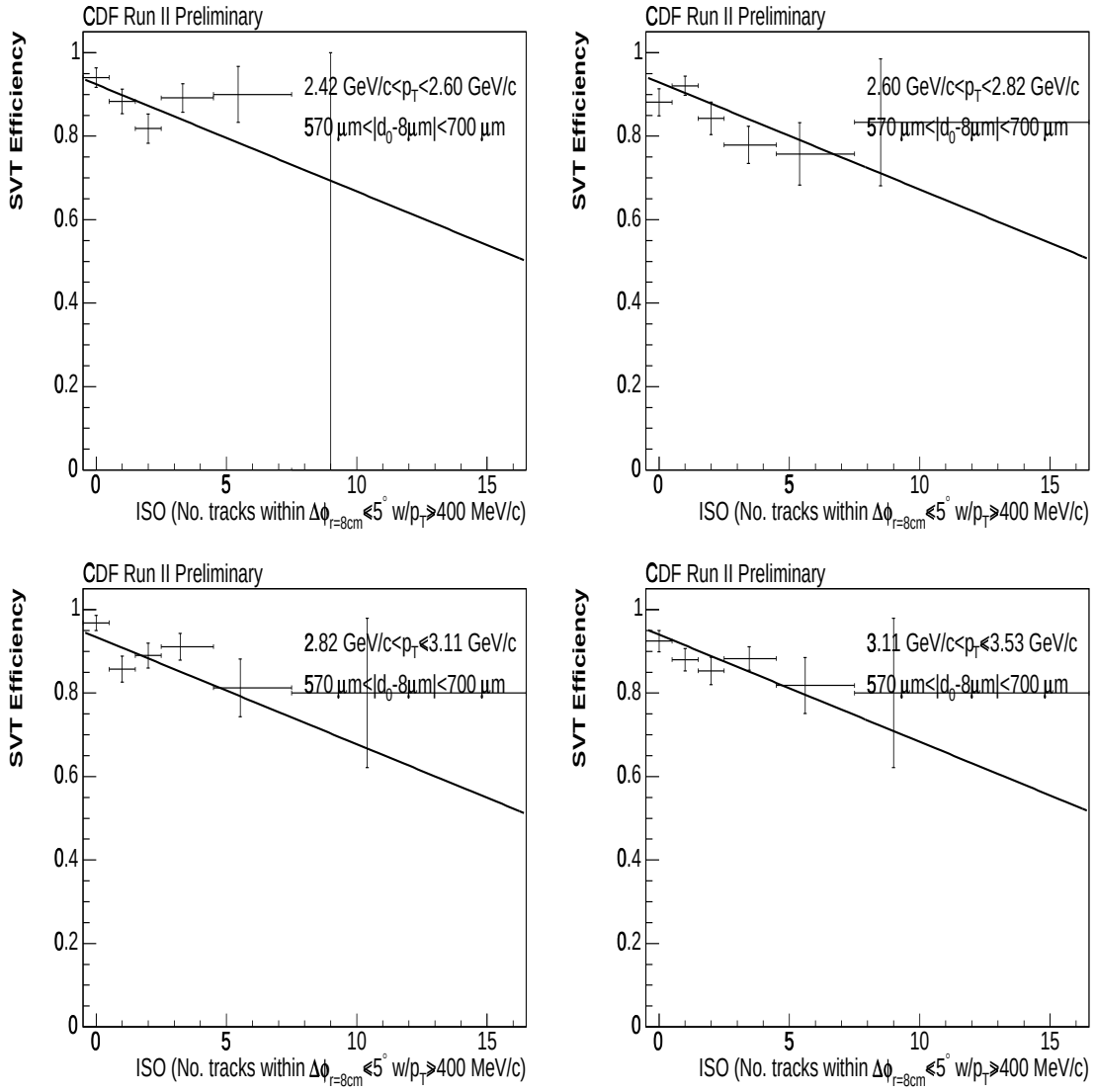

Figure B.62: SVT efficiency vs. ISO for various slices of transverse momentum and impact parameter. The curves are the one dimensional projections of the three dimensional binned fit to the data. Tracks with $|d_0 - 8\mu\text{m}| > 850$ microns have been excluded from the fit.

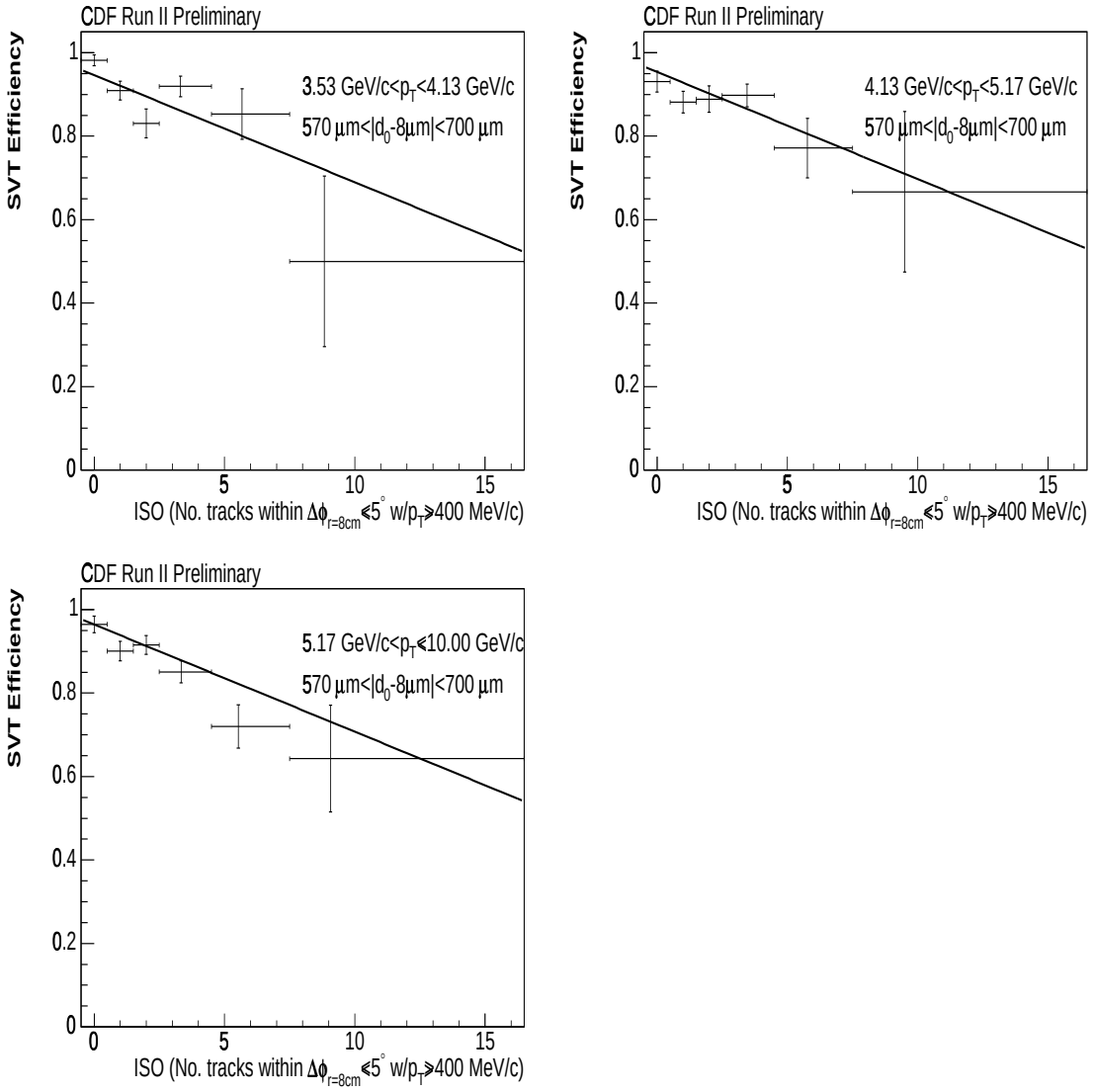

Figure B.63: SVT efficiency vs. ISO for various slices of transverse momentum and impact parameter. The curves are the one dimensional projections of the three dimensional binned fit to the data. Tracks with $|d_0 - 8\mu\text{m}| > 850$ microns have been excluded from the fit.

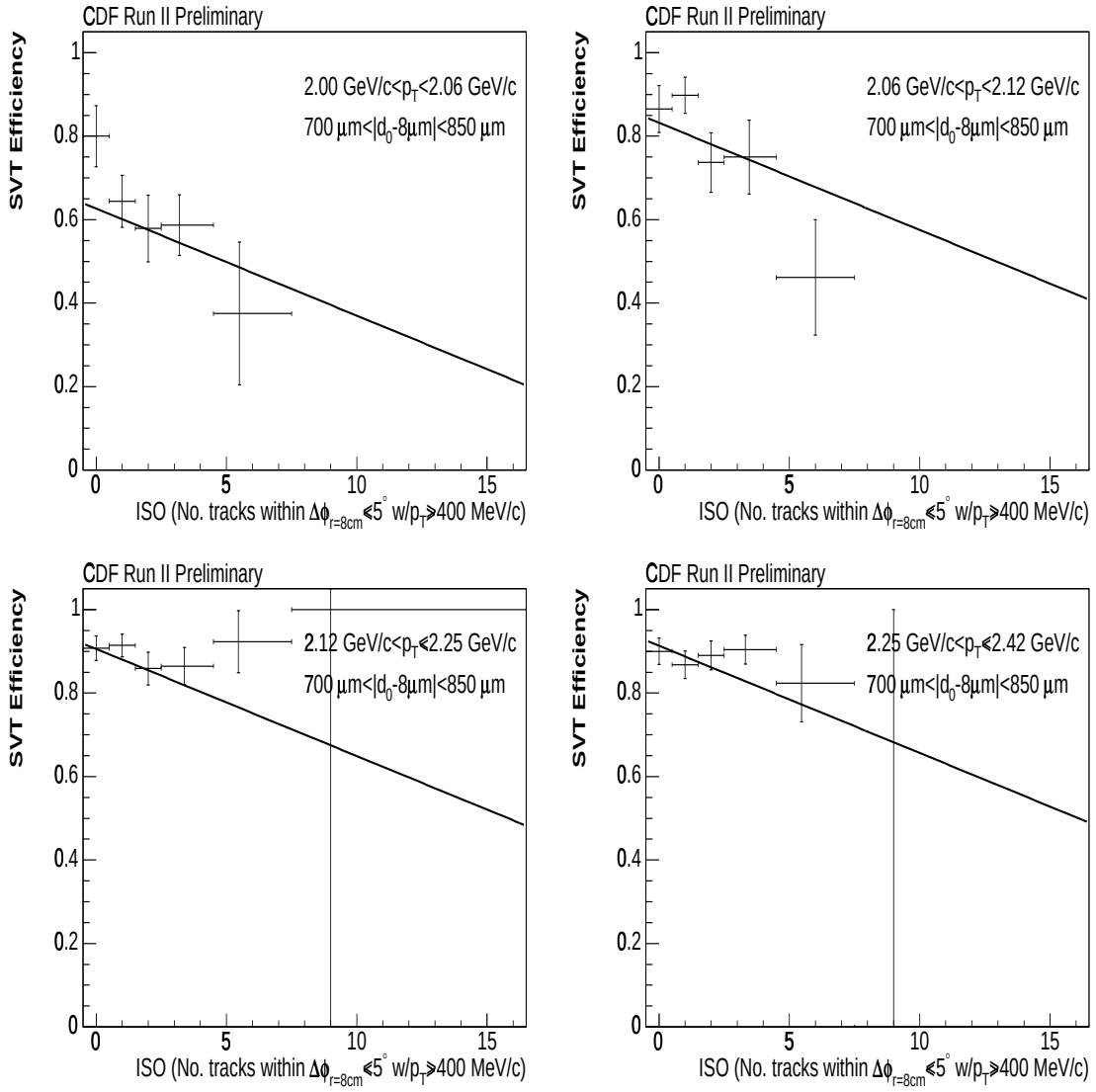

Figure B.64: SVT efficiency vs. ISO for various slices of transverse momentum and impact parameter. The curves are the one dimensional projections of the three dimensional binned fit to the data. Tracks with $|d_0 - 8\mu\text{m}| > 850$ microns have been excluded from the fit.

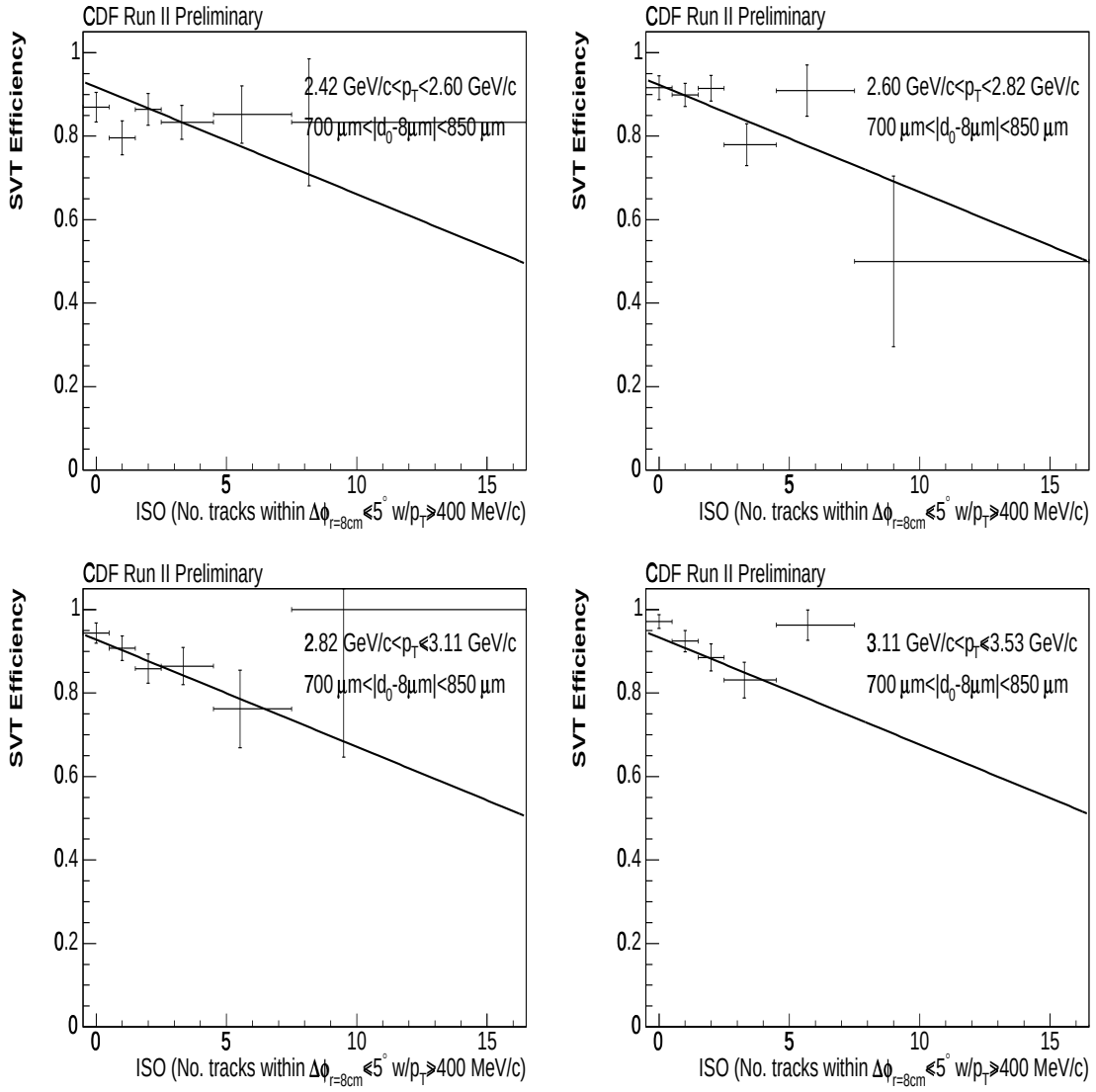

Figure B.65: SVT efficiency vs. ISO for various slices of transverse momentum and impact parameter. The curves are the one dimensional projections of the three dimensional binned fit to the data. Tracks with $|d_0 - 8\mu\text{m}| > 850$ microns have been excluded from the fit.

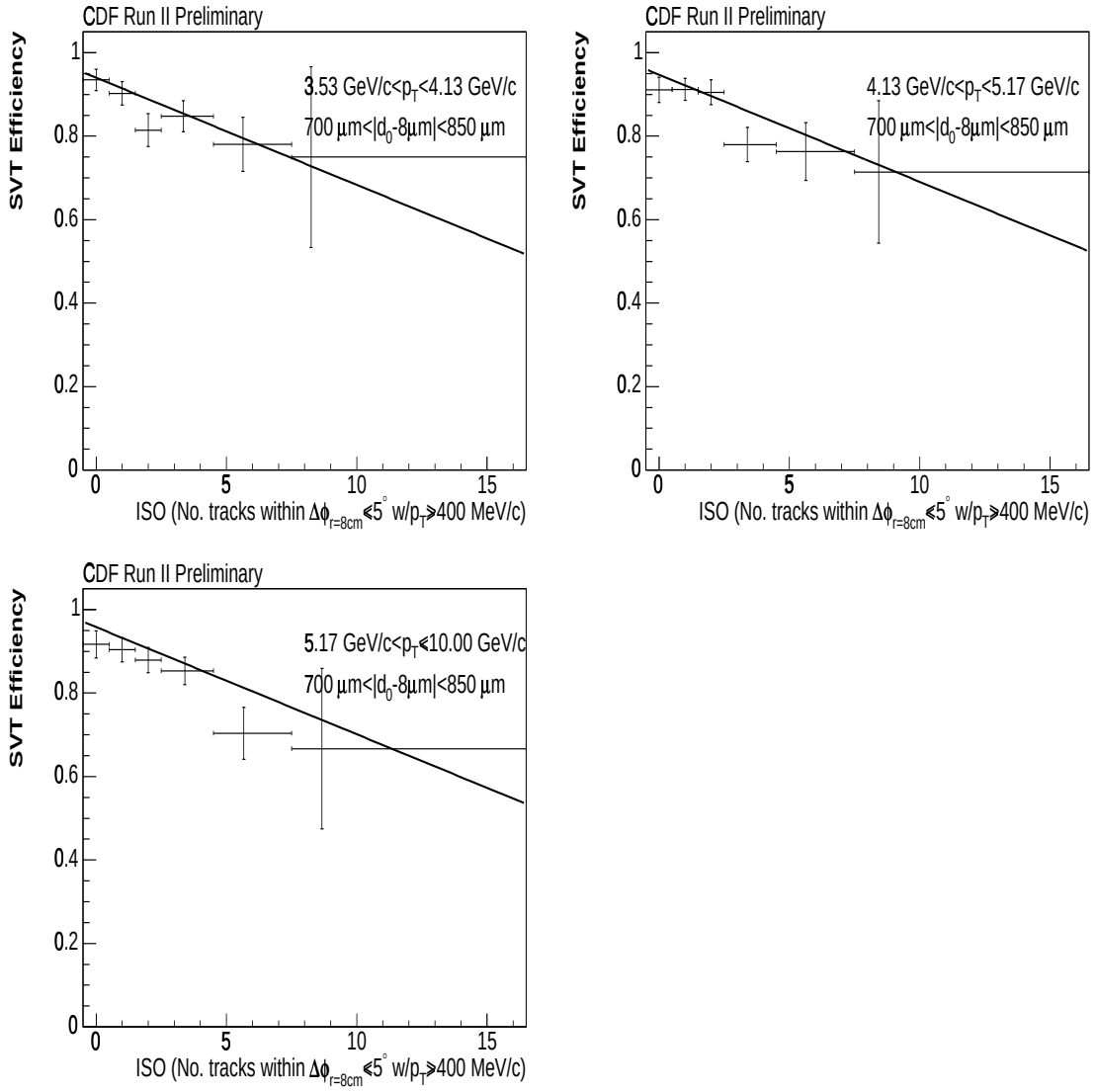

Figure B.66: SVT efficiency vs. ISO for various slices of transverse momentum and impact parameter. The curves are the one dimensional projections of the three dimensional binned fit to the data. Tracks with $|d_0 - 8\mu\text{m}| > 850$ microns have been excluded from the fit.

Appendix C

CDF Default Author List from July 2006 to January 2007

CDF Default Author List from July 2006 to January 2007:

A. Abulencia,[23] J. Adelman,[13] T. Aolder,[10] T. Akimoto,[55] M.G. Albrow,[16] D. Ambrose,[16] S. Amerio,[43] D. Amidei,[34] A. Anastassov,[52] K. Anikeev,[16] A. Annovi,[18] J. Antos, [1] M. Aoki,[55] G. Apollinari,[16] J.-F. Arguin,[33] T. Arisawa,[57] A. Artikov,[14] W. Ashmanskas,[16] A. Attal,[8] F. Azfar,[42] P. Azzi-Bacchetta,[43] P. Azzurri,[46] N. Bacchetta,[43] W. Badgett,[16] A. Barbaro-Galtieri,[28] V.E. Barnes,[48] B.A. Barnett,[24] S. Baroiant,[7] V. Bartsch,[30] G. Bauer,[32] F. Bedeschi,[46] S. Behari,[24] S. Belforte,[54] G. Bellettini,[46] J. Bellinger,[59] A. Belloni,[32] D. Benjamin,[15] A. Beretvas,[16] J. Beringer,[28] T. Berry,[29] A. Bhatti,[50] M. Binkley,[16] D. Bisello,[43] R.E. Blair,[2] C. Blocker,[6] B. Blumenfeld,[24] A. Bocci,[15] A. Bodek,[49] V. Boisvert,[49] G. Bolla,[48] A. Bolshov,[32] D. Bortoletto,[48] J. Boudreau,[47] A. Boveia,[10] B. Brau,[10] L. Brigliadori,[5] C. Bromberg,[35] E. Brubaker,[13] J. Budagov,[14] H.S. Budd,[49] S. Budd,[23] S. Budroni,[46] K. Burkett,[16] G. Busetto,[43] P. Bussey,[20] K. L. Byrum,[2] S. Cabrera,[15] M. Campanelli,[19] M. Campbell,[34] F. Canelli,[16] A. Canepa,[48] S. Carrillo,[17] D. Carlsmith,[59] R. Carosi,[46] S. Carron,[33] M. Casarsa,[54] A. Castro,[5] P. Catastini,[46] D. Cauz,[54] M. Cavalli-Sforza,[3] A. Cerri,[28] L. Cerrito,[30] S.H. Chang,[27] Y.C. Chen, [1] M. Chertok,[7] G. Chiarelli,[46] G. Chlachidze,[14] F. Chlebana,[16] I. Cho,[27] K. Cho,[27] D. Chokheli,[14] J.P. Chou,[21] G. Choudalakis,[32] S.H. Chuang,[59] K. Chung,[12] W.H. Chung,[59] Y.S. Chung,[49] M. Ciljak,[46] C.I. Ciobanu,[23] M.A. Ciocci,[46] A. Clark,[19] D. Clark,[6] M. Coca,[15] G. Compostella,[43] M.E. Convery,[50] J. Conway,[7] B. Cooper,[35] K. Copic,[34] M. Cordelli,[18] G. Cortiana,[43] F. Crescioli,[46] C. Cuenca Almenar,[7] J. Cuevas,[11] R. Culbertson,[16] J.C. Cully,[34] D. Cyr,[59] S. DaRonco,[43] S. D'Auria,[20] T. Davies,[20] M. D'Onofrio,[3] D. Dagenhart,[6] P. de Barbaro,[49] S. De Cecco,[51] A. Deisher,[28] G. De Lentdecker,[49] M. Dell'Orso,[46] F. Delli Paoli,[43] L. Demortier,[50] J. Deng,[15] M. Deninno,[5] D. De Pedis,[51] P.F. Derwent,[16] C. Dionisi,[51] B. Di Ruzza,[54] J.R. Dittmann,[4] P. DiTuro,[52] C. Dörr,[25] S. Donati,[46] M. Donega,[19] P. Dong,[8] J. Donini,[43] T. Dorigo,[43] S. Dube,[52] J. Efron,[39] R. Erbacher,[7] D. Errede,[23] S. Errede,[23] R. Eusebi,[16] H.C. Fang,[28] S. Farrington,[29] I. Fedorko,[46] W.T. Fedorko,[13] R.G. Feild,[60] M. Feindt,[25] J.P. Fernandez,[31] R. Field,[17] G. Flanagan,[48] A. Foland,[21] S. Forrester,[7] G.W. Foster,[16] M. Franklin,[21] J.C. Freeman,[28] I. Furic,[13] M.

Gallinaro,[50] J. Galyardt,[12] J.E. Garcia,[46] F. Garberson,[10] A.F. Garfinkel,[48] C. Gay,[60] H. Gerberich,[23] D. Gerdes,[34] S. Giagu,[51] P. Giannetti,[46] A. Gibson,[28] K. Gibson,[47] J.L. Gimmell,[49] C. Ginsburg,[16] N. Giokaris,[14] M. Giordani,[54] P. Giromini,[18] M. Giunta,[46] G. Giurgiu,[12] V. Glagolev,[14] D. Glenzinski,[16] M. Gold,[37] N. Goldschmidt,[17] J. Goldstein,[42] G. Gomez,[11] G. Gomez-Ceballos,[11] M. Goncharov,[53] O. González,[31] I. Gorelov,[37] A.T. Goshaw,[15] K. Goulianos,[50] A. Gresele,[43] M. Griths,[29] S. Grinstein,[21] C. Grosso-Pilcher,[13] R.C. Group,[17] U. Grundler,[23] J. Guimaraes da Costa,[21] Z. Gunay-Unalan,[35] C. Haber,[28] K. Hahn,[32] S.R. Hahn,[16] E. Halkiadakis,[52] A. Hamilton,[33] B.-Y. Han,[49] J.Y. Han,[49] R. Handler,[59] F. Happacher,[18] K. Hara,[55] M. Hare,[56] S. Harper,[42] R.F. Harr,[58] R.M. Harris,[16] M. Hartz,[47] K. Hatakeyama,[50] J. Hauser,[8] A. Heijboer,[45] B. Heinemann,[29] J. Heinrich,[45] C. Henderson,[32] M. Herndon,[59] J. Heuser,[25] D. Hidas,[15] C.S. Hill,[10] D. Hirschbuehl,[25] A. Hocker,[16] A. Holloway,[21] S. Hou,[1] M. Houlden,[29] S.-C. Hsu,[9] B.T. Human,[42] R.E. Hughes,[39] U. Husemann,[60] J. Huston,[35] J. Incandela,[10] G. Introzzi,[46] M. Iori,[51] Y. Ishizawa,[55] A. Ivanov,[7] B. Iyutin,[32] E. James,[16] D. Jang,[52] B. Jayatilaka,[34] D. Jeans,[51] H. Jensen,[16] E.J. Jeon,[27] S. Jindariani,[17] M. Jones,[48] K.K. Joo,[27] S.Y. Jun,[12] J.E. Jung,[27] T.R. Junk,[23] T. Kamon,[53] P.E. Karchin,[58] Y. Kato,[41] Y. Kemp,[25] R. Kephart,[16] U. Kerzel,[25] V. Khotilovich,[53] B. Kilminster,[39] D.H. Kim,[27] H.S. Kim,[27] J.E. Kim,[27] M.J. Kim,[12] S.B. Kim,[27] S.H. Kim,[55] Y.K. Kim,[13] N. Kimura,[55] L. Kirsch,[6] S. Klimenko,[17] M. Klute,[32] B. Knuteson,[32] B.R. Ko,[15] K. Kondo,[57] D.J. Kong,[27] J. Konigsberg,[17] A. Korytov,[17] A.V. Kotwal,[15] A. Kovalev,[45] A.C. Kraan,[45] J. Kraus,[23] I. Kravchenko,[32] M. Kreps,[25] J. Kroll,[45] N. Krumnack,[4] M. Kruse,[15] V. Krutelyov,[10] T. Kubo,[55] S. E. Kuhlmann,[2] T. Kuhr,[25] Y. Kusakabe,[57] S. Kwang,[13] A.T. Laasanen,[48] S. Lai,[33] S. Lami,[46] S. Lammel,[16] M. Lancaster,[30] R.L. Lander,[7] K. Lannon,[39] A. Lath,[52] G. Latino,[46] I. Lazzizzera,[43] T. LeCompte,[2] J. Lee,[49] J. Lee,[27] Y.J. Lee,[27] S.W. Lee,[53] R. Lefèvre,[3] N. Leonardo,[32] S. Leone,[46] S. Levy,[13] J.D. Lewis,[16] C. Lin,[60] C.S. Lin,[16] M. Lindgren,[16] E. Lipeles,[9] A. Lister,[7] D.O. Litvintsev,[16] T. Liu,[16] N.S. Lockyer,[45] A. Loginov,[36] M. Loreti,[43] P. Loverre,[51] R.-S. Lu,[1] D. Lucchesi,[43] P. Lujan,[28] P. Lukens,[16] G. Lungu,[17] L. Lyons,[42] J. Lys,[28] R. Lysak,[1] E. Lytken,[48] P. Mack,[25] D. MacQueen,[33] R. Madrak,[16] K. Maeshima,[16] K. Makhoul,[32] T. Maki,[22] P. Maksimovic,[24] S. Malde,[42] G. Manca,[29] F. Margaroli,[5] R. Marginean,[16] C. Marino,[25] C.P. Marino,[23] A. Martin,[60] M. Martin,[24] V. Martin,[20] M. Martínez,[3] T. Maruyama,[55] P. Mastrandrea,[51] T. Masubuchi,[55] H. Matsunaga,[55] M.E. Mattson,[58] R. Mazini,[33] P. Mazzanti,[5] K.S. McFarland,[49] P. McIntyre,[53] R. McNulty,[29] A. Mehta,[29] P. Mehtala,[22] S. Menzemer,[11] A. Menzione,[46] P. Merkel,[48] C. Mesropian,[50] A. Messina,[51] T. Miao,[16] N. Miladinovic,[6] J. Miles,[32] R. Miller,[35] C. Mills,[10] M. Milnik,[25] A. Mitra,[1] G. Mitselmakher,[17] A. Miyamoto,[26] S. Moed,[19] N. Moggi,[5] B. Mohr,[8] R. Moore,[16] M. Morello,[46] P. Movilla Fernandez,[28] J. Mülmenstädt,[28] A. Mukherjee,[16] Th. Muller,[25] R. Mumford,[24] P. Murat,[16] J. Nachtman,[16] A. Nagano,[55] J. Naganoma,[57] S. Nahn,[32] I. Nakano,[40] A. Napier,[56] V. Necula,[17] C. Neu,[45]

M.S. Neubauer,[9] J. Nielsen,[28] T. Nigmanov,[47] L. Nodulman,[2] O. Norniella,[3] E. Nurse,[30] S.H. Oh,[15] Y.D. Oh,[27] I. Oksuzian,[17] T. Okusawa,[41] R. Oldeman,[29] R. Orava,[22] K. Osterberg,[22] C. Pagliarone,[46] E. Palencia,[11] V. Papadimitriou,[16] A.A. Paramonov,[13] B. Parks,[39] S. Pashapour,[33] J. Patrick,[16] G. Pauletta,[54] M. Paulini,[12] C. Paus,[32] D.E. Pellett,[7] A. Penzo,[54] T.J. Phillips,[15] G. Piacentino,[46] J. Piedra,[44] L. Pinera,[17] K. Pitts,[23] C. Plager,[8] L. Pondrom,[59] X. Portell,[3] O. Poukhov,[14] N. Pounder,[42] F. Prokoshin,[14] A. Pronko,[16] J. Proudfoot,[2] F. Ptochos,[18] G. Punzi,[46] J. Pursley,[24] J. Rademacker,[42] A. Rahaman,[47] N. Ranjan,[48] S. Rappoccio,[21] B. Reisert,[16] V. Rekovic,[37] P. Renton,[42] M. Rescigno,[51] S. Richter,[25] F. Rimondi,[5] L. Ristori,[46] A. Robson,[20] T. Rodrigo,[11] E. Rogers,[23] S. Rolli,[56] R. Roser,[16] M. Rossi,[54] R. Rossin,[17] A. Ruiz,[11] J. Russ,[12] V. Rusu,[13] H. Saarikko,[22] S. Sabik,[33] A. Safonov,[53] W.K. Sakumoto,[49] G. Salamanna,[51] O. Saltó,[3] D. Saltzberg,[8] C. Sánchez,[3] L. Santi,[54] S. Sarkar,[51] L. Sartori,[46] K. Sato,[16] P. Savard,[33] A. Savoy-Navarro,[44] T. Scheidle,[25] P. Schlabach,[16] E.E. Schmidt,[16] M.P. Schmidt,[60] M. Schmitt,[38] T. Schwarz,[7] L. Scodellaro,[11] A.L. Scott,[10] A. Scribano,[46] F. Scuri,[46] A. Sedov,[48] S. Seidel,[37] Y. Seiya,[41] A. Semenov,[14] L. Sexton-Kennedy,[16] A. Sfyrla,[19] M.D. Shapiro,[28] T. Shears,[29] P.F. Shepard,[47] D. Sherman,[21] M. Shimojima,[55] M. Shochet,[13] Y. Shon,[59] I. Shreyber,[36] A. Sidoti,[46] P. Sinervo,[33] A. Sisakyan,[14] J. Sjolin,[42] A.J. Slaughter,[16] J. Slaunwhite,[39] K. Sliwa,[56] J.R. Smith,[7] F.D. Snider,[16] R. Snihur,[33] M. Soderberg,[34] A. Soha,[7] S. Somalwar,[52] V. Sorin,[35] J. Spalding,[16] F. Spinella,[46] T. Spreitzer,[33] P. Squillacioti,[46] M. Stanitzki,[60] A. Staveris-Polykalas,[46] R. St. Denis,[20] B. Stelzer,[8] O. Stelzer-Chilton,[42] D. Stentz,[38] J. Strologas,[37] D. Stuart,[10] J.S. Suh,[27] A. Sukhanov,[17] H. Sun,[56] T. Suzuki,[55] A. Taffard,[23] R. Takashima,[40] Y. Takeuchi,[55] K. Takikawa,[55] M. Tanaka,[2] R. Tanaka,[40] M. Tecchio,[34] P.K. Teng,[1] K. Terashi,[50] J. Thom,[16] A.S. Thompson,[20] E. Thomson,[45] P. Tipton,[60] V. Tiwari,[12] S. Tkaczyk,[16] D. Toback,[53] S. Tokar,[14] K. Tollefson,[35] T. Tomura,[55] D. Tonelli,[46] S. Torre,[18] D. Torretta,[16] S. Tourneur,[44] W. Trischuk,[33] R. Tsuchiya,[57] S. Tsuno,[40] N. Turini,[46] F. Ukegawa,[55] T. Unverhau,[20] S. Uozumi,[55] D. Usynin,[45] S. Vallecorsa,[19] N. van Remortel,[22] A. Varganov,[34] E. Vataga,[37] F. Vázquez,[17] G. Velev,[16] G. Veramendi,[23] V. Veszpremi,[48] R. Vidal,[16] I. Vila,[11] R. Vilar,[11] T. Vine,[30] I. Vollrath,[33] I. Volobouev,[28] G. Volpi,[46] F. Würthwein,[9] P. Wagner,[53] R.G. Wagner,[2] R.L. Wagner,[16] J. Wagner,[25] W. Wagner,[25] R. Wallny,[8] S.M. Wang,[1] A. Warburton,[33] S. Waschke,[20] D. Waters,[30] M. Weinberger,[53] W.C. Wester III,[16] B. Whitehouse,[56] D. Whiteson,[45] A.B. Wicklund,[2] E. Wicklund,[16] G. Williams,[33] H.H. Williams,[45] P. Wilson,[16] B.L. Winer,[39] P. Wittich,[16] S. Wolbers,[16] C. Wolfe,[13] T. Wright,[34] X. Wu,[19] S.M. Wynne,[29] A. Yagil,[16] K. Yamamoto,[41] J. Yamaoka,[52] T. Yamashita,[40] C. Yang,[60] U.K. Yang,[13] Y.C. Yang,[27] W.M. Yao,[28] G.P. Yeh,[16] J. Yoh,[16] K. Yorita,[13] T. Yoshida,[41] G.B. Yu,[49] I. Yu,[27] S.S. Yu,[16] J.C. Yun,[16] L. Zanello,[51] A. Zanetti,[54] I. Zaw,[21] X. Zhang,[23] J. Zhou,[52] and S. Zucchelli[5]

(CDF Collaboration)

[1] *Institute of Physics, Academia Sinica, Taipei, Taiwan 11529, Republic of China*

[2] *Argonne National Laboratory, Argonne, Illinois 60439*

[3] *Institut de Fisica d'Altes Energies, Universitat Autonoma de Barcelona, E-08193, Bellaterra (Barcelona), Spain*

[4] *Baylor University, Waco, Texas 76798*

[5] *Istituto Nazionale di Fisica Nucleare, University of Bologna, I-40127 Bologna, Italy*

[6] *Brandeis University, Waltham, Massachusetts 02254*

[7] *University of California, Davis, Davis, California 95616*

[8] *University of California, Los Angeles, Los Angeles, California 90024*

[9] *University of California, San Diego, La Jolla, California 92093*

[10] *University of California, Santa Barbara, Santa Barbara, California 93106*

[11] *Instituto de Fisica de Cantabria, CSIC-University of Cantabria, 39005 Santander, Spain*

[12] *Carnegie Mellon University, Pittsburgh, PA 15213*

[13] *Enrico Fermi Institute, University of Chicago, Chicago, Illinois 60637*

[14] *Joint Institute for Nuclear Research, RU-141980 Dubna, Russia*

[15] *Duke University, Durham, North Carolina 27708*

[16] *Fermi National Accelerator Laboratory, Batavia, Illinois 60510*

[17] *University of Florida, Gainesville, Florida 32611*

[18] *Laboratori Nazionali di Frascati, Istituto Nazionale di Fisica Nucleare, I-00044 Frascati, Italy*

[19] *University of Geneva, CH-1211 Geneva 4, Switzerland*

[20] *Glasgow University, Glasgow G12 8QQ, United Kingdom*

[21] *Harvard University, Cambridge, Massachusetts 02138*

[22] *Division of High Energy Physics, Department of Physics, University of Helsinki and Helsinki Institute of Physics, FIN-00014, Helsinki, Finland*

[23] *University of Illinois, Urbana, Illinois 61801*

[24] *The Johns Hopkins University, Baltimore, Maryland 21218*

[25] *Institut für Experimentelle Kernphysik, Universität Karlsruhe, 76128 Karlsruhe, Germany*

[26] *High Energy Accelerator Research Organization (KEK), Tsukuba, Ibaraki 305, Japan*

[27] *Center for High Energy Physics: Kyungpook National University, Taegu 702-701, Korea; Seoul National University, Seoul 151-742, Korea; and SungKyunKwan University, Suwon 440-746, Korea*

[28] *Ernest Orlando Lawrence Berkeley National Laboratory, Berkeley, California 94720*

[29] *University of Liverpool, Liverpool L69 7ZE, United Kingdom*

[30] *University College London, London WC1E 6BT, United Kingdom*

[31] *Centro de Investigaciones Energeticas Medioambientales y Tecnologicas, E-28040 Madrid, Spain*

[32] *Massachusetts Institute of Technology, Cambridge, Massachusetts 02139*

[33] *Institute of Particle Physics: McGill University, Montréal, Canada H3A 2T8; and University of Toronto, Toronto, Canada M5S 1A7*

[34] *University of Michigan, Ann Arbor, Michigan 48109*

[35] *Michigan State University, East Lansing, Michigan 48824*

[36] *Institution for Theoretical and Experimental Physics, ITEP, Moscow 117259, Russia*

[37] *University of New Mexico, Albuquerque, New Mexico 87131*

[38] *Northwestern University, Evanston, Illinois 60208*

[39] *The Ohio State University, Columbus, Ohio 43210*

[40] *Okayama University, Okayama 700-8530, Japan*

[41] *Osaka City University, Osaka 588, Japan*

[42] *University of Oxford, Oxford OX1 3RH, United Kingdom*

[43] *University of Padova, Istituto Nazionale di Fisica Nucleare, Sezione di Padova-Trento, I-35131 Padova, Italy*

[44] *LPNHE, Universite Pierre et Marie Curie/IN2P3-CNRS, UMR7585, Paris, F-75252 France*

[45] *University of Pennsylvania, Philadelphia, Pennsylvania 19104*

[46] *Istituto Nazionale di Fisica Nucleare Pisa, Universities of Pisa, Siena and Scuola Normale Superiore, I-56127 Pisa, Italy*

[47] *University of Pittsburgh, Pittsburgh, Pennsylvania 15260*

[48] *Purdue University, West Lafayette, Indiana 47907*

[49] *University of Rochester, Rochester, New York 14627*

[50] *The Rockefeller University, New York, New York 10021*

[51] *Istituto Nazionale di Fisica Nucleare, Sezione di Roma 1, University of Rome "La Sapienza," I-00185 Roma, Italy*

[52] *Rutgers University, Piscataway, New Jersey 08855*

[53] *Texas A&M University, College Station, Texas 77843*

[54] *Istituto Nazionale di Fisica Nucleare, University of Trieste/ Udine, Italy*

[55] *University of Tsukuba, Tsukuba, Ibaraki 305, Japan*

[56] *Tufts University, Medford, Massachusetts 02155*

[57] *Waseda University, Tokyo 169, Japan*

[58] *Wayne State University, Detroit, Michigan 48201*

[59] *University of Wisconsin, Madison, Wisconsin 53706*

[60] *Yale University, New Haven, Connecticut 06520*

(Dated: September 1, 2006)

References

[1] E. Segre. *Nuclei and Particles: An Introduction to Nuclear and Subnuclear Physics.* New York: W.A. Benjamin, Inc., 1964.

[2] M. Peskin and D. Schroeder. *An Introduction to Quantum Field Theory.* Cambridge, Mass.: Perseus Books, 1995.

[3] S. Eidelman *et. al.* (Particle Data Group) The Review of Particle Physics. *Physics Letters B*592:1-1109, 2004 and 2005 partial update for edition 2006 (URL: http://pdg.lbl.gov).

[4] P. Nason, S. Dawson and R.K. Ellis. *Nucl. Phys.* B303:607, 1988.

[5] P. Nason, S. Dawson and R.K. Ellis. *Nucl. Phys.* B327:49, 1989.

[6] M. Cacciari, M. Greco, and P. Nason. The p_T Spectrum in Heavy Flavour Hadroproduction. *JHEP*, 9805:007, 1998.

[7] A. D. Martin, W. J. Stirling and R. G. Roberts. New Information on Parton Distributions. *Phys. Rev. D* 47:867-882.

[8] A. D. Martin, R. G. Roberts, W. J. Stirling and R. S. Thorne. Parton Distributions: A New Global Analysis *Eur. Phys. J. C* 4:463-496, 1998.

[9] H. L. Lai *et al.* Global QCD Analysis of Parton Structure of the Nucleon. *Eur. Phys. J. C* 12:375-392, 2000.

[10] C. Peterson *et al.* Scaling Violations in Inclusive e^+e^- Annihilation Spectra. *Phys. Rev. D* 27:105-111, 1983.

[11] O.Biebel, P. Nason, and B.R. Webber. Jet Fragmentation in e^+e^- Annihilation. *hep-ph/0109282*, 2001.

[12] D. Acosta *et al.* Measurement of the J/ψ Meson and b-hadron Production Cross Sections in $p\overline{p}$ Collisions at $\sqrt{s} = 1960$ GeV. *Phys. Rev. D* 71:032001, 2005.

[13] P. Renton *Electroweak Interactions: An Introduction to the Physics of Quarks and Leptons.* Cambridge, U.K.: Cambridge University Press, 1990.

[14] G. Apollinari *et al.* Phenomenological Study of the Atypical Heavy Flavor Production Observed at the Fermilab Tevatron. *Phys. Rev. D*73:014025, 2006.

[15] M. Mangano. The Saga of Bottom Production in $p\overline{p}$ Collisions. *AIP Conf.Proc.* 753:247-260, 2005.

[16] F. Abe *et al.* A Measurement of the B Meson and b-quark Cross-Sections at $\sqrt{s} = 1.8$-TeV Using the Exclusive Decay $B^{\pm} \to J/\psi K^{\pm}$. *Phys. Rev. Lett.* 68:3404-3407, 1992.

[17] C. Albajar *et al.* Beauty Production at the CERN $p\overline{p}$ Collider. *Phys. Lett. B* 186:237-259, 1987.

[18] F. Abe *et al.* Measurement of Bottom Quark Production in 1.8 TeV $p\overline{p}$ Collisions Using Muons from b-quark Decays. *Phys. Rev. Lett.* 71:2396-2400, 1993.

[19] F. Abe *et al.* Inclusive J/ψ, $\psi(2s)$, and b-quark Production in $p\overline{p}$ Collisions at $\sqrt{s} = 1.8$ TeV. *Phys. Rev. Lett.* 69:3704-3708, 1992.

[20] F. Abe *et al.* Inclusive χ_c and b-quark Production in $p\overline{p}$ Collisions at $\sqrt{s} = 1.8$ TeV. *Phys. Rev. Lett.* 71:2537-2541, 1993.

[21] F. Abe *et al.* Measurement of Bottom-Quark Production Cross Section Using Semileptonic Decay Electrons in $p\overline{p}$ Collisions at $\sqrt{s} = 1.8$ TeV. *Phys. Rev. Lett.* 71:500-504, 1993.

[22] F. Abe *et al.* Measurement of the B Meson Differential Cross Section, $d\sigma/dp_T$, in $p\overline{p}$ Collisions $\sqrt{s} = 1.8$ TeV. *Phys. Rev. Lett.* 75:1451-1455, 1995.

[23] S. Abachi *et al.* Inclusive μ and b-quark Production Cross Sections in $p\overline{p}$ Collisions at $\sqrt{s} = 1.8$ TeV. *Phys. Rev. Lett.* 74:3548-3552, 1995.

[24] S. Abachi *et al.* J/ψ Production in $p\overline{p}$ collisions at $\sqrt{s} = 1.8$ TeV. *Phys. Lett.* B370:239-248, 1996.

[25] B. Abbott *et al.* The $b\overline{b}$ Production Cross-Section and Angular Correlations in $p\overline{p}$ Collisions at $\sqrt{s} = 1.8$ TeV. *Phys. Lett.* B487:264-272, 2000.

[26] B. Abbott *et al.* Small-Angle Muon and Bottom-Quark Production in $p\overline{p}$ Collisions at $\sqrt{s} = 1.8$ TeV. *Phys. Rev. Lett.* 84:5478-5483, 2000.

[27] C. Chen. A Measurement of the Direct Charm Meson Production Cross Section at CDF II. Ph.D. Thesis, University of Pennsylvania, 2003.

[28] CDF II Collaboration. The CDF Run II Technical Design Report. FERMILAB-Pub-96-390-E.

[29] H. Wenzel. Tracking in the SVX. CDF/DOC/SEC_VTX/CDFR/1790, 1998

[30] A. Affolder *et al.* CDF Central Outer Tracker. *Nucl.Instrum.Meth.* A526:249-299, 2004.

[31] D. Allspach *et al.* Aging in the Large CDF Axial Drift Chamber. *IEEE Trans.Nucl.Sci.* 52:2956-2962, 2005.

[32] A. Sill. CDF Run II Silicon Tracking Projects. *Nucl. Instrum. Meth.*, A447:1-8, 2000.

[33] F. Abe *et al.* Measurement of the Anti-Proton Proton Total Cross-Section at $s^{1/2} = 546$ GeV and 1800 GeV. *Phys. Rev.*, D50:5550-5561, 1994.

[34] J. Elias *et al.* Luminosity Monitor Based on Cherenkov Counters for p anti-p Colliders. *Nucl. Instrum. Meth.*, A441:366-373, 2000.

[35] D. Acosta *et al.* The CDF Cherenkov Luminosity Monitor. *Nucl. Instrum. Meth.*, A461:540-544, 2001.

[36] D. Acosta *et al.* The Performance of the CDF Luminosity Monitor. *Nucl. Instrum. Meth.*, A494:57-62, 2002.

[37] W. Ashmanskas *et al.* The CDF Silicon Vertex Tracker. FERMILAB-CONF-00238-E.

[38] W. Ashmanskas *et al.* Performance of the CDF Online Silicon Vertex Tracker. *IEEE Trans. Nucl. Sci.*, 49:1177-1184, 2002.

[39] ANSI/VIPA 23-1998, March 22, 1998.

[40] Motorola MVME2301, MVME2401 and MVME5500 processors have been used, http://www.motorola.com.

[41] E.J. Thomson et al., "Online Track Processor for the CDF Upgrade," IEEE Transactions on Nuclear Science, Vol. 49, No. 3 (2002).

[42] CDF Run2 Data Bases Queryer and Browser.
http://dbb2.fnal.gov:8520/cdfr2/databases?type=tf&fsrc=cdfofpr2&nsrc=cdfofpr2&gsrc=cdfofpr2&rc=n&dcbk=FILECATALOG

[43] P. Sphicas. A $b\bar{b}$ Monte Carlo Generator. CDF/DOC/BOTTOM/CDFR/2655, 1994. Bgenerator is a CDF specific MC generator used to create b quarks according to a input $p_T - y$ spectrum, and then hadronize the b quarks.

[44] K. Anikeev *et al.* Description of Bgenerator II: Bgenerator in its Run II Incarnation. CDF/DOC/BOTTOM/CDFR/5092, 1999.

[45] T. Sjostrand *et al.* Pythia 6.4 Physics and Manual. FERMILAB-PUB-06-052-CDF-T, 2006.

[46] D. Acosta *et al.* Measurements of Bottom Anti-Bottom Azimuthal Production Correlations in Proton-Antiproton Collisions at $\sqrt{s} = 1.8$ TeV. *Phys. Rev. D*71:091105, 2005.

[47] W. Bell *et al.* User Guide for EvtGen @ CDF. CDF/DOC/BOTTOM/CDFR/5618, 2003. Available online at http://cdfkits.fnal.gov/CdfCode/source/EvtGen/doc/CDF/CdfUserGuide.ps

[48] CERN Applications Software Group, Computing and Networks Division. GEANT-Detector Description and Simulation Tool. CERN Program Library Long Writeup W5013, 1993.

[49] D. Acosta *et al.* Measurement of Prompt Charm Meson Production Cross Sections in p anti-p Collisions at $\sqrt{s} = 1.96$ TeV. *Phys. Rev. Lett.* 91:241804, 2003.

[50] A. Varganov. The Production Cross Sections of the Weak Vector Bosons in $p\overline{p}$ Collisions at $\sqrt{s} = 1.96$ TeV and a Measurement of the W Boson Decay Width. Ph.D. Thesis, University of Michigan, 2004.

[51] D. Acosta *et al.* Search for $B_s^0 \to \mu^+\mu^-$ and $B_d^0 \to \mu^+\mu^-$ Decays in $p\overline{p}$ Collisions with CDF II. *Phys. Rev. Lett.* 95, 221805, 2005.

[52] The SiExpected method takes the COT track parameters and predicts which layers of the SVX (if any) the track is likely to have passed through. It also checks the run database to see if the layers of the SVX the track is expected to pass through were on in that run. See http://cdfkits.fnal.gov/CdfCode/source/TrackingSI/src/SiExpected.cc

[53] LeptonSvtSel forms a χ^2 based on the difference between the SVT and Offline curvature and ϕ_0.
H.-C. Fang *et al.* SemiLeptonicB/LeptonSvtSel– An Offline Filter Module for Lepton-SVT Data. CDF/DOC/BOTTOM/CDFR/6326, 2003.
See also http://cdfkits.fnal.gov/CdfCode/source/SemiLeptonicB/src/LeptonSvtSel.cc

[54] B. Riesert, [CDF]. Presentation at "Beauty 2006",
http://www.physics.ox.ac.uk/beauty2006/Talks/Burkard_Reisert_CDF_Charm_at_Beauty.pdf

[55] J. Marriner. Secondary Vertex Fit with Mass and Pointing Constraints (CTVMFT). CDF/DOC/SEC_VTX/PUBLIC/1996, 1993.
See also http://cdfkits.fnal.gov/CdfCode/source/VertexAlg/src/ctvmft.F,
and http://cdfkits.fnal.gov/CdfCode/source/VertexAlg/src/VertexFit.cc

[56] M. Cacciari *et al.* QCD Analysis of the First b Cross-Section Data at 1.96 TeV. *JHEP*, 0407:033, 2004.